frontiers | Research Topics

Studies on life at the energetic edge – from laboratory experiments to field-based investigations, volume II

Edited by
Bo Barker Jørgensen, Mark Alexander Lever,
Jan Amend, Victoria Orphan and Tori Hoehler

Published in
Frontiers in Microbiology

ISSN 1664-8714
ISBN 978-2-8325-4286-6
DOI 10.3389/978-2-8325-4286-6

About Frontiers

Frontiers is more than just an open access publisher of scholarly articles: it is a pioneering approach to the world of academia, radically improving the way scholarly research is managed. The grand vision of Frontiers is a world where all people have an equal opportunity to seek, share and generate knowledge. Frontiers provides immediate and permanent online open access to all its publications, but this alone is not enough to realize our grand goals.

Frontiers journal series

The Frontiers journal series is a multi-tier and interdisciplinary set of open-access, online journals, promising a paradigm shift from the current review, selection and dissemination processes in academic publishing. All Frontiers journals are driven by researchers for researchers; therefore, they constitute a service to the scholarly community. At the same time, the *Frontiers journal series* operates on a revolutionary invention, the tiered publishing system, initially addressing specific communities of scholars, and gradually climbing up to broader public understanding, thus serving the interests of the lay society, too.

Dedication to quality

Each Frontiers article is a landmark of the highest quality, thanks to genuinely collaborative interactions between authors and review editors, who include some of the world's best academicians. Research must be certified by peers before entering a stream of knowledge that may eventually reach the public - and shape society; therefore, Frontiers only applies the most rigorous and unbiased reviews. Frontiers revolutionizes research publishing by freely delivering the most outstanding research, evaluated with no bias from both the academic and social point of view. By applying the most advanced information technologies, Frontiers is catapulting scholarly publishing into a new generation.

What are Frontiers Research Topics?

Frontiers Research Topics are very popular trademarks of the *Frontiers journals series*: they are collections of at least ten articles, all centered on a particular subject. With their unique mix of varied contributions from Original Research to Review Articles, Frontiers Research Topics unify the most influential researchers, the latest key findings and historical advances in a hot research area.

Find out more on how to host your own Frontiers Research Topic or contribute to one as an author by contacting the Frontiers editorial office: frontiersin.org/about/contact

Studies on life at the energetic edge – from laboratory experiments to field-based investigations, volume II

Topic editors
Bo Barker Jørgensen — Aarhus University, Denmark
Mark Alexander Lever — The University of Texas at Austin, United States
Jan Amend — University of Southern California, United States
Victoria Orphan — California Institute of Technology, United States
Tori Hoehler — National Aeronautics and Space Administration (NASA), United States

Citation
Jørgensen, B. B., Lever, M. A., Amend, J., Orphan, V., Hoehler, T., eds. (2024).
Studies on life at the energetic edge – from laboratory experiments to field-based investigations, volume II. Lausanne: Frontiers Media SA.
doi: 10.3389/978-2-8325-4286-6

Table of contents

04 Editorial: Studies on life at the energetic edge – from laboratory experiments to field-based investigations, volume II
Tori M. Hoehler, Jan P. Amend, Bo Barker Jørgensen, Victoria J. Orphan and Mark A. Lever

07 Formate and hydrogen in hydrothermal vents and their use by extremely thermophilic methanogens and heterotrophs
James F. Holden and Harita Sistu

24 Characterization of microbiomic and geochemical compositions across the photosynthetic fringe
Katelyn Weeks, Elizabeth Trembath-Reichert, Grayson Boyer, Kristopher Fecteau, Alta Howells, Francesca De Martini, Gillian H. Gile and Everett L. Shock

39 Expanding the taxonomic and environmental extent of an underexplored carbon metabolism—oxalotrophy
Alexander Sonke and Elizabeth Trembath-Reichert

49 Metapangenomic investigation provides insight into niche differentiation of methanogenic populations from the subsurface serpentinizing environment, Samail Ophiolite, Oman
Patrick H. Thieringer, Eric S. Boyd, Alexis S. Templeton and John R. Spear

67 Liquid scintillation counting at the limit of detection in biogeosciences
Florian Schubert and Jens Kallmeyer

81 Cell-specific rates of sulfate reduction and fermentation in the sub-seafloor biosphere
Marion Jaussi, Bo Barker Jørgensen, Kasper U. Kjeldsen, Bente A. Lomstein, Christof Pearce, Marit-Solveig Seidenkantz and Hans Røy

98 Modeled energetics of bacterial communities in ancient subzero brines
Georges Kanaan, Tori M. Hoehler, Go Iwahana and Jody W. Deming

114 Corrigendum: Modeled energetics of bacterial communities in ancient subzero brines
Georges Kanaan, Tori M. Hoehler, Go Iwahana and Jody W. Deming

116 Aerobic methanotrophy increases the net iron reduction in methanogenic lake sediments
Hanni Vigderovich, Werner Eckert, Marcus Elvert, Almog Gafni, Maxim Rubin-Blum, Oded Bergman and Orit Sivan

133 Intact polar lipidome and membrane adaptations of microbial communities inhabiting serpentinite-hosted fluids
Kaitlin R. Rempfert, Emily A. Kraus, Daniel B. Nothaft, Nadia Dildar, John R. Spear, Julio Sepúlveda and Alexis S. Templeton

frontiers | Frontiers in Microbiology

TYPE Editorial
PUBLISHED 04 January 2024
DOI 10.3389/fmicb.2023.1351761

OPEN ACCESS

EDITED AND REVIEWED BY
Andreas Teske,
University of North Carolina at Chapel Hill,
United States

*CORRESPONDENCE
Tori M. Hoehler
✉ tori.m.hoehler@nasa.gov

RECEIVED 07 December 2023
ACCEPTED 11 December 2023
PUBLISHED 04 January 2024

CITATION
Hoehler TM, Amend JP, Jørgensen BB, Orphan VJ and Lever MA (2024) Editorial: Studies on life at the energetic edge – from laboratory experiments to field-based investigations, volume II.
Front. Microbiol. 14:1351761.
doi: 10.3389/fmicb.2023.1351761

Editorial: Studies on life at the energetic edge – from laboratory experiments to field-based investigations, volume II

Tori M. Hoehler[1]*, Jan P. Amend[2], Bo Barker Jørgensen[3], Victoria J. Orphan[4] and Mark A. Lever[5]

[1]Exobiology Branch, NASA Ames Research Center, Moffett Field, CA, United States, [2]Department of Earth Sciences and Department of Biological Sciences, University of Southern California, Los Angeles, CA, United States, [3]Department of Biology, Aarhus University, Aarhus, Denmark, [4]Department of Geological and Planetary Sciences, California Institute of Technology, Pasadena, CA, United States, [5]Marine Science Institute, The University of Texas at Austin, Austin, TX, United States

KEYWORDS

energy limitation, deep biosphere, aquatic sediments, cryopeg, serpentinizing systems, hydrothermal systems

Editorial on the Research Topic
Studies on life at the energetic edge – from laboratory experiments to field-based investigations, volume II

Among the diverse inhabitants of Earth's biosphere, microorganisms reign supreme in their capabilities to occupy an expansive range of ecological niches. We often conceive of the fringes of our biosphere in terms of physicochemical "extremes", but perhaps the most pervasive environmental challenge to microbial life is that of extreme energy limitation (Hoehler and Jørgensen, 2013; Lever et al., 2015; Bradley et al., 2020). Globally, for example, the marine deep biosphere occupies a volume and hosts a biomass comparable to that of the overlying oceans, yet that deep biosphere is sustained by an energy flux about 1,000 times lower (Hoehler et al., 2023). Both in the sub-seafloor and in the continental subsurface, these energy-starved organisms exist at the interface between the inhabited and uninhabited realms of our planet. To understand their physiology in the face of extreme energy limitation would, therefore, be to understand the capabilities and limitations of the ultimate arbiters of chemical exchange between the biosphere and the geosphere.

Our awareness and understanding of life at the energetic edge has grown considerably over the last few decades, yet much remains to be learned. What factors determine the minimal energy requirements of microorganisms, and how do those requirements vary with the physicochemical environment? What physiological traits promote survival under extreme energy limitation? Do those traits evolve as a specific adaptation to energy limitation, or are they a fortuitous result of adaptation to other conditions (exaptation)? Do any physiological differences relating to energy limitation translate to differing capabilities and limitations with respect to biogeochemical processing? Natural ecosystems provide a unique window into populations exposed to energy limitation over long timescales that are intractable in laboratory settings. This special Research Topic focuses on such systems: on advances being made at the frontiers of environmental microbiology.

Jaussi et al. quantified cell-specific catabolic energy yields in several marine sediments, for both the total cell population and for sulfate-reducing bacteria (SRB), specifically. They observed that cell-specific energy yields for the total population diminished over orders of magnitude with increasing sediment depth (age), but yields for SRB specifically appeared to reach a stable minimum much higher than that of the overall population. Taxonomic or metabolic differences thus appear to factor significantly into minimum energy requirements. This study leveraged sensitive radiotracer techniques to measure metabolic process rates. For those interested in pursuing similar techniques, Schubert and Kallmeyer have offered a deep dive into the methodology and optimization of liquid scintillation counting (LSC)—a "how-to" guide for pushing the sensitivity of radiotracer methods to the levels required for characterizing life at the energetic edge. Kanaan et al. modeled the energy requirements of microbes entrapped in a "cryopeg"—a volume of brine isolated within permafrost for 40,000 years. While subzero temperatures could potentially depress microbial energy requirements, the findings instead suggest that the need to produce extracellular enzymes and cryo- and osmoprotectant compounds results in an average per-cell requirement comparable to that observed by Jaussi et al. for SRB and well above that observed for non-SRB in cold marine sediments.

Two studies focused on microbial adaptations in serpentinizing systems, where water–rock reactions drive the fluid chemistry toward high pH and highly reducing and extremely CO_2-poor conditions. Thieringer et al. used metagenome analyses to investigate differences in ecophysiologies among three distinct populations of CO_2-reducing methanogens. While all were found to share the potential for DNA scavenging, possibly as a strategy to mitigate phosphorus and nitrogen limitation, genomic differences suggest that organisms inhabiting the most alkaline fluids adopt distinctly different strategies for coping with this energetically challenging environment—a niche differentiation that supports their coexistence. Working in the same system, Rempfert et al. performed a comprehensive analysis of membrane-forming intact polar lipids (IPLs). The lipidome, dominated by diether glycolipids, reflects a unique combination of membrane adaptations—including pervasive modifications likely associated with phosphate limitation—to enable microorganisms' survival in these conditions.

Three studies considered underexplored metabolic potential in the environment. Holden and Sistu reviewed the drivers of formate cycling by CO_2-reducing *Methanococci* and organotrophic *Thermococci*. Both have the genetic potential to produce H_2 from formate and subsequently catabolize H_2, but it is not known whether such production is prevalent relative to the direct utilization of environmental H_2. By considering H_2 and formate concentrations in hydrothermal fluids and environmental distributions, genomes, and biochemical data on *Methanococci* and *Thermococci*, Holden and Sistu argue that both preferentially utilize H_2, while formate becomes important primarily under low-H_2 conditions. Sonke and Trembath-Reichert analyzed published metagenomic and -transcriptomic datasets from a wide range of habitats to investigate the potential importance of oxalate as a microbial energy source. While oxalate is widespread in many environments, both in association with minerals and released by photosynthetic organisms, its typically very low dissolved concentrations suggest rapid turnover. Sonke and Trembath-Reichert demonstrate widespread potential for microbial oxalotrophy, especially in marine environments, where oxalotrophy is thermodynamically favorable and may represent a widely overlooked microbial energy source. Vigderovich et al. used a series of incubation experiments to explore the relationship between iron reduction and aerobic methanotrophy in lake sediments. Rates of methanotrophy and, perhaps surprisingly, accumulation of ferrous iron were both enhanced by the addition of oxygen to hematite-amended incubations. The results suggest a complex interplay between these aerobic and anaerobic microbially mediated processes and a potential role for iron recycling in the survival of aerobic methanotrophs under hypoxic conditions.

Finally, Weeks et al. considered "the edge" for photosynthetic microorganisms. Working in 12 Yellowstone hot springs, they characterized microbial community composition and a suite of physicochemical variables across the "photosynthetic fringe"—the region in which an outflow channel visibly transitions from chemotrophic to highly pigmented photosynthetic microbial communities. While changes in temperature, pH, and sulfide content have been previously proposed to control the location of the transition, such factors only explain about 35% of the variation in community composition, indicating that the microbial community of photosynthetic fringe environments is a more complex interplay of these and other factors.

With this special Research Topic, we invite you to explore these recent advances in understanding life at the energetic edge!

Author contributions

TH: Writing—original draft. JA: Writing—review & editing. BJ: Writing—review & editing. VO: Writing—review & editing. ML: Writing—original draft, Writing—review & editing.

Funding

The author(s) declare financial support was received for the research, authorship, and/or publication of this article. TH was supported by the NASA Planetary Science Division's ISFM program.

Acknowledgments

This special collection of articles accompanies the 4th International Workshop on Microbial Life under Extreme Energy Limitation (MicroEnergy 2022), which took place in Sandbjerg, Denmark, in September 2022. We gratefully acknowledge Kasper Urup Kjeldsen and Hans Røy for their many contributions to the organization of the workshop and the Aarhus University Research Foundation, the Carlsberg Foundation, the Center for Dark Energy Biosphere Investigations (C-DEBI), Frontiers in Microbiology, and the Gordon and Betty Moore Foundation for their financial support of the workshop.

Conflict of interest

The authors declare that the research was conducted in the absence of any commercial or financial relationships that could be construed as a potential conflict of interest.

The author(s) declared that they were an editorial board member of Frontiers, at the time of submission. This had no impact on the peer review process and the final decision.

Publisher's note

References

Bradley, J. A., Arndt, S., Amend, J. P., Burwicz, E., Dale, A. W., Egger, M., and LaRowe, D. E. (2020). Widespread energy limitation to life in global subseafloor sediments. *Sci. Adv.* 6, eaba0697. doi: 10.1126/sciadv.aba0697

Hoehler, T. M., and Jørgensen, B. B. (2013). Microbial life under extreme energy limitation, *Nature Rev. Microbiol.* 11, 83–94. doi: 10.1038/nrmicro2939

Hoehler, T. M., Mankel, D. J., Girguis, P. R., McCollom, T. M., Kiang, N. Y., and Jørgensen, B. B. (2023). The metabolic rate of the biosphere and its components, *Proc. Natl. Acad. Sci. U. S. A.* 120, e2303764120. doi: 10.1073/pnas.2303764120

Lever, M. A., Rogers, K. L., Lloyd, K. G., Overmann, J., Schink, B., Thauer, R. K., Hoehler, T. M., and Jørgensen, B. B. (2015). Life under Extreme Energy Limitation: A Synthesis of Laboratory- and Field-Based Investigations, *FEMS Microbiol. Rev.* 39, 688–728. doi: 10.1093/femsre/fuv020

frontiers | Frontiers in Microbiology

TYPE Review
PUBLISHED 06 March 2023
DOI 10.3389/fmicb.2023.1093018

OPEN ACCESS

EDITED BY
Mark Alexander Lever,
The University of Texas at Austin, United States

REVIEWED BY
Stefan M. Sievert,
Woods Hole Oceanographic Institution,
United States
Doug Bartlett,
Scripps Institution of Oceanography, University
of California, San Diego, United States

*CORRESPONDENCE
James F. Holden
✉ jholden@umass.edu

SPECIALTY SECTION
This article was submitted to
Extreme Microbiology,
a section of the journal
Frontiers in Microbiology

RECEIVED 08 November 2022
ACCEPTED 20 February 2023
PUBLISHED 06 March 2023

CITATION
Holden JF and Sistu H (2023) Formate
and hydrogen in hydrothermal vents and their
use by extremely thermophilic methanogens
and heterotrophs.
Front. Microbiol. 14:1093018.
doi: 10.3389/fmicb.2023.1093018

Formate and hydrogen in hydrothermal vents and their use by extremely thermophilic methanogens and heterotrophs

James F. Holden* and Harita Sistu

Department of Microbiology, University of Massachusetts, Amherst, MA, United States

Extremely thermophilic methanogens in the *Methanococci* and heterotrophs in the *Thermococci* are common in deep-sea hydrothermal vents. All *Methanococci* use H_2 as an electron donor, and a few species can also use formate. Most *Methanococci* have a coenzyme F_{420}-reducing formate dehydrogenase. All *Thermococci* reduce S^0 but have hydrogenases and produce H_2 in the absence of S^0. Some *Thermococci* have formate hydrogenlyase (Fhl) that reversibly converts H_2 and CO_2 to formate or an $NAD(P)^+$-reducing formate dehydrogenase (Nfd). Questions remain if *Methanococci* or *Thermococci* use or produce formate in nature, why only certain species can grow on or produce formate, and what the physiological role of formate is? Formate forms abiotically in hydrothermal fluids through chemical equilibrium with primarily H_2, CO_2, and CO and is strongly dependent upon H_2 concentration, pH, and temperature. Formate concentrations are highest in hydrothermal fluids where H_2 concentrations are also high, such as in ultramafic systems where serpentinization reactions occur. In nature, *Methanococci* are likely to use formate as an electron donor when H_2 is limiting. *Thermococci* with Fhl likely convert H_2 and CO_2 to formate when H_2 concentrations become inhibitory for growth. They are unlikely to grow on formate in nature unless formate is more abundant than H_2 in the environment. Nearly all *Methanococci* and *Thermococci* have a gene for at least one formate dehydrogenase catalytic subunit, which may be used to provide free formate for *de novo* purine biosynthesis. However, only species with a membrane-bound formate transporter can grow on or secrete formate. Interspecies H_2 transfer occurs between *Thermococci* and *Methanococci*. This and putative interspecies formate transfer may support *Methanococci* in low H_2 environments, which in turn may prevent growth inhibition of *Thermococci* by its own H_2. Future research directions include understanding when, where, and how formate is used and produced by these organisms in nature, and how transcription of *Thermococci* genes encoding formate-related enzymes are regulated.

KEYWORDS

formate, hydrogen, hydrothermal vent, hyperthermophiles, formate dehydrogenase, hydrogenase, *Thermococci*, *Methanococci*

1. Introduction

It was estimated that 40% of bacterial and archaeal global biomass is found in the rocky portion of the ocean crust below ocean sediments (Bar-On et al., 2018; Fleming and Wuertz, 2019). These microbes live in cracks and pores of the rocky subseafloor in the absence of sunlight and often in the absence of oxygen and rely on the gases, aqueous compounds (e.g., sulfide, sulfate, and nitrate), organic compounds, and minerals found locally for growth. In high-temperature anoxic environments, H_2 is generally considered to be the primary electron donor and CO_2 the primary carbon source for autotrophic metabolism. However, recently other electron donors and carbon sources such as formate have been considered as alternatives (Windman et al., 2007), especially in high pH environments where dissolved inorganic carbon precipitates as calcium carbonate and is largely unavailable to autotrophs (Lang et al., 2018; McGonigle et al., 2020; Brazelton et al., 2022). There are strong links between formate and H_2 in hydrothermal environments and in the physiology of microbes that consume and produce formate and H_2.

High-temperature microbes that use formate and H_2 are examined herein, namely methanogens (in the class *Methanococci* and the class *Methanopyri*) and heterotrophs (in the class *Thermococci*). These organisms are found in deep-sea hydrothermal vents on or near tectonic plate boundaries – both mid-ocean ridges and subduction zones. Thermophiles and hyperthermophiles are defined as those organisms with optimal growth temperatures above 50°C and 80°C, respectively (Stetter, 2006). In this review, the term 'extreme thermophile' will be used to describe organisms with optimal growth temperatures above 65°C. Extremely thermophilic *Methanococci* and *Thermococci* are among the more cosmopolitan and well-studied microbes found in hydrothermal vent environments. All *Methanococci* and the marine hyperthermophile *Methanopyrus kandleri* (the sole member of the *Methanopyri*) use H_2 and CO_2 as energy and carbon sources to produce CH_4, H_2O, and biomass (Thauer et al., 2008). All *Thermococci* use peptides and sugars as carbon and energy sources and reduce zero-valent sulfur (S^0) to a sulfide species or reduce 2 H^+ to H_2 in the absence of S^0 (Wu et al., 2018). However, some extremely thermophilic *Methanococci* and *Thermococci* grow using formate as an energy source only or as both energy and carbon sources (Belay et al., 1986; Kim et al., 2010; Lim et al., 2014). This raises questions about which organisms can use formate, when they use formate in nature, and for what purpose. This review describes how formate and H_2 are formed in hydrothermal vents, the concentrations of these compounds in pure hydrothermal fluids, the physiology of extremely thermophilic *Methanococci* and *Thermococci* as it relates to formate and H_2 use, transcriptional regulation of formate dehydrogenase and hydrogenase genes, and suggests likely roles for formate use by these organisms in nature.

2. Abiotic H_2 production in hydrothermal vents

Deep-sea hydrothermal vents provide one of the best access points to the hydrothermally influenced portion of the rocky subseafloor and are ideal starting points for understanding biogeochemical processes in these regions of the crust. Some hydrothermal fluids rise through the crust undiluted, so-called "end-member hydrothermal fluid," and exit the seafloor at temperatures generally above 300°C (**Table 1**). It can also mix with cold seawater on or below the seafloor creating habitats for extremely thermophilic anaerobes either within the host rock (e.g., basalt) or in metal sulfide mineral precipitates (e.g., black smoker chimneys). Most hydrothermal vent studies are focused on one of three types of sites: ultramafic sites along slow-to-ultraslow tectonic spreading centers, mafic sites along intermediate-to-fast spreading centers, and subduction-influenced sites near tectonic convergence zones (**Figure 1**).

The host rock in mafic and ultramafic sites have high concentrations of MgO and FeO, but they differ in their silica content, with ultramafic rocks having silica concentrations less than 45% (by weight), while mafic rocks have concentrations above 45%. Most abiotic formation of H_2 in hydrothermal vents occurs by hydrothermal alteration of the ultramafic rock peridotite (i.e., serpentinization) (**Table 1**). Serpentinization occurs in environments with limited magma supply where peridotite is present in the rock hosting hydrothermal circulation and is mostly associated with ultramafic sites. Olivine and orthopyroxene, the most abundant minerals in peridotite, are unstable under hydrothermal conditions, which causes dissolution-reprecipitation reactions and the formation of serpentine, magnetite, and H_2 [e.g., $6\ (Mg, Fe)_2SiO_4 + 7\ H_2O \rightarrow 3(Mg, Fe)Si_2O_5(OH)_4 + Fe_3O_4 + H_2$] (Klein et al., 2020). *Methanococci* and *Thermococci* are common in most ultramafic-influenced hydrothermal sites except at the Lost City hydrothermal vent field (**Table 1**). At Lost City, the high pH hydrothermal fluids formed by low temperature serpentinization lead to calcium carbonate precipitation and very low dissolved inorganic carbon concentrations. This likely hinders the growth of autotrophs such as *Methanococci* and *Methanopyri* unless they can grow on an aqueous carbon source such as formate.

Serpentinization is inhibited by silica and is thus less common in mafic and felsic rocks (felsic rocks are > 65% silica by weight). In mafic (basalt)-hosted hydrothermal systems, the oxidation of ferrous iron minerals, such as pyrrhotite to pyrite ($FeS + H_2S \rightarrow FeS_2 + H_2$) and magnetite to hematite ($2\ Fe_3O_4 + H_2O \rightarrow 3\ Fe_2O_3 + H_2$), and weathering of the ocean crust by oxygen-depleted water in the root zone of a hydrothermal system are also significant sources of H_2 in hydrothermal systems (Klein et al., 2020). H_2 and H_2S concentrations are controlled by chemical equilibrium between fluid and the pyrite-pyrrhotite-magnetite mineral assemblages present. Most H_2 and H_2S fluid compositions fall close to the metastable extension of pyrite-pyrrhotite equilibrium (Klein et al., 2020). H_2 concentrations in mafic hydrothermal fluids also increase significantly following a volcanic eruption as circulating fluids interact with newly injected rock (Lilley et al., 2003; Seewald et al., 2003; Von Damm and Lilley, 2004). Mafic hydrothermal vent sites generally tend to have *Thermococci* and *Methanococci* present (**Table 1**), especially following volcanic eruptions (Holden et al., 1998; Huber et al., 2002; Meyer et al., 2013), but *Methanococci* can become rare or undetectable during quiescent periods between eruptions when H_2 concentrations decrease or in low H_2 hydrothermal vents (Ver Eecke et al., 2009, 2012).

In contrast, hydrothermal vents that form along volcanic arcs at convergent plate boundaries have host rock with hydrous

TABLE 1 Physical, chemical, and microbial characteristics of hydrothermal vent sites.

Location	T_{max} (°C)	pH	H_2 (mM)[a]	Formate (μM)[a]	*Methanococci*	*Thermococci*
Ultramafic (peridotite)-influenced sites						
Kairei[b]	365	3.4–3.6	2.5–8.2	–	M	M
Logatchev[c]	350	6.2	5.9	–	F	ND
Lost City[d]	90	9.5–10.9	1.2–15.1	36–158	ND	M
Rainbow[e]	370	3.0–3.4	12.3–16.9	–	M	M
Von Damm[f]	226	5.6–6.1	9.9–18.3	82–669	F	F
Mafic (basalt-hosted) sites						
Axial Volcano[g]	351	3.5–4.4	0.06–0.43	–	F	F
Endeavor Segment[h]	352	3.7–4.5	0.03–0.17	–	M, F	M, F
9°50′N EPR[i]	386	3.1–5.2	0.33–8.9	–	M	M
Kilo Moana[j]	304	3.9–4.1	0.22–0.50	–	M	M
Lucky Strike[k]	324	3.6–3.9	0.03–0.07	–	ND	M
Piccard[l]	398	3.1–3.3	18.9–20.7	<1–4.8	F	F
Guaymas Basin[m]	315	5.9	–	–	M	M
Loki's Castle[n]	315	5.5–5.9	4.6–5.5	–	M	M
Subduction-influenced (andesite/dacite-hosted) sites						
Brothers Volcano[o]	303	2.1–4.4	0.01–0.02	–	M	M
Mariner Field[p]	359	2.4–2.7	0.03–0.18	–	ND	M
TOTO Caldera[q]	170	5.3	0.01	–	ND	M

The pH and concentrations of H_2 and formate are for end-member (zero-Mg^{2+}) hydrothermal fluid while the microbial data represent presence at the site in low-temperature fluids (F) and mineral samples (M). ND, not detected; –, not analyzed.

[a] Sometimes reported as mmol/kg or μmol/kg, respectively. [b] Takai et al. (2004b), Gallant and Von Damm (2006), Kumagai et al. (2008), and Han et al. (2018); [c] Perner et al. (2007); [d] Schrenk et al. (2004), Brazelton et al. (2006), Lang et al. (2010), and Lang et al. (2012); [e] Flores et al. (2011); [f] McDermott et al. (2015) and Reveillaud et al. (2016); [g] Ver Eecke et al. (2012), Topçuoğlu et al. (2016), and Fortunato et al. (2018); [h] Ding et al. (2005), Ver Eecke et al. (2012), Anderson et al. (2013), and Lin et al. (2016); [i] Von Damm and Lilley (2004), Ding et al. (2005), Kormas et al. (2006), McCliment et al. (2006), and Hou et al. (2020); [j] Flores et al. (2012); [k] Flores et al. (2011); [l] Reveillaud et al. (2016) and McDermott et al. (2018); [m] Von Damm et al. (1985) and Pagé et al. (2008); [n] Jaeschke et al. (2012) and Baumberger et al. (2016); [o] Takai et al. (2009) and Reysenbach et al. (2020); [p] Takai et al. (2008) and Flores et al. (2012); [q] Gamo et al. (2004) and Nakagawa et al. (2006).

FIGURE 1
Global map of the hydrothermal vents in Table 1. Hydrothermal vents hosted in ultramafic rock are shown in red; basalt, in black; and in subduction zones, in yellow-brown.

minerals, silica accumulation in aging oceanic crust, and more felsic character, such as dacite and andesite. The hydrothermal fluids from these rocks tend to have lower pH and lower H_2 (Table 1). While *Thermococci* are generally present at these sites, *Methanococci* tend to be rare or undetectable (Table 1) likely due to the very low H_2 concentrations (Ver Eecke et al., 2012).

Other more minor abiotic H_2 contributions in hydrothermal vents come from magmatic degassing at low hydrostatic pressures (e.g., shallow vent sites) and radiolysis of water (Klein et al., 2020). Biotic sources of H_2 at extremely thermophilic temperatures by *Thermococci* are described in Section "4. H_2 production by *Thermococci*."

3. H_2 use by methanogens

Hydrogen is used by extremely thermophilic *Methanococci*, specifically, the genera *Methanocaldococcus* (T_{opt} 80–85°C), *Methanotorris* (T_{opt} 75–88°C), *Methanofervidicoccus* (T_{opt} 70°C), and *Methanothermococcus* (T_{opt} 65°C), and in the *Methanopyri*, which consists solely of *Methanopyrus kandleri* (T_{opt} 98°C) (**Table 2**).

3.1. Hydrogenases in *Methanococci* and *Methanopyri*

The whole genome sequences of 10 extremely thermophilic *Methanococci* plus *M. kandleri* were analyzed for known hydrogenases (see **Supplementary materials**). All 11 of the *Methanococci* and *Methanopyri* in the genome survey have at least one of the following hydrogenase genes (see Greening et al., 2016 for a review): (1) *eha* and *ehb* operons, which encode for membrane-bound multimeric hydrogenases that couple H_2 oxidation to ferredoxin reduction and are H^+/Na^+ driven for anaplerotic (Eha) and anabolic (Ehb) purposes (Porat et al., 2006; Lie et al., 2012); (2) an *frh* operon, which encodes for a soluble complex that directly couples H_2 oxidation to coenzyme F_{420} reduction (Hendrickson and Leigh, 2008); (3) an *hmd* gene, which encodes a soluble methylenetetrahydromethanopterin dehydrogenase that couples oxidation of H_2 to the reduction of methenyltetrahydromethanopterin in the archaeal Wood-Ljungdahl CO_2 fixation pathway (Hendrickson and Leigh, 2008); and (4) a *vhu* operon, which encodes for soluble heterodisulfide reductase-linked complexes that bifurcate electrons from H_2 to heterodisulfide (coenzyme M-coenzyme B) and ferredoxin (Kaster et al., 2011). These hydrogenases are described and listed in **Figure 2**, **Table 2**, and **Supplementary Table 1**. Coenzyme F_{420}, ferredoxin, coenzyme M, and coenzyme B are soluble electron carriers in methanogens (Thauer et al., 2008). Extremely thermophilic *Methanococci* and *Methanopyri* will often have two or three copies of the genes encoding these enzymes (**Table 2** and **Supplementary Table 1**).

3.2. Growth of *Methanococci* on H_2

The growth of natural assemblages of extremely thermophilic *Methanococci* in hydrothermal vent fluids from Axial Seamount is largely dependent on H_2 availability and temperature (Topçuoğlu et al., 2016). The Monod kinetic half-saturation value (K_s) for growth of extremely thermophilic methanogens was 27–66 μM with maximum methane production rates of 24–43 fmol CH_4 produced $cell^{-1}$ h^{-1} (Ver Eecke et al., 2012; Stewart et al., 2019). *Methanocaldococcus jannaschii* and *Methanothermococcus thermolithotrophicum* were shown to grow by interspecies H_2 transfer when grown in co-culture with *Thermococcus celer*, *Thermococcus stetteri*, and *Pyrococcus furiosus* (Bonch-Osmolovskaya and Stetter, 1991). When *M. jannaschii* was grown in monoculture at high (80–83 μM) and low (15–27 μM) H_2 concentrations and in co-culture with the hyperthermophilic H_2 producer *Thermococcus paralvinellae* (representing very low H_2 flux), growth and cell-specific CH_4 production rates decreased with decreasing H_2 availability (Topçuoğlu et al., 2019). However, the number of cells produced per mole of CH_4 produced (i.e., cell yield) increased six-fold with decreasing H_2 indicating increased growth efficiency when growth was limited by H_2 (Topçuoğlu et al., 2019). Relative to high H_2 concentrations, isotopic fractionation of CO_2 to CH_4 was 16‰ larger for cultures grown at low H_2 concentrations and 45–56‰ larger in co-culture suggesting reversal of the Wood-Ljungdahl pathway during methanogenesis with low H_2 flux (Valentine et al., 2004; Topçuoğlu et al., 2019). While all four types of hydrogenases were synthesized by *M. jannaschii* with high and low H_2 flux, transcript levels of *hmd* and *eha* decreased with decreasing H_2 availability (Topçuoğlu et al., 2019).

4. H_2 production by *Thermococci*

Hydrogen is produced by *Thermococci*, specifically, the genera *Thermococcus* (T_{opt} 75–90°C), *Palaeococcus* (T_{opt} 83°C), and *Pyrococcus* (T_{opt} 96–105°C) (**Table 3**).

4.1. Hydrogenases in *Thermococci*

The whole genome sequences of 30 *Thermococci* were analyzed for known hydrogenases (see **Supplementary materials**). All 30 *Thermococci* analyzed have at least one of the following hydrogenase operons: (1) An *mbh* operon, which encodes for a membrane-bound hydrogenase that couples oxidation of ferredoxin to H_2 evolution with concomitant H^+/Na^+ translocation across the membrane using antiporters (Sapra et al., 2003); (2) an *sh* operon, which encodes for a soluble sulfhydrogenase that couples oxidation of H_2 oxidation to the reduction of $NAD(P)^+$ (Van Haaster et al., 2008); (3) an *frh* operon, which encodes for cytoplasmic coenzyme F_{420} reducing-type hydrogenase that oxidizes H_2 and passes electrons to a thioredoxin reductase (Jung et al., 2020); and (4) a *codh* operon, which encodes for a membrane-bound hydrogenase that couples oxidation of CO to H_2 evolution with concomitant H^+/Na^+ translocation across the membrane using antiporters (Bae et al., 2012; Moon et al., 2012). These hydrogenases are described and listed in **Figure 3**, **Table 3**, and **Supplementary Table 2**.

All *Thermococci* have at least one *mbh* operon and all but one have at least one *sh* operon (**Table 3**). These enzymes are the core hydrogenases for *Thermococci* (Schut et al., 2012; Boyd et al., 2014). Twelve of the 30 *Thermococci* in the survey have *frh* operons. Five of the 30 *Thermococci* have *codh* operons. It was shown that the growth of *Thermococcus* sp. strain AM4 and *Thermococcus onnurineus* can be supported by CO with concomitant H_2 production (Sokolova et al., 2004; Bae et al., 2012; Moon et al., 2012), although the physiological role of this enzyme in *Thermococcus* is yet to be determined for growth in its natural environment.

TABLE 2 Growth characteristics of the classes *Methanococci* and *Methanopyri* and presence of genes for formate transport (FT), formate dehydrogenase (*fdh*), hydrogenases (*eha*, *ehb*, *frh*, *vhu*, *hmd*), and purine biosynthesis (*purT*, *purP*).

Organism	T_{opt} (°C)	Growth*	FT	*fdh*	*eha*	*ehb*	*frh*	*vhu*	*hmd*	*purT*	*purP*
Methanocaldococcus jannaschii JAL-1[a]	85	–		●	●	●	●●	●	●●●	●	●
Methanocaldococcus bathoardescens JH146[b]	82	–		●	●	●	●●	●	●●●	●	●
Methanocaldococcus fervens AG86[c]	85	ND	●	●	●	●	●	●	●●	●	●
Methanocaldococcus infernus ME[d]	85	–			●	●	●	●	●	●	●
Methanocaldococcus vulcanius M7[e]	80	–		●	●	●	●●	●●	●●●	●	●
Methanotorris igneus Kol 5[f]	88	–		●	●	●	●●●	●●	●●	●	●
Methanotorris formicicus Mc-S-70[g]	75	+	+	+	+	+	+	+	+	+	+
Methanothermococcus okinawensis IH1[h]	65	+	●	●	●	●	●●	●●	●	●	●
Methanothermococcus thermolithotrophicus SN 1[i]	65	+	+	+	+	+	+	+	+	+	+
Methanofervidicoccus abyssi HHB[j]	70	–			+	+	+	+	+	+	+
Methanopyrus kandleri AV19[k]	98	–		●	●		●●	●	●		●

The number of circles per column represents the number of times the gene(s) for that complex appears in the organism's genome.

*Growth on formate; ND, not determined.

+ In protein columns indicates genes present in draft genome sequence.

References and genome accession numbers: [a]Jones et al. (1983a), L77117; [b]Ver Eecke et al. (2013), CP009149; [c]Zhao et al. (1988), CP001696; [d]Jeanthon et al. (1998), CP002009; [e]Jeanthon et al. (1999), CP001787; [f]Burggraf et al. (1990), CP002737; [g]Takai et al. (2004a), AGJL01000032; [h]Takai et al. (2002), CP002792; [i]Huber et al. (1982), AQXV01000039; [j]Sakai et al. (2019), BFAX0000000; [k]Kurr et al. (1991), AE009439.

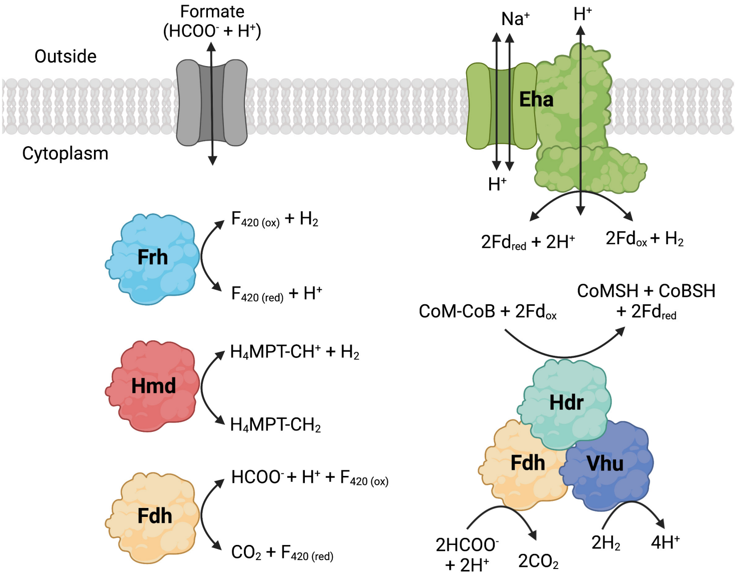

FIGURE 2

Formate dehydrogenase (Fdh), hydrogenase, and formate transporter proteins and their reactions that are found in *Methanococci* and *Methanopyri*. Fdh catalyzes the following formate oxidation reactions: cytoplasmic reduction of coenzyme F_{420} (F_{420}) and cytoplasmic reduction of coenzyme M (CoM), coenzyme B (CoB), and ferredoxin (Fd). The hydrogenases catalyze the following H_2 oxidation reactions: membrane-bound reduction of Fd (Eha), cytoplasmic reduction of F_{420} (Frh), cytoplasmic reduction of methenyl-tetrahydromethanopterin (CH-H_4MPT) (Hmd), and cytoplasmic reduction of CoM, CoB, and Fd. F_{420}, Fd, CoM, and CoB are cytoplasmic electron carriers. Methenyl-H_4MPT is an intermediate of the Wood-Ljungdahl CO_2 fixation pathway. Created with BioRender.com.

4.2. Growth of *Thermococci* with and without S^0

In *Thermococci*, the reduction of S^0 is the preferred route for electron disposal over the reduction of H^+ to H_2. In *P. furiosus*, the presence of S^0 in growth media resulted in decreases in Mbh and Sh hydrogenase specific activities, each by an order of magnitude (Adams et al., 2001). There was an immediate downregulation of *mbh* and an upregulation of *mbs* (membrane-bound sulfane reductase) (Wu et al., 2018) and *nsr* (NAD(P)H:S^0 reductase) in *P. furiosus* when S^0 was added to growth medium (Schut et al., 2001, 2007). A sulfur response regulator protein (SurR) was identified as the transcription factor regulating hydrogenase and sulfur responsive genes (Lipscomb et al., 2009, 2017). The proposed model suggests that SurR contains a redox-active cysteine disulfide that can reduce S^0 to H_2S (Yang et al., 2010). SurR is reduced

TABLE 3 Growth characteristics of the class *Thermococci* and presence of genes for formate transport (FT), formate dehydrogenase operons (*fhl, nfd*), and individuals (*fdhA*) with neighboring hydrogenase operons, individual hydrogenase operons (*mbh*, *sh*, *frh*, *codh*), and purine biosynthesis (*purT*, *purP*).

Organism	T_{opt} (°C)	H_2 ↔ formate*	FT	Group 1A: *frh-fhl-mbh*	Group 1B: *frh-nfd-mbh*	Group 2: *nfd-sh*	Group 3: *fhl-sh*	Group 4: *fhl* only	Group 5: *fdhA* only	*Mbh*	*sh*	*frh*	*codh*	*purT*	*purP*
Thermococcus paralvinellae ES1[d]	82	+[b,c]	●	●				●		●●	●	●	●		
Thermococcus barophilus CH5[a]	80	+[a,c]	●	●			●			●●	●○	●	●		●
Thermococcus onnurineus NA1[e]	80	+[a,c]	●●	●		●		●		●	●●	●	●		
Thermococcus gammatolerans EJ3[f]	88	+[a,c]	●	●				○	●	●		●	○	●	●
Thermococcus piezophilus CDGS[g]	75	+[c]	●	●		●		●		●	●●	●		●	●
Thermococcus cleftensis CL1[h]	88	+[c]	●		●				●	●	●●	●		●	●
Thermococcus nautili 30-1[i]	88	+[c]	●		●				●	●	●●	●		●	●
Thermococcus kodakarensis KOD1[j]	85	+[c]	●		Δ				●	●	●			●	●
Thermococcus chitonophagus GC74[k]	85	−[a,c]						●	●	●	●●			●	●
Thermococcus eurythermalis A501[l]	85	−[c]					●	●	●	●	●	●		●	●
Thermococcus pacificus P-4[m]	88	−[c]					●			●	●	●		●	●
Thermococcus litoralis NC-S[n]	88	−[c]					●		●	●●	●●			●	●
Thermococcus barophilus MP[o]	85	−[c]							●	●●	●●		●	●	●
Thermococcus sibiricus MM 739[p]	78	−[a,c]							●	●●	●●			●	●
Thermococcus guaymasensis TYS[q]	88	−[c]						○		●	●●	●	●	●	●
Thermococcus celer Vu 13[r]	88	−[a,c]							●	●	●●			●	●
Thermococcus peptonophilus OG-1[s]	90	−[a,c]						○	●	●	●●			●	●
Thermococcus barossii SHCK-94[t]	83	−[c]							●	●●	●●		○	●	●
Thermococcus siculi RG-20[u]	85	−[c]							●	●●	●●		○	●	●
Thermococcus radiotolerans EJ2[v]	88	−[c]							●	●●	●●		○	●	●
Thermococcus profundus DT 5432[w]	80	−[a,c]							●	●	●●		○	●	●
Thermococcus indicus IOH1[x]	80	ND							●	●●	●●	○		●	●
Thermococcus camini IRI35c[y]	80	–							●	●●	●●			●	●
Thermococcus gorgonarius W-12[z]	88	−[c]						○		●	●				
Palaeococcus pacificus DY20341[aa]	83	+[c]	●			●				●●	●●			●	●

(Continued)

TABLE 3 (Continued)

Organism	T_{opt} (°C)	H_2 ↔ formate*	FT	Group 1A: *frh-fhl-mbh*	Group 1B: *frh-nfd-mbh*	Group 2: *nfd-sh*	Group 3: *fhl-sh*	Group 4: *fhl* only	Group 5: *fdhA* only	*Mbh*	*sh*	*frh*	*codh*	*purT*	*purP*
Pyrococcus kukulkanii NCB100[ab]	105	$+^c$	●	●				●	●	●	●●	●		●	●
Pyrococcus yayanosii CH1[ac]	98	$+^c$	●	●						●	●●	●		●	●
Pyrococcus abyssi GE5[ad]	96	$-^c$						●	●	●	●●			●	●
Pyrococcus furiosus Vc1[ae]	100	$-^c$							●	●	●●			●	●
Pyrococcus horikoshii OT3[af]	98	$-^c$							●	●	●			●	●

The number of circles per column represents the number of times the gene(s) for that protein or operon appears in the organism's genome. Open circles represent incomplete operons; the open triangle, and *sh-nfd-mbh* operon configuration.

*Conversion of formate to H_2 or H_2 to formate; [a]Kim et al. (2010); [b]Topçuoğlu et al. (2018); [c]Le Guellec et al. (2021); ND, not determined. References and genome accession numbers: [d]Pledger and Baross (1989), CP006965; [a]Kim et al. (2010), CP013050; [e]Bae et al. (2006), CP000855; [f]Jolivet et al. (2003), CP001398; [g]Dalmasso et al. (2016), CP015520; [h]Holden et al. (2001), CP003651; [i]Gorlas et al. (2014), CP007264; [j]Atomi et al. (2004), AP006878; [k]Huber et al. (1995), LN999010; [l]Zhao et al. (2015), CP008887; [m]Miroshnichenko et al. (1998), CP015102; [n]Belkin et al. (1985), CP006670; [o]Marteinsson et al. (1999), CP002372; [p]Miroshnichenko et al. (2001), CP001463; [q]Canganella et al. (1998), CP007140; [r]Zillig et al. (1983), CP014854; [s]González et al. (1995), CP014750; [t]Duffaud et al. (1998), CP015101; [u]Grote et al. (1999), CP015103; [v]Jolivet et al. (2004), CP015106; [w]Kobayashi et al. (1994), CP014862; [x]Lim et al. (2020), CP040846; [y]Courtine et al. (2021), LR881183; [z]Miroshnichenko et al. (1998), CP014855; [aa]Zeng et al. (2013), CP006019; [ab]Callac et al. (2016), CP010835; [ac]Birrien et al. (2011), CP002779; [ad]Erauso et al. (1993), AL096836; [ae]Fiala and Stetter (1986), AE009950; [af]González et al. (1998), BA000001.

in a redox cascade involving NAD(P)H-dependent thioredoxin reductase (TrxR) and protein disulfide oxidoreductase (Pdo) as the electron donors (Lim et al., 2017). In the absence of S^0, SurR remains reduced, binds to GTTn$_3$AAC(n$_5$GTT), promotes the transcription of *mbh* and *sh* genes, and represses the expression of *mbs* and *nsr* genes (Lipscomb et al., 2009). *Thermococci* with the Frh hydrogenase also can reduce TrxR using H_2 as the electron donor (Jung et al., 2020).

5. Abiotic formate in hydrothermal vents

5.1. Formate production in hydrothermal fluids

Abiotic formation of formate, carbon monoxide, methane, and hydrocarbons in hydrothermal vents is of interest as potential growth substrates for microbes. Methane and hydrocarbons in vents were suggested to form through Fischer-Tropsch type reactions [$(2n + 1)H_2 + nCO \rightarrow C_nH_{2n+2} + nH_2O$] or leach from fluid inclusions in plutonic rocks (Berndt et al., 1996; Horita and Berndt, 1999; McCollom and Seewald, 2001; McDermott et al., 2015). In contrast to hydrocarbons, there is a strong thermodynamic drive toward rapid C-H-O equilibrium in hydrothermal fluids within hours to days. Kinetic barriers preclude the formation of CH_4 in this equilibrium (Shock, 1990). This permits the creation of metastable formate species ($H_2 + CO_2 \leftrightarrow HCOOH$), CO ($HCOOH \leftrightarrow CO + H_2O$), formaldehyde ($HCOOH + H_2 \leftrightarrow CH_2O + H_2O$), and methanol ($CH_2O + H_2 \leftrightarrow CH_3OH$) through the sequential reduction of CO_2 using H_2 as the reductant (Seewald et al., 2006).

The abundance of formate in chemical equilibrium with dissolved inorganic carbon is strongly dependent on H_2 concentration, pH, and temperature (McCollom and Seewald, 2003; Seewald et al., 2006). In a gold-titanium reaction cell, $HCOO^-$ was formed from CO_2 at 300°C and 350 bar in less than 24 h from H_2 generated from hydrothermal alteration of olivine serving as the reductant (McCollom and Seewald, 2001). In a separate study, incubation of a 175 mmol/kg HCOOH solution at 300°C and 350 bar in the gold reaction cell led to near complete conversion to H_2 and CO_2 within 48 h, CO reached 0.83 mmol/kg, and $HCOO^-$ + HCOOH (or ΣHCOOH) decreased to 0.38 mmol/kg (Seewald et al., 2006). Reducing the temperature to 200°C and then to 150°C each led to an increase in ΣHCOOH, a decrease in CO, and C-H-O equilibrium within 115 h and 71 h, respectively. Injection of 172 mmol/kg CO led to production of H_2, ΣCO_2, and ΣHCOOH, and decreasing CO. Alkaline conditions favored the formation of HCOOH, $HCO_3{}^-$, and $CO_3{}^{2-}$ (Seewald et al., 2006). Therefore, the abundance of formate, CO, and CH_3OH in seafloor hydrothermal systems will be regulated by the residence times of fluids in reactions zones, and physical and chemical conditions in the subsurface environments.

Formate is also generated across a pH gradient of more than three pH units using a mineral precipitate bridge at the interface of two fluids (Hudson et al., 2020). This may be relevant to the formation of formate on the early Earth or possibly in extraterrestrial oceans where high pH serpentinized fluids are

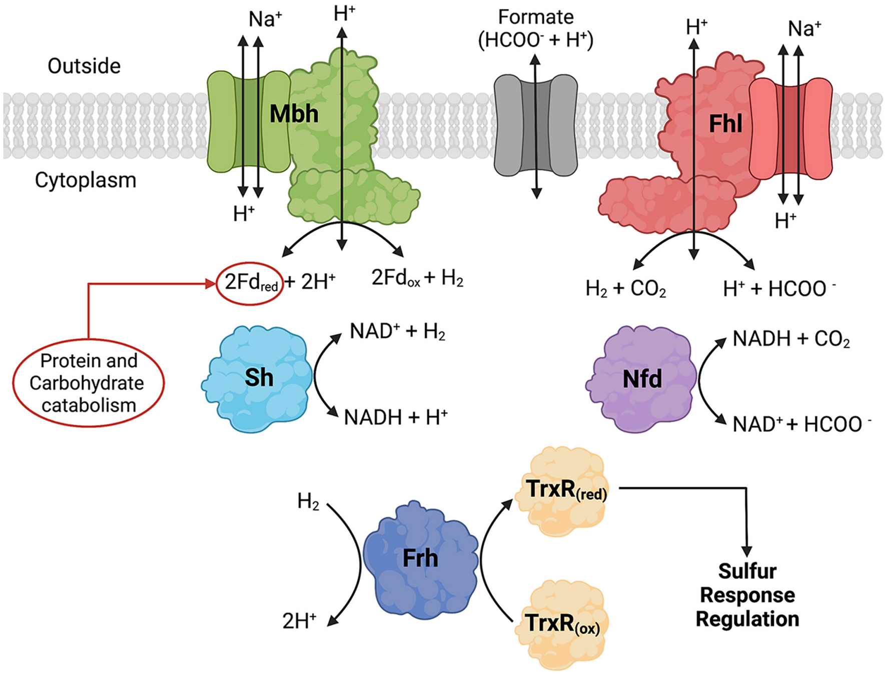

FIGURE 3
Formate dehydrogenase, hydrogenase, and formate transporter proteins and their reactions that are found in *Thermococci*. Formate hydrogenlyase (Fhl) catalyzes membrane-bound oxidation of formate to H_2 and CO_2. NAD(P)H: formate dehydrogenase (Nfd) catalyzes cytoplasmic oxidation of formate coupled with reduction of $NAD(P)^+$. The hydrogenases catalyze the following reactions: membrane-bound oxidation of ferredoxin (Fd) coupled with H_2 production (Mbh), cytoplasmic H_2 oxidation coupled with reduction of $NAD(P)^+$ (Sh), and cytoplasmic H_2 oxidation (Frd) coupled with reduction of thioredoxin reductase (TrxR). Fd and NAD(P)H are cytoplasmic electron carriers. TrxR is part of the redox cascade for sulfur response regulation using SurR. Created with BioRender.com.

emitted into an acid ocean. Under standard conditions, the generation of formate from H_2 and CO_2 is not thermodynamically favorable. However, H_2 in synthetic alkaline vent fluid (pH 12.3) passed electrons to dissolved CO_2 in a synthetic acid ocean (pH 3.9) at 25°C through a Fe(Ni)S mineral interface generating 1.5 μM $HCOO^-$ in the ocean fluid (Hudson et al., 2020). Isotopic labeling showed that protonation occurred using H_2O on the ocean side of the interface, not H_2 on the vent side. Weakening the pH gradient led to decreased concentrations of $HCOO^-$ produced. Nickel in the precipitate is a crucial part of the reduction mechanism as $HCOO^-$ yield dropped below detection without Ni in the ocean precipitation fluid.

5.2. Formate concentrations in hydrothermal fluids

There have been very few measurements of formate in natural hydrothermal fluids due in part to the analytical difficulty of measuring formate at low concentrations (Schink et al., 2017). Formate has been measured mostly at sites with high H_2 concentrations such as at the Lost City, Von Damm, and Piccard hydrothermal vent sites and were 36–669 μM (**Table 1**). Formate and H_2 were also measured at Snake Pit and TAG hydrothermal vents, which are mafic hydrothermal vents on the Mid-Atlantic Ridge, where formate concentrations were 1–2 nM and H_2 concentrations were 0.08–2.4 μM (Konn et al., 2022). At ultramafic sites, formate concentrations are generally 10–100 fold lower than that of H_2 at the same site (Lang et al., 2010; McDermott et al., 2015) while at mafic sites the formate concentration is often more than 1,000 fold lower than the H_2 concentration (McDermott et al., 2018; Konn et al., 2022).

6. Formate use by methanogens

6.1. Free formate use for *de novo* purine biosynthesis

Methanocaldococcus jannaschii was shown to incorporate ^{14}C-formate into biomass during growth (Sprott et al., 1993), which may be used in part for *de novo* purine biosynthesis. Inosine monophosphate (IMP) is a precursor for adenine and guanine synthesis for purine biosynthesis and is made from ribose-5-phosphate (**Figure 4**). In most organisms, the pathway intermediates glycinamide-ribose-5-phosphate (GAR) and aminoimidazole carboxamide-ribose-5-phosphate (AICAR) are formylated using N^{10}-formyl-tetrahydrofolate as the formyl donor. However, the genes for these enzymes are absent in *Methanococci* and *Methanopyri* and are replaced with genes that encode for enzymes that use free formate and energy from ATP to formylate their substrates (White, 1997; Brown et al., 2011). These enzymes are formylglycinamide-ribose-5-phosphate synthetase (PurT) and forminido imidazole carboxamide-ribose-5-phosphate synthetase (PurP) (**Figure 4**). *M. jannaschii* was shown to have PurP activity and that it produced free ^{13}C-formate in the cell when incubated with H_2 and $H^{13}CO_3$ (Ownby et al., 2005). Herein, a genome survey of the eleven extremely thermophilic methanogens showed that all the organisms have homologs for *purP* and all but *M. kandleri* have homologs for *purT* (**Table 2** and **Supplementary Table 1**). This suggests that these organisms have a mechanism for formate synthesis.

6.2. Formate dehydrogenases in *Methanococci* and *Methanopyri*

Nine of the 11 *Methanococci* and *Methanopyri* genomes have genes that encode for a cytoplasmic formate dehydrogenase (**Table 2** and **Supplementary Table 1**). Formate dehydrogenases catalyze the reversible oxidation of formate to CO_2 using various electron acceptors. The catalytic α subunit (FdhA) contains tungsten, selenocysteine, and a (Fe_4-S_4) cluster as cofactors while the β subunit (FdhB) contains three (Fe_4-S_4) clusters (Niks and Hille, 2019). FdhAB in *Methanococci* and *Methanopyri* is homologous to two formate dehydrogenases in the mesophilic methanogen *Methanococcus maripaludis*, also a *Methanococci*, that use coenzyme F_{420} as their redox partner (**Figure 2**; Wood et al., 2003; Lupa et al., 2008). *M. maripaludis* grows hydrogenotrophically on H_2 and CO_2 but also grows on formate in their absence (Jones et al., 1983b). When *fdhA1* was mutated in *M. maripaludis*, the organism was unable to grow on formate and formate dehydrogenase activity in cell extracts was undetectable (Lupa et al., 2008). Observations with hydrogenase mutants in *M. maripaludis* suggest that coenzyme F_{420} is an intermediate in formate-to-H_2 conversion (Lupa et al., 2008). An *M. maripaludis*Δ*fdhA1*Δ*fdhA2* double mutant grown in purine-free defined medium grew as well as the wild-type strain suggesting that formate dehydrogenase is not essential for *de novo* purine biosynthesis (Wood et al., 2003). The absence of *fdhAB* genes in *Methanocaldococcus infernus* and *Methanofervidicoccus abyssi* (**Table 2** and **Supplementary Table 1**) also supports the idea that formate dehydrogenase is not essential for purine biosynthesis. However, it is likely that H_2 and coenzyme F_{420} are electron donors for formate production and can help meet the cellular demand for formate for purine biosynthesis.

The formate dehydrogenase (FdhA1B1) from *M. maripaludis* also forms an enzyme complex with heterodisulfide reductase, the soluble hydrogenase Vhu, and formylmethanofuran dehydrogenase (**Figure 2**; Costa et al., 2010). It was necessary for the organism's growth on formate but not on H_2 (Costa et al., 2010). Therefore, in addition to coenzyme F_{420} reduction, this formate dehydrogenase also oxidizes formate to reduce the heterodisulfide coenzyme M-coenzyme B and ferredoxin through electron bifurcation. Coenzyme M, coenzyme B, and ferredoxin are cytoplasmic electron carriers in these methanogens. Expression of the second formate dehydrogenase gene (*fdhA2*) in *M. maripaludis* increased when cells were grown under H_2 limited conditions but was unchanged under formate limited conditions (Costa et al., 2013) and was not required for growth on formate (Lupa et al., 2008) suggesting that this isoenzyme may have a separate physiological function.

6.3. Formate transporters in *Methanococci*

For extremely thermophilic methanogens, it appears that a formate transporter is required for growth on formate. Formate transporters import or export formate across the cytoplasmic membrane and require co-translocation of a H^+ (**Figure 2**). Three thermophilic methanogens in our survey (*Methanotorris formicicus*, *Methanothermococcus okinawensis*, and *Methanothermococcus thermolithotrophicus*) grew on formate in the absence of H_2 and CO_2 but not any of the other methanogens examined (**Table 2**). Each of these methanogens that grew on formate has a gene that encodes for a membrane-bound formate transporter (*fdhC*) in its genome, which is absent in all other methanogens examined, except for *Methanocaldococcus fervens* which was not tested for growth on formate (**Table 2** and **Supplementary Table 1**). *M. maripaludis* has an *fdhC* gene in an operon with *fdhA1B1* (Sattler et al., 2013). In *M. fervens* and *M. okinawensis*, the formate transporter gene *fdhC* appears to be in the same operon as *fdhAB* suggesting they are co-transcribed (**Supplementary Table 1**).

7. Formate use by *Thermococci*

7.1. Free formate use for *de novo* purine biosynthesis

Like *Methanococci*, all *Thermococci* lack the enzymes that use N^{10}-formyl-tetrahydrofolate as the formyl donor for *de novo* purine biosynthesis (Brown et al., 2011). Instead, most *Thermococci* use formate-dependent enzymes (PurT and PurP) for *de novo* purine biosynthesis (**Figure 4**, **Table 3**, and **Supplementary Table 2**). Therefore, they depend on a source of free formate in the cell for *de novo* synthesis. However, some *Thermococcus* species (*T. paralvinellae*, *T. barophilus* CH5, *T. onnurineus*, and *T. gorgonarius*) lack most or all the genes for the purine biosynthesis pathway (Brown et al., 2011) and likely rely on environmental sources of purines.

7.2. Formate dehydrogenases in *Thermococci*

All 30 *Thermococci* genomes have at least one copy of the gene that encodes for the catalytic α subunit of formate dehydrogenase (FdhA) either in the form of formate hydrogenlyase, NAD(P)$^+$-dependent formate dehydrogenase, or the catalytic subunit alone (**Table 3** and **Supplementary Table 2**). The phylogeny of FdhA in extremely thermophilic *Methanococci*, *Methanopyri*, and *Thermococci* showed one clade for *Methanococci* and *Methanopyri* and five clades among the *Thermococci* (**Figure 5**). In *Thermococci*, hydrogenase operons often flank *fdhA*-containing operons in the genome (**Figure 6** and **Supplementary Table 2**) suggesting a close association between formate and H_2 in these organisms. In Groups 1 and 2 in **Figure 5**, *fdhA* was encoded in an operon with a formate transporter gene. For Group 1, in nearly all instances,

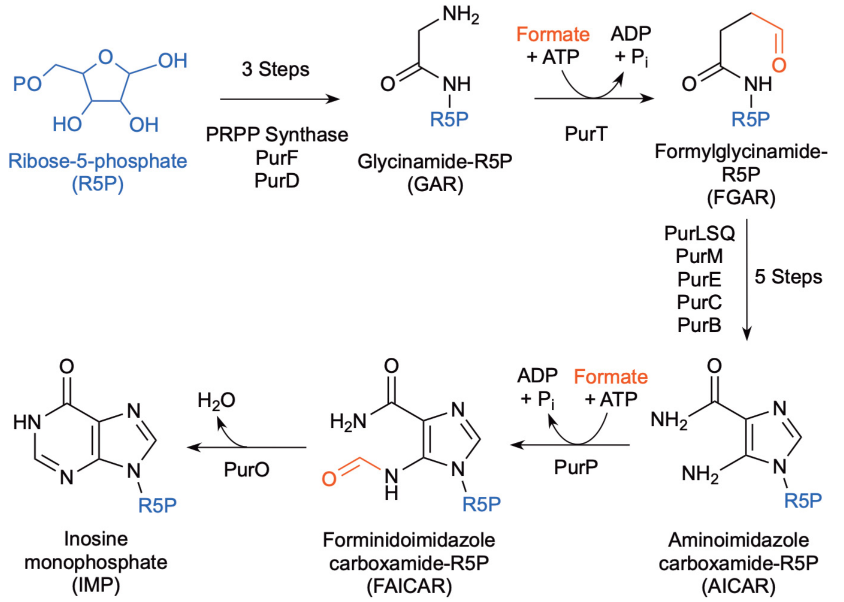

FIGURE 4
Biochemical pathway for *de novo* purine biosynthesis using free formate as the source of the formyl group (after Brown et al., 2011).

the *fdhA*-containing operon was immediately downstream from an *frh* operon and immediately upstream from one or two *mbh* operons on the same DNA strand suggesting that they may be co-transcribed (**Figure 6**). In Group 1A, *fdhA* was encoded in a formate hydrogenlyase (*fhl*) operon (Kim et al., 2010; Topçuoğlu et al., 2018; Le Guellec et al., 2021; **Table 3**; **Supplementary Table 2**). This enzyme reversibly couples formate oxidation to H_2 evolution on the cytoplasmic membrane with concomitant H^+/Na^+ translocation across the membrane *via* antiporter modules (**Figure 4**; Kim et al., 2010; Lim et al., 2014). In Group 1B, *fdhA* was encoded in a $NAD(P)^+$-dependent formate dehydrogenase (*nfd*) operon (**Figure 6**). This soluble enzyme catalyzes the reversible oxidation of formate using $NAD(P)^+$ or ferredoxin as its redox partner (Le Guellec et al., 2021; Yang et al., 2022; **Figure 4**). In Group 2, *fdhA* was encoded in an *nfd* operon but neighbored an *sh* operon in the genome instead of *frh* and *mbh* operons (**Figure 6**). These *nfd* and *sh* operons are transcribed in opposite directions from the same intergenic spacer region.

The *fdhA* from Groups 3 and 4 are in *fhl* operons that lack a formate transporter gene. In Group 3, the *fhl* operon was next to an *sh* operon (**Figure 6**). These *fhl* and *sh* operons are transcribed in opposite directions from the same intergenic spacer region. In Group 4, the *fhl* operon did not neighbor any hydrogenase operons in the genome, and in Group 5 the *fdhA* gene was the only formate dehydrogenase-related gene present in the genome (**Figure 6**). Often these solo genes in Group 5 are near the purine biosynthesis genes in genome sequences (**Supplementary Table 2**). In *T. sibiricus*, nearly all the genes for *de novo* purine biosynthesis (*purFCMTEDPSQL*) and *fdhA* are next to each other in the genome, although they are not all on the same DNA strand (**Figure 6**). In these organisms, it is unknown if *fdhA* alone encodes for a functional formate dehydrogenase or what the redox partner is for this putative enzyme. However, it is plausible that it might be used to produce formate for purine biosynthesis when other formate dehydrogenases and formate transport proteins are absent.

7.3. Formate transporters in *Thermococci*

Under defined growth conditions, 11 of the 30 *Thermococci* strains analyzed either oxidized added formate as an energy source (plus trace levels of organic compounds as a carbon source) and produced H_2 (Kim et al., 2010; Topçuoğlu et al., 2018) or secreted formate when grown on organic compounds in the presence of high background H_2 and the absence of added formate (Hensley et al., 2016; Topçuoğlu et al., 2018; Le Guellec et al., 2021). These 11 strains are the only *Thermococci* in the survey that have a formate transporter gene (**Table 3**). The other 19 *Thermococci* lack this gene and were unable to grow on formate or secrete formate (Kim et al., 2010; Le Guellec et al., 2021). Therefore, it appears that a formate transporter is required for *Thermococci* to secrete formate or, like *Methanococci*, for growth of *Thermococci* on formate. The presence of a formate transporter gene or transcript should be a criterion when determining if *Methanococci* or *Thermococci* are potentially using or producing formate in their natural habitat.

7.4. Formate production versus consumption by *Thermococci* in nature

The standard Gibbs energy for interconversion between formate and $H_2 + CO_2$ is small; therefore, the direction of the reaction is highly dependent upon the relative concentrations of formate and H_2 in the environment (Schink et al., 2017; Le Guellec et al., 2021). Le Guellec et al. (2021) calculated that CO_2 reduction to formate using H_2 is thermodynamically more favorable than formate oxidation to H_2 and CO_2 at

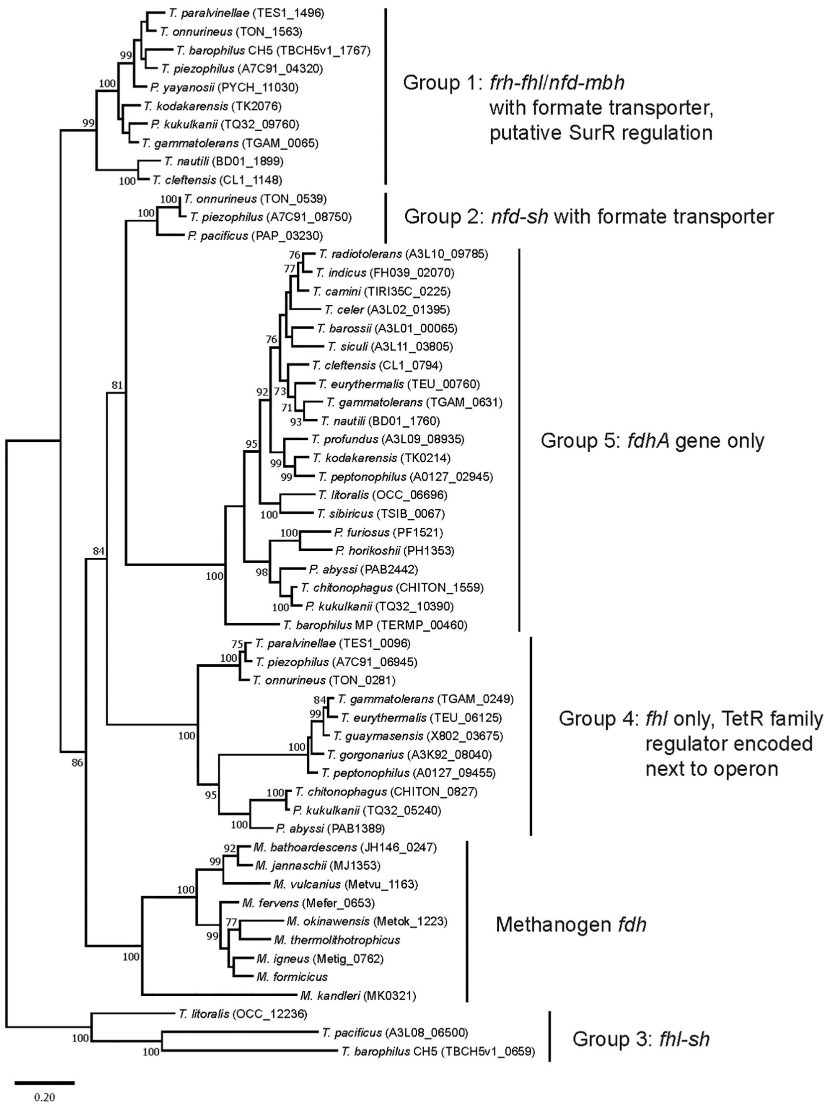

FIGURE 5

Phylogenetic tree based on catalytic subunit alpha (FdhA) for the various formate dehydrogenases found in extremely thermophilic *Methanococci*, *Methanopyri*, and *Thermococci*. The phylogeny of FdhA was inferred by using a maximum likelihood method and Jones-Taylor-Thornton (JTT) matrix-based modeling (Jones et al., 1992). After 1000 bootstrap constructions, the tree with the highest log likelihood (−31,270.37) is shown, with values next to nodes indicating the percentage of reconstructions in which the topology was preserved (values < 70% are omitted for clarity). There were a total of 736 positions in the final dataset. Branch lengths are to scale and indicate the number of substitutions per site. GenBank/EMBL/DDBJ open reading frame numbers are included in parentheses. Evolutionary analyses were conducted in MEGA11 (Tamura et al., 2021). Clade associations with operon arrangements on the genomes and the presence of a formate transporter or putative regulatory elements are shown.

Lost City, Von Damm, Rainbow, Lucky Strike, Snake Pit, and Ashadze 1 hydrothermal vent sites based on relative formate and H_2 concentrations in hydrothermal fluids. The physiological response of *Thermococcus* is in keeping with this idea. Growth of *T. paralvinellae* on a sugar or peptides when sparged with H_2 led to higher levels of *fhl1* expression and higher formate secretion relative to cultures sparged with N_2 (Topçuoğlu et al., 2018). It was concluded that *fhl* and *nfd* expression in *Thermococci* is primarily for the purpose of ameliorating H_2 inhibition rather than for growth on formate (Topçuoğlu et al., 2019; Le Guellec et al., 2021). *Thermococci* would require an environment where formate concentrations exceed H_2 concentrations to grow on formate. The formate produced by *Thermococci* may supplement the growth of *Methanococci* even when *Thermococci* produce H_2, as is observed with fermenter-methanogen relationships in mesophilic environments (Schink et al., 2017).

8. Transcriptional regulation of formate dehydrogenase genes

8.1. Transcriptional regulation in *Methanococci*

Formate consumption in *Methanococci* is closely associated with H_2 use in the cell. Therefore, a question that arises is whether

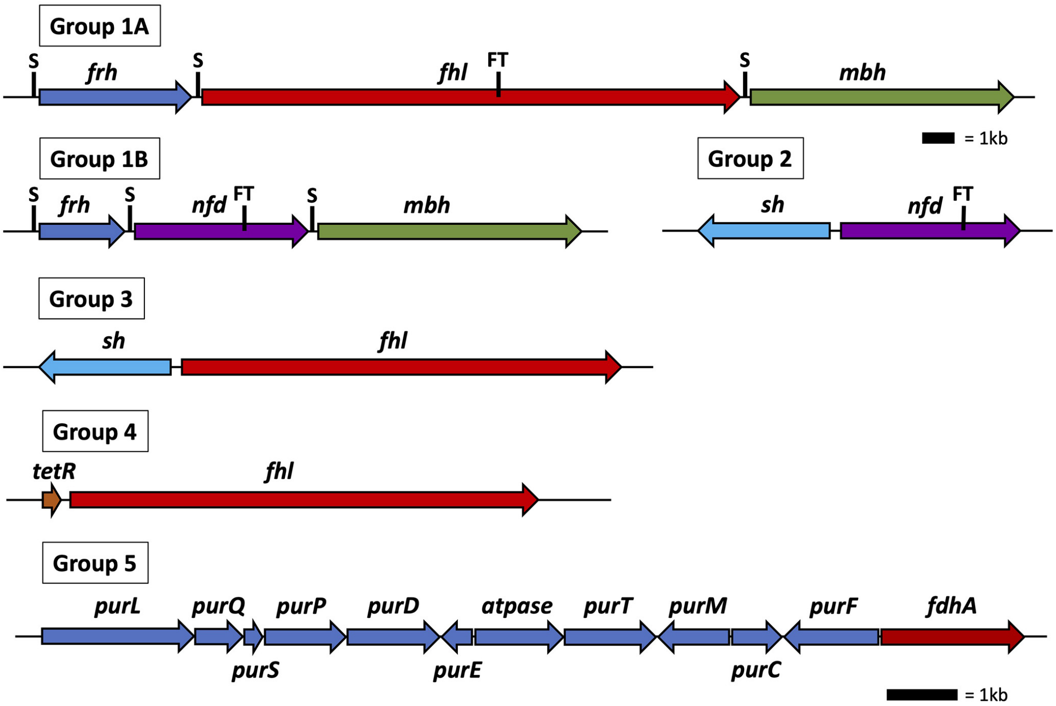

FIGURE 6

Operon and gene maps for *Thermococci* containing operons for formate hydrogenlyase (*fhl*), NAD(P)H: formate dehydrogenase (*nfd*), membrane hydrogenase (*mbh*), soluble hydrogenase (*sh*), and F_{420}-reducing-like hydrogenase (*frh*) (Groups 1–4) and genes for the catalytic subunit of formate dehydrogenase (*fdhA*), and purine biosynthesis (*pur*) (Group 5). Also shown are the locations of SurR binding sites (S), the *tetR* gene for transcriptional regulation, and the operons containing a formate transporter (FT) gene. The top scale bar is for the Group 1–4 operons; the bottom scale bar, the genes for Group 5.

formate or H_2 regulates *fdhAB* expression in these organisms. The thermophilic methanogen *Methanobacterium thermoformicicum* grows on H_2 and CO_2 as well as separately on formate. It has a formate transporter gene (*fdhC*) directly upstream of its formate dehydrogenase genes (*fdhAB*) (Nolling and Reeve, 1997). Transcripts of *fdhCAB* were present in *M. thermoformicicum* at all growth stages when grown on formate. When grown on H_2 and CO_2, *fdhCAB* transcripts were barely detectable in early exponential growth phase but increased dramatically as cells approached late exponential growth phase in a closed batch system when H_2 became more limiting. Similarly, *fdh* expression in *M. maripaludis* was controlled by the presence of H_2 and not formate (Wood et al., 2003). Using *fdhC-lacZ* gene fusions, β-galactosidase activity increased in *M. maripaludis* cells grown on H_2 and CO_2 as they approached late exponential growth phase, again when H_2 became limiting. When grown on formate, β-galactosidase activity was higher in cells with N_2 and CO_2 in the headspace relative to those with H_2 and CO_2 in the headspace. β-galactosidase activity increased in cells grown on formate plus H_2 and CO_2 after the H_2 and CO_2 was replaced mid-growth phase with N_2 and CO_2.

In *M. maripaludis*, genes for a putative response regulator and a histidine kinase are directly upstream of *fdhC*, which is three genes upstream of *fdhA1B1* and part of a putative five-gene operon (Sattler et al., 2013). Random mutagenesis showed that disruption of this putative response regulator led to slower growth of *M. maripaludis* on formate relative to the wild type. It also led to increased *fdhA1* transcriptional abundance regardless of whether H_2 and CO_2 or formate was the growth substrate. Impairment of derepression of the *fdhC-fdhA1B1* operon is a plausible explanation (Sattler et al., 2013). Therefore, H_2 present at high concentrations may interact with the histidine kinase and activate the response regulator in a two-component regulatory system that represses *fdhC-fdhA1B1* expression, which is derepressed when H_2 levels are low or absent.

8.2. Transcriptional regulation in *Thermococci*

Very little is known about transcriptional regulation of the *fhl* and *nfd* operons in *Thermococci*. Group 1 *Thermococci* genomes (**Figure 6**) encode syntenic *frh*, either *fhl* or *nfd*, and *mbh* operons with a formate transporter gene encoded in the *fhl* or *nfd* operon (**Figure 6**). These *frh*, *fhl*, *nfd*, and *mbh* operons each have GTTn$_3$AAC(n$_5$GTT) in their promoter region just upstream of BRE/TATA RNA polymerase binding sites suggesting they are also regulated and promoted by the sulfur response regulator protein SurR (see Section "4.2. Growth of *Thermococci* with and without S^0"). Furthermore, Frh was shown to oxidize H_2 and reduce TrxR (Jung et al., 2020), which reduces SurR *via* Pdo, suggesting that it might serve as a regulatory hydrogenase that promotes *frh*, *fhl*, *nfd*, and *mbh* expression when H_2 concentrations increase in the cell. Therefore, like *Methanococci*, H_2 abundance appears to regulate formate use in *Thermococci*. A remaining question is whether formate also regulates gene expression in *Thermococci*. In

T. paralvinellae, expression of the Group 1A *fhl* operon containing the formate transporter gene increased when cells were grown on formate relative to growth on maltose or peptides while expression of *mbh* either remained unchanged or decreased (Topçuoğlu et al., 2018). This suggests that in addition to SurR regulation, formate either directly or indirectly regulates gene expression in *T. paralvinellae* as well. Validation and the mechanism of this putative regulation is yet to be determined.

None of the promoter regions for the *nfd*, *fhl*, or *sh* operons in Groups 2–4 had a SurR nucleotide binding sequence. All but one of the Group 4 *fhl* operons have a gene encoding for a TetR/AcrR family transcriptional regulator that is ∼350 nucleotides upstream of and transcribed in the same direction as the *fhl* operon (**Supplementary Table 2**). TetR/AcrR family transcriptional regulators are one-component systems where a single protein contains both a sensory domain and a DNA-binding domain (Cuthbertson and Nodwell, 2013). They are widely associated with antibiotic resistance and the regulation of genes encoding small molecule exporters and are usually encoded alongside target operons (Colclough et al., 2019). In *T. paralvinellae*, expression of the Group 4 *fhl* operon decreased when cells were grown on formate relative to growth on maltose or peptides (Topçuoğlu et al., 2018). The mechanism for regulation of Group 2–5 formate dehydrogenase-related genes is unknown.

9. Conclusion

Formate and H_2 are linked both in hydrothermal vent environments and in the metabolisms of extremely thermophilic *Methanococci* and *Thermococci*. *Methanococci* prefer H_2 oxidation to formate oxidation but appear to switch to the latter when H_2 is limiting. Similarly, *Thermococci* appear to prefer H_2 production to formate production but switch to the latter when H_2 is excessive and inhibitory. H_2 is typically far more abundant than formate in hydrothermal vent fluids suggesting that in high H_2 environments formate is unlikely to be used by *Methanococci* and *Methanopyri* for growth. However, in hydrothermal environments that are very low H_2 environments but rich in organic compounds, *Thermococci* may produce H_2 and formate that are then used to support the growth of extremely thermophilic methanogens. Understanding where, when, and how formate is used by extreme thermophiles in nature is largely unknown and an area of future research. Furthermore, our understanding of transcriptional regulation of *fhl* and *nfd* in *Thermococci* is nascent. A key question is if and how formate influences gene expression, especially in concert with SurR regulation of hydrogenases and sulfur responsive genes.

Author contributions

JH and HS contributed to the conceptualization, original draft preparation, review, and editing of the manuscript. JH conducted bioinformatic analyses and data compilation. Both authors read and agreed to the published version of the manuscript.

Funding

This research was provided by the NASA Exobiology grant 80NSSC21K1240 and USDA National Institute of Food and Agriculture grant MAS00550 to JH.

Acknowledgments

We thank Briana Kubik, Gema Garcia, and Gabriella Rizzo for their constructive comments, and the reviewers for their helpful suggestions.

Conflict of interest

The authors declare that the research was conducted in the absence of any commercial or financial relationships that could be construed as a potential conflict of interest.

Publisher's note

Supplementary material

The Supplementary Material for this article can be found online at: https://www.frontiersin.org/articles/10.3389/fmicb.2023.1093018/full#supplementary-material

References

Adams, M. W. W., Holden, J. F., Lal Menon, A., Schut, G. J., Grunden, A. M., Hou, C., et al. (2001). Key role for sulfur in peptide metabolism and in regulation of three hydrogenases in the hyperthermophilic archaeon *Pyrococcus furiosus*. *J. Bacteriol.* 183, 716–724. doi: 10.1128/JB.183.2.716-724.2001

Anderson, R. E., Beltrán, M. T., Hallam, S. J., and Baross, J. A. (2013). Microbial community structure across fluid gradients in the Juan de Fuca ridge hydrothermal system. *FEMS Microbiol. Ecol.* 83, 324–339. doi: 10.1111/j.1574-6941.2012.01478.x

Atomi, H., Fukui, T., Kanai, T., Morikawa, M., and Imanaka, T. (2004). Description of *Thermococcus kodakaraensis* sp. nov., a well studied hyperthermophilic archaeon previously reported as *Pyrococcus* sp. KOD1. *Archaea* 1, 263–267.

Bae, S. S., Kim, T. W., Lee, H. S., Kwon, K. K., Kim, Y. J., Kim, M.-S., et al. (2012). H2 production from CO, formate, or starch using the hyperthermophilic archaeon, *Thermococcus onnurineus*. *Biotechnol. Lett.* 34, 75–79. doi: 10.1007/s10529-011-0732-3

Bae, S. S., Kim, Y. J., Yang, S. H., Lim, J. K., Jeon, J. H., Lee, H. S., et al. (2006). *Thermococcus onnurineus* sp. nov., a hyperthermophilic archaeon isolated from a deep-sea hydrothermal vent area at the pacmanus Field. *J. Microbiol. Biotechnol.* 16, 1826–1831.

Bar-On, Y. M., Phillips, R., and Milo, R. (2018). The biomass distribution on Earth. *Proc. Natl. Acad. Sci. U.S.A.* 115, 6506–6511. doi: 10.1073/pnas.1711842115

Baumberger, T., Früh-Green, G. L., Thorseth, I. H., Lilley, M. D., Hamelin, C., Bernasconi, S. M., et al. (2016). Fluid composition of the sediment-influenced loki's castle vent field at the ultra-slow spreading arctic mid-ocean ridge. *Geochim. Cosmochim. Acta* 187, 156–178. doi: 10.1016/j.gca.2016.05.017

Belay, N., Sparling, R., and Daniels, L. (1986). Relationship of formate to growth and methanogenesis by *Methanococcus thermolithotrophicus*. *Appl. Environ. Microbiol.* 52, 1080–1085. doi: 10.1128/aem.52.5.1080-1085.1986

Belkin, S., Wirsen, C. O., and Jannasch, H. W. (1985). Biological and abiological sulfur reduction at high temperatures. *Appl. Environ. Microbiol.* 49, 1057–1061. doi: 10.1128/aem.49.5.1057-1061.1985

Berndt, M. E., Allen, D. E., and Seyfried, W. E. Jr. (1996). Reduction of CO2 during serpentinization of olivine at 300°C and 500 bar. *Geology* 24, 351–354. doi: 10.1130/0091-76131996024<0351:ROCDSO<2.3.CO;2

Birrien, J.-L., Zeng, X., Jebbar, M., Cambon-Bonavita, M.-A., Quérellou, J., Oger, P., et al. (2011). *Pyrococcus yayanosii* sp. nov., an obligate piezophilic hyperthermophilic archaeon isolated from a deep-sea hydrothermal vent. *Int. J. Syst. Evol. Microbiol.* 61, 2827–2831. doi: 10.1099/ijs.0.024653-0

Bonch-Osmolovskaya, E. A., and Stetter, K. O. (1991). Interspecies hydrogen transfer in cocultures of thermophilic Archaea. *System. Appl. Microbiol.* 14, 205–208.

Boyd, E. S., Schut, G. J., Adams, M. W. W., and Peters, J. W. (2014). Hydrogen metabolism and the evolution of biological respiration. *Microbe* 9, 361–367.

Brazelton, W. J., McGonigle, J. M., Motamedi, S., Pendleton, H. L., Twing, K. I., Miller, B. C., et al. (2022). Metabolic strategies shared by basement residents of the lost city hydrothermal field. *Appl. Environ. Microbiol.* 88:e0092922. doi: 10.1128/aem.00929-22

Brazelton, W. J., Schrenk, M. O., Kelley, D. S., and Baross, J. A. (2006). Methane- and sulfur-metabolizing microbial communities dominate the lost city hydrothermal field ecosystem. *Appl. Environ. Microbiol.* 72, 6257–6270. doi: 10.1128/AEM.00574-06

Brown, A. M., Hoopes, S. L., White, R. H., and Sarisky, C. A. (2011). Purine biosynthesis in archaea: Variations on a theme. *Biol. Direct* 6:63. doi: 10.1186/1745-6150-6-63

Burggraf, S., Fricke, H., Neuner, A., Kristjansson, J., Rouvier, P., Mandelco, L., et al. (1990). *Methanococcus igneus* sp. nov., a novel hyperthermophilic methanogen from a shallow submarine hydrothermal system. *System. Appl. Microbiol.* 13, 263–269. doi: 10.1016/s0723-2020(11)80197-9

Callac, N., Oger, P., Lesongeur, F., Rattray, J. E., Vannier, P., Michoud, G., et al. (2016). *Pyrococcus kukulkanii* sp. nov., a hyperthermophilic, piezophilic archaeon isolated from a deep-sea hydrothermal vent. *Int. J. Syst. Evol. Microbiol.* 66, 3142–3149. doi: 10.1099/ijsem.0.001160

Canganella, F., Jones, W. J., Gambacorta, A., and Antranikian, G. (1998). *Thermococcus guaymasensis* sp. nov. and *Thermococcus aggregans* sp. nov., two novel thermophilic archaea isolated from the Guaymas basin hydrothermal vent site. *Int. J. Syst. Bacteriol.* 48, 1181–1185. doi: 10.1099/00207713-48-4-1181

Colclough, A. L., Scadden, J., and Blair, J. M. A. (2019). TetR-family transcription factors in gram-negative bacteria: Conservation, variation and implications for efflux-mediated antimicrobial resistance. *BMC Genomics* 20:731. doi: 10.1186/s12864-019-6075-5

Costa, K. C., Wong, P. M., Wang, T., Lie, T. J., Dodsworth, J. A., Swanson, I., et al. (2010). Protein complexing in a methanogen suggests electron bifurcation and electron delivery from formate to heterodisulfide reductase. *Proc. Natl. Acad. Sci. U.S.A.* 107, 11050–11055. doi: 10.1073/pnas.1003653107

Costa, K. C., Yoon, S. H., Pan, M., Burn, J. A., Baliga, N. S., and Leigh, J. A. (2013). Effects of H2 and formate on growth yield and regulation of methanogenesis in *Methanococcus maripaludis*. *J. Bacteriol.* 195, 1456–1462. doi: 10.1128/JB.02141-12

Courtine, D., Vince, E., Maignien, L., Philippon, X., Gayet, N., Shao, Z., et al. (2021). *Thermococcus camini* sp. nov., a hyperthermophilic and piezophilic archaeon isolated from a deep-sea hydrothermal vent at the mid-atlantic ridge. *Int. J. Syst. Evol. Microbiol.* 71:004853. doi: 10.1099/ijsem.0.004853

Cuthbertson, L., and Nodwell, J. R. (2013). The TETR family of regulators. *Microbiol. Mol. Biol. Rev.* 77, 440–475. doi: 10.1128/MMBR.00018-13

Dalmasso, C., Oger, P., Seva, G., Courtine, D., L'Harison, S., Garlaschelli, A., et al. (2016). *Thermococcus piezophilus* sp. nov., a novel hyperthermophilic and piezophilic archaeon with a broad pressure range for growth, isolated from a deepest hydrothermal vent at the mid-Cayman rise. *Syst. Appl. Microbiol.* 39, 440–444. doi: 10.1016/j.syapm.2016.08.003

Ding, K., Seyfried, W. E. Jr., Zhang, Z., Tivey, M. K., Von Damm, K. L., and Bradley, A. M. (2005). The in situ pH of hydrothermal fluids at mid-ocean ridges. *Earth Planet. Sci. Lett.* 237, 167–174. doi: 10.1016/j.epsl.2005.04.041

Duffaud, G. D., d'Hennezel, O. B., Peek, A. S., Reysenbach, A.-L., and Kelly, R. M. (1998). Isolation and characterization of *Thermococcus barossii*, sp. nov., a hyperthermophilic archaeon isolated from a hydrothermal vent flange formation. *System. Appl. Microbiol.* 21, 40–49.

Erauso, G., Reysenbach, A.-L., Godfroy, A., Meunier, J. R., Crump, B., Partensky, F., et al. (1993). *Pyrococcus abyssi* sp. nov., a new hyperthermophilic archaeon isolated from a deep-sea hydrothermalvent. *Arch. Microbiol.* 160, 338–349.

Fiala, G., and Stetter, K. O. (1986). *Pyrococcus furiosus* sp. nov. Represents a novel genus of marine heterotrophic archaebacteria growing optimally at 100°C. *Arch. Microbiol.* 145, 56–61.

Fleming, H.-C., and Wuertz, S. (2019). Bacteria and archaea on earth and their abundance in biofilms. *Nat. Rev. Microbiol.* 17, 247–260. doi: 10.1038/s41579-019-0158-9

Flores, G. E., Campbell, J. H., Kirshtein, J. D., Meneghin, J., Podar, M., Steinberg, J. I., et al. (2011). Microbial community structure of hydrothermal deposits from geochemically different vent fields along the mid-atlantic ridge. *Environ. Microbiol.* 13, 2158–2171. doi: 10.1111/j.1462-2920.2011.02463.x

Flores, G. E., Shakya, M., Meneghin, J., Yang, Z. K., Seewald, J. S., Wheat, C. G., et al. (2012). Inter-field variability in the microbial communities of hydrothermal vent deposits from a back-arc basin. *Geobiology* 10, 333–346. doi: 10.1111/j.1472-4669.2012.00325.x

Fortunato, C. S., Larson, B., Butterfield, D. A., and Huber, J. A. (2018). Spatially distinct, temporally stable microbial populations mediate biogeochemical cycling at and below the seafloor in hydrothermal vent fluids. *Environ. Microbiol.* 20, 769–784. doi: 10.1111/1462-2920.14011

Gallant, R. M., and Von Damm, K. L. (2006). Geochemical controls on hydrothermal fluids from the Kairei and Edmond vent fields, 23°-25°S, central Indian ridge. *Geochem. Geophys. Geosyst.* 7:Q06018. doi: 10.1029/2005GC001067

Gamo, T., Masuda, H., Yamanaka, T., Okamura, K., Ishibashi, J., Nakayama, E., et al. (2004). Discovery of a new hydrothermal venting site in the southernmost Mariana Arc: Al-rich hydrothermal plumes and white smoler activity associated with biogenic methane. *Geochem. J.* 38, 527–534. doi: 10.2343/geochemj.38.527

González, J. M., Kato, C., and Horikoshi, K. (1995). *Thermococcus peptonophilus* sp. nov., a fast-growing, extremely thermophilic archaebacterium isolated from deep-sea hydrothermal vents. *Arch. Microbiol.* 164, 159–164.

González, J. M., Masuchi, Y., Robb, F. T., Ammerman, J. W., Maeder, D. L., Yanagibayashi, M., et al. (1998). *Pyrococcus horikoshii* sp. nov., a hyperthermophilic archaeon isolated from a hydrothermal vent at the okinawa trough. *Extremophiles* 2, 123–130. doi: 10.1007/s007920050051

Gorlas, A., Croce, O., Oberto, J., Gauliard, E., Forterre, P., and Marguet, E. (2014). *Thermococcus nautili* sp. nov., a hyperthermophilic archaeon isolated from a hydrothermal deep-sea vent. *Int. J. Syst. Evol. Microbiol.* 64, 1802–1810. doi: 10.1099/ijs.0.060376-0

Greening, C., Biswas, A., Carere, C. R., Jackson, C. J., Taylor, M. C., Stott, M. B., et al. (2016). Genomic and metagenomic surveys of hydrogenase distribution indicate H2 is a widely utilized energy source for microbial growth and survival. *ISME J.* 10, 761–777. doi: 10.1038/ismej.2015.153

Grote, R., Li, L., Tamaoka, J., Kato, C., Horikoshi, K., and Antranikian, G. (1999). *Thermococcus siculi* sp. nov., a novel hyperthermophilic archaeon isolated from a deep-sea hydrothermal vent at the Mid-Okinawa Trough. *Extremophiles* 3, 55–62.

Han, Y., Gonnella, G., Adam, N., Schippers, A., Burkhardt, L., Kurtz, S., et al. (2018). Hydrothermal chimneys host habitat-specific microbial communities: Analogues for studying the possible impact of mining seafloor massive sulfide deposits. *Sci. Rep.* 8:10386. doi: 10.1038/s41598-018-28613-5

Hendrickson, E. L., and Leigh, J. A. (2008). Roles of coenzyme F420-reducing hydrogenases and hydrogen- and F420-dependent methlenetetrahydromethanopterin dehydrogenases in reduction of F420 and production of hydrogen during methanogenesis. *J. Bacteriol.* 190, 4818–4821. doi: 10.1128/JB.00255-08

Hensley, S. A., Moreira, E., and Holden, J. F. (2016). Hydrogen production and enzyme activities in the hyperthermophile *Thermococcus paralvinellae* grown on maltose, tryptone, and agricultural waste. *Front. Microbiol.* 7:167. doi: 10.3389/fmicb.2016.00167

Holden, J. F., Summit, M., and Baross, J. A. (1998). Thermophilic and hyperthermophilic microorganisms in 3-30°C hydrothermal fluids following a deep-sea volcanic eruption. *FEMS Microbiol. Ecol.* 25, 33–41. doi: 10.1111/j.1574-6941.1998.tb00458.x

Holden, J. F., Takai, K., Summit, M., Bolton, S., Zyskowski, J., and Baross, J. A. (2001). Diversity among three novel groups of hyperthermophilic deep-sea *Thermococcus* species from three sites in the Northeastern Pacific ocean. *FEMS Microbiol. Ecol.* 36, 51–60.

Horita, J., and Berndt, M. E. (1999). Abiogenic methane formation and isotopic fractionation under hydrothermal conditions. *Science* 285, 1055–1057. doi: 10.1126/science.285.5430.1055

Hou, J., Sievert, S. M., Wang, Y., Seewald, J. S., Natarajan, V. P., Wang, F., et al. (2020). Microbial succession during the transition from active to inactive stages of deep-sea hydrothermal vent sulfide chimneys. *Microbiome* 8:102. doi: 10.1186/s40168-020-00851-8

Huber, H., Thomm, M., König, H., Thies, G., and Stetter, K. O. (1982). *Methanococcus thermolithotrophicus*, a novel thermophilic lithotrophic methanogen. *Arch. Microbiol.* 132, 47–50. doi: 10.1007/BF00690816

Huber, J. A., Butterfield, D. A., and Baross, J. A. (2002). Temporal changes in archaeal diversity and chemistry in a mid-ocean ridge subseafloor habitat. *Appl. Environ. Microbiol.* 68, 1585–1594. doi: 10.1128/AEM.68.4.1585-1594.2002

Huber, R., Stöhr, J., Hohenhaus, S., Rachel, R., Burggraf, S., Jannasch, H. W., et al. (1995). *Thermococcus chitonophagus* sp. nov., a novel, chitin-degrading, hyperthermophilic archaeum from a deep-sea hydrothermal vent environment. *Arch. Microbiol.* 164, 255–264.

Hudson, R., de Graaf, R., Strandoo Rodin, M., Ohno, A., Lane, N., McGlynn, S. E., et al. (2020). CO2 reduction driven by a pH gradient. *Proc. Natl. Acad. Sci. U.S.A.* 117, 22873–22879. doi: 10.1073/pnas.2002659117

Jaeschke, A., Jørgensen, S. L., Bernasconi, S. M., Pedersen, R. B., Thorseth, I. H., and Früh-Green, G. L. (2012). Microbial diversity of loki's castle black smokers at the arctic mid-ocean ridge. *Geobiology* 10, 548–561. doi: 10.1111/gbi.12009

Jeanthon, C., L'Haridon, S., Reysenbach, A. L., Corre, E., Vernet, M., Messner, P., et al. (1999). *Methanococcus vulcanius* sp. nov., a novel hyperthermophilic methanogen isolated from east pacific rise, and identification of *Methanococcus* sp. DSM 4213T as *Methanococcus fervens* sp. nov. *Int. J. Syst. Microbiol.* 49, 583–589. doi: 10.1099/00207713-49-2-583

Jeanthon, C., L'Haridon, S., Reysenbach, A. L., Vernet, M., Messner, P., Sleytr, U. B., et al. (1998). *Methanococcus infernus* sp. nov., a novel hyperthermophilic lithotrophic methanogen isolated from a deep-sea hydrothermal vent. *Int. J. Syst. Bacteriol.* 48, 913–919. doi: 10.1099/00207713-48-3-913

Jolivet, E., Corre, E., L'Harison, S., Forterre, P., and Prieur, D. (2004). *Thermococcus marinus* sp. nov. and *Thermococcus radiotolerans* sp. nov., two hyperthermophilic archaea from deep-sea hydrothermal vents that resist ionizing radiation. *Extremophiles* 8, 219–227. doi: 10.1007/s00792-004-0380-9

Jolivet, E., L'Haridon, S., Corre, E., Forterre, P., and Prieur, D. (2003). *Thermococcus gammatolerans* sp. nov., a hyperthermophilic archaeon from a deep-sea hydrothermal vent that resists ionizing radiation. *Int. J. Syst. Evol. Microbiol.* 53, 847–851. doi: 10.1099/ijs.0.02503-0

Jones, D. T., Taylor, W. R., and Thornton, J. M. (1992). The rapid generation of mutation data matrices from protein sequences. *Comput. Appl. Biosci.* 8, 275–282.

Jones, W. J., Paynter, M. J. B., and Gupta, R. (1983b). Characterization of *Methanococcus maripaludis* sp. nov., a new methanogen isolated from salt marsh sediment. *Arch. Microbiol.* 135, 91–97. doi: 10.1007/BF00408015

Jones, W. J., Leigh, J. A., Mayer, F., Woese, C. R., and Wolfe, R. S. (1983a). *Methanococcus jannaschii* sp. nov., an extremely thermophilic methanogen from a submarine hydrothermal vent. *Arch. Microbiol.* 136, 254–261. doi: 10.1007/BF00425213

Jung, H.-C., Lim, J. K., Yang, T.-J., Kang, S. G., and Lee, H. S. (2020). Direct electron transfer between the frhAGB-encoded hydrogenase and thioredoxin reductase in the nonmethanogenic archaeon *Thermococcus onnurineus* NA1. *Appl. Environ. Microbiol.* 86, e2630–e2619. doi: 10.1128/AEM.02630-19

Kaster, A.-K., Moll, J., Parey, K., and Thauer, R. K. (2011). Coupling of ferredoxin and heterodisulfide reduction via electron bifurcation in hydrogenotrophic methanogenic archaea. *Proc. Natl. Acad. Sci. U.S.A.* 108, 2981–2986. doi: 10.1073/pnas.1016761108

Kim, Y. J., Lee, H. S., Kim, E. S., Bae, S. S., Lim, J. K., Matsumi, R., et al. (2010). Formate-driven growth coupled with H2 production. *Nature* 467, 352–355. doi: 10.1038/nature09375

Klein, F., Tarnas, J. D., and Bach, W. (2020). Abiotic sources of molecular hydrogen on Earth. *Elements* 16, 19–24. doi: 10.2138/gselements.16.1.19

Kobayashi, T., Kwak, Y. S., Akiba, T., Kudo, T., and Horikoshi, K. (1994). *Thermococcus profundus* sp. nov., a new hyperthermophilic archaeon isolated from a deep-sea hydrothermal vent. *Syst. Appl. Microbiol.* 17, 232–236.

Konn, C., Donval, J. P., Guyader, V., Germain, Y., Alix, A.-S., Roussel, E., et al. (2022). Extending the dataset of fluid geochemistry of the menez Gwen, lucky strike, rainbow, tag and snake pit hydrothermal vent fields: Investigation of temporal stability and organic contribution. *Deep Sea Res.* 179:103630. doi: 10.1016/j.dsr.2021.103630

Kormas, K. A., Tivey, M. K., Von Damm, K., and Teske, A. (2006). Bacterial and archaeal phylotypes associated with distinct mineralogical layers of a white smoker spire from a deep-sea hydrothermal vent site (9°N, east pacific rise). *Environ. Microbiol.* 8, 909–920. doi: 10.1111/j.1462-2920.2005.00978.x

Kumagai, H., Nakamura, K., Toki, T., Morishita, T., Okino, K., Ishibashi, J.-I., et al. (2008). Geological background of the Kairei and Edmond hydrothermal fields along the central Indian ridge: Implications of their vent fluids' distinct chemistry. *Geofluids* 8, 239–251. doi: 10.1111/j.1468-8123.2008.00223.x

Kurr, M., Huber, R., König, H., Jannasch, H. W., Fricke, H., Trincone, A., et al. (1991). *Methanopyrus kandleri*, gen. and sp. nov., represents a novel group of hyperthermophilic methanogens, growing at 110°C. *Arch. Microbiol.* 156, 239–247. doi: 10.1007/BF00262992

Lang, S. Q., Butterfield, D. A., Schulte, M., Kelley, D. S., and Lilley, M. D. (2010). Elevated concentrations of formate, acetate and dissolved organic carbon found at the lost city hydrothermal field. *Geochim. Cosmochim. Acta* 74, 941–952. doi: 10.1016/j.gca.2009.10.045

Lang, S. Q., Früh-Green, G. L., Bernasconi, S. M., Brazelton, W. J., Schrenk, M. O., and McGonigle, J. M. (2018). Deeply-sourced formate fuels sulfate reducers but not methanogens at lost city hydrothermal field. *Sci. Rep.* 8:755. doi: 10.1038/s41598-017-19002-5

Lang, S. Q., Früh-Green, G. L., Bernasconi, S. M., Lilley, M. D., Proskurowski, G., Méhay, S., et al. (2012). Microbial utilization of abiogenic carbon and hydrogen in a serpentinite-hosted system. *Geochim. Cosmochim. Acta* 92, 82–99. doi: 10.1016/j/gca.2012.06.006

Le Guellec, S., Leroy, E., Courtine, D., Godfroy, A., and Roussel, E. G. (2021). H2-dependent formate production by hyperthermophilic thermococcales: An alternative to sulfur reduction for reducing-equivalents disposal. *ISME J.* 15, 3423–3436. doi: 10.1038/s41396-021-01020-x

Lie, T. J., Costa, K. C., Lupa, B., Korpole, S., Whitman, W. B., and Leigh, J. A. (2012). Essential anaplerotic role for the energy-converting hydrogenase eha in hydrogenotrophic methanogenesis. *Proc. Natl. Acad. Sci. U.S.A.* 109, 15473–15478. doi: 10.1073/pnas.1208779109

Lilley, M. D., Butterfield, D. A., Lupton, J. E., and Olson, E. J. (2003). Magmatic events can produce rapid changes in hydrothermal vent chemistry. *Nature* 422, 878–881. doi: 10.1038/nature01569

Lim, J. K., Jung, H.-C., Kang, S. G., and Lee, H. S. (2017). Redox regulation of SurR by protein disulfide oxidoreductase in *Thermococcus onnurineus* NA1. *Extremophiles* 21, 491–498. doi: 10.1007/s00792-017-0919-1

Lim, J. K., Kim, Y. J., Yang, J.-A., Namirimu, T., Yang, S.-H., Park, M.-J., et al. (2020). *Thermococcus indicus* sp. nov., a Fe(III)-reducing hyperthermophilic archaeon isolated from the onnuri vent field of the central Indian ocean ridge. *J. Microbiol.* 58, 260–267. doi: 10.1007/s12275-020-9424-9

Lim, J. K., Mayer, F., Kang, S. G., and Müller, V. (2014). Energy conservation by oxidation of formate to carbon dioxide and hydrogen via a sodium ion current in a hyperthermophilic archaeon. *Proc. Natl. Acad. Sci. U.S.A.* 111, 11497–11502. doi: 10.1073/pnas.1407056111

Lin, T. J., Ver Eecke, H. C., Breves, E. A., Dyar, M. D., Jamieson, J. W., Hannington, M. D., et al. (2016). Linkages between mineralogy, fluid chemistry, and microbial communities within hydrothermal chimneys from the endeavour segment, Juan de Fuca ridge. *Geochem. Geophys. Geosyst.* 17, 300–323. doi: 10.1002/2015GC006091

Lipscomb, G. L., Keese, A. M., Cowart, D. M., Schut, G. J., Thomm, M., Adams, M. W. W., et al. (2009). SurR: A transcriptional activator and repressor controlling hydrogen and elemental sulfur metabolism in *Pyrococcus furiosus*. *Mol. Microbiol.* 71, 332–349. doi: 10.1111/j.1365-2958.2008.06525.x

Lipscomb, G. L., Schut, G. J., Scott, R. A., and Adams, M. W. W. (2017). SurR is a master regulator of the primary electron flow pathways in the order thermococcales. *Mol. Microbiol.* 104, 869–881. doi: 10.1111/mmi.13668

Lupa, B., Hendrickson, E. L., Leigh, J. A., and Whitman, W. B. (2008). Formate-dependent H2 production by the mesophilic methanogen *Methanococcus maripaludis*. *Appl. Environ. Microbiol.* 74, 6584–6590. doi: 10.1128/AEM.01455-08

Marteinsson, V. T., Birrien, J.-L., Reysenbach, A.-L., Vernet, M., Marie, D., Gambacorta, A., et al. (1999). *Thermococcus barophilus* sp. nov., a new barophilic and hyperthermophilic archaeon isolated under high hydrostatic pressure from a deep-sea hydrothermal vent. *Int. J. Syst. Bacteriol.* 49, 351–359.

McCliment, E. A., Voglesonger, K. M., O'Day, P. A., Dunn, E. E., Holloway, J. R., and Cary, S. C. (2006). Colonization of nascent, deep-sea hydrothermal vents by a novel archaeal and nanoarchaeal assemblage. *Environ. Microbiol.* 8, 114–125. doi: 10.1111/j.1462-2920.2005.00874.x

McCollom, T. M., and Seewald, J. S. (2001). A reassessment of the potential for reduction of dissolved CO2 to hydrocarbons during serpentinization of olivine. *Geochim. Cosmochim. Acta* 65, 3769–3778. doi: 10.1016/S0016-7037(01)00655-X

McCollom, T. M., and Seewald, J. S. (2003). Experimental constraints on the hydrothermal reactivity of organic acids and acid anions: I. Formic acid and formate. *Geochim. Cosmochim. Acta* 67, 3625–3644. doi: 10.1016/S0016-7037(03)00136-4

McDermott, J. M., Seewald, J. S., German, C. R., and Sylva, S. P. (2015). Pathways for abiotic organic synthesis at submarine hydrothermal fields. *Proc. Natl. Acad. Sci. U.S.A.* 112, 7668–7672. doi: 10.1073/pnas.1506295112

McDermott, J. M., Sylva, S. P., Ono, S., German, C. R., and Seewald, J. S. (2018). Geochemistry of fluids from Earth's deepest ridge-crest hot-springs: Piccard hydrothermal field, mid-Cayman rise. *Geochim. Cosmochim. Acta* 228, 95–118. doi: 10.1016/j.gca.2018.01.021

McGonigle, J. M., Lang, S. Q., and Brazelton, W. J. (2020). Genomic evidence for formate metabolism by chloroflexi as the key to unlocking deep carbon in lost city microbial ecosystems. *Appl. Environ. Microbiol.* 86, e2583–e2519. doi: 10.1128/AEM.02583-19

Meyer, J. L., Akerman, N. H., Proskurowski, G., and Huber, J. A. (2013). Microbiological characterization of post-eruption "snowblower" vents at axial seamount, Juan de Fuca ridge. *Front. Microbiol.* 4:153. doi: 10.3389/fmicb.2013.00153

Miroshnichenko, M. L., Gongadze, G. M., Rainey, F. A., Kostyukova, A. S., Lysenko, A. M., Chernyh, N. A., et al. (1998). *Thermococcus gorgonarius* sp. nov.

and *Thermococcus pacificus* sp. nov: Heterotrophic extremely thermophilic archaea from New Zealand submarine hot vents. *Int. J. Syst. Bacteriol.* 48, 23–29. doi: 10.1099/00207713-48-1-23

Miroshnichenko, M. L., Hippe, H., Stackebrandt, E., Kostrikina, N. A., Chernyh, N. A., Jeanthon, C., et al. (2001). Isolation and characterization of *Thermococcus sibiricus* sp. nov. From a western Siberia high-temperature oil reservoir. *Extremophiles* 5, 85–91. doi: 10.1007/s007920100175

Moon, Y.-J., Kwon, J., Yun, S.-H., Lim, H. L., Kim, M.-S., Kang, S. G., et al. (2012). Proteome analyses of hydrogen-producing hyperthermophilic archaeon *Thermococcus onnurineus* NA1 in different one-carbon substrate culture conditions. *Mol. Cell. Proteomics* 11:M111.015420. doi: 10.1074/mcp.M111.015420

Nakagawa, T., Takai, K., Suzuki, Y., Hirayama, H., Konno, U., Tsunogai, U., et al. (2006). Geomicrobiological exploration and characterization of a novel deep-sea hydrothermal system at the TOTO caldera in the Mariana volcanic Arc. *Environ. Microbiol.* 8, 37–49. doi: 10.1111/j.1462-2920.2005.00884.x

Niks, D., and Hille, R. (2019). Molybdenum- and tungsten-containing formate dehydrogenases and formylmethanofuran dehydrogenases: Structure, mechanism, and cofactor insertion. *Protein Soc.* 28, 111–122. doi: 10.1002/pro.3498

Nolling, J., and Reeve, J. N. (1997). Growth- and substrate-dependent transcription of the formate dehydrogenase (fdhCAB) operon in *Methanobacterium thermoformicicum* Z-245. *J. Bacteriol.* 179, 899–908. doi: 10.1128/jb.179.3.899-908.1997

Ownby, K., Xu, H., and White, R. H. (2005). A *Methanocaldococcus jannaschii* archaeal signature gene encodes for a 5-formaminoimidazole-4-carboxamide-1-β-D-ribofuranosyl 5′-monophosphate synthetase. *J. Biol. Chem.* 280, 10881–10887. doi: 10.1074/jbc.M413937200

Pagé, A., Tivey, M. K., Stakes, D. S., and Reysenbach, A.-L. (2008). Temporal and spatial archaeal colonization of hydrothermal vent deposits. *Environ. Microbiol.* 10, 874–884. doi: 10.1111/j.1462-2920.2007.01505.x

Perner, M., Kuever, J., Seifert, R., Pape, T., Koschinsky, A., Schmidt, K., et al. (2007). The influence of ultramafic rocks on microbial communities at the logatchev hydrothermal field, located 15°N on the Mid-Atlantic Ridge. *FEMS Microbiol. Ecol.* 16, 97–109. doi: 10.1111/j.1574-6941.2007.00325.x

Pledger, R. J., and Baross, J. A. (1989). Characterization of an extremely thermophilic archaebacterium from a black smoker polychaete (*Paralvinella* sp.) at the Juan de Fuca ridge. *System. Appl. Microbiol.* 12, 249–256.

Porat, I., Kim, W., Hendrickson, E. L., Xia, Q., Zhang, Y., Wang, T., et al. (2006). Disruption of the operon encoding Ehb hydrogenase limits anabolic CO2 assimilation in the archaeon *Methanococcus maripaludis. J. Bacteriol.* 188, 1373–1380. doi: 10.1128/JB.188.4.1373-1380.2006

Reveillaud, J., Reddington, E., McDermott, J., Algar, C., Meyer, J. L., Sylva, S., et al. (2016). Subseafloor microbial communities in hydrogen-rich vent fluids from hydrothermal systems along the mid-Cayman rise. *Environ. Microbiol.* 18, 1970–1987. doi: 10.1111/1462-2920.13173

Reysenbach, A.-L., St. John, E., Meneghin, J., Flores, G. E., Podar, M., Dombrowski, N., et al. (2020). Complex subsurface hydrothermal fluid mixing at a submarine arc volcano supports distinct and highly diverse microbial communities. *Proc. Natl. Acad. Sci. U.S.A.* 117, 32627–32638. doi: 10.1073/pnas.2019021117

Sakai, S., Takaki, Y., Miyazaki, M., Ogawara, M., Yanagawa, K., Miyazaki, J., et al. (2019). *Methanofervidicoccus abyssi* gen. nov., sp. nov., a hydrogenotrophic methanogen, isolated from a hydrothermal chimney in the mid-cayman spreading center, the Caribbean sea. *Int. J. Syst. Evol. Microbiol.* 69, 1225–1230. doi: 10.1099/ijsem.0.003297

Sapra, R., Bagramyan, K., and Adams, M. W. W. (2003). A simple energy-conserving system: Proton reduction coupled to proton translocation. *Proc. Natl. Acad. Sci. U.S.A.* 100, 7545–7550. doi: 10.1073/pnas.1331436100

Sattler, C., Wolf, S., Fersch, J., Goetz, S., and Rother, M. (2013). Random mutagenesis identifies factors involved in formate-dependent growth of the methanogenic archaeon *Methanococcus maripaludis*. *Mol. Genet. Genomics* 288, 413–424. doi: 10.1007/s00438-013-0756-6

Schink, B., Montag, D., Keller, A., and Müller, N. (2017). Hydrogen or formate: Alternative key players in methanogenic degradation. *Environ. Microbiol. Rep.* 9, 189–202. doi: 10.1111/1758-2229.12524

Schrenk, M. O., Kelley, D. S., Bolton, S. A., and Baross, J. A. (2004). Low archaeal diversity linked to subseafloor geochemical processes at the lost city hydrothermal field, mid-atlantic ridge. *Environ. Microbiol.* 6, 1086–1095. doi: 10.1111/j.1462-2920.2004.00650.x

Schut, G. J., Bridger, S. L., and Adams, M. W. W. (2007). Insights into the metabolism of elemental sulfur by the hyperthermophilic archaeon *Pyrococcus furiosus*: Characterization of a coenzyme A-dependent NAD(P)H sulfur oxidoreductase. *J. Bacteriol.* 189, 4431–4441. doi: 10.1128/JB.00031-07

Schut, G. J., Nixon, W. J., Lipscomb, G. L., Scott, R. A., and Adams, M. W. W. (2012). Mutational analyses of the enzymes involved in the metabolism of hydrogen by the hyperthermophilic archaeon *Pyrococcus furiosus*. *Front. Microbiol.* 3:163. doi: 10.3389/fmicb.2012.00163

Schut, G. J., Zhou, J., and Adams, M. W. W. (2001). DNA microarray analysis of the hyperthermophilic archaeon *Pyrococcus furiosus*: Evidence for a new type of sulfur-reducing enzyme complex. *J. Bacteriol.* 183, 7027–7036.

Seewald, J. S., Zolotov, M. Y., and McCollom, T. (2006). Experimental investigation of single carbon compounds under hydrothermal conditions. *Geochim. Cosmochim. Acta* 70, 446–460. doi: 10.1016/j.gca.2005.09.002

Seewald, J., Cruse, A., and Saccocia, P. (2003). Aqueous volatiles in hydrothermal fluids from the main endeavour field, northern Juan de Fuca ridge: Temporal variability following earthquake activity. *Earth Planet. Sci. Lett.* 216, 575–590. doi: 10.1016/S0012-821X(03)00543-0

Shock, E. L. (1990). Geochemical constraints on the origin of organic compounds in hydrothermal systems. *Orig. Life Evol. Biosph.* 20, 331–367. doi: 10.1007/BF01581580

Sokolova, T. G., Jeanthon, C., Kostrikina, N. A., Chernyh, N. A., Lebedinsky, A. V., Stackebrandt, E., et al. (2004). The first evidence of anaerobic CO oxidation coupled with H2 production by a hyperthermophilic archaeon isolated from a deep-sea hydrothermal vent. *Extremophiles* 8, 317–323. doi: 10.1007/s00792-004-0389-0

Sprott, G. D., Ekiel, I., and Patel, G. B. (1993). Metabolic pathways in *Methanococcus jannaschii* and other methanogenic bacteria. *Appl. Environ. Microbiol.* 59, 1092–1098. doi: 10.1128/AEM.59.4.1092-1098.1993

Stetter, K. O. (2006). History of discovery of the first hyperthermophiles. *Extremophiles* 10, 357–362. doi: 10.1007/s00792-006-0012-7

Stewart, L. C., Algar, C. K., Fortunato, C. S., Larson, B. I., Vallino, J. J., Huber, J. A., et al. (2019). Fluid geochemistry, local hydrology, and metabolic activity define methanogen community size and composition in deep-sea hydrothermal vents. *ISME J.* 13, 1711–1721. doi: 10.1038/s41396-019-0382-3

Takai, K., Gamo, T., Tsunogai, U., Nakayama, N., Hirayama, H., Nealson, K. H., et al. (2004b). Geochemical and microbiological evidence for a hydrogen-based, hyperthermophilic subsurface lithoautotrophic microbial ecosystem (HyperSLiME) beneath an active deep-sea hydrothermal field. *Extremophiles* 8, 269–282. doi: 10.1007/s00792-004-0386-3

Takai, K., Inoue, A., and Horikoshi, K. (2002). *Methanothermococcus okinawensis* sp. nov., a thermophilic, methane-producing archaeon isolated from a Western Pacific deep-sea hydrothermal vent system. *Int. J. Syst. Evol. Microbiol.* 52, 1089–1095. doi: 10.1099/00207713-52-4-1089

Takai, K., Nealson, K. H., and Horikoshi, K. (2004a). *Methanotorris formicicus* sp. nov., a novel extremely thermophilic, methane-producing archaeon isolated from a black smoker chimney in the central Indian ridge. *Int. J. Syst. Evol. Microbiol.* 54, 1095–1100. doi: 10.1099/ijs.0.02887-0

Takai, K., Nunoura, T., Horikoshi, K., Shibuya, T., Nakamura, K., Suzuki, Y., et al. (2009). Variability in microbial communities in black smoker chimneys at the NW caldera vent field, brothers volcano, kermadec Arc. *Geomicrobiol. J.* 26, 252–269. doi: 10.1080/01490450903304949

Takai, K., Nunoura, T., Ishibashi, J., Lupton, J., Suzuki, R., Hamasaki, H., et al. (2008). Variability in the microbial communities and hydrothermal fluid chemistry at the newly discovered mariner hydrothermal field, southern Lau basin. *J. Geophys. Res.* 113:G02031. doi: 10.1029/2007JG000636

Tamura, K., Stecher, G., and Kumar, S. (2021). MEGA11: Molecular evolutionary genetics analysis version 11. *Mol. Biol. Evol.* 38, 3022–3027. doi: 10.1093/molbev/msab120

Thauer, R. K., Kaster, A.-K., Seedorf, H., Buckel, W., and Hedderich, R. (2008). Methanogenic archaea: Ecologically relevant differences in energy conservation. *Nat. Rev. Microbiol.* 6, 579–591. doi: 10.1038/nrmicro1931

Topçuoğlu, B. D., Meydan, C., Nguyen, T. B., Lang, S. Q., and Holden, J. F. (2019). Growth kinetics, carbon isotope fractionation, and gene expression in the hyperthermophile *Methanocaldococcus jannaschii* during hydrogen-limited growth and interspecies hydrogen transfer. *Appl. Environ. Microbiol.* 85, e180–e119. doi: 10.1128/AEM.00180-19

Topçuoğlu, B. D., Meydan, C., Orellana, R., and Holden, J. F. (2018). Formate hydrogenlyase and formate secretion ameliorate H2 inhibition in the hyperthermophilic archaeon *Thermococcus paralvinellae*. *Environ. Microbiol.* 20, 949–957. doi: 10.1111/1462-2920.14022

Topçuoğlu, B. D., Stewart, L. C., Morrison, H. G., Butterfield, D. A., Huber, J. A., and Holden, J. F. (2016). Hydrogen limitation and syntrophic growth among natural assemblages of thermophilic methanogens at deep-sea hydrothermal vents. *Front. Microbiol.* 7:1240. doi: 10.3389/fmicb.2016.01240

Valentine, D. L., Chidthaisong, A., Rice, A., Reeburgh, W. S., and Tyler, S. C. (2004). Carbon and hydrogen isotope fractionation by moderately thermophilic methanogens. *Geochim. Cosmochim. Acta* 68, 1571–1590. doi: 10.1016/j.gca.2003.10.012

Van Haaster, D. J., Silva, P. J., Hagedoorn, P.-L., Jongejan, J. A., and Hagen, W. R. (2008). Reinvestigation of the steady-state kinetics and physiological function of the soluble NiFe-hydrogenase I of *Pyrococcus furiosus*. *J. Bacteriol.* 190, 1584–1587. doi: 10.1128/JB.01562-07

Ver Eecke, H. C., Akerman, N. H., Huber, J. A., Butterfield, D. A., and Holden, J. F. (2013). Growth kinetics and energetics of a deep-sea hyperthermophilic methanogen under varying environmental conditions. *Environ. Microbiol. Rep.* 5, 665–671. doi: 10.1111/1758-2229.12065

Ver Eecke, H. C., Butterfield, D. A., Huber, J. A., Lilley, M. D., Olson, E. J., Roe, K. K., et al. (2012). Hydrogen-limited growth of hyperthermophilic methanogens at deep-sea hydrothermal vents. *Proc. Natl. Acad. Sci. U.S.A.* 109, 13674–13679. doi: 10.1073/pnas.1206632109

Ver Eecke, H. C., Kelley, D. S., and Holden, J. F. (2009). Abundances of hyperthermophilic autotrophic Fe(III) oxide reducers and heterotrophs in hydrothermal sulfide chimneys of the Northeastern Pacific ocean. *Appl. Environ. Microbiol.* 75, 242–245. doi: 10.1128/AEM.01462-08

Von Damm, K. L., and Lilley, M. D. (2004). "Diffuse flow hydrothermal fluids from 9° 50' N east pacific rise: Origin, evolution and biogeochemical controls," in *The subseafloor biosphere at mid-ocean ridges*, eds W. S. D. Wilcock, E. F. DeLong, D. S. Kelley, and S. C. Cary (Washington, DC: American Geophysical Union Press), 245–268.

Von Damm, K. L., Edmond, J. M., Measures, C. I., and Grant, B. (1985). Chemistry of submarine hydrothermal solutions at Guaymas basin, gulf of California. *Geochim. Cosmochim. Acta* 49, 2221–2237. doi: 10.1016/0016-7037(85)90223-6

White, R. H. (1997). Purine biosynthesis in the domain archaea without folates or modified folates. *J. Bacteriol.* 179, 3374–3377. doi: 10.1128/jb.179.10.3374-3377.1997

Windman, T., Zolotova, N., Schwandner, F., and Shock, E. L. (2007). Formate as an energy source for microbial metabolism in chemosynthetic zones of hydrothermal ecosystems. *Astrobiology* 7, 873–890. doi: 10.1089/ast.2007.0127

Wood, G. E., Haydock, A. K., and Leigh, J. A. (2003). Function and regulation of the formate dehydrogenase genes of the methanogenic archaeon *Methanococcus maripaludis*. *J. Bacteriol.* 185, 2548–2554. doi: 10.1128/JB.185.8.2548-2554.2003

Wu, C.-H., Schut, G. J., Poole, F. II, Haja, D. K., and Adams, M. W. W. (2018). Characterization of membrane-bound sulfane reductase: A missing link in the evolution of modern day respiratory complexes. *J. Biol. Chem.* 293, 16687–16696. doi: 10.1074/jbc.RA118.005092

Yang, H., Lipscomb, G. L., Keese, A. M., Schut, G. J., Thomm, M., Adams, M. W. W., et al. (2010). SurR regulates hydrogen production in *Pyrococcus furiosus* by a sulfur-dependent redox switch. *Mol. Microbiol.* 77, 1111–1122. doi: 10.1111/j.1365-2958.2010.07275.x

Yang, J., Lee, S. H., Ryu, J. Y., Lee, H. S., and Kang, S. G. (2022). A novel NADP-dependent formate dehydrogenase from the hyperthermophilic archaeon *Thermococcus onnurineus* NA1. *Front. Microbiol.* 13:844735. doi: 10.3389/fmicb.2022.844735

Zeng, X., Zhang, X., Jiang, L., Alain, K., Jebbar, M., and Shao, Z. (2013). *Palaeococcus pacificus* sp. nov., an archaeon from deep-sea hydrothermal sediment. *Int. J. Syst. Evol. Microbiol.* 63, 2155–2159. doi: 10.1099/ijs.0.044487-0

Zhao, H., Wood, A. G., Widdel, F., and Bryant, M. P. (1988). An extremely thermophilic *Methanococcus* from a deep-sea hydrothermal vent and its plasmid. *Arch. Microbiol.* 150, 178–183. doi: 10.1007/BF00425159

Zhao, W., Zeng, X., and Xiao, X. (2015). *Thermococcus eurythermalis* sp. nov., a conditional piezophilic, hyperthermophilic archaeon with a wide temperature range for growth, isolated from an oil-immersed chimney in the Guaymas basin. *Int. J. Syst. Evol. Microbiol.* 65, 30–35. doi: 10.1099/ijs.0.067942-0

Zillig, W., Holz, I., Janekovic, D., Schäfer, W., and Reiter, W. D. (1983). The archaebacterium *Thermococcus* celer represents, a novel genus within the thermophilic branch of the archaebacteria. *System. Appl. Microbiol.* 4, 88–94. doi: 10.1016/S0723-2020(83)80036-8

frontiers | Frontiers in Microbiology

TYPE Original Research
PUBLISHED 28 April 2023
DOI 10.3389/fmicb.2023.1176606

OPEN ACCESS

EDITED BY
Bo Barker Jørgensen,
Aarhus University, Denmark

REVIEWED BY
Nancy Merino,
Lawrence Livermore National Laboratory (DOE), United States
Michael Hügler,
Technologiezentrum Wasser, Germany

*CORRESPONDENCE
Katelyn Weeks
✉ kmweeks1@asu.edu

RECEIVED 28 February 2023
ACCEPTED 12 April 2023
PUBLISHED 28 April 2023

CITATION
Weeks K, Trembath-Reichert E, Boyer G, Fecteau K, Howells A, De Martini F, Gile GH and Shock EL (2023) Characterization of microbiomic and geochemical compositions across the photosynthetic fringe.
Front. Microbiol. 14:1176606.
doi: 10.3389/fmicb.2023.1176606

Characterization of microbiomic and geochemical compositions across the photosynthetic fringe

Katelyn Weeks[1]*, Elizabeth Trembath-Reichert[2], Grayson Boyer[1], Kristopher Fecteau[1,2], Alta Howells[3,4], Francesca De Martini[3,5], Gillian H. Gile[3] and Everett L. Shock[1,2]

[1]School of Molecular Sciences, Arizona State University, Tempe, AZ, United States, [2]School of Earth and Space Exploration, Arizona State University, Tempe, AZ, United States, [3]School of Life Sciences, Arizona State University, Tempe, AZ, United States, [4]NASA Postdoctoral Program Fellow at NASA Ames Research Center, Moffett Field, CA, United States, [5]Department of Life Sciences, Mesa Community College, Mesa, AZ, United States

Hot spring outflow channels provide geochemical gradients that are reflected in microbial community compositions. In many hot spring outflows, there is a distinct visual demarcation as the community transitions from predominantly chemotrophs to having visible pigments from phototrophs. It has been hypothesized that this transition to phototrophy, known as the photosynthetic fringe, is a result of the pH, temperature, and/or sulfide concentration gradients in the hot spring outflows. Here, we explicitly evaluated the predictive capability of geochemistry in determining the location of the photosynthetic fringe in hot spring outflows. A total of 46 samples were taken from 12 hot spring outflows in Yellowstone National Park that spanned pH values from 1.9 to 9.0 and temperatures from 28.9 to 92.2°C. Sampling locations were selected to be equidistant in geochemical space above and below the photosynthetic fringe based on linear discriminant analysis. Although pH, temperature, and total sulfide concentrations have all previously been cited as determining factors for microbial community composition, total sulfide did not correlate with microbial community composition with statistical significance in non-metric multidimensional scaling. In contrast, pH, temperature, ammonia, dissolved organic carbon, dissolved inorganic carbon, and dissolved oxygen did correlate with the microbial community composition with statistical significance. Additionally, there was observed statistical significance between beta diversity and the relative position to the photosynthetic fringe with sites above the photosynthetic fringe being significantly different from those at or below the photosynthetic fringe according to canonical correspondence analysis. However, in combination, the geochemical parameters considered in this study only accounted for 35% of the variation in microbial community composition determined by redundancy analysis. In co-occurrence network analyses, each clique correlated with either pH and/or temperature, whereas sulfide concentrations only correlated with individual nodes. These results indicate that there is a complex interplay between geochemical variables and the position of the photosynthetic fringe that cannot be fully explained by statistical correlations with the individual geochemical variables included in this study.

KEYWORDS

Yellowstone National Park, hot spring, microbiome, photosynthetic fringe, geochemistry

1. Introduction

In hot spring outflow channels, there is a visual transition from predominantly chemotrophic microbial communities to those with larger contributions from phototrophs. This transition is marked by the occurrence of green, orange, yellow, brown, and/or purple pigments in biofilms associated with chlorophylls, carotenoids, and/or phycobiliproteins (Cox et al., 2011). The first transition to pigmented organisms is referred to as the photosynthetic fringe (Shock and Holland, 2007). This visual transition corresponds to geochemical transitions as the hot spring water flows away from its source and begins to cool and equilibrate with the atmosphere. This process leads to more oxygenation and increased pH as CO_2 degases, among other geochemical changes (Nordstrom et al., 2005).

Previous studies have attributed the visual appearance of the photosynthetic fringe to concurrent changes in geochemistry that are more conducive to phototrophs in hot spring outflows. Temperature, pH, and sulfide concentrations have been suggested as limiting factors of photosynthesis in hot spring outflows (Cox et al., 2011; Boyd et al., 2012; Hamilton et al., 2012). Previous work established an upper limit of photosynthesis between 73 and 75°C across environments (Kempner, 1963; Brock and Brock, 1966; Brock, 1978; Castenholz, 1969). However, the upper temperature limit of photosynthesis depends on pH (Cox et al., 2011; Boyd et al., 2012; Fecteau et al., 2022) and is reduced to ∼56°C under acidic conditions (Doemel and Brock, 1970, 1971). Though the upper temperature limit for photosynthesis was established based on observation, culture work, microbial activity, and pigment studies, the advent of sequencing methods challenges these earlier findings. Additionally, the reason for the upper temperature limit for photosynthesis is still debated. Possible limits on photosynthesis based on temperature include protein instability and the functionality of the CO_2-assimilating mechanism (Brock and Brock, 1966; Meeks and Castenholz, 1978). It is also uncertain why the temperature limit is lower in acidic conditions, but it is most likely due to the dominant phototrophs transitioning from bacteria to comparatively less thermotolerant eukaryotes at lower pH (Boyd et al., 2012; Fecteau et al., 2022). Sulfide concentration may also be a limiting factor for photosynthesis due to sulfide's ability to bind to metalloproteins and block electron flow to photosystem II (Oren et al., 1979; Miller and Bebout, 2004).

In the phototrophic communities of hot spring outflows in Yellowstone National Park (YNP), the composition of phototrophs changes with pH. In the phototrophic mats below the photosynthetic fringes of basic springs ($pH > 7$), the microbial communities consist predominantly of bacterial phototrophs, including Cyanobacteria and filamentous anoxygenic phototrophs (Inskeep et al., 2013; Bennett et al., 2022). The predominance of bacterial phototrophs in basic hot spring outflows has been supported by 16S rRNA gene sequencing, metagenomic sequencing, and *in situ* studies of bicarbonate and nitrogen fixation (Ward et al., 1990; Steunou et al., 2008; Klatt et al., 2011; Thiel et al., 2016). Below the photosynthetic fringe of acidic outflows ($pH < 4$), the phototrophs are typically eukaryotic and include acidophilic algae such as *Cyanidioschyzon* (Toplin et al., 2008; Skorupa et al., 2013). Both eukaryotic and bacterial phototrophs have been identified in the phototrophic mats of acidic to circumneutral hot springs (pH 4–7), combining the likes of Cyanobacteria and *Cyanidioschyzon* (Fecteau et al., 2022). Thus, in hot spring environments there exists a trend in microbial community composition from prokaryotic to eukaryotic phototrophs as pH decreases (Brock, 1973; Bennett et al., 2022; Fecteau et al., 2022).

The predominantly chemotrophic communities above the photosynthetic fringe of hot spring outflows also vary with pH (Swingley et al., 2012; Inskeep et al., 2013; Colman et al., 2016; Lindsay et al., 2018). In general, according to quantitative PCR amplification of 16S rRNA genes, Archaea dominate in the chemotrophic communities of acidic hot springs, whereas Bacteria are dominant in the chemotrophic communities of basic hot springs (Colman et al., 2018). In acidic hot springs ($pH < 4$), predominant archaeal constituents are Sulfolobales, Desulfurcoccales, and Thermoproteales (Inskeep et al., 2013; Colman et al., 2018). The predominant bacteria in acidic hot springs include Aquificales, Thermales, Firmicutes, and Proteobacteria (Inskeep et al., 2013; Colman et al., 2016). However, it should be noted that Aquificales and Proteobacteria are predominant bacterial constituents in hot spring outflows regardless of pH. These previous studies have provided characterizations of chemotrophic community compositions and implicate the importance of pH on the composition of the community.

The distinct compositions of microbial communities along hot spring outflows have been linked to differences in the concentrations of dissolved inorganic carbon (DIC) and dissolved organic carbon (DOC). Havig et al. (2011) investigated the presence versus absence of various carbon fixation pathways and connected the findings back to changes in carbon isotope fractionation ($\Delta^{13}C$) data as well as DIC and DOC concentrations. In the outflow of a basic spring, "Bison Pool," also discussed in this study as hot spring "BP," $\Delta^{13}C$ measurements of the biofilm became more negative down the outflow, indicating a possible shift in carbon fixation strategies (Havig et al., 2011). Additionally, DIC was observed to decrease down the outflow while DOC increases. Generally, DIC concentrations are dependent on CO_2 input from the hydrothermal source and decrease down hot spring outflows as CO_2 degasses and is microbially fixed. In contrast, DOC generally increases down the outflow, and, in the case of "Bison Pool," this is attributed to meteoric water input from the surrounding meadow (Swingley et al., 2012). In the "Bison Pool" outflow, the increase in DOC was connected to a transition in the microbial community composition from chemoautotrophs at the highest temperatures to heterotrophs and phototrophs further downstream, implicating the importance of DIC/DOC in the composition of the microbial community (Swingley et al., 2012).

Nitrogen availability in YNP hot spring outflows also contributes to the microbial community composition. According to isotopic observations by Havig et al. (2011), measurable N-fixation only occurs at and below the photosynthetic fringe of the "Bison Pool" outflow. This limitation on N-fixation was reflected in the distribution of nitrogen fixation (*nif*) genes only at and below the photosynthetic fringe. In contrast, the expression of *nif* genes was observed above the photosynthetic fringe at "Mound Spring," also discussed in this study as hot spring "MN" (Loiacono et al., 2012). *nif* genes have also been identified in acidic to circumneutral springs, suggesting that nitrogen fixation is not limited by pH in hot spring ecosystems (Hamilton et al., 2011a). This was supported further by enrichment of diazotrophs from acidic YNP hot springs that were shown to fix nitrogen *in situ* via acetylene reduction assays (Hamilton et al., 2011b). In contrast, *amoA*, a gene associated with ammonia oxidation, is predominantly found in circumneutral to basic hot springs, and ammonia-oxidizers have only been enriched from circumneutral to basic YNP hot springs (De la Torre et al., 2008; Hatzenpichler et al., 2008; Hamilton et al., 2011b; Boyd et al., 2013). It is hypothesized that ammonia-oxidizers outcompete diazotrophs in circumneutral to basic hot springs, consuming the bioavailable nitrogen, thereby producing a downstream niche for diazotrophs (Hamilton et al., 2014). Genetic and geochemical analyses both implicate nitrogen as a determining factor for microbial community composition in YNP hot spring outflows.

In this study, 12 hot spring outflows in YNP were selected for sampling above, at, and below the photosynthetic fringe spanning temperatures from 28.9 to 92.2°C, pH from 1.9 to 9.0, and sulfide concentrations from below the detection limit ($<$0.15 μmolal) to 52.6 μmolal (**Supplementary Table 1**). Due to this sampling scheme, each of the 12 hot spring outflows differ in both geochemical and microbiomic diversity and complexity, in addition to differing in history and geographic location. Site selection used linear discriminant analysis (LDA) of multiple geochemical parameters to estimate equidistant geochemical space above and below the visual photosynthetic fringe, for a total of 46 samples. Communities in sample sites above the photosynthetic fringe were expected to consist predominantly of chemotrophs, while those below the photosynthetic fringe were expected to contain a larger contribution of phototrophs. Samples at the photosynthetic fringe provided insight into the transition between the predominantly chemotrophic to the phototroph-containing microbial communities. From each sample site, geochemical measurements were taken including temperature, pH, conductivity, total sulfide, total dissolved silica, ferrous iron, dissolved oxygen gas (DO), DOC, DIC, and major cation and anion concentrations (**Supplementary Tables 1, 2**). In addition, 16S rRNA gene sequencing was performed using a sediment slurry from each sample location to determine the microbial community composition along the hot spring outflows (**Supplementary Table 3**). In combination, the geochemical measurements and sequencing data provide insights into how both the microbial community and the geochemistry change and interact down hot spring outflows and across the photosynthetic fringe. However, we find collapsing the complexity of these hot spring outflows into a list of geochemical variables was insufficient to determine the exact position of the photosynthetic fringe in geochemical space.

2. Materials and methods

2.1. Sample site selection via LDA

Sampling locations (**Supplementary Table 1**) were determined by linear discriminant analysis (LDA), in which at least three samples were collected to represent locations *below* (chemosynthetic and photosynthetic), *at* (fringe), and *above* (chemosynthetic) the photosynthetic fringe in hot spring outflow channels, though additional samples were taken at several sites to provide additional biogeochemical context. The LDA model (Equation 1) was trained to separate samples into photosynthetic and non-photosynthetic classes based on 20 variables measured across 56 samples collected from twenty-nine geochemically diverse hot springs in previous years. The 20 variables selected to construct the LDA model were chosen based on perceived biological relevance, specifically, temperature, pH, conductivity, DIC, DOC, DO, Fe(II), sulfide, phosphate, total ammonia, and total dissolved Mg, Co, Ni, Cu, Zn, As, Mo, Cd, W, and Pb. Fe(II) was used in place of total Fe because Fe(II) could be measured in the field spectrophotometrically. Additionally, representative variables were chosen per element, for example, total ammonia is representative for nitrogen species. Samples above the photosynthetic fringe tend to have greater negative LDA scores, while samples below tend to have greater positive scores. Photosynthetic fringe positions were determined visually when possible and by LDA when not discernable by eye. When testing the LDA model on 381 previously collected samples, where photosynthesis had been identified by the visual presence of photosynthetic pigments, an LDA score of 0.13 predicted photosynthetic and non-photosynthetic samples with the fewest number of false positives and negatives. In outflow channels where the fringe was not apparent, the location of the fringe was estimated by choosing a location where the LDA score was close to or equal to 0.13 based on temperature, pH, and conductivity measured in the field combined with historical data for the remaining 17 variables in the LDA model. In the outflow of CF and MO, the photosynthetic fringe was apparent but occurred at different temperatures throughout the hot spring outflow, hence multiple samples were taken throughout the outflows to account for these variations. Sampling locations were chosen such that they were chemically equidistant from the fringe as estimated by the LDA model. In other words, sampling was carried out such that the difference in LDA scores between the *at* and *below* samples was equal to the difference between *above* and *at* scores. The LDA model was trained using the lda function in the MASS package in R (RRID:SCR_019125) (Venables and Ripley, 2002; R Core Team, 2013).

Equation 1.

$$\begin{aligned} \textit{Line 1}:\ \textit{LDA score} &= \textit{1.028E} - \textit{1 pH} + \textit{6.769E} - \textit{5 conductivity} \\ &\quad (\mu S) - \textit{6.12E} - \textit{2 temperature}\ (^{\circ}C) \end{aligned}$$

$$\begin{aligned} \textit{Line 2}:\ & + \textit{2.037E} - \textit{4 DIC}\ (\textit{mg C/L}) + \textit{7.199E} - \textit{3 DOC} \\ & (\textit{mg C/L}) + \textit{1.746E} - \textit{1 DO}\ (\textit{ppm}) \end{aligned}$$

$$\begin{aligned} \textit{Line } 3:\ & - 2.610E - 2\ \ \textit{Fe(II)}\ (\textit{ppm}) - 9.36E - 5\ \Sigma HS^{-} (\textit{ppb}) \\ & - 2.242E^{-2}\ \Sigma PO_4^{3-}\ (\textit{ppm}) \end{aligned}$$

$$\begin{aligned} \textit{Line } 4:\ & - 1.615E - 3\ \Sigma NH_4^{+}\ (\textit{ppm}) - 2.57E - 5\ \Sigma Mg\ (\textit{ppb}) \\ & - 2.01E - 2\ \Sigma Co\ (\textit{ppb}) \end{aligned}$$

$$\textit{Line } 5: + 2.39E - 2\ \Sigma Ni\ (\textit{ppb}) + 2.89E - 3\ \Sigma Cu\ (\textit{ppb})$$

$$\begin{aligned} \textit{Line } 6:\ & - 2.77E - 3\ \Sigma Zn\ (\textit{ppb}) - 2.35E - 4\ \Sigma As\ (\textit{ppb}) \\ & - 6.35E - 3\ \Sigma Mo\ (\textit{ppb}) \end{aligned}$$

$$Line\,7: \; -7.15E-1\,\Sigma Cd\,(ppb) + \;2.44E-3\,\Sigma W\,(ppb) \\ -2.35E-2\,\Sigma Pb\,(ppb)$$

Sigma symbols indicate that the variable includes measured values of total solute concentrations and includes all protonation states and complexes.

2.2. Geochemical sampling and analyses

Temperature, pH, and conductivity were measured in the field as previously described (Boyer et al., 2020). Temperature and conductivity were measured using a YSI-30 portable meter (YSI, Yellow Springs, OH, USA). Measurements of pH were obtained using a WTW 3110 meter and SenTix 41 temperature-compensated probes (Xylem Analytics, Weilheim, Germany) calibrated daily at ambient temperature using buffered pH solutions. Dissolved oxygen was measured optically using a PreSens Fibox 4 meter and a DP-PSt3-L2.5-St10-YOP-HT sensor calibrated to 100°C (PreSens, Regensburg, Germany) as previously described (St Clair et al., 2019). Total dissolved sulfide was determined via the methylene blue method using Hach reagents and a DR1900 spectrophotometer on unfiltered water samples and analyzed immediately after collection.

Filtered (0.2 micron; Supor, Pall Corporation, Port Washington, NY, USA) water samples for laboratory analyses were collected and stored according to previously described procedures (Fecteau et al., 2022). Samples for anions were collected in 30 ml high-density polyethylene (HDPE) bottles that had been soaked and rinsed with deionized water multiple times; separate 30 ml samples for cations were collected in bottles that had been spiked with 6 M methanesulfonic acid resulting in a final concentration of ∼20 mM. These samples were frozen at –20°C as soon as possible after collection and maintained at that temperature until analysis. DIC samples were collected in acid-washed 40 ml amber class vials and sealed with black butyl rubber septa without any headspace. DOC samples were collected in combusted (450°C, 24 h) 40 ml amber glass vials spiked with 0.1 ml of 85% phosphoric acid (Thermo Scientific, Waltham, MA, USA) and sealed with Teflon-lined septa without any headspace.

Anions (F^-, Cl^-, $SO_4{}^{-2}$, Br^-, $NO_3{}^-$) and cations (Li^+, Na^+, K^+, Mg^{+2}, Ca^{+2}, $NH_4{}^+$) were determined on separate Dionex DX-600 4 mm ion chromatography systems using suppressed-conductivity detection as described elsewhere (Iacovino et al., 2020). Samples were injected via AS-40 autosamplers from 5 ml vials (2 injections per vial) onto 100 μl or 75 μl sample loops for anions or cations, respectively. Anions were separated using AG-/AS-18 columns and a hydroxide concentration gradient that was initially held isocratically at 5 mM for 10 min, followed by a non-linear (Chromeleon curve 8) (RRID:SCR_016874) gradient applied over 32 min to 55 mM hydroxide, after which the concentration was kept constant at 55 mM for 7 min, reduced back to 5 mM hydroxide over 1 min, and then the column was re-equilibrated at 5 mM hydroxide for 10 min before the next sample injection. The flow rate was held constant at 1 ml/min. Cations were separated isocratically using 19 mM methanesulfonic acid on CG-/CS-16 columns at 0.5 ml/min over 58 min. Suppressors were operated in external water mode and suppressor currents were 137 and 50 mA for anions and cations, respectively. Calibration curves were constructed from a series of dilutions of mixed-ion standards (Environmental Express, Charleston, SC, USA) and accuracy was verified daily by analysis of an independent mixed-ion standard (Thermo Scientific).

Analyses of DIC and DOC were performed with a OI Wet Oxidation TOC analyzer coupled to a Thermo Delta Plus Advantage mass spectrometer as previously described (Havig et al., 2011). Briefly, CO_2 was generated via addition of phosphoric acid (DIC) or sodium persulfate (DOC) and the ion chromatogram for the molecular ion (44 m/z) was used for quantification relative to calibration curves prepared with sodium bicarbonate (DIC) or glycine (DOC) standards. Three sample loops with volumes of 1 ml (calibration range 10–200 mg C L^{-1}), 5 ml (calibration range 2–50 mg C L^{-1}), and 25 ml (calibration range 0.25–8 mg C L^{-1}) were employed to capture the range of carbon concentrations across the sample set.

2.3. Biological sampling, extractions, and sequencing

Hot spring outflow sediment samples were collected and preserved for biological analyses (16S rRNA gene amplicon sequencing and subsequent microbial community diversity analyses). Samples were collected using a flame-sterilized spatula into a 1.8 ml cryovial. Once samples were collected, they were transferred into a container of dry ice and frozen until they could be stored at −80°C at ASU.

For DNA extraction, biological samples were homogenized, and DNA was extracted using a ZymoBIOMICS DNA Miniprep Kit (Catalog # D4300), binding capacity 25 μg, as previously described (Howells, 2020). A NanoDrop was used to spectrophotometrically analyze the purity of the DNA and a Qubit fluorometric assay kit from Invitrogen (Catalog # Q32850) was used to determine the concentration of purified DNA. The DNA was then sequenced for both bacterial and archaeal 16S rRNA gene amplicons at Arizona State University's Biodesign Institute using Illumina MiSeq v2 2 × 300 chemistry (RRID:SCR_020134) with the Earth Microbiome Project primers 505F and 806R (Thompson et al., 2017). The 16S rRNA gene amplicon library was prepared following Earth Microbiome Project protocol,[1] (Caporaso et al., 2012). All raw sequences were uploaded to the NCBI Sequence Read Archive (SRA) (RRID:SCR_004891) under BioProject ID PRJNA938133.

2.4. Bioinformatic analyses

FASTQC (v. 0.11.9) (RRID:SCR_014583) was used to quality filter the 16S rRNA amplicon sequences (Andrews, 2010). The resulting high quality fasta files were then processed using the QIIME2 (v. 2020.2) (RRID:SCR_021258) pipeline to produce amplicon sequence variants (ASVs) and were denoised using the DADA2 plug-in (Bolyen et al., 2019). The SILVA database (RRID:SCR_006423) was used for the taxonomic classification of ASVs (Quast et al., 2012). The produced ASV table was normalized by putting the sequence counts into relative abundances and

---

[1] http://www.earthmicrobiome.org/protocols-and-standards/16s/

multiplying them by the mean library size (**Supplementary Table 3**; Fullerton et al., 2021). Non-metric multidimensional scaling (NMDS) analyses were performed using VEGAN R software (v. 2.5-7) (RRID:SCR_011950) and Bray-Curtis Dissimilarity values (Oksanen et al., 2022). The envfit function from the VEGAN package was used to add geochemical vectors to the NMDS and to calculate the respective *p*-values for each geochemical vector. The percent contribution for each geochemical vector was determined using the redundancy analysis (RDA) function in the VEGAN package. To determine the significance of separating sites as above, at, or below the photosynthetic fringe, analysis was performed using the canonical correlation analysis (CCA) function from the VEGAN package and an ANOVA test was performed on each axis using the R stats package. For the co-occurrence network analysis, ASVs were filtered to only include ASVs that had more than 20 reads across all samples and occurrences across more than 3 sample sites. The remaining ASVs were used to construct a co-occurrence network using R's igraph package (v. 1.2.11) (RRID:SCR_021238), in which each node is an ASV, and each edge represents a Spearman's correlation coefficient greater than 0.7 between the two nodes (Csardi and Nepusz, 2006; Fullerton et al., 2021). Cliques were determined by using the Louvain membership algorithm (Csardi and Nepusz, 2006). The nodes were then plotted and colored in Gephi (v. 0.9.4) (RRID:SCR_004293) based on their Spearman correlation with the selected geochemical variables (Bastian et al., 2009).

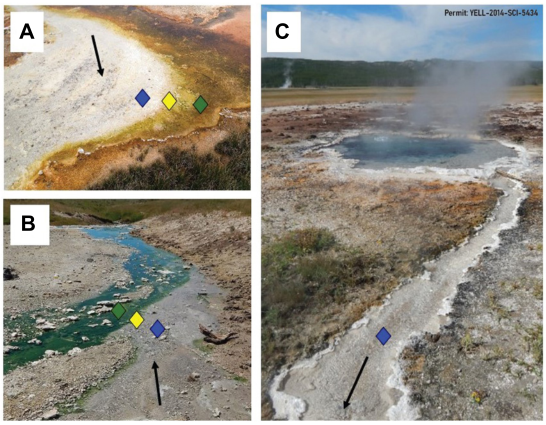

FIGURE 1
Hot spring outflows with depictions of the photosynthetic fringe. Locations above (blue), at (yellow), and below (green) the photosynthetic fringe are indicated by respective diamonds. Black arrows indicate a general flow of water away from the source. **(A)** The visual representation of the photosynthetic fringe in the outflow of a basic spring, BP, where the white sinter in the outflow meets orange phototrophic mats along the edge of the outflow. **(B)** The visual representation of the photosynthetic fringe in the outflow of an acidic spring, CF, where the clear outflow meets green phototrophic mats. **(C)** An example of the start of a hot spring outflow channel from a basic hot spring, BP, before reaching its photosynthetic fringe.

3. Results

3.1. Sampling locations and geochemical data

A total of twelve hot springs from eight separate locations within YNP were sampled to investigate the connection between the microbiomic and geochemical transitions that occur down hot spring outflows (**Supplementary Table 1** and **Supplementary Figure 1**).

To select sample sites, an LDA equation was developed (see section 2. Materials and methods) to determine the locations above and below the photosynthetic fringe such that sampling would be equidistant from the fringe in multivariate geochemical space. The photosynthetic fringe can often be visually confirmed as seen in example images of a sampled basic (**Figure 1A**) and an acidic (**Figure 1B**) hot spring outflow channel. An example of a sampled hot spring outflow before reaching the photosynthetic fringe is shown in **Figure 1C**. In 3 of the 12 hot spring outflows, the photosynthetic fringe could not be visually identified, so temperature, pH, and conductivity measurements were taken along the hot spring outflow and used in the LDA model to predict the location of the photosynthetic fringe.

In total, 46 samples were taken with the intention of spanning the temperature, pH, and sulfide ranges provided by YNP hot springs (**Figure 2** and **Supplementary Table 1**). Of the 12 hot spring outflows sampled, four were acidic ($pH < 4$) (CF, MO, GL, and CH), three were acidic to circumneutral (pH 4–7) (MU, FI, and EM), and five were considered basic (pH 7–9) (RN, OB, BP, PB, and MN). Additionally, Shannon diversity values were computed to assess the alpha diversity of the microbial community and range from 2.63 to 5.93 (**Supplementary Table 1**). This study includes additional geochemical measurements of total ammonia, nitrate, DIC, DOC, and DO concentrations (**Supplementary Table 1**). Of the major ions measured, total ammonia and nitrate were the two most significant ions, contributing 3.78 and 2.55%, respectively, to overall microbial community composition (**Supplementary Table 4**) determined via the VEGAN package in R using RDA. Total ammonia concentrations span a range of 0.63–1171 μmolal, whereas nitrate concentrations are 0.07–1.01 μmolal. DOC and DIC concentrations span a range of 0.20–1.89 mg C/L, and 0.04–66.98 mg C/L, respectively. All Pearson correlations between the geochemical measurements from each sample are included in **Supplementary Figure 3**. According to the Pearson correlation values, there are nine strongly correlated (> 0.50) geochemical parameters. There are strong positive correlations between temperature and pH (0.58), temperature and DIC (0.71), pH and DIC (0.79), and ammonia and DO (0.53). Strong negative correlations include temperature with total ammonia (−0.61), temperature with DO (−0.78), pH with ammonia (−0.57), pH with DOC (−0.77), ammonia with DIC (−0.53), and DIC with DOC (−0.68). There are no strong positive or negative correlations between sulfide or nitrate concentrations and any of the other geochemical parameters.

3.2. Microbial community composition

The relative abundance of taxonomic classes present in each of the 46 samples was determined by 16S rRNA gene sequencing to investigate the microbial community composition and diversity

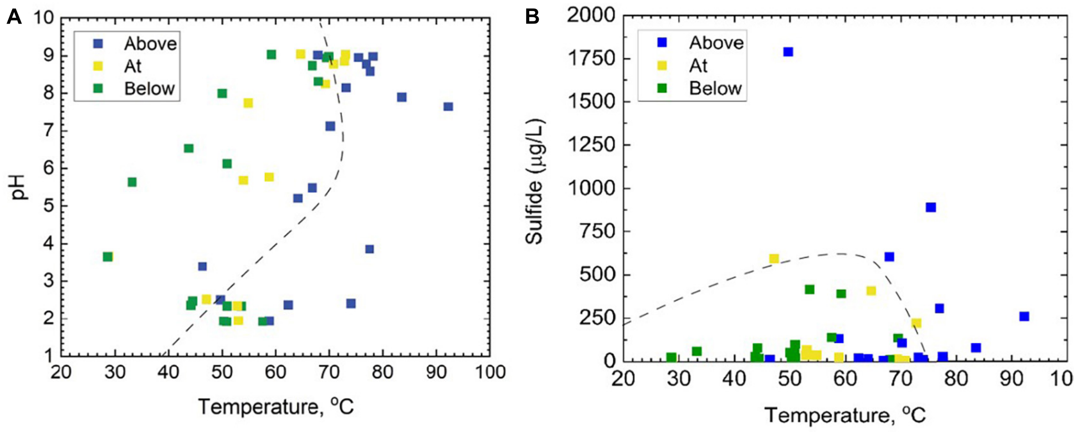

FIGURE 2
A total of 46 samples taken from the outflows of 12 separate hot springs above, at, and below the photosynthetic fringe, as determined by linear discriminant analysis, displayed as functions of **(A)** pH and temperature, and **(B)** total dissolved sulfide and temperature. In both panels **(A,B)**, the dashed line represents the photosynthetic limits defined by Cox et al. (2011).

along each outflow and among the hot springs sampled (**Figure 3**). In each of the hot springs sampled, ASVs associated with the taxonomic classes Thermotogae, Planctomycetia, Deinococci, Aquificae, Thermoprotei, and Nitrososphaeria were present. Aquificae and Deinococci were present in high relative abundances across all hot springs, up to 96.8 and 33.0%, respectively. In the four most basic springs sampled (RN, OB, MN, and PB), Deinococci reached relative abundances greater than 30%. Additionally, Nitrososphaeria occurred across all hot springs sampled with the highest relative abundances occurring in the basic sites, RN and OB, and above the photosynthetic fringe with relative abundances of 37.4 and 28.4%, respectively. Both Thermotogae and Planctomycetia occurred at all hot spring sites but had consistently low relative abundances, ranging from around 0.1–9.0 and 0.1–4.9%, respectively, when present. Additionally, there were unidentified bacteria present in each of the hot springs sampled with the highest relative abundances in acidic hot springs. As an example, below the photosynthetic fringe of GL, where the pH is 2.5, unidentified bacteria made up 21.2% of the community.

Amplicon sequence variants associated with photoautotrophs, including those in the phyla Cyanobacteria and Chloroflexi, such as *Leptococcus* and *Chloroflexus*, respectively, occurred with higher relative abundances in the circumneutral to basic hot spring outflows. Both Cyanobacteria and Chloroflexi occurred in nearly all hot spring outflows sampled, except, neither Cyanobacteria nor Chloroflexi occurred in the outflow of GL (49.7 °C, pH 2.5) or MO (74.0°C, pH 2.4), nor did Chloroflexi occur in the outflow of FI (64.1 °C, pH 5.2). Furthermore, neither Cyanobacteria nor Chloroflexi surpassed a relative abundance of 0.1% in the outflow of any of the acidic hot springs sampled. Chloroflexi reached relative abundances above 1% only at pH values greater than 7, while Cyanobacteria reached a relative abundance above 1% only at pH values greater than 8. In basic conditions, Chloroflexi and Cyanobacteria made up to 30.7 and 25.6% of the microbial community, respectively, at their highest relative abundances. Chloroflexi occurred above, at, and below the visually determined photosynthetic fringe. However, Chloroflexi reached higher relative abundances at (0.9–2.4%) and below (0.0–22.6%) the photosynthetic fringe compared to above (0.0–3.4%). Cyanobacteria were also identified above the visually detected photosynthetic fringe but did not surpass a relative abundance of 1.8% except at outflow sample BP0.5, where the relative abundance was 6.2%. In contrast, at and below the photosynthetic fringe, the relative abundances for Cyanobacteria made up to 25.6% of the microbial community. ASVs associated with putative photoheterotrophs were also present, including those in the taxonomic classes of Alphaproteobacteria and Acidobacteriia, such as *Acidiphilium, Acidisphaera*, and *Chloracidobacterium*, which, when combined, only surpass a relative abundance of 1% in a single sample, MU3, where they make up 4.0% of the community.

Samples at or below the photosynthetic fringe indicate an apparent cut-off for photosynthesis at ∼73°C for basic to circum neutral pH samples (**Figure 2A**). The temperature cut-off for photosynthesis is lower, ∼56°C, for the outflow of acidic hot springs (**Figure 2A**), consistent with previous studies (Cox et al., 2011; Boyd et al., 2012; Fecteau et al., 2022). However, it should be noted that there are samples categorized as being "above" the photosynthetic fringe that are within these temperature limits, indicating additional factors may be restricting the growth of photosynthetic organisms in individual locations. Common bacterial phototrophs, such as Cyanobacteria and Chloroflexi, are abundant in basic hot spring outflows at and below the photosynthetic fringe, but also occur in small relative abundances above the visually determined photosynthetic fringe (**Supplementary Figure 2**). None of the 46 sample sites that were below the photosynthetic fringe had total sulfide concentrations that exceeded 500 μg/L; however, there was one sample, GL2, assessed to be "at" the photosynthetic fringe that exceeded 500 μg/L, the suggested sulfide limit defined by Cox et al. (2011) (**Figure 2B**).

In addition to ASVs associated with photosynthetic taxa occurring in the circumneutral to basic hot spring outflows, ASVs associated with non-phototrophs in the taxonomic classes of Acetothermia, Kapabacteria, Fervidibacteria, Hydrothermae, Anaerolineae, and the phylum Armatimonadota were also present.

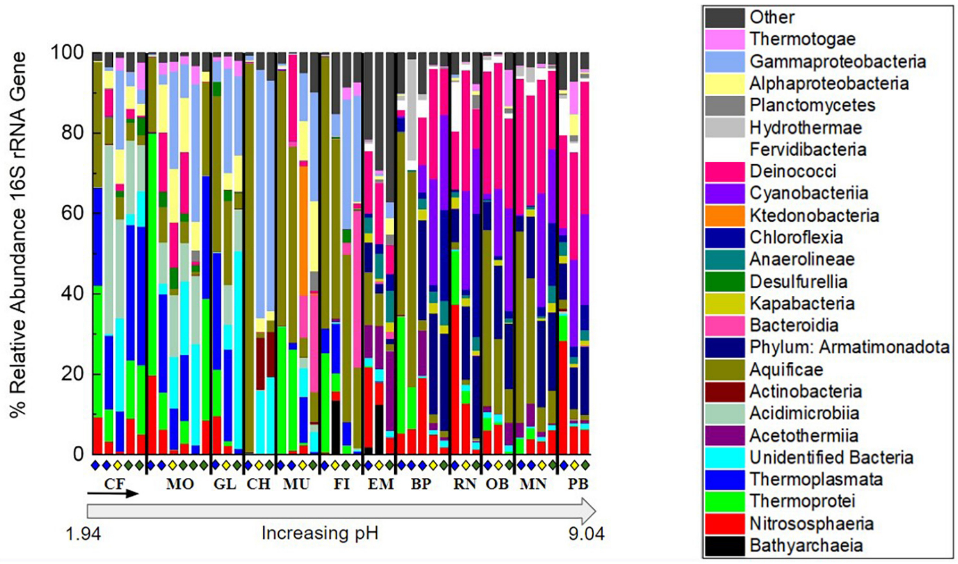

FIGURE 3
Percent relative abundance of the 16S rRNA gene sequencing results to the class level except for Armatimonadota, which is at the phylum level, and unidentified bacteria, which were binned together at the domain level. To focus on abundant features and overarching patterns, classes not occurring at >20% relative abundance when summed over all samples were binned into the "Other" category. Organization of hot spring sites, separated by black bars, follows the order of increasing pH shown in **Supplementary Table 1**. Within each site, samples are organized down the outflow with above (blue diamond), at (yellow diamond), and below (green diamond) the photosynthetic fringe indicated as in **Figure 1**.

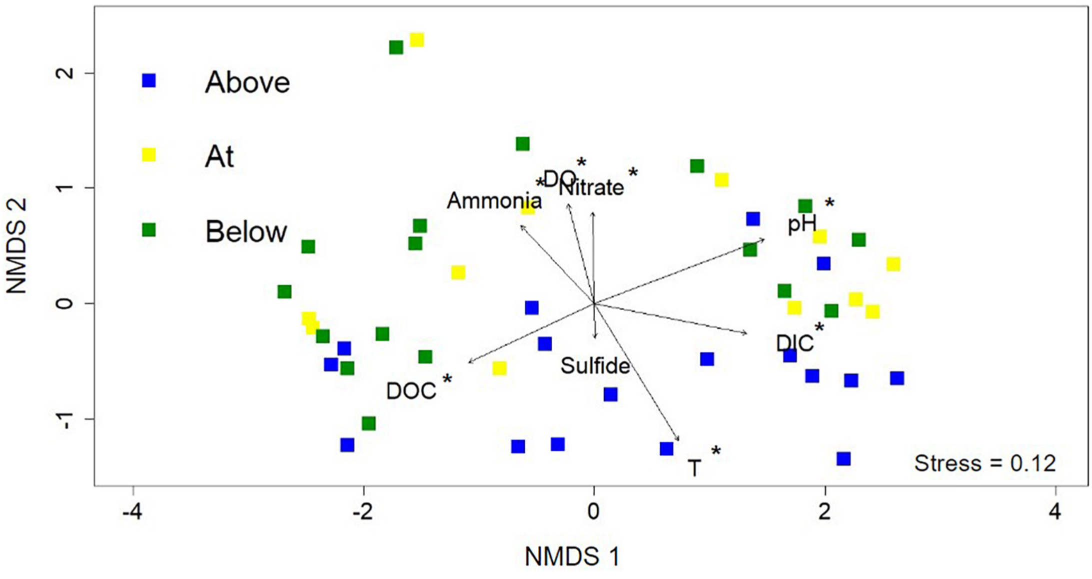

FIGURE 4
Non-metric multidimensional scaling (NMDS) analysis using the 16S rRNA gene sequencing data from each of the 46 samples. Each point represents the normalized microbial community composition determined in a hot spring sample while the distance between points represents the dissimilarity. Sample point colors (blue, yellow, and green) refer to the position along the photosynthetic fringe (above, at, below, respectively). Geochemical data are added as vectors; vectors that correlate with an ordination axis with a p-value < 0.05 are indicated by an asterisk.

Although Cyanobacteria and Chloroflexia were abundant within the outflow of basic hot springs, ASVs associated with the non-photosynthetic phylum Armatimonadota were also prevalent in these samples, occurring with an average relative abundance of 13.5% when present. Armatimonadota were present in every sample above a pH of 7, except for sample site 0.5 from BP. As for the ASVs associated with the taxonomic classes Acetothermia, Kapabacteria, Fervidibacteria, Hydrothermae, and Anaerolineae, they reached relative abundances above 1% only above a pH of 7 but none were as consistently predominant as ASVs associated with the phylum Armatimonadota.

The ASVs abundant in the lower pH sites (pH < 7) include ASVs from the following taxonomic classes: Gammaproteobacteria, Alphaproteobacteria, Desulfurellia,

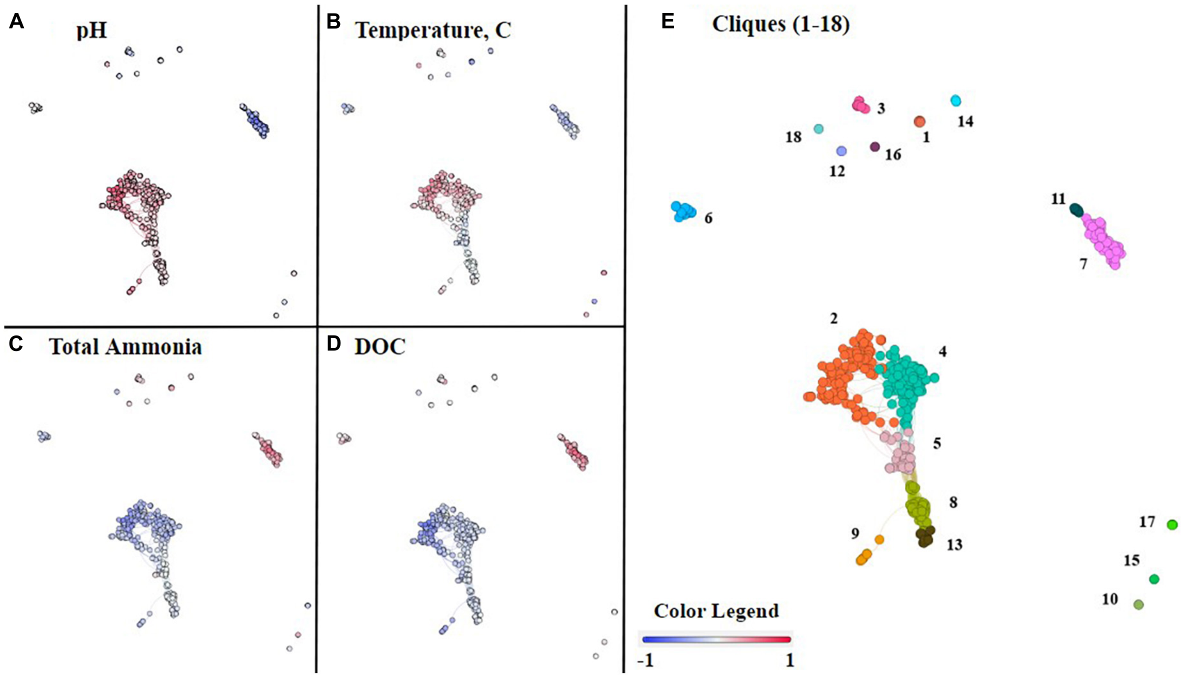

FIGURE 5
Co-occurrence network analysis of commonly occurring ASVs within the 46 hot spring samples. Each node represents an ASV, and nodes were organized into 18 cliques using Louvain's membership algorithm. The connections between nodes, also known as edges, represent a >0.7 Spearman's correlation coefficient. In panels **(A–D)**, each node is colored on a gradient of blue to red based on its Spearman's correlation, from negative one to positive one, respectively, with the following geochemical parameters, **(A)** pH, **(B)** temperature, **(C)** total ammonia, and **(D)** DOC. Each of the cliques is differentiated by color and number in panel **(E)**.

Actinobacteria, Acidimicrobiia, and Thermoplasmata. Gammaproteobacteria, Alphaproteobacteria, and Actinobacteria were present in at least one sample from each hot spring outflow but reached relative abundances above 1% only at acidic sites. Acidimicrobiia were present in all hot springs sampled except for in the outflow of MN (75.4°C, pH 9.0) and only reached a relative abundance over 10% at pH values below 3. Gammaproteobacteria had a high relative abundance of 61.8% at the photosynthetic fringe of hot spring CF where the temperature was 28.8°C and the pH was 3.7. Thermoplasmata and Desulfurellia were restricted to circumneutral and acidic sites, only occurring below a pH of 8.0 and 6.5, respectively, with Desulfurellia only making up to 5.3% of any microbial community composition, while Thermoplasmata reached up to 34.5% of the relative abundance of the microbial community composition below the photosynthetic fringe of CF.

Additionally, there were ASVs associated with three taxonomic classes that were restricted to circumneutral conditions, including Ktedonobacteria, Bacteroidia, and Bathyarchaea. Ktedonobacteria only occurred with a relative abundance higher than 1% at the photosynthetic fringe of MU, where they made up 32.2% of the community, which is at a pH of 5.7. Bacteroidia occurred across pH, but only made up more than 1% of the community in the outflows of MU, FI, and EM, which range in pH from 3.9 to 8.0. Below the photosynthetic fringe of FI, Bacteroidia made up 39.0% of the microbial community. Bathyarchaea were present in small relative abundances (<0.1%) in the outflows of RN and CF but occurred with relative abundances of 13.6 and 12.6% at the photosynthetic fringes of FI and EM, respectively. The photosynthetic fringe of FI occurred at a pH of 5.8 while the photosynthetic fringe of EM occurred at a pH of 7.8.

Overall, there were trends in microbial community composition across pH as well as down the outflows of the 12 sampled hot springs. In the lower pH sites, ASVs associated with taxonomic classes such as Thermoplasmata and Gammaproteobacteria dominated. In basic sites, ASVs associated with the phylum Armatimonadota dominated, as well as ASVs associated with the potentially photosynthetic phyla, Cyanobacteria and Chloroflexi. The relative abundance of potential bacterial photosynthetic taxa increased in relative abundance with increasing pH and increased down hot spring outflows. In contrast, the relative abundance of the taxonomic class Hydrothermae decreased down hot spring outflows. At all hot springs and outflows, ASVs for the taxonomic classes Aquificae and Deinococci were present and made up a considerable portion (19.0 and 10.8% when averaged across all samples, respectively) of the microbial community composition.

3.3. Geochemical influence on community composition

Non-metric multidimensional scaling (NMDS) analysis was used to interrogate the influence of geochemistry on microbial community composition across the photosynthetic fringe (Figure 4). The 16S rRNA gene sequencing data was used to determine the microbial community composition (Supplementary Table 5). Geochemical vectors for each of the geochemical measurements were initially added to indicate potential causes for differences in microbiome composition in the 46 sampled locations; however, only a subset of eight geochemical vectors were included due to either their hypothesized importance (sulfide), or their contribution to the variation of the microbial community composition determined by RDA (pH, Temperature, DIC, DOC, nitrate, total ammonia, and DO) (**Supplementary Table 4**). Of the eight included geochemical vectors, all correlated with changes in microbial community composition with statistical significance ($p > 0.05$) except for sulfide. Along NMDS2, the distribution of sites can be differentiated based on position relative to the photosynthetic fringe. However, only sites labeled as being above the photosynthetic fringe can be differentiated from the sample sites at or below the photosynthetic fringe with statistical significance according to CCA analysis (**Supplementary Figure 5**). The geochemical vectors that correlate with changes in microbial community composition along NMDS2 with statistical significance are ammonia, DO, temperature, and nitrate, all of which increase down the hot spring outflows. There is more variation in microbial community composition across NMDS1 which correlates with changes in pH, DIC, and DOC with statistical significance. This indicates that there is a complex interplay between geochemical parameters and microbial community composition.

While NMDS analyses provide insight into overall microbial community composition in relation to geochemical parameters, co-occurrence network analyses provide insight at the level of individual ASVs and their correlation(s) with geochemical parameters (Fullerton et al., 2021). In a co-occurrence network, each node is an ASV. All nodes were grouped into 18 unique cliques (statistically significant groups of ASVs) using the Louvain algorithm and consisted of at least two nodes (**Supplementary Table 6**; Fullerton et al., 2021). Clique analysis provides a mechanism for observing microbial patterns within guilds and individuals rather than as an entire assemblage (e.g., NMDS).

The co-occurrence network consisted of ten cliques with no interconnections (modular cliques), a central cluster consisting of six interconnected cliques, and a separate cluster of two cliques. This topology suggests there are groups of ASVs that uniquely co-occur (modular cliques) and groups of ASVs that co-occur predominantly with each other (main cluster cliques). Some members of the main cluster cliques co-occur with ASVs outside the clique as well. The statistical association of the cliques with geochemical parameters of interest was conducted by Spearman correlation. From these combined analyses we can observe how cliques and individual ASVs co-varied with pH, temperature, total ammonia, DIC, DOC, nitrate, and sulfide concentrations (**Figure 5**; **Supplementary Figure 6**).

Within the main cluster of six cliques (2, 4, 5, 8, 9, and 13) all ASVs correlated positively with an increase in pH (**Figure 5A**). The remaining cliques, outside the central cluster, are composed of ASVs that mostly occur in acidic or circumneutral samples, and, therefore, either correlate negatively or have no significant correlation with increasing pH. However, cliques 17 and 18 are an exception, and like the main cluster cliques, are correlated with an increase in pH.

The main cluster cliques consist of the phototrophs *Leptococcus*, *Roseiflexus*, and *Chloroflexus*, as well as non-phototrophs from the taxonomic classes Aquificae, Anaerolineae, Deinococci, Acetothermiia, and the phylum Armatimonadota among others listed in **Supplementary Table 6**. Due to the prevalence of Aquificae and Deinococci throughout the dataset, it is important to note that the genera present in the main cluster cliques are *Thermocrinis* and *Thermus*, respectively. Although all 6 cliques within the main cluster are correlated positively with an increase in pH, only cliques 2, 4, and 9, which include ASVs associated with the taxa *Thermocrinis,* Deinococci*, Leptococcus,* Acetothermia, and Armatimonadota, are positively correlated with temperature. Clique 5 is correlated slightly negatively with temperature and consists of the taxonomic classes Anaerolineae, Acetothermia, and the phylum Armatimonadota. Additionally, cliques 2, 4, and 9 are all correlated negatively with total ammonia, whereas the nodes in clique 5 are mixed between positive and negative correlations with total ammonia. The remaining cliques in the cluster (8 and 13) are not correlated with total ammonia. In contrast, all 6 cliques within the cluster are correlated negatively with DOC, although cliques 2 and 9 have a stronger negative correlation with DOC than cliques 4, 5, 8, or 13.

Outside of the main cluster cliques, there are five cliques (3, 7, 11, 12, and 15) that are correlated negatively with pH. Cliques 7 and 11 are interconnected and tend to follow similar trends. Cliques 7 and 11 include ASVs associated with the taxonomic classes Acidimicrobiia, Thermoplasmata, Deinococci, and Aquificae. In this case, Deinococci is represented by *Meiothermus*, and Aquificae is represented by *Hydrogenobaculum*. Cliques 7 and 11 are correlated positively with total ammonia and DOC concentrations but are correlated negatively with pH and temperature. The only major differences in trends for cliques 7 and 11 are displayed in **Supplementary Figure 6**, where clique 7 has a strong negative correlation with nitrate, whereas clique 11 has a slight positive correlation with nitrate.

The unconnected cliques, 3, 12, and 15, are also correlated negatively with pH. Cliques 3, 12, and 15, which contain the taxa *Meiothermus,* Acidimicrobiia, Gammaproteobacteria, Alphaproteobacteria, and Thermoprotei, are correlated positively with total ammonia and DOC concentrations. However, cliques 3 and 12 are correlated negatively with pH but not temperature, whereas clique 15 is negatively correlated with both temperature and pH.

In contrast to the previously mentioned cliques, cliques 17 and 18 are correlated positively with an increase in pH and are outside of the central cluster. Clique 18, which only contains two taxa, Fervidicoccaceae and *Ignisphaera*, a Thermoprotei, is positively correlated with both temperature and pH but negatively correlates with both total ammonia and DOC. Clique 17 contains Nitrososphaeria and Thermoprotei and is correlated positively with temperature, but has no strong correlation with total ammonia or DOC.

The remaining cliques, 1, 6, 10, 14, and 16, lack strong correlations with pH in either direction. Cliques 6, 10, and 16 are only correlated with temperature, cliques 6 and 16 correlated negatively with temperature, and clique 10 correlated positively with temperature. Clique 6 is correlated negatively with temperature and total ammonia concentration but is correlated positively with DOC. Besides temperature, cliques 10 and 16 cannot be differentiated based on pH, total ammonia, or DOC. However, clique 16 is correlated negatively with sulfide and is positively correlated with nitrate (**Supplementary Figure 6**). There are only 2 nodes in clique 16 representing the phylum

Armatimonadota and the genus *Thermoflavifilum*, whereas clique 10 contains the taxa Geoarchaeales and Corynebacterium. Clique 14 is unique in that it is correlated negatively with temperature but has a slight positive correlation with total ammonia. The taxa in clique 14 include *Meiothermus,* Betaproteobacteria, and Gammaproteobacteria. Clique 1, which consists of *Mycobacterium* and *Thiomonas*, is correlated positively with temperature and correlated negatively with total ammonia, but is not strongly correlated with temperature or DOC.

Overall, we find internal consistencies between the pH of samples where ASVs are abundant and the correlation with pH in the co-occurrence networks. For example, taxa associated with higher pH samples in **Figure 3** are located within the 6 cliques in the main cluster in **Figure 5** and are correlated positively with pH. Of the twelve remaining cliques surrounding the cluster, five of them are negatively correlated with pH, including 3, 7, 11, 12, and 15, and include taxa associated with low pH samples in **Figure 3**. Cliques 17 and 18 are correlated positively with pH and contain taxa associated with circumneutral to basic samples, as well as Thermoprotei, a taxonomic class found in all hot springs sampled. Finally, the remaining cliques, 6, 10, and 16, show no strong correlation with pH in either direction and contain taxa such as *Meiothermus*, from the class Deinococci, and Armatimonadota, both of which are found across all hot springs sampled.

4. Discussion

The stark visual differences in microbial community compositions above versus below the photosynthetic fringe of hot spring outflows were also observed in the NMDS analysis in the distribution of points relative to their location across the photosynthetic fringe, as determined by LDA analysis (see section 2. Material and methods; **Figure 4**). The difference in the microbial community composition above versus below the photosynthetic fringe was determined and verified to be statistically significant ($p < 0.05$) through an ANOVA test of the CCA axes (**Supplementary Figure 5**). In contrast, metrics of alpha diversity showed no significant correlation to the LDA-determined photosynthetic fringe (**Supplementary Figure 7**).

The photosynthetic fringe is not necessarily indicative of an ecotone as described by Meyer-Dombard et al. (2011) (**Supplementary Table 1**), which is a region where there is either an increase or a decrease in biological diversity where two or more communities mix (van der Maarel, 1990; Meyer-Dombard et al., 2011). Because the photosynthetic fringe represents a transition from a chemotrophic microbial community to a community also consisting of phototrophs, there is the potential that this transition promotes biological diversity. Ecotones have been identified at the photosynthetic fringe of hot spring outflows with streamer biofilm communities, but ecotones were not present at the photosynthetic fringe of hot spring outflows lacking streamer biofilm communities (Meyer-Dombard et al., 2011). Instead, hot spring outflows lacking streamer biofilm communities had higher diversity below the photosynthetic fringe transition. It should be noted that Meyer-Dombard et al. (2011) measured diversity by species richness and taxonomic complexity, whereas the measurement of diversity for this study (Shannon Diversity Index) accounts for both species richness and relative abundances. Overall, Shannon diversity values at the photosynthetic fringe were not higher than values above or below the photosynthetic fringe (**Supplementary Figure 7**). Instead, the mean Shannon diversity values were lower at the photosynthetic fringe, but not with statistical significance.

Beta diversity was investigated using NMDS analysis with the addition of geochemical vectors. Geochemical factors known to affect microbial community composition, as described in the introduction, including temperature, pH, total sulfide, total ammonia, nitrate, DIC, DOC, and DO concentrations, were added to the NMDS as geochemical vectors (Cox et al., 2011; Hamilton et al., 2011a; Havig et al., 2011; Inskeep et al., 2013). Each of these geochemical parameters, except for total sulfide, exhibited a statistically significant correlation with the overall microbial community composition. Additionally, there were observable patterns among cliques of ASVs and the geochemical parameters determined to correlate with microbial community composition with statistical significance (**Figure 5**). However, only individual nodes are correlated with sulfide and nitrate concentrations.

Both pH and temperature correlated with microbial community composition with statistical significance according to the NMDS analysis ($p < 0.05$) and were determined to contribute 7.33 and 4.85%, respectively, to variations in the microbial community compositions according to RDA, in agreement with previous studies (Inskeep et al., 2013; Colman et al., 2016; **Figure 4** and **Supplementary Table 4**). The extent of the roles of pH and temperature in affecting microbial community compositions are revealed in the co-occurrence network analysis as well as in the distribution of individual taxa in the 16S rRNA gene amplicon analysis (**Figures 3**, **5**, respectively). In acidic hot spring outflows, classes including Thermoplasmata, Acidimicrobiia, and Gammaproteobacteria are major constituents. In basic hot spring outflows, Cyanobacteria, Chloroflexi, and Deinococci are the major constituents. There are also taxonomic classes present in all samples regardless of pH, such as Aquificae and Nitrososphaeria. These findings are reflected in most of the cliques being correlated with pH (13 cliques) and/or temperature (16 cliques), whereas only 5 cliques are not correlated with pH and only two cliques are not correlated with temperature. There are no cliques that are not correlated with either temperature or pH. Although temperature and pH do contribute to microbial community composition, our analyses indicate that other geochemical factors are additionally contributing to the overall microbial community composition in hot spring outflow communities.

Sulfide concentrations are known to negatively impact oxygenic photosynthesis and have been linked to differences in microbial community composition (Cox et al., 2011; Hamilton et al., 2011b; Boyd et al., 2012; Inskeep et al., 2013; Jørgensen and Nelson, 1988), where the mechanism of sulfide's negative impact on phototrophs is most likely due to an inhibition of photosystem II (Oren et al., 1979; Miller and Bebout, 2004; Boyd et al., 2012). Rates of autotrophy in Yellowstone microbial mats have also been shown to be sulfide dependent, where acidic phototrophic communities were suppressed at 5 μM sulfide (Boyd et al., 2012). This suppression was not observed in basic mats. The suppression of acidic phototrophic communities at 5 μM sulfide, largely consisting of phototrophic algae, may be due to H_2S being the dominant form of sulfide in acidic environments. H_2S has been shown to more readily cross the cell membrane than HS^- (Howsley and Pearson, 1979).

Our samples were distributed across sulfide concentrations (below detection <0.15 μmolal to 52.6 μmolal) and pH (1.92–9.04). Two samples designated as being at the photosynthetic fringe occurred beyond the previously noted maximum range for photosynthesis of ∼15 μmolal (Cox et al., 2011), thereby expanding the possible sulfide range for photosynthesis in YNP hot springs (**Figure 2B**). Additionally, eukaryotic phototrophs have been identified in acidic samples with sulfide concentrations above 5 μM, the previously noted limit for phototrophic activity in acidic conditions (Boyd et al., 2012; Romero, 2018). Therefore, the concentrations of sulfide required to limit the presence of phototrophs in YNP hot springs may be higher than initially determined based on measurements coinciding with visual detection of the photosynthetic fringe or measurements of DIC uptake. However, in this study we only observed presence, not activity, under these sulfide concentrations.

When considering the overall microbial community composition, sulfide concentrations did not contribute to the composition with statistical significance even in acidic hot spring outflows ($pH < 4$, $p = 0.30$) (**Figure 4**). Additionally, sulfide concentrations only contributed 1.10% to overall variation in microbial community composition according to RDA. The lack of sulfide's statistical significance in microbial community composition is further supported by the co-occurrence network (**Supplementary Figure 6**), in which there are no trends between overall clique membership and sulfide concentrations. However, there are individual ASVs, or nodes, within cliques that are correlated with sulfide concentrations, including those representing taxa of known phototrophs, although this does not hold true for all nodes representative of phototrophic taxa. Overall, these findings corroborate the importance of sulfide concentrations in determining the distribution of individual taxa, but do not support the importance of sulfide concentrations in determining overall microbial community compositions, despite previous evidence for the suppression of phototrophic activity in acidic environments.

The gradient of increasing DO concentrations down hot spring outflows contributes 2.68% to changes in the microbial community composition according to RDA (Inskeep et al., 2013). The increase in DO down hot spring outflows is connected to the increased solubility of O_2 gas as temperature decreases and the increasing extent to which the reduced hydrothermal fluids have equilibrated with the atmosphere. In sulfidic systems, DO is quickly consumed in abiotic oxidation reactions, including the oxidation of reduced sulfur compounds (Inskeep et al., 2013). Examples include both the rapid oxidation of sulfide to polysulfides and the oxidation of sulfide to thiosulfate (the fate for up to 33% of sulfide present in pH 6–8 hot springs in YNP) (Nordstrom et al., 2005). The oxidation of reduced sulfide compounds affects the potential niche availability for sulfur-cyclers, therefore potentially contributing to microbial community composition (Nordstrom et al., 2005, 2009; Inskeep et al., 2013). Though DO in our samples is not correlated significantly with sulfide (−0.201 Pearson correlation), DO does increase with a decrease in temperature and is significantly correlated with temperature (−0.779 Pearson correlation). Therefore, the effects of DO on microbial community composition are difficult to disentangle from those of temperature, as observed by others (Inskeep et al., 2013), but cannot be ruled out in influencing overall microbial community composition.

Nitrogen species correlate with the abundance of subsets (specific cliques) within microbial communities, as well as overall microbial community composition down hot spring outflows. Ammonia and nitrate contribute 3.78 and 2.55% to the variation of overall microbial community (**Supplementary Table 4**). Furthermore, by including correlations with ammonia and nitrate concentrations in the co-occurrence network analysis, cliques can be further distinguished. Although clique 5 is not correlated with ammonia, it is 1 of only 3 cliques containing nodes representative of known ammonia-oxidizers, the other two cliques being cliques 2 and 13, both of which are correlated negatively with total ammonia. Only two taxa of ammonia-oxidizers, *Nitrosocaldus* and Nitrososphaeria, were identified in the 46 samples. Similar trends are present with nodes representing taxa of known phototrophic nitrogen fixers, such as *Leptococcus*, which trend negatively with ammonia and trend positively with pH. Spring pH could be a driver for N-cycler distribution, but acidic springs provide higher concentrations of N-compounds, such as ammonia, providing what seems to be a sparsely attended buffet for N-cyclers beyond N-fixers. Given these findings, the hypothesis by Hamilton et al. (2014) that ammonia-oxidizers consume the low levels of fixed nitrogen available in basic springs, leaving a niche for nitrogen fixers, would not apply in acidic YNP springs. Additionally, in acidic YNP hot springs, though *nif* genes and N-fixers are found abundantly, ammonia-oxidizers have not yet been identified definitively nor cultured from acidic YNP hot springs (Reigstad et al., 2008; Hamilton et al., 2011a,b; Boyd et al., 2013). However, the *amoA* gene responsible for the first step of ammonia oxidation has been identified in acidic hot springs but is less abundant than in circumneutral to basic hot springs (Boyd et al., 2013). Thus, the cycling of nitrogen in acidic YNP hot springs is ripe for further investigation to characterize the full nitrogen cycle.

According to the NMDS analysis, both DIC and DOC concentrations contribute significantly to differences in microbial community composition along NMDS1 with DIC and DOC contributing 8.20 and 3.60%, respectively, to the variation in the overall composition of microbial community compositions (**Figure 4** and **Supplementary Table 4**). DIC and DOC concentrations are correlated negatively with each other (−0.69 Pearson correlation) and are both strongly correlated with pH (0.79 and −0.77 Pearson correlations, respectively). The strong correlation between DIC and pH is attributed to the increased DIC input in high temperature, circumneutral to basic hot springs, due to being predominantly hydrothermally fed (Nordstrom et al., 2005). Additionally, there is the degassing of CO_2, which increases the pH for already circumneutral to basic hot springs (Nordstrom et al., 2005). In contrast, the strong negative correlation between DOC and pH has been attributed to increased soil input in acidic springs compared to basic springs which are commonly raised and/or surrounded by sinter, restricting DOC inputs to hydrothermal and microbial sources (Nye et al., 2020).

The effects of dissolved inorganic and organic carbon on microbial community composition are difficult to deconvolve; however, in hot spring outflow studies dissolved carbon and position along the photosynthetic fringe does correlate with changes in the presence or absence of genes associated with specific carbon cycling pathways (Havig et al., 2011). The dominant carbon fixation pathway down the outflow of BP was the reverse tricarboxylic acid cycle, a chemoautotrophic carbon fixation pathway, but below the photosynthetic fringe, the reductive pentose phosphate cycle, a carbon fixation pathway used by oxygenic phototrophs, also became abundant. The transition in the abundance of chemotrophic- versus phototrophic- associated carbon fixation pathway genes is not only indicative of changes in carbon metabolism down hot spring outflows but would be reflected in the microbial community composition. Therefore, at least in the case of a basic outflow, changes in DIC and DOC concentrations are reflected within the microbial communities.

In the present study, the significance of DIC and DOC in microbial distribution is reflected in the clique analysis, with cliques 2–9, 11, and 13 correlating with DOC concentrations (**Figure 5**). Clique 2 has the strongest negative correlation with DOC and includes taxa found in the outflows of basic sites, where DIC concentrations are comparatively high, and it includes taxa that are generally known as heterotrophs or phototrophs, such as Armatimonadota and *Synechococcus*. In contrast, clique 7 has a strong positive correlation with DOC and includes taxa found typically in cooler acidic sites but are generally known as chemoautotrophs, such as *Hydrogenobaculum* and Acidimicrobia. Even though DIC and DOC concentrations may be important down individual hot spring outflows, when analyzing the NMDS and breaking up the microbial data into cliques for co-occurrence analysis, it becomes more difficult to separate DIC and DOC from pH and temperature to gain meaningful information on the overall composition of hot spring microbial communities.

5. Conclusion

Although prior studies have focused on temperature, pH, and sulfide as determining factors for the position of the photosynthetic fringe, these geochemical variables, nor the geochemical variables included in this study, account for the true complexity of hot spring outflows and their hosted microbial communities. Each of the 12 hot spring outflows included in this study is geochemically complex as well as visually and geochemically unique. Though the stark differences visually observed between the predominantly chemotrophic communities above the photosynthetic fringe and the phototroph-containing communities below the photosynthetic fringe of each outflow were supported by CCA to be different in microbial community composition with statistical significance, statistical patterns in the geochemistry across all photosynthetic fringe locations studied are more nuanced. Even when including DIC, DOC, nitrate, ammonia, and DO concentrations, in addition to pH, temperature, and sulfide, the position of the photosynthetic fringe as defined by LDA could not be completely explained across the 12 hot spring outflows included in this study. While temperature and pH correlate with the composition of microbial communities and the position of the photosynthetic fringe down hot spring outflows, other variables, such as DIC, DOC, nitrate, ammonia, and DO concentrations act as supporting players, and are themselves correlated with pH and temperature. Though the co-occurrence analysis provides further differentiation on distribution based on taxa and geochemistry, especially when analyzing through the lens of dissolved carbon or ammonia concentrations, no single variable or set of variables could significantly predict community composition. However, according to both the NMDS analysis and the co-occurrence network analysis, the concentration of sulfide may play less of a role in overall microbial community composition than previously hypothesized. Overall, these findings mirror the complexity of the hot spring outflows studied. Further work inclusive of energy supplies and the rate of change in chemical concentrations down the hot spring outflows were not considered in this study but have been suggested as potential contributing factors in microbial community composition in hot spring outflows (Shock and Holland, 2007; Cox et al., 2011). Furthermore, these are active biological systems where factors of competition and adaptation could also explain departures from what chemical observations might predict (Leibold et al., 2022).

Data availability statement

The datasets presented in this study can be found in online repositories. The names of the repository/repositories and accession number(s) can be found in the article/**Supplementary material**.

Author contributions

ES, GB, and KF conceived the study and supervised the sampling. AH, FD, and GG carried out the DNA extractions, library prep, and sequencing efforts. KW, AH, and ET-R performed the sequence processing and bioinformatic analyses. KF performed the processing of water samples and ion chromatography (IC). KW and ET-R conducted the in-depth statistical analyses of geochemical and microbiomic data, including NMDS, and the co-occurrence network analysis. KW and ET-R wrote the manuscript with input from all authors. All authors contributed to the article and approved the submitted version.

Funding

This research was supported in part by the NASA Exobiology grant #NNX16AJ61G.

Acknowledgments

We acknowledge that Yellowstone National Park is situated on Native American lands with historical ties to 27 separate Native tribes including the Kiowa, Blackfeet, Cayuse, Coeur d'Alene, Shoshone, and Nez Perce. We recognize the enduring relationship that exists between these indigenous peoples and their ancestral territories. We also acknowledge that this research was performed with the permission of Yellowstone National Park under the permit YELL-2014-SCI-5434. We thank both Joseph Romero and Vince Debes for their efforts in assisting in DNA extraction, as well as Joseph Romero for his previous analyses on this dataset (Romero, 2018). We also thank Alysia Cox, Jason Raymond, and Jordan Okie for helpful discussions during the early stages of this project.

Conflict of interest

The authors declare that the research was conducted in the absence of any commercial or financial relationships that could be construed as a potential conflict of interest.

Publisher's note

Supplementary material

The Supplementary Material for this article can be found online at: https://www.frontiersin.org/articles/10.3389/fmicb.2023.1176606/full#supplementary-material

SUPPLEMENTARY FIGURE 1
Map of Yellowstone National Park depicting the 8 thermal areas (red stars) containing the 12 hot springs sampled as part of this study.

SUPPLEMENTARY FIGURE 2
A total of 46 samples taken from the outflows of 12 separate hot springs above (blue), at (yellow), and below (green) the photosynthetic fringe displayed across pH and temperature. X marks represent sites in which no Cyanobacteria or Chloroflexia were identified. Circles represent samples in which Cyanobacteria and Chloroflexia were identified, and the size of the circle corresponds to the percent relative abundance (RA) of these bacterial phototrophs in that sample. Asterisks indicate sites in which eukaryotic phototrophs were identified (Romero, 2018).

SUPPLEMENTARY FIGURE 3
A pairwise matrix analysis of trends between geochemical measurements including temperature, pH, total sulfide, total ammonia, dissolved oxygen, DOC, and DIC. Within each plot in the bottom left of the matrix, each point represents a single hot spring sample. The color of each point indicates whether the sample was taken above (blue), at (yellow), or below (green) the photosynthetic fringe. Corresponding with each plot, a box in the upper right of the matrix lists the overall Pearson correlation between the paired geochemical parameters, as well as the breakdown of the Pearson correlation between the paired geochemical parameters and the relative location of the samples to the photosynthetic fringe as determined by LDA.

SUPPLEMENTARY FIGURE 4
Percent relative abundance of the 16S rRNA gene sequencing results to the family level. Families not occurring at >20% relative abundance, when summed across all samples, were binned into the "Other" category. Organization of hot spring sites, separated by black bars, follows the order of increasing pH as in **Supplementary Table 1**. Within each site, samples are organized down the outflow with above (blue diamond), at (yellow diamond), and below (green diamond) the photosynthetic fringe indicated as in **Figure 1**.

SUPPLEMENTARY FIGURE 5
Canonical correspondence analysis (CCA) using the 16S rRNA gene sequencing data from each of the 46 sample sites separated by relative position to the photosynthetic fringe. Sample point colors (blue, yellow, and green) refer to the position along the photosynthetic fringe (above, at, below, respectively). Samples above the photosynthetic fringe are separated from samples at or below the photosynthetic fringe on the CCA1 axis with statistical significance ($p < 0.05$) as determined by an ANOVA test. Samples at and below the photosynthetic fringe are separated on the CCA2 axis but not with statistical significance.

SUPPLEMENTARY FIGURE 6
Co-occurrence network analysis of commonly occurring ASVs within the 46 hot spring samples. The ASVs are organized into 18 cliques using Louvain's membership algorithm. Edges represent a >0.7 Spearman's correlation coefficient. Each node is color-coded based on the strength of the Spearman correlation coefficient, negative 1 to positive 1 (blue to red, respectively) between the presence and abundance of the ASV with the following geochemical parameters, **(A)** pH, **(B)** temperature, **(C)** total ammonia, **(D)** DOC, **(E)** total dissolved sulfide, **(F)** nitrate, and **(G)** in relation to the photosynthetic fringe. Panel **(H)** shows all cliques differentiated by color and number of the clique.

SUPPLEMENTARY TABLE 1
Geochemical data, alpha diversity, and position in respect to the visually determined photosynthetic fringe for each sample. Samples are listed in the order in which they appear in **Figure 3**.

SUPPLEMENTARY TABLE 2
Extended geochemical data and position in respect to the visually determined photosynthetic fringe for each sample. All officially recognized hot spring names are listed along with citations. Samples are listed in the order in which they appear in **Figure 3**.

SUPPLEMENTARY TABLE 3
Sequence count data for each sample. The raw sequence count, the cleaned sequence count, and the sequence count after normalization are included for each sample.

SUPPLEMENTARY TABLE 4
Percent contribution for each geochemical variable included in this study on overall microbial community composition determined by RDA. Variables that were determined to contribute to overall community composition with statistical significance ($p < 0.05$) according to the NMDS analysis are bolded. Percent contributions calculated from a subset of sample data are marked with an asterisk.

SUPPLEMENTARY TABLE 5
ASV count table using the normalized sequence counts for each sample. The SILVA database was used to provide the taxonomic labels for each ASV using QIIME2 (v. 2020.2).

SUPPLEMENTARY TABLE 6
ASV node table organized by the assigned clique. All nodes present in the co-occurrence network analysis are provided in this table along with the associated ASV down to the lowest available taxonomic classification. The level of taxonomic classification for each ASV is also noted.

References

Andrews, S. (2010). *FastQC: A quality control tool for high throughput sequence data.* Available online at: http://www.bioinformatics.babraham.ac.uk/projects/fastqc (accessed June 1, 2022).

Bastian, M., Heymann, S., and Jacomy, M. (2009). Gephi: An open-source software for exploring and manipulating networks. *Proc. Int. AAAI Conf. Web Soc. Media* 3, 361–362.

Bennett, A. C., Murugapiran, S. K., Kees, E. D., Sauer, H. M., and Hamilton, T. L. (2022). Temperature and geographic location impact the distribution and diversity of photoautotrophic gene variants in alkaline Yellowstone hot springs. *Microbiol. Spectr.* 10:e146521. doi: 10.1128/spectrum.01465-21

Bolyen, E., Rideout, J., Dillon, M., Bokulich, N., Abnet, C., Al-Ghalith, G., et al. (2019). Reproducible, interactive, scalable and extensible microbiome data science using QIIME 2. *Nat. Biotechnol.* 37, 852–857. doi: 10.1038/s41587-019-0209-9

Boyd, E. S., Fecteau, K. M., Havig, J. R., Shock, E. L., and Peters, J. W. (2012). Modeling the habitat range of phototrophs in Yellowstone National Park: Toward the development of a comprehensive fitness landscape. *Front. Microbiol.* 3:221. doi: 10.3389/fmicb.2012.00221

Boyd, E. S., Hamilton, T. L., Wang, J., He, L., and Zhang, C. L. (2013). The role of tetraether lipid composition in the adaptation of thermophilic archaea to acidity. *Front. Microbiol.* 4:62. doi: 10.3389/fmicb.2013.00062

Boyer, G. M., Schubotz, F., Summons, R. E., Woods, J., and Shock, E. L. (2020). Carbon oxidation state in microbial polar lipids suggests adaptation to hot spring temperature and redox gradients. *Front. Microbiol.* 11:229. doi: 10.3389/fmicb.2020.00229

Brock, T. D. (1973). Lower pH limit for the existence of blue-green algae: Evolutionary and ecological implications. *Science* 179, 480–483. doi: 10.1126/science.179.4072.480

Brock, T. D. (1978). *Thermophilic microorganisms and life at high temperatures*. Berlin: Springer-Verlag.

Brock, T. D., and Brock, M. L. (1966). Temperature optima for algal development in Yellowstone and Iceland hot springs. *Nature* 209, 733–734.

Caporaso, J. G., Lauber, C. L., Walters, W. A., Berg-Lyons, D., Huntley, J., Fierer, N., et al. (2012). Ultra-high-throughput microbial community analysis on the Illumina HiSeq and MiSeq platforms. *ISME J.* 6, 1621–1624. doi: 10.1038/ismej.2012.8

Castenholz, R. W. (1969). Thermophilic blue-green algae and the thermal environment. *Bacteriol. Rev.* 33, 476–504.

Colman, D. R., Feyhl-Buska, J., Robinson, K. J., Fecteau, K. M., Xu, H., Shock, E. L., et al. (2016). Ecological differentiation in planktonic and sediment-associated chemotrophic microbial populations in Yellowstone hot springs. *FEMS Microbiol. Ecol.* 92:fiw137. doi: 10.1093/femsec/fiw137

Colman, D. R., Poudel, S., Hamilton, T. L., Havig, J. R., Selensky, M. J., Shock, E. L., et al. (2018). Geobiological feedbacks and the evolution of thermoacidophiles. *ISME J.* 12, 225–236. doi: 10.1038/ismej.2017.162

Cox, A., Shock, E. L., and Havig, J. R. (2011). The transition to microbial photosynthesis in hot spring ecosystems. *Chem. Geol.* 280, 344–351.

Csardi, G., and Nepusz, T. (2006). The igraph software package for complex network research. *Inter J. Compl. Syst.* 1695, 1–9.

De la Torre, J. R., Walker, C. B., Ingalls, A. E., Könneke, M., and Stahl, D. A. (2008). Cultivation of a thermophilic ammonia oxidizing archaeon synthesizing crenarchaeol. *Environ. Microbiol.* 10, 810–818. doi: 10.1111/j.1462-2920.2007.01506.x

Doemel, W. N., and Brock, T. D. (1970). The upper temperature limit of *Cyanidium caldarium*. *Arch. Microbiol.* 72, 326–332. doi: 10.1007/BF00409031

Doemel, W. N., and Brock, T. D. (1971). The physiological ecology of *Cyanidium caldarium*. *J. Gene. Microbiol.* 67, 17–32. doi: 10.1099/00221287-67-1-17

Fecteau, K. M., Boyd, E. S., Lindsay, M. R., Amenabar, M. J., Robinson, K. J., Debes, R. V., et al. (2022). Cyanobacteria and Algae meet at the limits of their habitat ranges in moderately acidic hot springs. *J. Geophys. Res. Biogeosci.* 127:e2021JG006446.

Fullerton, K. M., Schrenk, M. O., Yücel, M., Manini, E., Basili, M., Rogers, T. J., et al. (2021). Effect of tectonic processes on biosphere–geosphere feedbacks across a convergent margin. *Nat. Geosci.* 14, 301–306.

Hamilton, T. L., Boyd, E. S., and Peters, J. W. (2011a). Environmental constraints underpin the distribution and phylogenetic diversity of nifH in the Yellowstone geothermal complex. *Microb. Ecol.* 61, 860–870. doi: 10.1007/s00248-011-9824-9

Hamilton, T. L., Lange, R. K., Boyd, E. S., and Peters, J. W. (2011b). Biological nitrogen fixation in acidic high-temperature geothermal springs in Yellowstone National Park Wyoming. *Environ. Microbiol.* 13, 2204–2215. doi: 10.1111/j.1462-2920.2011.02475.x

Hamilton, T. L., Koonce, E., Howells, A., Havig, J. R., Jewell, T., de la Torre, J. R., et al. (2014). Competition for ammonia influences the structure of chemotrophic communities in geothermal springs. *Appl. Environ. Microbiol.* 80, 653–661. doi: 10.1128/AEM.02577-13

Hamilton, T. L., Vogl, K., Bryant, D. A., Boyd, E. S., and Peters, J. W. (2012). Environmental constraints defining the distribution, composition, and evolution of chlorophototrophs in thermal features of Yellowstone National Park. *Geobiology* 10, 236–249. doi: 10.1111/j.1472-4669.2011.00296.x

Hatzenpichler, R., Lebedeva, E. V., Spieck, E., Stoecker, K., Richter, A., Daims, H., et al. (2008). A moderately thermophilic ammonia-oxidizing crenarchaeote from a hot spring. *Proc. Natl. Acad. Sci. U.S.A* 105, 2134–2139. doi: 10.1073/pnas.0708857105

Havig, J. R., Raymond, J., Meyer-Dombard, D. A. R., Zolotova, N., and Shock, E. L. (2011). Merging isotopes and community genomics in a siliceous sinter-depositing hot spring. *J. Geophys. Res. Biogeosci.* 116.

Howells, A. E. G. (2020). *). A combined microbiome and geochemical approach, assessing drivers of microbial diversity, distribution and activity*. Ph.D thesis. Lake Havasu: Arizona State University.

Howsley, R., and Pearson, H. W. (1979). pH dependent sulphide toxicity to oxygenic photosynthesis in *Cyanobacteria*. *FEMS Microbiol. Lett.* 6, 287–292.

Iacovino, K., Guild, M. R., and Till, C. B. (2020). Aqueous fluids are effective oxidizing agents of the mantle in subduction zones. *Contrib. Mineral Petrol.* 175, 1–22.

Inskeep, W. P., Jay, Z. J., Tringe, S. G., Herrgård, M. J., Rusch, D. B., and Committee and Working Group Members (2013). The YNP metagenome project: Environmental parameters responsible for microbial distribution in the Yellowstone geothermal ecosystem. *Front. Microbiol.* 4:67. doi: 10.3389/fmicb.2013.00067

Jørgensen, B. B., and Nelson, D. C. (1988). Bacterial zonation, photosynthesis, and spectral light distribution in hot spring microbial mats of Iceland. *Microb. Ecol.* 16, 133–147. doi: 10.1007/BF02018909

Kempner, E. S. (1963). Upper temperature limit of life. *Science* 142, 1318–1319.

Klatt, C. G., Wood, J. M., Rusch, D. B., Bateson, M. M., Hamamura, N., Heidelberg, J. F., et al. (2011). Community ecology of hot spring *Cyanobacterial* mats: Predominant populations and their functional potential. *ISME J.* 5, 1262–1278. doi: 10.1038/ismej.2011.73

Leibold, M. A., Govaert, L., Loeuille, N., De Meester, L., and Urban, M. C. (2022). Evolution and community assembly across spatial scales. *Annu. Rev. Ecol. Evol. Syst.* 53, 299–326.

Lindsay, M. R., Amenabar, M. J., Fecteau, K. M., Debes, R. V., Fernandes Martins, M. C., Fristad, K. E., et al. (2018). Subsurface processes influence oxidant availability and chemoautotrophic hydrogen metabolism in Yellowstone hot springs. *Geobiology* 16, 674–692. doi: 10.1111/gbi.12308

Loiacono, S. T., Meyer-Dombard, D. A. R., Havig, J. R., Poret-Peterson, A. T., Hartnett, H. E., and Shock, E. L. (2012). Evidence for high temperature in situ *nifH* transcription in an alkaline hot spring of Lower Geyser Basin, Yellowstone National Park. *Environ. Microbiol.* 14, 1272–1283. doi: 10.1111/j.1462-2920.2012.02710.x

Meeks, J. C., and Castenholz, R. W. (1978). Photosynthetic properties of the extreme thermophile synechococcus lividus—II. Stoichiometry between oxygen evolution and CO_2 assimilation. *J. Thermal Biol.* 3, 19–24.

Meyer-Dombard, D. A. R., Swingley, W., Raymond, J., Havig, J., Shock, E. L., and Summons, R. E. (2011). Hydrothermal ecotones and streamer biofilm communities in the Lower Geyser Basin, Yellowstone National Park. *Environ. Microbiol.* 13, 2216–2231. doi: 10.1111/j.1462-2920.2011.02476.x

Miller, S. R., and Bebout, B. M. (2004). Variation in sulfide tolerance of photosystem II in phylogenetically diverse cyanobacteria from sulfidic habitats. *Appl. Environ. Microbiol.* 70, 736–744. doi: 10.1128/AEM.70.2.736-744.2004

Nordstrom, D. K., Ball, J. W., and McCleskey, R. B. (2005). "Ground water to surface water: Chemistry of thermal outflows in Yellowstone National Park," in *Geothermal biology and geochemistry in Yellowstone National Park*, eds W. Inskeep and T. McDermott (Bozeman: Montana State University), 73–94. doi: 10.1128/AEM.00357-07

Nordstrom, D. K., McCleskey, R. B., and Ball, J. W. (2009). Sulfur geochemistry of hydrothermal waters in Yellowstone National Park: IV Acid–sulfate waters. *Appl. Geochem.* 24, 191–207. doi: 10.1186/1467-4866-4-12

Nye, J. J., Shock, E. L., and Hartnett, H. E. (2020). A novel PARAFAC model for continental hot springs reveals unique dissolved organic carbon compositions. *Org. Geochem.* 141:103964.

Oksanen, J., Blanchet, F. G., Kindt, R., Legendre, P., Minchin, P. R., O'hara, R. B., et al. (2022). Package 'vegan'. *Commun. Ecol. Package Vers.* 2, 1–295.

Oren, A., Padan, E., and Malkin, S. (1979). Sulfide inhibition of photosystem II in *Cyanobacteria*. (blue-green algae) and tobacco chloroplasts. *Biochim. Biophys. Acta Bioenerg.* 546, 270–279. doi: 10.1016/0005-2728(79)90045-8

Quast, C., Pruesse, E., Yilmaz, P., Gerken, J., Schweer, T., Yarza, P., et al. (2012). The SILVA ribosomal RNA gene database project: Improved data processing and web-based tools. *Nucleic Acids Res.* 41, D590–D596. doi: 10.1093/nar/gks1219

R Core Team (2013). *R: A language and environment for statistical computing*. Vienna: R Foundation for Statistical Computing.

Reigstad, L. J., Richter, A., Daims, H., Urich, T., Schwark, L., and Schleper, C. (2008). Nitrification in terrestrial hot springs of Iceland and Kamchatka. *FEMS Microbiol. Ecol.* 64, 167–174. doi: 10.1111/j.1574-6941.2008.00466.x

Romero, J. T. (2018). *Changes in microbial communities and geochemical energy supplies across the photosynthetic fringe of hot spring outflows in Yellowstone National Park*. M.S. thesis. Arizona: Arizona State University.

Shock, E. L., and Holland, M. E. (2007). Quantitative habitability. *Astrobiology* 7, 839–851.

Skorupa, D. J., Reeb, V., Castenholz, R. W., Bhattacharya, D., and McDermott, T. R. (2013). Cyanidiales diversity in Yellowstone National Park. *Lett. Appl. Microbiol.* 57, 459–466. doi: 10.1111/lam.12135

St Clair, B., Pottenger, J., Debes, R., Hanselmann, K., and Shock, E. (2019). Distinguishing biotic and abiotic iron oxidation at low temperatures. *ACS Earth Space Chem.* 3, 905–921.

Steunou, A. S., Jensen, S. I., Brecht, E., Becraft, E. D., Bateson, M. M., Kilian, O., et al. (2008). Regulation of nif gene expression and the energetics of N_2 fixation over the diel cycle in a hot spring microbial mat. *ISME J.* 2, 364–378. doi: 10.1038/ismej.2007.117

Swingley, W. D., Meyer-Dombard, D. A. R., Shock, E. L., Alsop, E. B., Falenski, H. D., Havig, J. R., et al. (2012). Coordinating environmental genomics and geochemistry reveals metabolic transitions in a hot spring ecosystem. *PLoS One* 7:e38108. doi: 10.1371/journal.pone.0038108

Thiel, V., Wood, J. M., Olsen, M. T., Tank, M., Klatt, C. G., Ward, D. M., et al. (2016). The dark side of the mushroom spring microbial mat: Life in the shadow of chlorophototrophs. I. Microbial diversity based on 16S rRNA gene amplicons and metagenomic sequencing. *Front. Microbiol.* 7:919. doi: 10.3389/fmicb.2016.00919

Thompson, L. R., Sanders, J. G., McDonald, D., Amir, A., Ladau, J., Locey, K. J., et al. (2017). A communal catalogue reveals Earth's multiscale microbial diversity. *Nature* 551, 457–463. doi: 10.1038/nature24621

Toplin, J. A., Norris, T. B., Lehr, C. R., McDermott, T. R., and Castenholz, R. W. (2008). Biogeographic and phylogenetic diversity of thermoacidophilic cyanidiales in Yellowstone National Park, Japan, and New Zealand. *Appl. Environ. Microbiol.* 74, 2822–2833. doi: 10.1128/AEM.02741-07

van der Maarel, E. (1990). Ecotones and ecoclines are different. *J. Veg. Sci.* 1, 135–138.

Venables, W. N., and Ripley, B. D. (2002). *Modern Applied Statistics with S. Fourth Edition*. New York, NY: Springer.

Ward, D. M., Weller, R., and Bateson, M. M. (1990). 16S rRNA sequences reveal numerous uncultured microorganisms in a natural community. *Nature* 345, 63–65. doi: 10.1038/345063a0

frontiers | Frontiers in Microbiology

TYPE Original Research
PUBLISHED 04 May 2023
DOI 10.3389/fmicb.2023.1161937

OPEN ACCESS

EDITED BY
Mark Alexander Lever,
The University of Texas at Austin, United States

REVIEWED BY
Hans Karl Carlson,
Berkeley Lab (DOE), United States
Éric Verrecchia,
Université de Lausanne, Switzerland

*CORRESPONDENCE
Elizabeth Trembath-Reichert
✉ e.t.r@asu.edu

RECEIVED 08 February 2023
ACCEPTED 11 April 2023
PUBLISHED 04 May 2023

CITATION
Sonke A and Trembath-Reichert E (2023) Expanding the taxonomic and environmental extent of an underexplored carbon metabolism—oxalotrophy.
Front. Microbiol. 14:1161937.
doi: 10.3389/fmicb.2023.1161937

Expanding the taxonomic and environmental extent of an underexplored carbon metabolism—oxalotrophy

Alexander Sonke and Elizabeth Trembath-Reichert*

School of Earth and Space Exploration, Arizona State University, Tempe, AZ, United States

Oxalate serves various functions in the biological processes of plants, fungi, bacteria, and animals. It occurs naturally in the minerals weddellite and whewellite (calcium oxalates) or as oxalic acid. The environmental accumulation of oxalate is disproportionately low compared to the prevalence of highly productive oxalogens, namely plants. It is hypothesized that oxalotrophic microbes limit oxalate accumulation by degrading oxalate minerals to carbonates via an underexplored biogeochemical cycle known as the oxalate-carbonate pathway (OCP). Neither the diversity nor the ecology of oxalotrophic bacteria is fully understood. This research investigated the phylogenetic relationships of the bacterial genes *oxc*, *frc*, *oxdC*, and *oxlT*, which encode key enzymes for oxalotrophy, using bioinformatic approaches and publicly available omics datasets. Phylogenetic trees of *oxc* and *oxdC* genes demonstrated grouping by both source environment and taxonomy. All four trees included genes from metagenome-assembled genomes (MAGs) that contained novel lineages and environments for oxalotrophs. In particular, sequences of each gene were recovered from marine environments. These results were supported with marine transcriptome sequences and description of key amino acid residue conservation. Additionally, we investigated the theoretical energy yield from oxalotrophy across marine-relevant pressure and temperature conditions and found similar standard state Gibbs free energy to "low energy" marine sediment metabolisms, such as anaerobic oxidation of methane coupled to sulfate reduction. These findings suggest further need to understand the role of bacterial oxalotrophy in the OCP, particularly in marine environments, and its contribution to global carbon cycling.

KEYWORDS

oxalate, oxalotrophy, carbon sequestration, oxalate-carbonate pathway, carbon cycle, biosignature

1. Introduction

Plant production of oxalate biominerals appears to be widespread and oxalate minerals are stable over geologic time, yet oxalates are uncommon in the geologic record (Hofmann and Bernasconi, 1998; Stephens, 2012). Moreover, soil oxalate concentrations reported in the literature are often below detection limits, or on the order of a few micromolar—far less than would be expected given the apparent extent of production (Jones, 1998; Strobel, 2001). Limited accumulation appears to be due to degradation of oxalate minerals to carbonates by bacteria and fungi in an underexplored biogeochemical cycle known as the oxalate-carbonate pathway (OCP; Verrecchia, 1990). The global role of this pathway in carbon cycling is unconstrained but estimated to have significant influence on carbon fluxes and long-term sequestration. For example, deserts of the American Southwest and Mexico, where density of the oxalogenic Saguaro cactus is high, may accumulate as much as $1.8 \times 10^{11}\,\mathrm{g\,yr.}^{-1}$ of atmospheric carbon in oxalate biominerals (Garvie, 2006).

Oxalate occurs naturally as organic minerals and oxalic acid (Baran, 2014), forming by diagenesis, biomineralization, and abiotic processes such as radiolysis and ultraviolet (UV) irradiation (Vandenborre et al., 2021; Zhao et al., 2022). Calcium oxalate, in its monohydrate and dihydrate forms (known as whewellite and weddellite, respectively), is especially prevalent as a biomineral produced by plants, fungi, and lichens, and is present pathologically in animals (Bungartz et al., 2004; Franceschi and Nakata, 2005). In the plant kingdom, oxalogens are present in nearly 80% of families (McNair, 1932; Barth, 2020), and in some cases comprise up to 80% (w/w) of a plant's dry weight and 90% of its total calcium (Nakata, 2003). Oxalates have been observed to serve biochemical, photosynthetic, and reproductive purposes in plants (He et al., 2014).

By contrast, bacterial oxalate use has centered around metabolic needs. Six biologically mediated oxalate degradation pathways are documented in MetaCyc (Caspi et al., 2018). Three are widespread in bacteria (Types II, III, V; Figure 1), while other types (I, IV, and VI) are either more common in eukaryotes (mostly plants) or specific bacteria (acetogens). Type V is a single-step pathway that utilizes the *oxdC* gene to directly convert oxalate to formate (Tanner and Bornemann, 2000). Types II and III are multistep pathways that convert oxalate to formate (Type II) or to CO_2 (Type III). The key gene shared in both Type II and Type III pathways is *oxc*, which encodes oxalyl-CoA decarboxylase (Baetz and Allison, 1989; Lung et al., 1994).

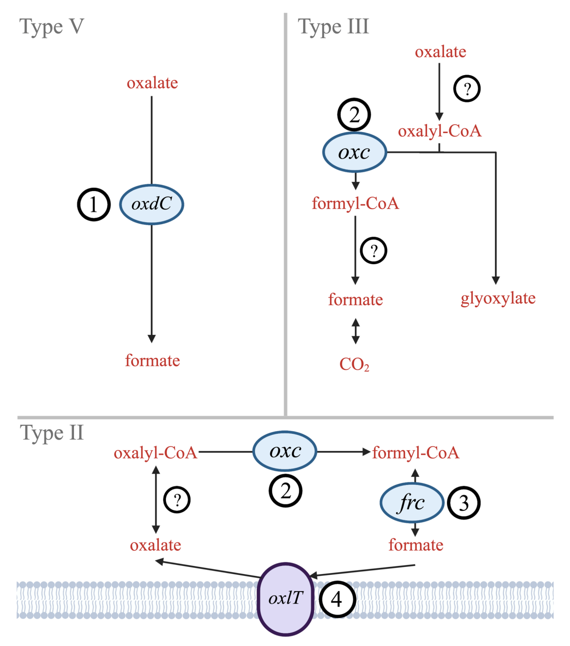

FIGURE 1
Simplified diagram of Type II, III, and V oxalate degradation pathways. Genes that encode key enzymes or proteins are labeled (1) *oxdC* – oxalate decarboxylase, (2) *oxc* – oxalyl-CoA decarboxylase, (3) *frc* – formyl-CoA transferase, and (4) *oxlT* – oxalate:formate antiporter. Hypothesized enzymes without known genes are indicated by (?) – oxalate CoA-transferase and formate-CoA hydrolase.

The Type II pathway also includes *frc*, which encodes formyl-CoA transferase (Baetz and Allison, 1990). While *frc* is well characterized, it is also ubiquitous across metabolisms and therefore not unique to oxalotrophy. Type II and III share EC 2.8.3.2 (oxalate CoA-transferase) as the initial catalyzing step in the pathway; however, no genes have been identified that encode this enzyme since its description in 1961 (Quayle et al., 1961). Similarly, Type III requires EC 3.1.2.10 (formyl-CoA hydrolase), which has not been associated with an encoding gene since its description in 1963 (Sly and Stadtman, 1963). The terminal step in Type III is formate dehydrogenase (Rusching et al., 1976). Types II, III, and V may all rely on an oxalate:formate antiporter, encoded by the *oxlT* gene. *oxlT* is thought to mediate transmembrane uptake of oxalate, which has been identified in fungi and many anaerobic bacteria, but only two strains of aerobic bacteria (Fu et al., 2001; Müller et al., 2016; Robertson and Meyers, 2022).

Therefore, this study investigated the taxonomic and environmental diversity of the key genes unique or essential to bacterial oxalotrophy: *oxdC* (1), *oxc* (2), *frc* (3), and *oxlT* (4) (Figure 1). Since presence of these genes in an organism guarantees neither metabolic function, nor microbial activity (Turroni et al., 2007; Bravo et al., 2013), we also provide transcript and protein amino acid conservation analysis. We investigated transcriptomes of contrasting ecosystems, evaluated the energetics of bacterial oxalotrophy, and compared conservation of key residues from characterized proteins across our gene alignments. In combination, these findings suggest novel taxa and environments where oxalotrophy may play a role in carbon cycling.

2. Materials and methods

2.1. Sequence data acquisition

Sequence data were obtained from NCBI using BLAST+ (v2.12.0; Altschul et al., 1997; Camacho et al., 2009). Each search consisted of FASTA-formatted amino acid sequences queried against nonredundant isolate and whole-genome sequencing (WGS) protein databases. Query sequences were obtained from reference oxalotrophic strains using their respective KEGG Orthology identifiers (KO IDs). Complexity of BLAST results was reduced to our target of fewer than 200 sequences by selecting for E-values less than $1e^{-50}$, percent identities below 0.87, and default BLAST+ parameters except where otherwise noted in Supplementary Table 1. Data processing was conducted with Unix commands in the MacOS Terminal bash shell.

Metatranscriptome searches were conducted using the IMG/MER OMICS/RefSeq database (Chen et al., 2023). Search queries were composed using the gene product name and the EC or KO ID listed in Table 1 to ensure accuracy. To evaluate the potential for active oxalotrophy in high temperature marine systems, we searched the one available hydrothermal RNA-seq dataset on IMG consisting of metatranscriptomes from hydrothermal plume and vent fluids of the Gulf of California and North Pacific Ocean (Anderson et al., 2019). From this, we recovered multiple genes related to oxalotrophy from plume samples, but only *frc* from vent fluids (Table 1). To compare with active oxalotrophy in a soil environment, we selected an available RNA-seq dataset looking at soil activation during spring snow melt (Brodie et al., 2017). From this we recovered high (>1,000 counts)

TABLE 1 Transcript counts for genes involved in oxalotrophy from 36 soil and 3 hydrothermal vent fluid and 2 hydrothermal vent plume metatranscriptomes.

Gene	Gene name		EC number	KO ID	Soil MetaT (n=36)	Vent MetaT (n=3)	Plume MetaT (n=2)	IMG isolate gene count
4	OFA family oxalate/formate antiporter-like MFS transporter	*oxlT*	–	K08177	3,178	0	2	38,263
3	Formyl-CoA transferase	*frc*	2.8.3.16	–	31,497	3	183	20,981
2	Oxalyl-CoA decarboxylase	*oxc*	4.1.1.8	–	2,452	0	13	9,997
1	Oxalate decarboxylase	*oxdC*	4.1.1.2	–	2,560	0	3	8,670

transcription of all oxalotrophy genes of interest (Table 1). For comparison, we also provided the total gene count for each gene in the IMG isolate database.

Sequences of fungal genes were obtained from FungiDB (Basenko et al., 2018) and included in the database prior to multiple sequence alignment in order to generate phylogenetic outgroups. In the case of *oxc*, the fungal sequences recovered represented predicted genes only. A neighbor-joining tree of all gene sequences used in this study suggested phylogenetic relationships that support the validity of using these fungal sequences, as well as those of the other genes investigated here, as outgroups (Supplementary Figure 1). Metadata for all sequences retained and used in this study are available in Supplementary Table 2.

2.2. Phylogenetic trees and sequence analysis

Multiple-sequence alignment was performed with MUSCLE (v3.8.1551) using default parameters (Edgar, 2004). Sequence metadata, such as source environment and taxonomy, were obtained from multiple sources: NCBI archival protein sequence records, the JGI Integrated Microbial Genomes and Microbiomes, the BioCyc, BacDive, and Genomes OnLine databases (Karp et al., 2019; Reimer et al., 2022; Chen et al., 2023; Mukherjee et al., 2023), and directly from source publications. GhostKOALA (v2.2) was used to assign taxonomies of metagenome-assembled genome (MAG) sequences that were otherwise unclassified in NCBI, and to confirm gene annotations of all other sequences (Kanehisa et al., 2016). RAxML was used to construct maximumlikelihood phylogenetic trees with PROTCATAUTO model settings and branch support values generated from 500 bootstrapping iterations (Stamatakis, 2014). Trees were visualized and annotated using Interactive Tree of Life (iTOL v6.6; Letunic and Bork, 2021). Several nodes on the *oxc* phylogenetic tree (Figure 2), which was significantly larger than the other trees, were collapsed for simplification; the fully expanded version can be viewed in Supplementary Figure 4.

Multiple-sequence alignments of each gene were evaluated in Jalview (v2.11.2.5; Waterhouse et al., 2009) in order to assess key residue conservation, an indicator of the preservation of structure and function in the proteins encoded by each gene. This was then visualized by generating pore logos in WebLogo 3 (Schneider and Stephens, 1990; Crooks et al., 2004). Key residues were identified from experimental mutagenesis publications referenced in the Uniprot Knowledgebase (UniprotKB) (The UniProt Consortium, 2021). These publications show varying effects of mutation between residues. For simplicity, all referenced residues were considered "key" and assessed for conservation (see Results and Discussion).

2.3. Energetics

The Water-Organic-Rock-Microbe (WORM) Portal was used for all energetics calculations (Boyer et al., 2022). Code is provided in Supplementary Data Sheet 1.

3. Results

3.1. Phylogeny

The phylogeny of OXC-encoding sequences partitioned into groups (I, II, and III) generally attributable to sequence taxonomy at the phylum and class levels (Figure 2). Group I consisted entirely of Actinobacteria (bootstrap value = 100). Source environments for this group were predominantly terrestrial, with one marine exception collected from tissue of a coral reef-inhabiting sea sponge in the South China Sea (WP_111862994). Group II consisted of several Proteobacteria-dominated clades largely of terrestrial origin. Conversely, Group III was homogeneously comprised of Alphaproteobacteria from marine source environments. The marine hydrothermal plume transcriptome sequences included in this tree were predicted in GhostKOALA to be from Alphaproteobacteria, consistent with their placement in Group III among other sequences of marine and hydrothermal source environments.

Within Group II, Clade I contained a mixed group of Proteobacteria sequences that were documented to have been specifically isolated from plant hosts (as opposed to being labeled simply as "soil" isolates, for example). All Group II non-Proteobacteria sequences, including those that may represent previously undescribed oxalotrophic diversity (e.g., Fusobacteria, Deltaproteobacteria, Acidobacteria, and a single sequence purportedly isolated from the

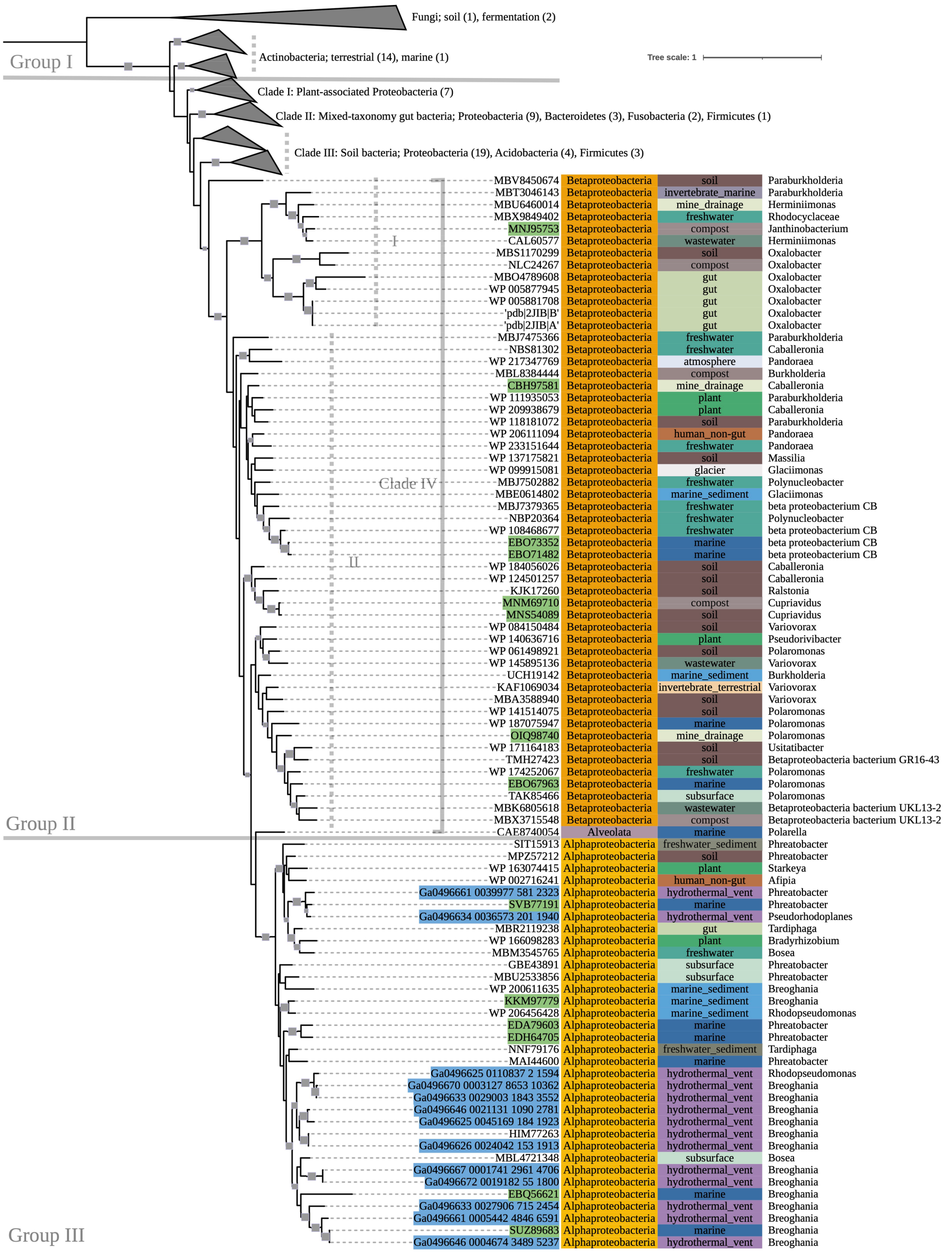

FIGURE 2
500-bootstrap maximum-likelihood phylogenetic tree of bacterial and predicted fungal *oxc* genes. Bootstrap values >50 displayed as gray boxes (min=50, max=100). Green-highlighted sequence identifiers indicate MAG genes. Blue-highlighted sequence identifiers indicate hydrothermal transcripts. Left-most annotation column indicates phylum taxonomy, class for Proteobacteria. Center column indicates source environment. Right-most column indicates genus taxonomy, or the next most exclusive classification available. Number of sequences included in collapsed nodes are indicated in parentheses.

dinoflagellate *Polarella glacialis*) grouped into Clades II and III, along with Proteobacteria sequences of similar source environments. Clade II consisted predominantly of gut-associated sequences, while Clade III consisted of soil-associated sequences. Clade IV consisted of Betaproteobacteria sequences of mixed source environments that grouped into two subclades (Clade IV.I, Clade IV.II, bootstrap value = 91).

The phylogenetic tree of OXDC-encoding sequences (Figure 3) also demonstrated grouping by taxonomy. Group I consisted primarily of mixed Proteobacteria, while Group II consisted of Terrabacteria. Notably, Proteobacteria and Firmicutes (Terrabacteria) sequences that were obtained from the same compost metagenome sample grouped with their respective taxonomic groups rather than with each other. Taxonomic predictions in GhostKOALA assigned three of the included marine hydrothermal plume transcriptome sequences as bacterial (two Alphaproteobacteria and one Bacteroidetes), and one as fungal. The Bacteroidetes-assigned sequence grouped with the Alphaproteobacteria-assigned sequences among other Group I Proteobacteria of mixed source environments, while the fungal sequence grouped with the tree's fungal outgroup.

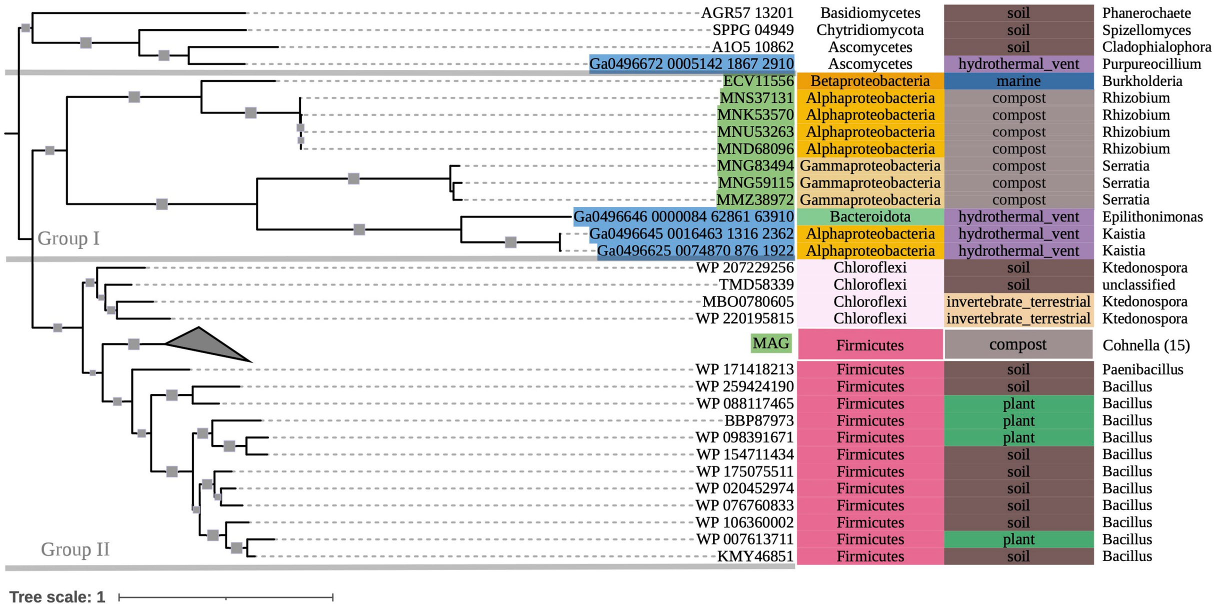

FIGURE 3
500-bootstrap maximum-likelihood phylogenetic tree of bacterial and fungal *oxdC* genes. Bootstrap values >50 displayed as gray boxes (min=50, max=100). Green-highlighted sequence identifiers indicate MAG genes. Blue-highlighted sequence identifiers indicate hydrothermal transcripts. Left-most annotation column indicates phylum taxonomy, class for Proteobacteria. Center column indicates source environment. Right-most column indicates genus taxonomy, or the next most exclusive classification available. Collapsed node represents 15 Firmicutes sequences from a single compost metagenome (NCBI BioProject PRJNA488358).

The phylogenetic tree of OXLT-encoding sequences (Figure 4) showed two main groups (bootstrap value = 90). Group I consisted of terrestrial-dominant Proteobacteria. Group II consisted mostly of terrestrial Firmicutes, with a single clade of terrestrial Betaproteobacteria within the group (bootstrap value = 100). Marine hydrothermal plume transcriptome sequences grouped together outside of Groups I and II (bootstrap value = 66), despite one of them appearing to share ancestry with sequences in Group II (Ga0496633_0000486_29460_30734).

The tree of *frc* sequences (Supplementary Figure 2) did not demonstrate distinct groupings. Rather, it showed numerous small clades of mixed taxonomic and environmental groups (bootstrap values ranged 1–80), which we attribute to the ubiquity and versatility of the formyl-CoA transferase enzyme. However, several sequences recovered from marine isolates and MAGs grouped with the hydrothermal vent transcriptome sequences included in our study.

3.2. Key residue conservation

Multiple-sequence alignments that included fungal outgroups and hydrothermal transcripts were compared to each gene's respective reference sequence in UniprotKB and assessed for key residue conservation. Key residues in the *oxc* gene (Figure 5 and Supplementary Figure 4) include E-56, Y-120, E-121, Y-483, S-553, and R-555 (Berthold et al., 2007). E-56 (Figure 5A) was conserved across all sequences (percentage identity; PID = 100%). Y-120 (Figure 5B) was conserved across all but two bacterial isolate sequences and two fungal sequences that all had phenylalanine substitutions (PID = 96.8%). E-121 (Figure 5B) was conserved across all but four bacterial isolate sequences and two fungal sequences that had glutamine substitutions (PID = 95.5%). Y-483 (Figure 5C) was conserved across all but three bacterial MAG sequences that terminated prior to this position (PID = 98.1%). Similarly, S-553 (Figure 5D) was conserved across all but eight bacterial sequences that terminated prior to said position and two fungal sequences which showed substitutions (PID = 93.5%). R-555 (Figure 5D) was conserved with only 50.3% consensus; many bacterial sequences either showed histidine substitution or terminated prior to this position.

Among a subset of 27 *oxc* genes of particular interest to this study, which include marine MAG sequences, hydrothermal transcripts, and sequences of taxa previously unknown to be oxalotrophic, key residue conservation was considerably high. E-56, Y-120, and E-121 were 100% conserved. Y–483 was conserved in all but three marine MAG sequences which terminated prior to this position (PID = 90.3%). S-553 was conserved in all but eight sequences (six MAGs, two hydrothermal transcripts; PID = 74.1% overall). R-555 showed similar conservation to the complete alignment, where terrestrial sequences had histidine substitutions, but marine sequences conserved arginine (74.1% occupancy, PID = 69.6% R).

Key residues in the *oxdC* gene (Supplementary Figure 4) include R-270, E-333, and Y-340 (Anand et al., 2002). R-270 was conserved across all sequences in our alignment (PID = 100%). E-333 was highly conserved among Terrabacteria sequences and fungi, but showed varying substitutions among nearly all non-Terrabacteria sequences (PID = 78%). Y-340 was highly conserved among non-Terrabacteria sequences, but showed frequent phenylalanine substitutions among Firmicutes and fungal sequences (PID = 52%). Our *oxdC* genes of interest (as detailed above) also had significant conservation of key residues. R-270 was completely conserved, while Y-340 had a single

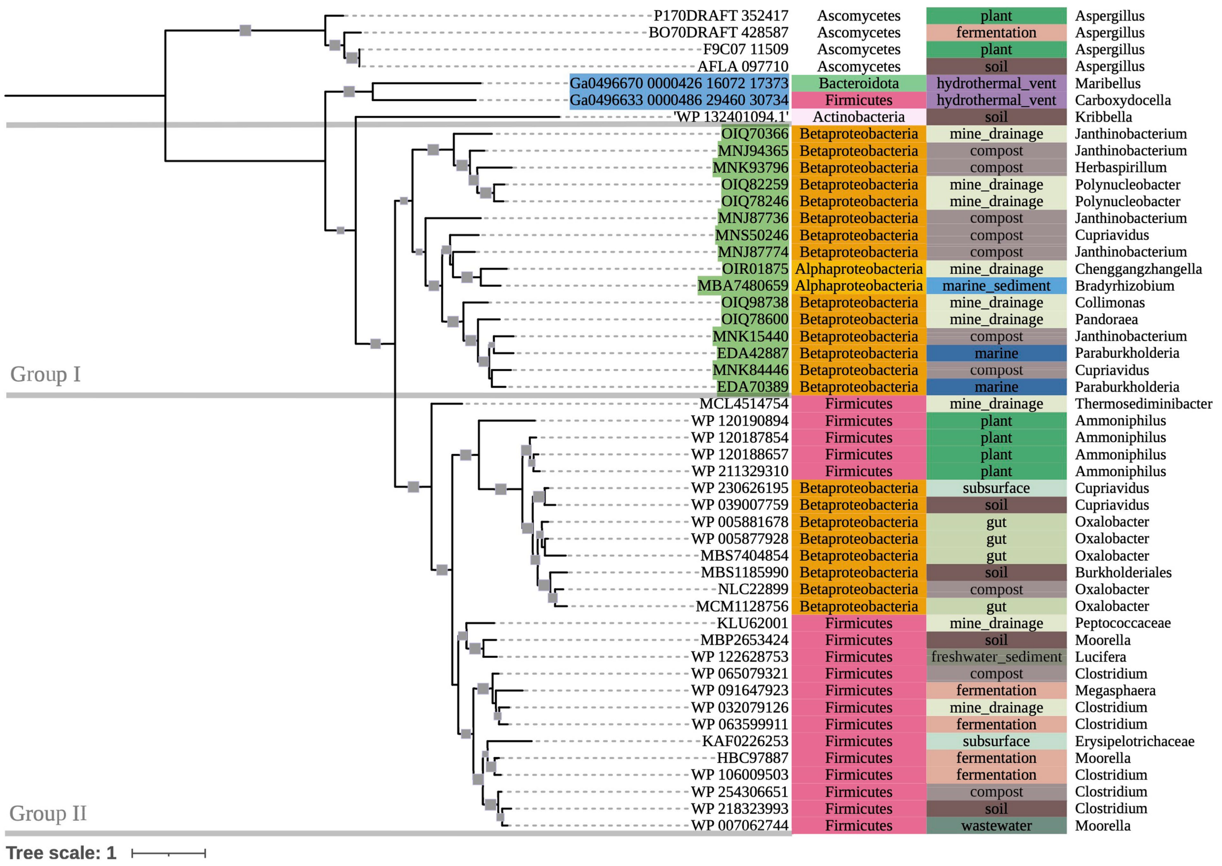

FIGURE 4
500-bootstrap maximum-likelihood phylogenetic tree of bacterial and fungal *oxlT* genes. Bootstrap values >50 displayed as gray boxes (min=50, max=100). Green-highlighted sequence identifiers indicate MAG genes. Blue-highlighted sequence identifiers indicate hydrothermal transcripts. Left-most annotation column indicates phylum taxonomy, class for Proteobacteria. Center column indicates source environment. Right-most column indicates genus taxonomy, or the next most exclusive classification available.

phenylalanine substitution in our hydrothermal fungal transcript (Ga0496672_0005142_1867_2910), consistent with our other fungal *oxdC* genes. E-333 was conserved among terrestrial sequences of interest (PID = 62.5%).

Key residues in the *frc* gene (Supplementary Figure 5) include Q-17, W-48, D-169, G-259, and G-260 (Toyota et al., 2008). Notably, all were completely conserved (PID = 100%) across all bacterial sequences in the alignment, with the exception of W-48 which was only present in seven of the sequences examined here (consensus Q 87.3%). Alternatively, fungal sequences had high conservation of D-240 only, and low conservation of the other key residues.

In the *oxlT* gene, 12 key residues are identified in UnitprotKB as having deleterious effects after mutagenic experimentation (Fu et al., 2001). Conservation of these residues ranged from 0 to 96%. However, a gene sequenced from *Kribbella albertanoniae* (the only Actinobacteria sequence on this tree), recently confirmed to be an aerobic oxalotroph that utilizes the OXLT enzyme (Bravo et al., 2013; Robertson and Meyers, 2022), showed conservation of only four of these 12 residues. Hence, we suspect that there may be greater variation in OXLT-encoding sequences than other key genes involved in oxalotrophy, and assessments of key residue conservation and subsequent conclusions about enzyme function in these organisms require more data of existing *oxlT* genotypes.

3.3. Energetics

The oxalotrophic reaction where bacteria catalyze the conversion of oxalate to calcite has been represented by Equation 1 (Garvie, 2006). This reaction represents the conversion of inorganic carbon into an organic component (represented by a generic CHO molecule) and inorganic bicarbonate formation in the presence of water. Based on known bacterial oxalotrophic catabolic pathways (Verrecchia et al., 2006), a more biologically relevant reaction would be oxalate converted to formate and bicarbonate. As a balanced overall reaction, this would be best represented by the oxalate ion and water converted to the formate ion and bicarbonate ion for circumneutral pH (Equation 2). Using Equation 2, we calculated the Gibbs free energy at standard state (ΔG_r°) for a range of temperatures (2, 20, 50, 100°C) and pressures (1.01 and 250 bar) representative of marine and hydrothermal conditions which host other chemolithotrophic metabolisms (Nakamura and Takai, 2014) using the WORM portal (see Methods). These values ranged from −25.0 to −33.2 kJ/mol, with slightly higher yield at atmospheric pressures (Table 2). Temperature was a larger factor in ΔG_r° than pressure, with the highest energy yield at the highest temperature (−33.1 and −33.2 kJ/mol at 1.01 and 250 bar, respectively). For comparison, the ΔG_r° of anaerobic oxidation of methane coupled to sulfate reduction (AOM-SR, Equation 3) ranges from 30.1 to −43.1 across the sample pressure/temperature space (Nakamura and Takai, 2014).

While there is a paucity of data regarding the concentrations of oxalate in hydrothermal fluids and plumes, we can approximate significant ranges for concentrations that would affect the favorability of Equation 2 using the WORM portal. First, we assumed an activity of 1 M, 10 μM, and 2 mM for water, formate, and bicarbonate, respectively. Then we evaluated a range of activities for oxalate. For 100°C, activity of oxalate below 0.1 μM (10^{-7} M) reduced the favorability of (increased) ΔG_r and activities of 1 μM (10^{-6} M) or 10 μM (10^{-5} M) increased the favorability (lowered) ΔG_r to 38.8 kJ/mol and − 41.1 kJ/mol, respectively.

$$C_2O_4^{2-} + H_2O + H^+ \rightarrow HCO + HCO_3^- \quad (1)$$

$$C_2O_4^{2-} + H_2O \rightarrow HCOO^- + HCO_3^- \quad (2)$$

$$SO_4^{2-} + CH_4 \rightarrow HS^- + HCO_3^- + H_2O \quad (3)$$

4. Discussion

Phylogenies of *oxc* and *oxdC* genes demonstrated grouping primarily by taxonomy. For example, *oxdC* clades of Proteobacteria and Terrabacteria from the same metagenomic compost sample grouped with their respective taxonomic groups rather than with each other, suggesting that their genes were inherited vertically (ancestrally) rather than by horizontal gene transfer (HGT). Although, some mixed-taxonomy clades (e.g., *oxc* Group II: Clades II and III)—including taxa not previously described as oxalotrophic—grouped by source environments instead of taxonomy, particularly from soil and gut microbiomes, where HGT is known to be prevalent (Heuer and Smalla, 2007; Berthold et al., 2016). HGT may still be a mechanism for gene proliferation among close relatives in these environments. As more oxalotrophic organisms are described from these novel environments, we hope to gain more resolution on these gene histories.

There may also be evidence for phylogenetic differences between *oxc* genes used in either predominantly anaerobic or aerobic oxalate degradation pathways (II and III, respectively; Figure 1). In Group II, some clades' (Clade II, Clade IV-I) source environments were possibly anoxic, while others (Clade III, Clade IV-II) appear to range between hypoxic and highly oxygenated. This possible distinction between oxalate degradation pathways may also explain some grouping on our *oxlT* tree, which placed a clade of Betaproteobacteria sequences from anaerobe-hosting source environments (gut microbiomes, anaerobic digesters, etc.) in Group II (Firmicutes of mixed terrestrial environments) rather than Group I (other terrestrial-dominant Proteobacteria). Further sequencing of oxalotrophs isolated under varying conditions may help to better characterize the phylogenetics of oxalate degradation pathways.

While the conservation of protein activity in the novel sequences recovered by bioinformatic approaches requires further research, the highly conserved key residues in our *oxc* and *frc* alignments supports the potential for similar function across the alignments. Moreover,

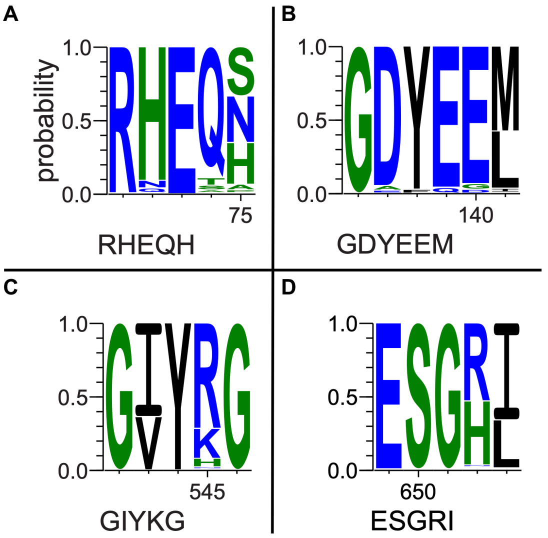

FIGURE 5
Selected oxc pore logos demonstrating conservation of **(A)** E-56, **(B)** Y-120, E-121, **(C)** Y-483, **(D)** S-553, and G-555 in a multiple-sequence alignment of bacterial isolate, MAG, and hydrothermal transcriptome genes and predicted fungal oxc genes. Letter strings below each logo represent partial reference gene sequences as documented in UniprotKB (The UniProt Consortium, 2021).

TABLE 2 Theoretical standard state Gibbs free energy ($\Delta G_r°$) for oxalotrophy (Equation 2) and anaerobic methanotrophy (Equation 3) across relevant marine temperatures and pressures.

Temperature (°C)	Pressure (bar)	EQ 2 $\Delta G_r°$ (kJ/mol)	EQ 3 $\Delta G_r°$ (kJ/mol)
2	1.01	−25.0	−30.6
20	1.01	−26.2	−33.0
50	1.01	−28.6	−36.9
100	1.01	−33.2	−43.1
2	250	−25.0	−30.1
20	250	−26.2	−32.6
50	250	−28.5	−36.6
100	250	−33.1	−43.0

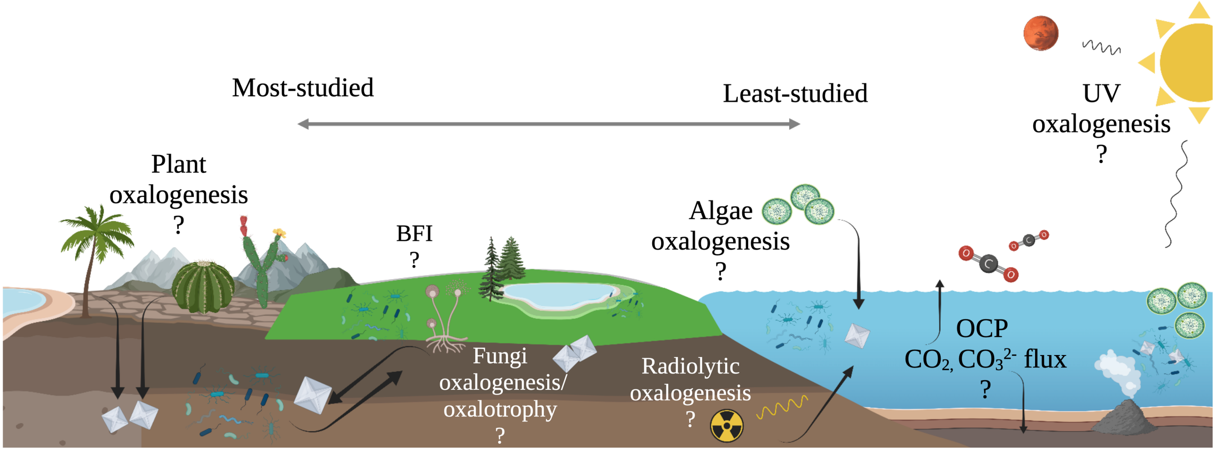

FIGURE 6
Illustration of unconstrained oxalate flux in the oxalate-carbonate pathway (OCP) and other possible, yet unexplored sub-cycles of global carbon cycling. Processes to the left are well-documented, while processes to the right are relatively unexplored.

conservation among predicted fungal *oxc* genes supports their annotation as OXC-encoding sequences. Most notably, marine MAG sequences, hydrothermal transcripts, and sequences from taxa not previously known to be oxalotrophic had near complete conservation of key residues, supporting the possibility of unexplored oxalotrophy in their respective ecosystems and taxonomic groups. Where some metagenomic sequences of interest did not show key residue conservation due to termination, we question if they may be incomplete assemblies. Key residue conservation was interpreted to be less significant in our assessment of our *oxlT* alignment considering high variability and poor conservation in *Kribbella albertanoniae*, which is known to actively utilize the oxalate:formate antiporter (see Results). Similarly, our *oxdC* alignment, which used a reference gene sequenced from *Bacillus subtilis* (a Terrabacterium), showed poor conservation among non-Terrabacteria sequences. In both cases, this may suggest that amino acid sequences for these genes vary too widely to be recovered with only a single reference sequence query.

The known diversity of oxalotrophic bacteria was limited to the phyla Proteobacteria, Actinobacteria, and Firmicutes until 2017 with the discovery of oxalotrophic Bacteroidetes in a mouse gut microbiome (Tanca et al., 2017). Furthermore, active oxalotrophic bacteria have only been documented in terrestrial ecosystems (soil, freshwater sediments, plants, gut microbiomes and other host-associations, etc.). This study recovered gene sequences from public datasets that were taxonomically assigned to Fusobacteria, Deltaproteobacteria, Chloroflexi, and Acidobacteria, all of which may represent additional oxalotrophic groups not previously described in the literature. The purported *oxc* sequence from a marine isolate of *Polarella glacialis* (CAE8740054), a species known for its relatively large genome (billions of base pairs; Stephens et al., 2020) may represent the discovery of an oxalotrophic protist, but verification of transcription or metabolic activity would be required to determine if the gene is functional or simply non-encoding "junk" DNA.

Isolates, MAGs, and transcriptome sequences were also recovered in this study from diverse marine environments. These sequences were sampled from ocean and arctic surface water, oxygen minimum mesopelagic water, and sediments and diffuse fluids around hydrothermal vents (Table 1 and Supplementary Table 2). Oxalate is produced in such environments by algae (Pueschel, 2019) and porifera (Cerrano et al., 1999), as well as abiotic processes (Vandenborre et al., 2021; Zhao et al., 2022). Our energy calculations for oxalotrophy have a theoretical $\Delta G_r°$ similar to low energy metabolisms such as AOM-SR (Nakamura and Takai, 2014), but are still energy-yielding. Therefore, oxalotrophy is plausible in marine systems, especially where hydrothermal fluids may provide both a source of oxalate and warmer temperatures. Overall, hot desert and tropical soils with oxalate sourced from plants may be the most energy-yielding environment for this metabolism.

5. Conclusion

The work presented here suggests the diversity of microbial oxalotrophs may be more extensive than previously recognized and oxalotrophs may occupy a significant niche in marine ecosystems, where oxalate sources are present but unconstrained (Figure 6). Furthermore, the abiotic processes that produce oxalate on Earth, and beyond, make oxalotrophy a candidate for astrobiological research. Oxalate minerals are thought to exist in a large, stable reservoir on Mars (Applin et al., 2015), and are known to be delivered to the inner solar system in meteorites (Peltzer et al., 1984; Shimoyama and Shigematsu, 1994). Continued study of the microbe-mineral interactions in the OCP may further elucidate their role in marine ecosystems, and thereby its role in global carbon cycling and as a potential signature of life in the universe.

Data availability statement

The original contributions presented in the study are included in the article/Supplementary material, further inquiries can be directed to the corresponding author.

Author contributions

AS and ET-R contributed to the conception and design of the study and read and approved the submitted version. AS developed the database, conducted the analyses, and wrote the first draft of the manuscript. ET-R contributed to the manuscript scope and revision. All authors contributed to the article and approved the submitted version.

Acknowledgments

We thank Prof. Laurence Garvie, Jon Lima-Zaloumis, and Veronica Mierzejewski for their helpful feedback on this manuscript. We acknowledge Research Computing at Arizona State University for providing high-performance computing resources that contributed to our research. Figures 1, 6 were created with BioRender.com (2023).

Conflict of interest

The authors declare that the research was conducted in the absence of any commercial or financial relationships that could be construed as a potential conflict of interest.

Publisher's note

Supplementary material

The Supplementary material for this article can be found online at: https://www.frontiersin.org/articles/10.3389/fmicb.2023.1161937/full#supplementary-material

References

Altschul, S. F., Madden, T. L., Schäffer, A. A., Zhang, J., Zhang, Z., Miller, W., et al. (1997). Gapped BLAST and PSI-BLAST: a new generation of protein database search programs. *Nucleic Acids Res.* 25, 3389–3402. doi: 10.1093/nar/25.17.3389

Anand, R., Dorrestein, P. C., Kinsland, C., Begley, T. P., and Ealick, S. E. (2002). Structure of oxalate decarboxylase from *Bacillus subtilis* at 1.75 Å resolution. *Biochemistry* 41, 7659–7669. doi: 10.1021/bi0200965

Anderson, R., Anantharaman, K., and Trembath-Reichert, E. (2019). Microbial and viral mediation of biogeochemical cycles from source to sink in hydrothermal vent systems. doi: 10.46936/10.25585/60001283

Applin, D. M., Izawa, M. R. M., Cloutis, E. A., Goltz, D., and Johnson, J. R. (2015). Oxalate minerals on Mars? *Earth Planet. Sci. Lett.* 420, 127–139. doi: 10.1016/j.epsl.2015.03.034

Baetz, A. L., and Allison, M. J. (1989). Purification and characterization of oxalyl-coenzyme a decarboxylase from Oxalobacter formigenes. *J. Bacteriol.* 171, 2605–2608. doi: 10.1128/jb.171.5.2605-2608.1989

Baetz, A. L., and Allison, M. J. (1990). Purification and characterization of formyl-coenzyme a transferase from Oxalobacter formigenes. *J. Bacteriol.* 172, 3537–3540. doi: 10.1128/jb.172.7.3537-3540.1990

Baran, E. J. (2014). Review: natural oxalates and their analogous synthetic complexes. *J. Coord. Chem.* 67, 3734–3768. doi: 10.1080/00958972.2014.937340

Barth, J.-G. (2020). Limestone and calcium in plants. *Elemente Naturwissenschaft* 112, 29–78. doi: 10.18756/edn.112.29

Basenko, E. Y., Pulman, J. A., Shanmugasundram, A., Harb, O. S., Crouch, K., Starns, D., et al. (2018). FungiDB: an integrated bioinformatic resource for fungi and oomycetes. *J Fungi* 4:39. doi: 10.3390/jof4010039

Berthold, T., Centler, F., Hübschmann, T., Remer, R., Thullner, M., Harms, H., et al. (2016). Mycelia as a focal point for horizontal gene transfer among soil bacteria. *Sci. Rep.* 6:36390. doi: 10.1038/srep36390

Berthold, C. L., Toyota, C. G., Moussatche, P., Wood, M. D., Leeper, F., Richards, N. G. J., et al. (2007). Crystallographic snapshots of oxalyl-CoA decarboxylase give insights into catalysis by nonoxidative ThDP-dependent decarboxylases. *Structure* 15, 853–861. doi: 10.1016/j.str.2007.06.001

Boyer, G., Robare, J., Ely, T., and Shock, E. (2022). AqEquil: Python package for aqueous geochemical speciation (0.15.3). Zenodo. doi: 10.5281/zenodo.6382932

Bravo, D., Martin, G., David, M. M., Cailleau, G., Verrecchia, E., and Junier, P. (2013). Identification of active oxalotrophic bacteria by Bromodeoxyuridine DNA labeling in a microcosm soil experiments. *FEMS Microbiol. Lett.* 348, 103–111. doi: 10.1111/15746968.12244

Brodie, E., Bouskill, N., Beller, H., Chakraborty, R., Hao, Z., Karaoz, U., et al. (2017). The synchronization of microbial and plant phenology in a mountainous watershed and its importance for nutrient retention under changing hydrologic regimes. *Award DOI Serv*. doi: 10.46936/fics.proj.2017.49991/60006232

Bungartz, F., Garvie, L. A. J., and Nash, T. H. (2004). Anatomy of the endolithic Sonoran Desert lichen *Verrucaria rubrocincta* Breuss: implications for biodeterioration and biomineralization. *Lichenologist* 36, 55–73. doi: 10.1017/S0024282904013854

Camacho, C., Coulouris, G., Avagyan, V., Ma, N., Papadopoulos, J., Bealer, K., et al. (2009). BLAST+: architecture and applications. *BMC Bioinformatics* 10:421. doi: 10.1186/1471-2105-10-421

Caspi, R., Billington, R., Fulcher, C. A., Keseler, I. M., Kothari, A., Krummenacker, M., et al. (2018). The MetaCyc database of metabolic pathways and enzymes. *Nucleic Acids Res.* 46, D633–D639. doi: 10.1093/nar/gkx935

Cerrano, C., Bavestrello, G., Arillo, A., Benatti, U., Bonpadre, S., Cattaneo-Vietti, R., et al. (1999). Calcium oxalate production in the marine sponge Chondrosia reniformis. *Mar. Ecol. Prog. Ser.* 179, 297–300. doi: 10.3354/meps179297

Chen, I.-M. A., Chu, K., Palaniappan, K., Ratner, A., Huang, J., Huntemann, M., et al. (2023). The IMG/M data management and analysis system v.7: content updates and new features. *Nucleic Acids Res.* 51, D723–D732. doi: 10.1093/nar/gkac976

Crooks, G. E., Hon, G., Chandonia, J.-M., and Brenner, S. E. (2004). WebLogo: a sequence logo generator: figure 1. *Genome Res.* 14, 1188–1190. doi: 10.1101/gr.849004

Edgar, R. C. (2004). MUSCLE: multiple sequence alignment with high accuracy and high throughput. *Nucleic Acids Res.* 32, 1792–1797. doi: 10.1093/nar/gkh340

Franceschi, V. R., and Nakata, P. A. (2005). Calcium oxalate in plants: formation and function. *Annu. Rev. Plant Biol.* 56, 41–71. doi: 10.1146/annurev.arplant.56.032604.144106

Fu, D., Sarker, R. I., Abe, K., Bolton, E., and Maloney, P. C. (2001). Structure/function relationships in OxlT, the oxalate-formate transporter of Oxalobacter formigenes. *J. Biol. Chem.* 276, 8753–8760. doi: 10.1074/jbc.M008417200

Garvie, L. A. J. (2006). Decay of cacti and carbon cycling. *Naturwissenschaften* 93, 114–118. doi: 10.1007/s00114-005-0069-7

He, H., Veneklaas, E. J., Kuo, J., and Lambers, H. (2014). Physiological and ecological significance of biomineralization in plants. *Trends Plant Sci.* 19, 166–174. doi: 10.1016/j.tplants.2013.11.002

Heuer, H., and Smalla, K. (2007). Horizontal gene transfer between bacteria. *Environ. Biosaf. Res.* 6, 3–13. doi: 10.1051/ebr:2007034

Hofmann, B. A., and Bernasconi, S. M. (1998). Review of occurrences and carbon isotope geochemistry of oxalate minerals: implications for the origin and fate of oxalate in diagenetic and hydrothermal fluids. *Chem. Geol.* 149, 127–146. doi: 10.1016/S00092541(98)00043-6

Jones, D. L. (1998). Organic acids in the rhizosphere – a critical review. *Plant Soil* 205, 25–44. doi: 10.1023/A:1004356007312

Kanehisa, M., Sato, Y., and Morishima, K. (2016). BlastKOALA and GhostKOALA: KEGG tools for functional characterization of genome and metagenome sequences. *J. Mol. Biol.* 428, 726–731. doi: 10.1016/j.jmb.2015.11.006

Karp, P. D., Billington, R., Caspi, R., Fulcher, C. A., Latendresse, M., Kothari, A., et al. (2019). The BioCyc collection of microbial genomes and metabolic pathways. *Brief. Bioinform.* 20, 1085–1093. doi: 10.1093/bib/bbx085

Letunic, I., and Bork, P. (2021). Interactive tree of life (iTOL) v5: an online tool for phylogenetic tree display and annotation. *Nucleic Acids Res.* 49, W293–W296. doi: 10.1093/nar/gkab301

Lung, H. Y., Baetz, A. L., and Peck, A. B. (1994). Molecular cloning, DNA sequence, and gene expression of the oxalyl-coenzyme a decarboxylase gene, oxc, from the bacterium Oxalobacter formigenes. *J. Bacteriol.* 176, 2468–2472. doi: 10.1128/jb.176.8.2468-2472.1994

McNair, J. B. (1932). The interrelation between substances in plants: essential oils and resins, cyanogen and oxalate. *Am. J. Bot.* 19, 255–272. doi: 10.2307/2436337

Mukherjee, S., Stamatis, D., Li, C. T., Ovchinnikova, G., Bertsch, J., Sundaramurthi, J. C., et al. (2023). Twenty-five years of genomes OnLine database (GOLD): data updates and new features in v.9. *Nucleic Acids Res.* 51, D957–D963. doi: 10.1093/nar/gkac974

Müller, D. B., Schubert, O. T., Röst, H., Aebersold, R., and Vorholt, J. A. (2016). Systems-level proteomics of two ubiquitous leaf commensals reveals complementary adaptive traits for Phyllosphere colonization. *Mol. Cell. Proteomics* 15, 3256–3269. doi: 10.1074/mcp.M116.058164

Nakamura, K., and Takai, K. (2014). Theoretical constraints of physical and chemical properties of hydrothermal fluids on variations in chemolithotrophic microbial communities in seafloor hydrothermal systems. *Prog Earth Planet Sci* 1:5. doi: 10.1186/21974284-1-5

Nakata, P. A. (2003). Advances in our understanding of calcium oxalate crystal formation and function in plants. *Plant Sci.* 164, 901–909. doi: 10.1016/S01689452(03)00120-1

Peltzer, E. T., Bada, J. L., Schlesinger, G., and Miller, S. L. (1984). The chemical conditions on the parent body of the Murchison meteorite: some conclusions based on amino, hydroxy and dicarboxylic acids. *Adv. Space Res.* 4, 69–74. doi: 10.1016/0273-1177(84)90546-5

Pueschel, C. M. (2019). Calcium oxalate mineralisation in the algae. *Phycologia* 58, 331–350. doi: 10.1080/00318884.2019.1578587

Quayle, J. R., Keech, D. B., and Taylor, G. A. (1961). Carbon assimilation by pseudomonas oxalaticus (OXI). 4. Metabolism of oxalate in cell-free extracts of the organism grown on oxalate. *Biochem. J.* 78, 225–236. doi: 10.1042/bj0780225

Reimer, L. C., Sardà Carbasse, J., Koblitz, J., Ebeling, C., Podstawka, A., and Overmann, J. (2022). BacDive in 2022: the knowledge base for standardized bacterial and archaeal data. *Nucleic Acids Res.* 50, D741–D746. doi: 10.1093/nar/gkab961

Robertson, C. F. M., and Meyers, P. R. (2022). Oxalate utilisation is widespread in the actinobacterial genus Kribbella. *Syst. Appl. Microbiol.* 45:126373. doi: 10.1016/j.syapm.2022.126373

Rusching, U., Müller, U., Willnow, P., and Höpner, T. (1976). CO_2 reduction to formate by NADH catalysed by formate dehydrogenase from pseudomonas oxalaticus. *Eur. J. Biochem.* 70, 325–330. doi: 10.1111/j.1432-1033.1976.tb11021.x

Schneider, T. D., and Stephens, R. M. (1990). Sequence logos: a new way to display consensus sequences. *Nucleic Acids Res.* 18, 6097–6100. doi: 10.1093/nar/18.20.6097

Shimoyama, A., and Shigematsu, R. (1994). Dicarboxylic acids in the Murchison and Yamato791198 carbonaceous chondrites. *Chem. Lett.* 23, 523–526. doi: 10.1246/cl.1994.523

Sly, W. S., and Stadtman, E. R. (1963). Formate metabolism. *J. Biol. Chem.* 238, 2632–2638. doi: 10.1016/S0021-9258(18)67878-0

Stamatakis, A. (2014). RAxML version 8: a tool for phylogenetic analysis and post-analysis of large phylogenies. *Bioinformatics* 30, 1312–1313. doi: 10.1093/bioinformatics/btu033

Stephens, W. E. (2012). Whewellite and its key role in living systems. *Geol. Today* 28, 180–185. doi: 10.1111/j.1365-2451.2012.00849.x

Stephens, T. G., González-Pech, R. A., Cheng, Y., Mohamed, A. R., Burt, D. W., Bhattacharya, D., et al. (2020). Genomes of the dinoflagellate Polarella glacialis encode tandemly repeated single-exon genes with adaptive functions. *BMC Biol.* 18:56. doi: 10.1186/s12915-020-00782-8

Strobel, B. W. (2001). Influence of vegetation on low-molecular-weight carboxylic acids in soil solution—a review. *Geoderma* 99, 169–198. doi: 10.1016/S0016-7061(00)00102-6

Tanca, A., Manghina, V., Fraumene, C., Palomba, A., Abbondio, M., Deligios, M., et al. (2017). Metaproteogenomics reveals taxonomic and functional changes between cecal and fecal microbiota in mouse. *Front. Microbiol.* 8:391. doi: 10.3389/fmicb.2017.00391

Tanner, A., and Bornemann, S. (2000). *Bacillus subtilis* YvrK is an acid-induced oxalate decarboxylase. *J. Bacteriol.* 182, 5271–5273. doi: 10.1128/JB.182.18.5271-5273.2000

The UniProt Consortium (2021). UniProt: the universal protein knowledgebase in 2021. *Nucleic Acids Res.* 49, D480–D489. doi: 10.1093/nar/gkaa1100

Toyota, C. G., Berthold, C. L., Gruez, A., Jónsson, S., Lindqvist, Y., Cambillau, C., et al. (2008). Differential substrate specificity and kinetic behavior of *Escherichia coli* YfdW and Oxalobacter formigenes formyl coenzyme a transferase. *J. Bacteriol.* 190, 2556–2564. doi: 10.1128/JB.01823-07

Turroni, S., Vitali, B., Bendazzoli, C., Candela, M., Gotti, R., Federici, F., et al. (2007). Oxalate consumption by lactobacilli: evaluation of oxalyl-CoA decarboxylase and formyl-CoA transferase activity in lactobacillus acidophilus. *J. Appl. Microbiol.* 103, 1600–1609. doi: 10.1111/j.1365-2672.2007.03388.x

Vandenborre, J., Truche, L., Costagliola, A., Craff, E., Blain, G., Baty, V., et al. (2021). Carboxylate anion generation in aqueous solution from carbonate radiolysis, a potential route for abiotic organic acid synthesis on earth and beyond. *Earth Planet. Sci. Lett.* 564:116892. doi: 10.1016/j.epsl.2021.116892

Verrecchia, E. P. (1990). Litho-diagenetic implications of the calcium oxalate-carbonate biogeochemical cycle in semiarid Calcretes, Nazareth, Israel. *Geomicrobiol J.* 8, 87–99. doi: 10.1080/01490459009377882

Verrecchia, E. P., Braissant, O., and Cailleau, G. (2006). "The oxalate–carbonate pathway in soil carbon storage: the role of fungi and oxalotrophic bacteria" in *Fungi in biogeochemical cycles*. ed. G. M. Gadd (Cambridge: Cambridge University Press), 289–310.

Waterhouse, A. M., Procter, J. B., Martin, D. M. A., Clamp, M., and Barton, G. J. (2009). Jalview version 2—a multiple sequence alignment editor and analysis workbench. *Bioinformatics* 25, 1189–1191. doi: 10.1093/bioinformatics/btp033

Zhao, J.-J., Zhang, Y.-F., Zhao, T.-L., Li, H., Yao, Q.-Z., Fu, S.-Q., et al. (2022). Abiotic formation of calcium oxalate under UV irradiation and implications for biomarker detection on Mars. *Astrobiology* 22, 35–48. doi: 10.1089/ast.2020.2416

frontiers | Frontiers in Microbiology

TYPE Original Research
PUBLISHED 03 July 2023
DOI 10.3389/fmicb.2023.1205558

Metapangenomic investigation provides insight into niche differentiation of methanogenic populations from the subsurface serpentinizing environment, Samail Ophiolite, Oman

Patrick H. Thieringer[1], Eric S. Boyd[2], Alexis S. Templeton[3] and John R. Spear[1]*

[1]Department of Civil and Environmental Engineering, Colorado School of Mines, Golden, CO, United States, [2]Department of Microbiology and Cell Biology, Montana State University, Bozeman, MT, United States, [3]Department of Geological Sciences, University of Colorado, Boulder, CO, United States

Serpentinization reactions produce highly reduced waters that have hyperalkaline pH and that can have high concentrations of H_2 and CH_4. Putatively autotrophic methanogenic archaea have been identified in the subsurface waters of the Samail Ophiolite, Sultanate of Oman, though the strategies to overcome hyperalkaline pH and dissolved inorganic carbon limitation remain to be fully understood. Here, we recovered metagenome assembled genomes (MAGs) and applied a metapangenomic approach to three different *Methanobacterium* populations to assess habitat-specific functional gene distribution. A Type I population was identified in the fluids with neutral pH, while a Type II and "Mixed" population were identified in the most hyperalkaline fluids (pH 11.63). The core genome of all *Methanobacterium* populations highlighted potential DNA scavenging techniques to overcome phosphate or nitrogen limitation induced by environmental conditions. With particular emphasis on the Mixed and Type II population found in the most hyperalkaline fluids, the accessory genomes unique to each population reflected adaptation mechanisms suggesting lifestyles that minimize niche overlap. In addition to previously reported metabolic capability to utilize formate as an electron donor and generate intracellular CO_2, the Type II population possessed genes relevant to defense against antimicrobials and assimilating potential osmoprotectants to provide cellular stability. The accessory genome of the Mixed population was enriched in genes for multiple glycosyltransferases suggesting reduced energetic costs by adhering to mineral surfaces or to other microorganisms, and fostering a non-motile lifestyle. These results highlight the niche differentiation of distinct *Methanobacterium* populations to circumvent the challenges of serpentinization impacted fluids through coexistence strategies, supporting our ability to understand controls on methanogenic lifestyles and adaptations within the serpentinizing subsurface fluids of the Samail Ophiolite.

KEYWORDS

serpentinization, subsurface, pangenomics, niche differentiation, geomicrobiology

Check for updates

OPEN ACCESS

EDITED BY
Mark Alexander Lever,
The University of Texas at Austin, United States

REVIEWED BY
Cody Sheik,
University of Minnesota Duluth, United States
Yinzhao Wang,
Shanghai Jiao Tong University, China

*CORRESPONDENCE
John R. Spear
✉ jspear@mines.edu

RECEIVED 14 April 2023
ACCEPTED 13 June 2023
PUBLISHED 03 July 2023

CITATION
Thieringer PH, Boyd ES, Templeton AS and Spear JR (2023) Metapangenomic investigation provides insight into niche differentiation of methanogenic populations from the subsurface serpentinizing environment, Samail Ophiolite, Oman.
Front. Microbiol. 14:1205558.
doi: 10.3389/fmicb.2023.1205558

Introduction

Earth's deep subsurface biosphere requires substrates created from water-rock interactions to support a continued source of chemical energy for microbial metabolisms. Serpentinization—the hydration and oxidation of ultramafic, olivine-rich rock connected to the reduction of water—produces the secondary minerals serpentine, iron oxides, as well as hydroxides, and molecular hydrogen (H_2; Sleep et al., 2004; Schulte et al., 2006; McCollom and Seewald, 2013). Surface derived inorganic carbon (CO_2) can be abiotically reduced to methane (CH_4) and other potential hydrocarbons or organic acids (Holm and Charlou, 2001; McCollom and Seewald, 2013; Miller et al., 2017). These water-rock reactions produce fluids that are geochemically reduced with very low oxidation–reduction potentials. These serpentinized-impacted waters generate conditions of alkaline to hyperalkaline pH values from 8 to greater than 12, while producing appreciable concentrations of H_2 and CH_4 that can readily serve as electron donors for subsurface microbial metabolisms (Russell et al., 2010; Brazelton et al., 2012; Schrenk et al., 2013; Miller et al., 2016; Suzuki et al., 2017). Serpentinization acts as a viable process for supporting chemolithoautotrophic life in the deep subsurface through abiotic reactions.

Sites of terrestrial serpentinization are distributed globally and show evidence of methanogenic and methanotrophic microbial members, including the Voltri Massif (Italy), Santa Elena Ophiolite (Costa Rica), the Chimaera Seeps (Turkey), and the Manleluag Spring National Park of Zamabales (Philippines; Brazelton et al., 2017; Crespo-Medina et al., 2017; Zwicker et al., 2018; Wang et al., 2022). Specifically, the Samail Ophiolite, Sultanate of Oman, offers the largest exposed ophiolite on Earth that is actively undergoing low temperature serpentinization (Neal and Stanger, 1985; Kelemen and Matter, 2008; Kelemen et al., 2011; Paukert et al., 2012; Miller et al., 2016). Recent work has determined the presence of an active CH_4 cycle in the subsurface fluids of the Samail Ophiolite, where methanogenic populations are most abundant and transcriptionally active in the hyperalkaline fluids (Kraus, 2021). Additional ^{14}C-labeled substrate microcosm assays confirmed the generation of CH_4 and assimilation of organic substrate into biomass from organisms within the subsurface fluids (Fones et al., 2019). Investigation into the methanogenic community has revealed the diversification of the genus *Methanobacterium*, reflecting species inhabiting the hyperalkaline fluids capable of potentially utilizing formate as an alternative carbon source and electron donor (Fones et al., 2021). These incubation studies have provided initial insights regarding the carbon metabolic capabilities of *Methanobacterium*, yet further investigation is required to understand the unique pH and nutrient limitation strategies employed by *Methanobacterium* populations to overcome environmental stressors controlling methanogenic activity in subsurface serpentinizing conditions.

The genomic relatedness of a group of organisms can be studied with the use of pangenomics to contrast population diversity and functional capabilities (Medini et al., 2005; Tettelin et al., 2005; Vernikos et al., 2015). The pangenome can identify the core genome shared across an entire group, as well as the accessory genome that is specific to individual members or sub-groups (Delmont and Eren, 2018). The taxonomic resolution of pangenomics can be applied at higher order rankings in order to demonstrate the relatedness of members and provide informative comparisons across phylogenetic or environmental associations (Simon et al., 2017; Utter et al., 2020). However, the application of pangenomics to environmental systems remains understudied. Pangenomic analyses have primarily focused on genomes of cultivars to describe the pangenome of a well-studied taxon. Contrastingly, pangenomic tools applied to organisms difficult to cultivate from the environment can reveal the genetic potential across a taxon of interest and the various sub-populations separated by environmental conditions. The combination of metagenomics and pangenomics allows for the opportunity to investigate microbial members across complex environmental conditions (Simmons et al., 2008; Kashtan et al., 2014). Sampling for metagenomes can provide information of microbial populations within their environmental setting, and pangenomic investigation can reveal the biogeography of microbial diversity and gene distribution (Delmont and Eren, 2018). This combination of tools termed "metapangenomics" can inform on adaptability to environmental conditions, and broadly investigate the evolution of microbial members across diverse habitats (Delmont and Eren, 2018). The Samail Ophiolite provides an ideal environmental system with distinct geochemical conditions across fluid types to investigate the adaptability of microbial populations within hyperalkaline settings. Methanogen populations serve as a prominent target for metapangenomic evaluation due to their abundance across pH and geochemical conditions to understand their biogeography and habitat-specific gene pools.

While preliminary work has highlighted some metabolic adaptations that enable *Methanobacterium* to function in the subsurface fluids of the Samail Ophiolite (Fones et al., 2019, 2021), further efforts to characterize how *Methanobacterium* overcome the polyextremic conditions in the hyperalkaline wells and maintain such a dominating presence are needed. Here we apply metagenomics to examine how *Methanobacterium* populations potentially overcome DIC limited and hyperalkaline pH conditions. A metapangenomic analysis was used to describe the adaptations of *Methanobacterium* populations spanning multiple subsurface wells at various pH conditions and depth profiles to highlight adaptive strategies through carbon utilization, use of transporters, and other survival mechanisms. The work herein helps to reveal how *Methanobacterium* populations exhibit niche differentiation for cohabitation and circumvent the energy limiting conditions induced from low temperature serpentinization in the subsurface fluids of the Samail Ophiolite.

Materials and methods

Site description and geochemical measurements

Three preexisting boreholes were sampled from a multi-borehole observatory established by the Oman Drilling Project and Oman Ministry of Regional Municipalities and Water Resources in Wadi Lawayni in the Wadi Tayin massif into the mantle section of the Samail Ophiolite (Kelemen et al., 2011; Templeton et al., 2021). Fluid samples were collected in February to March of 2020 using multiple devices to cover a range of depth intervals within each borehole. A Grundfos SQ 2–85 submersible pump (Grundfos Pumps Corp. Denmark) was used for "open" borehole pumping. This pumping method was conducted at 50 m in borehole WAB188 and 75 m in borehole BA3A. A Double Packer Standard System (SolExperts, France) was used in borehole NSHQ14. The packer system contains two inflatable rubber packers and a submersible pump, and one or both of the packers can be inflated to isolate depth intervals for discrete pumping of fluids as described in previous work (Nothaft et al., 2021a). The top packer was left uninflated to sample from the top of the water table (9 m) to 30 m where the bottom packer was set. The submersible pump and packer system were connected to a splitting manifold with field-washed Tygon tubing. An air-tight gas sampler was used in borehole BA3A by dropping at 100 and 275 m depth, capturing a ~1 m interval of approximately 5 L of fluid.

Prior to sampling, a field wash lasting ~20–30 min was performed on the pump, manifold, tubing and filter housing at each borehole. Fluids were collected for geochemical analysis by passing through a 0.2 μm polycarbonate filter into 15 mL Falcon tubes. Major cations were acidified with nitric acid in the field at the time of collection. As previously reported (Kraus, 2021), anion and cation concentrations were analyzed using inductively coupled plasma atomic emission spectroscopy (ICP-AES; Optima 5300, Perkin-Elmer, Freemont, CA) and ion chromatography (IC; ICS-90, Dionex, Sunnyville, CA) respectively at the Colorado School of Mines. Water temperature and pH were measured in the field with a Hach multiparameter field meter (HQ40D, Hach, Inc., Loveland, CO).

Sample collection, DNA extraction, and metagenomic sequencing

Biomass was collected from fluids passed through 0.2 μm polycarbonate filters when sampling from the submersible pump or packer system, or 0.1 μm filters from the air tight gas sampler. Approximately 5 L of fluid was passed through each filter or until noticeable particulates were collecting on the filter to ensure enough biomass was retrieved; in the case of the 0.1 μm filters, a minimum of 200 mL was passed through or until it was too difficult to deliver any liquid through the filter. Filters were immediately stored in DNA/RNA Shield™ (Zymo, Inc.) to be preserved until returned to the lab. DNA and RNA were extracted using the ZymoBIOMICS™ DNA/RNA Miniprep kit as described in previous work (Thieringer et al., 2021). Five samples representing each sampling depth from the boreholes described above were submitted for metagenomic sequencing on an Illumina NovaSeq platform (2 × 150 bp) and processed as a part of the Joint Genome Institute Pipeline, described in detail previously (Clum et al., 2021).

Metagenomic sequences were downloaded from the JGI/IMG portal, which already included steps of read quality filtering and trimming of adapters using BBduk (Bushnell, 2020). Reads were individually assembled using SPAdes with the "—meta" option for metagenomic data (Nurk et al., 2017). Individual reads were then mapped to contigs within each respective individual metagenome sample using Bowtie2 to generate coverage data (Langmead and Salzberg, 2012). Open reading frames (ORFs) were identified on the contigs with the program Prodigal and generated into contigs database files for downstream analysis with the program Anvi'o (Hyatt et al., 2010; Eren et al., 2015). Functional annotation of ORFs were identified with HMMER, Clusters of Orthologous Genes (COGS), Pfam, Kegg (through GhostKOALA), and with Interproscan using TIGRFAM and SUPERFAMILY (Zhang and Wood, 2003; Bateman, 2004; Kanehisa et al., 2007; Mulder and Apweiler, 2007; Haft et al., 2012; Galperin et al., 2021). Initial taxonomic annotation was provided by running the "anvi-estimate-scg-taxonomy" referencing the GTDB database, and helped guide binning efforts at the refinement stage (Eren et al., 2015). The contigs databases and BAM files created during the Bowtie2 mapping step were then created into a profile database within Anvi'o (Langmead and Salzberg, 2012; Eren et al., 2015). Initial binning was performed with CONCOCT, Maxbin2, and MetaBat2 software packages using default parameters (Alneberg et al., 2013; Wu et al., 2016; Kang et al., 2019). Bins were then integrated into DASTool to calculate the most optimized and non-redundant set of bins from each metagenome (Sieber et al., 2018). These binning results were imported into the profile database and then manually refined into metagenome assembled genomes (MAGs) within the Anvi'o interactive interface (Eren et al., 2015). MAGs were considered high-quality based upon >90% completion and <10% redundancy thresholds (Eren et al., 2015).

Phylogenomic analyses of *Methanobacterium* MAGs were conducted by using the program GtoTree (Lee, 2019). In brief, representative *Methanobacterium* genomes were downloaded as accession files from the Genome Taxonomy Database (GTDB), where only species cluster representatives were selected using the "—GTDB-representatives-only" flag. An outgroup genome representative was downloaded from NCBI for phylogenetic reconstruction, which included a genome for *Methanosarcina barkeri*. GtoTree was run with default settings except for the input single copy gene HMM sets using the "-H" flag, and the archaeal HMM target gene set was used for analysis which contains 76 marker genes. GtoTree then identifies target genes from MAGs and genomes using HMMER3, aligns each gene set with the MUSCLE program, and performs automated trimming with TrimAl (Zhang and Wood, 2003; Edgar, 2004; Capella-Gutierrez et al., 2009). The alignment and partitions files were then passed on to IQTree where a maximum likelihood phylogenetic analysis was conducted by identifying the optimal amino acid substitution model by implementing the "-m TEST" flag, and branch support was conducted with 1,000 ultrafast bootstraps (Minh et al., 2020). Tree files were then visualized and annotated with the Interactive Tree of Life (iTOL) web program (Letunic and Bork, 2007).

Metapangenomic workflow

Eight MAGs taxonomically identified as *Methanobacterium* considered high quality, from completion and redundancy scores, were examined through the pangenomic workflow outlined by Anvi'o (Eren et al., 2015; Utter et al., 2020). In brief, the workflow computes the amino acid identity level between all ORF pairs using BLASTp, and removes matches below a bitscore (at default value of 0.5; Altschul et al., 1990). Homologous gene clusters were grouped from ORFs using the Markov Clustering Algorithm (MCL; Eren et al., 2015; Utter et al., 2020). These gene clusters were then aligned using MUSCLE for interactive visualization (Edgar, 2004). Core genes and gene clusters are identified as sharing at least a fourth of the median coverage of where the sample gene originated from, otherwise the gene or gene cluster was determined to be accessory as described previously (Eren et al., 2015; Utter et al., 2020). The core and accessory genomes of groups were binned according to overlapping gene clusters identified in the Anvi'o interactive interface. Core and accessory genomic information determined from a metapangenomic approach does not differ from pangenomic analysis in terms of its meaning. Instead, a metapangenome incorporates metagenomic read recruitment to aid in identifying core and accessory genomic content across environmental conditions. The average nucleotide identity (ANI) of each MAG was calculated with the function "anvi-compute-genome-similarity" which calls the PyANI program (Pritchard et al., 2016). The "ANI_full_percent_identity" option was included in the final pangenome figure and used to compare the genome similarity of the eight *Methanobacterium* MAGs. This option takes into account both the percent identity of the aligned fraction from the MAGs being compared, as well as the aligned fraction or coverage of the MAGs. Inclusion of coverage/alignment fraction provides greater stress on the likelihood of the MAGs representing different species due to greater homology shared from greater alignment fractions (Pritchard et al., 2016). The command "anvi-summarize" was run on the pangenome and contigs databases to export the genes and gene clusters within each pangenome grouping (accessory or core). The exported text file was then curated in R and visualized with custom R scripts with the "ggplot2" package (Wickham, 2011; R Core Team, 2021).

A functional enrichment analysis was conducted on the eight MAGs assembled from this study in order to highlight gene clusters unique to the Oman *Methanobacterium* populations as a whole. Publicly available genomes ($n = 57$) for *Methanobacterium* were downloaded from the NCBI Genbank and Refseq databases, and the two other MAGs from wells NSHQ14 and WAB188, to contrast genes that may be unique to the MAGs from these hyperalkaline conditions within the Samail Ophiolite. In brief, a pangenome was conducted as above, this time including the MAGs identified in this study and external genomes (Supplementary Figure 1). The function "anvi-compute-functional-enrichment-in-pan" was run in order to identify which gene clusters are enriched a within the Oman *Methanobacterium* MAGs. Additional enrichment analyses were conducted on each *Methanobacterium* population against the others in order to compare and contrast genes that may serve as functionally core within each population type.

Results

Geochemical characterization of subsurface fluids

Subsurface fluids were sampled from three preexisting wells in the Samail Ophiolite for molecular biological and chemical analysis. The waters are classified based on previously reported data to reflect the geologic and hydrologic conditions of the fluids from each borehole—this includes Type I and Type II depending on the pH of the water and concentrations of Mg^{2+} and HCO_3^- or Ca^{2+} and OH^- (Rempfert et al., 2017). Hyperalkaline fluids retrieved from BA3A and NSHQ14 agree with previous classification, with pH values of 11.63 and 11.24, respectively, and are reflective of Type II waters resembling closed system—no exposure to atmospheric input—serpentinization. Samples collected from WAB188 represents a "contact" zone where faulted boundary between gabbro and peridotite bedrock exists and a neutral pH of 7.47 was measured and the fluid composition reflect Type I characterizations of open system serpentinization. DIC is typically in very small concentrations (~0.05–0.13 mM) in the hyperalkaline fluids of NSHQ14 and BA3A, and greater concentrations in the circumneutral fluids of WAB188 (~3 mM; Rempfert et al., 2017; Fones et al., 2021; Nothaft et al., 2021b). Other potential sources of carbon generated as a result of serpentinization include acetate and formate, which were present in variable concentration in all fluids sampled. Acetate concentrations within hyperalkaline fluids were nearly double the concentrations of formate (1.01–2.48 µM acetate and 0.53–1.24 µM formate), while both analytes remained nearly equal in the neutral fluids (1.59 µM acetate and 1.63 µM formate). NO_3^- concentrations are variable across fluid types. Nitrate was not detected in well BA3A, while measured in low concentrations (3.23×10^{-3} mM) within NSHQ14. Conversely, NO_3^- concentrations in WAB188 were observed at 0.13 mM. NH_4^+ was not measured for well WAB188, however, was detected in large concentrations within the hyperalkaline fluids of NSHQ14 and BA3A (7.59–88.81 µM). Measurements for phosphorous species were not resolved and have not been reported in recent work conducted at the Samail Ophiolite. Further details of geochemical measurements from the 2020 field sampling campaign are reported in Table 1.

Description of recovered MAGs

DNA collected from filtered biomass for metagenomic analysis provided eight high quality MAGs representative of *Methanobacterium* populations. One MAG was recovered from WAB188 at 50 m depth, and another at the shallow packer interval of 9–30 m from NSHQ14. The six remaining MAGs were all recovered from well BA3A where two MAGs were identified at

TABLE 1 Select geochemical compositions from subsurface waters recovered from wells BA3A, NSHQ14, and WAB188 collected from the Samail Ophiolite in 2020.

	WAB188	BA3A	NSHQ14	LOQ
Depth (m)	50	75	9–30	
pH	7.47	11.63	11.35	
Eh (mV)	–	−403	−169	
Temp. (°C)	35.3	36.8	35.9	
H_2 (µM)	0.92	–	21–164	0.45
DIC (mM)	3	–	0.05–0.13	0.1
Acetate (µM)	1.59	2.48	1.01	0.07
Formate (µM)	1.63	1.24	0.53	0.24
SO_4^{2-} (mM)	1.04	0.01	0.13	1.04×10^{-3}
∑Na (mM)	2.73	9.94	6.84	1.25×10^{-3}
∑Ca (mM)	1.21	6.2	3.35	1.22×10^{-4}
∑Mg (mM)	1.7	0.03	0.03	1.62×10^{-3}
NO_3^- (mM)	0.15	–	3.23×10^{-3}	1.61×10^{-3}
NH_4^+ (µM)	–	88.81	7.59	1
∑Fe (µM)	13.61	6.26	2.33	5.37×10^{-6}
∑Ni (µM)	0.14	0.1	0.14	2.39×10^{-5}

A dashed line (–) indicates the sample was not measured. The concentrations of H_2 and DIC were not possible and previous measurements from the 2015/2016 field season are reported from Rempfert et al. (2017) instead.

each sampling depth (75, 100, and 275 m). Phylogenomic analysis revealed the presence of three distinct populations of the *Methanobacterium* genus from subsurface fluids of the Samail Ophiolite. *Methanobacterium* populations are referred to by previous classification schemes reflecting the lithologic and hydrologic conditions reflected at the site of each MAG; Type I populations are indicative of alkaline conditions from near-surface water/rock interaction, whereas Type II populations reflect the highly serpentinized, closed-system conditions within hyperalkaline fluids in peridotite bedrock. The MAG from WAB188 represents the Type I population, while a distinct clade of 4 MAGs from BA3A and NSHQ14 represent the Type II population. Interestingly, the third population consisted of 3 MAGs and appeared to have recently diverged from the WAB188 Type I population and are phylogenetically distinct (Figure 1). This unique population shares the most phylogenetic relatedness to the Type I lineage, yet exists only in the most hyperalkaline well (BA3A, 11.63 pH). Therefore, this distinct population will hereafter be referred to as the "Mixed" population in order to distinctly evaluate the three populations throughout the remainder of this study. Comparatively, the Type II *Methanobacterium* MAGs exhibit the smallest genome size, while the Type I MAG contains the largest genomes size and Mixed population MAGs are slightly smaller than the Type I population (Table 2). This is consistent with previously observed genomes in other sites impacted by serpentinization, where genome streamlining allows for the reduction of energy demands within increasingly hyperalkaline conditions (Suzuki et al., 2017; Fones et al., 2019, 2021). While the MAGs from WAB188 and NSHQ14 only represent one sampling depth, the estimated relative abundance of the Mixed and Type II populations appear to increase with depth within well BA3A (Table 2).

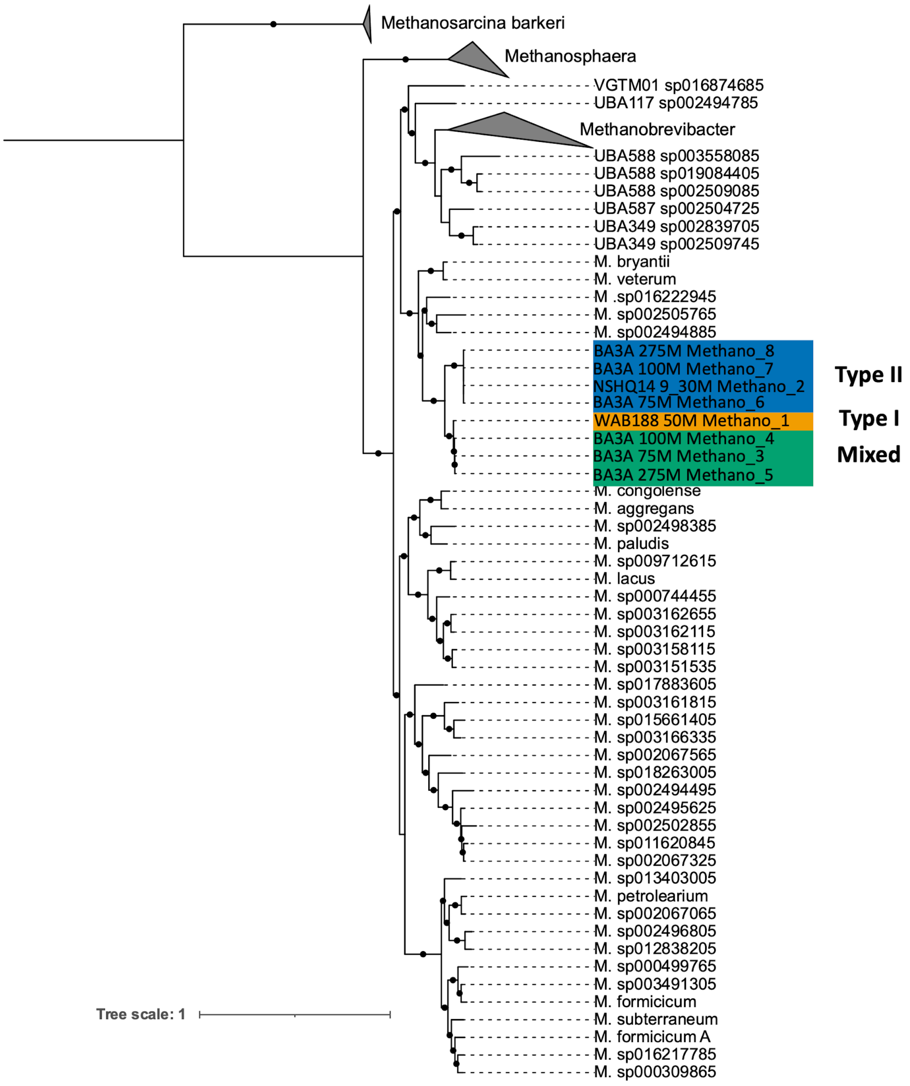

FIGURE 1
Maximum likelihood phylogenetic reconstruction of *Methanobacterium* metagenome assembled genomes based on 76 archaeal marker genes (Lee, 2019). The well and depth from which each MAG was collected is denoted in the sample name, along with the MAG ID. The MAGs are color-coded based on their population designation: blue=type II, green=mixed, yellow=type I. Bootstrap values ≥ 90% out of 1,000 bootstraps are denoted with black circles. *Methanosarcina barkeri* representatives were chosen as the outgroup.

TABLE 2 The statistics and information of assembling *Methanobacterium* MAGs recovered from the subsurface fluids.

MAG ID	Well	Depth (m)	Type	Est. comp. (%)	Est. red. (%)	Est. rel. abund. (%)	GC content (%)	Genome size (Mbp)
Methanobacterium								
Methano_1	WAB188	50	I	98.68	1.32	4.04	36.63	2.47
Methano_2	NSHQ14	9–30	II	98.67	0	5.03	34.76	1.64
Methano_3	BA3A	75	Mixed	98.62	1.31	1.67	36.64	2.07
Methano_4	BA3A	100	Mixed	98.68	1.32	7.57	34.15	2.12
Methano_5	BA3A	275	Mixed	94.76	2.63	7.91	34.59	2.29
Methano_6	BA3A	75	II	98.68	0	12.17	34.75	1.37
Methano_7	BA3A	100	II	98.67	0	13.08	35.03	1.59
Methano_8	BA3A	275	II	97.36	0	23.87	34.93	1.38

The relative abundance of each MAG was estimated by the percentage of overall reads mapped to a MAG within each of their corresponding metagenome. Est. comp., estimated completion; Est. red., estimated redundancy; Est. rel. abund., estimated relative abundance.

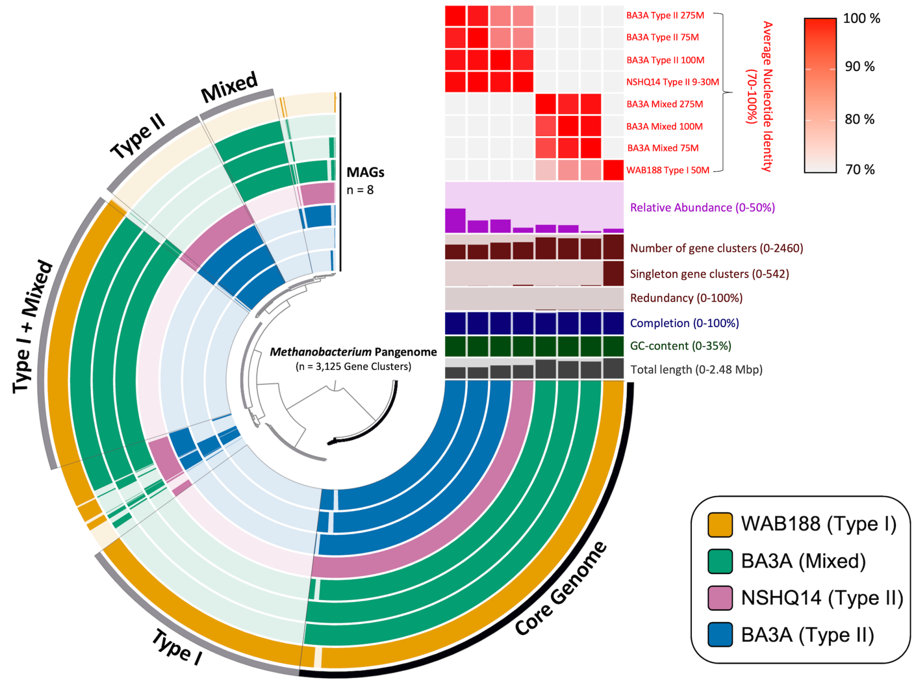

FIGURE 2
Visual depiction of the pangenome of *Methanobacterium*-affiliated metagenome assembled genomes (MAGs) recovered from subsurface fracture fluids from the Samail Ophiolite, Oman. The inner radial dendrogram shows the 3,125 protein-encoding genes homologs in the pangenome, clustered by presence/absence across MAGs. The 8 MAGs of the three different population "types" are plotted on the innermost 8 layers (270° arcs), ordered and spaced to reflect groupings based on genomic composition. The presence of gene clusters are indicated by filled and colored bars; unshaded bars indicate the lack of a gene cluster in a MAG. Gene clusters belonging to the core genome shared across all MAGs and environmental accessory genomes are binned and labeled with the according specificity on the outside of the outermost layer. The top right portion above the pangenome contains relevant information for each MAG, with the y-axis limits contained within the parentheses. The relative abundance is representative of each *Methanobacterium* MAG's percentage of overall reads within its corresponding metagenome.

Methanobacterium pangenome

Pangenomic analysis revealed sets of genes intrinsic to all *Methanobacterium* populations that may be vital in the subsurface serpentinized environment. The entire metapangenome of *Methanobacterium* MAGs contains 3,125 gene clusters, of which 36% (1,122 gene clusters) occupy the core genome (Figure 2). The accessory genome of each population appears to decrease in size when the population is found in more hyperalkaline conditions – 17% of total gene clusters (542 gene clusters) in the accessory genome of Type I, 6% (173 gene clusters) in the accessory genome of the Mixed population, and 8% (260 gene clusters) in the accessory genome of the Type II population. To further understand the relationship between the three populations, the average nucleotide identity (ANI) was calculated to determine the genome similarity between each MAG, and is represented in the upper right heatmap of the metapangenome

(Figure 2). Results further highlight the distinction of three *Methanobacterium* populations. Of particular note, the Mixed population only shares a stronger genome similarity with the Type I MAG (76 to 82% ANI) than compared to the Type II MAGs (28 to 41% ANI). This finding corroborates the likely short evolutionary separation of this population into hyperalkaline conditions.

Core genome

The core genome of the eight *Methanobacterium* MAGs (the bottom right portion of the metapangenome) represents all of the genes present among all observed populations (Figure 2). Metabolic reconstruction of annotated genes includes the necessary proteins to carry out the essential steps of the methanogenesis pathway, converting CO_2 into CH_4. Additional genes and gene clusters of interest can be inspected in Supplementary Table 1. All *Methanobacterium* MAGs contained the genes for trehalose-6-phophatase synthase and ureidoglycolate dehydrogenase, which serve as possible mechanisms to overcome energy limiting conditions (Kyryakov et al., 2012; Bird et al., 2019).

Comparison of all *Methanobactierum* MAGs to publicly available *Methanobacterium* genomes revealed that only six genes were functionally enriched specifically to the MAGs collected from the Samail Ophiolite with an adjusted q-value < 0.05 (Supplementary Table 2). Some of these genes included CRISPR/Cas associated proteins, mannose-6-phosphate isomerase, and zinc-dependent alcohol dehydrogenase. An additional nine gene annotations were enriched for the Oman MAGs and found in only 10% or less of external genomes. Of note, these annotations included a DNA protection under starvation (DPS) family protein, the zinc-exporting ATPase (*zntA*), and an ABC-type iron exporter (*fetB*; Supplementary Table 2).

Accessory genomes and functional enrichment

Genes that were present only in the accessory genome of each *Methanobacterium* population were extracted to identify adaptations to their environmental conditions. The number of genes present in each accessory genome were categorized into 22 observed Clusters of Orthologous Genes (COG) categories (Figure 3). The distribution of genes within accessory genomes discussed below reflects the gene total that falls within one of the COG categories. Additional genes that did not receive functional annotations were not included in the summary of genes belonging to these categories from each *Methanobacterium* population, as this does not reflect the total gene count within the accessory genomes found from each population. The Type I population displayed the largest number of accessory genes annotated by the COG database ($n = 133$) with most genes being placed within the general function prediction only, defense mechanisms, and cell wall/membrane/envelope biogenesis categories. The Type I population contains a large number of genes ($n = 19$) belonging to the radical SAM superfamily within the general function prediction category. Within the cell wall category, the Type I population contained 9 copy numbers of glycosyltransferase, of which 5 were encoded as glycosyltransferases involved in cell wall biosynthesis UDP-D-galactose:(glucosyl) LPS alpha-1,6-D-galactosyltransferase *rfaB* and 4 were annotated as putative colonic acid biosynthesis glycosyltransferase *wcaA* (Figure 4). Many genes appeared to be functionally enriched in the Type I MAG, however, this could be due to the larger genome size leading to an equally as sizeable accessory genome. The functional core of this genome did not reveal any clear distinction between the annotated genes and the environmental conditions observed at WAB188 (Supplementary Table 3).

Comparatively, the Mixed population's accessory genes with COG functional annotations decreased in size ($n = 107$). The cell wall/membrane/envelope biogenesis COG category was the Mixed population's standout accessory group with a total of 29 genes. Similar to Type I, the Mixed population contained 10 gene copy numbers of glycosyltransferase, making up more than a third of its dominant COG category. However, the Mixed population encoded only 1 copy of the *wcaA* gene while the rfaB stood out with the remaining *9* copy numbers (Figure 4). Additionally, this dominant category contained the spore coat biosynthesis proteins *spsFG*. The functional enrichment analysis of the Mixed population revealed 20 genes that were not present in any of the other two *Methanobacterium* populations (Supplementary Table 3). These gene annotations appeared to be related to DNA repair or stress and included DNA glycosylase *alkD*, recombinational DNA repair protein *RecF*, and the enamine deaminase of the YjgF/YER057c/UK114 family *ridA*. Additional genes for the presence of lipoprotein and cell wall biosynthesis included teichoic acid biosynthesis protein *tagB*, lysophospholipase *pldB*, and the spore coat biosynthesis proteins *spsFG*. Two acetyltransferases were identified as n-acetyltrasnferases *yhbS* and *rimL*, as well as the ADP-ribosylglycohydrolase *draG*.

The Type II population contained accessory genes ($n = 130$) with the greatest number of genes belonging to the energy production and conversion and defense mechanisms COG categories. Distinct from the other *Methanobacterium*, the Type II population contained genes encoding for type I ($n = 9$) and III ($n = 1$) restriction enzymes. Inspection into the cell wall/membrane/envelope category revealed no annotations for glycosyltransferase in the Type II population. The functionally enriched gene annotations revealed 23 genes that were unique to the Type II population (Supplementary Table 3). Distinct transporters included the ABC-type Fe^{3+} transport system *afuA* and an oxalate/formate antiporter *oxlT*. Potential antimicrobial and detoxification genes included the membrane protein *ydbS*, Zn-dependent glyoxylase *phnB*, cephalosporin hydroxylase *cmcI*, and bacterial immunity and signal transduction membrane protein *SdpI*. Additional genes that were functionally enriched within the Type II MAGs were aconitase hydratase (*acnA*) and isocitrate dehydrogenase (*Icd*) proteins which are responsible for carrying out steps in the tricarboxylic acid (TCA) cycle, though no other gene annotations were detected to form a complete TCA cycle.

Transporters

Gene annotations for different transports were inspected for their presence or absence across the different *Methanobacterium* populations in order to resolve potential adaptations through pH homeostasis or circumventing low nutrient availability. Transporter encoding genes were placed into custom categories defined by their

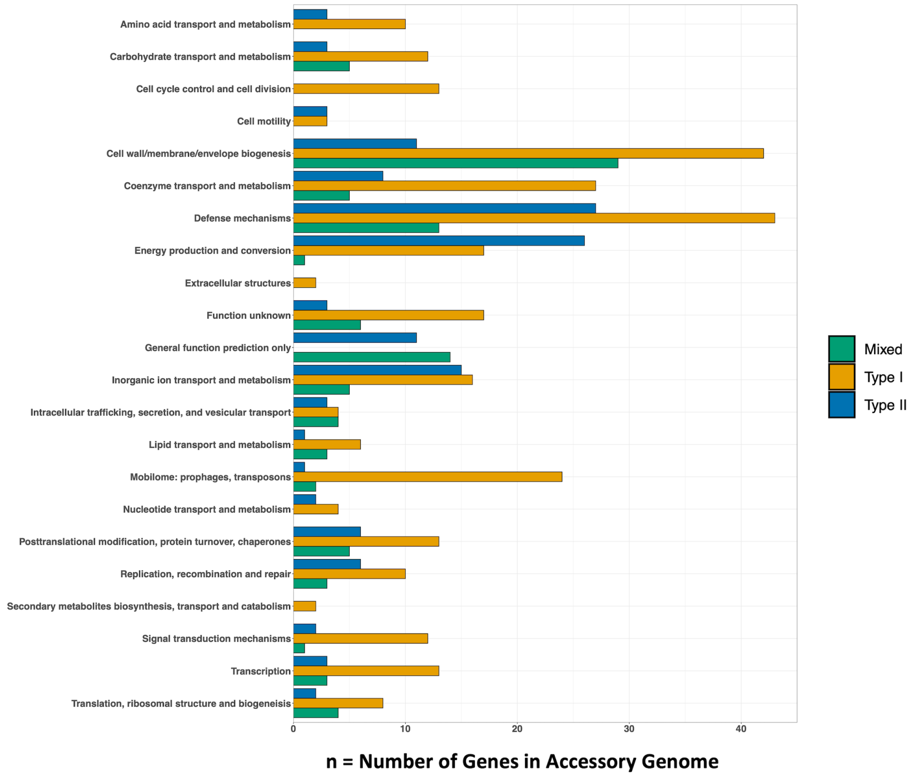

FIGURE 3
The number of genes within each *Methanobacterium* population's accessory metagenome assembled genome. The COG20 Category is listed on the y-axis and the x-axis denotes the number of genes that make up the category. The full list of genes found in the top categories of each population can be found in Supplementary Table 4.

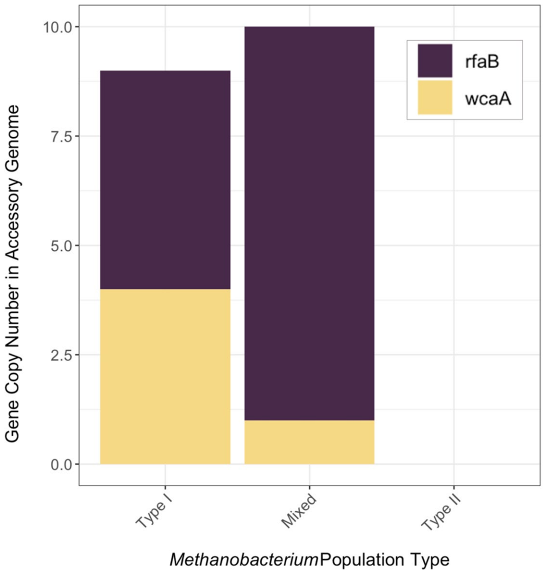

FIGURE 4
The gene copy number of genes (*rfaB* and *wcaA*) encoding glycosyltransferase in the accessory metagenome assembled genomes of each *Methanobacterium* population. The full list of genes within the accessory genome of each population can be found in Supplementary Table 4.

gene function and included: Fe, Na^+/K^+, Lipoprotein, Taurine, Other, Acetate and Formate, NH_4^+, Cation, and Phosphate transporters (Figure 5). All *Methanobacterium* populations shared the presence of all but two Fe transporters. Only the Type II population possessed the *afuA* Fe^{3+} transporter while exhibiting no detection of the *exbD* subunit. The Mixed and Type I population contain both *exb* subunits that are part of an iron uptake complex to transport ferrous iron in the form of siderophores (Noinaj et al., 2010). All *Methanobacterium* populations also contain the *fepBCD* iron siderophore complex (Schalk and Guillon, 2013). Similarly for Na^+/K^+ transporters, the Type II MAGs contained the presence of all the identified annotated genes for these transporters, but demonstrates the only presence of the *natB* component of the sodium transport system. Interestingly, the *natA* subunit component was not detected in any of the Type II MAGs. The Type I and Mixed populations contain the only detection of the *nhaP* sodium-hydrogen antiporter, which was absent in the Type II population.

The gene copy number of lipoprotein transport gene annotations was much larger in the Type I and Mixed population compared to the Type II population. Specifically, the *lolE* lipoprotein transport subunit and the *DedA* family protein involved in a variety of cell membrane transport and functions are 2x in gene copy number abundance of the Type I and Mixed populations compared to the Type II populations. Conversely, only the Type II population demonstrates the presence of all three

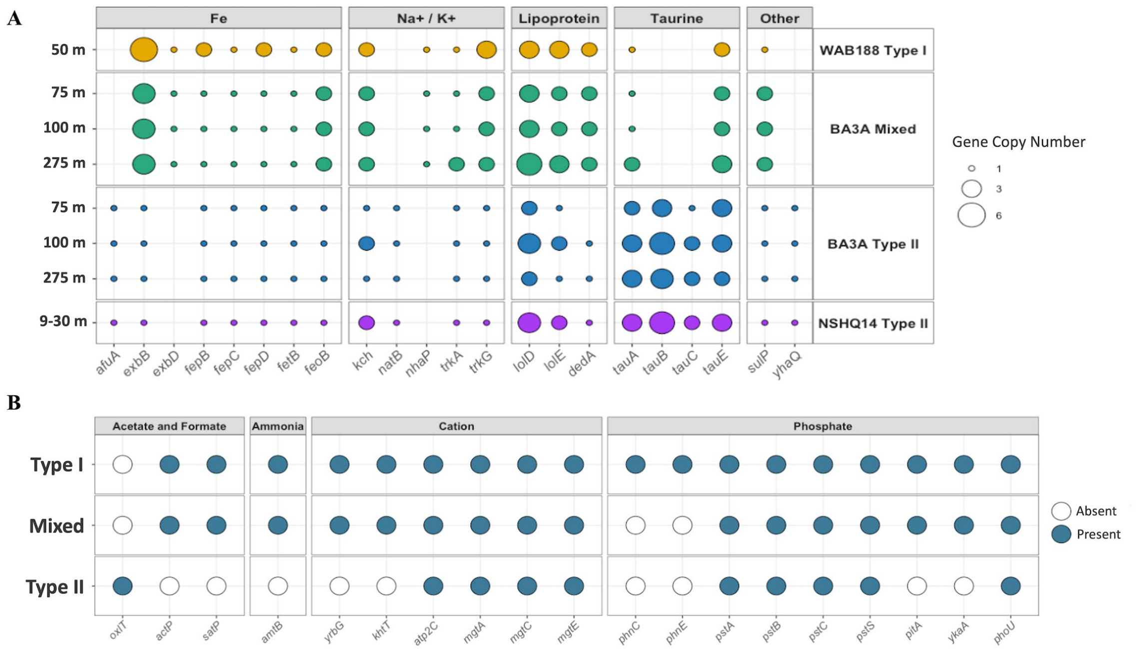

FIGURE 5
(A) The gene copy number of genes involved in transport mechanisms for various metabolites. The x-axis denotes the gene and are faceted (above) into custom transporter categories. The y-axis represents each MAG at the depth in which it was collected and is faceted (on the right) from the borehole in which it was sampled and the *Methanobacterium* population it belongs to. Each dot is also sized by the gene copy number. **(B)** The presence or absence of additional transporter genes across each population type. The presence of a gene is indicated by a filled in dot and represents all MAGs within the population containing the presence of the gene. The x-axis represents the transporter genes and are faceted (above) into custom categories. The y-axis represents the *Methanobacterium* population.

tauABC subunits in ≥2x gene copy number. However, all populations share the presence of the *tauE* sulfite exporter. Within the "Other" category of transporters, only the Type II population contained the putative ABC-transporter *yhaQ*. All *Methanobacterium* MAGs shared the presence of a sulfate permease (*SulP*) gene. The *SulP* gene from the Type II population was resolved through BlastP analysis and identified as a putative sulfate transporter. Further BlastP analysis did not resolve the *SulP* transporter from the Type I population, and was broadly characterized as an inorganic anion transporter belonging to *Methanobacterium* with 76% identity. However, only the Mixed population possessed both of these *SulP* encoded proteins.

The presence or absence of genes was extended to additional categories to further highlight potential adaptions in hyperalkaline fluids by the *Methanobacterium* populations (Figure 5). The Type II population contains the only detected formate transporter annotated as an oxalate:formate antiporter. Additionally, it appears that the Type II population does not possess an acetate transporter, while the Type I and Mixed populations share the same transporters, *actP* and *satP*, for potential acetate assimilation. Similarly, the Type II population demonstrates the absence of the ammonium transporter *amtB* and the potassium/hydrogen antiporter *khtT*. Only the Type I *Methanobacterium* population displays the presence of the *phnCE* subunits of the phosphonate transporters. The Type I and Mixed population share gene annotations for phosphate and metal symporter *pitA* and phosphate transport regulator *ykaA*. Additional gene absence, presence, and copy number are illustrated in Figure 5.

Carbon cycling

Multiple pathways for carrying out methanogenesis were investigated, and include suggested mechanisms from previous studies conducted at the Samail Ophiolite (Fones et al., 2021; Kraus, 2021). All *Methanobacterium* MAGs were queried for proteins involved in hydrogenotrophic, acetoclastic, and formatotrophic methanogenesis along with carbonic anhydrase to potentially convert bicarbonate into bioavailable CO_2. The variety of pathways for methanogenesis were examined in order to determine adaptability to available carbon substrates (Figure 6). Type I and Mixed *Methanobacterium* MAGs contained the full suite of proteins encoded to carry out the hydrogenotrophic methanogenesis pathway, reducing CO_2 in the presence of H_2 to CH_4 (Figure 6). In line with previously reported work, only Type II *Methanobacterium* populations encoded the presence of formate dehydrogenase (*fdhAB*), which allows for potentially using formate as an alternative and sole carbon source to circumvent low DIC in hyperalkaline conditions (Fones et al., 2021). None of the proteins required for carbonic anhydrase proteins were detected in any of the *Methanobacterium* populations. Furthermore, none of the MAGs encoded for the *ack*/*pta* proteins that are typically found in acetoclastic methanogens (Stams et al., 2019). All *Methanobacterium* MAGs contained the acetyl-CoA synthetase (*acs*) protein which allows for the conversion of acetate into acetyl-CoA (Hattori, 2008). However, the *Methanobacterium* populations are likely assimilating carbon from acetate for biosynthesis of various cell components rather than being incorporated into CH_4 production (Oberlies et al., 1980).

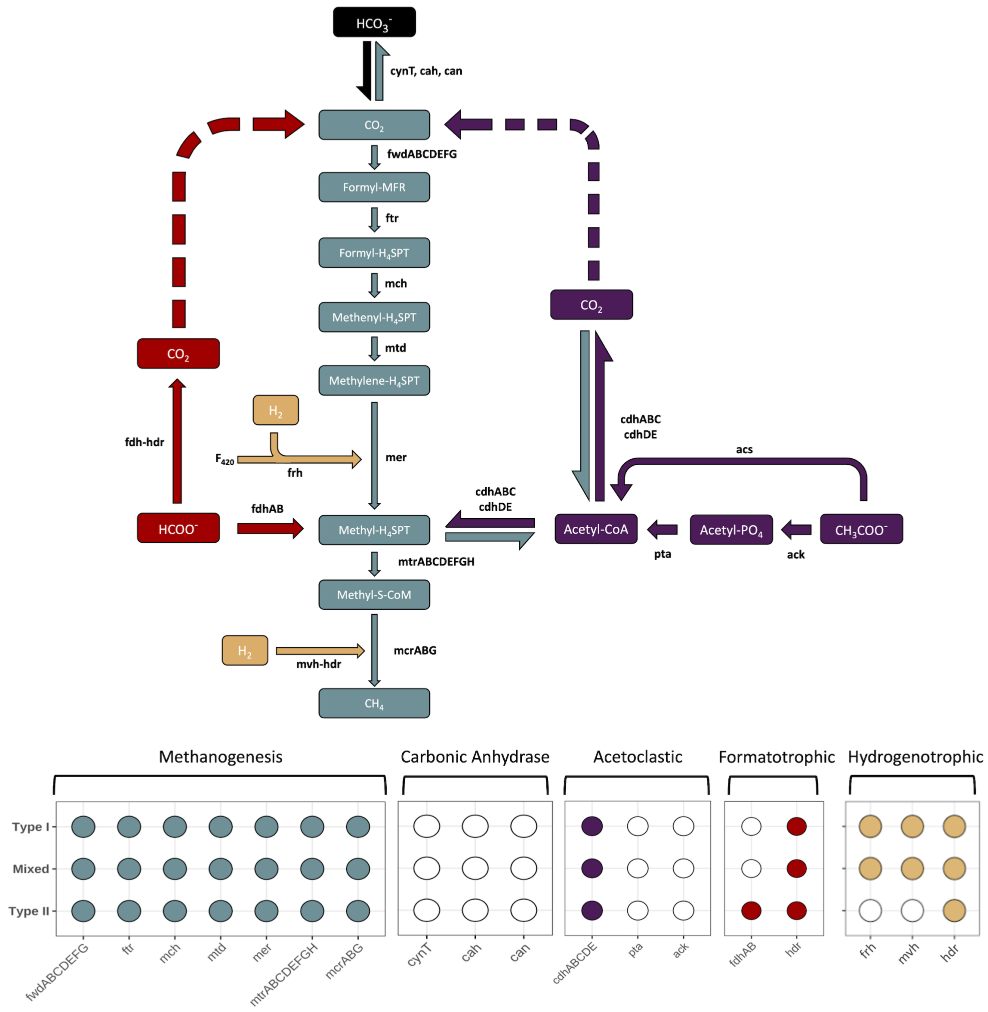

FIGURE 6

The different enzymatic pathways for the core methanogenesis pathway (gray), hydrogenetrophic (tan), acetoclastic (purple), formatotrophic (red) or steps involving conversion of bicarbonate into CO_2 for methanogenesis (black). Carbon substrates, intermediates, and products appear in rectangular boxes, while enzymes are in black lettering next to arrows that point in the direction of their end product. Dashed arrows indicate the potential use for the pathway to allow for intracellular CO_2 to be generated and subsequently reduced to CH_4. The enzymatic component of heterodisulfide reductase (hdr) is included in both formatotrophic and hydrogenetrophic pathways because each due to its similar function, but does not represent a different gene. The bottom of the figure contains a presence/absence diagram, where circles are filled in to represent the presence of a gene in the respective pathway and a white, unfilled circle indicates the absence of a gene. The rows of the presence/absence diagram are representative of each *Methanobacterium* population. Figure inspired by Carr et al. (2018). Genes: fwd, formylmethanofuran dehydrogenase; ftr, formylmethanofuran:H4SPT formyltransferase; mch, methenyl-H4SPT cyclohydrolase; mtd, F420-dependent methylene H4SPT dehydrogenase; mer, F420-dependent methylene-H4SPT reductase; mtr, methyl-H4SPT:coenzyme M methyltransferase; mcr, methyl-coenzyme M reductase; ack, acetate kinase; pta, phosphate acetyltransferase; acs, acetyl-CoA synthetase; cdh, carbon monoxide dehydrogenase; fdh, formate dehydrogenase; hdr, heterodisulfide reductase; mvh, methyl viologen-reducing [NiFe]-hydrogenase; frh, coenzyme F_{420} [NiFe]-hydrogenase; F_{420}, coenzyme F_{420}. Carbon compounds: CO_2, carbon dioxide; formyl-MFR, formyl-methanofuran; formyl-H4SPT, formyl-tetrahydrosarcinapterin; methenyl-H4SPT, methenyl-tetrahydrosarcinapterin; methylene-H4SPT, methylene-tetrahydrosarcinapterin; methyl-H4SPT, methylene-tetrahydrosarcinapterin; methylene-S-CoM, 2-(Methylthio) ethanesulfonate; Acetyl-CoA, acetyl-Coenzyme A; Acetyl-PO_4, acetylphosphate; CH_3COO^-, acetate; $HCOO^-$, formate.

Discussion

Methanobacterium core genome and shared strategies

Methanobacterium populations play a significant role as the primary methane producer in the hyperalkaline subsurface fluids of the Samail Ophiolite (Fones et al., 2019; Kraus, 2021). While previous work has elucidated a potential adaptation for circumventing DIC limitation in the subsurface by use of formate by *Methanobacterium*, more work is needed to fully unravel the strategies *Methanobacterium* uses to adapt to both a high pH and a nutrient limited environment (Fones et al., 2021). In this study, eight MAGs across various geochemical gradients have been exploited to investigate metabolic strategies for living in the conditions experienced in the most hyperalkaline wells. Results from phylogenomic analysis and ANI metrics reveal three distinct *Methanobacterium* populations exist in the subsurface serpentinizing fluids of the Samail Ophiolite (Figures 1, 2). Previous work in the Samail Ophiolite suggests that the diversification of methanogens and acetogens can be reflected by the fluid type in which those populations exist (Fones et al., 2021; Colman et al., 2022). This work corroborates the distinction between Type II *Methanobacterium* populations that exist in the hyperalkaline fluids and Type I populations collected from neutral waters. However, the most intriguing discovery includes the identification of a third Mixed *Methanobacterium* population. The Mixed *Methanobacterium* population likely represents an intermediary in the evolutionary history from Type I to Type II lineages. Interestingly, the Mixed population appears only within the most hyperalkaline borehole and was not detected in any other fluid source. This raises key questions regarding why a *Methanobacterium* population that is likely to be better suited to exist in more hospitable conditions only subsists within the most unfavorable geochemical regimes within the serpentinizing subsurface.

Evidence for genome streamlining is indicated by the decrease in genome size between methanogenic populations from neutral and hyperalkaline conditions. When organisms face selective pressures from their environment, a reduction in genome size allows for lessening the costs of energetics associated with the replication of their genome (Giovannoni et al., 2014). The DIC limited and high pH conditions found in the more serpentinizing impacted fluids results in both nutrient limitation and osmotic stress of organisms, and would suggest genome streamlining acts as a favorable adaptation to hyperalkaline fluids. The Type I *Methanobacterium* MAG displays the largest genome size and likely receives less environmental stress, given that surficial CO_2 can more readily mix into the fluids and prevent carbon limitation. The Type II population contains the smallest genome sizes, and reflects previous work where these hyperalkaline-adjusted-organisms have reduced their genome size to cut down energetic costs (Fones et al., 2021). The genome sizes of the Mixed *Methanobacterium* population are greater than Type II populations, yet smaller than Type I. This genome size variance could suggest that the Mixed population have not fully adapted to the nutrient limited and hyperalkaline conditions, and therefore have not yet fully streamlined to minimize energy demands. The presence and absence of the various transporter gene annotations between all *Methanobacterium* MAGs may highlight how the Type II population keeps necessary transporters for the metabolites that are under greatest demand in the hyperalkaline fluids (Figure 5). Additionally, genome streamlining may be the dominant strategy for adapting to hyperalkaline conditions observed by the *Methanobacterium* populations of the Samail Ophiolite compared to external *Methanobacterium* genomes. This potential adaptation strategy becomes emphasized by the lack of genes determined from functional enrichment analysis belonging specifically to the *Methanobacterium* populations from Oman. A reduction in genome size will decrease the number of shared genes across all three populations, and therefore makes it difficult to distinguish unique genes or adaptation strategies for circumventing the subsurface serpentinized fluids from the Samail Ophiolite. Instead, greater focus on the differences between the three populations identified within this study provide greater resolution of potential lifestyle strategies invoked by changes in local geochemistry across different boreholes and depths.

The pangenomic comparisons among these three *Methanobacterium* species allows for investigation of shared survival strategies and how each has adapted unique capabilities to overcome limiting conditions in the serpentinizing subsurface. Pangenomic analysis revealed sets of genes intrinsic to all *Methanobacterium* populations that may be necessary in the subsurface serpentinized environment. Trehalose-6-phophatase synthase was found in all *Methanobacterium* MAGs (and only 66% of publicly available genomes not from Oman), and has been suggested as a low-energy state strategy in other subsurface systems (Argüelles, 2000; Bird et al., 2019). This protein has been reported from other energy limiting systems in sediments of the Baltic Sea and Antarctic soils, where metagenomic sequencing has detected trehalose synthase to aid in stabilizing cellular membranes against osmotic stresses (Koo et al., 2018; Bird et al., 2019). This protein has been suggested to help by producing trehalose which prevents accumulation of degraded proteins, slow replication rates, and increase cellular longevity (Brauer et al., 2006; Kyryakov et al., 2012; Sipes et al., 2021).

Additionally, all *Methanobacterium* MAGs contain ureidoglycolate dehydrogenase which is involved in the degradation of allantoin in order to access detrital DNA (Bird et al., 2019; Sipes et al., 2021). Though it has been previously reported that ureidoglycolate dehydrogenase is employed under nitrogen starvation, work quantifying the cycling of nitrogen within the subsurface fluids of the Samail Ophiolite is replete (Rempfert et al., 2023). However, the dominant nitrogen species in the hyperalkaline fluids is NH_4^+. Additionally, the Type II population does not contain the presence of an NH_4^+ transporter (*amtB*) that the Mixed population possesses (Figure 5). The advantage for the Type II *Methanobacterium* to not contain a NH_4^+ transporter is not clear. In order to maintain internal cytoplasmic pH balance, the Type II population may have adapted to not assimilate NH_4^+ due to the cationic charge. NH_4^+ has also been demonstrated to become toxic to methanogens in bioreactors in large concentrations, yet not at the levels reported here or at the pH conditions seen at the Samail Ophiolite in hyperalkaline fluids (Capson-Tojo et al., 2020). Further, in pH 11 fluids the dominant nitrogen species will likely be NH_3, the uncharged form. *Methanobacterium* may be able to acquire NH_3 that passes through the cell without the need of an ion gradient. While the lack of an NH_4^+ transporter in the Type II population in not apparent, ureidoglycolate dehydrogenase may prove an effective strategy to overcome potential nitrogen limitation. The presence of these two encoded proteins indicates that *Methanobacterium* may employ strategies that involve maintaining a low-energy state for survival and scavenging during periods of nutrient starvation (Liang et al., 2019; Sipes et al., 2021). Within the hyperalkaline fluids, DNA scavenging tactics for phosphate may take place since DNA can serve as a source for phosphorous. Additionally, phosphorous species will precipitate out in the hyperalkaline Ca^{2+} and OH^- rich fluids further limiting it is availability. Scavenging for DNA supports an avenue for alternative phosphorous uptake in the hyperalkaline fluids that have been suggested to be phosphorous limited (Kraus, 2021; Rempfert et al., In Review). Maintaining low energy states may also explain how both the Type II and Mixed *Methanobacterium* populations comprise the greatest relative abundance within the more extreme fluids. By potentially employing strategies to reduce replication rates and lower energetic costs, the methanogenic populations within the hyperalkaline conditions may be able to retain greater cell concentrations, while other microbial members are unable to meet the energetic demands and cannot sustain replication rates to make up a significant portion of the subsurface community. In comparison, conditions within WAB188 contain inputs of surface derived DIC and greater access to other nutrients. Though, it is possible that Type I *Methanobacterium* are being out-competed by other microbial members for resources and may need to employ these survival techniques against contending microorganisms. These findings suggest that all *Methanobacterium* populations might use DNA scavenging and low-energy state strategies in order to overcome nutrient limitations imposed by environmental pressures or community competition and thus adapt to subsurface serpentinizing conditions.

Functional enrichment analysis revealed that all *Methanobacterium* populations share the iron exporter *fetB* that is only found in 3.5% of other observed *Methanobacterium* genomes (Supplementary Table 2). This protein has been reported to play a role in providing resistance to oxidative stress through iron homeostasis (Nicolaou et al., 2013). Reactive oxygen species such as the hydroxyl radical (•OH) can be threatening to DNA and lipids (van Erk et al., 2023). These reactive oxygen species can be formed through redox reactions or from the Fenton reaction in the presence of iron (Burns et al., 2010). Given the greater concentrations of ferrous iron from serpentine minerals, dissolved iron, and the dominance of OH^- primarily in the hyperalkaline fluids, the role of iron homeostasis may play a role in providing defense against oxidative stress imposed on the *Methanobacterium* populations not commonly observed from the external *Methanobacterium* genomes originating from non-serpentinizing environments. However, the generation of reactive oxygen species in the presence of iron usually results from the abundance of oxygen, which is not replete within the hyperalkaline subsurface (Burns et al., 2010). Therefore, it is not clear still why *fetB* would provide an advantage unless another oxidative stress from other geochemical analytes is imposed on the *Methanobacterium* MAGs observed in this study. Though reactive oxygen species may play a role in the hyperalkaline subsurface, the role of iron transport from *Methanobacterium* populations is influenced by the necessity for [NiFe]-hydrogenases that are requisite for methanogenesis. All *Methanobacterium* populations contain the *exbB* transporter gene, yet the Mixed and Type I population contain an incredibly large gene copy number compared to the Type II MAGs (Figure 5). This *exbB* protein is involved in the uptake of iron through siderophore uptake (Schalk et al., 2004). The Type II population contains the only presence of the putative iron ABC transporter *afuA*, which may allow this population an advantage toward accruing iron in hyperalkaline conditions. Overall, greater efforts are needed to resolve the microbially mediated iron acquisition and trafficking in serpentinizing systems.

Unique adaptation strategies resolved from accessory genomes and functional enrichment

The three different *Methanobacterium* populations' accessory genomes were evaluated to investigate unique gene clusters and individual genes that may promote an advantage to overcome environmental challenges in the subsurface of the Samail Ophiolite. Initial trends can be delineated from the three methanogenic populations between the dominant COG categories in which the most accessory genes fall under. Functional enrichment analysis further provided insight into the functional core set of genes unique to each population to reflect adaptations imposed by either hyperalkaline or circumneutral fluid conditions.

Type II *Methanobacterium*'s accessory genome demonstrates preference toward "Energy production and conversion" and "Defense Mechanisms." It is likely that the dominance of genes related to energy production is in line with Type II *Methanobacterium* being capable of potential formatotrophic methanogenesis due to the formate dehydrogenase genes (*fdhAB*) only appearing in the accessory genome of the Type II population. This may suggest that Type II *Methanobacterium* are well adapted to hyperalkaline fluids, and may be able to take advantage of unique sources of carbon and other nutrients to circumvent energy limitations. The presence of genes related to defense mechanisms is intriguing since the threat of potential viral infections and microbial competition may not be as extensive in hyperalkaline fluids, yet this needs greater efforts to resolve why this may aid Type II *Methanobacterium*. This defense mechanisms category is dominated by genes encoding for restriction enzymes and components of toxin/antitoxin systems which dually play a role in viral protection and potentially against other microorganisms (Supplementary Table 4). The 10 gene copy numbers of restriction enzymes belonging to the Type II population may play a further role in DNA scavenging strategies. An increase in restriction enzyme levels has been proposed as a mechanism mainly to protect cells from viral infection (Loenen et al., 2014). However, phosphate is a limiting nutrient in the hyperalkaline subsurface, often below a 5 μM detection limit (Rempfert et al., 2017, In Review. Table 1). Thus, restriction enzymes could function as a mechanism for cleaving detrital DNA as a source for phosphate uptake.

Intriguingly, the significant quantity of encoded proteins related to antimicrobial resistance and detoxification from the Type II population suggests a unique survival adaptation. The *ydbS* protein is reported to be involved in general resistance to antimicrobials, and *cmcI* is linked to detoxifying cephalosporins which act as compounds to disrupt cell wall synthesis (Öster et al., 2006). The *SdpI* protein is known to protect against a toxin that lyses cells open for feeding off the nutrients released from these dead cells. In a strain of *Bacillus subtulis*, this organism has been shown to produce a cannibalism toxin under nutrient limitation that will kill and lyse open cells within its own population (Povolotsky et al., 2010). The cells that display the activated *SdpI* protein are able to recognize the toxin and are immune to being lysed, and gain the opportunity to uptake nutrients from localized dead cells or scavenged DNA (Ellermeier et al., 2006). While the ability for Type II *Methanobacterium* to produce this toxin was not confirmed, this population may have acquired the resistance to a toxin possibly released by another subsurface microbial member. Therefore, we conjecture that the Type II *Methanobacterium* may be employing an adaptive strategy by scavenging from dead cells as a mechanism for potentially overcoming nutrient limitation, a viable approach due to phosphate limitation in the hyperalkaline fluids.

The Type I population contains the greatest number of unique genes in the "General function prediction only" category, though also shows great abundance in the "Cell wall/membrane/envelope biogenesis" and "Defense mechanisms" COG categories. Speculating from these categories, Type I *Methanobacterium* may require greater efforts for defending against viral infections or competition from other microbial members. Subsurface fluids with neutral pH conditions have been reported to contain a higher diversity and richness of microorganisms (Brazelton et al., 2012; Rempfert et al., 2017). These fluids typically are composed of a larger presence of stronger oxidants and limited by reductants such as H_2. Even more, at contact wells such as WAB188 where our Type I MAG exists, fluid mixing allows for greater fluctuation of geochemistry. Type I *Methanobacterium* populations might need to be flexible to the non-stagnant fluid chemistry observed at contact wells. Therefore, the greater competition of other microbial members for available reductants may require Type I *Methanobacterium* to employ ways to circumvent thermodynamic competition. While the viral community has not yet been explored in the subsurface fluids of the Samail Ophiolite, it is likely that the abundance of viral members would reflect similar trends in the microbial distribution among serpentinizing fluids. Therefore, defensive strategies to hold off viral infection may be greater in the Type I fluids compared to the deep hyperalkaline environments.

Interestingly, despite both Type II and Mixed *Methanobacterium* occupying hyperalkaline fluids, only the Mixed population's accessory genome is predominantly comprised of genes that fall under the "Cell wall/membrane/envelope biogenesis" COG20 category. The presence of spore coat polysaccharide biosynthesis proteins (*spsFG*) have been reported for entering a state of stasis until conditions become more favorable may imply sporulation as a mechanism for protecting Mixed populations (Liang et al., 2019). Sporulation has not been observed as a strategy imposed by methanogens, yet these genes may suggest a beneficial role to the membrane structure of the Mixed population to serve as an environmental stress defense. As the Mixed *Methanobacterium* population represents an intermediary between Type I and Type II methanogens, it is possible that the Mixed population have adapted to hyperalkaline conditions requiring greater cell membrane integrity preventing cell disruption. The functionally enriched genes of the Mixed population may reflect their adaptation mechanisms necessary for subsisting in the highly reduced fluids. The Mixed population contains the presence of the *pldB* lipophospholipase which may further help to provide membrane stability. Lipophospholipases, such as those encoded by *pldB*, are responsible for metabolizing lipophsopholipids which are responsible for cell signaling processes and regulation of the cellular membrane structure (Kobayashi et al., 1985). Additionally, it has been shown that lipophospholipases play a role in maintaining lipid homeostasis (Wepy et al., 2019). While these biomolecules have not been studied for their role in alkaline environments, we posit that the Mixed *Methanobacterium* population requires greater effort to organize its cell membrane in order provide membrane stability or support potential collaboration with other microbial members. Cell signaling processes may indicate the Mixed population is participating in biofilm interactions where lipophospholipases regulate intermediary exchanges of metabolites.

Accessory genome results from the Mixed *Methanobacterium* population indicate a role for glycosyltransferases to support niche adaptation within the high pH conditions and coexistence with Type II *Methanobacterium*. The incredible shift from Type I populations containing a near even distribution of the *rfaB* and *wcaA* glycosyltransferases to Mixed populations containing almost entirely *rfaB* signifies the importance of this gene for providing an advantage in the hyperalkaline fluids (Figure 4). Previous work has demonstrated under glucose limitation that the *wcaA* protein requires a greater energetic cost and is not expressed (Pradel et al., 1992; Wang et al., 2020). The lack of any glycosyltransferase genes in the Type II population's accessory genome further represents the niche differentiation of the Mixed population within the hyperalkaline fluids. The presence of the glycosyltransferase gene *rfaB* may indicate opportunities for biofilm interaction from methanogenic microbial members. The *rfaB* protein has been linked to biofilm formation and is necessary for certain microbes to participate within biofilms (Raaijmakers et al., 2010; Chai et al., 2012; Probst et al., 2014). In addition, the potential interaction with biofilm communities would increase the likelihood for a non-motile mode of habitation for the Mixed population. Postulating upon alternative adaptation strategies, Mixed *Methanobacterium* populations might require cooperation between additional microbial members in order to gain access to DIC. Specifically, other microbial members able to liberate bicarbonate from carbonate mineral veins or generate bioavailable CO_2 may require the Mixed population to interact directly through syntrophic partnership or interspecies electron transfer. Further transcriptomic analysis and physiological studies are necessary to corroborate the role of other microorganisms possessing carbonic anhydrase able to the speciation bicarbonate or aid methanogens by another metabolic mechanism. The increased gene copy number of *rfaB* in the Mixed *Methanobacterium* population's accessory genome would suggest biofilm interaction from Mixed *Methanobacterium* MAGs poses as a substantial environmental adaptation to circumvent the lack of available DIC in the hyperalkaline fluids.

The Type II and Mixed populations occupy a large abundance (up to 23.87% and 7.91% relative abundance, respectively) of the overall microbial community within the hyperalkaline fluids within BA3A. We hypothesize that niche differentiation is supporting the ability for coexistence, given the two *Methanobacterium* populations inhabit the same environmental ecosystem with accessory genomes highlighting very different lifestyles. These differences minimize overlap in their functions within the microbial community and allow for successful adaptation within the hyperalkaline fluids. The Type II population appears capable of a metabolic adaptation to utilize formate in the absence of a clear source of DIC. Contrastingly, the enriched number of glycosyltransferases, specifically *rfaB*, within the Mixed population may indicate greater interaction with biofilms or other microbial members. Further, this would suggest Mixed *Methanobacterium* occupy a more sessile mode of existence in order to reduce energetic demands in search for a source of DIC. Alternatively, the Mixed population could attach to abiotic surfaces to potentially acquire a source of nutrients. The lack of any genes related to cell motility within the accessory genome of the Mixed population further supports the possibility of a sessile lifestyle (Figure 3). Ultimately, the augmentation of glycosyltransferases in the Mixed *Methanobacterium* population supports the notion of facilitating strong niche differentiation from the Type II population to enable co-habitation within the hyperalkaline fluids.

Transporters demonstrate further niche differentiation

The contrast of different gene annotations to related transporters was explored to provide insight into adaptation to hyperalkaline conditions from Type II *Methanobacterium* as well as to compliment how the Mixed population may require additional osmoregulation or nutrient acquisition strategies. The Type II population contained a small subset of transporter genes that were not observed in the other two populations that might provide additional benefit in the hyperalkaline subsurface. The Na^+ transporter *natB* was only possessed by the Type II population, and may play some role in maintaining osmoregulation. Surprisingly, the Type II population was absent of the *nhaP* Na^+/H^+ antiporter and *khtT* K^+/H^+ antiporter, which would appear beneficial given the high H_2 concentration in hyperalkaline fluids. However, this antiporter may not be active at hyperalkaline pH, and may result in gene loss from genome streamlining of the Type II population. Fones et al. (2021) reported on the Mrp-MbH complex (not reported here) that is present in the Type II population and is predicted to help maintain pH homeostasis. Interestingly, the Type II *Methanobacterium* contained the only presence of the full suite of *tauABC* genes responsible for uptake of taurine. Taurine may provide a source of sulfur for Type II methanogens (Kraus, 2021). Sulfate concentrations are an order or two magnitude lesser in the hyperalkaline fluids of NSHQ14 and BA3A compared to WAB188, and taurine may prove as an alternate source of sulfur (Table 1). However, taurine may also serve as an osmoprotectant in order to balance the external osmotic pressure faced in the hyperalkaline fluids (Zhang et al., 2016; Yan et al., 2022). Methanogens and other microbiota have been reported to accumulate soluble organic compounds such as taurine or glycine betain, neutral molecules compatible with metabolic processes and cellular structure. These organic solutes are predicted to provide osmotic balance within the cell against environmental osmotic stress (Farwick et al., 1995; Yan et al., 2022). The ability for Type II *Methanobacterium* to accumulate taurine as a possible osmoprotectant highlights an additional adaptation strategy by this methanogenic population, though the source of taurine within the hyperalkaline subsurface is unclear.

It is additionally perplexing as to why the Type II population only possesses the ATP2C P-type Ca^{2+} transporter shared among all *Methanobacterium* populations and not additional Ca^{2+} transport mechanisms. The Type II population is absent of the yrbG cation:H^+ antiporter, yet demonstrates the presence of the Mg^{2+} transport system from *mgtACE* genes. One study demonstrated that *M. thermoautotrophicus* was directly dependent on Ca^{2+} availability for methane production and cell growth (Vancek et al., 2006). Ca^{2+} concentrations are incredibly high in the hyperalkaline fluids (3.35–6.2 mM) compared to the neutral fluids (1.21 mM). Additional cation transporters for the Type II *Methanobacterium* population may not be energetically favorable or have pH dependencies that are exceeded in the hyperalkaline conditions and may be excluded due to genome streamlining despite high Ca^{2+} concentrations in hyperalkaline waters. The absence of the NH_4^+ transporter in the Type II population is intriguing given the dominant source of nitrogen in the highly reduced fluids is NH_4^+. Contrastingly, phosphate may be a limiting nutrient in the serpentinizing subsurface (Kraus, 2021). The Type II population lacks the *ykaA* phosphate transport regulator, which may further indicate that the cells are under constant phosphate limitation and do not require regulation.

The Mixed *Methanobacterium* population demonstrates few transporter mechanisms that would suggest an adaptation or strategy to circumvent the high pH conditions found in borehole BA3A. The greater gene copy number of lipoprotein transporters compliments the presence of functionally enriched lipoprotein gene annotations found in the Mixed population. Specifically, the gene annotations for the *DedA* family proteins are involved in the transport of various phospholipids in order to rearrange the lipid dynamics of the cell membrane and provide improved membrane integrity (Kumar and Doerrler, 2015; Okawa et al., 2021). While the exact function of these proteins is not fully understood, the reoccurring theme of the Mixed population's focus on cell membrane arrangement suggests this population is actively combating the environmental stress imposed in the hyperalkaline subsurface fluids. The Mixed *Methanobacterium* MAGs also contain an additional sulfate permease gene compared to the other two populations. While the initial sulfate permease protein identified across Type II and Mixed *Methanobacterium* MAGs appears to be involved in sulfate transport, the additional *SulP* protein in the Mixed and Type I population shares homology to a generic inorganic anion transporter from BlastP analysis. Sulfate permeases compose a large family of proteins primarily responsible for sulfate transport, but recently recognized for anion:anion antiport exchange in some homologs (Felce and Saier, 2004). Bioinformatic analysis of various *SulP* genes demonstrated that many of them are fused to carbonic anhydrase homologs, including the bicarbonate transporter belonging to the *SulP* family within a marine cyanobacteria (Felce and Saier, 2004; Price et al., 2004). Further efforts are required to determine if the additional *SulP* protein identified in the Mixed population could act as an anion transporter to circumvent DIC limitation or provide another adaptation strategy in the hyperalkaline, reduced fluids. Physiological studies providing a better understanding of how Mixed *Methanobacterium* acquires cytoplasmic CO_2 are necessary to inform on how this population contributes to a significant proportion of the relative abundance within the deep subsurface hyperalkaline fluids of borehole BA3A.

Carbon substrate adaptability

Understanding how methanogens are able to survive in the hyperalkaline conditions despite an obvious source of DIC remains puzzling. Multiple pathways for carrying out methanogenesis were investigated, and include suggested mechanisms from previous studies conducted at the Samail Ophiolite (Kraus, 2021; Fones et al., 2021). Corroboration of Type II *Methanobacterium* MAGs possessing formate dehydrogenase encoded proteins to oxidize formate to generate cytoplasmic CO_2 matches previous findings and supports an alternative methanogenic pathway to overcome CO_2 limitations (Fones et al., 2019, 2021). Though, the significant presence of the Mixed *Methanobacterium* population within hyperalkaline waters not containing formate dehydrogenase genes suggests this methanogen population is being supported through another adaptation strategy or way of scavenging CO_2 from some other unknown mechanism. To corroborate that the Mixed population was not missing contig sequences that may indicate growth on formate, we looked for unbinned contigs encoding for formate dehydrogenase that may belong to *Methanobacterium*. While many formate dehydrogenases were identified, results from Blastp searches indicated the homology of these genes were not related to any *Methanobacterium* strains (Altschul et al., 1990). Therefore, Mixed *Methanobacterium* populations are demonstrating an alternative method to cope with DIC limitation while also being able to maintain an osmotic balance in the high pH fluids.

Acetate would seem a viable carbon source to support methanogenesis within the hyperalkaline conditions of fluids within the Samail Ophiolite. A study modeling the free energy yield of different substrates in the Santa Elena Ophiolite in Costa Rica demonstrated when acetate comprises a greater proportion of the dissolved organic carbon (DOC) concentration, then the free energy yield becomes more favorable to methanogens (Crespo-Medina et al., 2017). Thermodynamic modeling of biological methanogenesis reactions within the Samail Ophiolite indicates acetoclastic methanogenesis as the most favorable in hyperalkaline conditions (Nothaft et al., 2021b). Given the concentration of acetate is nearly double that of formate while DIC remains incredibly low in the Samail Ophiolite, acetate likely plays a valuable role in the subsurface carbon cycle (Table 1). Yet, the *Methanobacterium* populations here do not display the capacity to assimilate acetate for CH_4 generation.

It therefore remains puzzling that a metabolic mechanism was not identified within the Mixed population to circumvent limited DIC in the hyperalkaline fluids of borehole BA3A. Given the Mixed population constitutes a significant portion of the relative abundance for the microbial community composition, especially with increasing depth, another yet to be defined adaptation strategy must be at play that cannot be recognized through sequencing data alone. We postulate our hypotheses here as motivation to provide avenues of research benefiting our understanding of *Methanobacterium* populations and biological methanogenesis within the subsurface hyperalkaline system in the Samail Ophiolite. While the Type II population has demonstrated the ability to potentially acquire formate as alternative carbon source, it may be that the Mixed population survives by lowering energetic demands through a sessile lifestyle and increasing interactions with other microorganisms or attaching to a carbon substrate source implied by the enriched presence of glycosyltransferases. The cooperation of other microbiota could result in the oxidation of formate or acetate, analytes which are observed in considerable concentrations within the hyperalkaline fluids compared to other available oxidants. A microbial partner capable of oxidizing formate or acetate may be able to produce a localized source of CO_2 rapidly consumed by *Methanobacterium*. This collaborative metabolic framework would require a strict spatial proximity of the Mixed *Methanobacterium* population to avoid precipitation of CO_2 into carbonate minerals in the hyperalkaline conditions.

Acetogens and methanogens have received great attention in serpentinizing systems in efforts to understand early life on Earth, however, the role of additional microbial members in these systems have yet to be explored. Particularly, the ability for specific microorganisms to metabolically cooperate with other members in the community would seem a viable strategy in the nutrient limited hyperalkaline subsurface (Kraus, 2021). Metagenomic sequencing data reveals the presence of the organism *Bellilinea* belonging to the *Anaerolineaceae* family (Supplementary Table 5). *Anaerolineaceae* have been observed in consortia with methanogens in many environments, from anaerobic sludge digesters to marine sediments within Antarctica (Liang et al., 2015; Carr et al., 2018; Dyksma et al., 2020). *Anaerolineaceae* have been observed to degrade n-alkanes and subsequently produce acetate, then successively oxidize acetate into CO_2 through syntrophic cooperation to support methanogenesis (Callaghan, 2013; Liang et al., 2015). Future work to unravel the role of this organism in potentially aiding the Mixed *Methanobacterium* population and its capability for potential alkane degradation warrant further physiological and sequencing based studies. Whether through the cooperation of syntrophic activity or another metabolic mechanism, further research necessitates additional investigation into how Mixed *Methanobacterium* populations are circumventing DIC limitation in the hyperalkaline subsurface fluids. Future work should consider focusing on cultivated isolates from this system to support the role for niche differentiation and other adaptation strategies of *Methanobacterium* within the subsurface serpentinized fluids of the Samail Ophiolite.

Conclusion

Metagenomic sequences were collected from subsurface fluids contrasting various geochemical conditions and depths within the Samail Ophiolite, Sultanate of Oman, and allowed the reconstruction of *Methanobacterium* MAGs to investigate niche differentiation within high pH and DIC limitations resulting from hyperalkaline waters. Metapangenomic analysis determined the presence of three distinct *Methanobacterium* populations, where two inhabited the most hyperalkaline pH fluids sampled to date at the Samail Ophiolite. Core genome analysis revealed all *Methanobacterium* populations contain genes indicating DNA scavenging techniques may be a viable strategy to overcome nutrient limitation within the subsurface hyperalkaline, reduced fluids. Metabolic reconstruction corroborated the presence of formate dehydrogenase in Type II populations suggesting formate oxidation to generate intracellular CO_2 to overcome DIC limitation in hyperalkaline conditions. Further, the accessory genome and functional enrichment of genes unique to the Type II population highlighted proteins relevant to defense against antimicrobials, and the potential use of taurine as an osmoprotectant and source of sulfur. The Mixed population existing in the most hyperalkaline fluids revealed an accessory genome reflecting many cell membrane maintenance mechanisms. The accessory genome of the Mixed population revealed an abundance of various DNA repair genes that likely result from the pressures of osmotic stress on the cell. Additionally, lipoproteins and their associated transporters, as well as glycosyltransferases indicate greater potential for opportunities to interact with microbial biofilms or abiotic surfaces implying a more sessile lifestyle. The significant gene copy number of the *rfaB* glycosyltransferase highlights the need for future research to unravel how this methanogenic population may interact with other microorganisms or adopt another yet to be defined mechanism to overcome DIC limitation, despite a clear metabolic strategy to acquire CO_2 in the hyperalkaline waters.

The data reported here also highlights the benefits of a metapangenomic approach, and how it is capable of identifying unique properties of microbial members across diverse environmental conditions. This approach distinguished unique adaptations and strategies from *Methanobacterium* populations within the Samail Ophiolite, and would provide an insightful approach to deconvolute how other members may circumvent serpentinization impacted conditions. This work aids our ability to partition niche lifestyles of methanogens in this system to better develop methods for understanding life in other serpentinizing environments on Earth and other planetary bodies.

Data availability statement

The Methanobacterium MAG assemblies created as a part of this study are accessible under the NCBI Bioproject Number

PRJNA930444. The metagenomic sequencing data is available at the JGI IMG database under accession numbers: 3300045950, 3300045482, 3300045454, 3300045456, 3300045455. A reproducible methods document and additional files can be found on Github and includes the code used for this analysis (https://github.com/pthieringer/Metapangenomes_Oman2020).

Author contributions

PT wrote the manuscript along with help from EB, AT, and JS and conducted all bioinformatic analyses. PT, AT, and JS collected samples and designed the experiment. All authors contributed to the article and approved the submitted version.

Funding

This work was supported by the National Science Foundation Graduate Research Fellowship (grant no. 1646713): fellow identification number 2018254777 (PT). This work was additionally supported by the NASA Astrobiology Institute "Rock-Powered Life" NAI (NNA15BB02A). The funding agencies did not play a role in design of the study, data collection, or decision to submit the manuscript for publication.

Acknowledgments

The authors thank the Ministry of Regional Municipalities and Water Resources in the Sultanate of Oman for collaboration with sample collection. Additionally, we thank Tristan Caro, Libby Fones, Mike Kubo, and Tori Hoehler for help in collection of the fluid samples. A special thanks to Jeurg Matter, Amelia Paukert-Vankeuren, and Martin Stute for their guidance and knowledge for operating the packer system. Additional thanks to Emily Kraus for insightful and valuable comments on the manuscript. The authors acknowledge the Colorado School of Mines supercomputing resources (http://ciarc.mines.edu/hpc) made available for conducting research reported in this paper. A special thanks to Michael Robbert for his patience and guidance with setting up the necessary software to conduct our bioinformatic analyses.

Conflict of interest

The authors declare that the research was conducted in the absence of any commercial or financial relationships that could be construed as a potential conflict of interest.

Publisher's note

Supplementary material

The Supplementary material for this article can be found online at: https://www.frontiersin.org/articles/10.3389/fmicb.2023.1205558/full#supplementary-material

References

Alneberg, J., Bjarnason, B. S., de Bruijn, I., Schirmer, M., Quick, J., Ijaz, U. Z., et al. (2013). "CONCOCT: clustering CONtigs on COverage and CompositTion." arXiv [preprint]. Available at: http://arxiv.org/abs/1312.4038.

Altschul, S. F., Gish, W., Miller, W., Myers, E. W., and Lipman, D. J. (1990). Basic local alignment search tool. *J. Mol. Biol.* 215, 403–410.

Argüelles, J. C. (2000). Physiological roles of Trehalose in Bacteria and yeasts: a comparative analysis. *Arch. Microbiol.* 174, 217–224. doi: 10.1007/s002030000192

Bateman, A. (2004). The Pfam Protein Families Database. *Nucleic Acids Res.* 32, 138D–141D. doi: 10.1093/nar/gkh121

Bird, J. T., Tague, E. D., Zinke, L., Schmidt, J. M., Steen, A. D., Reese, B., et al. (2019). Uncultured microbial Phyla suggest mechanisms for multi-thousand-year subsistence in Baltic Sea sediments. *MBio* 10, e02376–e02318. doi: 10.1128/mBio.02376-18

Brauer, M. J., Yuan, J., Bennett, B. D., Wenyun, L., Kimball, E., Botstein, D., et al. (2006). Conservation of the Metabolomic response to starvation across two divergent microbes. *Proc. Natl. Acad. Sci.* 103, 19302–19307. doi: 10.1073/pnas.0609508103

Brazelton, W. J., Nelson, B., and Schrenk, M. O. (2012). Metagenomic evidence for H2 oxidation and H2 production by Serpentinite-hosted subsurface microbial communities. *Front. Microbiol.* 2:268. doi: 10.3389/fmicb.2011.00268

Brazelton, W. J., Thornton, C. N., Hyer, A., Twing, K. I., Longino, A. A., Lang, S. Q., et al. (2017). Metagenomic identification of active methanogens and Methanotrophs in Serpentinite Springs of the Voltri massif, Italy. *PeerJ* 5:e2945. doi: 10.7717/peerj.2945

Burns, J. M., Craig, P. S., Shaw, T. J., and Ferry, J. L. (2010). Multivariate examination of Fe(II)/Fe(III) cycling and consequent hydroxyl radical generation. *Environ. Sci. Technol.* 44, 7226–7231. doi: 10.1021/es903519m

Bushnell, B. (2020) "BBTools—DOE joint genome institute." Available at: https://jgi.doe.gov/data-and-tools/software-tools/bbtools/ (Accessed 11 October 2022).

Callaghan, A. V. (2013). Enzymes involved in the anaerobic oxidation of N-alkanes: from methane to long-chain Paraffins. *Front. Microbiol.* 4:89. doi: 10.3389/fmicb.2013.00089

Capella-Gutierrez, S., Silla-Martinez, J. M., and Gabaldon, T. (2009). TrimAl: a tool for automated alignment trimming in large-scale phylogenetic analyses. *Bioinformatics* 25, 1972–1973. doi: 10.1093/bioinformatics/btp348

Capson-Tojo, G., Moscoviz, R., Astals, S., Robles, Á., and Steyer, J.-P. (2020). Unraveling the literature Chaos around free Ammonia inhibition in anaerobic digestion. *Renew. Sustain. Energy Rev.* 117:109487. doi: 10.1016/j.rser.2019.109487

Carr, S. A., Schubotz, F., Dunbar, R. B., Mills, C. T., Dias, R., Summons, R. E., et al. (2018). Acetoclastic Methanosaeta are dominant methanogens in organic-rich Antarctic marine sediments. *ISME J.* 12, 330–342. doi: 10.1038/ismej.2017.150

Chai, Y., Beauregard, P. B., Vlamakis, H., Losick, R., and Kolter, R. (2012). Galactose metabolism plays a crucial role in biofilm formation by *Bacillus Subtilis*. *MBio* 3, e00184–e00112. doi: 10.1128/mBio.00184-12

Clum, A., Huntemann, M., Bushnell, B., Foster, B., Foster, B., Roux, S., et al. (2021). DOE JGI Metagenome workflow. *MSystems* 6, e00804–e00820. doi: 10.1128/mSystems.00804-20

Colman, D. R., Kraus, E. A., Thieringer, P. H., Rempfert, K., Templeton, A. S., Spear, J. R., et al. (2022). Deep-branching Acetogens in Serpentinized subsurface fluids of Oman. *Proc. Natl. Acad. Sci.* 119:e2206845119. doi: 10.1073/pnas.2206845119

Crespo-Medina, M., Twing, K. I., Sánchez-Murillo, R., Brazelton, W. J., McCollom, T. M., and Schrenk, M. O. (2017). Methane dynamics in a tropical Serpentinizing environment: the Santa Elena Ophiolite, Costa Rica. *Front. Microbiol.* 8:916. doi: 10.3389/fmicb.2017.00916

Delmont, T. O., and Eren, A. M. (2018). Linking Pangenomes and Metagenomes: the Prochlorococcus Metapangenome. *PeerJ* 6:e4320. doi: 10.7717/peerj.4320

Dyksma, S., Jansen, L., and Gallert, C. (2020). Syntrophic acetate oxidation replaces Acetoclastic Methanogenesis during Thermophilic digestion of biowaste. *Microbiome* 8:105. doi: 10.1186/s40168-020-00862-5

Edgar, R. C. (2004). MUSCLE: multiple sequence alignment with high accuracy and high throughput. *Nucleic Acids Res.* 32, 1792–1797. doi: 10.1093/nar/gkh340

Ellermeier, C. D., Hobbs, E. C., Gonzalez-Pastor, J. E., and Losick, R. (2006). A three-protein signaling pathway governing immunity to a bacterial cannibalism toxin. *Cells* 124, 549–559. doi: 10.1016/j.cell.2005.11.041

Eren, A. M., Esen, Ö. C., Quince, C., Vineis, J. H., Morrison, H. G., Sogin, M. L., et al. (2015). Anvi'o: An advanced analysis and visualization platform for 'omics data. *PeerJ* 3:e1319. doi: 10.7717/peerj.1319

Farwick, M., Siewe, R. M., and Krämer, R. (1995). Glycine Betaine uptake after hyperosmotic shift in *Corynebacterium Glutamicum*. *J. Bacteriol.* 177, 4690–4695. doi: 10.1128/jb.177.16.4690-4695.1995

Felce, J., and Saier, M. H. (2004). Carbonic anhydrases fused to anion transporters of the SulP family: evidence for a novel type of bicarbonate transporter. *Microbial Physiol* 8, 169–176. doi: 10.1159/000085789

Fones, E. M., Colman, D. R., Kraus, E. A., Nothaft, D. B., Poudel, S., Rempfert, K. R., et al. (2019). Physiological adaptations to Serpentinization in the Samail Ophiolite, Oman. *ISME J.* 13, 1750–1762. doi: 10.1038/s41396-019-0391-2

Fones, E. M., Colman, D. R., Kraus, E. A., Stepanauskas, R., Templeton, A. S., Spear, J. R., et al. (2021). Diversification of methanogens into Hyperalkaline Serpentinizing environments through adaptations to minimize oxidant limitation. *ISME J.* 15, 1121–1135. doi: 10.1038/s41396-020-00838-1

Galperin, M. Y., Wolf, Y. I., Makarova, K. S., Alvarez, R. V., Landsman, D., and Koonin, E. V. (2021). COG database update: focus on microbial diversity, model organisms, and widespread pathogens. *Nucleic Acids Res.* 49, D274–D281. doi: 10.1093/nar/gkaa1018

Giovannoni, S. J., Cameron Thrash, J., and Temperton, B. (2014). Implications of streamlining theory for microbial ecology. *ISME J.* 8, 1553–1565. doi: 10.1038/ismej.2014.60

Haft, D. H., Selengut, J. D., Richter, R. A., Harkins, D., Basu, M. K., and Beck, E. (2012). TIGRFAMs and genome properties in 2013. *Nucleic Acids Res.* 41, D387–D395. doi: 10.1093/nar/gks1234

Hattori, S. (2008). Syntrophic acetate-oxidizing microbes in Methanogenic environments. *Microbes Environ.* 23, 118–127. doi: 10.1264/jsme2.23.118

Holm, N. G., and Charlou, J. L. (2001). Initial indications of abiotic formation of hydrocarbons in the rainbow Ultrama¢c hydrothermal system, mid-Atlantic ridge. *Earth Planet. Sci. Lett.* 191, 1–8. doi: 10.1016/S0012-821X(01)00397-1

Hyatt, D., Chen, G.-L., LoCascio, P. F., Land, M. L., Larimer, F. W., and Hauser, L. J. (2010). Prodigal: prokaryotic gene recognition and translation initiation site identification. *BMC Bioinformatics* 11:119. doi: 10.1186/1471-2105-11-119

Kanehisa, M., Araki, M., Goto, S., Hattori, M., Hirakawa, M., Itoh, M., et al. (2007). KEGG for linking genomes to life and the environment. *Nucleic Acids Res.* 36, D480–D484. doi: 10.1093/nar/gkm882

Kang, D. D., Li, F., Kirton, E., Thomas, A., Egan, R., An, H., et al. (2019). MetaBAT 2: An adaptive binning algorithm for robust and efficient genome reconstruction from Metagenome assemblies. *PeerJ* 7:e7359. doi: 10.7717/peerj.7359

Kashtan, N., Roggensack, S. E., Rodrigue, S., Thompson, J. W., Biller, S. J., Coe, A., et al. (2014). Single-cell genomics reveals hundreds of coexisting subpopulations in wild Prochlorococcus. *Science* 344, 416–420. doi: 10.1126/science.1248575

Kelemen, P. B., and Matter, J. (2008). In situ carbonation of Peridotite for CO2 storage. *Proc. Natl. Acad. Sci.* 105, 17295–17300. doi: 10.1073/pnas.0805794105

Kelemen, P. B., Matter, J., Streit, E. E., Rudge, J. F., Curry, W. B., and Blusztajn, J. (2011). Rates and mechanisms of mineral carbonation in Peridotite: natural processes and recipes for enhanced, in situ CO_2 capture and storage. *Annu. Rev. Earth Planet. Sci.* 39, 545–576. doi: 10.1146/annurev-earth-092010-152509

Kobayashi, T., Kudo, I., Karasawa, K., Mizushima, H., Inoue, K., and Nojima, S. (1985). Nucleotide sequence of the PldB gene and Characteristics of deduced amino acid sequence of Lysophospholipase L2 in *Escherichia Coli*1. *J. Biochem.* 98, 1017–1025. doi: 10.1093/oxfordjournals.jbchem.a135347

Koo, H., Hakim, J., Morrow, C., Crowley, M., Andersen, D., and Bej, A. (2018). Metagenomic analysis of microbial community compositions and cold-responsive stress genes in selected Antarctic lacustrine and soil ecosystems. *Life* 8:29. doi: 10.3390/life8030029

Kraus, E. A. (2021). The endolithic and planktonic subsurface microbiome within zones of active low-temperature serpentinization in the Samail ophiolite of oman (order no. 28413788). Available from Dissertations & Theses @ Colorado School of Mines; ProQuest Dissertations & Theses Global. (2561055614). Available at: http://mines.idm.oclc.org/login?url=https://www.proquest.com/dissertations-theses/endolithic-planktonic-subsurface-microbiome/docview/2561055614/se-2

Kumar, S., and Doerrler, W. T. (2015). *Escherichia Coli* YqjA, a member of the conserved DedA/Tvp38 membrane protein family, is a putative Osmosensing transporter required for growth at alkaline PH. *J. Bacteriol.* 197, 2292–2300. doi: 10.1128/JB.00175-15

Kyryakov, P., Beach, A., Richard, V. R., Burstein, M. T., Leonov, A., Levy, S., et al. (2012). Caloric restriction extends yeast chronological lifespan by altering a pattern of age-related changes in Trehalose concentration. *Front. Physiol.* 3:256. doi: 10.3389/fphys.2012.00256

Langmead, B., and Salzberg, S. L. (2012). Fast gapped-read alignment with bowtie 2. *Nat. Methods* 9, 357–359. doi: 10.1038/nmeth.1923

Lee, M. D. (2019). GToTree: a user-friendly workflow for Phylogenomics. *Bioinformatics* 35, 4162–4164. doi: 10.1093/bioinformatics/btz188

Letunic, I., and Bork, P. (2007). Interactive Tree of life (ITOL): An online tool for phylogenetic Tree display and annotation. *Bioinformatics* 23, 127–128. doi: 10.1093/bioinformatics/btl529

Liang, R., Lau, M., Vishnivetskaya, T., Lloyd, K. G., Wang, W., Wiggins, J., et al. (2019). Predominance of anaerobic, spore-forming Bacteria in metabolically active microbial communities from ancient Siberian permafrost. *Appl. Environ. Microbiol.* 85, e00560–e00519. doi: 10.1128/AEM.00560-19

Liang, B., Wang, L.-Y., Mbadinga, S. M., Liu, J.-F., Yang, S.-Z., Ji-Dong, G., et al. (2015). Anaerolineaceae and Methanosaeta turned to be the dominant microorganisms in alkanes-dependent Methanogenic culture after long-term of incubation. *AMB Express* 5:37. doi: 10.1186/s13568-015-0117-4

Loenen, W. A. M., Dryden, D. T. F., Raleigh, E. A., and Wilson, G. G. (2014). Type I restriction enzymes and their relatives. *Nucleic Acids Res.* 42, 20–44. doi: 10.1093/nar/gkt847

McCollom, T. M., and Seewald, J. S. (2013). Serpentinites, hydrogen, and life. *Elements* 9, 129–134. doi: 10.2113/gselements.9.2.129

Medini, D., Donati, C., Tettelin, H., Masignani, V., and Rappuoli, R. (2005). The microbial Pan-genome. *Curr. Opin. Genet. Dev.* 15, 589–594. doi: 10.1016/j.gde.2005.09.006

Miller, H. M., Matter, J. M., Kelemen, P., Ellison, E. T., Conrad, M. E., Fierer, N., et al. (2016). Modern water/rock reactions in Oman Hyperalkaline Peridotite aquifers and implications for microbial habitability. *Geochim. Cosmochim. Acta* 179, 217–241. doi: 10.1016/j.gca.2016.01.033

Miller, H. M., Mayhew, L. E., Ellison, E. T., Kelemen, P., Kubo, M., and Templeton, A. S. (2017). Low temperature hydrogen production during experimental hydration of partially-Serpentinized Dunite. *Geochim. Cosmochim. Acta* 209, 161–183. doi: 10.1016/j.gca.2017.04.022

Minh, B. Q., Schmidt, H. A., Chernomor, O., Schrempf, D., Woodhams, M. D., von Haeseler, A., et al. (2020). IQ-TREE 2: new models and efficient methods for phylogenetic inference in the genomic era. *Mol. Biol. Evol.* 37, 1530–1534. doi: 10.1093/molbev/msaa015

Mulder, N., and Apweiler, R.. (2007) "InterPro and InterProScan," 12.

Neal, C., and Stanger, G. (1985). "Past and present Serpentinisation of ultramafic rocks; An example from the Semail Ophiolite Nappe of northern Oman" in *The chemistry of weathering*. ed. J. I. Drever (Dordrecht: Springer Netherlands), 249–275.

Nicolaou, S. A., Fast, A. G., Nakamaru-Ogiso, E., and Papoutsakis, E. T. (2013). Overexpression of FetA (YbbL) and FetB (YbbM), encoding an Iron exporter, enhances resistance to oxidative stress in *Escherichia Coli*. *Appl. Environ. Microbiol.* 79, 7210–7219. doi: 10.1128/AEM.02322-13

Noinaj, N., Guillier, M., Barnard, T. J., and Buchanan, S. K. (2010). TonB-dependent transporters: regulation, structure, and function. *Annu. Rev. Microbiol.* 64, 43–60. doi: 10.1146/annurev.micro.112408.134247

Nothaft, D. B., Templeton, A. S., Boyd, E. S., Matter, J. M., Stute, M., Paukert Vankeuren, A. N., et al. (2021a). Aqueous geochemical and microbial variation across discrete depth intervals in a Peridotite aquifer assessed using a packer system in the Samail Ophiolite, Oman. *J. Geophys. Res. Biogeo.* 126:6319. doi: 10.1029/2021JG006319

Nothaft, D. B., Templeton, A. S., Rhim, J. H., Wang, D. T., Labidi, J., Miller, H. M., et al. (2021b). Geochemical, biological, and clumped Isotopologue evidence for substantial microbial methane production under carbon limitation in Serpentinites of the Samail Ophiolite, Oman. *J. Geophys. Res. Biogeo.* 126:6025. doi: 10.1029/2020JG006025

Nurk, S., Meleshko, D., Korobeynikov, A., and Pevzner, P. A. (2017). MetaSPAdes: a new versatile metagenomic assembler. *Genome Res.* 27, 824–834. doi: 10.1101/gr.213959.116

Oberlies, G., Fuchs, G., and Thauer, R. K. (1980). Acetate Thiokinase and the assimilation of acetate in Methanobacterium Thermoautotrophicum. *Arch. Microbiol.* 128, 248–252. doi: 10.1007/BF00406167

Okawa, F., Hama, Y., Zhang, S., Morishita, H., Yamamoto, H., Levine, T. P., et al. (2021). Evolution and insights into the structure and function of the DedA superfamily containing TMEM41B and VMP1. *J. Cell Sci.* 134:jcs255877. doi: 10.1242/jcs.255877

Öster, L. M., Lester, D. R., Terwisscha, A., van Scheltinga, M., Svenda, M., van Lun, C., et al. (2006). Insights into Cephamycin biosynthesis: the crystal structure of CmcI from *Streptomyces Clavuligerus*. *J. Mol. Biol.* 358, 546–558. doi: 10.1016/j.jmb.2006.02.004

Paukert, A. N., Matter, J. M., Kelemen, P. B., Shock, E. L., and Havig, J. R. (2012). Reaction path modeling of enhanced in situ CO2 mineralization for carbon sequestration in the Peridotite of the Samail Ophiolite, Sultanate of Oman. *Chem. Geol.* 330-331, 86–100. doi: 10.1016/j.chemgeo.2012.08.013

Povolotsky, T. L., Orlova, E., Tamang, D. G., and Saier, M. H. (2010). Defense against cannibalism: the SdpI family of bacterial immunity/signal transduction proteins. *J. Membr. Biol.* 235, 145–162. doi: 10.1007/s00232-010-9260-7

Pradel, E., Parker, C. T., and Schnaitman, C. A. (1992). Structures of the RsfaB, RfaI, RfaJ, and RfaS genes of Escherichia coli K-12 and their roles in assembly of the lipopolysaccharide Core. *J. Bacteriol.* 174, 4736–4745. doi: 10.1128/jb.174.14.4736-4745.1992

Price, G. D., Woodger, F. J., Badger, M. R., Howitt, S. M., and Tucker, L. (2004). Identification of a SulP-type bicarbonate transporter in marine Cyanobacteria. *Proc. Natl. Acad. Sci.* 101, 18228–18233. doi: 10.1073/pnas.0405211101

Pritchard, L., Glover, R. H., Humphris, S., Elphinstone, J. G., and Toth, I. K. (2016). Genomics and taxonomy in diagnostics for food security: soft-rotting Enterobacterial plant pathogens. *Anal. Methods* 8, 12–24. doi: 10.1039/C5AY02550H

Probst, A. J., Weinmaier, T., Raymann, K., Perras, A., Emerson, J. B., Rattei, T., et al. (2014). Biology of a widespread uncultivated Archaeon that contributes to carbon fixation in the subsurface. *Nat. Commun.* 5:5497. doi: 10.1038/ncomms6497

R Core Team. (2021). *R a language and environment for statistical computing*. Vienna, Austria: R foundation for Statistical Computing.

Raaijmakers, J. M., De Bruijn, I., Nybroe, O., and Ongena, M. (2010). Natural functions of Lipopeptides from Bacillus and Pseudomonas: more than surfactants and antibiotics. *FEMS Microbiol. Rev.* 34, 1037–1062. doi: 10.1111/j.1574-6976.2010.00221.x

Rempfert, K. R., Kraus, E. A., Nothaft, D. B., Dildar, N., Spear, J. R., Sepulveda, J., et al. (In Review). Intact polar Lipidome and membrane adaptations of microbial communities inhabiting Serpentinite-hosted fluids. *Front. Microbiol.*

Rempfert, K. R., Miller, H. M., Bompard, N., Nothaft, D., Matter, J. M., Kelemen, P., et al. (2017). Geological and geochemical controls on subsurface microbial life in the Samail Ophiolite, Oman. *Front. Microbiol.* 8:56. doi: 10.3389/fmicb.2017.00056

Rempfert, K. R., Nothaft, D. B., Kraus, E. A., Evans, D., Spear, J. R., Matter, J. M., et al. (2023). Subsurface biogeochemical cycling of nitrogen in the actively serpentinizing Samail Ophiolite, Oman. *Front. Microbiol.* 14:1139633. doi: 10.3389/fmicb.2023.1139633

Russell, M. J., Hall, A. J., and Martin, W. (2010). Serpentinization as a source of energy at the origin of life: Serpentinization and the emergence of life. *Geobiology* 8, 355–371. doi: 10.1111/j.1472-4669.2010.00249.x

Schalk, I. J., and Guillon, L. (2013). Fate of Ferrisiderophores after import across bacterial outer membranes: different Iron release strategies are observed in the cytoplasm or Periplasm depending on the Siderophore pathways. *Amino Acids* 44, 1267–1277. doi: 10.1007/s00726-013-1468-2

Schalk, I. J., Yue, W. W., and Buchanan, S. K. (2004). Recognition of Iron-free Siderophores by TonB-dependent Iron transporters: Iron-free ligand recognition. *Mol. Microbiol.* 54, 14–22. doi: 10.1111/j.1365-2958.2004.04241.x

Schrenk, M. O., Brazelton, W. J., and Lang, S. Q. (2013). Serpentinization, carbon, and deep life. *Rev. Mineral. Geochem.* 75, 575–606. doi: 10.2138/rmg.2013.75.18

Schulte, M., Blake, D., Hoehler, T., and McCollom, T. (2006). Serpentinization and its implications for life on the early earth and Mars. *Astrobiology* 6, 364–376. doi: 10.1089/ast.2006.6.364

Sieber, C. M. K., Probst, A. J., Sharrar, A., Thomas, B. C., Hess, M., Tringe, S. G., et al. (2018). Recovery of genomes from Metagenomes via a Dereplication, aggregation and scoring strategy. *Nat. Microbiol.* 3, 836–843. doi: 10.1038/s41564-018-0171-1

Simmons, S. L., DiBartolo, G., Denef, V. J., Aliaga Goltsman, D. S., Thelen, M. P., and Banfield, J. F. (2008). Population genomic analysis of strain variation in Leptospirillum group II bacteria involved in acid mine drainage formation. *PLoS Biol.* 6:e177. doi: 10.1371/journal.pbio.0060177

Simon, M., Scheuner, C., Meier-Kolthoff, J. P., Brinkhoff, T., Wagner-Döbler, I., Ulbrich, M., et al. (2017). Phylogenomics of Rhodobacteraceae reveals evolutionary adaptation to marine and non-marine habitats. *ISME J.* 11, 1483–1499. doi: 10.1038/ismej.2016.198

Sipes, K., Almatari, A., Eddie, A., Williams, D., Spirina, E., Rivkina, E., et al. (2021). Eight Metagenome-assembled genomes provide evidence for microbial adaptation in 20,000- to 1,000,000-year-old Siberian permafrost. *Appl. Environ. Microbiol.* 87:e0097221. doi: 10.1128/AEM.00972-21

Sleep, N. H., Meibom, A., Fridriksson, T., Coleman, R. G., and Bird, D. K. (2004). H2-rich fluids from Serpentinization: geochemical and biotic implications. *Proc. Natl. Acad. Sci.* 101, 12818–12823. doi: 10.1073/pnas.0405289101

Stams, A. J. M., Teusink, B., and Sousa, D. Z. (2019). "Ecophysiology of Acetoclastic methanogens" in *Biogenesis of hydrocarbons*. eds. A. J. M. Stams and D. Sousa (Cham: Springer International Publishing), 1–14.

Suzuki, S., Ishii, S., Hoshino, T., Rietze, A., Tenney, A., Morrill, P. L., et al. (2017). Unusual metabolic diversity of Hyperalkaliphilic microbial communities associated with subterranean Serpentinization at the cedars. *ISME J.* 11, 2584–2598. doi: 10.1038/ismej.2017.111

Templeton, A. S., Ellison, E. T., Glombitza, C., Morono, Y., Rempfert, K. R., Hoehler, T. M., et al. (2021). Accessing the subsurface biosphere within rocks undergoing active low-temperature Serpentinization in the Samail Ophiolite (Oman drilling project). *J. Geophys. Res. Biogeo.* 126:6315. doi: 10.1029/2021JG006315

Tettelin, H., Masignani, V., Cieslewicz, M. J., Donati, C., Medini, D., Ward, N. L., et al. (2005). Genome analysis of multiple pathogenic isolates of *Streptococcus agalactiae*: implications for the microbial 'Pan-genome. *Proc. Natl. Acad. Sci.* 102, 13950–13955. doi: 10.1073/pnas.0506758102

Thieringer, P. H., Honeyman, A. S., and Spear, J. R. (2021). Spatial and temporal constraints on the composition of microbial communities in subsurface boreholes of the Edgar experimental mine. *Microbiol Spectr* 9:e0063121. doi: 10.1128/Spectrum.00631-21

Utter, D. R., Borisy, G. G., Murat Eren, A., Cavanaugh, C. M., and Mark, J. L. (2020). Metapangenomics of the Oral microbiome provides insights into habitat adaptation and cultivar diversity. *Genome Biol.* 21:293. doi: 10.1186/s13059-020-02200-2

van Erk, M. R., Bourceau, O. M., Moncada, C., Basu, S., Colleen, H., and De Beer, D. (2023). Reactive oxygen species affect the potential for mineralization processes in permeable intertidal flats. *Nat. Commun.* 14:938. doi: 10.1038/s41467-023-35818-4

Vancek, M., Vidová, M., Majerník, A. I., and Smigán, P. (2006). Methanogenesis is Ca^{2+} dependent in *Methanothermobacter Thermautotrophicus* strain ΔH. *FEMS Microbiol. Lett.* 258, 269–273. doi: 10.1111/j.1574-6968.2006.00232.x

Vernikos, G., Medini, D., Riley, D. R., and Tettelin, H. (2015). Ten years of Pan-genome analyses. *Curr. Opin. Microbiol.* 23, 148–154. doi: 10.1016/j.mib.2014.11.016

Wang, Y., Li, W., Baker, B. J., Zhou, Y., He, L., Danchin, A., et al. (2022). Carbon metabolism and adaptation of Hyperalkaliphilic microbes in Serpentinizing spring of Manleluag, the Philippines. *Environ. Microbiol. Rep.* 14, 308–319. doi: 10.1111/1758-2229.13052

Wang, C., Zhang, H., Wang, J., Chen, S., Wang, Z., Zhao, L., et al. (2020). Colanic acid biosynthesis in *Escherichia Coli* is dependent on lipopolysaccharide structure and glucose availability. *Microbiol. Res.* 239:126527. doi: 10.1016/j.micres.2020.126527

Wepy, J. A., Galligan, J. J., Kingsley, P. J., Xu, S., Goodman, M. C., Tallman, K. A., et al. (2019). Lysophospholipases cooperate to mediate lipid homeostasis and Lysophospholipid signaling. *J. Lipid Res.* 60, 360–374. doi: 10.1194/jlr.M087890

Wickham, H. (2011). Ggplot2. *Wiley Interdisciplin Rev Comput Stat* 3, 180–185. doi: 10.1002/wics.147

Wu, Y.-W., Simmons, B. A., and Singer, S. W. (2016). MaxBin 2.0: An automated binning algorithm to recover genomes from multiple metagenomic datasets. *Bioinformatics* 32, 605–607. doi: 10.1093/bioinformatics/btv638

Yan, Y., Yan, M., Angelidaki, I., Dafang, F., and Fotidis, I. A. (2022). Osmoprotectants boost adaptation and protect Methanogenic microbiome during Ammonia toxicity events in continuous processes. *Bioresour. Technol.* 364:128106. doi: 10.1016/j.biortech.2022.128106

Zhang, Z., and Wood, W. I. (2003). A Profile Hidden Markov Model for Signal Peptides Generated by HMMER. *Bioinformatics* 19, 307–308. doi: 10.1093/bioinformatics/19.2.307

Zhang, L., Zhu, K., and Li, A. (2016). Differentiated effects of Osmoprotectants on anaerobic Syntrophic microbial populations at saline conditions and its engineering aspects. *Chem. Eng. J.* 288, 116–125. doi: 10.1016/j.cej.2015.11.100

Zwicker, J., Birgel, D., Bach, W., Richoz, S., Smrzka, D., Grasemann, B., et al. (2018). Evidence for Archaeal Methanogenesis within veins at the onshore Serpentinite-hosted Chimaera seeps, Turkey. *Chem. Geol.* 483, 567–580. doi: 10.1016/j.chemgeo.2018.03.027

frontiers | Frontiers in Microbiology

TYPE Original Research
PUBLISHED 07 July 2023
DOI 10.3389/fmicb.2023.1194848

OPEN ACCESS

EDITED BY
Tori Hoehler,
National Aeronautics and Space Administration (NASA), United States

REVIEWED BY
Hans Røy,
Aarhus University, Denmark
Paraskevi Polymenakou,
Hellenic Center for Marine Research (HCMR), Greece

*CORRESPONDENCE
Jens Kallmeyer
✉ kallm@gfz-potsdam.de

RECEIVED 27 March 2023
ACCEPTED 15 June 2023
PUBLISHED 07 July 2023

CITATION
Schubert F and Kallmeyer J (2023) Liquid scintillation counting at the limit of detection in biogeosciences.
Front. Microbiol. 14:1194848.
doi: 10.3389/fmicb.2023.1194848

Liquid scintillation counting at the limit of detection in biogeosciences

Florian Schubert and Jens Kallmeyer*

GFZ German Research Center for Geosciences, Section Geomicrobiology, Potsdam, Germany

Liquid scintillation is widely used to quantify the activity of radioisotopes. We present an overview of the technique and its application to biogeosciences, particularly for turnover rate measurements. Microbial communities and their metabolism are notoriously difficult to analyze in low energy environments as biomass is exceedingly sparse and turnover rates low. Highly sensitive methods, such as liquid scintillation counting, are required to investigate low metabolic rates and conclusively differentiate them from the background noise of the respective analyzer. We conducted a series of experiments to explore the effects of luminescence, measurement time and temperature on scintillation measurements. Luminescence, the spontaneous emission of photons, disproportionally affects samples within the first few hours after sample preparation and can be minimized by following simple guidelines. Short measurement times will negatively affect liquid scintillation analysis or if background noise makes up a significant proportion of the detected events. Measurement temperature affected liquid scintillation analysis only when the temperature during the measurement reached approximately 30°C or higher, i.e. the liquid scintillation analyzer was placed in an environment without temperature control, but not in cases where chemicals were stored at elevated temperatures prior to measurement. Basic understanding on the functionality of a liquid scintillation analyzer and simple precautions prior to the measurement can significantly lower the minimum detection limit and therefore allow for determination of low turnover rates previously lost in the background noise.

KEYWORDS

background measurements, liquid scintillation, minimum detection limit, radioisotopes, biotic fringe

Introduction

The subsurface biosphere is the largest continuous ecosystem on the planet (Jørgensen and Boetius, 2007). The discovery of microorganisms hundreds or even thousands of meters below the ocean floor (Parkes et al., 1994; Inagaki et al., 2015) and in several kilometers depth in terrestrial habitats (Baker et al., 2003) illustrate that life in the subsurface is widely distributed.

Albeit extremely low microbial abundance and activity, the deep subsurface harbors ~15% of the world's living biomass due to its sheer volume (Kallmeyer et al., 2012; Bar-On et al., 2018; Magnabosco et al., 2018). The subsurface biosphere is the intermediary between the mainly biologically controlled surface biosphere and purely abiotic geosphere and thereby plays a key role in important element cycles (Hinrichs and Inagaki, 2012).

A reoccurring theme of the investigation of the subsurface biosphere is exploration of the biotic fringe (Shock, 2000). Extremophilic microorganisms have been found in a variety of seemingly uninhabitable environments (Heuer et al., 2020; Beulig et al., 2022) and the known boundaries of life have been steadily extended over the last decades (Cowan, 2004). Particularly in deep subsurface environments, the often very low cell abundances and therefore low biomass at the biotic fringe hampers detection and quantification of microorganisms (Morono and Inagaki, 2016). Molecular biological techniques rely on extraction of sufficient amounts of biomolecules like DNA or RNA. Insufficient amounts of DNA lead to problems with low-level contamination from reagents and laboratory equipment, thus deteriorating the ratio between sample and contaminants. Given the severe limitations in available sample volume from deep subsurface environments, the total amounts of extractable biomolecules from such samples are often too small for even the most sensitive molecular biological analyses (Heuer et al., 2020). Highly sophisticated methods, such as cell separation via flow cytometry and cell sorting (Morono et al., 2013), may allow for cell quantification, but usually fall short to collect sufficient cells for phylogenetic analyses. Hence, no information about the composition of the microbial community can be extracted. This is a hurdle that often cannot be overcome, deeming culture-independent techniques like sequencing impossible (Heuer et al., 2020).

Incubations with radiotracer allow highly sensitive measurements of several quantitatively important carbon mineralization processes such as sulfate reduction, methanogenesis, fermentation, and anaerobic oxidation of methane (Jørgensen, 1982; Beulig et al., 2018; Jørgensen et al., 2019), that can give insight into microbial activity beyond the limits of biomolecular analysis (Heuer et al., 2020; Beulig et al., 2022). Short incubation times also allow for separate analysis of both directions of bi-directional reactions or steady states (Csala et al., 2005).

Radioisotope Incubations

Radioisotope incubations are a standard technique for determination of catabolic and anabolic rates in sediments (Ivanov, 1956; Sorokin, 1962; Iversen and Blackburn, 1981; Smith and Klug, 1981). Major advantages of radioisotope incubations are their sensitivity and the fact that the concentration of the compound of interest does not significantly change, as the usually carrier-free tracer (i.e., without any non-radioactive components) has a very high specific activity and is only added in minute amounts. Microorganisms metabolize only a tiny fraction of the supplemented radioisotope and, in most cases, the radiolabeled product can still be analyzed. Additional sensitivity can be achieved by adding higher amounts of radiotracer to increase the chance of a labeled reagent being metabolized but comes with the burden of additional radioactive material.

Fossing (1995) outlined the major principles that have to be considered for radiotracer incubations:

The radiolabeled compound must be present only in trace amounts to keep the chemical and physical equilibrium of the system intact. The specific activity of the radioisotope [i.e., Bequerel (Bq) per mole of substrate] must be constant throughout the incubation. Therefore, a sufficiently short incubation time has to be chosen to keep turnover of the injected tracer <1%. As neither the concentration of the radioactive reagent nor the initial ratio of the reactants or other physicochemical parameters change significantly during the experiment, a constant turnover of the radiolabeled tracer throughout the entire incubation period can be assumed.

Jørgensen (2021) illustrates the significance of radioisotope techniques on the examples of sulfate reduction rate measurements by comparing the sensitivity of measuring changes in sulfate concentration via ion chromatography and ^{35}S sulfate via liquid scintillation counting. The ^{35}S method relies on conversion of ^{35}S sulfate to ^{35}S sulfide by sulfate reducing bacteria (SRB). Each sample is typically provided with 0.1–1 MBq ^{35}S sulfate but only a small fraction is reduced by SRB. Liquid scintillation counters are able to detect less than 1 Bq of activity (Røy et al., 2014), i.e., only a millionth of the injected ^{35}S, hence a millionth of the total sulfate pool. Ion chromatography has reproducibility of around 1%, so only concentration changes >1% can be safely detected. In conclusion, radiotracer techniques increase the sensitivity of measuring sulfate turnover about 10,000-fold.

Although turnover rate measurements do not provide any information about the composition of the microbial community, biological turnover of a specific (radiolabeled) compound can still be used to deduce the existence of a certain group of microorganisms even when microbial abundances are too low for molecular biological analyses (Heuer et al., 2020; Beulig et al., 2022). Additionally, while genomic data only provide information about metabolic potential but not about ongoing processes (these would require transcriptomic data), turnover of a radiolabeled substrate is unambiguous.

A combination of geochemical analyses and turnover rate measurements, e.g., anaerobic oxidation of methane, hydrogenase activity, methanogenesis, and sulfate reduction, can therefore provide novel insight into low biomass environments.

Liquid scintillation counting

Liquid scintillation counting is a standard method for the quantification of low energy alpha- and beta-emitting radioisotopes. Liquid scintillation counting offers high counting efficiency for common isotopes involved in various chemical and biological cycles like ^{3}H, ^{14}C, ^{32}P, ^{35}S, and ^{131}I and only requires relatively simple sample preparation. It is the method of choice for quantification of turnover and incorporation in a wide range of environments.

Liquid scintillation counting requires specific scintillation cocktails that consist of organic aromatic compounds and a suitable solvent. Decaying particles of the radioactive isotopes activate the aromatic solvent through electron excitation. The energy is then absorbed by the organic scintillator molecules, producing excited states of electrons and eventually emitting photons. The bursts of photons are detected by photomultiplier tubes (PMT) and converted into electric pulses. The amplitude of each electric pulse is hereby proportional to the decay energy. The electric pulses are then quantified and represent the detected signals given as output in the software of the liquid scintillation analyzer.

Due to the versatility of the liquid scintillation counting technique, it is used in a variety of fields such as medicine, meteorology, and physical sciences. Comprehensive literature about the Liquid scintillation counting method and functionality is available (Horrocks, 2012; Kobayashi, 2012; L'Annunziata, 2020; L'Annunziata et al., 2020) but almost exclusively focused on the previously mentioned main areas of application.

This publication aims to summarize relevant information for liquid scintillation counting in biogeosciences and to highlight important findings with respect to measurements near the absolute limit of detection.

History and development of liquid scintillation counting

In the late 1920s and early 30s scintillation counting required manual detection of scintillation events with a microscope (Meyer et al., 1927; Krebs, 1955) but the methodology was eventually abandoned due to its labor intensity, subjective nature and difficulty as well as the development and rise of the Geiger-Müller counter.

Initial investigations of organic compounds and certain dissolved solutes as efficient scintillation sources by Kallmann were disrupted by the Second World War. After the war however, multiple publications (Broser and Kallmann, 1947; Herforth, 1948; Kallmann, 1950; Reynolds et al., 1950) presented the viability of organic solutions as scintillation liquids.

Most of the early liquid scintillation counters (LSC) were only equipped with a single photomultiplier tube (Horrocks, 1974) and therefore not able to detect low-energy beta emitters due to the high inherent background signal. The first commercially available LSC, the Tri-Carb 314, and Packard Instrument Company, was produced in 1953 (Temple, 2015). Since the inception of commercially available LSCs, innovations mainly focused on the reduction of the background via physical or electronic improvements (see the section “Background Reduction”).

Commercial LS counters

The current market for LSC is shared by only a small number of manufacturers—PerkinElmer, Hidex, and Hitachi Aloka. Hitachi Alokas’ LB series is available almost exclusively in Japan and does not play a major role internationally. PerkinElmer’s Tri-Carb series is equipped with two main PMTs, facing the sample from opposite sides at one plane; some models have additional guard detectors with a PMT. The two-PMT design was also used in LSCs from Wallac Oy, Packard Bioscience, and Beckman. These companies discontinued their production, but their systems are still in use in many laboratories around the world. Hidex Scintillation Counters are a relatively recent addition to the market. Their two models (300/600SL) are both equipped with a triple PMT configuration, which enables determination of the triple-to-double-coincidence-ratio (TDCR). The TDCR method does not require an internal radiation source and allows to directly calculate counting efficiency. All of the above mentioned LSC allow for reliable determination of turnover rate measurements. Simple, portable analyzers like the Triathler LSC (Hidex) are also available for field measurements.

There are several factors that can influence the quantification of radioactivity via liquid scintillation counting. The most important ones are quenching and luminescence.

Quenching

Quenching is defined as incomplete transfer of the radioisotope’s decay energy to the PMT and results in an underestimation or loss of the amplitude of the signal. Different types of quench can occur, such as physical, chemical, color, and ionization quench (Figure 1).

Physical quench occurs when there is physical separation of the radioisotope and the scintillator, which can be a problem when working with solid scintillation techniques. It is of minor importance in the context of liquid scintillation counting as it can generally be avoided by proper homogenization of sample and scintillation cocktail. The properties of the cocktail should be checked to ensure its suitability for a given sample matrix in order to form a stable emulsion of sample and cocktail. Especially at very high or low pH values or high salt concentrations, the choice of the right LSC cocktail requires special consideration to suit the specific parameters. Also, the mixing ratio between cocktail and sample needs to be considered to ensure optimal counting efficiency (Røy et al., 2014).

Chemical quench describes the process of energy absorption between the radioisotope and the scintillator. The scintillation process is intercepted by chemical compounds in the sample or sample solution that scavenge excited molecules and produce heat instead of re-emitting the energy. Chemical quench represents the most frequent type of quench in liquid scintillation counting. Common chemical quenchers are Zn-ions, NaOH, ketones, organic acids, dissolved oxygen, aliphatic alkenes, and hydrocarbons (Cassette et al., 2000; Broda et al., 2007).

Color quench occurs when emitted photons are absorbed by coloration of particles or solutions before reaching the PMT. Examples for color quench include measurements of samples containing sediment or colored chemicals.

Ionization quench occurs when molecular damage is caused by a charged particle. The damage caused by the ionized molecule can either be temporary or permanent. Temporary molecule damage is characterized by high ionization density along the track of the ionizing particle. Permanent molecule damage is caused by long-term exposure of the scintillator to a high density of ionized molecules that negatively affect scintillation efficiency. The interaction between the liquid scintillator and a particle is a non-linear function of particle energy and non-linearity increases with stopping power of the particle (Broda et al., 2007). The stopping power is defined as loss of energy by ionizing radiation per unit of distance (Ashley, 1982). Photon emission of low-energy beta particles, such as those from ^{3}H, or electrons will exhibit greater non-linearity, therefore cause higher ionization quench, than high-energy beta particles or electrons as interaction of the charged particles.

Luminescence

One of the main contributors to the background (i.e., detection of events by the PMTs that are not associated with a sample’s radioactivity) is luminescence, which is a phenomenon caused by a low energetic single photon emission. Chemiluminescence and photoluminescence directly interfere with the assay of radioactive samples in scintillation cocktail and should be reduced and/or quantified for a reliable analysis.

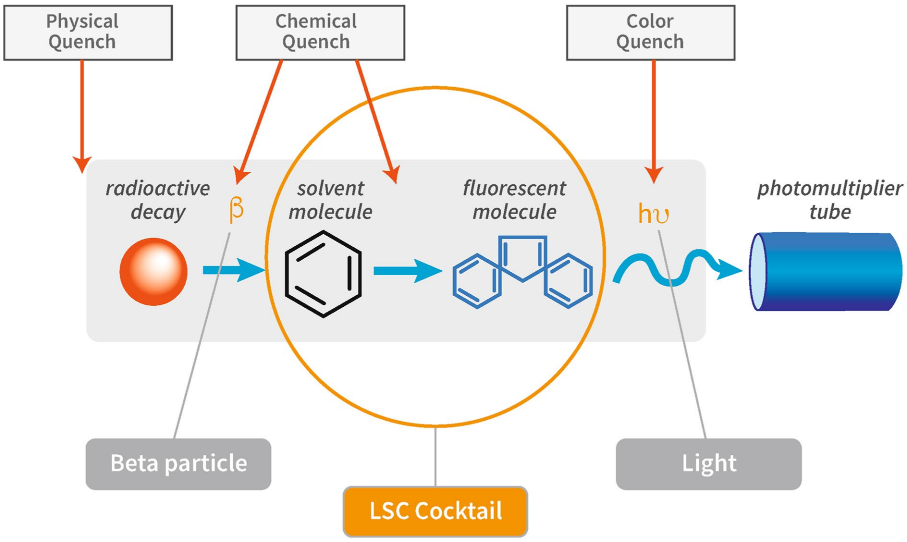

FIGURE 1
Schematic overview of the interference of quench on the different steps in the scintillation process. Modified after "PerkinElmer Introduction to Quench."

Chemiluminescence is caused by chemical reactions between the scintillation cocktail and the chemical solution or substrate. Such chemical interactions can cause molecular excitation and light emission (L'Annunziata et al., 2020). The light is emitted when the excited molecule, in a state of an elevated energy level, decays into its ground state, the lowest possible energy level. Storage of the samples for a few hours can significantly reduce chemiluminescence.

Photoluminescence describes the effect of photon emission due to excitations by ultraviolet light (e.g., sun light) in the sample-scintillation cocktail mixture (L'Annunziata et al., 2020). Temporary storage for approximately 15 min in the dark prior to the LSC measurement should eliminate any photoluminescence. Samples can either be stored in dark environments or a pre-count delay in the LSC itself can be programmed. A subtype of photoluminescence, phosphorescence, can be encountered during wipe tests for contamination control. Detergents or cleaning agents are taken up by the wipe and then cause a reaction with the scintillation cocktail that can be characterized by a lower decay constant and longer duration.

Triple-to-double coincidence rate

Liquid scintillation counters equipped with three instead of one or two PMTs allow for quantification of the Triple-to-Double Coincidence Rate (TDCR), which relies on a physical and statistical model of distribution and detection probability of scintillation photons. These models are the foundation for theoretical calculations of the counting efficiency, a critical parameter to evaluate the number of "true" counts. In TDCR systems, the PMTs are usually arranged in 120° angles to each other in one plane as it provides a geometrically optimal coverage of the measurement chamber. The underlying principle of TDCR is the comparison of counts that were measured by any combination of only two of the three PMTs and signals that were captured by all three PMTs and is calculated using the formula:

$$TDCR = \frac{Triple\ Counts}{Double\ Counts + Triple\ Counts} \qquad (1)$$

Triple-to-double-coincidence-ratio allows for the determination of a factor for quench correction, as common quenches such as color and chemical quench disproportionally affect the triple coincidences (Simpson and Meyer, 1994). The quench correction is a correlation between counting efficiency and measured TDCR and can routinely be applied to activity measurements of pure beta emitters irrespective of the states of quench. Counting efficiency can be determined by using external calculations (Simpson and Meyer, 1994) or is already included in the LSC-specific operating program. No external standard for the monitoring of quench level is needed and TDCR can be applied to both chemical and color quench, aqueous and organic samples as well as different scintillation cocktails and isotopes (L'Annunziata, 2020).

Triple-to-double-coincidence-ratio is also a viable analytical method for high-energy beta emitters, such as ^{32}P, ^{89}Sr, and ^{90}Y by Čerenkov counting (Kossert, 2010), i.e., the detection of Čerenkov photons that are emitted by high-energy beta decay when moving in a dielectric and transparent medium (Čerenkov, 1937). An in-depth description of functionality and theoretical approaches of TDCR can be found in Broda (2003) and Broda et al. (2007).

Background

The background is defined as the cumulative signal from external sources that are not associated with disintegrations in the sample. A variety of factors affects the background signal of a liquid scintillation counter, i.e., the inherent count rate: electrical noise of the analyzer, natural radioactivity in the instrument or in the vial material, ambient γ- and cosmic radiation, and the scintillation fluid. These interferences can be separated into a quenchable background and an unquenchable background. Quenchable background is caused by interactions of primarily cosmic radiation and natural radioactivity with the liquid scintillator solution whereas unquenchable background is caused by interactions outside the liquid scintillation cocktail (Horrocks, 1985).

Qualification and quantification of the counter background is of great significance for samples at or near the detection limit as an elevated or fluctuating background disproportionally affects such data. The same standards have to be applied for both counter background measurements and all actual samples, even those with count rates several orders of magnitudes above the background. For samples with high-count rates, the effect of the counter background on the data will be miniscule as the background only represents a tiny fraction of the signal but proper counter background assessment can help to identify potential contamination or carry-over of radioactivity in subsequent experiments.

A counter background measurement is carried out with a vial containing only scintillation cocktail and all other chemicals in the exact same ratio as in an actual sample but without any radionuclides. The identical ratio of chemicals will result in a comparable quench level between the counter background and sample measurements. The counter background then has to be measured for a sufficient length of time, optimally identical to the measurement time of the corresponding sample.

Background reduction

Liquid scintillation counters are equipped with various tools to reduce the background. Those tools can be of physical nature like passive shielding or guard detectors or electric, e.g., pulse discrimination electronics. Commercially available liquid scintillation counters are using a combination of various techniques to automatically reduce background count rates. More details and supporting visuals about the various background reduction techniques can be found in L'Annunziata (2020) and L'Annunziata et al. (2020).

Passive shielding

A lead shielding is employed to reduce environmental gamma photons, cosmic muons, secondary X-rays, and thermal neutrons (L'Annunziata et al., 2020). The lead shield is composed of low residual activity lead and equipped with a layer of cadmium to shield against neutrons and can have an additional copper lining against stray magnetic fields (Kojola et al., 1984). The shielding can have a total weight of several 100 kg. Still, passive shielding does not fully absorb all high-energy photons and energetic cosmic particles (L'Annunziata et al., 2020).

Active guard detector

An active guard detector includes additional PMTs that either surround the sample or are placed very close to it, but lack an optic path for scintillation photons from the sample to enter the tube. Any event simultaneously detected by the PMT of the active guard and the sample detector will be rejected, as it represents an external signal not associated with the disintegration of the sample. Photon detection by only the internal PMTs will be attributed to a decay inside the measurement chamber and counted as a sample-derived radioactive decay or luminosity, depending on the energy profile and duration of the pulse. An active guard is the most efficient way to reduce background and filters much of environmental gamma radiation and 99% of soft cosmic components (L'Annunziata, 2020; L'Annunziata et al., 2020).

Pulse discrimination electronics

Pulse shape analysis (PSA) and pulse amplitude comparison (PAC) can be applied to carry out pulse discrimination analysis.

The LSC detects different signals, namely nuclear decay or background events, which do not share the exact same properties. The shapes of the pulses of the detected signals are determined by their energy and decay time. Nuclear decays appear with a strong, prompt pulse and rapid decay whereas background events produce weaker pulses with a longer decay time. The photons emitted by the fast decay, from excited single states with paired electrons, have a duration of typically 2–8 ns while the delayed pulse, from annihilation of more stable triplet states with unpaired electrons, can persist for several hundred nanoseconds (L'Annunziata, 2020). Pulse shape analysis can be used to differentiate between a true nuclear decay and a background event due to their unique pulse shape. Optimization of the pulse shape analysis is specific to vial material and sample-cocktail chemistry (L'Annunziata et al., 2020). PSA is most effective for alpha counting but has also been used for background discrimination (Kaihola et al., 1991) and separation of background events from beta decay (L'Annunziata, 2020).

The ratio of pulse amplitudes detected by different PMTs can be analyzed via a pulse amplitude comparison. When PMTs detect photons generated by nuclear decay within the scintillation cocktail, the pulse amplitudes at the different PMTs will be very similar; hence, the ratio of pulse amplitudes between the PMTs will be close to 1. Cosmic radiation or naturally occurring decays in the material of the vial (e.g., in glass vials) will result in a higher amplitude on one PMT and a weaker amplitude at the other PMT(s) causing a dissimilar signal and hence a ratio deviating from 1. Pulse amplitude comparison should not be applied to measure low-energy beta-emitters or Čerenkov radiation as only a small number of photons is generated (L'Annunziata et al., 2020).

Physical background reduction (vial, cocktails)

The physical background of the sample can be reduced by choosing appropriate vials and scintillation cocktail. Vials can have an inherent background due to the material containing radioactive elements, e.g., ^{40}K in glass vials. While specific low ^{40}K glass vials are available, plastic vials provide multiple advantages including a lower background, as they are made from ^{14}C-dead hydrocarbons and should not contain any natural radioactive compounds. Plastic vials require a scintillation cocktail that will not dissolve the vials (i.e., cocktails not containing solvents such as benzene or toluene). Additionally, plastic vials may be affected by buildup of static charge, which leads to elevated count rates (L'Annunziata et al., 2020). Specific antistatic vials or a built-in deionizer in the LSC are efficient ways to circumvent the static charge build-up.

As mentioned above, it is important to use the same chemical composition, i.e., sample-cocktail ratio, for background and sample analysis. An optimal ratio should be determined for every specific LSC cocktail-sample mixture.

Stable counting environment

The liquid scintillation counter should be operated in a controlled environment as parameters, such as temperature, humidity, and sunlight can affect the background. Optimal temperature windows for LSC operations and scintillation cocktails are provided by the respective supplier, and deviations from those recommendations can significantly affect background levels and variation within the background. As mentioned previously, direct exposure of the samples to sunlight will lead to elevated rates of photoluminescence. Hence, environments without direct sunlight should be prioritized for the placement of the LSC.

Motivation

Increasing interest in and accessibility to deep subsurface sediment or other samples from environments near the biotic-abiotic fringe led to a growing need for measurements of turnover or incorporation rates close to the limit of detection. However, such measurements demand a deep understanding of the parameters that affect the limit of detection. A low limit of detection is the fundamental requirement to reliably detect turnover rates in samples from low biomass or low activity sites. Therefore, we investigate different parameters such as temperature and measurement time to monitor their effect on the limit of detection to provide recommendations and to improve detection of very small amounts of radioactivity as often encountered in low turnover rate analyses.

Materials and methods

Scintillation counting

Liquid scintillation analysis was conducted with a Hidex 600 SL LSC. The LSC is equipped with a triple PMT configuration that allows recording double coincidences (CPM2), counts that are detected only at two of the three PMTs, and triple coincidences (CPM3), which are simultaneously detected at all three PMTs, within a pre-defined coincidence time of 35 ns. Measuring CPM2 and CPM3 allows for the determination of the triple-to-double-coincidence ratio. Additionally, the LSC is equipped with an additional active guard PMT underneath the counting chamber to detect ambient radiation.

All background samples were prepared with a 7/8 mL sample/cocktail mixture; in case of counter background measurements, the sample consists of 7 mL 5% zinc acetate (ZnAc) without any added radioactivity. The composition of the counter background sample was chosen because the ZnAc is used as final trap in the cold chromium distillation (Kallmeyer et al., 2004), a widely used technique to measure sulfate reduction. This method uses ZnAc to capture the microbially produced $H_2{}^{35}S$ in the form of $Zn^{35}S$. All sample-cocktail mixtures were vortexed for 10 s to ensure homogeneity. Prior to analysis sample vials were cleaned with microfiber tissues moistened with ethanol to remove potential contaminants on the outside walls. The standard measurement time was 10 min, but dedicated measurements with a measurement time of 1, 2, and 60 min were also carried out.

Experiments that investigated luminosity and/or the effect of measurement time were carried out with the vial repeat option that allows measuring the same sample vial multiple times in a row without removing it from the measurement chamber, with a delay of a few seconds between each measurement.

Luminosity and counter background

For the assessment of the decline of luminosity with time and its effect on the background, a freshly prepared background sample containing 7 mL 5% ZnAc and 8 mL scintillation cocktail was put into the scintillation counter immediately after preparation and cleaning of the outside of the vial with ethanol. These background samples were measured consecutively for 200 times with a measurement time of 1 and 2 min and 100 times with a measurement time of 10 and 60 min, respectively. For each experiment, new counter background samples were freshly prepared—a total of 12 samples, one for each combination of the four measurement times and three scintillation cocktails. The assessment of luminosity and the counter background was carried out with the following scintillation cocktails with the same measurement time and number of measurements: ROTISZINT Eco Plus (Carl Roth, Germany), AquaLight+ (Hidex, Finland), and Ultima GOLD XR (PerkinElmer, United States). We will refer to these cocktails by the following abbreviations: ROTI, AL+, and UG, respectively.

Measurement temperature and storage temperature

We stored our scintillation cocktails in a dark environment at room temperature as per manufacturers' guidelines. In order to investigate the temperature optimum for LSC measurements, we conducted a series of tests. Eight counter background samples were measured at each of the temperature steps.

In a first experiment, we increased the measurement temperature from 10°C to over 35°C to simulate the approximate annual temperature range in a room without proper temperature control. For this test, we used ROTISZINT Eco Plus and Ultima GOLD XR scintillation cocktail.

In a second experiment, potential chemical effects of elevated storage temperatures on the scintillation cocktail were tested by heating background samples in an incubator to various temperatures between 25 and 60°C. We used the same cocktails, ROTI and UG, as in the previous experiment and prepared eight replicates of each cocktail. A triplicate of background samples kept at 20°C was used as a reference.

Results

Assessment of the counter background

Luminosity

We regularly observed noticeable differences in luminosity in our standard background measurements that we run at the beginning, middle, and end of each sample analysis. This difference correlated with time passed since the start of the measurement; with high luminosity in the samples measured early in the sequence and significantly lower luminosity at the end. For all measurements

(Figure 2), irrespective of scintillation cocktail or measurement time per sample an initial peak for luminosity was observed in the very first measurement repetitions followed by a asymptotic decline in luminosity over the next few hours, which eventually resulted in a plateau. While the general trend is similar between all measurements, significant differences were observed between the various measurement times and scintillation cocktails.

In terms of luminosity, the AL+ scintillation cocktail yielded low luminosity values from the start and also quickly established a plateau with low and consistent luminosity values. The cocktails ROTI and UG show a compareable luminosity profile. Both have initial luminosity values of >20% that decline below 10% after *ca.* 10 h and experience a constant decline even after a measurement time of more than 4 days. The UG cocktail had a slightly less pronounced initial peak and lower minimum values than the ROTI cocktail. In terms of luminosity, the 1-min measurement experiment with UG cocktail showed significant scatter of almost 30% even after almost 5 h of measurement time.

Counter background

Independent of the scintillation cocktail, the measured counter background in the various experiment revealed almost identical trends. Comparing the background experiments with 1, 2, 10, and 60 min of measurement time, the scatter of measured background activity is declining with increasing measurement time (Tables 1–3), i.e., while data of the 1-min measurement time experiments show a range of >20 CPM2 or > 0.75 Bq, data of the 60-min measurement time experiment are confined within ~5 CPM2 or < 0.1 Bq. For measurement times of 2 min and longer all cocktails performed equally realiable.

TABLE 1 Performance of selected scintillation cocktails at various measurement times.

[CPM2]	1 min	2 min	10 min	60 min
ROTISZINT	23.48 ± 5.38	21.59 ± 4.28	20.60 ± 2.30	19.32 ± 0.99
AquaLight+	19.70 ± 4.56	18.07 ± 3.33	19.75 ± 1.42	20.04 ± 0.64
Ultima Gold XR	23.07 ± 77.95	14.58 ± 2.87	15.96 ± 1.60	14.94 ± 0.63

Performance is presented by CPM2 (events counted by two of the three PMTs) of the counter background values and respective standard deviation.

CPM2 vs. CPM3

Initial measurements of CPM2 seem to follow the trends of luminosity for approximately 300 min, although the asymptotic decline is less pronounced. This effect is especially visible for shorter measurement times. After the first 300 min, double detections (Figure 2) follow a linear trend around 20 CPM2 for the ROTI and AL+ and 15 cpm for UG scintillation cocktails (Table 1). Overall, UG reveals the lowest values for CPM2 and CPM3 while AL+ has lowest luminosity of all cocktails. However, UG is also heavily affected by outliers, especially during the first hour, for measurement times of 1 min that result in extremely elevated values for CPM2 and standard deviation (Table 1).

With the exception of the 1-min measurements, each of the cocktails shows relatively small variability in their average cpm values, but their standard deviation decreases drastically with increasing measurement time (Table 1). While for a measurement time of 1 min AL+ appears to perform slightly better than the other two cocktails, UG outperforms the other cocktails at longer measurement times, revealing both lowest CPM2 values and smallest standard deviation.

Triple detections (CPM3) behave similar to the CPM2 but detected values are significantly lower. The CPM3 values do not seem to be influenced by luminosity as the initial spike in luminosity that can be observed within the first few hours of measurements is not visible. Additionally, CPM3 values are extremely consistent from the first to the last measurement. In comparison, the first 100 min of measurements of CPM2 in the presence of high luminosity (e.g., for ROTI) are vastly different from the last 100 min of measurements (Figure 2). This effect, much like in the luminosity profiles, is more pronounced for shorter measurement times and the ROTI and UG scintillation cocktail. ROTI and AL+ show an average of around 12 CPM3 (Table 2) while the average of the UG cocktail is around 8 CPM3. Again, measurement time only has a minimal influence on the CPM3 with slightly elevated values for the 1-min measurements while standard deviation decreases with increased measurement time. The 1-min measurements of the UG cocktail show highly increased values during the first 2 h of measurements, which leads to a significantly higher standard deviation (Table 2). Between CPM2 and CPM3, CPM3 has a lower average cpm value and lower standard deviation (Tables 1, 2).

TABLE 2 Performance of selected scintillation cocktails at various measurement times.

[CPM3]	1 min	2 min	10 min	60 min
ROTISZINT	13.49 ± 3.56 (±3.67)	12.49 ± 2.63 (± 2.50)	12.62 ± 1.14 (±1.12)	12.52 ± 0.49 (±0.45)
AquaLight+	12.92 ± 3.76 (±3.59)	11.82 ± 2.42 (±2.43)	12.97 ± 1.17 (±1.14)	13.32 ± 0.55 (±0.47)
Ultima Gold XR	10.31 ± 36.25 (±3.21)	8.03 ± 1.97 (±2.00)	7.80 ± 0.91 (±0.88)	7.90 ± 0.42 (±0.36)

Performance is presented by CPM3 (events counted by all three PMTs) of the counter background values and respective standard deviation. Values in parentheses are calculated values based on the Poisson distrubution. Except for the 1-min measurement of Ultima Gold XR, the calculated and measured values are in good agreement.

TABLE 3 Counter background of selected scintillation cocktails at various measurement times.

[Bq]	1 min	2 min	10 min	60 min
ROTISZINT	0.48 ± 0.16 (0.96)	0.45 ± 0.12 (0.81)	0.44 ± 0.05 (0.59)	0.45 ± 0.04 (0.57)
AquaLight+	0.49 ± 0.16 (0.97)	0.45 ± 0.14 (0.87)	0.49 ± 0.04 (0.61)	0.50 ± 0.02 (0.56)
Ultima Gold XR	0.73 ± 2.80 (9.31)	0.39 ± 0.11 (0.72)	0.45 ± 0.06 (0.63)	0.45 ± 0.02 (0.51)

Performance is presented by the average Becquerel of the counter background values and respective standard deviation. The resulting minimum detection limit (MDL), calculated as counter (background plus three times standard deviation is given in parentheses).

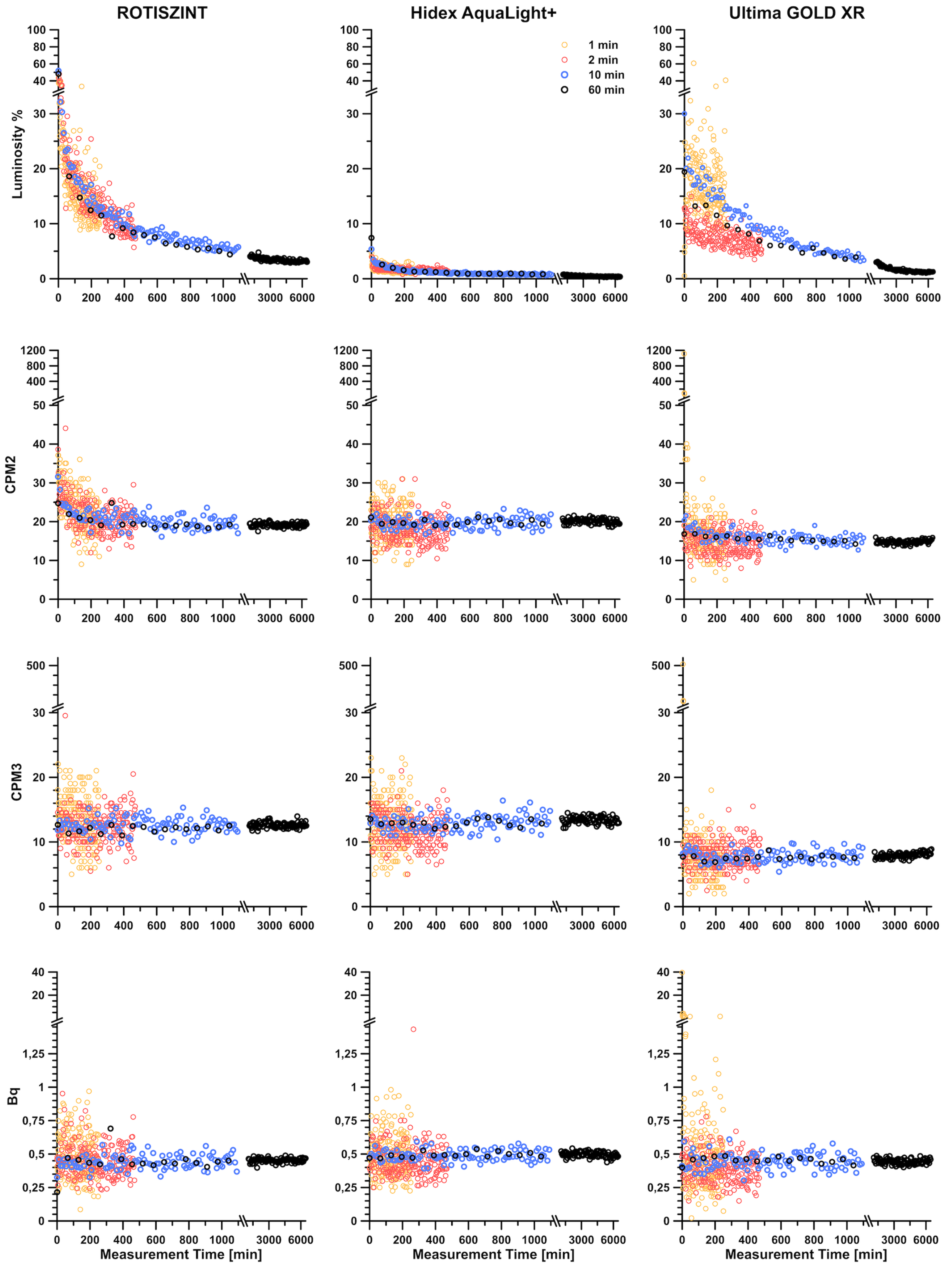

FIGURE 2
Contribution of luminosity on detected counts and related double detections (CMP2), triple detections (CPM3), and Becquerel values over a measurement period of up to 4 days, with varying measurement times and different scintillation cocktails. Counter background measurements were carried out with 1, 2, 10, and 60min of measurement time. A time series for each background measurement was established by repeating the analysis of the sample for 200 times (for experiment with a measurement time of 1 and 2min) and 100 times (for experiments with a measurement time of 10 and 60min). Three different scintillation cocktails (ROTISZINT, Carl Roth; AquaLight+, Hidex; and Ultima GOLD XR, and Perkin Elmer) were investigated with the above mentioned measurement times.

Becquerel values

The calculated Becquerel values incorporate features of the three parameters above. For all cocktails and measurement times, the Bq values average around 0.45 Bq (Table 3) with only one major excursion in the UG 1-min measurement time data set. This excursion is mainly influenced by the generally poor performance of the cocktail at 1-min measurement time, especially with regard to its luminosity. The standard deviation visibly decreases with measurement time and is reduced to 25–12.5% of its original values between the 1- and 60-min measurement experiments.

Impact of measurement temperature on background measurements

Our data show that at measurement temperatures of 10–20°C, all background measurements remain consistently below 1 Bq with only one minor excursions at 14°C with six out of eight vials having an activity >1 Bq for the UG scintillation cocktail (Figure 3). Around 25°C, the background measurements for both scintillation cocktails increase to mean values around 1.5 Bq. As soon as the measurement temperature reached 28°C, we observed a drastic jump to 5–7 Bq for both cocktails. Values remained at this level up to the highest measurement temperature of 36.5°C. Except for the minor excursion in the low temperature range, the response to measurement temperature was consistent for both scintillation cocktails analyzed. The cocktails performed reliably at 10–20°C and started to jump to highly elevated values around the 30°C mark.

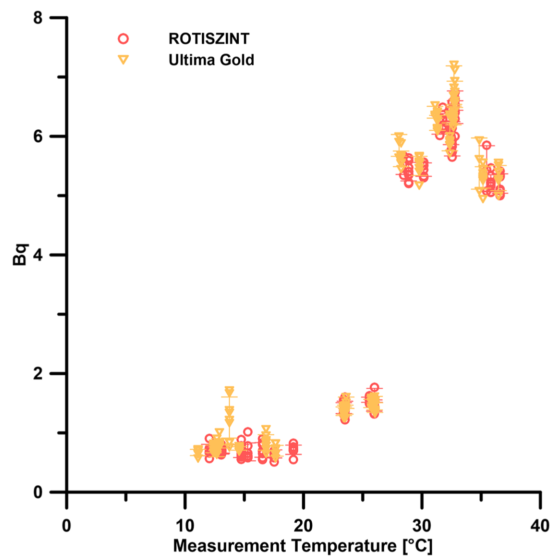

FIGURE 3
Effect of measurement temperature on the background measurements of different scintillation cocktails. Error bars indicate one standard deviation.

Effect of storage temperature on background measurements

The data of the temperature-dependent background measurements, irrespective of the incubation temperature, are generally similar to the 20°C reference background (Figure 4)—around ±20%. The UG scintillation cocktail performed consistent throughout the temperature range of 20–60°C with a maximum range of 80–140% of the 20°C reference measurements. While the ROTI cocktail mostly lies in the range of 70–130% of the reference values, elevated values of up to 190% of the 20°C reference can be observed at 35–36°C.

Discussion

Luminosity

L'Annunziata et al. (2020) mention that photoluminescence will generally disappear if the sample is stored in a dark environment for 15 min and chemiluminescence is expected to last for an approximate 4–6 h. Luminosity will affect samples disproportionately within the first few hours and generally drops below 10% after 8–10 h. However, only after 4 days a plateau is reached. The AL+ scintillation cocktail with its initial low luminosity appears to be a preferable choice for measurements where luminosity is of concern. Our experimental setup does not allow for the distinction between photo- and chemiluminescence, but the high initial peak likely reflects a superimposed signal of both prevalent luminescence components that quickly changes to an asymptotic decline once the influence of photoluminescence wears off. This effect is pronounced for shorter measurement times, especially the 1-min measurements, due to low numbers of photon detections per measurement. Interestingly, the 1-min measurements of the UG cocktail also show some strong negative outliers within these first few minutes.

The effect of luminosity can be mitigated by computational means that modern LSC are equipped with, but additional consistency can be achieved by simply storing sample vials in the dark for at least 1 day, preferably 3 or 4 days prior to the measurement, or by utilizing a scintillation cocktail that naturally shows low luminosity. For background measurements, a measurement time of at least 10 min should be targeted as it represents a good compromise between statistical significance and duration (Figure 2). If measurement time is of no concern, a longer measurement time of, e.g., 60 min will improve performance, although the improvement is not dramatic, as illustrated by the changes in background counts and standard deviation at different measurement times (Table 2).

In general, a consistent measurement protocol and precautions such as sufficient time between sample preparation and measurement allows for better comparability of the samples and avoids potential discrepancies between different measurements caused by changes in luminescence over time.

CPM in double and triple PMT setups

With the increasing availability and popularity of commercial LSCs with a triple PMT configuration, a distinction between cpm values of different types of liquid scintillation counting has to be made. On a double PMT setup, both PMTs (PMT A and PMT B) oppose each other and are arranged at a 180° angle inside the measurement

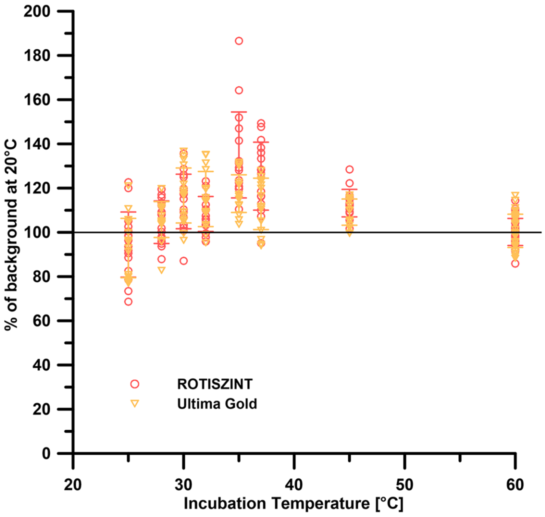

FIGURE 4
Effect of storage temperature on background measurements of different scintillation cocktails. Error bars indicate one standard deviation.

chamber. Photon detection on both PMTs (AB) will equate to one count of sample-associated radioactive decay. In comparison, the PMTs in a triple PMT setup (PMT A, PMT B, and PMT C) are orientated at 120° angles and sample-associated decay requires the detection on all three PMTS (ABC).

Due to the different geometries and number of PMTs, the detection limits with regard to cpm values may differ between machines, with a lower limit of detection achieved by the geometrically more complex triple PMT setups. Next to the advantage of having an extra PMT to improve photon detection, the TDCR method also allows for statistical modeling of expected double and triple coincidences and compares expected detections to the ratio of measured CPM2 and CPM3. In turn, the comparison of double detections will result in higher CPM2 values in the triple PMT setup as a double detection can result from multiple PMT combinations (i.e., AB, AC, and BC). TDCR in a triple PMT setup will include the detection on only two of its three PMTs and perform a quench correction that provides the opportunity to calculate the respective Bq value on the basis of the ratio of double detections (CPM2), triple detections (CPM3), and luminosity.

The formula for our luminosity corrected TDCR values is the following:

$$TDCR_{corr} = \frac{CPM2}{CPM3 - Lumi} \qquad (2)$$

Where Lumi represents all detected decays not associated with radioactive decay of the sample which are determined via probabilistic distribution of double and triple counts. On the basis of the luminosity-corrected TDCR, the luminosity-corrected Bq can be calculated using the formula:

$$Bq_{corr} = \left. \frac{CPM2}{TDCR^2} \middle/ 60 \right. \qquad (3)$$

The use of cpm, even between different PMT setups, has the advantage of more direct comparability, although cpm values are likely skewed toward lower numbers for the triple PMT setups. The utilization of the TDCR method and calculated luminosity-corrected Bq values are only possible with triple PMT LSC as the statistical foundation for calculating Bq values requires both CPM2 and CPM3.

Measurement time

Accuracy of the measurement increases with measurement time as the measurement time is correlated to the number of detected signals, i.e., a 10-fold increase of measurement time approximately results in a 10-fold increase in detected events (Røy et al., 2014). A visualization of this statement can be seen for our 1- and 2-min experiment (Tables 1–4) that consistently performed much worse in terms of consistency than the 10- and 60-min measurements. Radioactive decay are random, independent events that occur at a fixed mean rate, i.e., decays follow Poisson distribution. Thus, the rate of decay of the targeted radioisotope and ambient and cosmic radiation has an underlying variability. These statistical fluctuations within the background signal or radioactive decay result in minute variations for any specific time frame. Therefore, longer measurement times are preferred to reduce variations between measurements as they cover a larger number of expected decays. These fluctuations can be reduced significantly by targeting a measurement time of at least 10 min. Throughout all measured scintillation cocktails, we found a decrease in standard deviation between the 1- and 10-min background measurements to less than 30% of their initial cpm and Bq values. For our experiments and throughout all tested scintillation cocktails, experiments of 60-min measurement time yielded the best results but come with the burden of prolonged time investment especially for large numbers of samples. A measurement time of 10 min provides a good compromise between low and consistent measurements and short measurement time.

Further, we can compare the observed (standard deviation of Table 2) to the expected standard deviation (Table 2) of the counter background to evaluate if variability within the background fully matches the Poisson process. The standard variation of the Poisson process is calculated with $\sqrt{\lambda} * t^{-1}$ where λ is the total amount of counts over the respective measurement interval and t is the measurement time. The comparison shows that both observed and expected value are extremely close ($\Delta \approx <0.1$). Thus, the counter background is Poisson distributed and the standard deviation is inherited by the Poisson process. The only exception and significant deviation of the observed and expected standard deviation is the aforementioned 1 min measurement of the UG scintillation cocktail that shows an observed variance of 10 times the expected value. However, it is unclear what exactly attributes to the stark difference between the observed and expected value.

A compromise between statistical significance and duration of a measurement has to be made, as data sets can be comprised of several hundreds of individual measurements. Short measurement times will significantly increase the impact of background noise (Figure 2) while long measurement times will be statistically sounder but more time consuming. Røy et al. (2014) mention that the number of counts will reach a point of diminishing returns, a reduction in statistical significance per time spent. Generally, a counting time of 10 min is accepted as a good compromise between statistical significance and time and is used by many studies (Kallmeyer et al., 2004; Beulig et al., 2022; Nagakura et al., 2022). However, many publications do not provide any information about their measurement time (Boetius et al., 2000; Böning et al., 2004; Kallmeyer and Boetius, 2004; Treude et al., 2005; Røy et al., 2014). In samples with medium to high activity, the number of detected decay events is several orders of magnitude higher than in low turnover samples and therefore well above the minimum detection limit set by the blank measurements. Measurement protocols that exceed the 10-min counting time can be applied to increase the number of counts and therefore decrease variance of the background noise (Røy et al., 2014). Other studies that operate at the limit of detection utilize longer measurement times (30 min; Glombitza et al., 2016). Our results show that an extended measurement time will have an improved detection limit by 1–2 cpm or 0.05 Bq if measurement time is increased from 10 to 60 min (Table 4).

Kallmeyer et al. (2004) investigated the effect of measurement time on the minimum detection limit and proposed that 10 min is a sufficient amount of time and further increase will not lower the detection limit any further. Furthermore, Røy et al. (2014) presented a statistical analysis focusing on the number of detected decay events and concluded that a higher number of detected events leads to statistically better results. However, the improvement of the results is affected by diminishing returns and eventually leads to impractical long measurement times. Our results (Tables 2, 3) support the concept of diminishing returns on measurement time, although still show a benefit of measurement times >10 min for determination of the minimum detection limit. Nevertheless, a significantly further extension of measurement time beyond 60-min will not lead to a markedly improved minimum detection limit due to diminishing returns. Additionally, hour-long measurement times can only be applied to small sample sets due to the time constraints. The effect of the diminishing returns is illustrated in Table 2. Comparing the standard deviation of the 2-, 10-, and 60-min measurements, i.e., increasing measurement time 5 or 30 times, leads to a reduction of standard deviation by ~50 or 75%, respectively. The standard deviation for CPM3 drops from 2 to 2.6 cpm of the 2-min measurements to approximately 0.5 cpm for the 60-min measurement. The diminishing returns are even more obvious for Bq measurements (Table 3) as the 60-min measurement already reaches a standard deviation of almost zero (~0.02 Bq). Extensive measurement times would result in a large enough number of expected decays to no longer have any variation between measurements but also would be impractically long.

Figure 2 illustrates the effect of insufficient counting times. The figure shows consecutive background measurements, but while counting times of 2 min or higher show an exponential decline of luminosity over time, a counting time of 1 min does not show this trend. Moreover, the 1-min data show significant scatter of more than three times the standard deviation of the 10-min measurement. This scatter can also be seen in the corresponding calculated activity values (Figure 2; Bq).

The effects of different measurement times on the minimum detection limit can be shown by using, e.g., the CPM3 values for AL+ (Table 2). The minimum detection limit (Kaiser, 1970) is defined as:

$$MDL = b + 3 \times \sigma_b \tag{4}$$

Where b is the average value of all counter background measurements and σ_b is the standard deviation of the blank signal. A factor of 3 is chosen to reflect the approximate 95% confidence interval of the counter background. This calculation of the MDL is used as an approximation due to its simplicity. A statistically correct treatment based on the true distribution of counter background that is used in Røy et al. (2014) to present detection near the absolute limit of detection on the example of sulfate reduction is available in Brüchle (2003).

The MDL (4) for the UG cocktail will be 13.94 cpm (2 min), 10.53 cpm (10 min), and 9.16 cpm (60 min), thus result in a difference of >4 cpm or > 33% between 2- and 60-min measurement times. The effect of counting times on microbial turnover rate experiments is more directly visible and easier to understand when using Becquerel values (Table 3). For the UG cocktail, the MDLs (4) for the 2, 10, and 60 min measurements are 0.72, 0.63, and 0.51 Bq, respectively. An increase in measurement time for the UG scintillation cocktail from 2 to 10 or from 10 to 60 min results in a reduction of the detection limit by approximately one 10th of a Bq. Recent studies that target the biotic-abiotic fringe use tracer activities of up to 5 MBq per sample for quantification of sulfate reduction rates in the sub-picomolar range (Glombitza et al., 2016; Beulig et al., 2022; Nagakura et al., 2022). With these low microbial turnover activities a reduction of a single cpm or fraction of a Becquerel can be decisive on whether a measurement is above or below MDL and therefore potentially change the conclusions derived from such a dataset. In the following, we show how small changes in the counter background affect the MDL, using a typical sample for quantification of sulfate reduction rate measurements as an example. Sulfate reduction rates are calculated according to the following formula:

$$SRR = \left[SO_4\right] \times P_{SED} \times \frac{a_{TRIS}}{a_{TOT}} \times t^{-1} \times 1.06 \times 10^6 \tag{5}$$

Where SRR is the sulfate reduction rate in pmol cm^{-3} day^{-1}; [SO$_4$] is the sulfate concentration in the porewater of the sediment in mmol L^{-1}; P$_{SED}$ is the porosity of the sediment in mL porewater cm^{-3} sediment; a$_{TRIS}$ is the radioactivity of the total reduced inorganic sulfur, a$_{TOT}$ the total radioactivity used; t the incubation time in days; 1.06 the correction factor of the isotopic fractionation (Jørgensen and Fenchel, 1974); and 10^6 the factor for the change of units from mmol L^{-1} to pmol cm^{-3}.

Assuming [SO$_4$] of 10 mM, P$_{SED}$ of 0.6, a total radioactivity used of 5 MBq, incubation time of 10 days and a SRR of 0.1 pmol cm^{-3} day^{-1}, the amount of radioactivity in the TRIS fraction (a$_{TRIS}$) is 0.79 Bq. This correlates to a turnover of less than 1 millionth of the total radioactivity used. For a 10-min measurement time of the tested cocktails, this measurement is still detectable as the MDL (Eq. 4) lies between 0.59–0.63 Bq for the different cocktails (4). These values correspond to minimum detection limits of 0.075–0.08 pmol cm^{-3} day^{-1}. A 60-min measurement time would reduce the MDL (4) of SRR to 0.065–0.071 pmol cm^{-3} d^{-1}. These hypothetical values compare well to low turnover rate measurements with similar parameters in the literature that can be found in the range of approximately 0.1–10 pmol cm^{-3} d^{-1} (Beulig et al., 2022; Nagakura et al., 2022).

For methods that rely on measurements via gas solubility such as anaerobic oxidation of methane, these reductions of the minimum detection limit are especially important as the amount of radiotracer cannot be increased as freely as for other processes such as sulfate

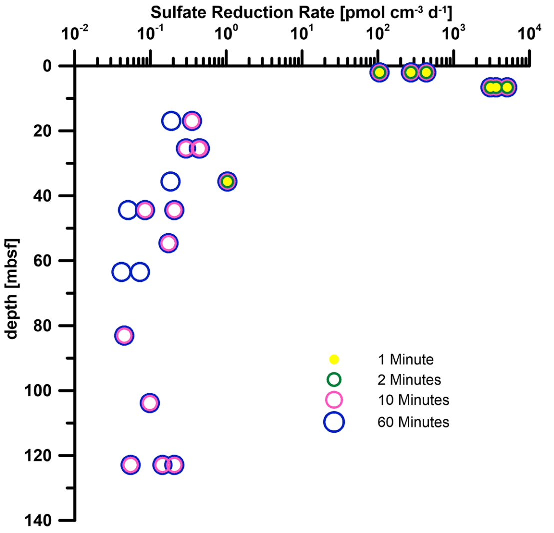

FIGURE 5
Sulfate reduction rates of IODP Exp. 385 Site U1545 (Nagakura et al., 2022), calculated by using standard deviations from different measurement times (Table 3). Measurements were carried out with AquaLight+ scintillation cocktail.

TABLE 4 Minimum detection limit of selected scintillation cocktails at various measurement times.

MDL [CPM3]	1 min	2 min	10 min	60 min
ROTISZINT	24.17	20.38	16.04	13,99
AquaLight+	24.20	19.08	16.48	14.97
Ultima Gold XR	119.06	13.94	10.53	9.16

The miminum detection limit is presented based on CPM3 of the counter background values (Table 2).

reduction or methanogenesis due to the constrains of dissolution of the tracer in the media (Beulig et al., 2022). We highly encourage the inclusion of the measurement time in the method description in all studies to allow for better comparability and reproducibility of data. Reduced standard deviation (Table 3, AquaLight+) can have significant impact on data (Figure 5) from the deep biosphere (Nagakura et al., 2022) as the margin of detection is slim for turnover rates near the limit of detection. The high variance in our 1- and 2-min measurements only covers SRR values above 0.1 pmol cm^{-3} day^{-1}. Almost two more magnitudes of data (just slightly above 1 fmol cm^{-3} day^{-1}) are detectable by switching from 1 and 2 min measurement time to 10 or 60 min with their reduced variance. As a result, turnover rates over the entire depth range can be observed instead of only the samples from the shallowest depth.

Temperature

Temperature can have a strong influence on liquid scintillation counting as the scintillation process can be accelerated with increasing temperatures (Birks, 1964) and counting efficiency can decrease (Homma and Murase, 1987). Generally, conditions around 20°C are advised by the manufacturers of the scintillation cocktails. As for many other parameters, it is advisable to keep the LSC in a temperature-controlled environment with as little fluctuation as possible.

Our experiment shows that between 10 and 20°C, temperature does not influence the background measurements (Figure 3). At temperatures around the upper limit of the recommended operating temperatures, i.e., above *ca.* 25°C slightly elevated background measurements can be observed. While this increase will not be noticeable during most measurements, as the number of detected events it is still negligible compared to the events caused by decays of the radioisotope in the sample, it might already be critical for measurements close to the lower limit of detection. At temperatures of 28°C and higher, the counter background increases significantly to values that are almost an order of magnitude above the counter background at 20°C, hence on a level that precludes low turnover measurements due to the drastically increased detection limit.

We also investigated potential chemical alterations of the scintillation cocktail due to increased storage temperatures. While the measurement temperature had a significant effect on the background (Figure 3), the storage temperature only has a minimal to no effect (Figure 4). While samples of all storage temperatures are roughly spread around the 20°C control, measurements around 36°C storage temperature visibly deviate to up to 190% of the 20°C reference samples. This increase can be attributed solely to the measurements of the ROTI scintillation cocktail. The effect of storage temperature on the counter background still is minimal to negligible compared to the measurement temperature.

We repeated both the storage and measurement temperature experiments with a UG scintillation cocktail that was exposed to extended periods of intense heating due to sunlight. Compared to the same cocktail stored according to the manufacturer's guidelines no significant difference was observed (data not shown).

Conclusion

It is vital to understand the mechanisms and parameters surrounding liquid scintillation measurements, especially when working close to the minimum detection limit. Samples with low microbial activity are especially susceptible to minor variations within the counter background as these fluctuations are disproportionally affecting the detection limit. To avoid a negative impact of luminosity on measurements, samples should be stored prior to measurement at least 1 day and up to 4 days, depending on the scintillation cocktail. Both samples and the liquid scintillation analyzer should be kept at temperatures at around 20°C to avoid elevated counter background. While scintillation cocktails perform equally well under standard conditions (room temperature, appropriate measurement time), cocktails should be selected to meet the needs of specific experiments and parameters. At last, we showed that for low activity measurements such as the counter background or samples with low turnover, a measurement time of 10–60 min should be chosen. Information about counting times should be included in the respective method section of each manuscript to provide a more concise picture of the analytical conditions.

Data availability statement

The raw data supporting the conclusions of this article will be made available by the authors, without undue reservation.

Author contributions

FS and JK designed the study. FS conducted all experiments, and wrote the manuscript with input from JK. All authors contributed to the article and approved the submitted version.

Funding

FS was funded through DFG grant (#651694) to JK.

Acknowledgments

The authors would like to thank Simone Bernsee and Axel Kitte for analytical assistance.

Conflict of interest

The authors declare that the research was conducted in the absence of any commercial or financial relationships that could be construed as a potential conflict of interest.

Publisher's note

References

Ashley, J. (1982). Stopping power of liquid water for low-energy electrons. *Radiat. Res.* 89, 25–31. doi: 10.2307/3575681

Baker, B. J., Moser, D. P., MacGregor, B. J., Fishbain, S., Wagner, M., Fry, N. K., et al. (2003). Related assemblages of sulphate-reducing bacteria associated with ultradeep gold mines of South Africa and deep basalt aquifers of Washington state. *Environ. Microbiol.* 5, 267–277. doi: 10.1046/j.1462-2920.2003.00408.x

Bar-On, Y. M., Phillips, R., and Milo, R. (2018). The biomass distribution on earth. *Proc. Natl. Acad. Sci.* 115, 6506–6511. doi: 10.1073/pnas.1711842115

Beulig, F., Røy, H., Glombitza, C., and Jørgensen, B. (2018). Control on rate and pathway of anaerobic organic carbon degradation in the seabed. *Proc. Natl. Acad. Sci.* 115, 367–372. doi: 10.1073/pnas.1715789115

Beulig, F., Schubert, F., Adhikari, R. R., Glombitza, C., Heuer, V. B., Hinrichs, K.-U., et al. (2022). Rapid metabolism fosters microbial survival in the deep, hot subseafloor biosphere. *Nat. Commun.* 13, 1–9. doi: 10.1038/s41467-021-27802-7

Birks, J. (1964). *The Theory and Practice of Scintillation Counting*. Oxford, England: Pergamon Press

Boetius, A., Ravenschlag, K., Schubert, C. J., Rickert, D., Widdel, F., Gieseke, A., et al. (2000). A marine microbial consortium apparently mediating anaerobic oxidation of methane. *Nature* 407, 623–626. doi: 10.1038/35036572

Böning, P., Brumsack, H.-J., Böttcher, M. E., Schnetger, B., Kriete, C., Kallmeyer, J., et al. (2004). Geochemistry of Peruvian near-surface sediments. *Geochim. Cosmochim. Acta* 68, 4429–4451. doi: 10.1016/j.gca.2004.04.027

Broda, R. (2003). A review of the triple-to-double coincidence ratio (TDCR) method for standardizing radionuclides. *Appl. Radiat. Isot.* 58, 585–594. doi: 10.1016/S0969-8043(03)00056-3

Broda, R., Cassette, P., and Kossert, K. (2007). Radionuclide metrology using liquid scintillation counting. *Metrologia* 44, S36–S52. doi: 10.1088/0026-1394/44/4/S06

Broser, I., and Kallmann, H. (1947). Über den Elementarprozeß der Lichtanregung in Leuchtstoffen durch α-Teilchen, schnelle Elektronen und γ-Quanten II. *Zeitschrift für Naturforschung A* 2, 642–650. doi: 10.1515/zna-1947-11-1206

Brüchle, W. (2003). Confidence intervals for experiments with background and small numbers of events. *Radiochim. Acta* 91, 71–80. doi: 10.1524/ract.91.2.71.19989

Cassette, P., Broda, R., Hainos, D., and Terlikowska, T. (2000). Analysis of detection-efficiency variation techniques for the implementation of the TDCR method in liquid scintillation counting. *Appl. Radiat. Isot.* 52, 643–648. doi: 10.1016/S0969-8043(99)00224-9

Čerenkov, P. A. (1937). Visible radiation produced by electrons moving in a medium with velocities exceeding that of light. *Phys. Rev.* 52, 378–379. doi: 10.1103/PhysRev.52.378

Cowan, D. A. (2004). The upper temperature for life–where do we draw the line? *Trends Microbiol.* 12, 58–60. doi: 10.1016/j.tim.2003.12.002

Csala, M., Senesi, S., Bánhegyi, G., Mandl, J., and Benedetti, A. (2005). Characterization of sulfate transport in the hepatic endoplasmic reticulum. *Arch. Biochem. Biophys.* 440, 173–180. doi: 10.1016/j.abb.2005.06.017

Fossing, H. (1995). *35S-Radiolabeling to Probe Biogeochemical Cycling of Sulfur*. Washington, DC: ACS Publications.

Glombitza, C., Adhikari, R. R., Riedinger, N., Gilhooly, W. P. III, Hinrichs, K.-U., and Inagaki, F. (2016). Microbial sulfate reduction potential in coal-bearing sediments down to~ 2.5 km below the seafloor off Shimokita peninsula, Japan. *Front. Microbiol.* 7:1576. doi: 10.3389/fmicb.2016.01576

Herforth, L., (1948). *Die Fluoreszenzanregung Organischer Substanzen Mit Alphateilchen, Schnellen Elektronen und Gammastrahlen*. Berlin: Technische Universität

Heuer, V. B., Inagaki, F., Morono, Y., Kubo, Y., Spivack, A. J., Viehweger, B., et al. (2020). Temperature limits to deep subseafloor life in the Nankai trough subduction zone. *Science* 370, 1230–1234. doi: 10.1126/science.abd7934

Hinrichs, K.-U., and Inagaki, F. (2012). Downsizing the deep biosphere. *Science* 338, 204–205. doi: 10.1126/science.1229296

Homma, Y., and Murase, Y. (1987). Energy resolution of liquid scintillator for α-particles and internal conversion electrons at lower temperatures. *J. Radioanal. Nucl. Chem.* 119, 355–365. doi: 10.1007/BF02162046

Horrocks, D. L. (1974). *Applications of Liquid Scintillation*. Academic Press, New York and London: Citeseer.

Horrocks, D. L. (1985). Studies of background sources in liquid scintillation counting. *Int. J. Appl. Radiat. Isot.* 36, 609–617. doi: 10.1016/0020-708X(85)90001-8

Horrocks, D. (2012). *Applications of Liquid Scintillation Counting*. Cambridge, Massachusetts, USA: Elsevier.

Inagaki, F., Hinrichs, K.-U., Kubo, Y., Bowles, M. W., Heuer, V. B., Hong, W.-L., et al. (2015). Exploring deep microbial life in coal-bearing sediment down to ~2.5 km below the ocean floor. *Science* 349, 420–424. doi: 10.1126/science.aaa6882

Ivanov, M. V. (1956). Isotopes in the determination of the sulfate-reduction rate in Lake Belovod. *Microbiologiya* 25, 305–309.

Iversen, N., and Blackburn, T. H. (1981). Seasonal rates of methane oxidation in anoxic marine sediments. *Appl. Environ. Microbiol.* 41, 1295–1300. doi: 10.1128/aem.41.6.1295-1300.1981

Jørgensen, B. B. (1982). Mineralization of organic matter in the sea bed—the role of sulphate reduction. *Nature* 296, 643–645. doi: 10.1038/296643a0

Jørgensen, B. B. (2021). Sulfur biogeochemical cycle of marine sediments. *Geochem. Perspect.* 10, 145–307. doi: 10.7185/geochempersp.10.2

Jørgensen, B. B., and Boetius, A. (2007). Feast and famine—microbial life in the deep-sea bed. *Nat. Rev. Microbiol.* 5, 770–781. doi: 10.1038/nrmicro1745

Jørgensen, B., and Fenchel, T. (1974). The sulfur cycle of a marine sediment model system. *Mar. Biol.* 24, 189–201. doi: 10.1007/BF00391893

Jørgensen, B. B., Findlay, A. J., and Pellerin, A. (2019). The biogeochemical sulfur cycle of marine sediments. *Front. Microbiol.* 10:849. doi: 10.3389/fmicb.2019.00849

Kaihola, L., Ross, H., Noakes, J., and Spaulding, J., (1991). *Liquid Scintillation Counting Performance Using Glass Vials in the Wallac 1220 Quantulus. Liquid Scintillation Counting and Organic Scintillators*. Chelsea: Lewis Publishers. 495–500

Kaiser, H. (1970). Report for analytical chemists. II. Quantitation in elemental analysis. *Lab. Guide Instrum. Equip. Chem.* 42, 26A–59A. doi: 10.1021/ac60286a027

Kallmann, H. (1950). Scintillation counting with solutions. *Phys. Rev. D. Partic. Fields* 78, 621–622. doi: 10.1103/PhysRev.78.621.2

Kallmeyer, J., and Boetius, A. (2004). Effects of temperature and pressure on sulfate reduction and anaerobic oxidation of methane in hydrothermal sediments of Guaymas Basin. *Appl. Environ. Microbiol.* 70, 1231–1233. doi: 10.1128/AEM.70.2.1231-1233.2004

Kallmeyer, J., Ferdelman, T. G., Weber, A., Fossing, H., and Jørgensen, B. B. (2004). A cold chromium distillation procedure for radiolabeled sulfide applied to sulfate reduction measurements. *Limnol. Oceanogr. Methods* 2, 171–180. doi: 10.4319/lom.2004.2.171

Kallmeyer, J., Pockalny, R., Adhikari, R. R., Smith, D. C., and D'Hondt, S. (2012). Global distribution of microbial abundance and biomass in subseafloor sediment. *Proc. Natl. Acad. Sci.* 109, 16213–16216. doi: 10.1073/pnas.1203849109

Kobayashi, Y. (2012). *Biological Applications of Liquid Scintillation Counting*. Cambridge, Massachusetts, USA: Elsevier.

Kojola, H., Polach, H., Nurmi, J., Oikari, T., and Soini, E. (1984). High resolution low-level liquid scintillation β-spectrometer. *Int. J. Appl. Radiat. Isot.* 35, 949–952. doi: 10.1016/0020-708X(84)90208-4

Kossert, K. (2010). Activity standardization by means of a new TDCR-Čerenkov counting technique. *Appl. Radiat. Isot.* 68, 1116–1120. doi: 10.1016/j.apradiso.2009.12.038

Krebs, A. T. (1955). Early history of the scintillation counter. *Science* 122, 17–18. doi: 10.1126/science.122.3157.17

L'Annunziata, M. F. (2020). *Handbook of Radioactivity Analysis*, 2 Cambridge, Massachusetts, USA: Radioanalytical Applications. Academic Press.

L'Annunziata, M. F., Tarancón, A., Bagán, H., and García, J. F. (2020). *Liquid Scintillation Analysis: Principles and Practice, Handbook of Radioactivity Analysis* Cambridge, Massachusetts, USA: Elsevier, 575–801.

Magnabosco, C., Lin, L.-H., Dong, H., Bomberg, M., Ghiorse, W., Stan-Lotter, H., et al. (2018). The biomass and biodiversity of the continental subsurface. *Nat. Geosci.* 11, 707–717. doi: 10.1038/s41561-018-0221-6

Meyer, S., Schweidler, E., Meyer, S., and Schweidler, E. (1927). *Die Radioaktiven Substanzen*. Wiesbaden, Germany: Springer.

Morono, Y., and Inagaki, F. (2016). Analysis of low-biomass microbial communities in the deep biosphere. *Adv. Appl. Microbiol.* 95, 149–178. doi: 10.1016/bs.aambs.2016.04.001

Morono, Y., Terada, T., Kallmeyer, J., and Inagaki, F. (2013). An improved cell separation technique for marine subsurface sediments: applications for high-throughput analysis using flow cytometry and cell sorting. *Environ. Microbiol.* 15, 2841–2849. doi: 10.1111/1462-2920.12153

Nagakura, T., Schubert, F., Wagner, D., Kallmeyer, J., and Party, S. S. (2022). Biological sulfate reduction in deep subseafloor sediment of Guaymas Basin. *Front. Microbiol.* 462 doi: 10.3389/fmicb.2022.845250

Parkes, R. J., Cragg, B. A., Bale, S., Getlifff, J., Goodman, K., Rochelle, P. A., et al. (1994). Deep bacterial biosphere in Pacific Ocean sediments. *Nature* 371, 410–413. doi: 10.1038/371410a0

Reynolds, G. T., Harrison, F. B., and Salvini, G. (1950). Liquid scintillation counters. *Phys. Rev. D. Partic. Fields* 78:488. doi: 10.1103/PhysRev.78.488

Røy, H., Weber, H. S., Tarpgaard, I. H., Ferdelman, T. G., and Jørgensen, B. B. (2014). Determination of dissimilatory sulfate reduction rates in marine sediment via radioactive 35S tracer. *Limnol. Oceanogr. Methods* 12, 196–211. doi: 10.4319/lom.2014.12.196

Shock, E. (2000). Characterizing the biotic fringe in hydrothermal ecosystems. Goldschmidt Conference, Oxford, UK *J. Conf. Abstr.*:923.

Simpson, B., and Meyer, B. (1994). Direct activity measurement of pure beta-emitting radionuclides by the TDCR efficiency calculation technique. *Nucl. Instrum. Methods Phys. Res. Sect. A* 339, 14–20. doi: 10.1016/0168-9002(94)91771-X

Smith, R. L., and Klug, M. J. (1981). Electron donors utilized by sulfate-reducing bacteria in eutrophic lake sediments. *Appl. Environ. Microbiol.* 42, 116–121. doi: 10.1128/aem.42.1.116-121.1981

Sorokin, Y. I. (1962). Experimental investigation of bacterial sulfate reduction in the Black Sea using S 35. *Microbiology* 31, 329–335.

Temple, S. (2015). Liquid scintillation counting: how has it advanced over the years and what does the future hold? *Bioanalysis* 7, 503–505. doi: 10.4155/bio.15.10

Treude, T., Niggemann, J., Kallmeyer, J., Wintersteller, P., Schubert, C. J., Boetius, A., et al. (2005). Anaerobic oxidation of methane and sulfate reduction along the Chilean continental margin. *Geochim. Cosmochim. Acta* 69, 2767–2779. doi: 10.1016/j.gca.2005.01.002

frontiers | Frontiers in Microbiology

TYPE Original Research
PUBLISHED 24 July 2023
DOI 10.3389/fmicb.2023.1198664

EDITED BY
Jesse G. Dillon,
California State University,
United States

REVIEWED BY
Jennifer F. Biddle,
University of Delaware, United States
William D. Orsi,
Ludwig Maximilian University of Munich,
Germany

*CORRESPONDENCE
Hans Røy
✉ hans.roy@bio.au.dk

RECEIVED 01 April 2023
ACCEPTED 05 July 2023
PUBLISHED 24 July 2023

CITATION
Jaussi M, Jørgensen BB, Kjeldsen KU, Lomstein BA, Pearce C, Seidenkantz M-S and Røy H (2023) Cell-specific rates of sulfate reduction and fermentation in the sub-seafloor biosphere.
Front. Microbiol. 14:1198664.
doi: 10.3389/fmicb.2023.1198664

Cell-specific rates of sulfate reduction and fermentation in the sub-seafloor biosphere

Marion Jaussi[1], Bo Barker Jørgensen[1], Kasper U. Kjeldsen[1], Bente A. Lomstein[1], Christof Pearce[2], Marit-Solveig Seidenkantz[2] and Hans Røy[1]*

[1]Department of Biology, Aarhus University, Aarhus, Denmark, [2]Department of Geoscience, Aarhus University, Aarhus, Denmark

Microorganisms in subsurface sediments live from recalcitrant organic matter deposited thousands or millions of years ago. Their catabolic activities are low, but the deep biosphere is of global importance due to its volume. The stability of deeply buried sediments provides a natural laboratory where prokaryotic communities that live in steady state with their environments can be studied over long time scales. We tested if a balance is established between the flow of energy, the microbial community size, and the basal power requirement needed to maintain cells in sediments buried meters below the sea floor. We measured rates of carbon oxidation by sulfate reduction and counted the microbial cells throughout ten carefully selected sediment cores with ages from years to millions of years. The rates of carbon oxidation were converted to power (Js^{-1} i.e., Watt) using the Gibbs free energy of the anaerobic oxidation of complex organic carbon. We separated energy dissipation by fermentation from sulfate reduction. Similarly, we separated the community into sulfate reducers and non-sulfate reducers based on the *dsrB* gene, so that sulfate reduction could be related to sulfate reducers. We found that the per-cell sulfate reduction rate was stable near 10^{-2} fmol C cell^{-1} day^{-1} right below the zone of bioturbation and did not decrease with increasing depth and sediment age. The corresponding power dissipation rate was 10^{-17} W sulfate-reducing cell^{-1}. The cell-specific power dissipation of sulfate reducers in old sediments was similar to the slowest growing anaerobic cultures. The energy from mineralization of organic matter that was not dissipated by sulfate reduction was distributed evenly to all cells that did not possess the *dsrB* gene, i.e., cells operationally defined as fermenting. In contrast to sulfate reducers, the fermenting cells had decreasing catabolism as the sediment aged. A vast difference in power requirement between fermenters and sulfate reducers caused the microbial community in old sediments to consist of a minute fraction of sulfate reducers and a vast majority of fermenters.

KEYWORDS

cell-specific carbon oxidation rates, basal power requirement, sulfate reducing microorganisms, fermentative microorganisms, deep biosphere

1. Introduction

As continued deposition gradually buries marine sediments, they become increasingly isolated from the surface world. Dissolved electron acceptors can be supplied to the isolated microbial community from above, but the pool of organic carbon that fuels microbial life is mostly constrained to the stationary solid phase (e.g., Komada et al., 2013). Thus, a microbial community must live from the finite amount of organic carbon buried with it in the sediment. The anaerobic food chain is inefficient, and repeated cycles of cell death and reassimilation of necromass would lead to rapid loss of carbon (Orsi et al., 2020). Nevertheless, we find microorganisms in ancient sediments that are still thriving and are slowly degrading the old and refractory organic matter (Røy et al., 2012). This implies that the rates of mineralization are exceedingly low. Indeed, the reactivity of organic matter decreases steeply in aging sediment (Middelburg, 1989; Boudreau and Ruddick, 1991; Shang, 2023).

As the rates of carbon mineralization decrease with increasing age, so does the size of the microbial community (Røy et al., 2012). Although the assembly of the deep biosphere community conserves a part of the surface community (Starnawski et al., 2017), the decreasing community size with increasing age and depth in the sediment is not merely due to a slow death of the surface community. This can be seen by the continuous production of dead microbial cells (necromass) far in excess of the size of the original community (Lomstein et al., 2012), and by the fact that the estimated biomass turnover times of the sedimentary microbes is much shorter than the age of the sediment they live in Biddle et al. (2006), Hoehler and Jørgensen (2013), Braun et al. (2017). Thus, the microbial community in the deep sediment column must largely be in steady state with respect to their basal power requirement and the local availability of energy at any time. As the rate of liberation of labile carbon substrates from the refractory organic matter decreases with time, the size of the microbial community is decreasing accordingly. If the energy supply were in excess, the community would grow and thereby reduce the energy flux available per cell to approach the basal power requirement. If the energy supply falls below the basal power requirement, some cells will die, and this increases the per-cell energy availability (LaRowe and Amend, 2015b). Thus, we expect that the ever-decreasing energy turnover in aging marine sediments will force cells in the deep biosphere to constantly exist at the lowest power dissipation that will sustain their community (Hoehler and Jørgensen, 2013; Lever et al., 2015).

The lower limit, i.e., the basal power requirement, of prokaryotic cells is, most likely, set by physical and chemical decay processes in the cells such as the rate of leakage of membrane potential, the rate of depurination of nucleic acids, and the rate of racemization of amino acids. None of these processes are, however, constrained well enough to confidently calculate the basal power requirement of the individual cells (Lever et al., 2015). Yet, the intrinsic rate of racemization of aspartic acid, which is the amino acid with the highest rate of racemization, indicate that this process leads to the largest unavoidable loss of energy (Brinton et al., 2002; Onstott et al., 2014). Indeed, a gene encoding the enzyme (Protein-L-iso aspartate(D-aspartate) O-methyltransferase), which recognizes damaged L-isoapartyl and D-aspartyl residues in proteins and catalyzes their repair while still within the protein, was found widely distributed and expressed in deeply buried sediments in the Baltic Sea (Mhatre et al., 2019).

The lowest basal power requirement for prokaryotes in the deep biosphere is difficult to determine in the laboratory yet experiments with axenic bacterial cultures maintained without addition of substrates for prolonged time under so-called long-term stationary phase have shown general mechanisms of adaptation in cell respiration to extreme nutrient limitation (e.g., Riedel et al., 2013; Robador et al., 2019). To avoid artifacts related to laboratory cultivation, we have searched for the basal power requirement of cells in the natural environment by relating the catabolic rate of a community to the community size (Hoehler and Jørgensen, 2013) directly in sediments of varying age, ranging from tens to millions of years old. To limit the number of variables in the data, we focused on the sulfatic zone (Canfield and Thamdrup, 2009; Jørgensen, 2021), where anaerobic respiration is dominated by sulfate reduction. The goal of our study was to identify if, and how, the availability of energy controlled the microbial community size and the per-cell metabolic rate in the energy-starved deep biosphere. In addition, we compared the community size of the two main metabolic guilds, fermenters and sulfate reducers, living syntrophically in sulfate-rich sediments, with the power available to each of the guilds.

2. Materials and methods

2.1. Sampling sites

Gravity-cores from eight different geographic locations were retrieved for this study during 2012–2014. When possible, the gravity-cores were supplemented with either box-cores or Rumohr cores from the same site. Two additional datasets were retrieved from the databases of the Ocean Drilling Program (ODP) Leg 201 and Integrated Ocean Drilling Program (IODP) Leg 323. The goal of the site selection was to access samples from an extensive range of well-constrained sediment ages within the sulfatic sediment zone. In addition, the sedimentary and geochemical settings were selected such that the rate of dissimilatory sulfate reduction could be determined with good accuracy. The sampling sites can be found in Table 1, in Supplementary Figure S1, and at https://drive.google.com/open?id=1rYE3drQ6eSkWIjRFQtpxwL265bM&usp=sharing.

2.2. Subsampling of sediment cores

Gravity-cores were retrieved specifically for the study and the greatest care was taken to avoid oxygen exposure and heating. Thus, the cores were sectioned into 1-meter sections immediately after core recovery and the full core sections were capped and placed horizontally near *in situ* temperature. Rumohr cores were capped with overlying water and stored vertically until processing. All cores were taken at high latitudes, which helped to avoid elevated temperatures in the upper water column and on deck.

Extraction of pore water and solid-phase sampling were completed within 4–48 h after sediment recovery. Pore-water was extracted with Rhizon soil-moisture samplers (Rhizosphere Research Products, Wageningen, Netherlands) through 4 mm holes drilled through the plastic core-liners every 10–25 cm within the top 1 m of the gravity-cores and Rumohr Lot cores. Below 1 m, the sample resolution in the gravity-cores was 20 to 25 cm. The first milliliter of extracted pore water was discarded, and the rest of the pore water was collected in evacuated Exetainers (Labco) before distribution for further analyses. Solid phase samples were collected with sterile plastic syringes with cut-off tip through windows cut into the core liner with a vibrating saw (Røy et al., 2014), after the outer sediment in contact

TABLE 1 Coordinates of the coring sites and general description of the cores.

Site	Drilling hole/ core name	Water depth (m)	Latitude	Longitude	Temp. (°C)*	Length of core (m)	Age (year)§
Little Belt	SKA14-05-B25	38	55°00.258′ N	10°06.519′E	9	0.035	20
Greenland Glacier Fjord	SA13-ST8-47G	475	64°40.7078′ N	50°17.4672′ W	2	5.67	200
Greenland Main Fjord	SA13-ST5-30G	622	64°25.3479′ N	51°30.6209′ W	2	6.06	466
Greenland Side Fjord	SA13-ST6-40G, SA13-ST6-35R	389	64°29.0604′ N	50°42.3240′ W	2	5.61	4,600
Iceland Basin	DA12-11-1-GC01	2120	61°37.04′ N	20°43.26′ W	3	4.20	12,500
Greenland Continental Shelf	SA13-ST3-20G, SA13-ST3-17R	498	64°26.742′ N	52°47.6478′ W	4	5.92	12,600
Faroe Bank	DA12-11-ST2-GC03	742	60°46.94′ N	009°47.62’W	8	5.89	55,100
South Azores	DA14-ST1-GC01	2515	37°17.773 N	27°04.934 W	3.2	5.96	300,000
Bering Sea	IPDP Exp. 323, Hole U1342-B	818	54° 49.7004′ N	176° 55.0232′ E	2–6	43	1,000,000
Eastern Equatorial Pacific	ODP Leg 201, Hole 1,226-B	3297	3°5.24′S	90°49.12′ W	1.7–25.6	417	15,600,000

*Bottom water temperature (or temperature gradient down through the sediment for Eastern Equatorial Pacific and Bering Sea long cores). § approximated age at the bottom of the cores.

with the liner had been removed. The solid-phase samples were taken from the same depths as the pore water and care was taken to only sample one side of the core (working half of the core). For selected cores, the archive-half was scanned by an ITRAX x-ray diffraction core scanner (Croudace et al., 2006).

2.3. Determination of age-models

The loss of sediment from the top of the gravity-cores, due to the core catcher and the violent penetration of the sediment surface, was estimated by matching the pore water profiles of NH_4^+, SO_4^{2-}, and $\delta^{13}C_{DIC}$. The estimated sediment loss was then used to extend the age-models of the cores all the way to the sediment–water interface (see section 3.4 for analytical details). The matched pore water profiles can be found in the cited literature for each individual cores.

The average age of the upper 5 few cm of sediment in Little Belt core (SKA14-05-B25) was estimated based on correlation to IODP expedition 347 site M0059 (Andrén et al., 2015), which was retrieved at the same location.

The age of the rapidly accumulating sediment in the Glacier Fjord (core SA13-ST8-47G) was analyzed via short-lived natural gamma emitters (^{210}Pb and ^{226}Ra). The sedimentation rate was estimated from the least-squares fit to the natural log of excess ^{210}Pb in the core and the output of a one-dimensional two-layer advection–diffusion model that accounted for both biomixing and compaction with depth (Lavelle et al., 1985; Kuzyk et al., 2015). The data and the procedures are described in detail in Pelikan et al. (2019).

Calcareous mollusk shells and organic worm-tubes were collected in the Greenland Continental Shelf (core SA13-ST3-20G), Main Fjord of Nuuk Kangerlua (also known as Nuuk Fjord or Godthåbsfjord; SA13-ST5-30G), Side Fjord Kapisillit Kangerluat of Nuup Kangerlua (SA13-ST6-40G), Iceland Basin (DA12-11-ST1-GC01), and Faroe Bank (DA12-11-ST2-GC03) sediment cores for ^{14}C age determination by Accelerator Mass Spectrometry at Aarhus AMS Centre, Aarhus University. The ^{14}C ages were calibrated using the Marine13 radiocarbon calibration curve (Reimer et al., 2013) with no further regional reservoir correction ($\Delta R = 0$). The age models were reported as calibrated ^{14}C years BP (Before Present, where present = AD 1950). For the analysis of the organic matter reactivity here, however, the ages were calculated to years before collection (AD 2013) to relate to mineralization age. The procedures and data are described in detail in Petro et al. (2019).

The age-depth model of the South Azores core (DA14-ST1-GC01) was developed from the sediment description and from calcium (Ca) and iron (Fe) measurements using an ITRAX x-ray fluorescence (XRF) core scanner (Croudace et al., 2006). The profile of Ca/Fe, which may here be considered a proxy for marine productivity, was aligned with marine isotope stages and the age of the stages was determined according to LR04 Benthic Stack (Lisiecki and Raymo, 2005).

The age-depth model of the Bering Sea site (IODP Exp323, Hole U1342B) was retrieved from Knudson and Ravelo (2015), who based their age model on calcite $\delta^{18}O$ of benthic foraminifera, which they too correlated to the LR04 Benthic Stack (Lisiecki and Raymo, 2005). The depths were converted into ages using a linear interpolation between the measurements. Below 35 mbsf (meters below seafloor), there was a shift in stratigraphic unit (Unit II), where the age versus depth was not clearly resolved (Expedition 323 Scientists, 2011). Therefore, data below this depth were excluded from our study.

The age-depth model for the Eastern Equatorial Pacific core (ODP Leg 201, Hole 1,226-B) was based on one unique ^{14}C measurement and six biostratigraphic boundaries from the Pleistocene to the Middle Miocene (Shipboard Scientific Party, 2003; D'Hondt et al., 2004), previously assessed at site 846 of ODP Leg 138 (Shipboard Scientific Party, 1992). The depths were converted into ages using a linear interpolation between the seven age points. Below 388 mbsf, the age model was interpolated linearly, based on a basement age of 16.5 million years at the base of the core.

2.4. Pore water analyses

2.4.1. Ammonium

Aliquots of 1 mL pore water for analysis of dissolved ammonium were transferred to 2.5 mL Eppendorf tubes and frozen at −20°C until analysis. Ammonium concentrations were analyzed by spectrophotometry of the blue indophenols formed when ammonium is dissolved in a weak alkaline solution with salicylate, hypochlorite, and sodium nitroprusside (Bower and Holm-Hansen, 1980). After dilution of the pore water samples with MilliQ water (up to 50 times), 1 mL of the dilution was first mixed with 120 μL salicylic acid catalyst, then 200 μL of alkaline-hypochlorite solution (1 part of alkaline-citrate solution and 9 parts of 5% sodium hypochlorite) was added to the reaction tube. After incubating the reaction mix for 1 h, the absorbance was measured at 650 nm on a spectrophotometer (FLUOstar Omega, BMG Labtech GMBH, Ortenberg, Germany).

2.4.2. Dissolved inorganic carbon

Pore-water for analysis of dissolved inorganic carbon (DIC) was transferred to glass vials (Zinsser) filled up to the brim (*ca.* 2 mL), closed without headspace and stored at 4°C until analysis. Subsamples were transferred to 10 mL helium-flushed exetainers and the DIC was transferred to the headspace as CO_2 by reaction with phosphoric acid. The CO_2 content of the headspace was then analyzed by gas chromatography using a GC-IRMS with helium as carrier gas (CTC Analytics GC-pal autosampler, Thermo scientific GasBench II, Thermo scientific ConFlo IV, Thermo scientific Finnigan Delta V plus IRMS). The carbon isotopic composition ($\delta^{13}C$) of the CO_2 was determined relative to the VPDB standard using LSVEC ($\delta^{13}C$: -46.4‰ $_{VPDB}$) and NBS 19 ($\delta^{13}C$: +1.95‰ $_{VPDB}$) for calibration.

2.4.3. Sulfate

Aliquots of 300 μL pore water for analysis of sulfate (SO_4^{2-}) were transferred to 2.5 mL Eppendorf tubes and ventilated at room temperature for 20 min (only samples with low H_2S and high SO_4^{2-}) or flushed with humidified CO_2 to remove hydrogen sulfide before storage at 4°C until analysis. The pore water was then diluted with MilliQ water (10–100 times), and the sulfate concentration was determined by ion chromatography (Dionex ICS 2500 with AS 18 column and ED 50 electrochemical detector). An initial KOH eluent concentration of 20 mmol L^{-1} was used for the analysis, followed by a column flush at 32 mmol L^{-1} (Røy et al., 2014). In samples from Greenlandic waters, the measured sulfate concentrations were normalized to the chloride concentration to correct for possible dilution and evaporation errors.

2.5. Solid phase analyses

2.5.1. Porosity and density

Porosity and density of the sediment were determined using 2 cm^3 of wet sediment and calculated from the weight loss of sediment after drying at 100°C until constant weight. Porosity was calculated from water content multiplied by wet density.

2.5.2. Total organic carbon

Total organic carbon (TOC) was determined by combusting dry ball-mill-powdered sediment in an elemental analyzer [FLASH EA (1112 series), Thermo Scientific]. To remove the inorganic carbon, the sediment samples were pre-treated with 5% (w/w) sulfurous acid until the samples no longer produced CO_2 bubbles (Braun et al., 2017). Once re-dried and homogenized, aliquots of 50 mg acidified sediment were packed into tin cups and burned in the elemental analyzer. The content of organic matter is given as nmol C cm^{-3} fresh wet sediment, calculated based on the carbon content, the porosity, and the dry density. By this volume-specific unit, the organic carbon content can be directly compared to its volume-specific rate of oxidation.

2.5.3. Total cell abundance

Samples for total cell abundance determination were taken with 2.5 mL cut-off syringes. 1 mL of sediment was transferred into 4 mL sterile and saline paraformaldehyde solution (35 g L^{-1} NaCl and 2 g L^{-1} paraformaldehyde, final concentration of PFA in preserved samples 0.1%), mixed thoroughly and stored at 4°C until analysis. Microbial cells were quantified by fluorescence microscopy of cell extracts based on Kallmeyer et al. (2008) and Morono et al. (2013). The cell extraction consisted of a chemical detachment by a detergent mix (100 mM EDTA, 100 mM sodium pyrophosphate, and 1% (v/v) Tween 80) and methanol, followed by a mechanical detachment by three times 10 s sonication at 7 W. After each detachment treatment, the microbial cells were separated from sediment particles using density centrifugation with 50% Nycodenz (AXIS-SHIELD PoC AS). The cell extracts were pooled and filtrated on black polycarbonate membrane filters (25 mm, GTBP, 0.2 μm pore size) and stained with DAPI solution on the filter. A minimum of 400 cells were counted on at least 12 fields of view with an epifluorescence microscope (Axiovert 200 M Zeiss, Germany). An additional dissolution with acetic acid (Kallmeyer et al., 2008) was tested at all sites, but only applied to the calcareous Faroe Bank sediment.

2.5.4. Relative abundance of sulfate reducers

The relative abundance of sulfate-reducer cells compared to total cell abundance was determined by quantitative PCR (qPCR) of *dsrB* and *16S* rRNA- genes in extracted DNA. Mud samples were taken in cut-off 5 mL syringes that were immediately frozen at −80°C. Total nucleic acids were extracted from 0.5 to 1.0 g thawed sediment with a combination of enzymatic and chemical pre-treatment and the FastDNA Spin Kit for Soil (MP Biomedicals) as described by Kjeldsen et al. (2007). The abundance of *dsrB*- and of bacterial and archaeal *16S* rRNA gene copies in the DNA extracts were quantified by SYBR green-based qPCR according to Jochum et al. (2017) and Starnawski et al. (2017). The *dsrB* gene encodes for the β-subunit of dissimilatory (bi)sulfite reductase, which is a diagnostic marker gene for sulfate-reducing prokaryotes. Triplicate reactions were performed for each DNA extract. For 2–3 samples from each core the qPCR assays were performed on ten-fold serial dilutions of the DNA extract to test for the presence of co-extracted PCR inhibitors (inhibition effects were not observed). The *dsrB* gene qPCR assay conditions and performance were reported previously (Jochum et al., 2017). The assay standard curves were linear within a range of 10^2 to 10^8 target gene copies μL^{-1} template, with an efficiency between 102 and 107% and with $R^2 > 0.99$. The relative abundance of sulfate-reducing microorganisms in the total microbial community was calculated from *dsrB* gene copy numbers and the sum of bacterial and archaeal *16S* rRNA gene copy numbers assuming that sulfate reducers on average harbor 1 *dsrB* copy per genome (Jochum et al., 2017) while bacterial and archaeal cells on average harbor 4 and 2 *16S* rRNA gene copies, respectively (Suna et al., 2013). Based on analysis of DNA extraction negative control samples and using 2 µL DNA template, the limit of quantification of the *dsrB* assay was approx. 7400 *dsrB* gene copies per gram of wet sediment. The limit of quantification in gene copies cm^{-3} wet sediment varied from site to site depending on porosity and density, but was always close to 10^4. See supplementary information for primer sequences and further details.

2.6. Volume-specific carbon oxidation rates

2.6.1. Sulfate reduction rates by $^{35}SO_4^{2-}$ tracer incubation

Sulfate reduction rates (SRR) were measured experimentally by $^{35}SO_4^{2-}$ tracer incubation in cut-off 5 mL syringes according to Røy et al. (2014). Ten µL of carrier free $^{35}SO_4^{2-}$ tracer (100 to 250 kBq) was injected in the center of each sediment sample. The samples were incubated at *in situ* temperature for 6 to 24 h in the dark, under anoxic conditions in air-tight plastic bags with an oxygen scrubber inside (Oxoid™ AnaeroGen™, Thermo Scientific). The incubations were stopped by freezing the mini-cores at −20°C or − 80°C. Later, the samples were distilled to separate the total reduced inorganic sulfur (TRIS) from sulfate by a cold chromium distillation (Kallmeyer et al., 2004, including modifications as recommended by Røy et al., 2014). The total radioactivity of the sediment before distillation and the distilled fraction of total reducible inorganic sulfur (TRIS) were measured separately by liquid scintillation counting (Packard Tri-Carb 2,900 TR). Killed blank samples that consisted of sediment transferred to ZnAc (20% w/v) before tracer injection were used to test the procedure background and limits of quantification. The sulfate reduction rates (SRR) were calculated according to Jørgensen (1978a).

$$\mathrm{SRR} = [\mathrm{sulfate}] \times \varphi \times \left(\frac{a_{\mathrm{TRIS}}}{a_{\mathrm{TOT}}}\right) \times 1.06 \times t^{-1} \tag{1}$$

where [sulfate] is the pore-water sulfate concentration, A is the porosity, a_{TRIS} the radioactivity of TRIS, a_{TOT} the sediment radioactivity before distillation, t the incubation time, 1.06 a correction factor for the estimated isotope discrimination against $^{35}SO_4^{2-}$ (Jørgensen and Fenchel, 1974).

The measured rates of dissimilatory sulfate reduction were related to the oxidation of complex organic matter with the net-formula $C_{27}H_{28}O_7$ (LaRowe and Amend, 2015a). This implies a nominal oxidation state of carbon of −0.52 and a C:S ratio of 1.77:1 according to the stoichiometry:

$$\begin{aligned} &\mathrm{C_{27}H_{28}O_7} + 13\,\mathrm{H_2O} + 15.25\,\mathrm{SO_4^{2-}} \rightarrow \\ &27\,\mathrm{HCO_3^-} + 15.25\,\mathrm{HS^-} + 11.75\,\mathrm{H^+} \end{aligned} \tag{2}$$

Sulfate reduction rates can be measured with $^{35}SO_4^{2-}$ tracer down to 0.02 pmol SO_4^{2-} cm^{-3} day^{-1}, especially if the concentration of sulfate is low (Glombitza et al., 2016). We refrained from measurements in old and sulfide-free sediments to avoid reoxidation of reduced radiotracer, avoid contaminating with atmospheric oxygen in samples with poor redox-buffer, and avoid slow drift away from *in situ* conditions during long incubations. Thus, the incubation times could be held shorter than 24 h and the injected activity of $^{35}SO_4^{2-}$ tracer could be held below 250 kBq per sample.

2.6.2. Carbon oxidation rates based on modeling of NH_4^+ profiles

Complete mineralization of organic matter under sulfate-reducing conditions releases DIC and NH_4^+ in the same ratio as the C:N ratio of the organic matter that is being mineralized. But DIC is involved in precipitation and dissolution of carbonates, and the net rate of DIC production does not always correspond to the rate of carbon mineralization. We therefore used the NH_4^+ production rates to indirectly determine the carbon oxidation rates with greater accuracy in older sediments far from the sediment–water interface, where the rates were too low for determination with $^{35}SO_4^{2-}$ but the long diffusive distances increased the sensitivity of reaction–diffusion modeling. Ammonium production rates were determined by fitting a reaction–diffusion model to NH_4^+concentration profiles, assuming steady state and one-dimensionality (Boudreau, 1996) using the software PROFILE (Berg et al., 1998). The program solves the mass balance of NH_4^+ in the pore water:

$$R_{NH_4^+} = -\frac{\mathrm{d}}{\mathrm{d}z}\left(\varphi \times (D_s)\frac{\mathrm{d}C}{\mathrm{d}z}\right) \tag{3}$$

where R_{NH4+} is the rate of production of ammonium in the pore water, z is the sediment depth in meters below seafloor, φ the porosity of the sediment, D_s the diffusion coefficient of ammonium in the sediment, C the pore water ammonium concentration. The boundary conditions of the model were based on the measured concentrations of NH_4^+ at the upper and lower boundaries; exceptions are mentioned in Supplementary Table S1. The diffusion coefficient of ammonium in the sediment (D_s) was determined using the relation:

$$D_s = \frac{D_0}{\left(1 + 3 \times (1 - \varphi)\right)} \tag{4}$$

where D_0 is the diffusion coefficient in seawater corrected for salinity and temperature (Boudreau, 1996).

2.6.2.1. Calculation of diffusion coefficients in sediment with low porosity

For the site 1226-B in the Eastern Equatorial Pacific, the D_s for NH_4^+ was calculated from formation factors (FF), because this approach is more appropriate than Eq. 4 in very compact sediment, and because this approach has been used by previous authors who worked on data from the same site (Wang, 2006). The FF were interpolated from the measurements by a locally weighted least squares fit (*loess function*, in the R Stats Package (R Core Team, 2013), smoothing parameter =0.25). At the bottom of the core (374–418 mbsf), where FF measurements were not available, these factors were determined according to the empirical equation of Archie's law:

$$FF = \varphi^{-1.8812} \times 10^{0.1916} \tag{5}$$

(Wang, 2006). FF was used to calculate the tortuosity (τ^2) according to Boudreau (1996):

$$\tau^2 = \left(FF \times \varphi\right) \tag{6}$$

The sediment diffusion coefficient (D_s) was then calculated by dividing the temperature-corrected molecular diffusion coefficient of ammonium in pore water (D_0) by the tortuosity.

$$D_s = \frac{D_0}{\tau^2} \tag{7}$$

2.6.2.2. Temperature-correction of diffusion coefficients In thermal gradients

The software PROFILE does not directly allow the diffusion coefficient (D_0) to vary with depth, which is necessary in deep cores due to the geothermal gradient. To accommodate this deficiency, we calculated the difference between the diffusion coefficients calculated by PROFILE according to Eq. 4, and the temperature-corrected D_s at each depth. This difference was fed into the model as D_b. At runtime, PROFILE will add D_s and D_b, resulting in a correct diffusion coefficient (Wehrmann et al., 2011).

The reaction zones solved by PROFILE were fixed to a minimum of three zones when the model allowed. Data from the top and bottom reaction zones were rejected due to poor sensitivity, unconstrained transport coefficients, and strong influence of the boundary conditions, leaving a central reaction zone with high confidence in the calculated ammonium production rates.

2.6.2.3. Calculation of carbon oxidation from NH_4^+ production

The ratio between DIC and NH_4^+ production rates in pore water can be calculated from the ratio between the concentrations of DIC and NH_4^+ without calculating the actual fluxes (Jørgensen and Parkes, 2010). The procedure is less sensitive to noise in the DIC data than reaction–diffusion modeling, it is independent of porosity-effects on diffusion coefficients, and it allowed us to transform our ammonium production rates (section 3.6.2.2) into the equivalent DIC production rates. Thus, the DIC: NH_4^+ production rate for each site was found as the slope of so-called parameter plots of NH_4^+ vs. DIC concentrations in the pore water, multiplied by the ratio of D_0 of HCO_3^- and D_0 of NH_4^+ to account for the fact that NH_4^+ diffuses away faster than DIC. As the precipitation of calcium carbonate influences the DIC concentration, and therefore the apparent C:N ratio of mineralized organic matter, we determined the DIC: NH_4^+ production rate only in non-carbonate sediments. As all calculated DIC: NH_4^+ ratios fell in a narrow range we used the median value from all stations to transform the volume-specific rates of NH_4^+ production to volume-specific rates of carbon oxidation.

2.7. Reactivity of organic matter

The reactivity of the sedimentary organic matter was assessed in each sediment sample from the momentary first-order rate constant of its decay (k, in y^{-1}):

$$C_{ox\,rate} = k \times TOC \tag{8}$$

$$k = \frac{C_{ox\,rate}}{TOC} \tag{9}$$

where $C_{ox\,rate}$ is the rate of organic carbon mineralization based on SRR or NH_4^+ production rates (nmol C cm^{-3} y^{-1}) and TOC is the measured concentration of total organic carbon (nmol C cm^{-3}) at the same depth. The relation between k and sediment age was then derived by fitting a non-biased linear model to log–log transformed data and transposing this relation back to linear space according to Flury et al. (2016).

2.8. Mean cell-specific carbon oxidation rates

The mean cell-specific carbon oxidation rates were calculated by dividing the volume-specific carbon oxidation rates by the total cell abundance at the same depth. Similarly, the mean cell-specific sulfate reduction rates were assessed by dividing the volume-specific sulfate reduction rates by the number of sulfate-reducing cells. The latter was estimated by multiplying the relative abundance of *dsrB* genes (in %) by the total cell abundance at each depth.

2.9. Thermodynamic calculations

Complex sedimentary organic matter was represented by the net-formula $C_{27}H_{28}O_7$ (LaRowe and Amend, 2015a), which has a nominal oxidation state of carbon (NOSC) of −0.52.

Since the standard free energy of organic matter is closely linked to the mean oxidation state of carbon, we can assess ΔG^0_{ox} of the half reaction from $C_{27}H_{28}O_7$ to CO_2 per carbon atom via the relationship presented by LaRowe and Van Cappellen (2011) at 25°C and 1 bar:

$$\Delta G^0_{ox} = 60.3 - 28.5 \times NOSC \tag{10}$$

We summed ΔG^0_{ox} and the standard free energy of the sulfate reduction half-reaction (ΔG^0_{red}) calculated from tabulated Gibbs energy of formation for HS^-, SO_4^{2-} and H^+ (Kulik and Harff, 1993). The total Gibbs energy of the reaction (ΔG_r) was then calculated from ΔG^0 and the pore water concentrations of HS^-, SO_4^{2-}, HCO_3^- and H^+:

$$\Delta G_r = \Delta G^0 + R \times T \times \ln \prod_i a_i^{\nu_i} \tag{11}$$

where R is the gas constant (0.00831 kJ mol $^{-1}$ K^{-1}), and T is the temperature (K).

$\prod_i a_i^{v_i} = \left(\frac{\prod_i a_{i(product)}^{v_i}}{\prod_i a_{i(substrate)}^{v_i}} \right)$ is the mass action expression where a_i is the activity of the i^{th} component of the reaction, and vi is its stoichiometric ratio.

We used activity coefficients: 0.172 for SO_4^{2-}, 0.6592 for HS^-, 0.6843 for HCO_3^-, retrieved from (Kulik and Harff, 1993) at an ionic strength of 0.647. Organic matter as a solid has an activity of 1 regardless of its concentration. We assumed a pH of 7, which influenced the activity of HCO_3^- based on DIC concentration and HS^- based on total H_2S concentration. For simplicity, the calculation was done at 25°C (298 K).

Likewise, ΔG_r of acetate (CH_3COO^-) oxidation to CO_2 with sulfate as electron acceptor was calculated from Eq. 12, using the following stoichiometry:

$$CH_3COO^- + SO_4^{2-} \rightarrow 2HCO_3^- + HS^- \qquad (12)$$

For acetate, we used the same activity coefficient as HCO_3^- and assumed pH = 7. Acetate concentrations in the Greenland cores were available from Glombitza et al. (2015), but such data are rare because acetate is difficult to measure in saline water at the relevant concentrations (Glombitza et al., 2014). But the most complete datasets indicate that the acetate concentrations in cold marine sediments are remarkedly constant due to thermodynamic constraints (Glombitza et al., 2019; Beulig et al., 2022). We therefore use the mean value of the acetate concentration in the Greenlandic cores (5.96 µM ± 1.6) in the calculation of ΔG_r for the Eastern Equatorial Pacific sediments where no measurements were available. To estimate the Gibbs energy liberated by fermentation, we subtracted ΔG_r from oxidation of acetate to CO_2 via sulfate reduction from the total ΔG_r from $C_{27}H_{28}O_7$ all the way to CO_2.

2.10. ODP and IODP data

The data from ODP Leg 201, site 1226, in the Eastern Equatorial Pacific were retrieved from the Janus Web Database.[1] Pore-water NH_4^+ concentration and porosity were obtained from Hole 1226-B and the porosity measurements were interpolated to the same depth resolution as NH_4^+. Cell counts from Hole 1226-B were retrieved from Parkes et al. (2005), who used direct counts with acridine orange, fluorescent dye, without cell extraction. TOC data (weight %) were retrieved from Janus web database and recalculated to nmol cm^{-3}. Note that most TOC concentrations were measured in hole 1226-E.

Data from IODP expedition 323, site U1342, in the Bering Sea were retrieved from the Janus database and from published studies. The depth-matching between parameters (porosity from Hole C, pore water from Hole B) was done via the corrected composite depth scale (CCSF-A) in meter core composite depth below seafloor. This depth scale was constructed by Expedition 323 Scientists (2011) based on multiple drillings holes, A–D, and was calculated by adding a specific cumulative offset to the CSF-A depth scale of each core. We used ammonium concentration as our reference sample resolution. Porosity was matched to this resolution using linear interpolation between measurements, except for the top and bottom depths, where we used the closest porosity data point. D_s was calculated from porosity based on Eq. 4, as the data quality of the measured formation factors was low. After matching the parameter depths, the CCSF-B scale (mbsf) was used for the modeling, which corrected CCSF-A for the core expansion during drilling by dividing the CCSF-A-depth by 1.06 (Expedition 323 Scientists, 2011). Cell count samples were retrieved from the Hole U1342B, published in Kallmeyer et al. (2012) and derived via cell extraction based on Kallmeyer et al. (2008) and SYBR Green I dye. If the samples were counted multiple times, we used the mean value. TOC data (weight %) were retrieved from the LIMS database and transformed into nmol C cm^{-3}.

3. Results

3.1. Site descriptions

The Little Belt core (SKA14-05-B25) was co-located with IODP expedition 347 site M0059. Samples from the same site and day were designated SKA05-B25 by Deng et al. (2020), who describes the link between bioturbation and the microbial community. Information on benthic infauna and mineralization pathways can be found in Kristensen et al. (2018). The site was situated in a local depression prone to seasonal anoxia and, at the time of sampling, the bottom water had just barely re-oxygenated. Thus, the sediment was still thoroughly reduced and devoid of fauna (Kristensen et al., 2018). The sedimentation rate was 5 to 7 mm yr^{-1}, based on the preliminary age-model of IODP Expedition 347 site M0059 retrieved from the same site (Andrén et al., 2015); paleoclimatic and paleoenvironmental data from the site are presented by Kotthoff et al. (2017). SKA14-05-B25 provided the youngest sulfate-reducing sediment available (average age ca 10 years), when sampling the upper 3.5 cm with cut-off syringes directly through the sediment–water interface in a box-core.

Greenland Glacier Fjord core SA13-ST8-47G was sampled in the innermost part of Nuup Kangerlua (Godthåbsfjord), close to the marine-terminating glaciers Narsap Sermia and Kangilinnguata Sermia [see Glombitza et al. (2015) and Pelikan et al. (2019) for details on all Greenland cores, including age models and geochemistry]. The glacier at the head of the fjord delivered large amounts of clastic material to the seabed, giving a mean sedimentation rate 2.9 cm yr^{-1} (95% confidence interval 2.2–4.1 cm yr^{-1} based on excess ^{210}Pb activity) (Pelikan et al., 2019; Supplementary Figure S2), Thus, the 6-m long core provided samples with ages in the range of 0–200 years.

Greenland Main Fjord core (SA13-ST5-30G) was sampled in Nuup Kangerlua in the path of the ice-flow from the glaciers, but more distant from the glacier front, resulting in lower sedimentation rates and higher ages than the Glacier Fjord Core (SA13-ST8-47G). One bivalve shell was found at 39 cmbsf (cm below seafloor) and dated to 265 ± 42 cal yrs BP, a second at 553 cmbsf was dated to 457 ± 26 cal yrs BP. This dating could be ascribed to a dramatic change in sedimentation rate occurring sometime between the upper 39 cm (0.15 cm yr^{-1}) and the rest of the core below (2.68 cm yr^{-1}). A more likely explanation is that the shell found at 39 cmbsf was redeposited from an older deposit. Thus, the sediment accumulation rate was

---

[1] http://www-odp.tamu.edu/database/

estimated to 1.2 cm yr^{-1} from linear extrapolation between the sediment surface and the age of the deepest shell (Supplementary Figure S2). According to this, the site provided samples in the age range from 80 to 600 years.

Greenland Side Fjord core (SA13-ST6-40G) was sampled in a side-fjord (Kapisillit Kangerluat) of Nuup Kangerlua; this side fjord is currently not connected to the Greenland ice-cap at its head. Matching of Rumohr cores and Gravity-cores indicated a loss of 10 cm from the top of the gravity-core. The core was dated to 4.6 ka cal. BP at 270 cmbsf, which implied an accumulation rate of 0.6 mm yr^{-1} (Supplementary Table S1). The surface sediment was heavily bioturbated and burrows were observed down to 43 cmbsf. The sediment was homogeneous in structure down 340 cmbsf, where the material changed from silty-clay to mud with an abundance of small ice-rafted pebbles. Data from below the deepest datable fossil at 270 cmbsf was rejected due to unknown age. The site provided usable sediment in the range from 200 to 4,600 years old (Supplementary Figure S2).

Iceland Basin gravity-core (DA12-11/1-GC01) and a box-core from the same site were collected from 2021 m deep water in the North Atlantic. The age model, the paleo-climate, and the paleo-circulation are described in Van Nieuwenhove et al. (2018), Orme et al. (2018), and Braun et al. (2017). Matching of pore-water profiles between gravity-core and box-core indicated a loss of 14 cm from the top of the gravity-core. The sediment was rich in carbonates and contained four distinct horizons of volcanic ash. Sulfate reduction rates were measured in the upper parts of the core with radiotracer, at sediment ages of 100–380 years. The sulfate reduction rates in the deeper parts of the core were below our level of quantification, but the ammonium profile in the entire core could be modelled (Figure 1E). Discarding the modelled rates of mineralization in the shallowest and deepest intervals left data with good confidence in the age-interval from 4,000 to 8,200 years (Supplementary Figure S2).

Greenland Continental Shelf core (SA13-ST3-20G) and a Rumohr Lot core (SA13-ST3-17R) were both retrieved at the same site on the West Greenlandic Shelf in the Labrador Sea. Matching of the two cores indicated that the upper 18 cm was lost from the top of the gravity-core. The sediment accumulation rate was on average 0.48 mm yr^{-1}, with a higher sedimentation rate during the recent 2,000 years (0.86 mm yr^{-1}, 0–163.5 cmbsf, Supplementary Figure S2). From 253 to 568 cmbsf the core was weakly laminated, changing to millimeter-thick laminations (silty-sand) from 568 cmbsf to the bottom of the core, indicative of permanent ice cover during the Weichelian ice age (see Allan et al., 2021, for age model, stratigraphic and paleoenvironmental details). The core provided sulfate reduction rates at sediment ages ranging from 300 to 10,000 years and useful modeled rates based on pore water profiles of ammonium in the overlapping age range from 1,000 to 8,000 years old (Supplementary Figure S2; Figure 2).

Faroe Bank core (DA12-11-ST2-GC03) and a box-core were collected from 742 m deep water SW of the Faroe Islands. The sediments were carbonaceous with more than 14 cm of accumulated foraminiferal tests at the surface. Matching of Rumohr and gravity-cores indicated a loss of 18 cm from the top of the gravity-core. The sediment was too old for reliable determination of sulfate reduction rates with radiotracer but provided useful rates of carbon mineralization modeled from ammonium profiles in an age range from 22,000 to 35,000 years (Supplementary Figure S2, age model published in Braun et al., 2017).

South Azores core (DA14-ST1-GC01) was collected from 2,500 m deep water between the Azores Archipelago and the East Azores Fracture zone. The sediment consisted of calcareous deep-sea ooze covering the past 300,000 years. No attempts were made to measure reduction of ^{35}S tracer as the younger layers of sediment, where tracer-incubations could have been feasible, were assumed not to be sulfate reducing. The model could not resolve more than one reaction zone from the ammonium profile. The calculated rate of mineralization was, therefore, only associated with the central third of the core where the age ranged from 100,000 to 200,0000 years (Supplementary Figures S2, S3).

Bering Sea IODP Leg 323 Bower Ridge Site U1342 was drilled in the southern Bering Sea under the Integrated Ocean Drilling Program (IODP). The data were retrieved from IODP LIMS Online Report http://web.iodp.tamu.edu/LORE/. The temperature at the seafloor was 1.9°C and increased by 0.0977°C m^{-1} down-core (Takahashi et al., 2011). The core covered the past 1,000,000 years, and mineralization of organic matter could be modelled with good confidence in the age-range from 400.000 to 700.000 years (Supplementary Figure S2).

Eastern Equatorial Pacific IODP Leg 201 Site 1,226 was drilled 300 km south of the Galapagos Islands. The temperature at the seafloor was 1.74°C and increased by 0.0572°C m^{-1} down-core (Shipboard Scientific Party, 2003; Wang et al., 2008). The core penetrated the 417 m thick sediment column all the way to the basaltic basement and covered the past 15,600,000 years. The core had an unusual geochemical profile due to diffusion of oxygen, nitrate, and sulfate from the basaltic basement (Jørgensen et al., 2006). Therefore, the core lacked a methanic zone and instead had a very deep penetration of sulfate. This unique core provided rates of carbon mineralization modelled from ammonium production in the sulfatic sediment in an age interval of 2–3.75 million years, after discarding data from the upper and lower reaction zones from PROFILE (Supplementary Figure S2).

3.2. Mineralization rates of organic carbon

The content of organic carbon differed between sites but did not decrease systematically with increasing sediment age in the individual cores (Figure 3). The lowest carbon content was found near the glaciers in the Greenlandic fjord (site DA13-ST8-47G), where the organic matter was diluted by a large influx of glacially-derived clastic material, and in old deep-water deposits (ODP Leg 201/1226-B from the Eastern Equatorial Pacific). A continuous loss of organic material over time was partly balanced by compaction, when expressed in the volume-specific unit applied here, and the trajectory down-core was mostly determined by the depositional history. This is for example seen in the core from the Greenlandic continental shelf (SA13-ST3-20G), where the content of organic matter decreased abruptly in the early Holocene 6,000–10,000 years ago, when ocean circulation and climate changed dramatically after the Last Glaciation (the Weichselian; Figure 3). The total variation in organic matter content in the entire dataset was mostly between 2×10^5 and 2×10^6 nmol C cm^{-3}.

In sharp contrast to the low variability of organic carbon concentrations, the volume-specific carbon oxidation rates spanned 8

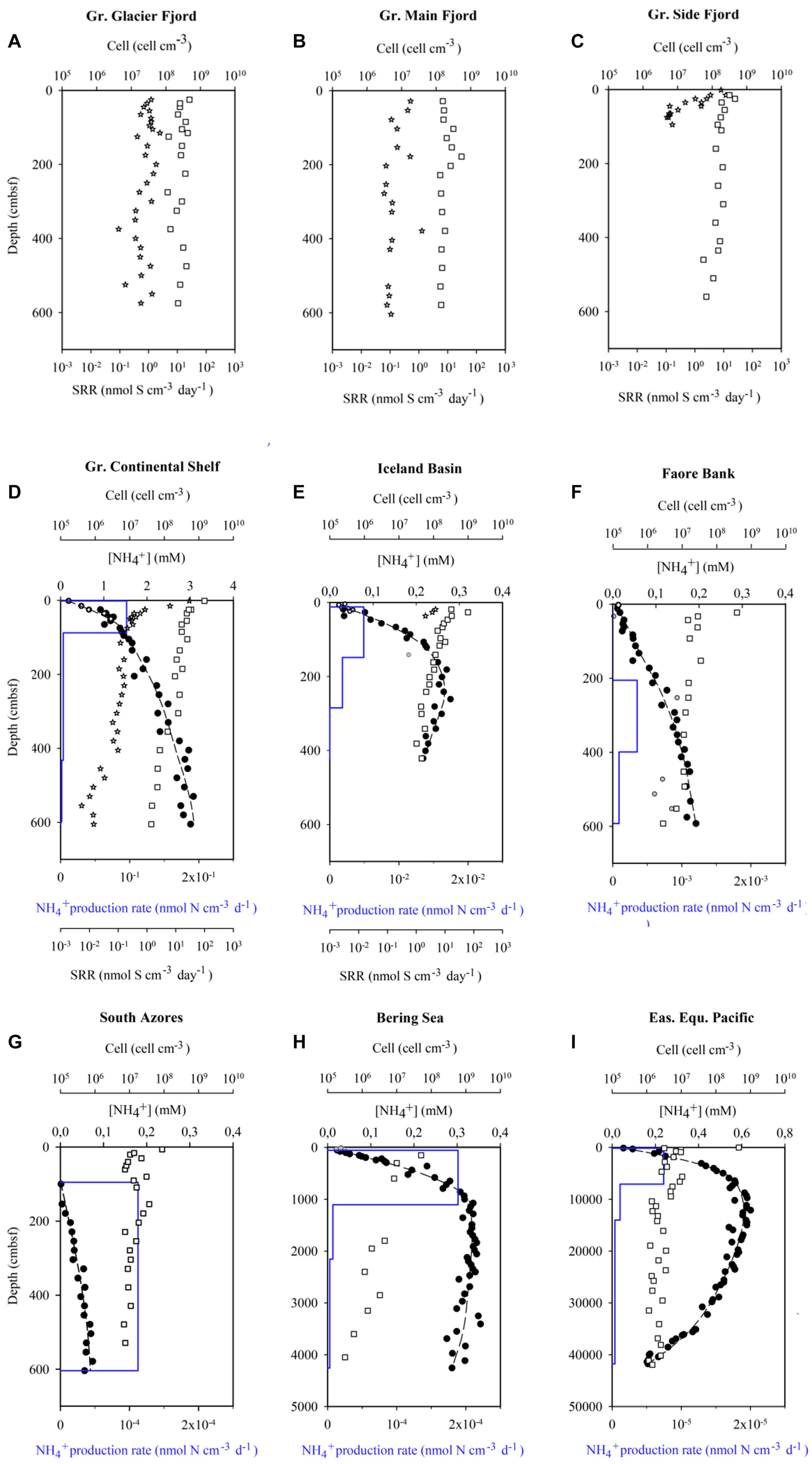

FIGURE 1
Nine of the datasets used to calculate mean cell-specific carbon oxidation rates showing pore water ammonium concentrations ([NH_4^+, filled circles]), model fits to the ammonium data (dashed line), modeled ammonium production rates (blue line), measured sulfate reductions rates (SRR, stars), and cell abundance (squares). Near-surface ammonium data marked with open circles was not included in the model fit. The South Azores model (G) starts at 0.95 mbsf because above this depth, ammonium concentrations were below the limit of quantification. Sulfate reduction rates from the Greenlandic cores were published in Glombitza et al. (2015), while the ammonium profiles were published in Pelikan et al. (2019). The data from Little Belt was not resolved in depth and, therefore, not plotted.

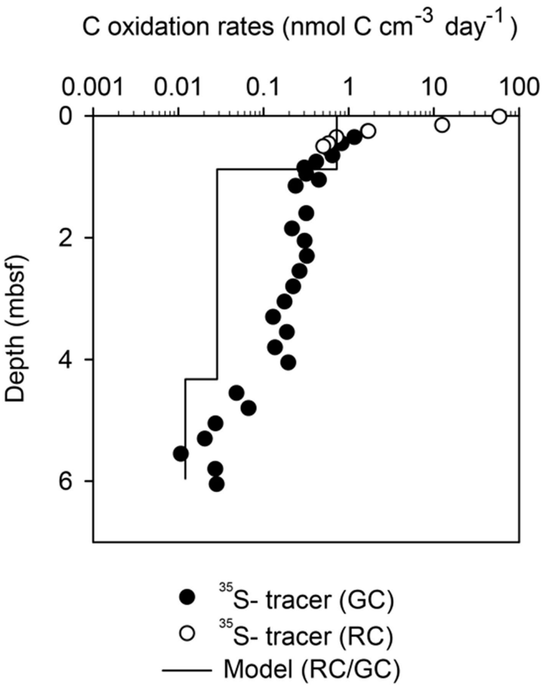

FIGURE 2
Comparison between carbon oxidation rates based on the modeling of ammonium concentration profiles, and carbon oxidation rates based on ^{35}S-radiotracer incubation in Greenland Continental Shelf Sediments. The data was derived from Figure 1D by multiplying the sulfate reduction rates by 1.77 according to the C:S stoichiometry in Eq. 2 and multiplying the ammonium production rates by 7.59 according to the C:N stoichiometry from parameter plots (Supplementary Figure S4). RC is data from the Rumhor core and GC is data from the gravity-core.

orders of magnitude from 7×10^2 to 8×10^{-6} nmol C cm^{-3} day^{-1} (Figures 1A–I, 4A). The highest rates of mineralization of organic matter were found in the youngest sediments using ^{35}S-radiotracer measurements. Conversely, the lowest rates of mineralization were determined in the oldest sediments using modeling of ammonium profiles. Fortunately, the geochemical settings on the Greenlandic shelf (SA13-ST3-20G) allowed both methods to be used on the same age interval (Figure 2). As expected, the modeled rates of ammonium production could not resolve the steep decrease in sulfate reduction in the upper meters, and the average rates given by the model systematically underestimated the measured rate of carbon mineralization in the top of the sediment and overestimated the rate in the lower half of the upper reaction zone. Deeper in the core, where the sulfate reduction rate changed more gradually, the two methods dropped in parallel, although with up to one order of magnitude discrepancy.

The reactivity of the organic matter, quantified as the momentary first order rate constant (k), decreased systematically with increasing age. There was no offset in the trend between data derived from incubations with radiotracer and data derived from modeling of ammonium profiles (Figure 4C). The best power-law fit to the relationship between k and sediment age was:

$$k = 0.180 \times \text{sediment age}^{-1.11} \qquad (13)$$

The exponent of −1.11 in the power function signified that the reactivity of organic carbon decreased by 1.11 order of magnitude each time the age increased by one order of magnitude. The exponent in the fit to the rate constant vs. depth (−1.11, Figure 5) was less negative than exponent in the fit to the sulfate reduction rate vs. depth (−1.23, Figure 4A). The faster drop in the rate of sulfate reduction compared to the rate constant was caused by a relatively fast initial drop in carbon concentration, and because loss of pore-space at depth concentrated the remaining volumetric carbon content.

3.3. Abundance of prokaryotic cells

The total cell abundance decreased with increasing sediment age, but only by three orders of magnitude, from 3.9×10^9 to 1.9×10^6 cells cm^{-3} (Figures 1A–I, 4B). The corresponding exponent of the fitted power function was −0.63. As the cell counts decreased relatively less than the volume-specific organic carbon oxidation rates (Figure 4A Figure 4B), the mean cell-specific carbon oxidation rate decreased continuously with sediment depth and age over ~5 orders of magnitude from 1.8×10^{-1} to 1.4×10^{-6} fmol C cell^{-1} day^{-1}, with no indication that the decrease was tapering off in the oldest sediment (Figure 4D).

The relative proportion of *dsrB* vs. *16S* rRNA gene copies, and thus the proportion of potentially sulfate-reducing microorganisms within the total microbial community, was up to 40% in the youngest sediments but decreased rapidly with increasing sediment age (Figure 5). In sediments older than 10,000–100,000 years, the abundance of *dsrB* gene copies fell below the limit of quantification (10^4 cm^{-3}). The decreasing proportion of sulfate-reducing microorganisms did not follow a common function with increasing age, but if the individual cores were treated separately, then the decrease followed power functions with exponents of −0.77 to −0.86 (Figure 5). We disregard the calculated exponent from the Iceland Basin here because the surface of this deep-sea core was most likely iron-reducing rather than sulfate reducing, and because the high calculated percentages of sulfate-reducing cells deep in the sediment were interspersed with samples below the level of quantification which skewed the fit.

The cell numbers decreased with an exponent of −0.63 and the proportion of sulfate-reducing cells decreased with an exponent of −0.82. Combined, this caused the number of sulfate-reducing cells to decrease with an exponent of −1.45, which is closely matched by the rate at which the mineralization of organic carbon decreased (exponent of −1.36). Thus, the combined effect of decreasing cell numbers and decreasing proportion of sulfate-reducing cells caused the quantified abundance of sulfate-reducing cells to decrease as steeply as the rate of carbon mineralization over sediment ages from 10^1 and at least to 10^4 years old. Accordingly, the sulfate reduction rates per sulfate-reducing cell remained surprisingly constant in the order of 10^{-2} fmol sulfate cell^{-1} day^{-1}, although the overall cell-specific community metabolism decreased by 4 orders of magnitude. We could not resolve how the sulfate reduction rate per sulfate-reducing cell developed in even older sediments ranging from 10^4 up to 10^7 years because our methods were not sensitive enough to quantify the number of *dsrB* gene copies.

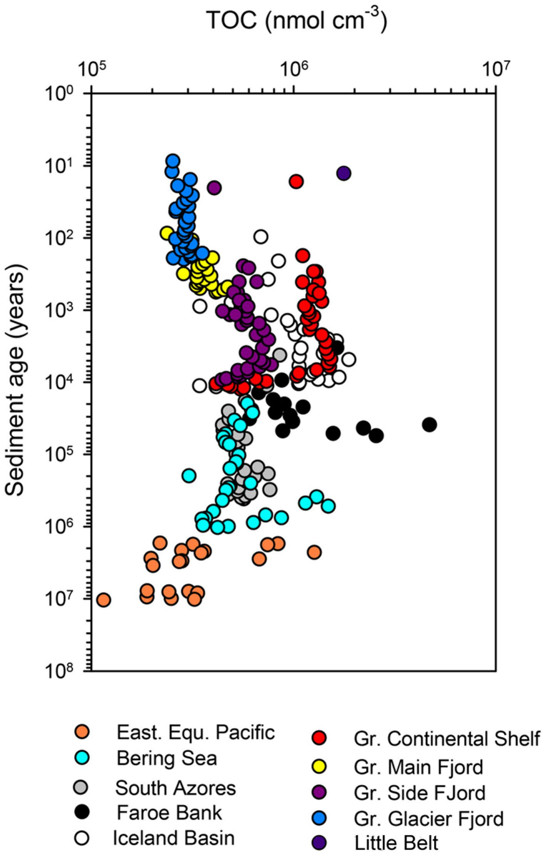

FIGURE 3
Total organic carbon concentration in all cores.

4. Discussion

4.1. Reaction rate and reactivity of organic matter in old sediments

The careful selection of sites and methods allowed us to determine the rate of mineralization of organic matter in sulfatic sediments (Canfield and Thamdrup, 2009; Jørgensen, 2021) with ages from 10 years to 3,750,000 years. The data extended the power law of organic matter decay constants, first presented by Middelburg (1989), to even older sediments and overcame the original need for a site-specific “initial age,” possibly because our data were more uniform with respect to temperature and geochemical zone. In contrast to previous data syntheses [e.g., Middelburg (1989) and Katsev and Crowe (2015)], our approach did not rely on a measurable decrease in the concentration of organic matter with increasing depth and age of the sediment. In fact, we found little correlation between depth in the sediment column and the concentration of organic matter (Figure 3). Our correlation predicted a slightly faster loss of reactivity with $k = 0.180 \times \text{sediment age}^{-1.11}$ (Eq. 13), compared to models based on, or verified from, vertical profiles of organic carbon, which have exponents ranging from -0.8 to -1 (Shang, 2023). Power-law models with exponents close to -1 demonstrate that the overwhelming factor responsible for decreasing rates of microbial catabolism in ageing sediments is not so much the loss of organic carbon, but rather the loss of organic carbon reactivity (Figures 3, 4D). Conceptually, this corresponds well with the increasing molecular complexity of degrading organic matter (e.g., Estes et al., 2019; Hach et al., 2020), but poorly with models that assume concurrent degradation of multiple pools of organic matter with individual degradability (Jørgensen, 1978b; Shang, 2023). Note, however, that the two types of models provide equally good fits to empirical data (Arndt et al., 2013).

4.2. The link between sediment age, community size, and respiration rate

Cell numbers decreased as a function of sediment depth and age, as seen in several previous studies (Whitman et al., 1998; Kallmeyer et al., 2012). The decrease in total cell abundance with increasing age of the sediment was much slower than the decrease in carbon oxidation rates (Figure 4A vs. Figure 4B), which implied a large drop in the mean cell-specific rates of catabolism (Figure 4D). The degradation of organic matter in sulfatic marine sediments is, however, divided between two major guilds of cells, one guild that hydrolyses and ferments complex organic matter to volatile fatty acids and hydrogen, and a second guild that oxidizes these fermentation products to CO$_2$ and water while reducing sulfate to sulfide. The rate-limiting step in mineralization of complex organic matter is the initial hydrolysis (Beulig et al., 2018) and the fermenters will take up the resulting monomers so efficiently that their concentrations are mostly too low to even detect. The community that oxidizes the fermentation products via anaerobic respiration is equally efficient, and fermentation products do not normally accumulate above a few μM (Postma and Jakobsen, 1996; Wang et al., 2010; Glombitza et al., 2015). The metabolic guild that has the most energetic respiratory metabolism will deplete the fermentation products to such low concentrations that energy conservation via proton translocation across the cell membrane is only barely possible. This excludes energy conservation from respiration with less energetic electron acceptors and causes the characteristic geochemical redox-zonation with limited overlap between utilization of different external electron acceptors (Postma and Jakobsen, 1996). We can, therefore, assume a tight link between fermentation and sulfate reduction regardless of which specific fermentation processes that were active: The fermenters oxidize some organic carbon to CO$_2$, while concurrently producing more reduced carbon or H$_2$ in the process. When these electron-rich substrates are then used by the sulfate reducers, it balances the stoichiometric ratio between sulfate consumption and total CO$_2$ production to the same value as if the sulfate reducer had mineralized the original organic matter with no fermentation involved (Eq. 2). This way, the electrons from complex organic matter must pass through both fermentation and sulfate reduction for the carbon to be funneled fully to CO$_2$, and the rate of sulfate reduction is a measure of the flow of carbon and electrons through both processes. Even syntrophic interactions with direct electron transfer do not change the overall stoichiometry between mineralized organic carbon/CO$_2$ and sulfate.

The fermentation product acetate is instrumental in the transfer of reducing equivalents from fermentation to sulfate reduction, and oxidation of acetate accounts for 30–65% of the sulfate reduction rate in sulfatic sediments (Christensen and Blackburn, 1982; Finke et al., 2007; Beulig et al., 2018). We specifically selected sediments for the study where all other electron accepters than sulfate and CO$_2$ had

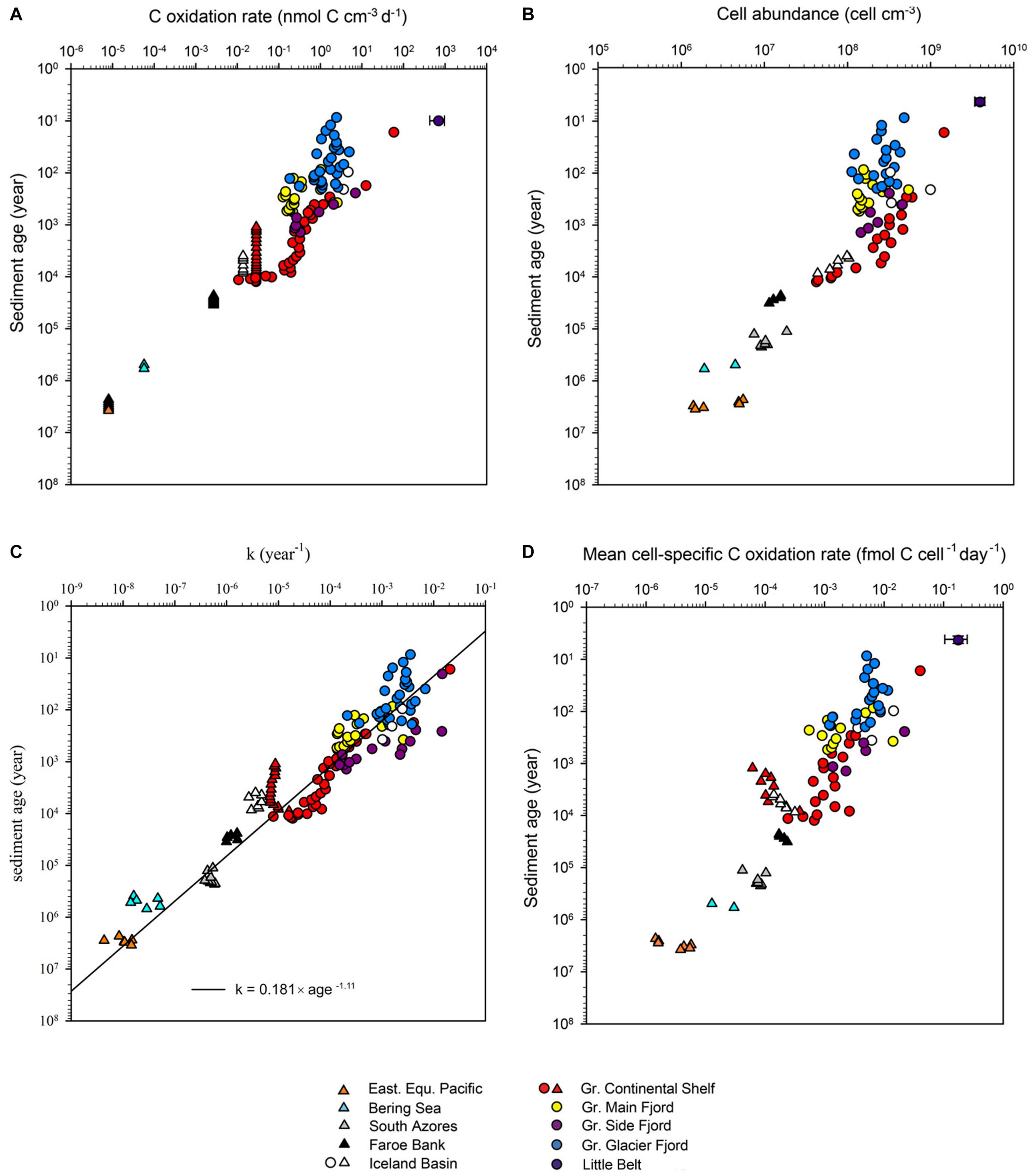

FIGURE 4
(A) Volume-specific organic carbon oxidation rates versus the age of the sediment. Datapoints represented by triangles were measured by radiotracer while datapoints represented by circles were measured by modeling of ammonium profiles. The error bar for Little Belt shows the standard deviation of multiple samples at the same depth. **(B)** Cell abundance versus age of the sediment. **(C)** Relation between the first order rate constant of organic matter mineralization (k) and the age of the sediment. The 95% confidence interval of the calculated exponent of the power function was –1.06 to –1.14 year^{-1}. **(D)** Mean cell-specific carbon oxidation rates versus age of the sediment.

already been depleted. Under these conditions, sulfate reduction is the primary terminal electron accepting process, and all known prokaryotes that respire via sulfate use the *dsrB* gene. The gene is also used in sulfide oxidation, but the sediment strata that we analyzed did not contain suitable electron accepters for this process. We therefore assumed that all cells that contained the *dsrB* gene were potential sulfate reducers, and as they were found in sulfate-reducing sediment, we assumed that all potential sulfate reducers were active. This allowed us to calculate the per-cell sulfate reduction rate. We found elevated rates of per-cell sulfate reduction in upper centimeters of sediment with active bioturbation. But when both the decreasing cell numbers and the decreasing proportion of sulfate reducers were considered, the

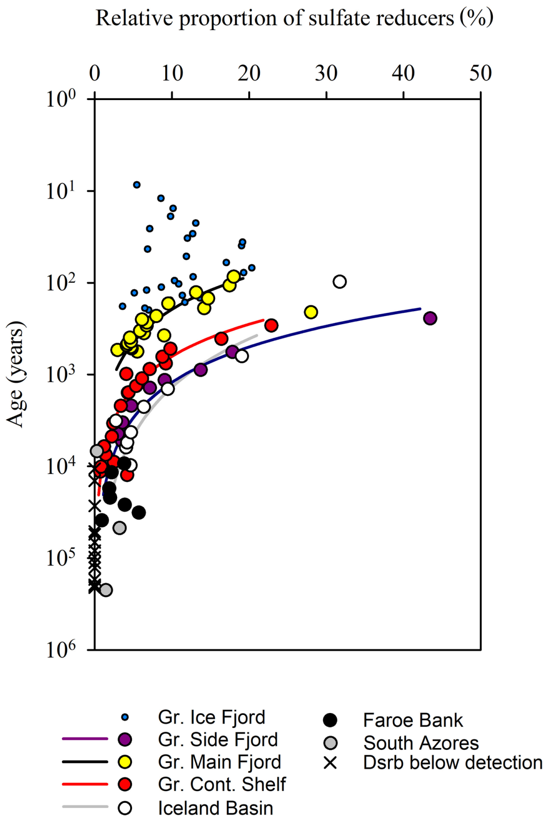

FIGURE 5
Relative proportion of sulfate-reducing microorganisms based on quantitative PCR of *dsrB* genes and *16S* rRNA genes from Bacteria and Archaea. In sediments older than 10^4 years, sulfate reducers could not be detected in 14 out of 23 samples. The lines represent fits to power functions with exponents of −0.84 (−0.71 to 1.00) for Gr. Main Fjord, −0.86 for Gr. Cont. Shelf (−0.77 to −0.92), −0.78 (0.55 to 0.89) for Gr. Side Fjord and −0.57 (−0.36 to −72) for the Iceland Basin (95% confidence interval).

cell-specific carbon oxidation rate by sulfate-reducing microorganisms in the subsurface stayed remarkably constant on the order of 10^{-2} fmol C cell^{-1} day^{-1}, despite increasing depth and a drop in sulfate reduction rates of four orders of magnitude (Figure 5).

Previous studies have shown relatively high cell-specific rates of sulfate reduction in the very surface of coastal sediments, gradually decreasing to an organic carbon oxidation rate of 10^{-3} to 10^{-2} fmol C cell^{-1} day^{-1} between 30 and 100 cm below seafloor (Hoehler and Jørgensen, 2013; Petro et al., 2019). Interpretation of the data deeper in the sediment from these coastal sites is difficult because of the transition from the sulfatic zone and into the methanic zone, and because the early qPCR protocols and primers used (Leloup et al., 2007, 2009) lacked the necessary resolution. In an attempt to predict the cell specific rates of sulfate reduction deeper in the sediment, Lever et al. (2015) extended the estimate of Hoehler and Jørgensen (2013) into deeply buried sediments of the Peru Margin by assuming that sulfate reducers constituted 10% of the total microbial community regardless of sediment depth and age. This assumption resulted in calculation of constantly decreasing per-cell rates of sulfate reduction in deeper sediment, but later studies have not confirmed the proportion of sulfate reducers to be constant (Webster et al., 2006; Petro et al., 2019). Thus, the constant cell specific sulfate reduction rates across depth and age up to 20,000 years seen in our study do not contradict the more recent studies and might imply that the size of the sulfate-reducing community is indeed controlled by a fixed minimum energy requirement of these microorganisms, as hypothesized by Hoehler and Jørgensen, (2013). Further, this minimum metabolic rate of sulfate reducers in deeply buried marine sediments might not be far from that seen below the depth of bioturbation in sediment that is buried only 30 cm deep and is only 300 years old (Petro et al., 2019).

Our attempt to detect sulfate-reducing prokaryotes in sediments older than 26,000 years was not successful as the *dsrB* gene copy numbers fell below our limit of quantification of ~10^4 gene copies cm^{-3}. Thus, it awaits more sensitive experimental methods to see if the proportion of sulfate reducers continue to drop with increasing sediment age beyond 26,000 years, which is necessary for the cell specific sulfate reduction rates to stay at the constant level of 10^{-2} fmol C cell^{-1} day^{-1} that we observed down to this depth. There are, however, indications that this could indeed be the case: Studies have revealed (a) low abundance of functional genes related to sulfate reduction (*dsrAB* genes) or methanogenesis (methyl-coenzyme M reductase, *mcr* genes) in deep sediments (<1% of total community, Schippers and Neretin, 2006; Lever, 2013), (b) fermentation-related genes that were much more abundant than *dsr* or *mcr* genes in metagenomes (Kirchman et al., 2014; Gaboyer et al., 2015), and (c) apparent virtual absence of genes related to sulfate reduction in metagenomes from deep sulfatic sediments of the Bering Sea (Biddle et al., 2008). The apparent difficulty in detection and quantification of dsr genes in the diverse pool of DNA extracted form sediment from deep below the sea floor on the Peru Margin indicate that terminal-oxidizing prokaryotes are present at low abundance (Webster et al., 2006), while the consistent detection of mRNA transcript of dsr (Orsi et al., 2013, 2016) indicate that sulfate reduction play a larger role in community activity than the low proportion of sulfate-reducing prokaryotes suggests.

4.3. Division of Gibbs free energy between fermentation and sulfate reduction

To assess the division of Gibbs free energy (ΔG_r) between fermenters and sulfate reducers, we calculated the Gibbs free energy (ΔG_r) by complete oxidation of organic matter to CO_2 via Eqs 11, 12 according to LaRowe and Van Cappellen (2011). We also calculated ΔG_r for oxidation of acetate to CO_2 with sulfate as electron acceptor based on measured concentrations of reactants and products (Eqs 12, 13). By subtracting the energy yield of this terminal oxidation from the total energy yield, we could estimate the energy yield of fermentation under *in situ* conditions without needing to know the molecular identity or the concentrations of fermentation substrates (i.e., the products of hydrolysis). This is a rather crude approximation, as fermentation processes produce other products than acetate, and sulfate reducers oxidize H_2 and other volatile fatty acids, such as formate or propionate, in addition to acetate (Glombitza et al., 2015). Moreover, this calculation overestimates the energy available for the fermenters, as the free energy from extracellular hydrolysis cannot be coupled to energy conservation (i.e., to ATP). Note also that our operational definition of "fermenters" includes all organisms involved in production of acetate regardless of the actual biochemical pathway. Thus, the purpose was not to calculate the accurate ΔG_r of the processes or to compare energy yields close to thermodynamic thresholds. But to test if the overwhelming dominance of fermenting cells could be explained by an inequal sharing of energy between fermentation and sulfate reduction. Thus, we calculated the division of energy between fermentation and sulfate reduction on the four Greenland cores and in the oldest core from the Eastern Equatorial Pacific, where we had the most complete data on pore water chemistry that is needed.

In the core from the Greenland Continental Shelf (SA13-ST3-20G), the ΔG_r liberated by fermentation 1 m below seafloor was -43 kJ (mol C)$^{-1}$, while the ΔG_r liberated by acetate oxidation was -24 kJ (mol C)$^{-1}$. At 5.9 meters below seafloor, the values changed only slightly to -42 kJ (mol C)$^{-1}$ and -18 kJ (mol C)$^{-1}$, respectively. The remaining Greenlandic cores (SA13-ST5-30G, SA13-ST6-40G, SA13-ST8-47G) were in the same range, with even less variation down-core. In the core from the Eastern Equatorial Pacific (ODP Leg 201, Hole 1,226-B), the fermenters and the terminal oxidizers shared the energy in a similar manner with -42 to -43 kJ (mol C)$^{-1}$ for the fermenters and -35 to -26 kJ (mol C)$^{-1}$ for the sulfate reducers. Similar values of -42.9 ± 2.7 kJ mol acetate^{-1} have previously been reported for sulfate reduction coupled to acetate oxidation for most of the sediment column at ODP Site 1226 (Wang et al., 2010), and -32 kJ mol C^{-1} for global marine sediments in general (Bradley et al., 2020).

The assumptions and approximations in the thermodynamic calculations above were coarse. Most notably the assumed temperature of 25°C, while the effects of the pressure between one bar and *in situ* were negligible (Helgeson, 1969). But effects of pressure and temperature on thermodynamic calculations are much less severe than the effects on kinetics (Jannasch, 1997), and even the temperature effect does not influence the conclusions drawn here: The standard Gibbs energy of sulfate reduction per mole acetate, for example, only change from -48.1 to -44.5 kJ (mol acetate)$^{-1}$ between reference temperature and pressure (25°C, 1 bar) and *in situ* conditions (2°C, 50 bar) at the Greenlandic sites. Thus, the coarse calculations still allow us to conclude that ΔG_r from mineralization of organic carbon to CO_2 was shared between the guilds of fermenters and terminal oxidizers in a ratio of roughly 1:1 regardless of site and sediment age. Since the fermentation products do not accumulate in the sediment, there must be a balance between fermentation and sulfate reduction, whereby rates of fermentation limit and control the rates of sulfate reduction (Jørgensen, 2021). Thus, the carbon flow through fermentation must be similar to the carbon flow through sulfate reduction. As non-sulfate-reducing bacteria outnumbered the sulfate reducers by >100-fold, the energy dissipation (i.e., power) available to the individual fermenters was much lower than the power available to the individual sulfate reducers.

Volume-specific power of reactions in the sediment (Watt cm^{-3} or Joule s^{-1} cm^{-3}) was calculated by multiplying ΔG_r of the reaction (J mol^{-1}\C) by the rates of reaction (mol C cm^{-3} s^{-1}). The mean cell-specific sulfate reduction rates in the Greenland cores were in the order of 10^{-2} fmol C cell^{-1} day^{-1}, which was not far outside the range from 10^{-1} to 10^{1} fmol C cell^{-1} day^{-1} seen in cultures of mesophilic and psychrophilic sulfate-reducing bacteria (Canfield et al., 2000). The 10^{-2} fmol C cell^{-1} day^{-1} translates to a power dissipation of 10^{-17} W cell^{-1} if we assume an energetic yield of -42 kJ (mol C)$^{-1}$ (see above and note that J/s equals W). This rate of energy dissipation is similar to the value calculated for coastal surface sediments by Lever et al. (2015), and similar to the per-cell power dissipation in slow-growing axenic cultures of *Desulfotomaculum putei* (Davidson et al., 2009). It is also similar to the power dissipation of extremely low-light adapted green sulfur bacteria in the Black Sea (1.9×10^{-17} W cell^{-1}; Marschall et al., 2010). Conversely, the values are far above the per-cell power dissipation calculated for deeply buried sulfate reducers on the Peru Margin by Lever et al. (2015), even though our estimation of the carbon oxidation rates in the same deep Pacific sediment based on NH_4^+ agrees well with calculations based on sulfate (Wang et al., 2008). The difference between our relatively high and invariant estimate of power dissipation by deeply buried sulfate reducers, and the low and age-dependent power dissipation reported by Lever et al. (2015) is that these authors assumed a constant 10% proportion of sulfate-reducing microorganisms (see above). The fact that the power dissipation we calculated per sulfate-reducing cell did not continue to drop with depth and age in the sediment, is because the estimated number of sulfate reducers decreased in near perfect balance with the decrease in sulfate reduction rates. This could indicate that 10^{-17} W cell^{-1} approaches a minimum power requirement of sulfate reducers in deeply buried sediments. As the same range of power dissipation can be observed only 30 cm below the sediment–water interface in eutrophic coastal sediments and in axenic cultures, this suggests that the sulfate reducers in the deep biosphere do not necessarily have any unique physiological adaptations to low energy availability.

The cell-specific power dissipation of extremely old oxic sediments has been calculated to 5×10^{-18} W cell^{-1} in the North Pacific Gyre, and within the range from 3.5×10^{-18} down to 4.9×10^{-20} in the South Pacific Gyre (LaRowe and Amend, 2015a). These calculations assume an energetic yield of -443 kJ (mol C)$^{-1}$ for aerobic oxidation of organic matter all the way to CO_2 in a single step (Lever et al., 2015). The low values from the SPG were calculated based on an assumed constant rate of carbon burial across the 75 million years and is, most likely, less accurate than the data from the North Pacific Gyre (NPG) that was based directly on modelled oxygen consumption rates (Røy et al., 2012). Thus, the apparent maintenance power of aerobic and anaerobic respiration come within one order of magnitude of each other. And in contrast to the per cell power dissipation of the "fermenters" (or the total carbon oxidation per total cells), both aerobic and anaerobic respiration appears to converge at fixed rates of per cell power dissipation rather than dropping continuously with increasing sediment age. The difference in the two levels is not understood, as the higher energetic cost of biomolecule synthesis aerobes (McCollom and Amend, 2005) would suggest that the minimum maintenance power of aerobes should be larger than that of anaerobes.

It is possible to estimate the power dissipation by the guild of fermenters in the deep sulfatic sediments older than 26,000 years that we studied, even though the proportion of fermenters vs. terminal oxidizers was not known. This is because the number of fermenters is essentially equal to the total cell numbers, only offset by 1% sulfate reducers or less. In contrast to the situation for sulfate reducers, the per cell power dissipation for the fermenters did not reach a plateau that could indicate a minimum power requirement of fermenting cells, although such a limit must exist. The lowest values reached in our dataset was 7×10^{-22} W cell^{-1}. This rate of power dissipation is so low that the cells would just barely cover the lowest estimate of the repair cost associated with spontaneous racemization of aspartic acid

(Lever et al., 2015). But there are no indications in the data that 10^{-6} fmol C cell^{-1} d^{-1}, corresponding to 10^{-22} W cell^{-1} is the lower limit, it is simply where our dataset ends. In principle, the correlation could extend further back in time. But extrapolation of log–log plots back in time from 4 million years would rapidly reach the age of Planet Earth.

In conclusion, we found that the population size of sulfate-reducing microorganisms was in balance with the rate of sulfate reduction in sub-surface sediments. The minimum per-cell sulfate reduction rate, and thus the minimum per cell power dissipation, in 10,000 to 100,000 years old sediment was not radically different from the much shallower sub-surface. Thus, we do not expect sulfate reducers in the deep subsurface to have a fundamentally different maintenance metabolism compared to organisms thriving less than 1 m below the seafloor in coastal seas (Starnawski et al., 2017). We did not see a lower threshold for metabolic activity of cells not involved in terminal oxidation, although there was a clear log–log correlation between the total number of cells and the rate of carbon mineralization. It is unknown which physiological properties make the fermenters able to apparently subside with a minute fraction of the power needed for sulfate reducers. The large number of cells relative to the extremely low rates of mineralization in the deep biosphere therefore remain enigmatic.

Data availability statement

The original contributions presented in the study are included in the article/Supplementary material, further inquiries can be directed to the corresponding author.

Author contributions

HR and BJ designed the study. HR, CP, M-SS, BL, KK, and MJ retrieved the cores and collected pore water and the solid phase samples. MJ performed geochemical, microbiological analyses, and thermodynamic estimations. KK supervised the molecular work. M-SS, and CP built the age models. MJ and HR wrote the manuscript. All authors contributed with comments, corrections, and discussions.

Funding

This work was supported by the Graduate School of Science and Technology at Aarhus University, the Danish National Research Foundation [n° DNRF104], the European Research Council, EU FP7 ERC Advanced Grant (n° 294200, MICROENERGY). Cruise funding was provided by the Danish Center for Marine Research and the Arctic Research Centre of Aarhus University. M-SS was supported through the European Union's Horizon 2020 research and innovation program under grant agreement no. 869383 (ECOTIP) (M-SS) and the Independent Research Fund Denmark (grant no. 0135-00165B GreenShelf).

Acknowledgments

We thank Karina Bomholt Oest, Trine Bech Søgaard, Jeanette Pedersen, Trine Ravn-Jonsen and Lykke B. Poulsen for assistance in the laboratory. The captain and the crew of R/V Sanna, R/V Dana, R/V Aurora, and participants of these cruises for assistance in the field. We thank Yuki Morono and team for the help with flow cytometry and hosting in Japan, Jens Kallmeyer for sharing cell abundance in site U1342, Clemens Glombitza for thoughtful discussions on thermodynamics, Nils Risgaard-Petersen for help with the depth scale in site U1342, and Fatima Abrantes for compiling the age model from the Azores core. Finally, we thank two reviewers for thorough and constructive reviews that helped improve the manuscript.

Conflict of interest

The authors declare that the research was conducted in the absence of any commercial or financial relationships that could be construed as a potential conflict of interest.

Publisher's note

Supplementary material

The Supplementary material for this article can be found online at: https://www.frontiersin.org/articles/10.3389/fmicb.2023.1198664/full#supplementary-material

References

Allan, E., de Vernal, A., Seidenkrantz, M. S., Briner, J. P., Hillaire-Marcel, C., Pearce, C., et al. (2021). Insolation vs. meltwater control of productivity and sea surface conditions off SW Greenland during the Holocene. *Boreas* 50, 631–651. doi: 10.1111/bor.12514

Andrén, T., Jørgensen, B. B., Cotterill, C., and Green, S.IODP expedition 347 scientific party (2015). IODP expedition 347: Baltic Sea basin paleoenvironment and biosphere. *Sci. Drill.* 20, 1–12. doi: 10.2204/iodp.proc.347.2015

Arndt, S., Jørgensen, B. B., LaRowe, D. E., Middelburg, J. J., Pancost, R. D., and Regnier, P. (2013). Quantifying the degradation of organic matter in marine sediments: a review and synthesis. *Earth Sci. Rev.* 123, 53–86. doi: 10.1016/j.earscirev.2013.02.008

Berg, P., Risgaard-Petersen, N., and Rysgaard, S. (1998). Interpretation of measured concentration profiles in sediment pore water. *Limnol. Oceanogr.* 43, 1500–1510. doi: 10.4319/lo.1998.43.7.1500

Beulig, F., Røy, H., Glombitza, C., and Jørgensen, B. B. (2018). Control on rate and pathway of anaerobic organic carbon degradation in the seabed. *Proc. Natl. Acad. Sci. U. S. A.* 115, 367–372. doi: 10.1073/pnas.1715789115

Beulig, F., Schubert, F., Adhikari, R. R., Glombitza, C., Heuer, V. B., Hinrichs, K. U., et al. (2022). Rapid metabolism fosters microbial survival in the deep, hot subseafloor biosphere. *Nat. Commun.* 13:312. doi: 10.1038/s41467-021-27802-7

Biddle, J. F., Fitz-Gibbon, S., Schuster, S. C., Brenchley, J. E., and House, C. H. (2008). Metagenomic signatures of the Peru Margin subseafloor biosphere show a genetically distinct environment. *Proc. Natl. Acad. Sci. U. S. A.* 105, 10583–10588. doi: 10.1073/pnas.0709942105

Biddle, J. F., Lipp, J. S., Lever, M. A., Lloyd, K. G., Sørensen, K. B., Anderson, R., et al. (2006). Heterotrophic *Archaea* dominate sedimentary subsurface ecosystems off Peru. *Proc. Natl. Acad. Sci. U. S. A.* 103, 3846–3851. doi: 10.1073/pnas.0600035103

Boudreau, B.P. (1996). *Diagenetic models and their implementation: modelling transport and reactions in aquatic sediments*. Springer-Verlag, Berlin, Germany.

Boudreau, B. P., and Ruddick, B. R. (1991). On a reactive continuum representation of organic matter diagenesis. *Am. J. Sci.* 291, 507–538. doi: 10.2475/ajs.291.5.507

Bower, C. E., and Holm-Hansen, T. (1980). A salicylate-hypochlorit method for determining ammonia in seawater. *Can. J. Fish. Aquat. Sci.* 37, 794–798. doi: 10.1139/f80-106

Bradley, J. A., Arndt, S., Amend, J. P., Burwicz, E., Dale, A. W., Egger, M., et al. (2020). Widespread energy limitation to life in global subseafloor sediments. *Sci. Adv.* 6, eaba0697–eaba0699. doi: 10.1126/sciadv.aba0697

Braun, S., Mhatre, S. S., Jaussi, M., Røy, H., Kjeldsen, K. U., Pearce, C., et al. (2017). Microbial turnover times in the deep seabed studied by amino acid racemization modelling. *Sci. Rep.* 7:5680. doi: 10.1038/s41598-017-05972-z

Brinton, K. L. F., Tsapin, A. I., Gilichinsky, D., and McDonald, G. D. (2002). Aspartic acid racemization and age–depth relationships for organic carbon in Siberian permafrost. *Astrobiology* 2, 77–82. doi: 10.1089/153110702753621358

Canfield, D. E., Habicht, K. S., and Thamdrup, B. (2000). The Archean sulfur cycle and the early history of atmospheric oxygen. *Science* 288, 658–661. doi: 10.1126/science.288.5466.658

Canfield, D. E., and Thamdrup, B. (2009). Towards a consistent classification scheme for geochemical environments, or, why we wish the term 'suboxic' would go away. *Geobiology* 7, 385–392. doi: 10.1111/j.1472-4669.2009.00214.x

Christensen, D., and Blackburn, T. H. (1982). Turnover of C-14-labeled acetate in marine-sediments. *Mar. Biol.* 71, 113–119. doi: 10.1007/Bf00394618

Croudace, I. W., Rindby, A., and Rothwell, R. G. (2006). "ITRAX: description and evaluation of a new multi-function X-ray core scanner" in *New techniques in sediment Core Analysis*. ed. R. G. Rothwell, vol. *267* (London, UK: Geological Society of London), 51–63.

Davidson, M. M., Bisher, M. E., Pratt, L. M., Fong, J., Southam, G., Pfiffner, S. M., et al. (2009). Sulfur isotope enrichment during maintenance metabolism in the thermophilic sulfate reducing bacterium *Desulfotomaculum putei*. *Appl. Environ. Microbiol.* 75, 5621–5630. doi: 10.1128/AEM.02948-08

Deng, L. H., Bolsterli, D., Kristensen, E., Meile, C., Su, C. C., Bernasconi, S. M., et al. (2020). Macrofaunal control of microbial community structure in continental margin sediments. *Proc. Natl. Acad. Sci. U. S. A.* 117, 15911–15922. doi: 10.1073/pnas.1917494117

D'Hondt, S., Jørgensen, B. B., Miller, D. J., Batzke, A., Blake, R., Cragg, B. A., et al. (2004). Distributions of microbial activities in deep subseafloor sediments. *Science* 306, 2216–2221. doi: 10.1126/science.1101155

Estes, E. R., Pockalny, R., D'Hondt, S., Inagaki, F., Morono, Y., Murray, R. W., et al. (2019). Persistent organic matter in oxic subseafloor sediment. *Nat. Geosci.* 12, 783–784. doi: 10.1038/s41561-019-0423-6

Expedition 323 Scientists (2011). "Site U1342" in *Proceeding IODP, 323*. eds. K. Takahashi, A. C. Ravelo and C. A. Alvarez Zarikian, and the Expedition 323 Scientists (Tokyo, Integrated Ocean Drilling Program Management International, Inc), 1–71.

Finke, N., Vandieken, V., and Jørgensen, B. B. (2007). Acetate, lactate, propionate, and isobutyrate as electron donors for iron and sulfate reduction in Arctic marine sediments, Svalbard. *FEMS Microbiol. Ecol.* 59, 10–22. doi: 10.1111/j.1574-6941.2006.00214.x

Flury, S., Røy, H., Dale, A. W., Fossing, H., Toth, Z., Spiess, V., et al. (2016). Controls on subsurface methane fluxes and shallow gas formation in Baltic Sea sediment (Aarhus Bay, Denmark). *Geochim. Cosmochim. Acta* 188, 297–309. doi: 10.1016/j.gca.2016.05.037

Gaboyer, F., Burgaud, G., and Alain, K. (2015). Physiological and evolutionary potential of microorganisms from the Canterbury Basin subseafloor, a metagenomic approach. *FEMS Microbiol. Ecol.* 91:91. doi: 10.1093/femsec/fiv029

Glombitza, C., Adhikari, R. R., Riedinger, N., Gilhooly, W. P. III, Hinrichs, K.-U., and Inagaki, F. (2016). Microbial sulfate reduction potential in coal-bearing sediments down to ~ 2.5 km below the seafloor off Shimokita Peninsula, Japan. *Front. Microbiol.* 7:1576. doi: 10.3389/fmicb.2016.01576

Glombitza, C., Egger, M., Røy, H., and Jørgensen, B. B. (2019). Controls on volatile fatty acid concentrations in marine sediments (Baltic Sea). *Geochim. Cosmochim. Acta* 258, 226–241. doi: 10.1016/j.gca.2019.05.038

Glombitza, C., Jaussi, M., Røy, H., Seidenkrantz, M.-S., Lomstein, B. A., and Jørgensen, B. B. (2015). Formate, acetate and propionate as substrates for sulfate reduction in sub-arctic sediments of Southwest Greenland. *Front. Microbiol.* 6:846. doi: 10.3389/fmicb.2015.00846

Glombitza, C., Pedersen, J., Røy, H., and Jørgensen, B. B. (2014). Direct analysis of volatile fatty acids in marine sediment porewater by two-dimensional ion chromatography-mass spectrometry. *Limnol. Oceanogr. Methods* 12, 455–468. doi: 10.4319/lom.2014.12.455

Hach, P. F., Marchant, H. K., Krupke, A., Riedel, T., Meier, D. V., Lavik, G., et al. (2020). Rapid microbial diversification of dissolved organic matter in oceanic surface waters leads to carbon sequestration. *Sci. Rep.* 10:13025. doi: 10.1038/s41598-020-69930-y

Helgeson, H. C. (1969). Thermodynamics of hydrothermal systems at elevated temperatures and pressures. *Am. J. Sci.* 267, 729–804. doi: 10.2475/ajs.267.7.729

Hoehler, T. M., and Jørgensen, B. B. (2013). Microbial life under extreme energy limitation. *Nat. Rev. Microbiol.* 11, 83–94. doi: 10.1038/nrmicro2939

Jannasch, H. W. (1997). Small is powerful: recollections of a microbiologist and oceanographer. *Annu. Rev. Microbiol.* 51, 1–45. doi: 10.1146/annurev.micro.51.1.1

Jochum, L. M., Chen, X. H., Lever, M. A., Loy, A., Jørgensen, B. B., Schramm, A., et al. (2017). Depth distribution and assembly of sulfate reducing microbial communities in marine sediments of Aarhus Bay. *Appl. Environ. Microbiol.* 83:e01547–17. doi: 10.1128/AEM.01547-17

Jørgensen, B. B. (1978a). A comparison of methods for the quantification of bacterial sulfate reduction in coastal marine sediments. I. Measurement with radiotracer techniques. *Geomicrobiol. J.* 1, 11–27. doi: 10.1080/01490457809377721

Jørgensen, B. B. (1978b). A comparison of methods for the quantification of bacterial sulfate reduction in coastal marine sediments. II. Calculation from mathematical models. *Geomicrobiol. J.* 1, 29–47. doi: 10.1080/01490457809377722

Jørgensen, B. B. (2021). Sulfur biogeochemical cycle of marine sediments. *Geochem. Perspect.* 10, 145–307. doi: 10.7185/geochempersp.10.2

Jørgensen, B. B., D'Hondt, S. L., and Miller, D. J. (2006). Leg 201 synthesis: controls on microbial communities in deeply buried *sediments*, Ocean Drill. *Prog. Sci. Results* 201, 1–45.

Jørgensen, B. B., and Fenchel, T. (1974). The sulfur cycle of a marine sediment model system. *Mar. Biol.* 24, 189–201. doi: 10.1007/BF00391893

Jørgensen, B. B., and Parkes, R. J. (2010). Role of sulfate reduction and methane production by organic carbon degradation in eutrophic fjord sediments (Limfjorden, Denmark). *Limnol. Oceanogr.* 55, 1338–1352. doi: 10.4319/lo.2010.55.3.1338

Kallmeyer, J., Ferdelman, T. G., Weber, A., Fossing, H., and Jørgensen, B. B. (2004). A cold chromium distillation procedure for radiolabeled sulfide applied to sulfate reduction measurements. *Limnol. Oceanogr. Methods* 2, 171–180. doi: 10.4319/lom.2004.2.171

Kallmeyer, J., Pockalny, R., Adhikari, R. R., Smith, D. C., and D'Hondt, S. (2012). Global distribution of microbial abundance and biomass in subseafloor sediment. *Proc. Natl. Acad. Sci. U. S. A.* 109, 16213–16216. doi: 10.1073/pnas.1203849109

Kallmeyer, J., Smith, D. C., Spivack, A. J., and D'Hondt, S. (2008). New cell extraction procedure applied to deep subsurface sediments. *Limnol. Oceanogr. Methods* 6, 236–245. doi: 10.4319/lom.2008.6.236

Katsev, S., and Crowe, S. A. (2015). Organic carbon burial efficiencies in sediments: the power law of mineralization revisited. *Geology* 43, 607–610. doi: 10.1130/G36626.1

Kirchman, D. L., Hanson, T. E., Cottrell, M. T., and Hamdan, L. J. (2014). Metagenomic analysis of organic matter degradation in methane-rich Arctic Ocean sediments. *Limnol. Oceanogr.* 59, 548–559. doi: 10.4319/lo.2014.59.2.0548

Kjeldsen, K. U., Loy, A., Jakobsen, T. F., Thomsen, T. R., Wagner, M., and Ingvorsen, K. (2007). Diversity of sulfate reducing bacteria from an extreme hypersaline sediment, Great Salt Lake (Utah). *FEMS Microbiol. Ecol.* 60, 287–298. doi: 10.1111/j.1574-6941.2007.00288.x

Knudson, K. P., and Ravelo, A. C. (2015). North Pacific intermediate water circulation enhanced by the closure of the bering strait. *Paleoceanography* 30, 1287–1304. doi: 10.1002/2015PA002840

Komada, T., Burdige, D. J., Crispo, S. M., Druffel, E. R. M., Griffin, S., Johnson, L., et al. (2013). Dissolved organic carbon dynamics in anaerobic sediments of the Santa Monica Basin. *Geochim. Cosmochim. Acta* 110, 253–273. doi: 10.1016/j.gca.2013.02.017

Kotthoff, U., Groeneveld, J., Ash, J., Fanget, A. S., Krupinski, N., Peyron, O., et al. (2017). Reconstructing Holocene temperature and salinity variations in the western Baltic Sea region: a multi-proxy comparison from the Little Belt (IODP Expedition 347, Site M0059). *Biogeosciences* 14, 5607–5632. doi: 10.5194/bg-14-5607-2017

Kristensen, E., Røy, H., Debrabant, K., and Valdemarsen, T. (2018). Carbon oxidation and bioirrigation in sediments along a Skagerrak-Kattegat-Belt Sea depth transect. *Mar. Ecol. Prog. Ser.* 604, 33–50. doi: 10.3354/meps12734

Kulik, D. A., and Harff, J. (1993). Physicochemical modelling of the Baltic Sea eater-sediment column: I. reference ion-association models of normative seawater and of Baltic Sea brackish waters at salinities 1–40‰, 1 bar total pressure and 0 to 30°C temperature (system Na-Mg-Ca-K-Sr-Li-Rb-Cl-S-C-Br-F-B-N-Si-P-H-O). *Meerwisserschaftliche Berichte Warnemünde* 6, 1–80.

Kuzyk, Z. A., Macdonald, R. W., and Johannessen, S. C. (2015). "Calculating rates and dates and interpreting contaminant profiles in biomixed sediments" in *Environmental contaminants: Using natural archives to track sources and long-term trends of pollution*. eds. J. M. Blais, M. R. Rosen and J. P. E. Smol (Dordrecht: Springer), 547.

LaRowe, D., and Amend, J. (2015a). Power limits for microbial life. *Front. Microbiol.* 6:718. doi: 10.3389/fmicb.2015.00718

LaRowe, D. E., and Amend, J. P. (2015b). Catabolic rates, population sizes and doubling/replacement times of microorganisms in natural settings. *Am. J. Sci.* 315, 167–203. doi: 10.2475/03.2015.01

LaRowe, D. E., and Van Cappellen, P. (2011). Degradation of natural organic matter: a thermodynamic analysis. *Geochim. Cosmochim. Acta* 75, 2030–2042. doi: 10.1016/j.gca.2011.01.020

Lavelle, J.W., Massoth, G.J., and Crecelius, E.A. (1985). "*Sedimentation rates in Puget Sound from* ^{210}*Pb measurements*". Pacific Marine Environmental Laboratory, Seattle, WA.

Leloup, J., Fossing, H., Kohls, K., Holmkvist, L., Borowski, C., and Jørgensen, B. B. (2009). Sulfate reducing bacteria in marine sediment (Aarhus Bay, Denmark): abundance and diversity related to geochemical zonation. *Environ. Microbiol.* 11, 1278–1291. doi: 10.1111/j.1462-2920.2008.01855.x

Leloup, J., Loy, A., Knab, N. J., Borowski, C., Wagner, M., and Jørgensen, B. B. (2007). Diversity and abundance of sulfate reducing microorganisms in the sulfate and methane zones of a marine sediment, Black Sea. *Environ. Microbiol.* 9, 131–142. doi: 10.1111/j.1462-2920.2006.01122.x

Lever, M. A. (2013). Functional gene surveys from ocean drilling expeditions – a review and perspective. *FEMS Microbiol. Ecol.* 84, 1–23. doi: 10.1111/1574-6941.12051

Lever, M. A., Rogers, K. L., Lloyd, K. G., Overmann, J., Schink, B., Thauer, R. K., et al. (2015). Life under extreme energy limitation: a synthesis of laboratory- and field-based investigations. *FEMS Microbiol. Rev.* 39, 688–728. doi: 10.1093/femsre/fuv020

Lisiecki, L. E., and Raymo, M. E. (2005). A Pliocene-Pleistocene stack of 57 globally distributed benthic δ^{18}O records. *Paleoceanography* 20:PA1003. doi: 10.1029/2004PA001071

Lomstein, B. A., Langerhuus, A. T., D'Hondt, S., Jørgensen, B. B., and Spivack, A. J. (2012). Endospore abundance, microbial growth and necromass turnover in deep sub-seafloor sediment. *Nature* 484, 101–104. doi: 10.1038/nature10905

Marschall, E., Jogler, M., Henßge, U., and Overmann, J. (2010). Large-scale distribution and activity patterns of an extremely low-light-adapted population of green sulfur bacteria in the Black Sea. *Environ. Microbiol.* 12, 1348–1362. doi: 10.1111/j.1462-2920.2010.02178.x

McCollom, T. M., and Amend, J. P. (2005). A thermodynamic assessment of energy requirements for biomass synthesis by chemolithoautotrophic micro-organisms in oxic and anoxic environments. *Geobiology* 3, 135–144. doi: 10.1111/j.1472-4669.2005.00045.x

Mhatre, S. S., Kaufmann, S., Marshall, I. P. G., Obrochta, S., Andren, T., Jørgensen, B. B., et al. (2019). Microbial biomass turnover times and clues to cellular protein repair in energy-limited deep Baltic Sea sediments. *FEMS Microbiol. Ecol.* 6. doi: 10.1093/femsec/fiz068

Middelburg, J. J. (1989). A simple rate model for organic matter decomposition in marine sediments. *Geochim. Cosmochim. Acta* 53, 1577–1581. doi: 10.1016/0016-7037(89)90239-1

Morono, Y., Terada, T., Kallmeyer, J., and Inagaki, F. (2013). An improved cell separation technique for marine subsurface sediments: applications for high-throughput analysis using flow cytometry and cell sorting. *Environ. Microbiol.* 15, 2841–2849. doi: 10.1111/1462-2920.12153

Onstott, T. C., Magnabosco, C., Aubrey, A. D., Burton, A. S., Dworkin, J. P., Elsila, J. E., et al. (2014). Does aspartic acid racemization constrain the depth limit of the subsurface biosphere? *Geobiology* 12, 1–19. doi: 10.1111/gbi.12069

Orme, L. C., Miettinen, A., Divine, D., Husum, K., Pearce, C., Van Nieuwenhove, N., et al. (2018). Subpolar North Atlantic Sea surface temperature since 6 ka BP: indications of anomalous ocean-atmosphere interactions at 4-2 ka BP. *Quat. Sci. Rev.* 194, 128–142. doi: 10.1016/j.quascirev.2018.07.007

Orsi, W. D., Edgcomb, V. P., Christman, G. D., and Biddle, J. F. (2013). Gene expression in the deep biosphere. *Nature* 499, 205–208. doi: 10.1038/nature12230

Orsi, W. D., Jørgensen, B. B., and Biddle, J. F. (2016). Transcriptional analysis of sulfate reducing and chemolithoautotrophic sulfur oxidizing bacteria in the deep subseafloor. *Environ. Microbiol. Reports* 8, 452–460. doi: 10.1111/1758-2229.12387

Orsi, W. D., Schink, B., Buckel, W., and Martin, W. F. (2020). Physiological limits to life in anoxic subseafloor sediment. *FEMS Microbiol. Rev.* 44, 219–231. doi: 10.1093/femsre/fuaa004

Parkes, R. J., Webster, G., Cragg, B. A., Weightman, A. J., Newberry, C. J., Ferdelman, T. G., et al. (2005). Deep sub-seafloor prokaryotes stimulated at interfaces over geological time. *Nature* 436, 390–394. doi: 10.1038/nature03796

Pelikan, C., Jaussi, M., Wasmund, K., Seidenkrantz, M. S., Pearce, C., Kuzyk, Z. Z. A., et al. (2019). Glacial runoff promotes deep burial of sulfur cycling-associated microorganisms in marine sediments. *Front. Microbiol.* 10:2558. doi: 10.3389/fmicb.2019.02558

Petro, C., Zancker, B., Stamawski, P., Jochum, L. M., Ferdelman, T. G., Jørgensen, B. B., et al. (2019). Marine deep biosphere microbial communities assemble in near-surface sediments in Aarhus Bay. *Front. Microbiol.* 10:758. doi: 10.3389/fmicb.2019.00758

Postma, D., and Jakobsen, R. (1996). Redox zonation: equilibrium constraints on the Fe(III)/SO4-reduction interface. *Geochim. Cosmochim. Acta* 60, 3169–3175. doi: 10.1016/0016-7037(96)00156-1

R Core Team (2013). *R: A language and environment for statistical computing [Online]* Vienna, Austria: R Foundation for Statistical Computing

Reimer, P. J., Bard, E., Bayliss, A., Beck, J. W., Blackwell, P. G., Ramsey, C. B., et al. (2013). IntCal13 and Marine13 radiocarbon age calibration curves 0–50,000 years cal BP. *Radiocarbon* 55, 1869–1887. doi: 10.2458/azu_js_rc.55.16947

Riedel, T. E., Berelson, W. M., Nealson, K. H., and Finkel, S. E. (2013). Oxygen consumption rates of bacteria under nutrient-limited conditions. *Appl. Environ. Microbiol.* 79, 4921–4931. doi: 10.1128/Aem.00756-13

Robador, A., Amend, J. P., and Finkel, S. E. (2019). Nanocalorimetry reveals the growth dynamics of *Escherichia coli* cells undergoing adaptive evolution during long-term stationary phase. *Appl. Environ. Microbiol.* 15:e00968–19 doi: 10.1128/AEM.00968-19

Røy, H., Kallmeyer, J., Adhikari, R. R., Pockalny, R., Jørgensen, B. B., and D'Hondt, S. (2012). Aerobic microbial respiration in 86-million-year-old deep-sea red clay. *Science* 336, 922–925. doi: 10.1126/science.1219424

Røy, H., Weber, H. S., Tarpgaard, I. H., Ferdelman, T. G., and Jørgensen, B. B. (2014). Determination of dissimilatory sulfate reduction rates in marine sediment via radioactive 35S tracer. *Limnol. Oceanogr. Methods* 12, 196–211. doi: 10.4319/lom.2014.12.196

Schippers, A., and Neretin, L. N. (2006). Quantification of microbial communities in near-surface and deeply buried marine sediments on the Peru continental margin using real-time PCR. *Environ. Microbiol.* 8, 1251–1260. doi: 10.1111/j.1462-2920.2006.01019.x

Shang, H. T. (2023). A generic hierarchical model of organic matter degradation and preservation in aquatic systems. *Commun. Earth Environ.* 16. doi: 10.1038/s43247-022-00667-4

Shipboard Scientific Party (1992). "SITE 846" in *Ocean drilling program. Initial reports*. eds. L. Mayer, N. Pisias and T. Janeceket al. (College Station, TX: Ocean Drilling Program)

Shipboard Scientific Party (2003). "7. SITE 1226" in *Ocean drilling program. Initial reports*. eds. S. L. D'Hondt, B. B. Jørgensen and D. J. Miller (College Station, TX: Texas A&M University, Ocean Drilling Program) 77845–9547, United States, 1–96.

Starnawski, P., Bataillon, T., Ettema, T. J. G., Jochum, L. M., Schreiber, L., Chen, X., et al. (2017). Microbial community assembly and evolution in subseafloor sediment. *Proc. Natl. Acad. Sci. U. S. A.* 114, 2940–2945. doi: 10.1073/pnas.1614190114

Suna, D.-L., Jianga, X., Wub, Q. L., and Zhoua, N.-Y. (2013). Intragenomic heterogeneity of 16S rRNA genes causes overestimation of prokaryotic diversity. *Appl. Environ. Microbiol.* 79, 5962–5969. doi: 10.1128/AEM.01282-13

Takahashi, K., Ravelo, A. C., and Alvarez Zarikian, C. A.the Expedition 323 Scientists (2011). Expedition 323 summary. *Proc. Integr. Ocean Drill. Progr.* 323, 1–53. doi: 10.2204/iodp.proc.323.101.2011

Van Nieuwenhove, N., Pearce, C., Knudsen, M. F., Røy, H., and Seidenkrantz, M. S. (2018). Meltwater and seasonality influence on Subpolar Gyre circulation during the Holocene. *Palaeogeogr. Palaeoclimatol. Palaeoecol.* 502, 104–118. doi: 10.1016/j.palaeo.2018.05.002

Wang, G., Arthur, J., Spivack, Rutherford, S., Manor, U., and D'Hondt, S. (2006). Quantification of co-occurring reaction rates in deep subseafloor sediments. *Geochimica et Cosmochimica Acta* 72, 3479–3488. doi: 10.1016/j.gca.2008.04.024

Wang, G. Z., Spivack, A. J., and D'Hondt, S. (2010). Gibbs energies of reaction and microbial mutualism in anaerobic deep subseafloor sediments of ODP Site 1226. *Geochim. Cosmochim. Acta* 74, 3938–3947. doi: 10.1016/j.gca.2010.03.034

Wang, G., Spivack, A. J., Rutherford, S., Manor, U., and D'Hondt, S. (2008). Quantification of co-occurring reaction rates in deep subseafloor sediments. *Geochim. Cosmochim. Acta* 72, 3479–3488. doi: 10.1016/j.gca.2008.04.024

Webster, G., Parkes, R. J., Cragg, B. A., Newberry, C. J., Weightman, A. J., and Fry, J. C. (2006). Prokaryotic community composition and biogeochemical processes in deep subseafloor sediments from the Peru Margin. *FEMS Microbiol. Ecol.* 58, 65–85. doi: 10.1111/j.1574-6941.2006.00147.x

Wehrmann, L. M., Risgaard-Petersen, N., Schrum, H. N., Walsh, E. A., Huh, Y., Ikehara, M., et al. (2011). Coupled organic and inorganic carbon cycling in the deep subseafloor sediment of the northeastern Bering Sea Slope (IODP Exp. 323). *Chem. Geol.* 284, 251–261. doi: 10.1016/j.chemgeo.2011.03.002

Whitman, W. B., Coleman, D. C., and Wiebe, W. J. (1998). Prokaryotes: the unseen majority. *Proc. Natl. Acad. Sci. U. S. A.* 95, 6578–6583. doi: 10.1073/pnas.95.12.6578

Frontiers in Microbiology

TYPE Original Research
PUBLISHED 26 July 2023
DOI 10.3389/fmicb.2023.1206641

OPEN ACCESS

EDITED BY
William J. Brazelton,
The University of Utah, United States

REVIEWED BY
Marco J. L. Coolen,
Curtin University, Australia
Elizabeth Trembath-Reichert,
Arizona State University, United States

*CORRESPONDENCE
Georges Kanaan
✉ gkanaan@uw.edu

RECEIVED 16 April 2023
ACCEPTED 06 July 2023
PUBLISHED 26 July 2023

CITATION
Kanaan G, Hoehler TM, Iwahana G and Deming JW (2023) Modeled energetics of bacterial communities in ancient subzero brines.
Front. Microbiol. 14:1206641.
doi: 10.3389/fmicb.2023.1206641

Modeled energetics of bacterial communities in ancient subzero brines

Georges Kanaan[1]*, Tori M. Hoehler[2], Go Iwahana[3] and Jody W. Deming[1]

[1]School of Oceanography and Astrobiology Program, University of Washington, Seattle, WA, United States, [2]NASA Ames Research Center, Moffett Field, CA, United States, [3]International Arctic Research Center, University of Alaska Fairbanks, Fairbanks, AK, United States

Cryopeg brines are isolated volumes of hypersaline water in subzero permafrost. The cryopeg system at Utqiaġvik, Alaska, is estimated to date back to 40 ka BP or earlier, a remnant of a late Pleistocene Ocean. Surprisingly, the cryopeg brines contain high concentrations of organic carbon, including extracellular polysaccharides, and high densities of bacteria. How can these physiologically extreme, old, and geologically isolated systems support such an ecosystem? This study addresses this question by examining the energetics of the Utqiaġvik cryopeg brine ecosystem. Using literature-derived assumptions and new measurements on archived borehole materials, we first estimated the quantity of organic carbon when the system formed. We then considered two bacterial growth trajectories to calculate the lower and upper bounds of the cell-specific metabolic rate of these communities. These bounds represent the first community estimates of metabolic rate in a subzero hypersaline environment. To assess the plausibility of the different growth trajectories, we developed a model of the organic carbon cycle and applied it to three borehole scenarios. We also used dissolved inorganic carbon and nitrogen measurements to independently estimate the metabolic rate. The model reconstructs the growth trajectory of the microbial community and predicts the present-day cell density and organic carbon content. Model input included measured rates of the *in-situ* enzymatic conversion of particulate to dissolved organic carbon under subzero brine conditions. A sensitivity analysis of model parameters was performed, revealing an interplay between growth rate, cell-specific metabolic rate, and extracellular enzyme activity. This approach allowed us to identify plausible growth trajectories consistent with the observed bacterial densities in the cryopeg brines. We found that the cell-specific metabolic rate in this system is relatively high compared to marine sediments. We attribute this finding to the need to invest energy in the production of extracellular enzymes, for generating bioavailable carbon from particulate organic carbon, and the production of extracellular polysaccharides for cryoprotection and osmoprotection. These results may be relevant to other isolated systems in the polar regions of Earth and to possible ice-bound brines on worlds such as Europa, Enceladus, and Mars.

KEYWORDS

cryopeg, Arctic, extremophiles, permafrost, maintenance energy

1. Introduction

On Earth, bacteria often encounter energy-limited environments. Their prevalent physiological state is understood to be energy-limited (Lever et al., 2015). For example, the vast subsurface biosphere is energy-limited (Jørgensen and Boetius, 2007), yet sustains abundant microbial life (Teske, 2005; Jørgensen and Marshall, 2016). Understanding the strategies that allow bacteria to survive in such extreme environments prompts the question: what is their minimum metabolic requirement? Here we investigate the energetic needs over time of bacterial communities in cryopeg brine, a subzero hypersaline environment geologically isolated from surface inputs. We seek to answer the question posed by estimating the cell-specific metabolic rates of the bacterial communities residing in these extreme settings.

Cryopeg brines are considered extreme for various reasons, one of which is their assumed energetic isolation. These brines are volumes of hypersaline subzero liquid water found in permafrost well below the surface. The Utqiaġvik system of cryopegs in the high Alaskan Arctic at approximately 8 m below surface has a temperature around −6°C and total salt concentration around 120 ppt (Cooper et al., 2019). Carbon-14 (^{14}C) measurements suggest the brines have been enclosed for approximately 40 ka BP (Iwahana et al., 2021). Two types of cryopeg brines exist within the permafrost here: those encased by a layer of frozen marine sediments and those encased by massive ice. Both types are thought to be isolated hydrologically (Iwahana et al., 2021). Together, these properties describe an environment that is not only energy-limited, but also energetically costly to inhabit due to challenging conditions. Despite these conditions, cell densities range from 10^5 to 10^8 cells mL^{-1} brine (Cooper et al., 2019), comparable to previously sampled cryopeg brines across the Arctic (Gilichinsky et al., 2003, 2005; Bakermans et al., 2006). Metagenomic analyses show the presence of overwhelmingly heterotrophic bacterial communities dependent on organic carbon for their source of energy (Rapp et al., 2021; Cooper et al., 2022).

Investigations of cryopeg systems are relevant not only to our understanding of Earth-bound ecosystems but, excitingly, can inform our understanding of possible extraterrestrial life. Life within the icy mantles of Europa or Enceladus, and possibly the subsurface of Mars, could be inhabiting similarly extreme, energy-limited environments (Marion et al., 2003; Priscu and Hand, 2012; Sholes et al., 2019; Gomez-Buckley et al., 2022). To our knowledge, no estimate of cell-specific metabolic rate in subzero hypersaline environments is available. The objective of this study was to develop such estimates and contribute to our understanding of the habitability of subsurface subzero brines, be they Earth-bound or extraterrestrial.

We considered that the key to understanding the Utqiaġvik cryopeg system was to reconcile high cell densities with potential microbial kinetics and the available energy pool. We hypothesized that the minimum metabolic rate of the brine residents would be relatively high due to the extreme conditions and corresponding need to synthesize protective compounds, making the requirement for organic carbon correspondingly high to account for the observed cell densities. To test this hypothesis, we first made a series of simplifying assumptions to enable a first-order analysis of the system. The objective was to estimate the cell-specific metabolic rate of a resident community, assuming organic carbon as the sole energy source and considering two microbial growth trajectories to provide an upper and lower bound of this rate. This approach required us to measure the quantity of organic carbon in the sediments surrounding the brines. We then constructed a model of the organic carbon cycle within the brine, which allowed us to reconstruct microbial growth trajectories and relate them to available organic carbon. A sensitivity analysis of model parameters was performed to understand their relevance to model results and thus the limitations of our model. These parameters included the enzymatic conversion of particulate organic carbon (POC) to dissolved organic carbon (DOC) in the brine. POC represents the dominant form of organic carbon in surrounding permafrost yet is not available to bacteria until hydrolyzed to smaller molecular weight compounds (DOC).

Finally, we compared the model predictions to the available observations, which together allowed us to propose the system's microbial history under energetic isolation. We produced plausible simulations hinging on the precision of key parameters, and thus could identify research areas that would further advance understanding of bacterial energetics in extreme environments.

2. Physical and biological context for the model

To provide context for our model we outline the relevant environmental characteristics of cryopeg brines in this section. The physical characteristics guided the development of the equations governing environmental interactions in the model. Microbial energetics of the bacteria found in the cryopeg brine constrained our analyses and provided an understanding of the biology that the model attempts to resolve. Together, the physics and biology of the cryopeg brine underlie the design of our work, and the thoughts behind the analyses conducted.

2.1. Physical characteristics of cryopeg brines

Cryopeg brines are volumes of hypersaline water that occur in cryopeg, a basal layer in permafrost of unfrozen sediment perennially at subzero temperatures (van Everdingen, 2005). The brines studied herein were collected from below the Barrow Permafrost Tunnel at a depth of approximately 8 m below the surface, on the northernmost coast of Alaska. They are thought to have formed from saturated marine sediments in a lagoonal environment (Iwahana et al., 2021). As sea level fell during glaciation, these sediments would have been exposed to the atmosphere and become desiccated, causing previously dissolved solutes to concentrate and, following entrainment into permafrost, depress the freezing point of water to yield brine (Gilichinsky et al., 2003, 2005; Iwahana et al., 2021). This cryoconcentration effect leads to high salinities and possibly to concentrated organic matter. The marine origin of these brines is supported by ionic and microbiological evidence (Colangelo-Lillis et al., 2016; Iwahana et al., 2021). The temperature of these Alaskan brines perennially falls within a narrow range of −6 to −8°C and is thought to have remained within this range over their lifespan (Colangelo-Lillis et al., 2016; Cooper et al., 2019; Iwahana et al., 2021; Osman et al., 2021). The salinity of these brines ranges from 109 to 140‰ salt (Cooper et al., 2019). These brines are hydrologically isolated from each other as evidenced by the different pressure heads and equilibrium brine levels (Iwahana et al., 2021). Moreover, the combination of ice content plugging sediment pores and bacteria attached to surfaces is thought to preclude input of cells into the brine from the surrounding environment (Gilichinsky et al., 2005). However, possible input during partial melting at the brine/ice boundary cannot be excluded given slight seasonal temperature oscillations. They may be relevant to the observed microbiological similarities between proximate massive ice and sediment brines (Cooper et al., 2019).

The Utqiaġvik cryopeg system presents brines encased by marine sediments, as previously observed in other cryopegs, as well as those newly discovered to be encased by massive ice, respectively called intra-sediment and intra-ice brines (Iwahana et al., 2021). Intra-ice brines are thought to have migrated along the temperature gradient into the massive ice around 11 ka BP. This migration is suggested by the equal age of organic carbon in the brine and the massive ice surrounding it (Iwahana et al., 2021).

We considered brines sampled from three distinct cryopeg boreholes in the Barrow Permafrost Tunnel (Figure 1): two intra-sediment brines from boreholes CB1 and CB4, and one intra-ice brine from borehole CBIW. CBIW was sampled twice, in 2017 and 2018. All brines were sampled in May and were at −6°C when sampled, with salinities of 115, 121 and 140‰ salt, respectively (Cooper et al., 2019). No *in situ* oxygen measurements have been made in these or other tunnel boreholes, but anaerobic conditions are expected within the brines (Iwahana et al., 2021).

Cryopeg brines considered here featured POC concentrations of 2–12 mM and DOC concentrations of 30–102 mM, which are high when compared to the typical micromolar concentrations in seawater (Mathis et al., 2005; Goñi et al., 2021). The DOC concentrations are also high when compared to porewaters of nearby (unfrozen) marine sediments (e.g., < 7 mM on the Alaskan north slope; Coffin et al., 2017) and other Arctic marine sediments (1–6 mM, Arnosti and Jørgensen, 2006; < 1 mM, Rossel et al., 2020). Measured inorganic nutrients were also relatively high: nitrate, nitrite, and phosphate were present in micromolar concentrations, while ammonium concentrations were at millimolar levels (Cooper et al., 2019). Sulfate concentrations were

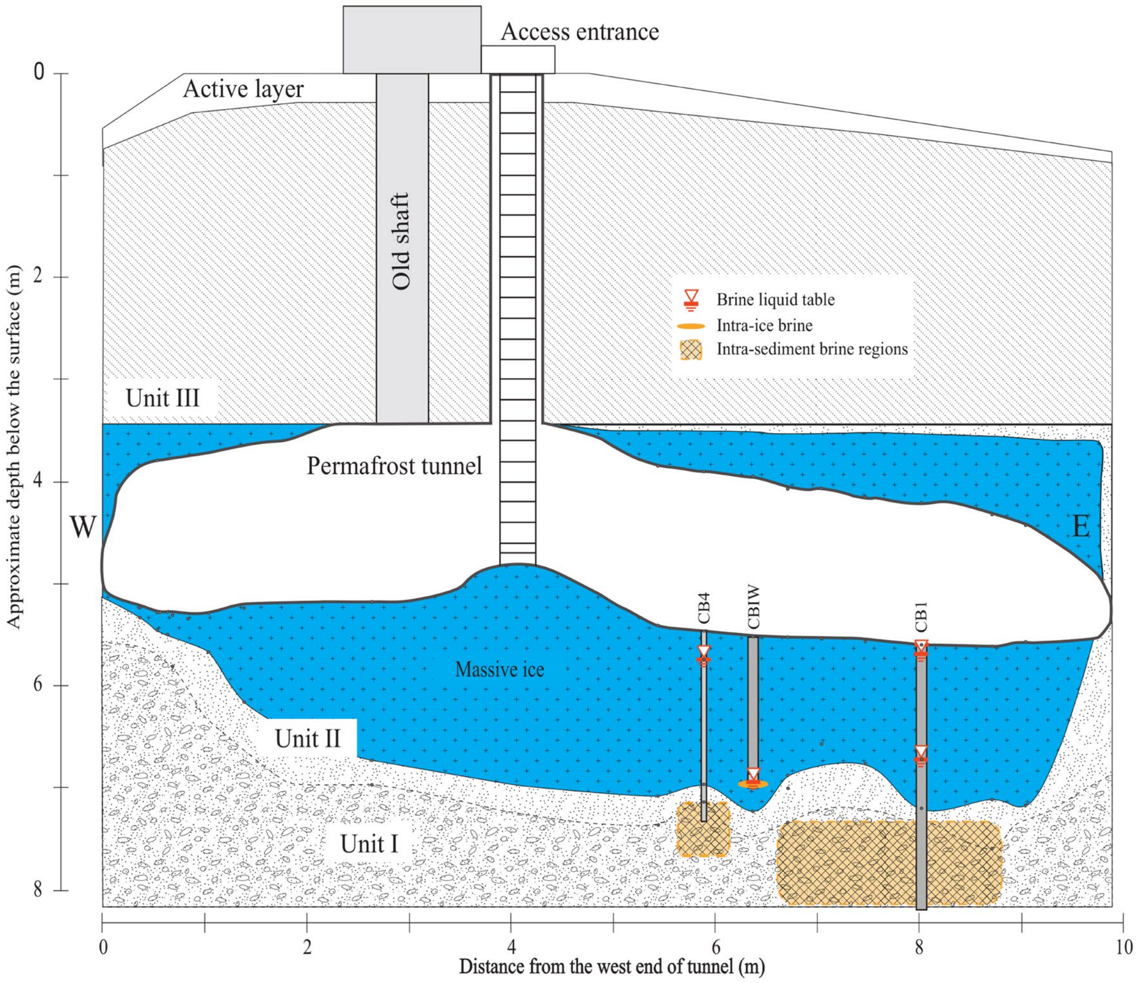

FIGURE 1
NNW-facing cross-sectional diagram of the Barrow Permafrost Tunnel providing access to cryopeg brines near Utqiaġvik, Alaska. Depicted are the cryopeg boreholes CB1, CBIW and CB4 considered in this study. CB1 and CB4 accessed intra-sediment brines 7–8 m below the massive ice; CBIW accessed intra-ice brine thought to have migrated upwards into the massive ice 11,000 years BP (Iwahana et al., 2021). Units I-III refer to permafrost regions (Meyer et al., 2010). Figure adapted from Iwahana et al. (2021).

similar to those in Chukchi Sea water, potentially drawn down in the brines from more concentrated values due to sulfate reduction or to mirabilite formation (Marion et al., 1999; Iwahana et al., 2021).

2.2. Microbial energetics of cryopeg brines

Across the Arctic, cryopeg brines have been found to harbor sizeable microbial communities, ranging between 10^5 and 10^8 cells mL^{-1} (Gilichinsky et al., 2003, 2005; Cooper et al., 2019). These brine communities are composed of a diverse set of organisms, which can include species of *Marinobacter*, *Psychrobacter*, *Gillisia*, *Frigoribacterium*, *Rhodococcus*, *Polaribacter*, and *Sulfurospirillum* (Bakermans et al., 2003, 2006; Bakermans and Nealson, 2004; Gilichinsky et al., 2005; Colangelo-Lillis et al., 2016; Cooper et al., 2019). Community composition appears to differ between Arctic regions, but the use of different methods across studies limits this assessment. The cryopeg brines below the Barrow Permafrost Tunnel, however, have been the subject of in-depth microbiological characterization.

The dominant bacterium in the brines from CB1 and CBIW, two of the brines we considered in this study, was a novel species of *Marinobacter*, recently brought into culture (Cooper et al., 2022). On average it comprised 49% of the total community (Cooper et al., 2019). In the brine from CB4, this *Marinobacter* sp. was abundant, but the dominant bacterium was *Psychrobacter* sp. at 54% of the total community (Cooper et al., 2019). Model parameters for microbial community kinetics were therefore based on the available data for these organisms. Regarding bacterial densities by epifluorescence microscopy, the brines from CB1, CB4 and CBIW (averaged over both sampling years) harbored 5.70×10^6, 1.14×10^7 and 1.30×10^8 cells mL^{-1}, respectively, with dividing cells observed in all three brines (Cooper et al., 2019). Dissolved extracellular polysaccharides (dEPS) made up between 19 and 28% of the DOC pool. Particulate extracellular polysaccharides (pEPS) made up between 2 and 13% of the POC pool (Colangelo-Lillis et al., 2016; Cooper et al., 2019).

Organisms reliant upon a range of metabolisms have been detected in cryopeg brines, including heterotrophs, sulfate reducers, acetogens and methanogens (Gilichinsky et al., 2003, 2005; Cooper et al., 2019). The genus *Marinobacter* features a highly versatile set of metabolisms, allowing its members to inhabit a wide diversity of environmental niches. Species of this genus, including from cryopeg brines, possess a complete tricarboxylic acid (TCA) cycle and glyoxylate shunt. The glyoxylate shunt bypasses the production of carbon dioxide and may play a role in oxidative stress response (Ahn et al., 2017). A genomic analysis of four strains of the dominant *Marinobacter* sp. isolated from Utqiaġvik cryopeg brines further reveals its metabolic potential (Cooper et al., 2022). This *Marinobacter sp.* possesses the genes required to derive energy from a wide range of organic compounds, including all 20 amino acids (with the possible exception of asparagine). As a substitute for glycolysis, it encodes the Entner–Doudoroff pathway, considered an adaptation for energy efficiency at low temperatures (Czajka et al., 2018). Its pathways for nitrogen cycling include nitrate oxidation and reduction, dissimilatory nitrate reduction, nitric oxide reduction, and nitrous oxide reduction. A C-P lyase system encoded in its genome may facilitate the scavenging of phosphate from organophosphates. The variety of nitrogen, sulfur and metal-based redox reactions encoded in its genome supports a facultative anaerobic lifestyle.

For a heterotrophic *Psychrobacter* sp. isolated from Siberian cryopeg, Bakermans et al. (2003) measured resazurin reduction rate (as a proxy for respiration) and growth rate across a temperature range of −10 to 22°C. From ratios of these rates, they concluded that cell metabolic requirements increase substantially at subzero temperatures. Such an increase is unexpected when considering that base energetic needs scale predominantly as a function of temperature, increasing with warming (Tijhuis et al., 1993; Price and Sowers, 2004). Given the subzero temperature of cryopeg brines, a relatively low cell-specific metabolic rate would be reasonable to expect. However, multiple constraints may impose a higher energetic cost to life in this extreme brine system.

Constrained habitat volume and high cell density in cryopeg brines lead to higher rates of cell-to-cell (and virus-to-cell) contact than occur in seawater. Increased cell-to-cell contact rates exacerbate resource and space competition. An analysis of cryopeg brine metagenomes found high abundance of cells associated with the type VI secretion system and microcin C, both tools to lyse neighboring competitors (Rapp et al., 2021). This microbial weaponry can be understood within the framework of an energetic arms race. Such competition-associated costs could raise the energetic cost of living in this system.

Moreover, cryopeg brines host abundant viral communities of marine origin that appear to have mediated the exchange of genetic information (Colangelo-Lillis et al., 2016; Zhong et al., 2020). Viral interactions contribute to the rate of cell death by lysis, influencing the organic carbon cycle through release of cellular carbon content (Showalter, 2020). Thus, we can hypothesize a high turnover of cell biomass leading to increased energetic cost to maintain a steady-state population.

The required production of certain compounds may also increase the energetic cost of life in this system. Subzero brines are relatively viscous (Cox and Weeks, 1975), and must be especially viscous when they contain millimolar concentrations of EPS (Cooper et al., 2019), known for cryoprotection and osmoprotection (Marx et al., 2009; Deming and Young, 2017). Viscosity may lead to the creation of microscale environmental niches, for example, as cell lysis alters local biochemistry. Metagenomics on cryopeg brines revealed the abundance of genes encoding two-component signaling systems (Rapp et al., 2021). These systems would allow a bacterium to respond to a changing energetic landscape more rapidly to outcompete its immediate neighbors (Rapp et al., 2021). A microbial response to localized patches of high molecular weight organic matter may take the form of extracellular enzyme production. Extracellular enzyme activity (EEA) has been measured in cryopeg brines (Showalter, 2020), providing evidence of proactive management of substrate concentrations by the bacterial community. The production of extracellular compounds, from EPS to enzymes, is an additional energetic cost.

Although the current genomic data available provide promising insights into the metabolisms supported by cryopeg brines, they do not allow us to determine whether these brines have supported energetically isolated microbial communities for 40,000 years. To understand the energetics of the Utqiaġvik brines, their energetic histories need to be reconstructed. This effort necessarily involves the reconstruction of the microbial growth trajectory over the lifespan of the brine. Figure 2 illustrates several possible growth trajectories. The different fluctuations or constancy in cell densities over time in each case lead to different

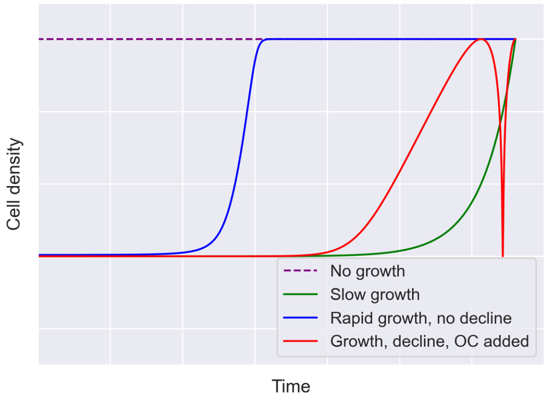

FIGURE 2
Hypothetical growth trajectories to account for a given endpoint cell density. Four possible cases for growth are illustrated here to describe why endpoint measurements leave open many possible trajectories. The case for rapid initial growth followed by stasis is presented in blue. The case for slow growth leading to the observed cell density is presented in green. In red, an intermediate growth rate, followed by decline due to insufficient energy and then an input of organic carbon (OC), depicts recovery of the community to the given endpoint. The no growth scenario, requiring the starting community to be as dense as the endpoint, is indicated by the dashed purple line. Growth lines are intended to be logarithmic, but all lines are conceptual (not drawn to scale).

energetic requirements. Simplistically, a community that spent most of its history at 10^5 cells mL^{-1} will not require the same amount of energy as one at 10^8 cells mL^{-1}. More complex trajectories could also have occurred, such as when a microbial community declines due to insufficient energy, then recovers after an energy input (e.g., when intra-sediment brine is assumed to have migrated into massive ice).

3. Materials and methods

Here we indicate the methods used to quantify key variables, such as organic carbon, and show the equations developed to model the different processes involved in microbial energetics. Along with the mathematical outline of our model, we also present fundamental assumptions and limitations. All of the code used to describe and calculate the equations below and plot the results shown is available online on GitHub. The contents of this paper were generated from the most recent commit on the "paper" branch. Python v3.9 and Julia v1.8.2 (Bezanson et al., 2017) are used throughout, and plots were generated using Matplotlib v3.6.2 and Seaborn v0.12.1 (Hunter, 2007; Waskom, 2021).

3.1. Organic carbon and nitrogen in sediment and massive ice

To determine the POC content of sediments surrounding the cryopeg brines, we used the method of Verardo et al. (1990). Duplicate samples of approximately 20 g of material were cleanly removed from previously collected sediments (Iwahana et al., 2021) that had been stored frozen (−20°C) until analysis. In each case, the sediment material was placed in a 50-cc polypropylene tube, weighed, dried in an oven at 60°C for at least 48 h, and weighed again to obtain dry weight. Samples were then homogenized to a fine powder in a ceramic mortar and pestle and kept in the drying oven until further processing. In the Marine Chemistry Lab (School of Oceanography, University of Washington), 4–6 mg of each sample were weighed in duplicate in combusted silver "boats" after having been fumed in HCl for 24 h to remove inorganic carbonates. Samples were dried again in the 60°C oven while acetanilide standards were prepared. Before analysis, the samples were cooled in a desiccator for at least 24 h. The sediment organic carbon and nitrogen content was measured using a Model 440 CHN/O/S Elemental Analyzer and a combustion temperature of 1,050°C. The organic carbon and nitrogen content of massive ice from this site was already available (Colangelo-Lillis et al., 2016).

To convert our sediment carbon measurements to *in-situ* concentrations we assumed a dry sediment density of 2.625 g mL^{-1}, the average of the density of kaolinite and sand. This assumption is guided by the fact that nearby sediment is composed of undefined clay minerals and sand (Iwahana et al., 2021). An expansion factor was needed to account for the fact that carbon quantification methods require thawing porewater, and that water density changes between its solid and liquid phases. We used a common expansion factor of 9.05% for permafrost porewater, and 8.042% for massive ice. Values for the volumetric ice content of permafrost, needed to determine the density of sediment *in situ*, were 73.1% in both CB1 and CBIW sediment, and 52.7% in CB4 sediment.

To determine DOC of porewater in the frozen sediment surrounding the cryopeg brines, subsamples of the sediment and ice were shaved off core sections with a sterile scalpel onto sterile aluminum foil. These subsamples were placed in 50-cc polypropylene tubes, weighed, and allowed to thaw at 4°C for 15 min before centrifuging for 10 min at 2,000 rpm in a benchtop centrifuge (IEC, Model HN-SII IM201) at 2°C. The resulting supernatant was decanted and filtered into a clean EPA vial using a 0.2-μm syringe filter, then frozen until analyzed. The tube of leftover sediment was reweighed for porewater/sediment normalization. DOC was measured using a Shimadzu TOC-VCSH DOC analyzer according to standard protocols in the Marine Chemistry Lab (School of Oceanography, University of Washington). In the case of massive ice, we lacked suitable samples for DOC analysis, so measurements of dEPS (Colangelo-Lillis et al., 2016) were used as a proxy for DOC.

3.2. Dissolved inorganic carbon

Dissolved inorganic carbon (DIC) was measured for a sample of CBIW brine taken in 2017 as an auxiliary to the ^{14}C dating procedure (Iwahana et al., 2021). Brine sample of approximately 200 mL was degassed under vacuum by pumping to the 10^{-4} Torr range. Dissolved carbon dioxide was liberated by the addition of anhydrous phosphoric acid. Purified carbon dioxide was isolated from other gases by gas distillation. DIC was then measured by the University of Arizona, Accelerator Mass Spectrometry Lab.

3.3. Modeling scenarios

We considered three separate scenarios for modeling purposes. Each scenario is based on a unique occurrence of cryopeg brine below the permafrost tunnel. The scenarios are named after the borehole that yielded the brine they describe: CB1, CB4, and CBIW. The following variables define a scenario: brine cell density, brine POC and DOC concentration, surrounding POC and DOC concentration, post-enclosure carbon addition, bacterial growth rate, and carbon content per cell.

The CB1 scenario was chosen to represent the multiple intra-sediment brines in the Utqiaġvik region of common geology and microbial composition. It was paired with organic carbon measurements made on regional permafrost from the nearby Barrow Environmental Observatory (BEO). As the dominant organism in this brine was the newly isolated *Marinobacter* sp., its growth rate and a literature-informed approximation of its carbon content were used to represent the microbial community.

The CB4 scenario describes an intra-sediment brine that differs from the others in terms of its dominant organism, *Psychrobacter* sp. The published growth rate and carbon content for Arctic *Psychrobacter* sp. (Bakermans et al., 2003, 2006) were used to represent the microbial community. In this scenario we used our measurements of organic carbon in sediment immediately surrounding this brine.

The CBIW scenario represents cryopeg brine encased in massive ice instead of sediment. This brine is thought to have originated as intra-sediment brine, then migrated upwards into massive ice around 11,000 years BP to become surrounded by ice. This ^{14}C-dating provided evidence of a possible mechanism for addition of organic carbon from the ice into the brine (Iwahana et al., 2021). The CBIW scenario is therefore the only one for which we have modeled an addition of organic carbon past the initial stage of brine enclosure. We used a lower bound estimate of the amount of carbon added, based on the amount of carbon in the massive ice currently surrounding the brine (Colangelo-Lillis et al., 2016). As CBIW brine was dominated by the new *Marinobacter* sp., we used its traits to represent the microbial community.

Specific values for the variables we used to define a model scenario are provided in Table 1. For scenarios CB1 and CBIW, where *Marinobacter* sp. dominated the brine community, the cell carbon content, $\pm_D$, was taken from an average value for Arctic sea-ice bacteria from Nguyen and Maranger (2011), the closest relevant estimates for a subzero brine environment that we could find. For the CB4 scenario we took the average size for a proxy of its dominant bacterium, *Psychrobacter sp.*, as 0.365 μ m^3 (Bakermans et al., 2006), using 148 fg C μ m^{-3} as the carbon conversion factor (Kirchman et al., 2009). The maximum growth rate, μ_{max}, for scenarios CB1 and CBIW was derived from lab experiments with the *Marinobacter* sp. isolated from these cryopeg brines. The cultures were grown in nutrient-replete media under *in-situ* temperature and salinity (Cooper et al., 2022). For the CB4 scenario, we used the growth rate determined for a culture of *Psychrobacter sp.* grown in nutrient-replete media at −10°C (Bakermans et al., 2003). The model assumes these rates to be the *in-situ* growth rates, as they are the closest approximations available. We note that they were determined not only under nutrient-replete conditions but also under aerobic culture conditions, and therefore likely represent over-estimations of the *in-situ* growth rates given that cryopeg brine is assumed to be an anaerobic environment.

3.4. Cell-specific metabolic rate

A primary goal was to develop an equation to estimate the cell-specific metabolic rate of the microbial community, which is described below (Equation 1). The cell-specific metabolic rate term was inspired by Pirt (1982), who proposed a constant base maintenance energy term and a second growth-dependent term without distinguishing different types of metabolisms. In our model, we have abstracted the total organic carbon (TOC) consumed to a cell-specific metabolic rate term, as we do not have a good approximation of the growth-dependent term. Metabolic rate as a function of growth rate would be needed to more accurately approximate the growth-dependent term. We account for organic carbon usage for biomass production (growth) separately.

We assumed that the brine upon initial enclosure contained POC and DOC pools equivalent to those present in the continuously frozen

TABLE 1 Variables and values used to define each of three cryopeg brine scenarios.

Variable	Symbol (units)	CB1 scenario (source^a)	CB4 scenario (source^a)	CBIW scenario (source^a)
Cell density	N_f (cells mL^{-1})	5.70 × 10^6 (CB1; Colangelo-Lillis et al., 2016)	1.14 × 10^7 (CB4; Cooper et al., 2019)	1.39 × 10^8 (CBIW; Cooper et al., 2019)
Sediment POC	P_0 (fg C cm^{-3})	1.64 × 10^{13} (BEO; this study)	1.75 × 10^{13} (CB4; this study)	1.64 × 10^{13} (BEO; this study)
Sediment DOC	D_0 (fg C cm^{-3})	3.41 × 10^{10} (BEO; this study)	6.17 × 10^{11} (CB4; this study)	3.41 × 10^{10} (BEO; this study)
Brine POC	P_f (fg C mL^{-1})	1.49 × 10^{11} (CB1; Cooper et al., 2019)	4.97 × 10^{10} (CB4; Cooper et al., 2019)	2.38 × 10^{10} (CBIW; Cooper et al., 2019)
Brine DOC	D_f (fg C mL^{-1})	1.23 × 10^{12} (CB1; Cooper et al., 2019)	1.02 × 10^{12} (CB4; Cooper et al., 2019)	3.60 × 10^{11} (CBIW; Cooper et al., 2019)
Added DOC^b	D_{in} (fg C mL^{-1})	0	0	3.88 × 10^{10} (massive ice; Colangelo-Lillis et al., 2016)
Added POC^b	P_{in} (fg C mL^{-1})	0	0	1.86 × 10^{10} (massive ice; Colangelo-Lillis et al., 2016)
Cell carbon content	α_D (fg C cell^{-1})	15.7 (Nguyen and Maranger, 2011)	54.04 (Bakermans et al., 2006; Kirchman et al., 2009)	15.7 (Nguyen and Maranger, 2011)
Net growth rate^c	μ_{max} (day^{-1})	0.06 (Cooper, 2021)	0.016 (Bakermans et al., 2003)	0.06 (Cooper, 2021)

^{a}CB1, CB4, and CBIW indicate boreholes; BEO indicates Barrow Environmental Observatory. CB1 and CBIW were dominated by *Marinobacter* sp.; CB4, by *Psychrobacter* sp. ^{b}Single addition at 29,000 years (11,000 years BP) into the 40,000-year trajectory. ^{c}Net (community) growth rate was set to the maximum growth rate of the dominant bacterium (see Section 3.7).

material currently surrounding the brines. In the CBIW scenario, we considered the surroundings to have been equal in TOC content to regional frozen sediment at depth in the permafrost (sampled at BEO). We then took the difference between starting TOC and TOC measured in the brines. This calculation accounted for any carbon addition during the 40,000-year period by adding it to the starting TOC quantity. We subtracted from this difference the quantity of organic carbon diverted toward biomass.

To obtain bounds for our approximation we considered two cases of cell growth. The lower bound case requires the available quantity of organic carbon to be divided among as many cells as possible to minimize this per-cell quantity. This case corresponds to one in which no growth occurs (Pirt, 1982). The upper bound case minimizes the cell quantity to maximize the cell-specific metabolic rate. This approach is intuitive by realizing that biomass is the only sink of carbon in this equation. Therefore, the upper bound case is represented by the slowest possible rate of exponential growth.

To calculate the slowest possible rate of exponential growth, we determined the growth rate of a community over the simulation time of 40,000 years by fitting an exponential function between the starting cell density of 10^5 cells mL^{-1} and the observed ending cell density. The resulting rate is called the "minimum growth rate." This approach assumes that the microbial community was growing over the entire lifespan of the enclosed brine, and hence does not allow for death or dormancy. Inherent to Equation 1 is that our system is feasible under the minimum growth rate with either cell-specific metabolic rate bounds.

The cell-specific metabolic rate, *m*, is given in femtograms of carbon per cell per day by:

$$m = \frac{\left(S_0 + S_i\right) - S_f - \alpha_D\left(N_f - N_0\right)}{\int_0^f N(t)\,dt} \tag{1}$$

where α_D denotes the quantity of organic carbon content per cell in femtograms of carbon per cell; S, the concentration of TOC in femtograms of carbon per milliliter; N, the cell density in number of cells per milliliter, and 0 and f, the start and end times, respectively, in days. S_i is any organic carbon added at time *i*. Sympy v1.11.1 was used to calculate the integral (Meurer et al., 2017). We took N_f to be the observed cell density in the cryopeg brine of reference for each scenario (Table 1). We took N_0 to be 10^5 cells mL^{-1}, the order of magnitude of cell densities observed in coastal sea ice (Cooper et al., 2019). The use of a coastal sea ice value is based on physical similarities between the two environments, and the potential that coastal sea ice of 40,000 years ago, being a frozen, brine-containing surface environment, supported a microbiome resembling that of cryopeg brine when first formed.

3.5. Extracellular enzyme activity

Measurements of EEA in cryopeg brines are available (Showalter, 2020), but we sought to calculate EEA rate bounds to understand whether EEA might hint at the age and energetic requirements of the microbial community. These bounds were calculated similarly to those for the cell-specific metabolic rate, using Equation 2:

$$\gamma_{\text{cell}} = \frac{\left(P_0 + P_i\right) - P_f}{\int_0^f N(t)\,dt} \tag{2}$$

where cell-specific EEA rate, γ_{cell}, is given in femtograms of carbon per cell per day and *P* denotes quantity of POC. We thus considered the difference in POC quantity between the brine and its surroundings, accounting for any additional POC input to the brine, with the resulting quantity divided by cell density over time. The bounding growth trajectories were identical to those used to estimate the cell-specific metabolic rate. Using Equation 2, we could also predict the timespan of the system by replacing γ_{cell} with measured EEA rate and solving for t. We solved for the timespan using the growth case with the minimum calculated growth rate starting at 10^5 cells mL^{-1}.

3.6. Model description

To determine the plausibility of the calculated cell-specific metabolic rate value, and to understand the energetic requirements of the system, we developed a model of the organic carbon cycle in Utqiaġvik cryopeg brines. In this section we offer a non-mathematical description and schematic representation (Figure 3) of the model. The central assumptions are presented in the next section.

The model keeps track of four quantities: POC, DOC, DIC, and cell abundance. Five processes structure these quantities: respiration of DOC to DIC by bacteria, cell growth, cell death, hydrolysis of POC to DOC by extracellular enzymes, and organic carbon additions to the system.

Here the rate of respiration, as well as all other utilizations of organic carbon (e.g., cell growth, production and release of extracellular compounds), is encompassed in the cell-specific metabolic rate. Each unit of organic carbon respired is removed from

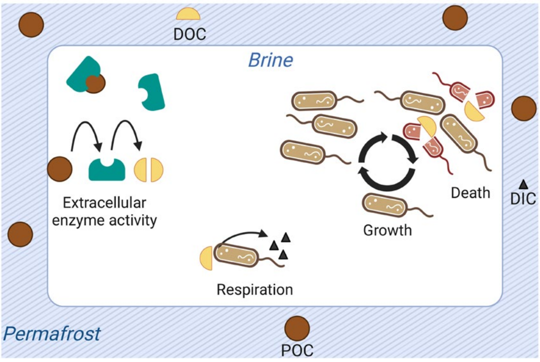

FIGURE 3
Graphical representation of processes and quantities modeled for permafrost-enclosed cryopeg brine. Particulate organic carbon (POC) is shown as dark brown circles; dissolved organic carbon (DOC), as yellow semi-circles; and dissolved inorganic carbon (DIC), as black triangles. Extracellular enzymes (teal-colored shapes) produced and released by bacteria hydrolyze POC to DOC. Bacteria take up DOC, respiring it to dissolved DIC or assimilating it into biomass to grow and reproduce. They release DOC back to the brine upon death, attributed explicitly to starvation in the model.

the DOC pool and added to the DIC pool. The quantity of DIC in the model runs presented here are modified solely by this cellular respiration of DOC. Cells grow according to an equation relating their maximum growth rate to substrate concentration (Monod, 1949). As a cell grows, the quantity of DOC it contains is removed from the DOC pool. Conversely, cells release the DOC they contain upon death. Cell death is explicitly considered to occur when the quantity of available DOC is less than the cell-specific metabolic rate and thus is referred to as starvation death. Other death processes are abstracted by net growth rate. Extracellularly, the enzymatic conversion of POC to DOC contributes to the DOC pool.

As used in the CBIW scenario, the model allows for the addition of organic carbon to the system, beyond that available at time zero. A model feature not used here would allow consideration of a punctuated or a constant input of DIC through processes other than respiration, such as carbonate dissolution. Possible chemoautotrophy to remove DIC and generate new biomass (Rapp et al., 2021) would require modifications that are being considered for a future modeling effort.

3.7. Model assumptions and limitations

Due to the sparse data available on cryopeg brines, reconstructing their microbial history requires assumptions to obtain the first-order approximation of their energetics. These assumptions inherently introduce limitations to our results. We address the central assumptions here to contextualize our results.

A key assumption in our analyses is that the cryopeg brines started with an amount of organic carbon equivalent to the quantity observed in their contemporary surroundings. This assumption is required, as obtaining precise information on a cryopeg system at the time of its formation 40,000 years ago is not possible. The assumption is not unreasonable given the hydrological isolation of the brines and the temperatures that have kept their surroundings frozen throughout their lifetimes (Iwahana et al., 2021; Osman et al., 2021).

Our model does not account for diffusion of material throughout the brine, which neglects the likelihood of environmental niches (Rapp et al., 2021). Without *in situ* microscale observations of these remote systems, we cannot parameterize niches or differentiate the energetic requirements of inhabiting them. For the purposes of conducting an overarching energetic analysis of the system, the lack of diffusivity may not be a critical limitation. The analysis is simply spread uniformly across the environment and the microbes.

We assumed that every cell in the system grows at the same rate. Of course, different subpopulations of cells express different phenotypes and levels of activity, including dormancy, at different times in their life histories. This assumption likely leads to an overestimation of the community growth rate and, in turn, an underestimation of the cell-specific metabolic rate. However, as will be seen in our results, the cell-specific metabolic rate compares reasonably well to existing estimations.

We also assumed that every cell in the system has the same carbon content throughout its lifetime. Of course, bacterial communities exhibit a range of cell sizes, with size and potentially content changing as a function of growth conditions, growth phase, starvation conditions, and dormancy. Until distribution data for cryopeg brines are obtained, the use of a uniform distribution of cell size and carbon content in our analyses leaves some uncertainty to our results. As will be seen, our model simulations are not overly sensitive to this parameter.

We have attributed cell death to starvation, but other processes can lead to cell death in these cryopeg brines. In particular, cell lysis following viral infection and "bacterial warfare" may contribute significantly (Rapp et al., 2021). Use of a net community growth rate includes such death processes implicitly. Our use of growth rates determined in cultures as net community growth rates likely represents an overestimation of the net rate. As a future research direction, this model could be modified to account explicitly for death mechanisms other than starvation.

We assumed that microbial community kinetics could be represented by those of the dominant bacterium. Many bacterial species exist within the cryopeg brine, each with presumably distinct kinetics. However, overall diversity was low and the dominant species was strongly dominant in each scenario considered, accounting for half or more of the community. Making this assumption allowed a first-order approximation despite the unknown complexities of community kinetics.

We assumed that all POC is inaccessible to the brine community until hydrolyzed enzymatically to DOC, and that all DOC is accessible and labile. An absence of data on the chemical composition and lability of either of these pools of organic carbon limits our analysis, as does the assumption that EEA rate is constant. Bacteria regulate their production of extracellular enzymes in response to environmental substrates, but we lack data to model this kinetic or enzyme lifetime. These assumptions could lead to biased results in EEA rate calculations and final carbon quantities (Supplementary Figure S1).

Finally, we assumed that organic compounds are the only limiting source of carbon, nutrients and energy for cell respiration and growth. Sources of inorganic nutrients are plentiful in cryopeg brines (Cooper et al., 2019), but are not included explicitly in our model. While data on the existence of other sources of chemical energy in the system are limited, the levels of POC and DOC in the brines indicate this assumption to be reasonable. The microbial communities in the brines examined were dominated overwhelmingly by organoheterotrophs, further supporting the assumption.

3.8. Model equations

The model was solved using the DifferentialEquations.jl package v7.6.0 (Rackauckas and Nie, 2016) using a Rosenbrock23 solver (Shampine and Reichelt, 1997) set up to solve an initial-value problem.

The growth term, G, is solved with a straightforward Monod equation (Monod, 1949) that relates the maximum net growth rate, $\mu_{\max}$, to substrate concentration, D, using a half-velocity term, K_D, where the substrate is DOC (Equation 3):

$$G = \mu_{\max} * \frac{D}{K_D + D} * N * \left(1 - \frac{N}{N_{\max}}\right) \tag{3}$$

A logistic growth term has been added to cap the growth as the cell density, N, approaches carrying capacity, $N_{\max}$. If cell density declined to zero at the time of a carbon addition (e.g., in the CBIW scenario), we set $N = 1$ to simulate a viable cell able to respond to the addition.

The death term, Δ, corresponds to deaths by starvation (Equation 4):

$$\Delta = \frac{\max\left(mN - D,0\right)}{m} \tag{4}$$

This term accounts for the assumption that cells will lyse if they do not have enough substrate to maintain their integrity, i.e., cannot satisfy their metabolic need (m). Other death-inducing processes such as viral infection or bacterial warfare are included implicitly in net growth rate (Equation 3). The net change in cell density is the difference between growth and death by starvation (Equation 5):

$$\frac{dN}{dt} = G - \Delta \tag{5}$$

While the cell-specific EEA rate remains constant throughout our simulations, the absolute EEA rate, γ, must be lower or equal to the available quantity of substrate, P. To satisfy this constraint, we used a minimum function (Equation 6):

$$\gamma = \min\left(\gamma_{cell} * N,P\right) \tag{6}$$

where P is the quantity of POC, which is given by the sum of two terms. The first term, P_{in}, represents any addition of POC into the system. The second term is the absolute EEA rate, ˀ, subtracted to remove the quantity of POC hydrolyzed to DOC.

$$\frac{dP}{dt} = P_{in} - \gamma \tag{7}$$

The quantity of DOC in the system is the sum of five terms (Equation 8):

$$\frac{dD}{dt} = D_{in} + \alpha_D\left(\Delta - G\right) - m\left(N - \Delta\right) + \gamma + \min\left(I_{xr},I\right) \tag{8}$$

The first term is any addition of organic carbon into the system, D_{in}, which allows the simulation of single or repeated carbon additions from the surrounding environment into the cryopeg brine. The second term is DOC sequestered or released by biomass, equal to the change in cell abundance multiplied by the quantity of organic carbon per cell, α_D. The third term accounts for the metabolism of the remaining population. The fourth term, γ, is the quantity of POC converted to DOC by EEA. The final term simulates autotrophy in the system by taking a DIC fixation rate, I_{xr}, which removes carbon from the DIC pool and adds to the DOC pool. This rate cannot be smaller than the quantity of DIC. In this work, we have set this term to zero, for lack of measurements of I_{xr} in cryopeg brines and expecting the rate to be minor based on metagenomic information (Rapp et al., 2021). If such rates become available for future simulations, the model would need modification to accommodate the flow of DIC into new cell biomass instead of directly into DOC (Section 3.7).

The equation for change in DIC is constructed similarly, though the EEA term is absent as it need not be considered (Equation 9):

$$\frac{dI}{dt} = I_{in} + \alpha_I\left(\Delta - G\right) + m\left(N - \Delta\right) - \min\left(I_{xr},I\right) \tag{9}$$

In this equation, α_I is the quantity of DIC per cell. While α_I and I_{xr} are set to zero here, they could be used in a future study to model autotrophy in this system.

3.9. Model inputs and simulations

In addition to the variables defined for each cryopeg brine scenario (Table 1), a set of constants were input to the model (Table 2). For each constant, we used the most accurate estimate we could find. In some cases, the chosen value was less relevant to our unique environment than we had hoped. However, given that we are striving for order of magnitude estimations, we expect these to be adequate, especially when considering the results of our sensitivity analysis (Sections 3.10 and 4.4).

K_D was derived by taking an average of the values for amino acid uptake rates measured at −1°C in Arctic seawater by Yager and Deming (1999), then taking the dissolved combined amino acids to be 41% carbon (as in Rowe and Deming, 1985). No adjustment was made for temperature, as the original data, determined across a range of temperatures, showed no conventional Q10 effect (Yager and Deming, 1999).

We ran simulations to obtain growth trajectories (changes in cell density over time) for each of the three cryopeg scenarios under different boundary conditions. Each simulation represents one of 8 unique combinations of the lower or upper bound of three variables: m, μ_{max}, and γ_{cell}. Simulations thus address minimum and maximum growth rate, lower and upper bound cell-specific metabolic

TABLE 2 Constants used to model cryopeg brine scenarios.

Constant	Symbol (unit)	Value	Reference
Carrying capacity	N_{max} (cells mL^{-1})	10^9	Assumed, based on Schmidt et al. (1998)
Monod half-velocity constant	K_D (fg C mL^{-1})	8.82×10^5	Estimated from Rowe and Deming (1985) and Yager and Deming (1999)
Cell density at t_0	N_0 (cells mL^{-1})	10^5	Assumed, based on density in coastal sea ice (Cooper et al., 2019)
Extracellular enzyme activity rate	γ_{max} (fg C cell^{-1} day^{-1})	1.22×10^{-2}	Measured in CBIW (Showalter, 2020)
Simulation timespan	t_f (years)[a]	40,000	Measured (Iwahana et al., 2021)

[a]Converted to days for all calculations.

rate, and calculated and measured extracellular enzyme activity. They also track POC and DOC during the 40,000-year time span of the resulting growth trajectories.

3.10. Sensitivity analysis

To understand how the accuracy of our estimates affect model results, we conducted a sensitivity analysis of model parameters. Using GlobalSensitivity.jl package v2.1.2 (Ma et al., 2021) we executed a global sensitivity analysis using a variation of the Sobol variance decomposition method and estimator (Sobol, 2001; Sobol et al., 2007). The analysis was allowed to converge to obtain a satisfactory confidence interval at a confidence level of at least 95%.

Briefly, this variance decomposition method varies each parameter within given bounds and measures the corresponding variance of the output. The resulting first-order Sobol index of a parameter is a measure of how much variance in the output can be attributed to that parameter. The total-effect Sobol index encompasses interactions between the variance of that parameter and the others in the analysis. The bounds passed for each parameter aim to encompass the range of microbiologically plausible values; these can be found in Table 3.

The sensitivity analysis was executed on the CB1 scenario, excluding environmental parameters. This choice was made to understand the influence of bacterial parameters, such as carbon content per cell and growth rate, on our results. Furthermore, these constitute the few parameters that future lab work may attempt to quantify, whereas more accurate environmental data is elusive.

TABLE 3 Parameter bounds of the sensitivity analysis.

Parameter (units)	Lower bound	Upper bound
Growth rate (day^{-1})	1×10^{-6}	1×10^{2}
Cell-specific metabolic rate (fg C cell^{-1} day^{-1})	1×10^{-5}	5×10^{2}
Cell carbon content (fg C cell^{-1})	1×10^{2}	5×10^{2}
EEA rate (fg C cell^{-1} day^{-1})	0	1×10^{2}
Monod half-velocity constant (fg C)	1×10^{3}	1×10^{8}
Carrying capacity (cells mL^{-1})	1×10^{8}	1×10^{9}
Starting cell density (cells mL^{-1})	1	1×10^{8}

TABLE 4 Cell-specific metabolic rate bounds and calculated maximum doubling time and minimum growth rate for each cryopeg brine scenario.

Parameter (units)	CB1 scenario	CB4 scenario	CBIW scenario
Cell-specific metabolic rate (fg C cell^{-1} day^{-1})	0.181–0.743	0.099–0.474	0.008–0.057
Maximum doubling time (years)	6,860	5,850	3,870
Minimum growth rate (day^{-1})	2.77×10^{-7}	3.24×10^{-7}	4.95×10^{-7}

4. Results

Here we provide the results of the different measurements made to fill gaps and complement the datasets available in the literature, and thus enable our model simulations. These measurements include sediment carbon and nitrogen content of cryopeg and regional sediments and brine DIC for one borehole sample. Estimates of cell-specific metabolic rate and extracellular enzyme rate are shown for the three different scenarios examined. Finally, a sensitivity analysis of model parameters and the model predictions are presented.

4.1. Sediment carbon and nitrogen measurements

To improve the accuracy of our model, we measured the quantity of organic carbon in sediment permafrost previously sampled at two locations in the BEO. The average value for POC was 0.0232 ± 0.0006 μg C μg sediment^{-1} at a depth of 367–383 cm ($n = 4$). The porewater salt concentration was 6‰. The concentration of DOC in this porewater was 51.2 μg C mL^{-1}. The nitrogen content of the sediment was 0.0016 ± 0.00005 μg N μg sediment^{-1}, for a molar C:N ratio of 15.8 mol C mol N^{-1}.

We also measured the concentration of organic carbon in sediment surrounding the CB4 cryopeg brine. For POC, the average value in this sediment layer was 0.0136 ± 0.0012 μg C μg sediment^{-1} ($n = 3$). The porewater salt concentration ranged between 22‰ and 30‰. The concentration of DOC in this porewater at 187-cm depth was 1,286 μg C mL^{-1}. The nitrogen content of the sediment was 0.0010 ± 0.00015 μg N μg sediment^{-1}. CB4 sediment thus had a C:N ratio of 15.8 mol C mol N^{-1}.

4.2. Brine dissolved inorganic carbon

The dissolved inorganic carbon content of CBIW brine (in 2017) was measured as 6.93 × 10^{10} fg C mL^{-1}. The dissolved inorganic carbon content of frozen sediment from CBIW (in 2018) was 4.9 × 10^{10} fg C mL^{-1}. We do not have DIC measurements for other brines.

4.3. Estimates of cell-specific metabolic rate

The lower and upper bounds of the cell-specific metabolic rate that we estimated for each of the three cryopeg brine scenarios ranged from 0.008 to 0.743 fg C cell^{-1} day^{-1} (Table 4). As expected, due to the input of organic carbon, the lowest of these rates was obtained for the CBIW scenario. The calculated minimum growth rate ranged between 2.77×10^{-7} and 4.95×10^{-7} day^{-1}. These extremely low growth rates, which correspond to doubling times on the order of 10^{3} years, are due to the significant age of the system and rely upon our assumption of a starting cell population of 10^{5} cells mL^{-1}.

4.4. Extracellular enzyme activity rate estimates and predicted timespan

We calculated the EEA rate required to hydrolyze the difference between surrounding sediment POC and brine POC. In the case of the CB1 scenario, the bounds of estimated EEA rates were 0.195

and 0.802 fg C cell^{-1} day^{-1}. At the measured EEA rate of 0.012 fg C cell^{-1} day^{-1}, the time required to hydrolyze the POC difference in this scenario would have been 81,200 years. In the CB4 scenario, the estimated bounds of EEA rates were 0.101 and 0.483 fg C cell^{-1} day^{-1}, with a predicted timespan of 71,000 years. Finally, in the CBIW scenario (that received organic input), the estimated bounds of EEA rates were 0.806 and 0.584, with a predicted timespan of 48,700 years, much closer to the observed age of the cryopeg system. In all cases, this independent estimation of the system's timespan is near to or less than double the measured timespan, well within the goal of obtaining order of magnitude estimates.

4.5. Model sensitivity analysis

A sensitivity analysis of model parameters revealed the importance of the three parameters at the heart of the Monod growth term (Figure 4): growth rate, cell-specific metabolic rate, and half-velocity constant. These are the only parameters with notable first-order indices. They have a measurable direct impact on model output, whereas cell carbon content and initial cell density do not. The total-effect indices offer more nuance. These indices reflect the added importance of carrying capacity. As a whole, this sensitivity analysis offers insight into which parameters account for much of the variability in the model results.

4.6. Model predictions

In two of the eight sets of conditions used for model simulations, our model fully or partially succeeds in explaining the cell densities observed at 40,000 years. With conditions of minimum growth rate paired with low cell-specific metabolic rate and calculated EEA, all three cryopeg brine scenarios reach their observed cell densities (Figure 5A). With measured EEA (Figure 5B), the observed cell density is reached only for the CBIW scenario; CB1 and CB4 scenarios fall short of their densities (Figure 5B). The CBIW scenario succeeds in reaching the observed cell density because it includes an addition of DOC, while the other two depend upon the hydrolysis of existing POC to generate DOC for bacterial growth. Insufficient POC is hydrolyzed toward the end of the trajectory (Supplementary Figure S1) to support these other two communities.

By Equation 1, minimum growth rate paired with the upper bound cell-specific metabolic rate should yield the observed cell densities. However, this is not the case. Common to all the minimum growth rate simulations (Figures 5A–D) is a long plateau for the first few thousand years. In those simulations where minimum growth rate and upper bound cell-specific metabolic rate are paired, the populations subsequently grow weakly before declining (Figures 5C,D). Given that abundant POC remains in the system in all cases (Supplementary Figure S1), these results are explained by an EEA rate inferior to the cell-specific metabolic rate requirements. The CBIW population does start to recover due to addition of DOC at 29,000 years, but the growth rate is too low to allow recovery to the observed cell densities before the simulation ends (Figures 5C,D).

When the maximum growth rate is used, the microbial populations rapidly reach the system carrying capacity (Figures 5E–H). Once they consume all available DOC, the populations decline. The time elapsed before the decline is governed by the demand for DOC driven by the cell-specific metabolic rate. Because CBIW sees a punctual addition of DOC at 29,000 years, the high growth rate allows the population to recover for a short time before declining again

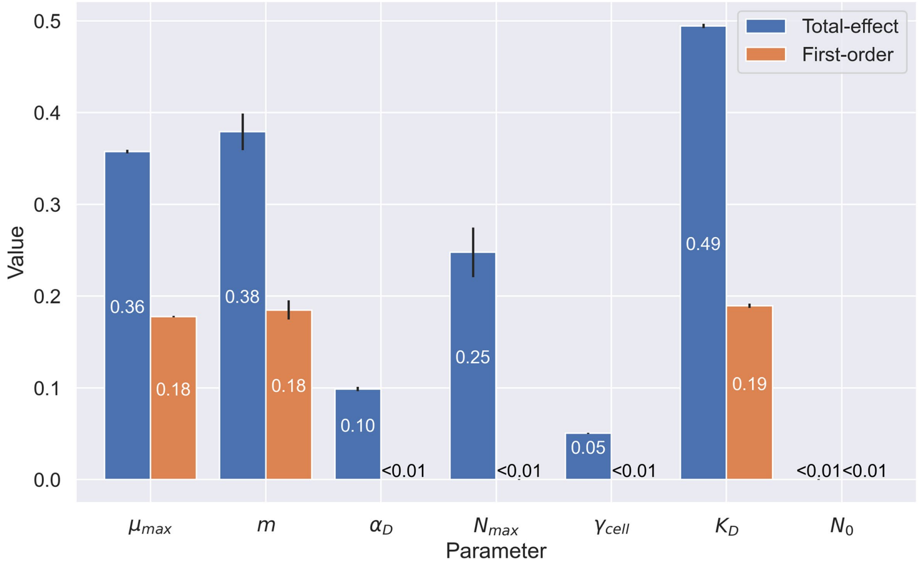

FIGURE 4
Sensitivity analysis of microbial parameters used in the organic carbon model. Numerical values represent the first-order (in orange) and total-effect (in blue) Sobol indices of the selected parameters: maximum growth rate (μ_{max}), cell-specific metabolic rate (m), cell carbon content (α_D), carrying capacity (N_{max}), cell specific extracellular enzyme activity (γ_{cell}), half-velocity constant for carbon uptake (K_D), and starting cell density (N_0). First-order indices show the sensitivity of the model when varying only the parameter in question. Total-effect indices show the sensitivity of the model when varying the selected parameter in conjunction with the other parameters selected in this analysis. Values shown are rounded at 10^{-2}.

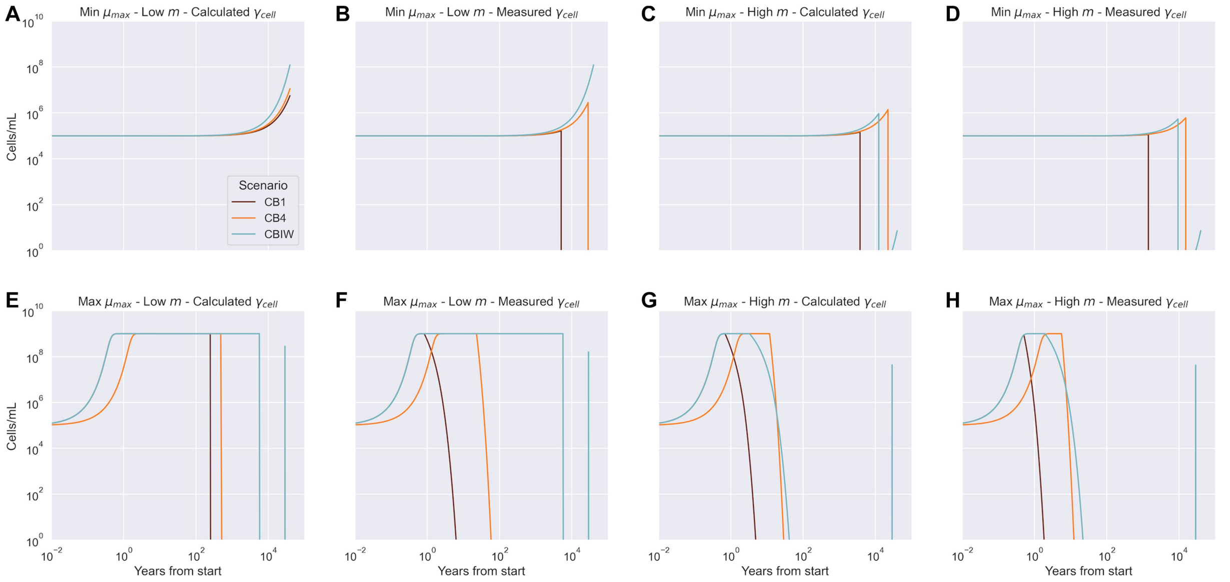

FIGURE 5

Model predictions of cell density over the lifetime of the system for each cryopeg brine scenario. Measured cell densities at 40,000 years are recreated by the model only under conditions shown in panel **A**: lower bound net growth rate (μ_{max}), lower bound cell-specific metabolic rate (m), and the calculated cell-specific extracellular enzyme activity (γ_{cell}); and for CBIW in panel **B**: lower bound net growth rate (μ_{max}), lower bound cell-specific metabolic rate (m), and the measured cell-specific extracellular enzyme activity (γ_{cell}). Panels **C** through **H** depict cases where the predicted end cell density did not match the observed cell density, regardless of the combination of bounds applied.

(Figure 5 panels E-H). However, not enough carbon has been added to sustain the population to the end of this simulation.

5. Discussion

Our overall approach can be considered a bulk energetic analysis. We have made the fundamental assumption that the total energy use of the system corresponds to the difference in organic carbon between the permafrost and the cryopeg brine, assuming these started with equal amounts. This approach mitigates the lack of a secondary metabolic state (i.e., dormancy) in our model. In this way, our cell-specific metabolic rate calculations provide bounds on the average energy requirement of a bacterium in this setting.

Multiple analyses increase our confidence in the mentioned assumption and our model predictions. Using the measured rate of EEA and following our assumption on total energy use in this system, we calculated an expected timespan of the system equal or less than double the measured timespan. We also used the measured C:N ratio of CB4 sediment and the previously measured quantity of ammonia in the brine from Cooper et al. (2019) to estimate the amount of organic carbon consumed. We obtained a value of 8.59×10^{11} fg C mL^{-1}, two orders of magnitude below the quantity produced by our assumption. This calculation is expected to produce a lower bound quantity given that it does not consider nitrogen cycling or the concentration of other nitrogen species in the brine. Thus, this quantity does not contradict our assumption or prediction. Similarly, the DIC value measured is three orders of magnitude below our expectations based on DOC consumed in CBIW. This analysis indicates that we may be overestimating DIC in the model by not accounting for the complexities of the inorganic carbon system in a subzero brine (Marion et al., 1999), supported by the measured DIC in surrounding frozen sediment. Together these results confirm the plausibility of our assumptions, while providing crucial context for our results. Future work could focus on modeling the DIC sinks of these brines in order to increase the fidelity of this model and understand the potential role for autotrophy in this extreme microbial community.

To understand the biological plausibility of our metabolic rate estimates we sought to compare them to existing measurements and estimates of metabolic rates in other remote and energy-limited environments. Assuming an energetic yield of 30 kJ mol C^{-1} our cell-specific metabolic rate values range on the order of 10^{-17} to 10^{-19} W cell^{-1}. This range overlaps at the high end of the range for estimated energy turnover from cold anoxic subsurface marine sediments, the closest analog we can find, on the order of 10^{-19} W cell^{-1} and 10^{-20} W cell^{-1} (Hoehler and Jørgensen, 2013; Lever et al., 2015). For deep crustal fluids, another energy-limited but open and oxygenated environment, sample incubations amended with ^{13}C-substrates at 4°C yielded potential anabolic rates that range from 10^{-3} to 30 fg C cell^{-1} day^{-1} (Trembath-Reichert et al., 2021). Our metabolic rates, which represent net anabolic and catabolic activities at −6°C, fall at the low end of this range (order of 10^{-3} to 10^{-1} fg C cell^{-1} day^{-1}; Table 4), as expected given the significant differences between these environments.

Thus, the cell-specific metabolic rate values we obtained, being framed by other existing rates, are biologically plausible. Our calculation of the cell-specific metabolic rate implicitly includes every cellular process but growth, including membrane, protein and other adaptations to low temperature and high salinity. The relatively high cell-specific metabolic rate of bacteria in the cryopeg brine system, compared to deep subsurface marine sediments, can be accounted for at least partly by the production of extracellular compounds. Moreover, cell carbon mass in these environments may be larger than cells in deep sediments, which could also account for some of the difference in cell-specific metabolic rate between cryopeg brines and cold (unfrozen) marine sediments.

Extracellular enzyme activity has been documented in cryopeg brines (Showalter, 2020). Producing extracellular enzymes is a costly endeavor, with the price reflected in higher cell-specific metabolic rate requirements (Vetter et al., 1998; Lever et al., 2015). Extracellular polysaccharides are also present in high concentrations in cryopeg brines (Cooper et al., 2019). These polysaccharides take on many critical functions, offering cell protection against the effects of both subzero temperatures and hypersaline conditions (Krembs et al., 2002, 2011; Carillo et al., 2015; Deming and Young, 2017). While extracellular polysaccharides appear to be fundamental in allowing a cryopeg microbial community to exist, their chemical nature and high concentration in cryopeg brines implies a significant energetic cost, again implicitly built into our cell-specific metabolic rate calculation.

We calculated the minimum growth rate of bacteria in this system, making an important assumption on the starting cell concentration of these brines. While we have made an informed assumption in using cell density in sea ice, the value remains at best an educated guess. We have no data on the actual starting cell concentration of these cryopeg brines. Nevertheless, our sensitivity analysis suggests little influence of this parameter on model output. Assuming a starting cell concentration of 10^5 cells mL^{-1}, we obtain maximum doubling times on the order of 10^3 years. This result is microbiologically feasible, based on similarly long doubling times (20–2,500 years) calculated for other, related energy-limited environments, particularly marine and deep subsurface sediments (Hoehler and Jørgensen, 2013; Lever et al., 2015; Jørgensen and Marshall, 2016), which are thermally more growth-permissive environments than subzero cryopeg brines. As we discuss below, very slow doubling times are not necessary in all cases to explain our observations.

The sensitivity analysis reflects the importance of the parameters we chose to manipulate in our simulations. Growth rate, cell-specific metabolic rate, and Monod half-velocity constant each have high first-order and total-effect Sobol indices. These high indices reflect an important interplay between the parameters in determining the outcome of the model. The EEA rate also presents a high total-effect index in its role of determining the quantity of DOC in the system. Surprisingly, EEA rate does not exhibit a high first-order index, despite other data suggesting this variable is key to cryopeg brine energetics. In fact, EEA does have a high Sobol index when only considering the end concentration of POC in the system (not shown).

In all but two (of 8) sets of conditions for simulations, the model fails to reconstruct a cell growth trajectory that yields the observed cell densities. In these cases, cell density collapses to zero due to the lack of available DOC to meet community energetic requirements. However, in most cases, plenty of POC, a potential source of energy, remains (Supplementary Figure S1). The extinction of available DOC in these simulations (Supplementary Figure S1) is caused by the cell-specific metabolic rate being higher than the cell-specific EEA rate. In other words, individual cells are consuming DOC faster than their enzymes can convert POC to DOC.

While the half-velocity constant presents high Sobol indices, this result must be nuanced. First, the chosen value is orders of magnitude lower that the quantity of DOC present in the system. Thus, the impact of this term at the beginning of the simulation is low, and growth proceeds unimpeded. A higher value might slow growth, but the timespan here is long enough that the effect would be negligible. When the quantity of DOC in the system is closer to or below the value chosen, the community is typically on a trajectory toward extinction in the model. Hence, the half-velocity constant, while important because it modulates growth, does not alone explain why the model is limited in explaining our observations.

Simulations based on the CBIW scenario provide some insight on model success versus failure in predicting the observations. In this scenario, the lower bound cell-specific metabolic rate is lower than the extracellular enzyme activity rate used, whether the calculated or measured value (Table 4, Section 4.3). Thus, with abundant DOC available, the model can reproduce the observed cell density using the minimum growth rate (Figures 5A,B). Observed cell densities are also obtained for the CB1 and CB4 scenarios if the calculated EEA rate is used (Figure 5A). In contrast, using the maximum growth rate in conjunction with the calculated EEA rate leads to the depletion of the POC pool, unless carrying capacity is reduced by one order of magnitude (not shown).

Clearly, the EEA rate has the potential to make bioavailable a significant energy source in the system: POC. We note that the observed cell-specific rate of EEA used in the simulations is the average of activities measured on only three substrates in CBIW brine. This rate is kept constant throughout every simulation. This simplification does not accurately reflect the number and specificity of enzymes produced in a cryopeg brine, their complex kinetics, the regulation of their production, or their lifetimes under subzero brine conditions. The cell-specific EEA rate surely fluctuated over the lifespan of the brine as a function of cell density, DOC concentration, and extracellular enzyme turnover time. We were thus led to calculate the range of EEA rates that would allow for enough POC to be hydrolyzed to sustain the microbial community. For the CB1 and CB4 scenarios, these calculated rates are an order of magnitude higher than the measured rate used. Conversely, we calculated the amount of time needed for the chosen EEA rate to hydrolyze the required amount of POC. The results point to a longer lifespan for the cryopeg brines than the measured 40,000 years (by carbon dating), as high as 81,200 years in one case. This discrepancy, based on the chosen EEA rates being too low, provides one explanation as to why our model fails in many cases to explain the observed cell densities. A lack of data to account for cell size differences between *in vitro* and *in situ* measurements may represent another. Future research on extracellular enzyme production and kinetics at subzero temperatures and high salinities, coupled with cell-size measurements, could allow for an improved understanding of bacterial energetics in cryopeg brines.

Despite being detected (Colangelo-Lillis et al., 2016; Cooper et al., 2019), hydrogen sulfide is not considered here as a potential source of chemical energy in these cryopeg brines. Most members of the bacterial communities as revealed by metagenomics are not known to utilize it (Rapp et al., 2021), bacterial kinetics for those that do are not available under *in-situ* conditions, and hydrogen sulfide concentrations are not known. However, the presence of sulfur-oxidizing and sulfur-reducing bacteria was recorded in these brines (Cooper et al., 2019).

Therefore, a large enough endogenous source of hydrogen sulfide in the cryopeg brines could change the energetic balance of these communities. We also note that sulfur concentration may be impacted by abiotic processes such as mirabilite precipitation (Marion et al., 1999). Armed with the relevant kinetics, a future study could establish an upper bound on the possible energetic contribution of hydrogen sulfide to this system. A more detailed analysis could account for metabolically different bacterial populations and different metabolic states.

6. Conclusion

Here we have produced a first estimation of cell-specific metabolic rate in cryopeg brines, ancient, geologically isolated, subzero hypersaline liquids in Arctic permafrost. Comparing our estimates to the few other estimates available on natural microbial systems is difficult, given the use of different approaches and reporting units. Our estimates suggest that cell-specific metabolic rate in a cryopeg system is much higher than in subsurface marine sediments (Hoehler and Jørgensen, 2013), the closest parallel we can find. Although both are sediment-based systems, the differences between them are marked: subsurface marine sediments are neither subzero nor hypersaline and they lack the energy resources that surround a cryopeg system. However, our estimates of cell-specific metabolic rate may be high primarily because we define cell-specific metabolic rate to include every cellular process but growth. The energetically costly production of extracellular enzymes and extracellular polysaccharides may best explain our result of high cell-specific metabolic rate.

To further understand the energetics of the cryopeg system, we developed a model of a simplified organic carbon cycle in subzero cryopeg brines. The results of a selective sensitivity analysis of this model suggest that growth rate, cell-specific metabolic rate and EEA rate are key parameters in determining the fate of the microbial community. Running simulations representative of different energetic bounds for each cryopeg brine improved our understanding of the history of a cryopeg microbial community. In most cases, the energetic requirement is too high and the microbial community collapses. A higher EEA rate would allow the community to take advantage of the energy locked within the high amounts of POC in the system. Where we modeled a punctual addition of DOC into the system, the population was either too slow growing to achieve the observed cell density, or the quantity of DOC was insufficient to sustain it. In cases where the lower bound cell-specific metabolic rate was inferior to the EEA rate, the model was successful in reproducing the observed cell densities after 40,000 years. In calculating the required EEA rate to satisfy the energetic requirements in each of the cryopeg brine scenarios considered, we concluded that the 40,000-year timespan could be reconciled with the measured EEA rate if the energetic requirements of the bacterial community are low enough. The calculated EEA based on our assumption on starting DOC and POC conditions yields an expected system timespan within a factor of two of the measured timespans. This result increases our confidence in the assumptions underlying our energetic analyses.

Although our model unavoidably relies on numerous assumptions, it has produced testable hypotheses for the continued study of cryopeg brines. It also leads us to conclude that the microbial densities observed today in cryopeg brines could well have been reached in energetic isolation over an estimated system lifespan of 40,000 years. In general, the success of these communities would have required a lower growth rate than that observed under *in-situ* conditions in the lab and higher average rate of EEA. The calculated cell-specific metabolic rate of bacteria in these systems can be met by the assumed available quantity of POC and DOC in the system and appears to be biologically plausible, particularly for bacteria functioning under the extreme conditions of subzero temperature and hypersalinity. Finally, this model could be tuned in its parameters to describe theoretical astrobiologically relevant environments within the icy crusts of Europa or Enceladus.

Data availability statement

The original contributions presented in the study are included in the article/Supplementary material, further inquiries can be directed to the corresponding author. The code to reproduce the analyses in this study can be found in the GitHub repository of this project at https://github.com/Ge0rges/Cryopeg-Carbon-Model.

Author contributions

GK developed the carbon model, estimated the cell-specific metabolic rate values, performed all calculations, model runs, and lab work, and drafted the manuscript. TH provided the methodological ideas required to estimate cell-specific metabolic rate, crucial feedback on the model, including the suggestion to conduct a sensitivity analysis, and critical revisions to the manuscript. GI provided organic and inorganic carbon data, expansion factors for ice, interpretation of dating measurements, and edits to the manuscript. JD supervised all work, advised GK, administered the grant, provided lab facilities, and revised and edited the manuscript. All authors approved this submission.

Funding

This work was initially supported by the Gordon and Betty Moore Foundation (grant number GBMF5488). GK also received support from a private sponsorship and the Karl M. Banse professorship to JD.

Acknowledgments

We thank the many people who provided helpful discussions, data, and encouragement to develop the model and associated calculations: Shelly Carpenter for help in the lab and with the sediment carbon measurements; Hajo Eicken for providing important input that stimulated this effort; Zac Cooper and Josephine Rapp for helpful discussions about brine genomics; Max Showalter for the critical EEA data and helpful modeling discussions; and Jodi Young and Kaitlin Harrison for discussion regarding the potential for chemoautotrophy in cryopeg brines. GK would also like to thank the organizers of the Microenergy Conference 2022 for the opportunity to present and discuss an early version of this work, Scott Martin for helpful mathematical discussion, and Mario Nohra for reviewing and auditing the project's codebase.

Conflict of interest

The authors declare that the research was conducted in the absence of any commercial or financial relationships that could be construed as a potential conflict of interest.

Publisher's note

Supplementary material

The Supplementary material for this article can be found online at: https://www.frontiersin.org/articles/10.3389/fmicb.2023.1206641/full#supplementary-material

References

Ahn, S., Jung, J., Jang, I.-A., Madsen, E. L., and Park, W. (2017). Role of glyoxylate shunt in oxidative stress response. *J. Biol. Chem.* 291, 11928–11938. doi: 10.1074/jbc.m115.708149

Arnosti, C., and Jørgensen, B. B. (2006). Organic carbon degradation in arctic marine sediments, Svalbard: a comparison of initial and terminal steps. *Geomicrobiol J.* 23, 551–563. doi: 10.1080/01490450600897336

Bakermans, C., Ayala-del-Río, H. L., Ponder, M. A., Vishnivetskaya, T., Gilichinsky, D., Thomashow, M. F., et al. (2006). *Psychrobacter cryohalolentis* sp. nov. and *Psychrobacter arcticus* sp. nov., isolated from Siberian permafrost. *Int. J. Syst. Evol. Micr.* 56, 1285–1291. doi: 10.1099/ijs.0.64043-0

Bakermans, C., and Nealson, K. H. (2004). Relationship of critical temperature to macromolecular synthesis and growth yield in *Psychrobacter cryopegella*. *J. Bacteriol.* 186, 2340–2345. doi: 10.1128/jb.186.8.2340-2345.2004

Bakermans, C., Tsapin, A. I., Souza-Egipsy, V., Gilichinsky, D. A., and Nealson, K. H. (2003). Reproduction and metabolism at −10°C of bacteria isolated from Siberian permafrost. *Environ. Microbiol.* 5, 321–326. doi: 10.1046/j.1462-2920.2003.00419.x

Bezanson, J., Edelman, A., Karpinski, S., and Shah, V. B. (2017). Julia: a fresh approach to numerical computing. *SIAM Rev.* 59, 65–98. doi: 10.1137/141000671

Carillo, S., Casillo, A., Pieretti, G., Parrilli, E., Sannino, F., Bayer-Giraldi, M., et al. (2015). A unique capsular polysaccharide structure from the psychrophilic marine bacterium *Colwellia psychrerythraea* 34H that mimics antifreeze (glyco)proteins. *J. Am. Chem. Soc.* 137, 179–189. doi: 10.1021/ja5075954

Coffin, R. B., Smith, J. P., Yoza, B., Boyd, T. J., and Montgomery, M. T. (2017). Spatial variation in sediment organic carbon distribution across the Alaskan Beaufort Sea shelf. *Energies* 10:1265. doi: 10.3390/en10091265

Colangelo-Lillis, J., Eicken, H., Carpenter, S. D., and Deming, J. W. (2016). Evidence for marine origin and microbial-viral habitability of sub-zero hypersaline aqueous inclusions within permafrost near Barrow, Alaska. *FEMS Microbiol. Ecol.* 92:fiw053. doi: 10.1093/femsec/fiw053

Cooper, Z. S. (2021). *Microbial evolution and ecology in subzero hypersaline environments*. Seattle, WA: University of Washington.

Cooper, Z. S., Rapp, J. Z., Carpenter, S. D., Iwahana, G., Eicken, H., and Deming, J. W. (2019). Distinctive microbial communities in subzero hypersaline brines from Arctic coastal sea ice and rarely sampled cryopegs. *FEMS Microbiol. Ecol.* 95:fiz166. doi: 10.1093/femsec/fiz166

Cooper, Z. S., Rapp, J. Z., Shoemaker, A. M. D., Anderson, R. E., Zhong, Z.-P., and Deming, J. W. (2022). Evolutionary divergence of *Marinobacter* strains in cryopeg brines as revealed by pangenomics. *Front. Microbiol.* 13:879116. doi: 10.3389/fmicb.2022.879116

Cox, G. F. N., and Weeks, W. F. (1975). *Brine drainage and initial salt entrapment in sodium chloride ice*. Hanover, NH: US Army Corps Engineers Cold Regions Research and Engineering Laboratory.

Czajka, J. J., Abernathy, M. H., Benites, V. T., Baidoo, E. E. K., Deming, J. W., and Tang, Y. J. (2018). Model metabolic strategy for heterotrophic bacteria in the cold ocean based on *Colwellia psychrerythraea* 34H. *Proc. Natl. Acad. Sci.* 115, 12507–12512. doi: 10.1073/pnas.1807804115

Deming, J. W., and Young, J. N. (2017). "The role of exopolysaccharides in microbial adaptation to cold habitats" in *Psychrophiles: From biodiversity to biotechnology*. ed. R. Margesin (Cham: Springer).

Gilichinsky, D., Rivkina, E., Bakermans, C., Shcherbakova, V., Petrovskaya, L., Ozerskaya, S., et al. (2005). Biodiversity of cryopegs in permafrost. *FEMS Microbiol. Ecol.* 53, 117–128. doi: 10.1016/j.femsec.2005.02.003

Gilichinsky, D., Rivkina, E., Shcherbakova, V., Laurinavichuis, K., and Tiedje, J. (2003). Supercooled water brines within permafrost: an unknown ecological niche for microorganisms: a model for astrobiology. *Astrobiology* 3, 331–341. doi: 10.1089/153110703769016424

Gomez-Buckley, A. C., Showalter, G. M., and Wong, M. L. (2022). Modeling virus and bacteria populations in Europa's subsurface ocean. *Life* 12:620. doi: 10.3390/life12050620

Goñi, M. A., Juranek, L. W., Sipler, R. E., and Welch, K. A. (2021). Particulate organic matter distributions in the water column of the Chukchi Sea during late summer. *J. Geophys. Res. Oceans* 126:664. doi: 10.1029/2021jc017664

Hoehler, T. M., and Jørgensen, B. B. (2013). Microbial life under extreme energy limitation. *Nat. Rev. Microbiol.* 11, 83–94. doi: 10.1038/nrmicro2939

Hunter, J. D. (2007). Matplotlib: a 2D graphics environment. *Comput. Sci. Eng.* 9, 90–95. doi: 10.1109/mcse.2007.55

Iwahana, G., Cooper, Z. S., Carpenter, S. D., Deming, J. W., and Eicken, H. (2021). Intra-ice and intra-sediment cryopeg brine occurrence in permafrost near Utqiaġvik (Barrow). *Permafrost Periglac.* 32, 427–446. doi: 10.1002/ppp.2101

Jørgensen, B. B., and Boetius, A. (2007). Feast and famine — microbial life in the deep-sea bed. *Nat. Rev. Microbiol.* 5, 770–781. doi: 10.1038/nrmicro1745

Jørgensen, B. B., and Marshall, I. P. (2016). Slow microbial life in the seabed. *Annu. Rev. Mar. Sci.* 8, 311–332. doi: 10.1146/annurev-marine-010814-015535

Kirchman, D. L., Hill, V., Cottrell, M. T., Gradinger, R., Malmstrom, R. R., and Parker, A. (2009). Standing stocks, production, and respiration of phytoplankton and heterotrophic bacteria in the western Arctic Ocean. *Deep Sea Res Part I Top Stud Oceanogr* 56, 1237–1248. doi: 10.1016/j.dsr2.2008.10.018

Krembs, C., Eicken, H., and Deming, J. W. (2011). Exopolymer alteration of physical properties of sea ice and implications for ice habitability and biogeochemistry in a warmer Arctic. *Proc. Natl. Acad. Sci.* 108, 3653–3658. doi: 10.1073/pnas.1100701108

Krembs, C., Eicken, H., Junge, K., and Deming, J. W. (2002). High concentrations of exopolymeric substances in Arctic winter sea ice: implications for the polar ocean carbon cycle and cryoprotection of diatoms. *Deep Sea Res. Part Oceanogr Res. Pap.* 49, 2163–2181. doi: 10.1016/s0967-0637(02)00122-x

Lever, M. A., Rogers, K. L., Lloyd, K. G., Overmann, J., Schink, B., Thauer, R. K., et al. (2015). Life under extreme energy limitation: a synthesis of laboratory-and field-based investigations. *FEMS Microbiol. Rev.* 39, 688–728. doi: 10.1093/femsre/fuv020

Ma, Y., Dixit, V., Innes, M. J., Guo, X., and Rackauckas, C. (2021). "A comparison of automatic differentiation and continuous sensitivity analysis for derivatives of differential equation solutions," in *2021 IEEE High Performance Extreme Computing Conference (HPEC)*, Waltham, MA, USA. 1–9.

Marion, G. M., Farren, R. E., and Komrowski, A. J. (1999). Alternative pathways for seawater freezing. *Cold Reg. Sci. Technol.* 29, 259–266. doi: 10.1016/s0165-232x(99)00033-6

Marion, G. M., Fritsen, C. H., Eicken, H., and Payne, M. C. (2003). The search for life on Europa: limiting environmental factors, potential habitats, and earth analogues. *Astrobiology* 3, 785–811. doi: 10.1089/153110703322736105

Marx, J. G., Carpenter, S. D., and Deming, J. W. (2009). Production of cryoprotectant extracellular polysaccharide substances (EPS) by the marine psychrophilic bacterium *Colwellia psychrerythraea* strain 34H under extreme conditions. *Can. J. Microbiol.* 55, 63–72. doi: 10.1139/w08-130

Mathis, J. T., Hansell, D. A., and Bates, N. R. (2005). Strong hydrographic controls on spatial and seasonal variability of dissolved organic carbon in the Chukchi Sea. *Deep Sea Res. Part Ii Top Stud. Oceanogr.* 52, 3245–3258. doi: 10.1016/j.dsr2.2005.10.002

Meurer, A., Smith, C. P., Paprocki, M., Čertík, O., Kirpichev, S. B., Rocklin, M., et al. (2017). SymPy: symbolic computing in Python. *Peerj Comput. Sci.* 3:e103. doi: 10.7717/peerj-cs.103

Meyer, H., Schirrmeister, L., Andreev, A., Wagner, D., Hubberten, H.-W., Yoshikawa, K., et al. (2010). Lateglacial and Holocene isotopic and environmental history of northern coastal Alaska – results from a buried ice-wedge system at Barrow. *Quat. Sci. Rev.* 29, 3720–3735. doi: 10.1016/j.quascirev.2010.08.005

Monod, J. (1949). The growth of bacterial cultures. *Ann. Rev. Microbiol.* 3, 371–394. doi: 10.1146/annurev.mi.03.100149.002103

Nguyen, D., and Maranger, R. (2011). Respiration and bacterial carbon dynamics in Arctic Sea ice. *Polar Biol.* 34, 1843–1855. doi: 10.1007/s00300-011-1040-z

Osman, M. B., Tierney, J. E., Zhu, J., Tardif, R., Hakim, G. J., King, J., et al. (2021). Globally resolved surface temperatures since the last glacial maximum. *Nature* 599, 239–244. doi: 10.1038/s41586-021-03984-4

Pirt, S. J. (1982). Maintenance energy: a general model for energy-limited and energy-sufficient growth. *Arch. Microbiol.* 133, 300–302. doi: 10.1007/bf00521294

Price, P. B., and Sowers, T. (2004). Temperature dependence of metabolic rates for microbial growth, maintenance, and survival. *Proc. Natl. Acad. Sci.* 101, 4631–4636. doi: 10.1073/pnas.0400522101

Priscu, J. C., and Hand, K. P. (2012). Microbial habitability of icy worlds: as our exploration of space begins its sixth decade, we have new tools and techniques to probe questions of planetary habitability. *Microbe Mag.* 7, 167–172. doi: 10.1128/microbe.7.167.1

Rackauckas, C., and Nie, Q. (2016). Differential equations. Jl – a performant and feature-rich ecosystem for solving differential equations in Julia. *J. Open Res. Softw.* 5:15. doi: 10.5334/jors.151

Rapp, J. Z., Sullivan, M. B., and Deming, J. W. (2021). Divergent genomic adaptations in the microbiomes of Arctic subzero sea-ice and cryopeg brines. *Front. Microbiol.* 12:701186. doi: 10.3389/fmicb.2021.701186

Rossel, P. E., Bienhold, C., Hehemann, L., Dittmar, T., and Boetius, A. (2020). Molecular composition of dissolved organic matter in sediment porewater of the arctic deep-sea observatory HAUSGARTEN (Fram Strait). *Front. Mar. Sci.* 7:428. doi: 10.3389/fmars.2020.00428

Rowe, G. T., and Deming, J. W. (1985). The role of bacteria in the turnover of organic carbon in deep-sea sediments. *J. Mar. Res.* 43, 925–950. doi: 10.1357/002224085788453877

Schmidt, J. L., Deming, J. W., Jumars, P. A., and Keil, R. G. (1998). Constancy of bacterial abundance in surficial marine sediments. *Limnol. Oceanogr.* 43, 976–982. doi: 10.4319/lo.1998.43.5.0976

Shampine, L. F., and Reichelt, M. W. (1997). The MATLAB ODE suite. *SIAM J. Sci. Comput.* 18, 1–22. doi: 10.1137/s1064827594276424

Sholes, S. F., Krissansen-Totton, J., and Catling, D. C. (2019). A maximum subsurface biomass on Mars from untapped free energy: CO and H_2 as potential antibiosignatures. *Astrobiology* 19, 655–668. doi: 10.1089/ast.2018.1835

Showalter, G. M. (2020). *Acquisition, degradation, and cycling of organic matter within sea-ice brines by bacteria and their viruses*. Seattle, WA: University of Washington.

Sobol, I. M. (2001). Global sensitivity indices for nonlinear mathematical models and their Monte Carlo estimates. *Math. Comput. Simulat.* 55, 271–280. doi: 10.1016/S0378-4754(00)00270-6

Sobol, I. M., Tarantola, S., Gatelli, D., Kucherenko, S. S., and Mauntz, W. (2007). Estimating the approximation error when fixing unessential factors in global sensitivity analysis. *Reliab. Eng. Syst. Safe.* 92, 957–960. doi: 10.1016/j.ress.2006.07.001

Teske, A. P. (2005). The deep subsurface biosphere is alive and well. *Trends Microbiol.* 13, 402–404. doi: 10.1016/j.tim.2005.07.004

Tijhuis, L., Loosdrecht, M. C. M. V., and Heijnen, J. J. (1993). A thermodynamically based correlation for maintenance Gibbs energy requirements in aerobic and anaerobic chemotrophic growth. *Biotechnol. Bioeng.* 42, 509–519. doi: 10.1002/bit.260420415

Trembath-Reichert, E., Shah Walter, S. R., Ortiz, M. A. F., Carter, P. D., Girguis, P. R., and Huber, J. A. (2021). Multiple carbon incorporation strategies support microbial survival in cold subseafloor crustal fluids. *Sci. Adv.* 7:eabg0153. doi: 10.1126/sciadv.abg0153

van Everdingen, R.. (2005). *Multi-language glossary of permafrost and related ground-ice terms*. Boulder, CO: National Snow and Ice Data Center/World Data Center for Glaciology.

Verardo, D. J., Froelich, P. N., and McIntyre, A. (1990). Determination of organic carbon and nitrogen in marine sediments using the Carlo Erba NA-1500 analyzer. *Deep Sea Res. Part Oceanogr. Res. Pap.* 37, 157–165. doi: 10.1016/0198-0149(90)90034-s

Vetter, Y. A., Deming, J. W., Jumars, P. A., and Krieger-Brockett, B. B. (1998). A predictive model of bacterial foraging by means of freely released extracellular enzymes. *Microbial. Ecol.* 36, 75–92. doi: 10.1007/s002489900095

Waskom, M. (2021). Seaborn: statistical data visualization. *J. Open Source Softw.* 6:3021. doi: 10.21105/joss.03021

Yager, P. L., and Deming, J. W. (1999). Pelagic microbial activity in an arctic polynya: testing for temperature and substrate interactions using a kinetic approach. *Limnol. Oceanogr.* 44, 1882–1893. doi: 10.4319/lo.1999.44.8.1882

Zhong, Z.-P., Rapp, J. Z., Wainaina, J. M., Solonenko, N. E., Maughan, H., Carpenter, S. D., et al. (2020). Viral ecogenomics of Arctic cryopeg brine and sea ice. *Msystems* 5, e00246–e00220. doi: 10.1128/msystems.00246-20

Frontiers in Microbiology

TYPE Correction
PUBLISHED 10 January 2024
DOI 10.3389/fmicb.2023.1355342

EDITED AND REVIEWED BY
William J. Brazelton,
The University of Utah, United States

*CORRESPONDENCE
Georges Kanaan
✉ gkanaan@uw.edu

RECEIVED 13 December 2023
ACCEPTED 19 December 2023
PUBLISHED 10 January 2024

CITATION
Kanaan G, Hoehler TM, Iwahana G and Deming JW (2024) Corrigendum: Modeled energetics of bacterial communities in ancient subzero brines. *Front. Microbiol.* 14:1355342. doi: 10.3389/fmicb.2023.1355342

Corrigendum: Modeled energetics of bacterial communities in ancient subzero brines

Georges Kanaan[1]*, Tori M. Hoehler[2], Go Iwahana[3] and Jody W. Deming[1]

[1]School of Oceanography and Astrobiology Program, University of Washington, Seattle, WA, United States, [2]NASA Ames Research Center, Moffett Field, CA, United States, [3]International Arctic Research Center, University of Alaska Fairbanks, Fairbanks, AK, United States

KEYWORDS

cryopeg, Arctic, extremophiles, permafrost, maintenance energy

A corrigendum on
Modeled energetics of bacterial communities in ancient subzero brines

Kanaan, G., Hoehler, T. M., Iwahana, G., and Deming, J. W. (2023). *Front. Microbiol.* 14:1206641. doi: 10.3389/fmicb.2023.1206641

In the published article, there was an error. The temperature of the permafrost is incorrectly characterized as near-constant; although temperature was always below freezing, some changes occurred during the period considered.

A correction has been made to Material and Methods, Model assumptions and limitations, 2. This sentence previously stated:

"The assumption is not unreasonable given the hydrological isolation of the brines and the near-constant temperatures that have kept their surroundings frozen throughout their lifetimes (Iwahana et al., 2021; Osman et al., 2021)."

The corrected sentence appears below:

"The assumption is not unreasonable given the hydrological isolation of the brines and the temperatures that have kept their surroundings frozen throughout their lifetimes (Iwahana et al., 2021; Osman et al., 2021)."

There was another error resulting from a typo. The stated exponent for the value of dissolved inorganic carbon in CBIW is incorrect because the multiplier 10 was typed twice.

A correction has been made to Results, Brine dissolved inorganic carbon, 1. This sentence previously stated:

"The dissolved inorganic carbon content of frozen sediment from CBIW (in 2018) was $4.9 \times 10 \times 10^{10}$ fg C mL−1".

The corrected sentence appears below:

"The dissolved inorganic carbon content of frozen sediment from CBIW (in 2018) was 4.9×10^{10} fg C mL−1".

The authors apologize for these errors and state that they do not change the scientific conclusions of the article in any way. The original article has been updated.

Publisher's note

frontiers | Frontiers in Microbiology

TYPE Original Research
PUBLISHED 27 July 2023
DOI 10.3389/fmicb.2023.1206414

EDITED BY
Bo Barker Jørgensen,
Aarhus University, Denmark

REVIEWED BY
Pinaki Sar,
Indian Institute of Technology Kharagpur, India
Axel Schippers,
Federal Institute For Geosciences and Natural Resources, Germany

*CORRESPONDENCE
Hanni Vigderovich
✉ hannil@post.bgu.ac.il

RECEIVED 15 April 2023
ACCEPTED 10 July 2023
PUBLISHED 27 July 2023

CITATION
Vigderovich H, Eckert W, Elvert M, Gafni A, Rubin-Blum M, Bergman O and Sivan O (2023) Aerobic methanotrophy increases the net iron reduction in methanogenic lake sediments. *Front. Microbiol.* 14:1206414.
doi: 10.3389/fmicb.2023.1206414

Aerobic methanotrophy increases the net iron reduction in methanogenic lake sediments

Hanni Vigderovich[1]*, Werner Eckert[2], Marcus Elvert[3], Almog Gafni[1], Maxim Rubin-Blum[4], Oded Bergman[1,2] and Orit Sivan[1]

[1]Department of Earth and Environmental Sciences, Ben-Gurion University of the Negev, Beer Sheva, Israel, [2]The Yigal Allon Kinneret Limnological Laboratory, Israel Oceanographic and Limnological Research, Migdal, Israel, [3]MARUM—Center for Marine Environmental Sciences and Faculty of Geosciences, University of Bremen, Bremen, Germany, [4]Israel Oceanographic and Limnological Research, National Institute of Oceanography, Haifa, Israel

In methane (CH_4) generating sediments, methane oxidation coupled with iron reduction was suggested to be catalyzed by archaea and bacterial methanotrophs of the order Methylococcales. However, the co-existence of these aerobic and anaerobic microbes, the link between the processes, and the oxygen requirement for the bacterial methanotrophs have remained unclear. Here, we show how stimulation of aerobic methane oxidation at an energetically low experimental environment influences net iron reduction, accompanied by distinct microbial community changes and lipid biomarker patterns. We performed incubation experiments (between 30 and 120 days long) with methane generating lake sediments amended with ^{13}C-labeled methane, following the additions of hematite and different oxygen levels in nitrogen headspace, and monitored methane turnover by ^{13}C-DIC measurements. Increasing oxygen exposure (up to 1%) promoted aerobic methanotrophy, considerable net iron reduction, and the increase of microbes, such as *Methylomonas*, *Geobacter*, and *Desulfuromonas*, with the latter two being likely candidates for iron recycling. Amendments of ^{13}C-labeled methanol as a potential substrate for the methanotrophs under hypoxia instead of methane indicate that this substrate primarily fuels methylotrophic methanogenesis, identified by high methane concentrations, strongly positive $\delta^{13}C_{DIC}$ values, and archaeal lipid stable isotope data. In contrast, the inhibition of methanogenesis by 2-bromoethanesulfonate (BES) led to increased methanol turnover, as suggested by similar ^{13}C enrichment in DIC and high amounts of newly produced bacterial fatty acids, probably derived from heterotrophic bacteria. Our experiments show a complex link between aerobic methanotrophy and iron reduction, which indicates iron recycling as a survival mechanism for microbes under hypoxia.

KEYWORDS

aerobic methanotrophy, iron reduction, lake sediments, iron recycling, methylotrophy, methanogenesis

Highlights

- Stimulation of aerobic methanotrophy with oxygen levels up to 1% increases the net iron reduction in energy-limited methane-generating lake sediments.
- Iron reduction is performed either by iron-reducing bacteria, such as *Desulfuromonas* or *Geobacter*, or by the methanotrophs themselves in a survival mode.
- Under hypoxia, methanol is not involved as a substrate for the methanotrophs instead of methane.

1. Introduction

Methane (CH_4) is a very efficient and potent greenhouse gas, 28 times more efficient than CO_2 on a 100-year time scale (Myhre et al., 2013). It is microbially produced in anoxic marine and freshwater settings. Freshwater environments contribute greatly to methane emissions (Bastviken et al., 2011), despite taking up a much smaller portion of the Earth's surface than oceans (Downing et al., 2006). The methane formed in the sediments can be attenuated by oxidation with available electron acceptors. Methane oxidation is microbially mediated in two fashions, anaerobically or aerobically. Anaerobic oxidation of methane (AOM) in marine sediments is mainly coupled to sulfate reduction via anaerobic methanotrophs (ANMEs; Knittel and Boetius, 2009). In freshwater sediments, which are usually depleted in sulfate, AOM is coupled to other electron acceptors like nitrate, nitrite, metal oxides, and humic substances. It is performed mostly by different ANMEs (mainly by ANME-2) with or without a bacterial partner (Raghoebarsing et al., 2006; Haroon et al., 2013; Nordi and Thamdrup, 2014; Ettwig et al., 2016; Lu et al., 2016; Scheller et al., 2016; Cai et al., 2018; Elul et al., 2021).

Aerobic methane oxidation is found in the oxic-anoxic transition zone (Bender and Conrad, 1994; He et al., 2012), usually at the sediment–water interface or the oxycline in the water column of stratified systems, and is performed by different methanotrophic bacteria (type-I, II, X; McDonald et al., 2008; Trotsenko and Murrell, 2008; Smith and Wrighton, 2019). Generally, during aerobic methanotrophy, bacteria use the enzyme complex methane monooxygenase (MMO) to oxidize methane with oxygen to methanol. The methanol is then oxidized to formaldehyde, which is finally oxidized to CO_2 (Dalton, 2005).

Interestingly, growing evidence in recent years indicates aerobic methanotrophs and methylotrophs activity below the oxic-anoxic zone in the anoxic hypolimnion of freshwater lakes (Blees et al., 2014; Oswald et al., 2016a) and sediments (Beck et al., 2013; Bar-Or et al., 2015; Martinez-Cruz et al., 2017; Su et al., 2022). Concomitantly, obligate anaerobic microbes, such as methanogens and iron reducers, were observed there (Elul et al., 2021; Van Grinsven et al., 2021; Steinsdóttir et al., 2022; Su et al., 2022).

Three possible scenarios can explain this co-occurrence of aerobic and anaerobic microorganisms; (1) Microlevel oxygen is trapped and survive this environment (Wang et al., 2018). The oxygen is slowly released so it does not poison the obligatory anaerobes. In this case, long-term anoxic conditions will terminate aerobic activity (Vigderovich et al., 2022). (2) Low oxygen levels are continuously produced in the anoxic environment and are immediately used by these methanotrophs. This has been demonstrated for the aerobic bacteria *Methylomirabilis* (NC10), which produce and utilize oxygen during a unique denitrification process to oxidize methane (Ettwig et al., 2010). Similarly, the archaeon *Nitrosopulimus maritimus* is suggested to produce oxygen upon depletion (to 1 nM) to mediate ammonia oxidation (Kraft et al., 2022). Alphaproteobacterial methanotrophs have been shown to survive under hypoxia by utilizing methanobactins to generate oxygen and fuel their methanotrophic activity (Dershwitz et al., 2021). (3) Under hypoxia conditions, aerobic methanotrophs survival is mediated by anaerobic metabolism. Recent experiments with sediments and pure cultures of methanotrophic bacteria show that these methanotrophs can use electron acceptors other than oxygen under hypoxia. The Gammaproteobacterial methanotrophs *Methylomonas* and *Methylosinus* were suggested to perform methane oxidation coupled with the reduction of metal oxides (Zheng et al., 2020). The Alphaproteobacterial methanotroph *Methylocystis* sp., strain SB2 was shown to couple methane oxidation with iron reduction (Dershwitz et al., 2021). *Methylomonas denitrificans* strain FJG1 expresses genes that encode for nitrate reduction (Kits et al., 2015; Orata et al., 2018). In addition, it is suggested that the Gammaproteobacteria *Methylocaldum* can couple methane oxidation to N_2O reduction in wetland sediments under anoxic conditions (Cheng et al., 2021). It should be noted that the presence of aerobic methanotrophic bacteria in a highly reduced environment without detectable oxygen raises the question whether the environment accounts as anoxic or hypoxic. In this study, we define hypoxia as a reduced environment with down to undetectable oxygen levels (below our detection limit of 1 ppb) but with evidence for active aerobic metabolism. The conditions are anoxic when oxygen is not detected and there is no evidence for aerobic activity.

Lake Kinneret (Sea of Galilee) is a monomictic lake in northern Israel. Its average depth is 24 m, and its maximum depth is 42 m at the center (station A). The lake is stratified between March and December, leading to about 20 m of hypolimnion with undetectable oxygen concentrations most of the stratified period (Adler et al., 2011). Sulfate is depleted in the upper few centimeters of the sediment and the methane zone below is characterized by low redox conditions (−200 mv) and unmeasurable oxygen levels (Eckert and Conrad, 2007). Despite this, *pmoA* gene-bearing methanotrophic bacteria together with *mcr* gene-bearing archaea were suggested to mediate methane oxidation coupled with iron reduction (Bar-or et al., 2017; Elul et al., 2021; Vigderovich et al., 2022) in these sediments. Aerobic type-I Gammaproteobacteria methanotrophs were observed, and evidence for aerobic methanotrophy has been demonstrated by the presence of specific fatty acids, the *pmoA* functional gene, and metagenomic analysis of incubation experiments (Bar-Or et al., 2015, 2017; Elul et al., 2021). These aerobic methanotrophs operate alongside methanogenesis and iron reduction in the methane generating sediments (Elul et al., 2021). This phenomenon was observed also in other sediments of shallow lakes (Martinez-Cruz et al., 2017; Su et al., 2022). Given that *pmoA* activity must involve oxygen (Dalton, 2005), and that it appears only in the natural (fresh) methane-generating sediments and incubations (and not in long-term two-stage incubations; Vigderovich et al., 2022), it seems that remnant microlevels of oxygen would be the most plausible scenario responsible for the methanotrophs' activity, making this environment hypoxic and not completely anoxic (with remnant oxygen but low enough redox values that enable the life of strictly anaerobes) However, it is unknown how the aerobic microbes survive and whether their survival is linked to the observed iron reduction coupled with methane oxidation in these sediments.

Here, we explored the potential link between aerobic methanotrophy and iron reduction in methane generating sediments by injecting low (micro) levels of oxygen into lake sediment slurries and quantified its effect on net iron reduction. This is by a set of slurry incubations with methane generating sediments of Lake Kinneret amended with ^{13}C-labeled methane, hematite, and with and without inhibition of methanogenesis by BES. Finally, we tested whether methanotrophic bacteria can operate under hypoxia by using the potential intermediate methanol as a substrate by another set of slurry incubations with ^{13}C-labeled methanol.

2. Materials and methods

2.1. Study site

The sediments and the extracted porewater used in this study were from the methane-generating depth (below 20 cm from the water–sediment interface from station A). They are mostly carbonatic-clay and contained 7% iron oxides (Vigderovich et al., 2022) and about 3% total organic carbon (TOC). Dissolved sulfate concentrations decrease from about 0.5 mM at the surface sediment to depletion around 10 cm depth, where dissolved Fe(II) appears and increases with depth up to 80 µM at 30 cm depth. Dissolved methane concentrations increase with sediment depth, reaching a maximum of 2 mM at 10–15 cm depth. The concentrations decrease then to 0.5 mM at 30 cm depth. The dissolved organic carbon (DOC) concentrations in the porewater increase with sediment depth, from ~6 mg C L^{-1} at the sediment–water interface to 17 mg C L^{-1} at 25 cm depth (Adler et al., 2011; Sivan et al., 2011; Bar-Or et al., 2015).

2.2. Sediment sampling

Sediment cores were collected using a gravity corer on four day-long sampling campaigns (Table 1), on the research vessel *Lillian*, between 2017 and 2021 from station A in the center of the lake (water depth 42 m). In each campaign, 1–2 Perspex cores of 50 cm long were collected for the incubation experiment, and another 10 cores were collected for porewater extractions. For the porewater extraction, sediment from the methane-generating zone (sediment depth > 20 cm) of each core was transferred to a 5 L plastic container onboard. The cores and the container were brought to the lab, and the cores were kept at 4°C, while porewater was extracted on the same day by centrifugation as described in Vigderovich et al. (2022).

2.3. Experimental settings

Five experiments are presented in this study, one of them (experiment C) is a slurry experiment set up with freshly collected sediment and is described below. The other four experiments (A, B, D, and E) are long-term two-stage slurry experiments (details in Vigderovich et al., 2022). In short, sediments from the methane generating zone of the collected cores were transferred within 48 h of their collection, under anaerobic conditions, to a 250 mL pre-autoclaved glass bottle and diluted with porewater extracted from the methane generating sediments to reach a 1:1 sediment-to-porewater ratio (pre-incubated slurry). The incubations were flushed with N_2 (99.999%, MAXIMA, Israel) and methane ($^{12}CH_4 + ^{13}CH_4$, 99.99%, MAXIMA, Israel and 99%, Sigma-Aldrich, respectively) was injected into the incubations to reach 20% of the headspace. After at least 3 months of incubation, sub-samples (18–20 g each) from each pre-incubated slurry were transferred under a laminar hood, with continuous flushing of N_2 to 60 mL pre-autoclaved glass bottles. The slurry was then diluted with filtered (0.22 µm) fresh anoxic porewater from the same depth as the sediments to reach a 1:3 sediment-to-porewater ratio. All experiments were kept in the dark at 20°C. The bottles were shaken before every porewater sampling point, before oxygen measurements, and after every oxygen injection. This was to ensure a homogeneous distribution of the oxygen and the dissolved constituents. We describe below each experiment; details summary of the experiments can be found in Table 1 and Figure 1.

In experiment A, seven sub-samples of pre-incubated (set-up in August 2017) slurry were transferred to seven 60 mL experiment glass bottles. Hematite (Sigma-Aldrich, <5 µm, 99%) was added to six of the bottles to reach final concentration of 10 mM, as was done previously in Vigderovich et al. (2022). Each slurry was further diluted with fresh, filter-sterilized, and anoxic porewater and was crimped-sealed. The final headspace volume in the experiment bottles was 20 mL. The bottles were flushed with N_2 for 5 min, shaken vigorously, and flushed again thrice (Sivan et al., 2014) to confirm anoxic starting conditions. This was verified with an optical oxygen sensor (details in the analytical methods below). The killed control bottle was autoclaved twice, cooled and only then hematite was added to the killed control bottle. Finally, 1.5 mL of methane was injected into all the experiment bottles (1 mL $^{12}CH_4$ + 0.5 mL $^{13}CH_4$) to reach final concentration of 7.5% methane in the headspace. The experiment consisted of four treatments, 0% O_2 + hematite, 1% O_2 + hematite, 0.1% O_2 + hematite, and killed control with 1% O_2 + hematite ("% O_2" refers to the oxygen concentrations in the headspace). The treatments were set up in duplicates. The duration of this experiment was 70 days. During that time porewater samples were taken for dissolved Fe(II) concentrations and δ^{13}C-DIC analyses. Oxygen gas (99.999%, MAXIMA, Israel) was injected into the specific bottles once a week and the oxygen levels in the headspace were monitored. A sample was taken from the 1% O_2 treatment at the start of the experiment and after 52 days for metagenome analysis. The experiment bottles were kept after the experiment ended, and a sample for lipid analysis was taken after 558 days.

Experiment B was set-up from pre-incubated slurry (set-up in September 2018), similarly to experiment A. It consisted with the seven following treatments $^{13}CH_4$, 10 mM hematite, hematite + BES, 0.3% O_2 + hematite, 1% O_2 + hematite, 20% O_2 + hematite, 1% O_2 + hematite + BES, and killed control + 1% O_2 + hematite + BES. 1 mL

TABLE 1 Experiments detail summary.

Experiment	Sediment collection time	Treatment	No. of bottles	$^{12}CH_4$ [mL]	$^{13}CH_4$ [mL]	CH_4 in headspace [%]	Hematite [mM]	O_2 in headspace [%]	$^{13}CH_3OH$ [mM]	BES [mM]	Sampling point for metagenome/16S rRNA gene [days]	Duration
A	Aug-17	$^{13}CH_4$ + hematite+1% O_2	2	1	0.5	7.5	10	1			0, 52	70
		$^{13}CH_4$ + hematite+0.1% O_2	2	1	0.5		10	0.1				
		$^{13}CH_4$ + hematite	2	1	0.5		10					
		killed+$^{13}CH_4$ + hematite+1% O_2	1	1	0.5		10	1				
B	Sep-18	$^{13}CH_4$	2		1	5						111
		$^{13}CH_4$ + hematite	2		1		10					
		$^{13}CH_4$ + hematite+BES	2		1		10			20		
		$^{13}CH_4$ + hematite+0.3% O_2	2		1		10	0.3				
		$^{13}CH_4$ + hematite+1% O_2	2		1		10	1				
		$^{13}CH_4$ + hematite+20% O_2	2		1		10	20				
		$^{13}CH_4$ + hematite+1% O_2 + BES	2		1		10	1		20		
		Killed+$^{13}CH_4$ + hematite+1% O_2 + BES	2		1		10	1		20		
C	Mar-21	CH_4 + hematite+1% O_2	5	1.5		4.2	10	1				37
		N_2 + hematite+1% O_2	3				10	1				
D	Dec-18	no additions	3								0 (two samples)	147
		$^{13}CH_3OH$	3						0.56		459	
		$^{13}CH_4$	3		1	4.2						
		Killed+$^{13}CH_3OH$	2						0.56			
E	Dec-18	no additions	2								0	129
		$^{13}CH_3OH$	2						0.56			
		$^{13}CH_3OH$ + BES	2						0.56	20	284	
		$^{13}CH_3OH$ + hematite	2				10		0.56		284	
		hematite	2				10					

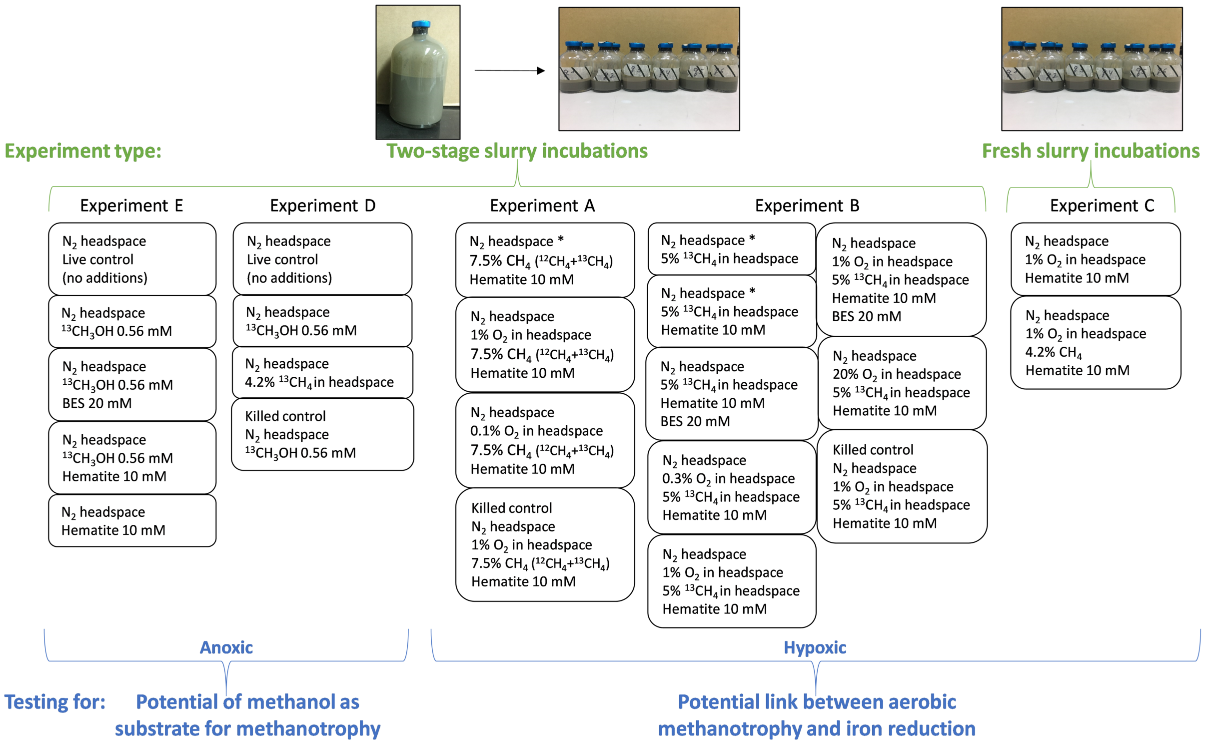

FIGURE 1
Summary of the experimental settings. Two experiment types are presented (in green): “fresh slurry incubations” with freshly collected methane-generating sediments and porewater from the same depth in a 1:3 sediment-to-porewater ratio. This type includes only experiment C. The second type is “two-stage slurry incubations.” Methane-generating sediments are incubated first in a 1:1 sediment-to-porewater ratio with ^{13}C-labeled methane. In the second stage, the slurry is divided into smaller incubations with different amendments and diluted to a 1:3 sediment-to-porewater ratio. This type includes experiments A, B, D, and E. The experiments are divided according to their purpose (in blue). Experiments A–C test the link between aerobic methanotrophy and iron reduction by oxygen injections; thus, they are hypoxic experiments. In these experiments, $\delta^{13}C_{DIC}$, dissolved Fe(II) and oxygen concentrations in the headspace were measured regularly. A sample from the 1% O_2 treatment in experiment A was taken for metagenome and lipid analyses. Experiments D and E test methanol as a potential intermediate in methanotrophy under anoxic conditions. In these experiments, $\delta^{13}C_{DIC}$, dissolved Fe(II) and CH_4 concentrations were measured. Samples from both experiments were taken for 16S rRNA gene amplicon-based sequencing and lipid analysis. Asterisks denote treatments without oxygen injections (i.e., 0% O_2 in the headspace).

of BES stock solution (0.8 M) was injected into the specific treatment bottles to reach a final concentration of 20 mM, as was previously shown to inhibit the AOM in these sediments (Bar-Or et al., 2017). The final headspace volume of the bottles was 24 mL. The treatments were set up in duplicates. Due to a mistake, ^{13}C-labeled methane was injected into all experiment bottles in two pulses, 200 μL in the beginning of the experiment and another 1 mL after 21 days, reaching 5% methane in the headspace. It should be noted that in this experiment (and in experiment D) only ^{13}C-labeled methane was injected into the bottles, in a lower volume than experiment A. The methane concentrations were enough to sustain methane oxidation, and the higher labeling resulted in a faster ^{13}C-labeling of the DIC in the bottles without oxygen. During the experiment time of 111 days, water samples were taken for dissolved Fe(II) concentrations and $\delta^{13}C_{DIC}$. In addition, the oxygen levels were monitored in the headspace, and oxygen gas was injected into the specific bottles once a week.

Fresh sediments for experiment C were collected from the methane generating zone of a core collected in March 2021, were cut under anaerobic conditions into a zip lock bag, and 7 g of sediment sample was transferred to eight pre-autoclaved 60 mL glass bottles under a laminar hood. Hematite was added to all bottles (final concentration of 10 mM). Fresh, filter-sterilized, and anoxic porewater from the same depth as the sediments was added to reach a 1:3 sediment-to-porewater ratio. The final headspace volume was 32 mL. The bottles were crimped-sealed and flushed with N_2 for 1 h and stored in the dark at 4°C for 5 days. To the headspace of each bottle, 1.5 mL of air was injected to reach 1% oxygen in the headspace. 1.5 mL of methane was added to five of the bottles, and 1.5 mL of N_2 to the rest. Methane concentrations in the bottles headspace were 4.2%. The experiment consisted of two treatments: hematite + O_2 + CH_4 in a N_2 headspace and hematite + O_2 in a N_2 headspace. Oxygen concentrations were monitored in the headspace daily and when the levels depleted, the bottles were flushed with N_2, subsequently, air was reinjected to all bottles, and CH_4 to the relevant treatment bottles. The experiment bottles were sampled for dissolved Fe(II) concentrations and metagenome analysis (not presented here). The experiment's duration was 37 days.

Experiment D was set-up from a pre-incubated slurry (set-up in December 2018) in the same fashion as experiment B and consisted of four treatments, $^{13}CH_3OH$, $^{13}CH_4$, killed control +$^{13}CH_3OH$, and live control (no additions). For the methanol labeling, a stock of 101 mM concentration of ^{13}C-labeled methanol was prepared. Then, 0.2 mL of the stock was injected into the relevant experiment bottles. The final $^{13}CH_3OH$ concentration in the bottles was 0.56 mM. The killed control bottles were autoclaved twice and cooled, only then $^{13}CH_3OH$ was injected into them. The final head space volume in the experiment bottles was 24 mL. One milliter of ^{13}C-labeled methane was injected into the relevant treatment bottles (4.2% methane in the headspace). All the treatments were set up in triplicates except for the killed control, which was set up in duplicates due to the limited amount of the original 1:1 slurry that was used for this experiment. The duration of this experiment was 147 days, in which porewater was sampled for dissolved Fe(II) concentrations and $\delta^{13}C_{DIC}$, and the headspace was sampled for methane concentrations and $\delta^{13}C_{CH4}$. Two samples for 16S rRNA amplicon-based sequencing were taken from the unamended slurry at the beginning of the experiment (as t_0), and another sample, after the experiment ended, at day 459 of incubation from the $^{13}CH_3OH$ treatment. Samples for lipid analysis from the $^{13}CH_4$ and $^{13}CH_3OH$ treatments were taken after 462 days.

Experiment E was set-up from a pre-incubated slurry (set-up in December 2018) similarly to experiment D and consisted of five treatments, live control (no additions), $^{13}CH_3OH$, $^{13}CH_3OH$ + BES, $^{13}CH_3OH$ + hematite, and hematite. Each treatment was set up in duplicates. Hematite (Sigma-Aldrich, <5 μm, 99%) was added to reach a final concentration of 10 mM. BES was added to the bottles as in experiment B, and $^{13}CH_3OH$ was added as in experiment D. The final head space volume in the experiment bottles was 24 mL. All treatments were set up in duplicates. The duration of this experiment was 129 days, in which porewater was sampled for dissolved Fe(II) concentrations and $\delta^{13}C_{DIC}$, and the headspace was sampled for methane concentrations. Samples for 16S rRNA amplicon-based sequencing were taken from the unamended slurry at the beginning of the experiment and after the experiment ended, at day 284 of incubation, from the $^{13}CH_3OH$ + BES and $^{13}CH_3OH$ + hematite treatments. Samples for lipid analysis from the same treatments were taken after 287 days.

2.4. Analytical methods

2.4.1. Geochemical measurements

Dissolved Fe(II) samples were analyzed using the ferrozine method (Stookey, 1970) by a Hanon i2 visible spectrophotometer at a 562 nm wavelength with a detection limit of 1 μM. Samples for $\delta^{13}C_{DIC}$ and $\delta^{13}C_{CH4}$ values were measured on a DELTA V Advantage Thermo Scientific isotope-ratio mass spectrometer (IRMS) with a precision of ±0.1‰. Reported results refer to the Vienna Pee Dee Belemnite (VPDB) standard. Oxygen concentrations in the headspace were measured by a fiber optic oxygen meter (Fibox 3 trace, PreSens), using an optical oxygen sensor (type PSt6) glued to the inside of the experiment bottle, with a detection limit of 1 ppb. Methane concentrations were measured on a gas chromatograph (FOCUS GC, Thermo Fisher), equipped with a flame ionization detector (FID) with a detection limit of 1 nmol of methane.

2.4.2. Lipid analysis and calculation of new production

A sub-set of samples (Table 2) was investigated for the assimilation of ^{13}C-labeled methane into polar lipid-derived fatty acids (PLFAs) and ether lipid-derived hydrocarbons. A total lipid extract (TLE) was obtained according to Sturt et al. (2004) based on a modified Bligh & Dyer protocol. Before extraction, 1 μg each of 1,2-diheneicosanoyl-sn-glycero-3-phosphocholine and 2-methyloctadecanoic acid was added as internal standard. PLFAs in the TLE were converted to fatty acid methyl esters (FAMEs) using saponification with KOH/MeOH and derivatization with BF_3/MeOH (Elvert et al., 2003). Total ether lipid-derived biomarkers in the TLE were obtained using ether cleavage with BBr_3 followed by reduction with lithium triethylborohydride, forming hydrocarbons (Lin et al., 2010). For the O_2-treated sample, ether lipid-derived hydrocarbons were obtained from the intact polar fraction, which was separated from the apolar archaeal lipid compounds using preparative liquid chromatography (Meador et al., 2014) and processed as those present in the TLE. Both FAMEs and ether-cleaved hydrocarbons were analyzed by a GC–mass spectrometry (GC–MS; Thermo Finnigan TRACE GC coupled to a TRACE MS) for identification and by GC-IRMS (Thermo Scientific TRACE GC coupled via a GC IsoLink interface to a DELTA V Plus) to determine $\delta^{13}C$ values using column and temperature program settings described by Aepfler et al. (2019). $\delta^{13}C$ values are reported with an analytical precision better than 1‰ as determined by long-term measurements of an *n*-alkane standard with known isotopic composition of each compound. The incorporation of ^{13}C-methane or ^{13}C-methanol into PLFAs was calculated as the product of excess ^{13}C and the amount of PLFA carbon based on quantification via GC-FID measurements. Excess ^{13}C is the difference between the fractional abundance (F) of ^{13}C in PLFAs after relative to the t_0 sample where $F = {}^{13}C/({}^{13}C + {}^{12}C) = R/(R + 1)$, with R being derived from the measured $\delta^{13}C$ values as $R = (\delta^{13}C/1000 + 1) \times RVPDB$.

2.4.3. DNA extraction, 16S rRNA gene V4 amplicon-sequencing, and metagenomics

DNA was extracted from six sediment slurries samples (stored at −20°C) of the experiments D and E. Two samples from t_0 of experiment D and one sample from the $^{13}CH_3OH$ treatment. From experiment E one sample of t_0 and one sample from each of the following treatments $^{13}CH_3OH$ + BES and $^{13}CH_3OH$ + hematite. This was done by using the PowerSoil™ DNA Isolation Kit (QIAGEN, Hilden, Germany), according to the manufacturer's instructions and stored at −80°C. The 16S rRNA gene amplicon-based sequencing targeting the V4 region was performed using modified primer pair with consensus sequence CS1_515F (ACACTGACGACATGGTTCTA CAGTGCCAGCMGCCGCGGTAA) and CS2_806R (TACGGT AGCAGAGACTTGGTCTGG ACTACHVGGGTWTCTAAT; Sigma-Aldridge, Israel; Walters et al., 2015). 25 μL reactions of the first PCR contained 12.5 μL KAPA HiFi HotStart ReadyMix (KAPA Biosystems, Wilmington, WA, United States) and 0.75 μL forward and reverse primers at a final concentration of 300 nM each. The PCR conditions were an initial denaturation at 95°C for 3 min, followed by 25 cycles of 98°C for 20 s, 60°C for 15 s, and 72°C for 30 s. PCR products were visualized on a 2% agarose gel to measure the bands' relative intensity. Samples were pooled and purified using calibrated Ampure XP beads and used for library preparation. PCR visualization, purification, library preparation, and sequencing (2 × 250 bp pair-end reads) were performed at HyLabs (Israel) and sequenced on an Illumina MiSeq platform. Metagenomic libraries were constructed using NEBNext® Ultra™ IIDNA Library Prep Kit (Cat No. E7645) and sequenced as *circa* 100 million 150 bp paired-end reads using the Illumina NovaSeq at Novogene (Singapore). For metagenomics, we used the genomic

TABLE 2 Isotope change (in ‰) of most diagnostic bacterial fatty acids and archaeol-derived phytane compared to DIC as an overall indicator of methane/methanol turnover (complete isotopic pattern can be found in Supplementary Table S5).

Experiment	Treatment	$iC_{15:0}$	$C_{16:1\omega7}$	Phytane	$\delta^{13}C_{DIC}$	Sum of ^{13}C in bacterial fatty acids (ng ^{13}C/g dw)
D	$^{13}CH_4$	−27	−42	−3	300	1.2
D	$^{13}CH_3OH$	170	−7	2,300	2,500	7.8
E	$^{13}CH_3OH$ + BES	710	850	−5	2,500	20.3
E	$^{13}CH_3OH$ + hematite	710	140	1,600	2,800	16.1
A	$^{13}CH_4$ + hematite+1% O_2	480	4,100	16	2,500	57.9

In addition, the calculated sum of newly produced bacterial fatty acids is presented. Samples were taken from experiments D and E after 462 and 287 days of incubation, respectively.

DNA from two samples of the 1% O_2 + hematite treatment of experiment A: (i) at beginning of the experiment (t0) and (ii) after 52 days. Total genomic DNA was extracted using the DNeasy PowerLyzer PowerSoil Kit (Qiagen). Genomic DNA was eluted using 50 μL of elution buffer and stored at −20°C. Metagenomics libraries were prepared at the sequencing core facility at the University of Illinois Chicago using the Nextera XT DNA library preparation kit (Illumina, United States). Between 19 and 40 million, 2 × 150 bp paired-end reads per library were sequenced using Illumina NextSeq 500 metagenomes.

2.4.4. Bioinformatics

For the amplicon reads, QIIME2 V.2020–11 (Bolyen et al., 2019) was used for demultiplexing of the paired-end reads and following analysis. Sequence quality was assessed using the q2-demux plugin. Merging of reads into Amplicon Sequence Variants (ASVs) was done with DADA2 (Callahan et al., 2016), using the q2-dada2 plugin. To account for length variations, ASVs were defined by clustering at 100% similarity (Rognes et al., 2016). The 138-SILVA QIIME-release database was used for taxonomy assignment, at 99% clustering (Quast et al., 2012). The q2-feature-classifier plugin (Bokulich et al., 2018) was used to build the classifier (Extract-reads and fit-classifier-naive-bayes methods). Classification of the ASVs was done via the classify-sklearn method (ver. 0.23.1; Pedregosa et al., 2011). Downstream analysis in R was performed using the packages phyloseq (McMurdie and Holmes, 2013), and ggplot2 (Wickham, 2016). The QIIME2 feature-table plugin was used to generate the Heatmaps (Hunter, 2007; McDonald et al., 2012).

For metagenomics, read quality control, assembly, and binning were performed within ATLAS v2.1 framework (Kieser et al., 2020), using SPAdes v3.14 (Prjibelski et al., 2020) as assembler, as well as binning using metabat (Kang et al., 2015) and maxbin2 (Wu et al., 2016), finalized by DASTool (Sieber et al., 2018). Metagenome-assembled genomes were dereplicated using the 0.975 cutoffs with dRep (Olm et al., 2017). The relative read abundance was estimated by mapping the metagenomic reads at 0.9 identities to the genomes using BBMap (Bushnell, B., https://sourceforge.net/projects/bbmap/).

2.5. Statistical analysis

We measured the change in Fe(II) concentrations after the addition of methane or nitrogen in experiment C in four time points (after 0, 11, 23, and 37 days). To assess the change over time, we performed a separate statistical analysis for both treatments, via one-way repeated measures ANOVA. To analyze the differences between treatments, Two-way repeated measures ANOVA was performed. *Post hoc* tests were performed by pairwise *t*-tests, with Bonferroni correction for multiple testing. To achieve normality Fe(II) concentrations were Log10 transformed. Analysis was performed in R using the rstatix package.

3. Results

3.1. Aerobic methanotrophy and iron reduction

Three incubation experiments (A, B, and C) tested how exposure to limited amounts of oxygen affects the methanotrophy and iron reduction in methane-generating sediments of Lake Kinneret. In experiment A, oxygen was injected repeatedly to reach two final concentrations (1 and 0.1%) in the headspace. The $\delta^{13}C_{DIC}$ values of the 1% O_2 treatment increased intensively and reached up to 2,500‰ (Figure 2A; Supplementary Table S1). In the 0.1% treatment, the values increased by 37‰ during the experiment. The values of the bottles without the addition of oxygen also increased during the experiment, but only by 19‰. The average initial dissolved Fe(II) concentrations were 20 ± 8 μM. The highest Fe(II) concentrations change was in the 1% O_2 treatment (Figure 2B; Supplementary Table S2). The change in Fe(II) concentrations of the control and the 0.1% O_2 treatments were 16 and 11 μM, respectively. Using the more frequent O_2 measurements in the beginning of the experiment, the oxygen consumption rate was calculated to be 0.03% O_2 per g sediment per day (Figure 2C).

To corroborate the findings obtained in experiment A and to extend our comprehension of the impact of oxygen on iron reduction, experiment B (Figure 3; Supplementary Figure S1) was set up. Oxygen was injected to reach three different concentrations of 0.3, 1, and 20% in the headspace. The $\delta^{13}C_{DIC}$ values of the 20% O_2 treatment were the highest (>10,000‰), and the 1% O_2 treatments, with and without BES, reached approximately 2,000‰ after 60 days (Figure 3A; Supplementary Table S3). Both treatments were not measured for $\delta^{13}C_{DIC}$ after 60 days because of a memory effect of the IRMS (due to the very high isotopic values). The $\delta^{13}C_{DIC}$ values of the 0.3% oxygen treatment reached 2,381‰ at the end of the experiment. The isotopic values of the $^{13}CH_4$-only and hematite treatments increased as well and reached 261 and 210‰ (respectively) by the end of the experiment. The $\delta^{13}C_{DIC}$ values of the hematite and BES treatment did not change throughout the experiment (Supplementary Figure S1). The average

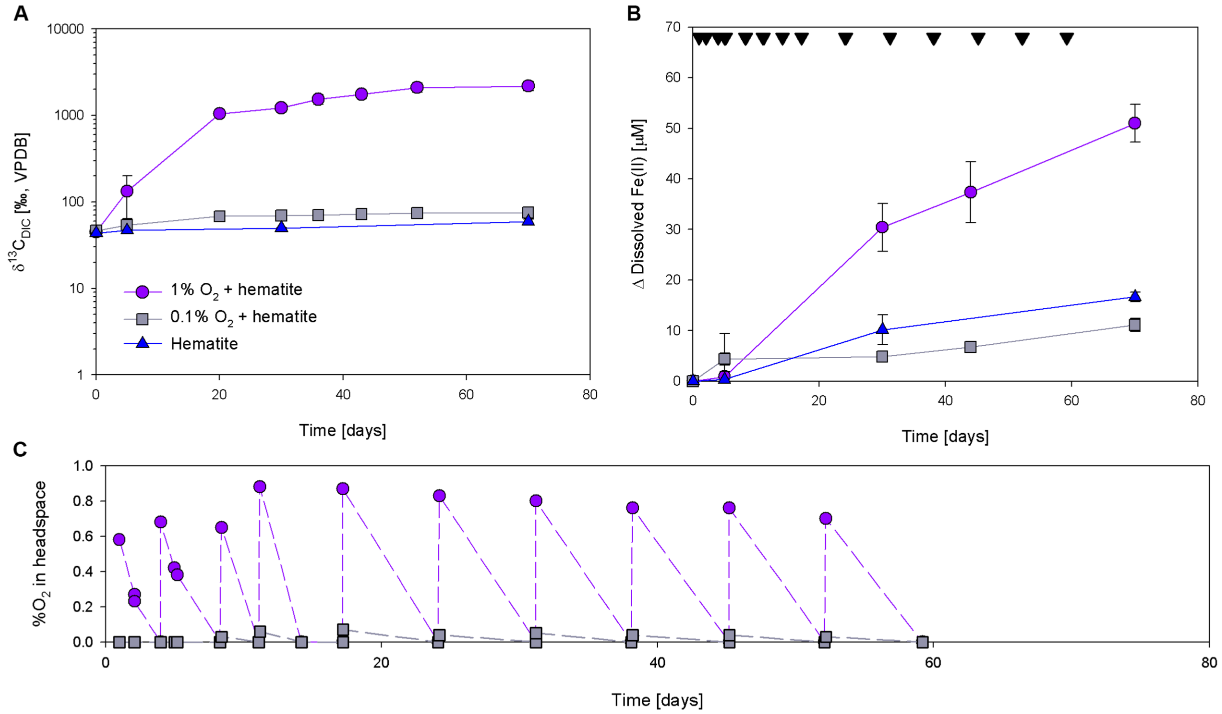

FIGURE 2

Development of $\delta^{13}C_{DIC}$ **(A)**, Δ dissolved Fe(II) **(B)**, and $\%O_2$ **(C)** during experiment A with the additions of ^{13}C-labeled methane, 10 mM hematite and injection of oxygen. Black upside-down triangles in panel **(B)** represent oxygen injections time. Error bars represent the average deviation from the mean of duplicate bottles.

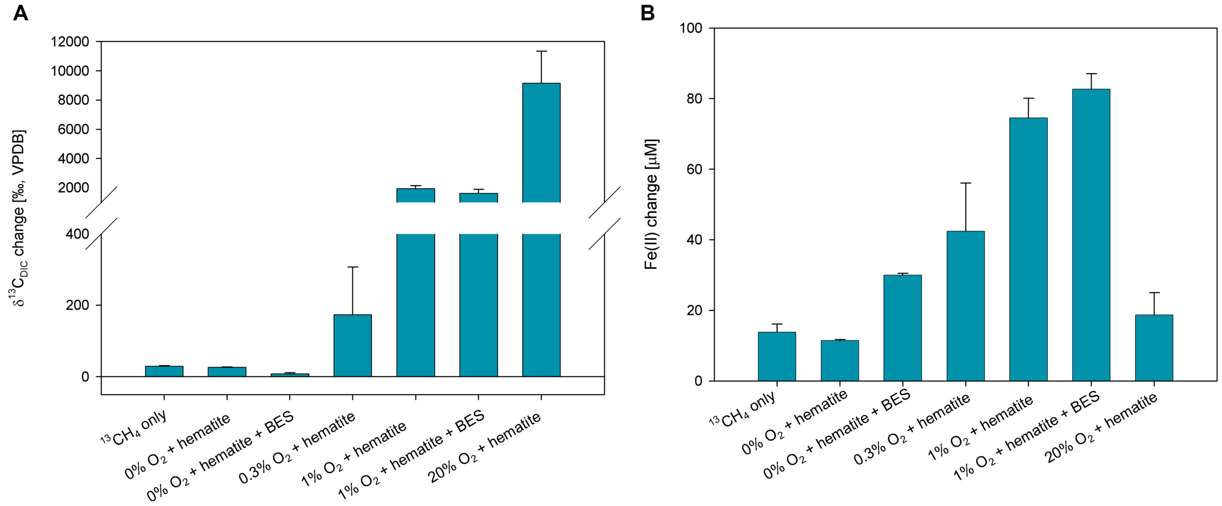

FIGURE 3

Net change of $\delta^{13}C_{DIC}$ after 61 days **(A)** and dissolved Fe(II) after 111 days **(B)** of experiment B, where 10 mM hematite and 20 mM BES were added in addition to ^{13}C-labeled methane and oxygen injections. Error bars represent the average deviation from the mean of the duplicate bottles.

initial dissolved Fe(II) concentrations were 40 ± 6 µM. The change in the Fe(II) concentrations increased in all treatments, except for the 20% O_2 treatment which remained the same with low concentrations (Figure 3B; Supplementary Table S4). The highest change was in the 1% O_2 treatment with the addition of BES, then the treatment with 1% O_2 without BES, then 0.3% O_2 treatment. Dissolved Fe(II) concentrations of the treatments without oxygen increased as well, however much lower than the treatments to which oxygen was injected.

The third experiment (experiment C) used fresh sediments and consisted of two treatments, one with a headspace of N_2 and methane and the other with a headspace of only N_2. Air was injected into both treatments to reach a 1% O_2 concentration in the headspace and reinjected each time the oxygen depleted. The average initial dissolved

Fe(II) concentrations were 27 ± 3 μM. Fe(II) concentrations measured in the treatment with methane addition did not alter significantly throughout the experiment. A slight non-significant average decrease (of 8 μM) was noted between day 0 and day 11. Final concentrations after 37 days were 24.3 ± 5 μM. In the treatment without methane, concentrations decreased significantly ($F = 122.1$, $p = 9.1 \times 10^{-6}$). Fe concentrations were lower at the end of the experiment after 37 days by 22.7 μM ($t = 11.1$, $p = 0.032$) and stood at 4.5 ± 1.2 μM. Similarly, *post hoc* pairwise comparisons indicate concentrations were higher at day 0, compared to the other time points (Figure 4; Supplementary Data). Two-way repeated measured ANOVA showed a significant correlation between time and treatment ($F = 73.7$, $p = 4 \times 10^{-5}$). *Post hoc* analysis revealed Fe(II) concentrations did not differ at day 0. Subsequently, at the following time points (11, 23, and 37 days), concentrations were significantly and consistently lower at the treatment without methane (Figure 4; Supplementary Data).

Metagenomic analysis was performed on the 1% O_2 + hematite treatment at t_0 and after 52 days. The results show an increase in the relative abundance of the methanotrophic bacteria *Methylomonas* (5.4%), *Methylobacter* (2%), and the methylotrophic bacterium *Methylotenera* (1.5%) during the experiment (Figure 5A). A small increase was also observed in the relative abundance of *Desulfuromonas* (0.02%) and *Geobacter* (0.04%). In this treatment, a decrease of 0.2 and 2.7% in the relative abundance of archaea *Methanothrix* and the Methanofastidiosales order (respectively) was observed.

Isotopes and concentrations analyses of PLFAs during the oxygen experiment provide a base for calculating the production of newly formed fatty acids. Our analysis shows a pattern indicative of aerobic methanotrophs being highly stimulated (Figure 5B), with new ^{13}C production ranging between 4 and 20 ng ^{13}C/g dw observed for dominating $C_{14:0}$, $C_{16:1\omega7}$, $C_{16:1\omega5}$, and $C_{16:0}$. This PLFA pattern matches the one provided by Bar-Or et al. (2017) (Supplementary material), but the new production is four times higher during active addition of oxygen, as performed here.

3.2. Methanol intermediate as a potential substrate for methanotrophy

We explored the involvement of methanol in methanotrophy and iron reduction, due to our former suggestion of potential methane activation by archaea and the release of available intermediates to the methanotrophs (Bar-Or et al., 2017). Of those, methanol would be the most probable candidate. During those anoxic slurry experiments, we observed an inhibition of the overall process by BES addition. Using ^{13}C-labeled methanol, two incubation experiments (D and E) tested the involvement of methanol. In experiment D (Figure 6; Supplementary Figure S2), the methane concentrations increased in all treatments except for the killed control. The highest change in methane concentrations was observed in the methanol treatment (6.2 μmol/g dw). The change in methane concentrations was the same in the no-addition and the methane treatments (2.6 μmol/g dw; Figure 6A). The $\delta^{13}C_{CH4}$ values in the ^{13}C-labeled methanol treatment reached the highest value (67,000‰) compared to the no-addition value (−18‰) and the killed control (300‰; Figure 6B). Throughout the experiment $\delta^{13}C_{DIC}$ values of the ^{13}C-labeled methanol treatment increased to ~2,500‰ in, and to 260‰ in the ^{13}C-labeled methane treatment (Figure 6D). The average initial dissolved Fe(II) concentrations were 28 ± 6 μM. The dissolved Fe(II) concentrations increased in all treatments except for the killed control treatment, with the highest increase noted in the ^{13}C-labeled methane treatment (13.8 μM; Figure 6C).

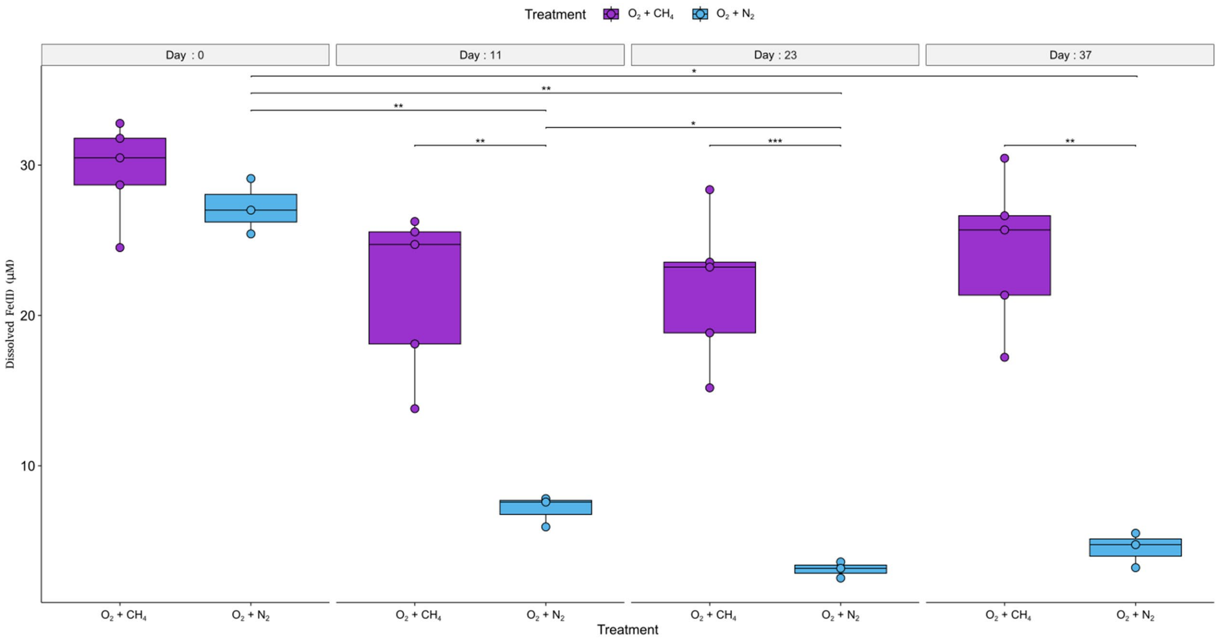

FIGURE 4
Development of dissolved Fe(II) concentrations over time in experiment C are presented as boxplots, with (purple) and without (cyan) methane in the headspace. The error bars indicate the measurements of replicate bottles. Significance levels; $*p \leq 0.05$; $**p \leq 0.01$; $***p \leq 0.001$. Air was injected into the bottles to reach 1% O_2 in the headspace at the following time points: 2, 5, 10, 11, 12, 13, 14, 15, 18, 21, and 23 (days from the start of the experiment).

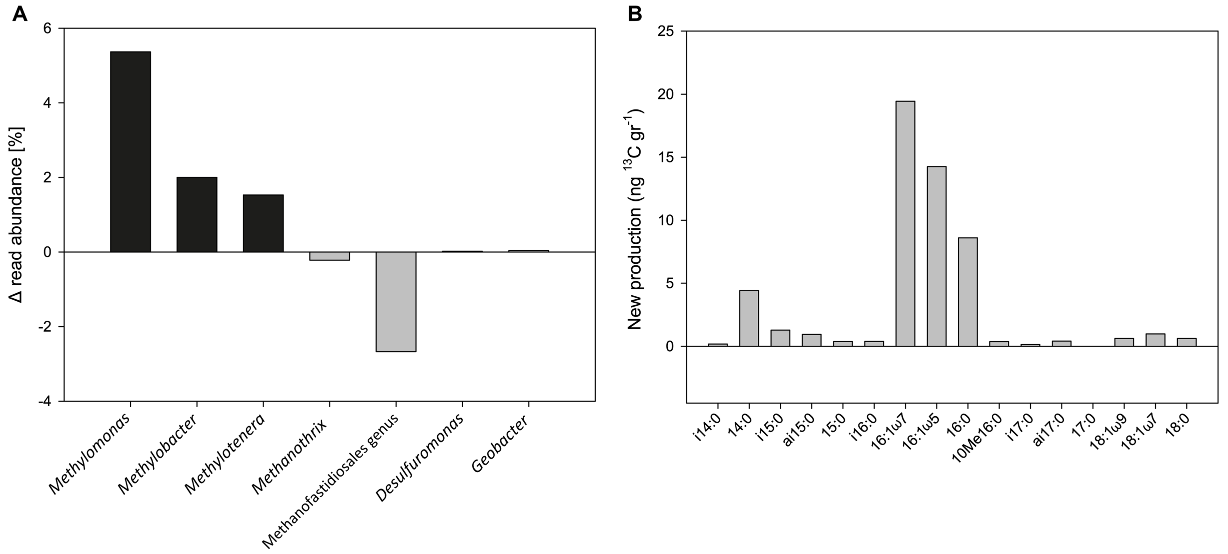

FIGURE 5
(A) Change in the relative abundance of the 16S rRNA gene from metagenome analysis of the 1% O_2 with hematite addition treatment of Experiment A (sampled after 52 days). **(B)** Newly produced fatty acids of the same treatment (in ng ^{13}C/g dw) after 558 days.

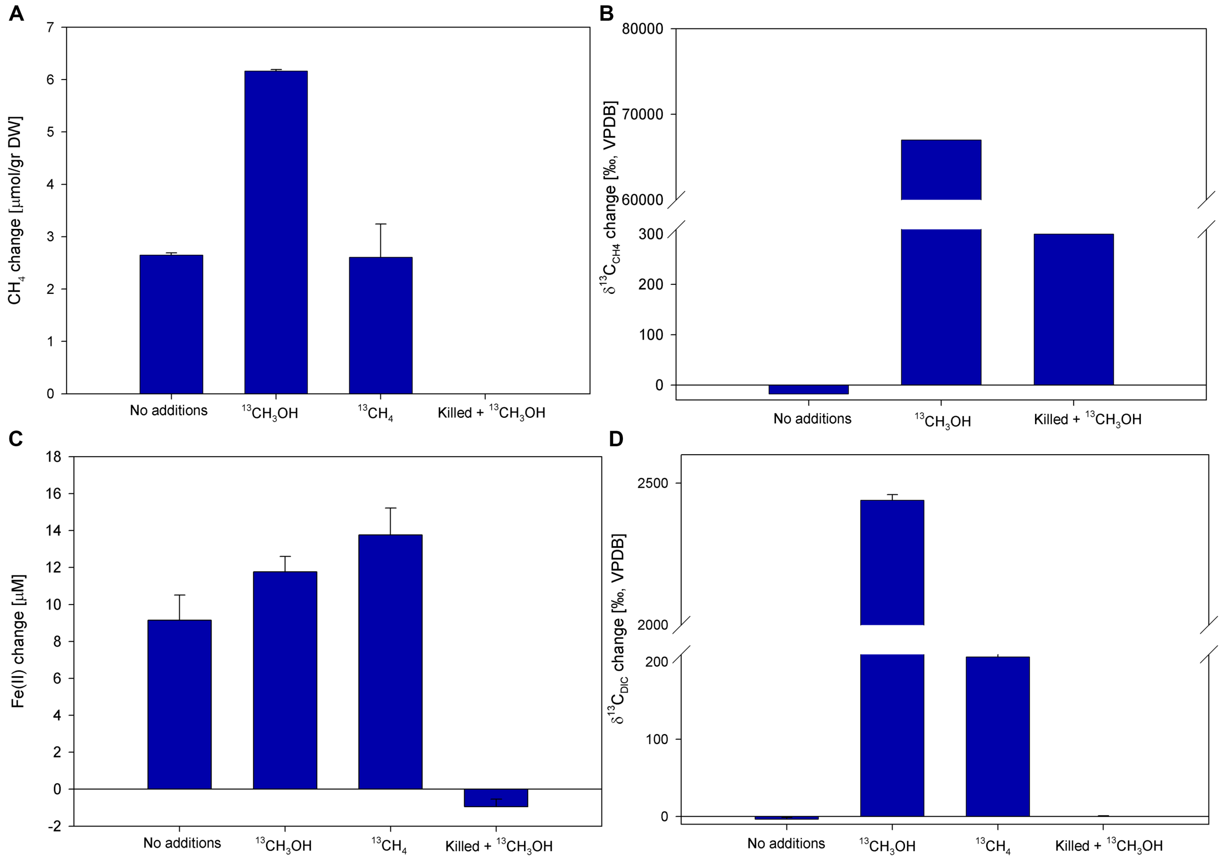

FIGURE 6
Net changes of CH^4 **(A)**, $\delta^{13}C_{CH4}$ **(B)**, dissolved Fe(II) **(C)**, and $\delta^{13}C_{CH4}$ **(D)** after 147 days of Experiment D with the addition of ^{13}C-labeled methanol ($\delta^{13}C_{CH4}$ was measured after 61 days). Error bars represent the average deviation from the mean of triplicate bottles.

In experiment E, BES and hematite were added to the slurries in addition to ^{13}C-labeled methanol to test the involvement of methanogens. Methane concentrations increased in all treatments except for the methanol + BES treatment. The methanol and the methanol + hematite treatments show the highest change of 5.7 μmol/g dw, while the no-addition and hematite treatments increased by 3 and

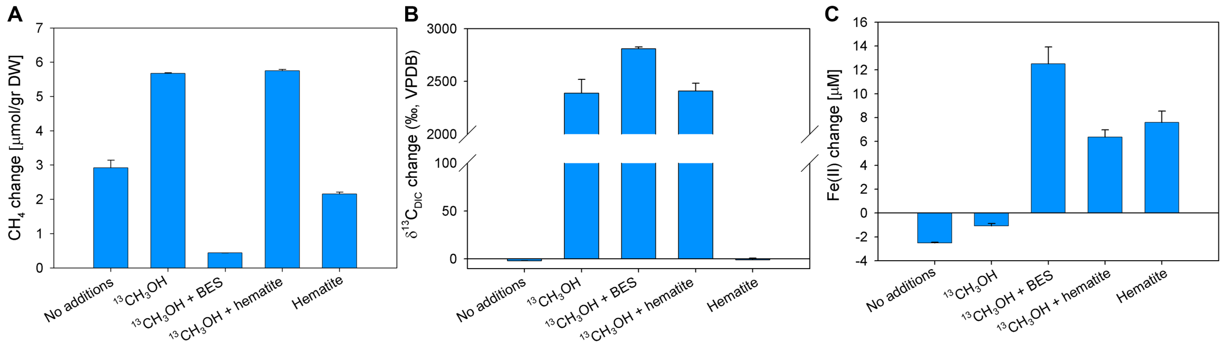

FIGURE 7
Net changes of CH_4 **(A)**, $\delta^{13}C_{DIC}$ **(B)**, and dissolved Fe(II) **(C)** after 129 days of Experiment E with the addition of ^{13}C-labeled methanol, hematite, and BES. Error bars represent the average deviation from the mean of duplicate bottles.

2 µmol/g, respectively (Figure 7A). The $\delta^{13}C_{DIC}$ values in the methanol and the methanol + hematite treatments increased during the experiment by 2,389 and 2,409‰, respectively (Figure 7B). The $\delta^{13}C_{DIC}$ of the methanol + BES increased by the end of the experiment by 2,809‰; however, the slope during the first 14 days was relatively low compared to the slope between day 14 and the end of the experiment (Supplementary Figure S3). The average initial dissolved Fe(II) concentrations were 50 ± 7 µM. Dissolved Fe(II) concentrations increased by about 7 µM in the hematite and methanol + hematite treatments (Figure 7C). In the methanol + BES treatment, the concentrations increased by 12 µM throughout the experiment. The concentrations of the no-addition and methanol treatments remained the same.

Samples from experiments D and E were analyzed for the isotopic composition of bacterial fatty acids and archaeal-derived isoprenoid hydrocarbons (Table 2; Supplementary Table S5). The $\delta^{13}C$ values of the archaeol-derived phytane in the ^{13}C-methanol treatments with and without hematite addition were 1,600 and 2,300‰, respectively. In contrast, in treatments with methane and ^{13}C-methanol plus BES $\delta^{13}C$ values were − 3 and − 5‰, respectively. Fatty acids mostly indicative of heterotrophic bacteria ($iC_{15:0}$, Aepfler et al., 2019) from the ^{13}C-labeled methanol treatment were slightly enriched in ^{13}C. The enrichment was more pronounced in the treatments with the addition of BES and hematite. In addition, there was a strong ^{13}C-enrichment in the fatty acid $C_{16:1\omega7}$, which can be affiliated with methylotrophic bacteria (Guckert et al., 1991), specifically considering the conditions applied here. The highest value was found in the treatment with BES (up to 850‰), then with hematite, and a small enrichment in the treatment with methanol only. No change in $\delta^{13}C$ values of fatty acids was observed in the methane treatment. A combination of fatty acid carbon isotope values and their corresponding concentrations were used to calculate the portion of newly produced fatty acids (in ng ^{13}C/g dw; Supplementary Figure S7). These patterns are different from that observed for the oxygen experiment which is highly specific for aerobic methanotrophs and shows much higher ^{13}C incorporation. Nonetheless, new production is still fairly high in the methanol treatments with new production ranging from 0.5 to 4.5 ng ^{13}C/g dw for the most diagnostic fatty acids $iC_{15:0}$ and $C_{16:1\omega7}$. Other fatty acids such as $aiC_{15:0}$, $C_{16:0}$, and $C_{18:1\omega7}$ are also showing new production values higher than 1.0 ng ^{13}C/g dw, especially when methanogens were inhibited or when iron reduction was stimulated by hematite additions. This trend is also visible using the sum of all newly produced bacterial fatty acids as an indicator of the overall turnover capacity of bacteria during the different treatments (Table 2). The highest amount of new production was found when oxygen is introduced (57.9 ng ^{13}C/g dw), whereas the lowest amount was detected during addition of $^{13}CH_4$ (1.2 ng ^{13}C/g dw). Methanol additions resulted in new productions of 7.8 ng ^{13}C/g dw, and 20.3 and 16.1 ng ^{13}C/g dw, when BES and hematite was used, respectively.

To study the microbial community associated with methanotrophy related to methanol addition, samples supplemented with methanol (experiment D), methanol and BES, and methanol and hematite (experiment E) were sent for 16S rRNA amplicon-based sequencing. Following taxonomic classification, our analysis indicated archaea accounted for a significant percentage of the microbial population of all treatments (between 28.3 and 37.5%, Supplementary File 1), and the remaining reads were assigned to bacteria. All ASVs of both experiments are also presented in Supplementary File 1. A substantially larger number of Bacterial Classes and Orders was noted (experiments D: 129 classes and 228 Orders; experiment E: 112 classes and 199 Orders), compared to Archaea (experiment D: 17 classes and 24 Orders; experiment E: 18 classes and 28 Orders). Supplementary Figure S4 presents the most abundant (>1%) Bacterial Classes and Archaeal Orders in experiments D and E. Six prominent bacterial Classes accounted for about 50% of the bacterial reads, with slight alteration observed from T0 to the methanol, methanol + BES and methanol + hematite additions: Anaerolineae, Dehalococcoidia, Gammaproteobacteria, Sva0485, Thermodesulfovibrionia, and Aminicenantia (Supplementary Figure S4B). Similarly, the six prominent Archaea orders, accounted for over 80% of the archaeal reads, with minor variations: Bathyarchaeia, Methanomicrobiales, Marine Benthic Group D and DHVEG-1, Woesearchaeales, Methanosarciniales and Methanofastidiosales (Supplementary Figure S4A).

We identified methanogens of the orders Methanosarciniales, Methanomassiliicoccales, Methanomicrobiales, Methanocellales, *Ca.* Methanomethyliales and *Ca.* Methanofastidiosales. Methanogens of the genus *Methanomethylovorans* (0.6% of total reads), were only detected after methanol addition to the slurries, compared to t_0 of experiment D (Supplementary Figures S5A, S6A). Similarly, the genus *Methanosarcina* (2.4% of total reads) was predominantly found after methanol addition. An increase in the relative abundance of *Ca.*

Methanomethylicus was noted (from 0.16 to 0.32% of total reads). In contrast, the relative abundance of the *Methanomassiliicoccaceae* family was reduced (from 0.38 to 0.28% of total reads) in the presence of methanol. Slight decreases were observed after methanol addition in the genera *Methanosaeta* (2.6–1.9% of total reads), *Methanoregula* (1.36–1.5% of total reads), and *Methanolinea* (3.2–2.75% of total reads). As expected, after BES addition, the relative abundance of all the methanogens decreased compared to t_0 of experiment E, excluding *Methanosarcina* which was only observed after BES addition (Supplementary File 1).

Aerobic methanotrophs were also observed in both experiments (Supplementary Figures S5B, S6B). The Gammaproteobacteria family *Methylophilaceae*, comprising type I aerobic methanotrophs (Deng et al., 2019), was detected at low relative abundance (0.02 and 0.05% of total reads) after the addition of methanol. The family *Methylococcaceae* (class Gammaproteobacteria), which is also comprised of type I methanotrophs (Taubert et al., 2019), was found in all samples of both experiments. After methanol addition, *Methylococcaceae* relative abundance decreased (from 0.28 to 0.21% of total reads). An increase (from 0.2 to 0.3%) was noted after the addition of hematite. *Methylocystis* (Alphaproteobacteria), a type II strictly aerobic methanotroph (Bowman, 2006; Belova et al., 2011), was observed in both experiments at low relative abundance (between 0.04 and 0.08% of total reads). Although *Methylocystis* relative abundance did not change significantly after methanol addition, when methanol and hematite were added, it increased compared to t_0 (from 0.05 to 0.08% of total reads). Methanol addition also increased the relative abundance of bacteria capable of iron-reduction: *ca. Omnitrophus* (from 1.1 to 1.64% of total reads), *Anaeromyxobacter* (from 0.34 to 0.47% of total reads), *Desulfuromonas* (from 0.07 to 0.15% of total reads) and *Thermoanaerobaculum* (from 1.44 to 1.57% of total reads). Even more profound increases were observed for most of the aforementioned iron reducers in the presence of hematite (Supplementary Figures S5C, S6C, Supplementary File 1).

4. Discussion

4.1. Aerobic conditions (re)activate methanotrophy and promote net iron reduction

Methane oxidation in Lake Kinneret sediments has been observed in pore-water profiles, models, on-top core, and incubation experiments; however, the observed oxidation was considered anaerobic due to the anoxic nature of the sediments (Adler et al., 2011; Sivan et al., 2011; Bar-Or et al., 2017; Vigderovich et al., 2022). Nevertheless, evidence for aerobic methanotrophy was presented in different microbial profiles (Bar-Or et al., 2015) and incubation experiments (Bar-Or et al., 2017; Elul et al., 2021) of Lake Kinneret sediments and, similarly, in other highly reduced freshwater environments around the world (Blees et al., 2014; Milucka et al., 2015; Oswald et al., 2016b; Martinez-Cruz et al., 2017; Van Grinsven et al., 2020, 2021; Su et al., 2022). This may be due to the slow release of remnant oxygen from clay-containing sediments, as proposed in Wang et al. (2018), or due to the continuous production of low oxygen levels in the anoxic environment, which is immediately used by methanotrophs and thus does not poison the anaerobes (Ettwig et al., 2010; Dershwitz et al., 2021; Kraft et al., 2022). An alternative explanation may be the potential survival of methanotrophs performing anaerobic metabolism under hypoxia conditions (Kits et al., 2015; Orata et al., 2018; Zheng et al., 2020; Cheng et al., 2022). In Lake Kinneret, aerobic methanotrophs and Fe-AOM co-occur at the same depth, raising the possibility that iron reduction is somehow associated with aerobic activity. Here we explored the potential aerobic methanotrophy in hypoxic methane-generating sediments of Lake Kinneret and assessed its influence on iron reduction.

The link between aerobic methanotrophy and iron reduction was investigated by repeated oxygen injections into three sets of initially anoxic slurry incubation experiments with/out of methane in the headspace and with/out inhibition of methanogenesis. Our results indicate first that the aerobic methanotrophs in these sediments can be activated by even small oxygen levels, which means that they are in a dormant-like state or possess the ability to survive under anoxic conditions by using other electron acceptors as was previously shown with related methanotrophs (Kits et al., 2015; Orata et al., 2018; Zheng et al., 2020; Cheng et al., 2021).

Second, interestingly, the net iron reduction increased along with the oxygen levels, up to 1% O_2 treatment. This increase was unexpected since dissolved Fe(II) was thought to be oxidized quickly when oxygen is introduced to the system, as can be seen in the 20% O_2 treatment (Figure 3). Generally, Fe(III) reduction is considered to occur mainly under anoxic conditions, where it acts as an electron acceptor instead of oxygen, and the produced Fe(II) is stable (Straub et al., 2001; Lovley et al., 2004). Nevertheless, iron reduction under aerobic conditions has recently been demonstrated in pure culture of iron reducers (Zhang et al., 2019). Zhang et al. (2019) also noted a delay in Fe(II) oxidation under oxic conditions due to metabolites (citric and gluconic acids) and self-produced-siderophores secreted by the specific iron reducers (Actinobacteria) that were tested. These metabolites can bind Fe(II) to form stable complexes. In our slurries, a net increase in Fe(II) was observed in all the treatments where oxygen was injected. Higher levels of injected oxygen (up to 1%) resulted in higher Fe(II) levels. In experiment C, where fresh sediments were incubated (Figure 4), it seems that there is no Fe(II) build-up without the presence of methane, suggesting that methanotrophy is required to explain the increase in net iron reduction. This implies that the methanotrophs/methylotrophs contribute to the observed iron reduction, perhaps by secreting metabolites that are actively used by iron reducers (as a carbon source, for instance) or by functioning as Fe(II)-binding ligands.

The iron reduction in the methane-generating sediments could be performed by iron-reducing bacteria, but also by methanogens (Sivan et al., 2016) and even by aerobic methanotrophs (Zheng et al., 2020); all three have been found in this depth of Lake Kinneret sediments (Bar-Or et al., 2015). It seems that before oxygen injection, natural iron reduction occurs in anoxic sediments by different iron reducers and perhaps by methanogens (Elul et al., 2021). When oxygen is injected, it is used for aerobic methanotrophy and biotic/abiotic Fe(II) oxidation. As a result, new and highly reactive (less crystalline) iron oxides precipitate. The increase in reactive iron oxides encourages iron reduction when oxygen levels are low and net iron reduction increases. In addition, some of the aerobic methanotrophs (i.e., *Methylomonas* and *Methylosinus* species) are known to be able to switch to iron reduction metabolism when oxygen levels are low (Zheng et al., 2020), this contributes to the increase in net Fe(II) concentrations. Experiment C indicates that when methanotrophy is scarce, there is no increase in the net iron reduction. This suggests that dissolved Fe(II) does not only increase due to the presence of oxygen but that methanotrophic bacteria activity is necessary for Fe(II) to accumulate, as was shown by Zhang et al. (2019). This potentially encourages iron reduction due to metabolites or an intermediate release during methanotrophy.

Hematite is considered a less reactive and more stable iron oxide compared to non-crystalline Fe-oxides, such as ferrihydrite, goethite or other iron(hydr)oxide (Poulton et al., 2004). Here, hematite was chosen to be the Fe(III)-oxide added to the slurries due to its stable nature, so that it will not disturb the system and shift it toward iron cycling. In addition, it is found naturally in the sediments and was shown to be the most available iron oxide for Fe-coupled AOM in incubations with Lake Kinneret sediments (Bar-Or et al., 2017). Here, in the hypoxic incubations, where oxygen was injected regularly, an aerobic metabolic pathway for methanotrophy was observed that promoted the iron reduction. It could be that addition of more reactive iron oxide to the experiments would cause more intense iron reduction.

From the results of the metagenome analysis on the 1% O_2 treatment of experiment A, it is evident that the methane oxidation is most likely performed by the type I methanotrophs *Methylomonas* and *Methylobacter* (Figure 4A). This is in line with previous observations from Lake Kinneret sediments, where the Methylococales order was detected in a microbial sediment profile and a slurry incubation experiment (Bar-Or et al., 2015, 2017; Elul et al., 2021). These methanotrophs were also noted in other anoxic/hypoxic freshwater environments (Martinez-Cruz et al., 2017; Cabrol et al., 2020; Van Grinsven et al., 2020, 2021; Su et al., 2022). Another aerobic bacterium detected in experiment A is the non-methane-oxidizing methylotroph *Methylotenera*. This methylotroph is known to co-occur with both *Methylomonas* and *Methylobacter* and oxidizes methanol excreted by the latter two as an intermediate during the methanotrophy process (Beck et al., 2013; Oshkin et al., 2015; Cao et al., 2019). The iron reducers *Geobacter* and *Desulfuromonas* abundance increased as well. Both are well-documented anaerobic iron-reducing bacteria in aquatic sediments and soils (Lovley et al., 2011; An and Picardal, 2015). As expected, the abundance of most methanogens and ANME-1 did not change during the experiment. The decrease in abundance of *Methanothrix* and the order Methanofastidiosales during the experiment suggests that ANME and methanogens are not involved in the observed methanotrophy, as indicated by the geochemical results. The results of the lipid analysis of the 1% O_2 treatment are in line with the metagenomic results (Figure 5B). There is a similar pattern of the PLFAs to the one previously observed in an anaerobic incubation experiment (Bar-Or et al., 2017) but given the apparent amount of new production in $iC_{15:0}$ (1.3 ng ^{13}C/g dw) we can speculate that this is the result of concomitant heterotrophic activity (Aepfler et al., 2019).

4.2. The role of methanol in Lake Kinneret sediments

To explain the results of the previous anaerobic incubation experiment (Bar-Or et al., 2017), the production of potential intermediates that can be channeled from archaea to aerobic methanotrophs was suggested. As the most probable candidate is methanol, its role was tested in anoxic methane-generating sediments in two slurry incubation experiments. Our results indicate that under anaerobic conditions, methanol additions fueled methylotrophic methanogenesis rather than methanol oxidation, as opposed to the fatty acids analyses of the 1% O_2 experiment (Figure 5B; Supplementary Figure S8) and previous observations (Bar-Or et al., 2017). In general, methanol addition increased methane concentrations and higher $\delta^{13}C_{DIC}$ values, originating from methylotrophic methanogenesis. This aligns with the strong ^{13}C-enrichment of methylotrophic methanogen lipids (i.e., phytane and phytenes; Table 2; Supplementary Table S5). These isoprenoid hydrocarbons are indirect indicators of archaeol and hydroxyarchaeols produced by methylotrophic methanogens of the order *Methanosarcinales* (Sprott et al., 1993). Accordingly, the 16S rRNA sequencing results fit the biogeochemical observations and show changes in the relative abundance of various methanogens during the experiment. These ranged from acetoclastic and hydrogenotrophic methanogens, i.e., *Methanosaeta*, *Methanoregula,* and *Methanolinea* (Jetten et al., 1992; Oren, 2014), to methylotrophic methanogens of the genera *Methanosarcina, Methanomethylovorans,* and *Methanomethylicus* (Smith, 1978; Ranalli, 1986; Lomans, 1999; Vanwonterghem, 2016; Supplementary Figures S5A, S6A). In the methanol treatment (experiment D), there was just a slight ^{13}C-enrichment and hence an incorporation of methanol into bacterial fatty acids (Table 2). Nonetheless, this suggests that methanol addition also stimulated the activity of bacteria, either directly as a substrate or by consuming $^{13}CO_2$ derived from methylotrophic methanogenesis, as expected in this kind of environment (Dijkhuizen and Harder, 1984).

In experiment E, some slurries were amended with BES and hematite, in addition to ^{13}C-methanol, to test the potential of methanol turnover when methanogenesis is inhibited or additional electron acceptors available. Similarly, high $\delta^{13}C_{DIC}$ values in these treatments (Figure 7) suggest the direct oxidation of methanol by bacteria, which is also reflected in higher ^{13}C-incorporations compared to those observed during the methanol-only experiment (Table 2). Even though the FA $C_{16:1\omega7}$ is associated with methylotrophs (Guckert et al., 1991), they were not detected in the 16S rRNA sequencing results (Supplementary File 1). Alternatively, this FA could indicate the involvement of aerobic methanotrophs; however, their relative abundance decreased compared to the t_0 treatment (Supplementary Figure S6). Considering the increase in Fe(II) concentrations, these new production patterns of bacterial fatty acids may indicate the activity of iron reducers (Teece et al., 1999; Zhang et al., 2003). When methanogenesis was inhibited, there was a marginal ^{13}C-enrichment in phytane and phytenes compared to the original values in the sediment (−32‰, Vigderovich et al., 2022). These results indicate that methylotrophic methanogens very likely outcompete heterotrophic bacteria for methanol in a natural system.

Hematite addition with and without methanol mostly encouraged net iron reduction. According to the $\delta^{13}C_{DIC}$ results, hematite does not appear to influence methanol oxidation. However, the isotopic composition of bacterial fatty acids revealed a more complex picture. It seems that the addition of hematite doubled the activity of the heterotrophic bacteria (Table 2), indicating a shortage of electron acceptors in the slurry. The sequencing analysis showed a similar picture, where the relative abundance of several bacteria capable of iron reduction (i.e., *ca. Omnitrophus*, *Anaeromyxobacter,* and *Thermoanaerobaculum*) increased during the incubation time. Similar results were noted for the phylums Zixibacteria and Sva0485. Prior reports identified iron-reducing genes in both members (Treude, 2003; Kerin, 2006; Losey, 2013; Tan, 2019; Garber, 2020; Casar, 2021; Williams, 2021). Interestingly, the type I aerobic methanotroph family *Methylococcaceae* was found in all treatments; however, it only increased in the methanol and hematite treatment. Members of this family have been previously found in suboxic and anoxic environments, such as lake sediments (Bar-Or et al., 2015; Martinez-Cruz et al., 2017; Elul et al., 2021; Su et al., 2022) and in the anoxic hypolimnion of freshwater lakes (Blees et al., 2014; Oswald et al., 2016a; Rissanen et al., 2021). This increase could indicate a potential metabolism that can sustain these methanotrophs in natural anaerobic environments.

5. Conclusion

Aerobic methanotrophs were previously discovered in anaerobic methane generating Lake Kinneret sediments. However, their ability to perform the aerobic activity and its potential link to iron reduction as the AOM in these sediments is unclear. By injecting different oxygen concentrations, we show that methanotrophs *Methylomonas* and *Methylobacter* are activated under low levels of oxygen (i.e., 1%). Furthermore, adding oxygen promoted an unexpected increase in net iron reduction in hypoxic slurries. We propose this may occur due to one or a combination of the following processes (i) ferrous iron recycling by its aerobic oxidation to low crystalline minerals available for reduction, (ii) methanotrophs switch from oxygen to iron reduction metabolism when oxygen concentrations are low, and (iii) the methanotrophs' activity promotes iron reduction by excretion of metabolites, which can be used as Fe(II)-binding ligands. By testing whether methanotrophic bacteria can operate under anoxic conditions we show that methanol is less likely to act as an intermediate between methanogens and methanotrophs, and that methanotrophs do not incorporate methanol. The results of these incubations indicate that methylotrophic methanogens outcompete heterotrophic bacteria as long as the methanogens are not inhibited. Adding hematite to the incubation stimulates iron reducers and possibly methanotrophic bacteria, while methylotrophic methanogens are active. Our findings open new avenues for elucidating microbial networks in reducing environments and indicate that methanotrophs and methylotrophs sustain anaerobic conditions from which they can be revived.

Data availability statement

The raw reads generated in this study have been deposited in the European Nucleotide Archive (ENA) Database (https://www.ebi.ac.uk/ena/browser/home) as BioProject accession number PRJEB59988. Additional data are available under the Supplementary material and Supplementary Data sections.

Author contributions

HV, WE, and OS designed the research. HV, ME, MR-B, AG, and OB analyzed the samples and the data. WE and OS supervised HV and provided resources and funding. HV and OS synthesized the data and wrote the original draft. All authors contributed to the article and approved the submitted version.

Funding

This research work was supported by ERC Consolidator (818450) and Israel Science Foundation (857–2016) grants awarded to OS. Funding for ME was provided by the Deutsche Forschungsgemeinschaft (DFG) under Germany's Excellence Strategy through the cluster of excellence EXC 2077 "The Ocean Floor – Earth's Uncharted Interface" (project no. 390741601). Funding for MR-B is funded by the Israel Ministry of Science and Technology Grant 001126 and the Israel Ministry of Energy (Grants 219-17-015 and 221-17-002). HV was supported by a student fellowship from the Israel Water Authority and by a short-term post-doctoral scholarship of the Kreitman School.

Acknowledgments

The authors would like to thank Benni Sulimani and Oz Tzabari from the Yigal Allon Kinneret Limnological Laboratory for their onboard technical assistance. We thank all of OS lab members for their help during sampling and express especially heartfelt thanks to Noam Lotem for helping with the lab work, and to Efrat Eliani-Russak for her technical assistance. Clemens Roettgen is thanked for his help during lipid biomarker extraction and clean-up.

Conflict of interest

The authors declare that the research was conducted in the absence of any commercial or financial relationships that could be construed as a potential conflict of interest.

Publisher's note

Supplementary material

The Supplementary material for this article can be found online at: https://www.frontiersin.org/articles/10.3389/fmicb.2023.1206414/full#supplementary-material

References

Adler, M., Eckert, W., and Sivan, O. (2011). Quantifying rates of methanogenesis and methanotrophy in Lake Kinneret sediments (Israel) using pore-water profiles. *Limnol. Oceanogr.* 56, 1525–1535. doi: 10.4319/lo.2011.56.4.1525

Aepfler, R. F., Bühring, S. I., and Elvert, M. (2019). Substrate characteristic bacterial fatty acid production based on amino acid assimilation and transformation in marine sediments. *FEMS Microbiol. Ecol.* 95, 1–15. doi: 10.1093/femsec/fiz131

An, T. T., and Picardal, F. W. (2015). Desulfuromonas carbonis sp. nov., an Fe(III)-, S0- and Mn(IV)-reducing bacterium isolated from an active coalbed methane gas well. *Int. J. Syst. Evol. Microbiol.* 65, 1686–1693. doi: 10.1099/ijs.0.000159

Bar-Or, I., Ben-Dov, E., Kushmaro, A., Eckert, W., and Sivan, O. (2015). Methane-related changes in prokaryotes along geochemical profiles in sediments of Lake Kinneret (Israel) methane-related changes in prokaryotes along geochemical profiles in sediments of Lake Kinneret (Israel). *Biogeosciences* 12, 2847–2860. doi: 10.5194/bg-12-2847-2015

Bar-or, I., Elvert, M., Eckert, W., Kushmaro, A., Vigderovich, H., Zhu, Q., et al. (2017). Iron-coupled anaerobic oxidation of methane performed by a mixed bacterial-archaeal community based on poorly-reactive minerals. *Environ. Sci. Technol.* 51, 12293–12301. doi: 10.1021/acs.est.7b03126

Bastviken, D., Tranvik, L. J., Downiing, J. A., Crill, P. M., and Enrich-Prest, A. (2011). Freshwater methane emissions offset the continental carbon sink. *Science.* 331:50. doi: 10.1126/science.1196808

Beck, D. A. C., Kalyuzhnaya, M. G., Malfatti, S., Tringe, S. G., del Rio, T. G., Ivanova, N., et al. (2013). A metagenomic insight into freshwater methane-utilizing communities and evidence for cooperation between the Methylococcaceae and the Methylophilaceae. *PeerJ* 2013, 1–23. doi: 10.7717/peerj.23

Belova, S. E., Baani, M., Suzina, N. E., Bodelier, P. L. E., Liesack, W., and Dedysh, S. N. (2011). Acetate utilization as a survival strategy of peat-inhabiting Methylocystis spp. *Environ. Microbiol. Rep.* 3, 36–46. doi: 10.1111/j.1758-2229.2010.00180.x

Bender, M., and Conrad, R. (1994). Methane oxidation activity in various soils and freshwater sediments: occurrence, characteristics, vertical profiles, and distribution on grain size fractions. *J. Geophys. Res.* 99, 16,531–16,540. doi: 10.1029/94jd00266

Blees, J., Niemann, H., Wenk, C. B., Zopfi, J., Schubert, C. J., Kirf, M. K., et al. (2014). Micro-aerobic bacterial methane oxidation in the chemocline and anoxic water column of deep south-alpine Lake Lugano (Switzerland). *Limnol. Oceanogr.* 59, 311–324. doi: 10.4319/lo.2014.59.2.0311

Bokulich, N. A., Kaehler, B. D., Rideout, J. R., Dillon, M., Bolyen, E., Knight, R., et al. (2018). Optimizing taxonomic classification of marker-gene amplicon sequences with QIIME 2's q2-feature-classifier plugin. *Microbiome* 6, 1–17. doi: 10.1186/s40168-018-0470-z

Bolyen, E., Rideout, J. R., Dillon, M. R., Bokulich, N. A., Abnet, C. C., Al-Ghalith, G. A., et al. (2019). Reproducible, interactive, scalable and extensible microbiome data science using QIIME 2. *Nat. Biotechnol.* 37, 852–857. doi: 10.1038/s41587-019-0209-9

Bowman, J. (2006). "The methanotrophs-the families methylococcaceae and methylocystaceae" in *The Prokaryotes. 3rd*, eds. M. Dworkin, S. Falkow, E. Rosenberg, K.H. Schleifer, E. Stackebrandt, (Springer), 266–289.

Cabrol, L., Thalasso, F., Gandois, L., Sepulveda-Jauregui, A., Martinez-Cruz, K., Teisserenc, R., et al. (2020). Anaerobic oxidation of methane and associated microbiome in anoxic water of northwestern Siberian lakes. *Sci. Total Environ.* 736:139588. doi: 10.1016/j.scitotenv.2020.139588

Cai, C., Leu, A. O., Jianhua, G. X., Yuexing, G., Zhao, F. J., and Tyson, G. W. (2018). A methanotrophic archaeon couples anaerobic oxidation of methane to Fe (III) reduction. *ISME J*, 12. doi: 10.1038/s41396-018-0109-x

Callahan, B. J., McMurdie, P. J., Rosen, M. J., Han, A. W., Johnson, A. J. A., and Holmes, S. P. (2016). DADA2: high-resolution sample inference from Illumina amplicon data. *Nat. Methods* 13, 581–583. doi: 10.1038/nmeth.3869

Cao, Q., Liu, X., Ran, Y., Li, Z., and Li, D. (2019). Methane oxidation coupled to denitrification under microaerobic and hypoxic conditions in leach bed bioreactors. *Sci. Total Environ.* 649, 1–11. doi: 10.1016/j.scitotenv.2018.08.289

Casar, C. P., Momper, L. M., Kruger, B. R., and Osburn, M. R. (2021). Iron-fueled life in the continental subsurface: deep mine microbial observatory, South Dakota, USA. *Applied and Environmental Microbiology.* 87, 1–14. doi: 10.1128/AEM.00832-21

Cheng, C., He, Q., Zhang, J., Chen, B., and Pavlostathis, S. G. (2022). Is the role of aerobic methanotrophs underestimated in methane oxidation under hypoxic conditions? *Sci. Total Environ.* 833, 1–4. doi: 10.1016/j.scitotenv.2022.155244

Cheng, C., Zhang, J., He, Q., Wu, H., Chen, Y., Xie, H., et al. (2021). Exploring simultaneous nitrous oxide and methane sink in wetland sediments under anoxic conditions. *Water Res.* 194, 1–10. doi: 10.1016/j.watres.2021.116958

Dalton, H. (2005). The Leeuwenhoek lecture 2000 the natural and unnatural history of methane-oxidizing bacteria. Philosophical transactions of the Royal Society of London. Series B. *Biol. Sci.* 360, 1207–1222. doi: 10.1098/rstb.2005.1657

Deng, Y., Gui, Q., Dumont, M., Han, C., Deng, H., Yun, J., et al. (2019). Methylococcaceae are the dominant active aerobic methanotrophs in a Chinese tidal marsh. *Environ. Sci. Pollut. Res.* 26, 636–646. doi: 10.1007/s11356-018-3560-3

Dershwitz, P., Bandow, N. L., Yang, J., Semrau, J. D., McEllistrem, M. T., Heinze, R. A., et al. (2021). Oxygen generation via water splitting by a novel biogenic metal ion-binding compound. *Appl. Environ. Microbiol.* 87, 1–14. doi: 10.1128/aem.00286-21

Dijkhuizen, L., and Harder, W. (1984). Current views on the regulation of autotrophic carbon dioxide fixation via the Calvin cycle in bacteria. *Anton. Leeuw. Int. J. Gen. Mol. Microbiol.* 50, 473–487.

Downing, A. J., Prairie, T. Y., Cole, J. J., Duarte, C. M., Tranvik, L. J., Striegl, R. G., et al. (2006). The global abundance and size of lakes, ponds and impooundments. *Limnology and Oceanography* 51, 2388–2379. doi: 10.4319/lo.2006.51.5.2388

Eckert, W., and Conrad, R. (2007). Sulfide and methane evolution in the hypolimnion of a subtropical lake: athree-year study. *Biogeochemistry* 82, 67–76. doi: 10.1007/s10533-006-9053-3

Elul, M., Rubin-Blum, M., Ronen, Z., Bar-Or, I., Eckert, W., and Sivan, O. (2021). Metagenomic insights into the metabolism of microbial communities that mediate iron and methane cycling in Lake Kinneret sediments. *Biogeosci. Discuss.* 2091–2106. doi: 10.5194/bg-2020-329

Elvert, M., Boetius, A., Knittel, K., and Jørgensen, B. B. (2003). Characterization of specific membrane fatty acids as chemotaxonomic markers for sulfate-reducing bacteria involved in anaerobic oxidation of methane. *Geomicrobiol J.* 20, 403–419. doi: 10.1080/01490450303894

Ettwig, K. F., Butler, M. K., Le Paslier, D., Pelletier, E., Mangenot, S., Kuypers, M. M. M., et al. (2010). Nitrite-driven anaerobic methane oxidation by oxygenic bacteria. *Nature* 464, 543–548. doi: 10.1038/nature08883

Ettwig, K. F., Zhu, B., Speth, D., Keltjens, J. T., Jetten, M. S. M., and Kartal, B. (2016). Archaea catalyze iron-dependent anaerobic oxidation of methane. *Proc. Natl. Acad. Sci.* 113, 12792–12796. doi: 10.1073/pnas.1609534113

Garber, A. I., Nealson, K. H., Okamoto, A., McAllister, S. M., Chan, C. S., Barco, R. A., et al. (2020). FeGenie: a comprehensive tool for identification of iron genes and iron gene neighborhoods in genome and metagenome assemblies. *Frontiers in Microbiology.* 11, 1–23. doi: 10.3389/fmicb.2020.00037

Guckert, J. B., Ringelberg, D. B., White, D. C., Hanson, R. S., and Bratina, B. J. (1991). Membrane fatty acids as phenotypic markers in the polyphasic taxonomy of methylotrophs within the Proteobacteria. *J. Gen. Microbiol.* 137, 2631–2641. doi: 10.1099/00221287-137-11-2631

Haroon, M. F., Hu, S., Shi, Y., Imelfort, M., Keller, J., Hugenholtz, P., et al. (2013). Anaerobic oxidation of methane coupled to nitrate reduction in a novel archaeal lineage. *Nature* 500, 567–570. doi: 10.1038/nature12375

He, R., Wooller, M. J., Pohlman, J. W., Quensen, J., Tiedje, J. M., and Leigh, M. B. (2012). Diversity of active aerobic methanotrophs along depth profiles of arctic and subarctic lake water column and sediments. *ISME J.* 6, 1937–1948. doi: 10.1038/ismej.2012.34

Hunter, J. D. (2007). Matplotlib: a 2D graphics environment. *Comput. Sci. Eng.* 9, 90–95. doi: 10.1109/MCSE.2007.55

Jetten, M. S. M., Stams, A. J. M., and Zhender, A. J. B. (1992). Methanogenesis from acetate metabolism in Methanothrix soehngenii and Methanosarcina spp. *FEMS Microbiology Reviews.* 88, 181–198. doi: 10.1111/j.1574-6968.1992.tb04987.x

Kang, D. D., Froula, J., Egan, R., and Wang, Z. (2015). Meta BAT, an efficient tool for accurately reconstructing single genomes from complex microbial communities. *PeerJ* 2015, 1–15. doi: 10.7717/peerj.1165

Kerin, E. J., Gilmour, C. C., Roden, E., Suzuki, M. T., Coates, J. D., and Mason, R. P. (2006). Mercury methylation by dissimilatory iron-reducing bacteria. *Applied and Environmental Microbiology.* 72, 7919–7921. doi: 10.1128/AEM.01602-06

Kieser, S., Brown, J., Zdobnov, E. M., Trajkovski, M., and McCue, L. A. (2020). ATLAS: a Snakemake workflow for assembly, annotation, and genomic binning of metagenome sequence data. *BMC Bioinformatics* 21, 1–8. doi: 10.1186/s12859-020-03585-4

Kits, K. D., Klotz, M. G., and Stein, L. Y. (2015). Methane oxidation coupled to nitrate reduction under hypoxia by the Gammaproteobacterium Methylomonas denitrificans, sp. nov. type strain FJG1. *Environ. Microbiol.* 17, 3219–3232. doi: 10.1111/1462-2920.12772

Knittel, K., and Boetius, A. (2009). Anaerobic oxidation of methane: Progress with an unknown process. *Annu. Rev. Microbiol.* 63, 311–334. doi: 10.1146/annurev.micro.61.080706.093130

Kraft, B., Jehmlich, N., Larsen, M., Bristow, L. A., Könneke, M., Thamdrup, B., et al. (2022). Oxygen and nitrogen production by an ammonia-oxidizing archaeon. *Science* 375, 97–100. doi: 10.1126/science.abe6733

Lin, Y. S., Lipp, J. S., Yoshinaga, M. Y., Lin, S. H., Elvert, M., and Hinrichs, K. U. (2010). Intramolecular stable carbon isotopic analysis of archaeal glycosyl tetraether lipids. *Rapid Commun. Mass Spectrom.* 24, 2817–2826. doi: 10.1002/rcm.4707

Losey, N. A., Stevenson, B. S., Busse, H. J., Sinninghe Damsté, J. S., Rijpstra, W. I. C., Rudd, S., et al. (2013). Thermoanaerobaculum aquaticum gen. nov., sp. nov., the first cultivated member of Acidobacteria subdivision 23, isolated from a hot spring. *International Journal of Systematic and Evolutionary Microbiology.* 63, 4149–4157. doi: 10.1099/ijs.0.051425-0

Lomans, B. P., Maas, R., Luderer, R., Op den Camp, H. J. M., Pol, A., Van der Drift, C., et al. (1999). Isolation and characterization of Methanomethylovorans hollandica gen. Nov., sp. Nov., isolated from freshwater sediment, a methylotrophic methanogen able to grow on dimethyl sulfide and methanethiol. *Applied and Environmental Microbiology*. 65, 3641-3650. doi: 10.1128/AEM.65.8.3641-3650.1999

Lovley, D. R., Holmes, D. E., and Nevin, K. P. (2004). Dissimilatory Fe(III) and Mn(IV) reduction. *Adv. Microb. Physiol.* 49, 219–286. doi: 10.1016/S0065-2911(04)49005-5

Lovley, D. R., Ueki, T., Zhang, T., Malvankar, N. S., Shrestha, P. M., Flanagan, K. A., et al. (2011). Geobacter. The microbe electric's physiology, ecology, and practical applications. *Adv. Microb. Physiol.* 59, 1–100. doi: 10.1016/B978-0-12-387661-4.00004-5

Lu, Y. Z., Fu, L., Ding, J., Ding, Z. W., Li, N., and Zeng, R. J. (2016). Cr (VI) reduction coupled with anaerobic oxidation of methane in a laboratory reactor. *Water Res.* 102, 445–452. doi: 10.1016/j.watres.2016.06.065

Martinez-cruz, K., Leewis, M., Charold, I., Sepulveda-jauregui, A., Walter, K., Thalasso, F., et al. (2017). Science of the Total environment anaerobic oxidation of methane by aerobic methanotrophs in sub-Arctic lake sediments. *Sci. Total Environ.* 607–608, 23–31. doi: 10.1016/j.scitotenv.2017.06.187

Meador, T. B., Gagen, E. J., Loscar, M. E., Goldhammer, T., Yoshinaga, M. Y., Wendt, J., et al. (2014). Thermococcus kodakarensis modulates its polar membrane lipids and elemental composition according to growth stage and phosphate availability. *Frontiers in Microbiology.* 5, 1–13. doi: 10.3389/fmicb.2014.00010

McDonald, I. R., Bodrossy, L., Chen, Y., and Murrell, J. C. (2008). Molecular ecology techniques for the study of aerobic methanotrophs. *Appl. Environ. Microbiol.* 74, 1305–1315. doi: 10.1128/AEM.02233-07

McDonald, D., Clemente, J. C., Kuczynski, J., Rideout, J. R., Stombaugh, J., Wendel, D., et al. (2012). The biological observation matrix (BIOM) format or: how I learned to stop worrying and love the ome-ome. *Giga Science* 464, 1–6. doi: 10.1186/2047-217X-1-7

McMurdie, P. J., and Holmes, S. (2013). Phyloseq: An R package for reproducible interactive analysis and graphics of microbiome census data. *PLoS One* 8, 1–11. doi: 10.1371/journal.pone.0061217

Milucka, J., Kirf, M., Lu, L., Krupke, A., Lam, P., Littmann, S., et al. (2015). Methane oxidation coupled to oxygenic photosynthesis in anoxic waters. *ISME J.* 9, 1991–2002. doi: 10.1038/ismej.2015.12

Myhre, G., Shindell, D., Bréon, F. M., Collins, W., Fuglestvedt, J., and Huang, J. (2013). "Anthropogenic and Natural Radiative Forcing. In: Climate Change 2013: The Physical Science Basis" in *Contribution of Working Group I to the Fifth Assessment Report of the Intergovernmental Panel on Climate Change*. eds. T. F. Stocker, D. Qin, G.-K. Plattner, M. Tignor, S. K. Allen, J. Boschung, A. Nauels, Y. Xia, V. Bex and P. M. Midgley (NY, USA: Cambridge University Press).

Nordi, K. A., and Thamdrup, B. (2014). Nitrate-dependent anaerobic methane oxidation in a freshwater sediment. *Geochim. Cosmochim. Acta* 132, 141–150. doi: 10.1016/j.gca.2014.01.032

Oren, A. (2014). "The family Methanoregulaceae" in *The Procaryotes*. ed. E. Rosenberg (Springer), 253–258.

Olm, M. R., Brown, C. T., Brooks, B., and Banfield, J. F. (2017). DRep: a tool for fast and accurate genomic comparisons that enables improved genome recovery from metagenomes through de-replication. *ISME J.* 11, 2864–2868. doi: 10.1038/ismej.2017.126

Orata, F. D., Kits, K. D., and Stein, Y. (2018). Complete genome sequence of Methylomonas denitrificans strain FJG1, an obligate aerobic Methanotroph that can couple methane oxidation with denitrification. *Genome Announc.* 6, 1–2. doi: 10.1128/genomeA.00276-18

Oshkin, I. Y., Beck, D. A. C., Lamb, A. E., Tchesnokova, V., Benuska, G., Mctaggart, T. L., et al. (2015). Methane-fed microbial microcosms show differential community dynamics and pinpoint taxa involved in communal response. *ISME J.* 9, 1119–1129. doi: 10.1038/ismej.2014.203

Oswald, K., Jegge, C., Tischer, J., Berg, J., Brand, A., Miracle, M. R., et al. (2016a). Methanotrophy under versatile conditions in the water column of the ferruginous meromictic Lake La Cruz (Spain). *Front. Microbiol.* 7, 1–16. doi: 10.3389/fmicb.2016.01762

Oswald, K., Milucka, J., Brand, A., Hach, P., Littmann, S., Wehrli, B., et al. (2016b). Aerobic gammaproteobacterial methanotrophs mitigate methane emissions from oxic and anoxic lake waters. *Limnol. Oceanogr.* 61, S101–S118. doi: 10.1002/lno.10312

Pedregosa, F., Varoquaux, G., Gramfort, A., Michel, V., Thirion, B., Grisel, O., et al. (2011). Scikit-learn: machine learning in Python. *J. Mach. Learn. Res.* 127, 2825–2830. doi: 10.1289/EHP4713

Poulton, S. W., Krom, M. D., and Raiswell, R. (2004). A revised scheme for the reactivity of iron (oxyhydr)oxide minerals towards dissolved sulfide. *Geochem. Cosmochim. Acta* 68, 3703–3715. doi: 10.1016/j.gca.2004.03.012

Prjibelski, A., Antipov, D., Meleshko, D., Lapidus, A., and Korobeynikov, A. (2020). Using SPAdes De novo assembler. *Curr. Protoc. Bioinformatics* 70, 1–29. doi: 10.1002/cpbi.102

Quast, C., Pruesse, E., Yilmaz, P., Gerken, J., Schweer, T., Yarza, P., et al. (2012). The SILVA ribosomal RNA gene database project: improved data processing and web-based tools. *Nucleic Acids Res.* 41, 590–596. doi: 10.1093/nar/gks1219

Raghoebarsing, A. A., Pol, A., Van De Pas-Schoonen, K. T., Smolders, A. J. P., Ettwig, K. F., Rijpstra, W. I. C., et al. (2006). A microbial consortium couples anaerobic methane oxidation to denitrification. *Nature* 440, 918–921. doi: 10.1038/nature04617

Ranalli, G., Whitmore, T. N., and Lloyd, D. (1986). Methanogenesis from methanol in Methanosarcina barkeri studied using membrane inlet mass spectroscopy. *FEMS Microbiology Letters.* 35, 119–122. doi: 10.1111/j.1574-6968.1986.tb01512.x

Rissanen, A. J., Saarela, T., Jäntti, H., Buck, M., Peura, S., Aalto, S. L., et al. (2021). Vertical stratification patterns of methanotrophs and their genetic controllers in water columns of oxygen-stratified boreal lakes. *FEMS Microbiol. Ecol.* 97, 1–16. doi: 10.1093/femsec/fiaa252

Rognes, T., Flouri, T., Nichols, B., Quince, C., and Mahé, F. (2016). VSEARCH: a versatile open source tool for metagenomics. *PeerJ* 2016, 1–22. doi: 10.7717/peerj.2584

Scheller, S., Yu, H., Chadwick, G. L., McGlynn, S. E., and Orphan, V. J. (2016). Artificial electron acceptors decouple archaeal methane oxidation from sulfate reduction. *Science* 351, 1754–1756. doi: 10.1126/science.aad7154

Sieber, C. M. K., Probst, A. J., Sharrar, A., Thomas, B. C., Hess, M., Tringe, S. G., et al. (2018). Recovery of genomes from metagenomes via a dereplication, aggregation and scoring strategy. *Nat. Microbiol.* 3, 836–843. doi: 10.1038/s41564-018-0171-1

Sivan, O., Adler, M., Pearson, A., Gelman, F., Bar-Or, I., John, S. G., et al. (2011). Geochemical evidence for iron-mediated anaerobic oxidation of methane. *Limnol. Oceanogr.* 56, 1536–1544. doi: 10.4319/lo.2011.56.4.1536

Sivan, O., Antler, G., Turchyn, A. V., Marlow, J. J., and Orphan, V. J. (2014). Iron oxides stimulate sulfate-driven anaerobic methane oxidation in seeps. *Proc. Natl. Acad. Sci. U. S. A.* 111, E4139–E4147. doi: 10.1073/pnas.1412269111

Sivan, O., Shusta, S., and Valentine, D. L. (2016). Methanogens rapidly transition from methane production to iron reduction. *Geobiology* 190–203. doi: 10.1111/gbi.12172

Smith, M. R., and Mah, R. A. (1978). Growth and methanogenesis by Methanosarcina Strain 227 on acetate and methanol. *Applied and Environmental Microbiology.* 36, 870–879. doi: 10.1128/aem.36.6.870-879.1978

Smith, G. J., and Wrighton, K. C. (2019). Metagenomic approaches unearth methanotroph phylogenetic and metabolic diversity. *Curr. Issues Mol. Biol.* 33, 57–84. doi: 10.21775/cimb.033.057

Sprott, G. D., Dicaire, C. J., Choquet, C. G., Patel, G. B., and Ekiel, I. (1993). Hydroxydiether lipid structures in Methanosarcina spp. and *Methanococcus voltae*. *Appl. Environ. Microbiol.* 59, 912–914. doi: 10.1128/aem.59.3.912-914.1993

Steinsdóttir, H. G. R., Gómez-Ramírez, E., Mhatre, S., Schauberger, C., Bertagnolli, A. D., Pratte, Z. A., et al. (2022). Anaerobic methane oxidation in a coastal oxygen minimum zone: spatial and temporal dynamics. *Environ. Microbiol.* 24, 2361–2379. doi: 10.1111/1462-2920.16003

Stookey, L. L. (1970). Ferrozine-a new spectrophotometric reagent for iron. *Anal. Chem.* 42, 779–781. doi: 10.1021/ac60289a016

Straub, K. L., Benz, M., and Schink, B. (2001). Iron metabolism in anoxic environments at near neutral pH. *FEMS Microbiol. Ecol.* 34, 181–186. doi: 10.1016/S0168-6496(00)00088-X

Sturt, H. F., Summons, R. E., Smith, K., Elvert, M., and Hinrichs, K. U. (2004). Intact polar membrane lipids in prokaryotes and sediments deciphered by high-performance liquid chromatography/electrospray ionization multistage mass spectrometry - New biomarkers for biogeochemistry and microbial ecology. *Rapid Communication in Mass Spectrometry.* 18, 617–628. doi: 10.1002/rcm.1378

Su, G., Zopfi, J., Niemann, H., and Lehmann, M. F. (2022). Multiple groups of methanotrophic bacteria mediate methane oxidation in anoxic lake sediments. *Front. Microbiol.* 13:864630. doi: 10.3389/fmicb.2022.864630

Tan, S., Liu, J., Fang, Y., Hedlund, B. P., Lian, Z. H., Huang, L. Y., et al. (2019). Insights into ecological role of a new deltaproteobacterial order Candidatus Acidulodesulfobacterales by metagenomics and metatranscriptomics. *ISME.* 13, 2044–2057. doi: 10.1038/s41396-019-0415-y

Taubert, M., Grob, C., Crombie, A., Howat, A. M., Burns, O. J., Weber, M., et al. (2019). Communal metabolism by Methylococcaceae and Methylophilaceae is driving rapid aerobic methane oxidation in sediments of a shallow seep near Elba. *Environ. Microbiol.* 21, 3780–3795. doi: 10.1111/1462-2920.14728

Teece, M. A., Fogel, M. L., Dollhopf, M. E., and Nealson, K. H. (1999). Isotopic fractionation associated with biosynthesis of fatty acids by a marine bacterium under oxic and anoxic conditions. *Org. Geochem.* 30, 1571–1579. doi: 10.1016/S0146-6380(99)00108-4

Treude, N., Rosencrantz, D., Liesack, W., and Schnell, S. (2003). Strain FAcl2, a dissimilatory iron reducing member of the Anaeromyxobacter subgroup of Myxococcales. *FEMS Microbiology Ecology.* 44, 261–269. doi: 10.1016/S0168-6496(03)00048-5

Trotsenko, Y. A., and Murrell, J. C. (2008). Metabolic Aspects of Aerobic Obligate Methanotrophy. *Advances in AppTlied Microbiology, Academic Press*. *63*, 183–229. doi: 10.1016/S0065-2164(07)00005-6

Van Grinsven, S., Oswald, K., Wehrli, B., Jegge, C., Zopfi, J., Lehmann, M. F., et al. (2021). Methane oxidation in the waters of a humic-rich boreal lake stimulated by photosynthesis, nitrite, Fe(III) and humics. *Biogeosciences* 18, 3087–3101. doi: 10.5194/bg-18-3087-2021

Van Grinsven, S., Sinninghe Damste, J. S., Abdala, A. A., Engelmann Harrison, J., and Villanueva, L. (2020). Methane oxidation in anoxic lake water stimulated by nitrate and sulfate addition. *Environ. Microbiol.* 22, 766–782. doi: 10.1111/1462-2920.14886

Vanwonterghem, I., Evans, P. N., Parks, D. H., Jensen, P. D., Woodcroft, B. J., Hugenhultz, P., et al. (2016). *Nature Microbiology.* 1, 1–9. doi: 10.1038/nmicrobiol.2016.170

Vigderovich, H., Eckert, W., Elul, M., Rubin-Blum, M., Elvert, M., and Sivan, O. (2022). Long-term incubations provide insight into the mechanisms of anaerobic oxidation of methane in methanogenic lake sediments. *Biogeosciences* 19, 2313–2331. doi: 10.5194/bg-19-2313-2022

Walters, W., Hyde, E. R., Berg-lyons, D., Ackermann, G., Humphrey, G., Parada, A., et al. (2015). Transcribed spacer marker gene primers for microbial community surveys. *Am. Soc. Microbiol.* 1, 1–10. doi: 10.1128/mSystems.00009-15

Wang, L., Miao, X., Ali, J., Lyu, T., and Pan, G. (2018). Quantification of oxygen Nanobubbles in particulate matters and potential applications in remediation of anaerobic environment. *ACS Omega* 3, 10624–10630. doi: 10.1021/acsomega.8b00784

Wickham, H. (2016). *ggplot2: Elegant Graphics for Data Analysis* (*35*). New York: Springer-Verlag

Williams, T. J., Allen, M. A., Berengut, J. F., and Cavicchioli, R. (2021). *Frontiers in Microbiology.* 12, 1–16. doi: 10.3389/fmicb.2021.741077

Wu, Y. W., Simmons, B. A., and Singer, S. W. (2016). MaxBin 2.0: An automated binning algorithm to recover genomes from multiple metagenomic datasets. *Bioinformatics* 32, 605–607. doi: 10.1093/bioinformatics/btv638

Zhang, C. L., Li, Y., Ye, Q., Fong, J., Peacock, A. D., Blunt, E., et al. (2003). Carbon isotope signatures of fatty acids in Geobacter metallireducens and *Shewanella algae*. *Chem. Geol.* 195, 17–28. doi: 10.1016/S0009-2541(02)00386-8

Zhang, L., Zeng, Q., Liu, X., Chen, P., Guo, X., Ma, L. Z., et al. (2019). Iron reduction by diverse actinobacteria under oxic and pH-neutral conditions and the formation of secondary minerals. *Chem. Geol.* 525, 390–399. doi: 10.1016/j.chemgeo.2019.07.038

Zheng, Y., Wang, H., Liu, Y., Zhu, B., Li, J., and Yang, Y. (2020). Methane-dependent mineral reduction by aerobic Methanotrophs under hypoxia. *Environ. Sci. Technol. Lett.* 7, 606–612. doi: 10.1021/acs.estlett.0c00436

Frontiers in Microbiology

TYPE Original Research
PUBLISHED 10 November 2023
DOI 10.3389/fmicb.2023.1198786

OPEN ACCESS

EDITED BY
Mark Alexander Lever,
The University of Texas at Austin, United States

REVIEWED BY
Jeffrey M. Dick,
Central South University, China
Ees Ahmad,
National Bureau of Agriculturally Important
Microorganisms (ICAR), India

*CORRESPONDENCE
Kaitlin R. Rempfert
✉ kaitlin.rempfert@colorado.edu
Alexis S. Templeton
✉ alexis.templeton@colorado.edu

RECEIVED 02 April 2023
ACCEPTED 25 September 2023
PUBLISHED 10 November 2023

CITATION
Rempfert KR, Kraus EA, Nothaft DB, Dildar N, Spear JR, Sepúlveda J and Templeton AS (2023) Intact polar lipidome and membrane adaptations of microbial communities inhabiting serpentinite-hosted fluids. *Front. Microbiol.* 14:1198786. doi: 10.3389/fmicb.2023.1198786

Intact polar lipidome and membrane adaptations of microbial communities inhabiting serpentinite-hosted fluids

Kaitlin R. Rempfert[1]*, Emily A. Kraus[2], Daniel B. Nothaft[1], Nadia Dildar[1], John R. Spear[2,3], Julio Sepúlveda[1] and Alexis S. Templeton[1]*

[1]Department of Geological Sciences, University of Colorado, Boulder, CO, United States, [2]Department of Civil and Environmental Engineering, Colorado School of Mines, Golden, CO, United States, [3]Department of Quantitative Biosciences and Engineering, Colorado School of Mines, Golden, CO, United States

The generation of hydrogen and reduced carbon compounds during serpentinization provides sustained energy for microorganisms on Earth, and possibly on other extraterrestrial bodies (e.g., Mars, icy satellites). However, the geochemical conditions that arise from water-rock reaction also challenge the known limits of microbial physiology, such as hyperalkaline pH, limited electron acceptors and inorganic carbon. Because cell membranes act as a primary barrier between a cell and its environment, lipids are a vital component in microbial acclimation to challenging physicochemical conditions. To probe the diversity of cell membrane lipids produced in serpentinizing settings and identify membrane adaptations to this environment, we conducted the first comprehensive intact polar lipid (IPL) biomarker survey of microbial communities inhabiting the subsurface at a terrestrial site of serpentinization. We used an expansive, custom environmental lipid database that expands the application of targeted and untargeted lipodomics in the study of microbial and biogeochemical processes. IPLs extracted from serpentinite-hosted fluid communities were comprised of >90% isoprenoidal and non-isoprenoidal diether glycolipids likely produced by archaeal methanogens and sulfate-reducing bacteria. Phospholipids only constituted ~1% of the intact polar lipidome. In addition to abundant diether glycolipids, betaine and trimethylated-ornithine aminolipids and glycosphingolipids were also detected, indicating pervasive membrane modifications in response to phosphate limitation. The carbon oxidation state of IPL backbones was positively correlated with the reduction potential of fluids, which may signify an energy conservation strategy for lipid synthesis. Together, these data suggest microorganisms inhabiting serpentinites possess a unique combination of membrane adaptations that allow for their survival in polyextreme environments. The persistence of IPLs in fluids beyond the presence of their source organisms, as indicated by 16S rRNA genes and transcripts, is promising for the detection of extinct life in serpentinizing settings through lipid biomarker signatures. These data contribute new insights into the complexity of lipid structures generated in actively serpentinizing environments and provide valuable context to aid in the reconstruction of past microbial activity from fossil lipid records of terrestrial serpentinites and the search for biosignatures elsewhere in our solar system.

KEYWORDS

serpentinization, habitability, intact polar lipids, lipid membrane adaptations, untargeted lipidomics, polyextreme conditions, Samail ophiolite, subsurface microbiome

1. Introduction

Efforts to detect life on other planetary bodies can be informed by investigating the distribution, diversity, and adaptations of extant life in planetary analog environments on Earth. Of particular interest are serpentinizing settings because the reducing conditions that arise during the hydration of ultramafic rock can yield abundant energy for microbial metabolism through the generation of hydrogen and organic compounds (Schulte et al., 2006; Russell et al., 2010). Both physiological and phylogenetic evidence support the hypothesis that microbial metabolisms dependent on substrates derived from serpentinization were among the first metabolisms on early Earth (Russell et al., 2010; Weiss et al., 2016; Boyd et al., 2020), and diverse microbial communities have been found to inhabit modern serpentinite-hosted fluids (Brazelton et al., 2013; Suzuki et al., 2013; Postec et al., 2015; Rempfert et al., 2017). Because ultramafic rocks are common not just in the Earth's mantle, but also on Mars and in the cores of icy satellites, the potential for serpentinization to provide sufficient energy to support life is widespread throughout the solar system and through time (Vance et al., 2007; Quesnel et al., 2009; Sleep et al., 2011; Tarnas et al., 2018).

While extended water-rock reaction may provide ample reducing power for microbial metabolism, the geochemical conditions that result from serpentinization also pose challenges to the physiology of microorganisms and influence the distribution and composition of microbial communities in these settings (Brazelton et al., 2013; Suzuki et al., 2013, 2017; Cardace et al., 2015; Meyer-Dombard et al., 2015; Postec et al., 2015; Woycheese et al., 2015; Miller et al., 2016; Crespo-Medina et al., 2017; Rempfert et al., 2017; Twing et al., 2017; Fones et al., 2019; Sabuda et al., 2020; Seyler et al., 2020; Kraus et al., 2021). Reacted fluids are often highly reduced and hyperalkaline ($pH > 11$), limiting the availability of oxidants for microbial metabolism and complicating maintenance of a proton motive force across the cellular membrane (Schrenk et al., 2013). As an additional consequence of the high pH of reacted fluids, dissolved inorganic carbon and nutrients, such as phosphate, are rapidly depleted through precipitation of minerals and sorption which limits microbial carbon fixation and biosynthesis in this environment (Chavagnac et al., 2013; Schrenk et al., 2013). Microbial life capable of harnessing energy from water-rock reaction in serpentinites must adapt to these polyextreme conditions to survive.

A primary strategy microorganisms employ to adapt to extreme environments is to modify their cellular membranes, as the cell membrane plays an integral role in both shielding the cell from its environment and in preserving disequilibrium in chemical energy for metabolism (Siliakus et al., 2017). Lipids, as a bilayer or monolayer, are the primary components of the cytoplasmic membrane of microbial cells. The physical properties of lipid membranes are dependent on the chemical structures of the individual lipids that comprise the membrane, and microorganisms are capable of rapidly adjusting the composition of their lipid membrane in order to maintain membrane integrity and functionality (Benning et al., 1995; Rowlett et al., 2017; Okur et al., 2019; Chwastek et al., 2020). Membrane lipid remodeling may also be an important adaptation to reduce energetic costs of biosynthesis or the need for specific macronutrients that may be limited (Schubotz, 2019; Boyer et al., 2020). Modifications to lipids include altering the polar lipid headgroup, configuration of the backbone linking the polar head group to the hydrophilic chains, or saturation and branching of hydrophobic chains, however all adjustments require an underlying genetic capability, and consequently can be specific to taxonomic groups (Parsons and Rock, 2013; Sohlenkamp and Geiger, 2016; Siliakus et al., 2017). In polyextreme environments, the lipidome thus reflects a combination of evolved physiological adaptations to the challenging conditions, short-term regulated enzymatic remodeling in response to changing environmental parameters, and the overall microbial community composition.

Due to the recalcitrant nature of lipids compared to other biomolecules (e.g., DNA, RNA, proteins; Brocks and Summons, 2003; Walters et al., 2004; Eigenbrode, 2008), numerous studies have identified lipids in serpentinizing settings with the goal of determining signatures that can be used to trace ancient microbial activity on Earth or even to inform the search for life on extraterrestrial bodies (Klein et al., 2015; Zwicker et al., 2018; Newman et al., 2020; Rattray et al., 2022). Accordingly, studies of serpentinite-hosted lipids have focused almost exclusively on core lipid moieties that are retained in rock (Klein et al., 2015; Zwicker et al., 2018; Newman et al., 2020), and not on intact polar lipids (IPLs), which represent a more recent lipid signature, since covalently-bound headgroups are susceptible to hydrolysis after cell death (White et al., 1979; Harvey et al., 1986; Logemann et al., 2011; Sturt et al., 2004). Because IPLs reflect modern microbial communities and carry additional structural information (e.g., lipid headgroup and backbone configuration), IPLs are more suitable molecules for correlating lipid adaptations to ambient geochemistry than core lipids. A recent study by Rattray et al. (2022) reported complex IPLs in calcite and brucite veins in serpentinite rock at the Chimera Seeps in Turkey, illustrating a need to explore the conditions under which diverse lipids are produced in serpentinizing environments. To our knowledge, the IPL composition of extant biomass has only been comprehensively investigated in serpentinized fluids at one site of active serpentinization, the Lost City Hydrothermal Field, a marine hydrothermal system (~90° C) venting into oxygenated seawater (Bradley et al., 2009a,b). Inventorying the fluid-hosted lipidome of a terrestrial site of serpentinization would provide an opportunity to isolate lipid membrane modifications specific to the geochemical conditions imposed by water-rock reaction, in the absence of additional osmotic pressures and temperature. Elucidating the source and type of lipid membrane adaptations that occur in the subsurface of terrestrial serpentinizing settings would improve interpretation of preserved lipid signatures in serpentinite rock and inform potential sampling efforts for biosignature detection on other planetary bodies such as Mars.

Here, we present the first IPL survey of serpentinized fluids from a terrestrial site of low-temperature serpentinization, in the Samail Ophiolite of Oman. We examined the distribution and diversity of IPL compounds in subsurface, serpentinite-hosted fluids that spanned both a large range of pH (7.6–11.3) and reduction potential (Eh +269 to −253 mV). We developed an expansive theoretical database (> 2 million lipids) to be able to classify diverse IPLs from this setting. The intact lipidome of these fluids was characterized within the framework of aqueous geochemistry and microbial community composition, which allows us to infer source organisms for lipid signatures and identify potential membrane modifications to improve understanding of the adaptations that enable microbial life to inhabit this polyextreme environment.

2. Materials and methods

2.1. Site description and sampling of subsurface fluids

In February 2017, subsurface fluids were pumped from six preexisting wells previously drilled into the crust–mantle section of the Samail Ophiolite by the Oman Ministry of Regional Municipalities and Water Resources (Table 1).

At each well, a Grundfos SQ2-85 submersible pump (Grundfos Pumps Corp., Denmark, Netherlands) attached to a splitting manifold and Teflon tubing was utilized to collect water at depth (Table 1). The pump, manifold, tubing, and filter housings were flushed with site water for 20–30 min (~100 L of water) prior to sampling. Biomass was concentrated for lipid analysis on combusted (450° C, 8 h) 0.3 μm Advantec (Advantec MFS, Inc., Dublin, CA) glass fiber filters in a Millipore 47 mm stainless steel housing (Millipore Sigma, Burlington, MA), and for DNA/RNA analysis on 0.2 μm Millipore polycarbonate filters in a 47 mm Pall (Pall Corporation, Cortland, NY) polycarbonate filter housing. The volume of water filtered at each well was measured by collecting the filtrate in a graduated cylinder. Biomass for DNA/RNA analysis was suspended in bead tubes with lysis/stabilization solution (Zymo Research Inc., Irvine, CA) and frozen in a liquid nitrogen dewar on site. Glass fiber filters with concentrated biomass for lipid analysis were placed in combusted aluminum foil and frozen inside sterile cryovials until analysis. Measured volumes of well water filtered for lipid analysis are listed in Table 1.

Water temperature, conductivity, pH, and oxidation–reduction potential (Eh) were measured in the field with a Hach HQ40D Portable Multi Meter (Loveland, CO). Aqueous phase gas sampling was conducted using the "bubble strip" method (modified from Kampbell et al., 1998, Nothaft, 2019). Additionally, filtered well water (passed through the 0.22 μm filter) was collected in 15 mL Falcon® tubes (Corning Inc., Corning, NY) for quantification of major anions and cations, with the latter acidified with nitric acid in the field at the time of collection to a final pH <2. Aliquots for dissolved inorganic carbon quantification were injected through 0.22 μm polyethersulfone Basix syringe filters (Thermo Fisher Scientific, Waltham, MA) into butyl-stoppered vials that had previously been evacuated, acid-washed, and combusted.

2.2. Aqueous geochemical analyses

Protocols for aqueous geochemical analyses are described in detail in Kraus et al. (2021). Briefly, dissolved H_2 and CH_4 were measured using an SRI 8610C gas chromatograph (SRI instruments, Torrance, CA) with a 2 × 1 mm ID micropacked ShinCarbon ST column (Agilent, Santa Clara, CA) and N_2 as the carrier gas. Peak intensities were measured on a thermal conductivity detector for H_2 and a flame ionization detector for CH_4. Peak intensities were calibrated (±2%) with standard gas mixes (Supelco Analytical, Bellefonte, PA) with a relative standard deviation of ~5% over the calibrated range. Concentrations of cations and anions were measured via inductively coupled plasma atomic emission spectroscopy (ICP-AES; Optima 5,300, Perkin-Elmer, Fremont, CA) and ion chromatography (IC; ICS-90; Dionex, Sunnyvale, CA) at the Colorado School of Mines. For DIC analyses, 6 mL aliquots of samples were transferred to helium-purged Exetainer® tubes (Labco, Ceredigion, United Kingdom) and converted to CO_2 for analysis by addition of boiled 85% phosphoric acid (H_3PO_4). Equilibrated and converted samples were then quantified using a Delta V Isotope Ratio Mass Spectrometer equipped with a Thermo Gasbench II gas preparation and introduction system (Thermo Fisher Scientific) at the Earth Systems Stable Isotope Laboratory at the University of Colorado, Boulder.

2.3. DNA and RNA extraction, sequencing, and processing

Prior to extraction, cells were lysed by bead beating in one-minute intervals for a total of 5 mins (with one-minute rests between beating intervals to cool the sample tubes to prevent sample degradation). DNA and RNA were then extracted in parallel using the Zymo microbiomics soil/fecal DNA miniprep extraction kit (Zymo Research Inc.) according to manufacturer instructions. DNA was quantified by the Qubit double-stranded DNA high-sensitivity assay (ThermoFisher Scientific) and then frozen at −80°C. Extracted RNA was first converted to cDNA through reverse transcription-PCR as described previously (Kraus et al., 2021) and then quantified and stored frozen.

SSU rRNA genes were amplified from both DNA and cDNA using the 515-Y M13 and 926R primer set (Parada et al., 2016; Kraus et al., 2018) which spans the V4 and V5 hypervariable regions. PCR conditions and barcode reactions utilized in this study were described

TABLE 1 Locations of wells and borehole sampling parameters.

Well	WAB188	WAB105	WAB104	WAB55	WAB71	NSHQ14
Lithology	gabbro	peridotite	peridotite	peridotite	peridotite	peridotite
UTM Easting	671,123	644,678	643,099	634,777	670,322	675,495
UTM Northing	2,529,798	2,536,524	2,541,124	2,506,101	2,533,981	2,529,716
elevation (masl)	514	738	842	531	608	526
well depth (m)	78	120.5	120.4	102	136.5	304
screened interval (mbc)	34.5–51	110–117	100.8–104	8–97	128–131	open below casing
depth to water (mbc)	9.5	16.2	35	7.7	7.7	10[a]
pump depth (mbl)	78	50	28	26	50	85
L filtered for lipid analysis	16.3	162	9.9	115.9	20.2	67.3

[a] indicates data from 2017 was not available and replaced with 2016 data published by Rempfert et al. (2017).

by Kraus et al. (2018). Final products were purified with Pure beads (Kapa Biosystensm Wilmington, MA) and pooled in equimolar amounts before concentration to a final volume of 80 μL on a Ultracel-30 K membrane (Millipore Sigma) within an Amicon Ultra 0.5 mL centrifugal filter (Millipore Sigma). The prepared DNA/cDNA library was sequenced using V2 PE250 chemistry on an Illumina MiSeq sequencer (Illumina Inc., San Diego, CA) at the Duke Center for Genomic and Computational Biology.[1] All raw sequences are available under accession PRJNA560313 on the NCBI Sequence Read Archive.

Sequence files were demultiplexed and trimmed using Cutadapt (Martin, 2011) and quality filtered using Figaro v1.1.1.[2] Amplicon sequence variants (ASVs) were then identified in the "DADA2" R package (Callahan et al., 2016) and assigned taxonomy to the genus level using the RDP classifier (Wang et al., 2007) trained on the Silva SSU 138 reference database (Quast et al., 2013). Sequences assigned to mitochondria, chloroplasts, eukaryotes, or not assigned at the domain level (collectively <1% of sequences), were removed. Processing scripts are available online[3] under folder "OM17."

2.4. Lipid extraction and analysis

Intact polar lipids were extracted from glass-fiber filters loaded with biomass using a modified (Wörmer et al., 2015) Bligh and Dyer method (Bligh and Dyer, 1959). Samples were subjected to a total of five sequential extractions by ultrasonication. Two extractions were performed using 2:1:0.8 v:v:v methanol/dichloromethane/phosphate buffer (50 mM dipotassium phosphate monobasic, adjusted to pH 7.4), followed by two extractions in 2:1:0.8 v:v:v methanol/dichloromethane/TCA buffer (5% trichloroacetic acid, adjusted to pH 2), and a final extraction in 5:1 v:v methanol/dichloromethane. Prior to extraction, 200 ng of C16-PAF (Avanti Polar Lipids, Inc., Alabaster, Alabama) was added to each sample as an extraction standard to assess yield. Entire glass fiber filters were extracted using 4 mL of extraction buffer per extraction step. Supernatant from each extraction step was pooled in a separatory funnel. We separated and collected the organic fraction of the total lipid extract (TLE) after addition of 1:1 v:v dichloromethane/water in an amount equal to the total buffer utilized throughout the combined extraction steps. TLEs were then concentrated under a gentle flow of nitrogen gas (UHP grade) using a turbovap® evaporator, filtered through a 0.45 μm polytetrafluoroethylene syringe filter, re-dissolved in 100 uL of 9:1 v:v dichloromethane/methanol, and transferred to a 2 mL vial with insert prior to analysis. 1 ng of deuterated standard (d9-DGTS, Avanti Polar Lipids) was added to each insert to correct for sample matrix effects on ionization and to monitor retention times between samples.

Lipid extracts were analyzed by high performance liquid chromatography with heated electrospray ionization high resolution mass spectrometry (HPLC-HESI-HRMS) on a Thermo Scientific UltiMate 3000 system coupled to a Q Exactive Focus hybrid Quadrupole-Orbitrap mass spectrometer at the Organic Geochemistry Lab in the University of Colorado, Boulder. Untargeted screening of all samples was performed in full scan coupled to TopN data-dependent MS–MS mode (full scan-ddMS2) with dual positive and negative ionization in which a full scan of parent ions across the entire mass range was obtained and the top three parent ions at any given time were successively isolated and fragmented in the next scan. Separation of IPL headgroups was achieved using hydrophilic interaction liquid chromatography (HILIC) under conditions described by Wörmer et al. (2013) on an Acquity BEH Amide column (1.7 μm, 2.1 by 150 mm column, Waters Corporation, Eschborn, Germany). Eluent A consisted of 75:25 v:v acetonitrile/dichloromethane with 0.01% formic acid and 0.01% ammonium hydroxide; eluent B consisted of 50:50 v:v methanol/water with 0.4% formic acid and 0.4% ammonium hydroxide. Gradient elution was performed at a constant flow rate of 0.4 mL/min under the following gradients: 1% B for 2.5 min, 1 to 5% B from 2.5 to 4 min, 5 to 25% B from 4 to 22.5 min, 25% B to 40% B from 22.5 to 26.5 min, held at 40% B from 26.5 to 27.5 min, dropped to 1% B from 27.5 to 28.5 min and then held at 1% B to re-equilibrate the column until the end of the run (total run time 50 min). The column was kept at 40°C throughout the duration of each run, and 10 μL of sample dissolved in 9:1 v:v dichloromethane/methanol was injected per run. Optimal electrospray source parameters for ionization of lipid classes as either hydrogen or ammonium adducts with positive ionization, or formate or deprotonated adducts with negative ionization, were used: spray voltage of 3.5 kV, sheath gas flow of 40 arbitrary units (AU), auxiliary gas flow of 5 AU, S-lens RF level of 55 AU, capillary temperature of 200°C, and auxiliary gas heater temperature of 250°C. A scan range of 400–2000 m/z was used and mass resolution was set to the maximum possible value of 70,000 (FWHM at 200 m/z) for full-scan and 17,500 for MS2, with an AGC target of 1e5, minimum AGC target of 1e4, 200 ms maximum injection time, stepped collisional energy (nce: 10, 30, 70), and 3 m/z isolation window for MS2 scans.

The mass spectrometer was calibrated for mass resolution and accuracy weekly through direct infusion of Pierce LTQ Velos ESI Positive (88323) and Negative (88324) Ion Calibration Solution (ThermoFisher Scientific). Real-time mass accuracy and correction was performed using the lock mass of a low-level eluent contaminant polysiloxane (391.28429).

2.5. Generation of theoretical intact polar lipids database

We developed a custom *in silico* IPL database for environmental lipids by adapting "LOBSTAHS" (Collins et al., 2016), an existing bioinformatic software package in R (R Core Team, 2020). We modified the LOBSTAHS "generateLOBdbase.R" script to allow for the addition of mixed acyl/ether glycerol (AEG), monoether glycerol (MEG), diether glycerol (DEG), ceramide (Cer), 1,2 alkanediol (AD), and fatty amide (FA) backbone structures in addition to the diacyl glycerol (DAG) and monoacyl glycerol (MAG) backbones already included in the package structure. Additionally, we increased the number of allowed chains from 2 to 4 to include cardiolipins and triglyceride lipids. Possible headgroups were expanded through compilation of previously identified headgroup structures from environmental IPLs from published literature. Chemical formulas and references (Kates, 1993; Benning et al., 1995; Karlsson et al., 1998; Ferreira et al., 1999; Kawahara et al., 2002; Sturt et al., 2004;

---

[1] https://www.genome.duke.edu

[2] https://github.com/Zymo-Research/figaro

[3] https://github.com/danote/Samail_16S_compilation

Yang et al., 2006, 2010; Zhang et al., 2009; Murphy and Axelsen, 2011; Rossel et al., 2011; Moore et al., 2013; Popendorf et al., 2013; Diercks et al., 2015; Schubotz et al., 2013, 2015, 2018; Lobasso et al., 2015; Moore et al., 2015, 2016; Wang et al., 2015; Wörmer et al., 2015; Yoshinaga et al., 2011, 2012, 2015; Becker et al., 2016; Bosak et al., 2016; Hewelt-Belka et al., 2016; Li et al., 2017; Slavetinsky et al., 2017; Luo et al., 2018; Bale et al., 2019; Boyer et al., 2020; Tsugawa et al., 2020) for included headgroups are reported in Supplementary Table S1.

For generation of the database, the summed formulas of headgroup and backbone combinations (Supplementary Table S1) were inputted as separate entries in the LOBSTAHS-formatted component table for iterative calculation. Additionally, formulas for the full IPL structure of ladderane and isoprenoidal diether and tetraether lipids were entered as unique components to the table. For database components calculated iteratively, we used parameters specified for lipid chains as described by Foster et al. (2013). Chains were allowed to vary in length from 2 to 30 carbons, and double bonds were allowed to vary from 0 to 6 per chain (with a minimum spacing of "3n + 2," where n is any non-negative integer which fits within the length of the chain). Chains were also allowed to have up to 3 hydroxylations, as reported in previous studies (Smułek et al., 2015; Nowak et al., 2016).

For unique components, we used custom R scripts to combine headgroup and core (backbone + chains) formulas. These include archaeol (1–8 unsaturations, 0–2 hydroxylations, 0–1 methylations, 0–2 extensions and 0–1 abridgements of an isoprene unit), glycerol dialkyl glycerol tetraethers (GDGTs) of both branched (br-GDGTs; 0–14 methylations) and isoprenoidal varieties (0–12 double bond equivalents, 0–2 methylations, 0–2 unsaturations) and the glycerol dialkyl diether (GDD) modification of these structures, as well as ladderane lipids with 3 and 5 cyclobutane rings and 18–22 carbons in the ladderane chain. The final database contained 91 headgroups corresponding to 2,139,073 unique ionized IPLs. Custom scripts and modified LOBSTAHS scripts for database generation are publicly available.[4]

2.6. Identification of intact polar lipids

Intact polar lipid datafiles in the raw Thermo file format were first converted to mzXML files using the software msConvert in centroid mode according to vendor format (Adusumilli and Mallick, 2017). The resulting mzXML files were read into R (R Core Team, 2020) using the package "MSnbase" (Gatto and Lilley, 2011; Gatto et al., 2021). Peak detection, grouping, and alignment was performed using the package "xcms" (Smith et al., 2006; Tautenhahn et al., 2008; Benton et al., 2010) with parameters optimized for the dataset in the package "IPO" (Libiseller et al., 2015). The package "CAMERA" was then utilized to aggregate peak groups into pseudospectra and annotate secondary isotopic features in the dataset (Kuhl et al., 2012). Peak groups were screened preliminarily with our custom environmental IPL database in "LOBSTAHS" (Collins et al., 2016). MS2 spectra were extracted for peak groups using the "featureSpectra" function in "xcms" and spectra across samples pertaining to the same peakgroup were combined to a composite MS2 spectra using "combineSpectra."

Only peak groups that had corresponding MS2 data for confirmation of "LOBSTAHS" identifications were included for downstream analysis. Due to the size of the custom database, multiple isomers exist for any given lipid of interest. These isomers represent different lipid structures in either core chain, backbone, or headgroup composition, but the same chemical formula, and thus measured mass on the Orbitrap. While the HILIC chromatography we employed separated lipid classes according to the polarity of their polar headgroup, we found that retention time screening by headgroup class did not entirely resolve isomer identification. Chain length and hydroxylation of core chains can result in retention time shifts of a few minutes, well within the range of typical separation between headgroup classes. We used a custom helper script to putatively annotate diagnostic MS2 fragments and neutral losses (diagnostic masses listed in Supplementary Table S2) and then manually screened annotations before final assignment of lipid identity. Positively ionized MS2 spectra were used to characterize headgroup composition, and negatively ionized MS2 were utilized to probe core lipid structure, as ester-linked fatty acids are lost from the intact structure at the collisional energies induced in our experimental method.

Identified compounds are reported as composite formulas in the format of "(headgroup abbrv.)- (backbone abbrv.) (# of carbons):(# of unsaturations) + (# of hydroxylations)O," e.g., "PG-DAG 34:0 + 1O" for a phosphatidylglycerol diacylglycerol with two saturated chains adding up to 34C in total, with one chain hydroxylation. Because the ionization response of IPLs was poorer for negative adducts, many IPLs with diagnostic positive MS2 spectra did not have complimentary negative ion data. For this reason, and because diether lipids diagnostically lack fragmentation as negative adducts, we did not specify their individual chain lengths and properties (see Supplementary Datasheet 1 for further elaboration on assumptions for DEG assignments). In the event that no corresponding negative MS2 data existed for any lipid structure that had been putatively annotated as one of multiple structural isomers of the same headgroup, an assignment was made to the linkage of a nearby (retention time < 15 s) lipid compound of the same headgroup with negative ion confirmation, or if that was not present, to the structural isomer that did not require hydroxylation.

Raw spectrometry files are available in the MetaboLights database (Haug et al., 2020) under study identifier MTBLS7570 and processing scripts and parameters are available.[5]

2.7. Quantification of intact polar lipids

Prior to quantification, annotated lipids found in solvent blanks were subtracted from sample data (Broadhurst et al., 2018). Only lipids with peak areas 10-fold greater than blank averages were considered for downstream analysis. To account for any sample matrix effects on ionization efficiency, we corrected all peak areas in each sample with the ratio of the peak response for the deuterated reference compound d9-DGTS spiked as an internal standard compared to the

---

[4] https://github.com/krempfert/Samail_fluid_IPLs

[5] https://github.com/krempfert/Samail_fluid_IPLs

peak response of the pure compound. Following matrix factor correction, IPL concentrations were calculated through application of analytical response factors from 31 commercially-available IPL external standards (Avanti Polar Lipids, see Supplementary Table S3). Response factors were estimated by taking the linear slope of the injected masses vs. the integrated peak areas across a 5-point dilution series (0.1, 1.0, 2.5, 5.0, 10.0 ng on column; see Supplementary Figure S1). Because authentic standards are not available for every IPL structure present in nature, or even headgroup, IPL analysis is only considered semi-quantitative. When no authentic standard was available, we assigned response factors on the basis of similarity of headgroups to existing standards, and for lipid classes with multiple measured standards, the average response factor for that class was applied. All aminolipids (e.g., OL, 3Me-OL, DGCC) were assigned to the DGTS response factor, all IPL glycolipids with nitrogen-bearing groups (e.g., NAcG-G, NAcG-P, G-GA) were assigned to the DG-Cer standard, and all glycolipids with more than one glycosyl group (e.g., GAc-G) to the DG-DAG standard.

2.8. Calculations and statistical analyses

Abundance-weighted properties of IPLs were calculated according to Boyer et al. (2020) using the following equation:

$$\Xi = \frac{\sum_i \Xi_{ipl,i} \cdot x_i}{\sum_i n_{component,i} \cdot x_i}$$

where Ξ represents the average property of interest (e.g., number of aliphatic carbons, number of unsaturations), Ξipl,i represents the property summed across all components in the ith IPL (e.g., 36 carbons in the alkyl chains of a 36:0 DAG) with ncomponent,i instances (e.g., 2 alkyl chains in a DAG), and xi represents the mole fraction of the ith IPL.

The oxidation state of carbon (Z_c) was calculated for IPLs and their component parts (e.g., headgroup, backbone, combined core chains) using the equation:

$$\mathrm{Zc} = \frac{2o + 3n - 5p - 4s - h + Z}{c}$$

where Z indicates the net charge and c, h, n, o, p, and s are the number of atoms of carbon, hydrogen, nitrogen, oxygen, phosphorus, and sulfur, respectively, in the chemical formula. Abundance-weighted properties and Zc calculations were conducted using scripts provided[6] by Boyer et al. (2020).

To correlate taxa abundances with IPLs, Pearson's correlations of the relative abundance matrices of DNA and IPLs were calculated with Bonferroni-corrected *p*-values according to Probst et al. (2020) with modifications to the scripts provided[7] to allow for more than one assignment for each IPL to potential source organism.

To investigate lipid distribution in relation to aqueous geochemistry, constrained analysis of principle coordinates (CAP) was performed using the "capscale" function in the R package vegan (Dixon, 2003) on the Gower dissimilarity matrix of Hellinger-transformed IPL compound relative abundances. A variation inflation factor (VIF) was calculated to ensure that there was no significant multicollinearity (VIF <10) of constrained parameters for the CAP analysis. The significance level in the CAP model was assessed by 500 data permutations.

3. Results

3.1. Geochemical characterization of subsurface fluids

Subsurface fluids were sampled from a series of six government monitoring wells previously drilled into crustal gabbro and mantle peridotite bedrock in the Samail Ophiolite, Sultanate of Oman. The chemical characterization of each well is summarized in Table 2. The pH of recovered fluids varied from 7.6 to 11.3. Hyperalkaline (pH >10) fluids sampled from wells NSHQ14 and WAB71 were also characterized by negative oxidation–reduction potentials (Eh) and low (<0.2 mM) concentrations of dissolved inorganic carbon (DIC). Potential electron acceptors were limited in these fluids, with measured sulfate and nitrate concentrations of or below 42 μM and 2.5 μM, respectively. Conversely, alkaline fluids (pH <10) hosted in the peridotite wells WAB104, WAB105, and WAB55 exhibited positive Eh values, oxidant concentrations an order of magnitude higher (sulfate ≥292 μM, nitrate ≥118 μM) than hyperalkaline fluids, and DIC concentrations up to 3 mM. WAB188, the only sampled well hosted within gabbro, was characterized by the highest concentration of sulfate (1.13 mM), and greater concentrations of potential reductants such as hydrogen and methane (0.99 μM H2, 1.8 μM CH4) compared to alkaline fluids hosted in peridotite. While dissolved aqueous-phase methane was detected in every fluid sampled, the greatest concentrations were measured in hyperalkaline fluids (14.8–106 μM). Hydrogen was only detected in hyperalkaline fluids and fluids hosted within gabbro, and was highest in concentration (253 uM) in well NSHQ14. Ammonium concentrations were highest (130 uM) in hyperalkaline fluids in well WAB71. Phosphate was below the detection limit (5.26 μM) in all fluids.

3.2. Custom intact polar lipid database generation

To be able to probe the diversity of IPL structures anticipated in this geologic setting, we developed a custom *in silico* IPL database for environmental lipids by adapting the existing bioinformatic software package "LOBSTAHS" (Collins et al., 2016). The LOBSTAHS package was developed in part to calculate the monoisotopic mass for theoretical lipid structures through user-specified combinations of IPL headgroups, acyl chain lengths, unsaturations, and hydroxylations for acylglycerol lipids. However, because this package was designed to annotate oxylipins of marine algae, the default database is limited to a few common marine lipid headgroups with ester-linkages of aliphatic chains to the lipid backbone. We expanded possible backbone

---

[6] https://gitlab.com/gmboyer/polarlipidzc

[7] https://github.com/AJProbst/lip_metgen

TABLE 2 Geochemical composition of sampled fluids in the 2017 field season previously reported by Kraus et al. (2021).

Well	WAB188	WAB105	WAB104	WAB55	WAB71	NSHQ14	LOQ (μM)
pump depth (mbl)	78	50	28	26	50	85	-
L filtered for lipid analysis	16.3	162	9.9	115.9	20.2	67.3	-
pH	7.6^{a}	8.3^{a}	8.5	9.2	10.6	11.3	-
Eh (mV)	214	178^{a}	180^{a}	269	−133	−253	-
SO_4^{2-} (μM)	1.13E+03	2.92E+02	4.77E+02	8.75E+02	4.20E+01	2.00E+00	1.04E+00
NO_2^- (μM)	6.00E+00	BLOQ	BLOQ	8.00E+00	1.40E+01	1.60E+01	2.17E+00
NO_3^- (μM)	1.18E+02	1.35E+02	1.23E+02	1.43E+02	2.50E+00	BLOQ	1.61E+00
NH_4^+ (μM)	BLOQ	BLOQ	6.41E+00	BLOQ	1.00E+02	1.30E+01	1.00E+00
PO_4^{3-}(μM)	BLOQ	BLOQ	BLOQ	BLOQ	BLOQ	BLOQ	5.26E+00
H_2 (μM)	9.92E-01	BLOQ	BLOQ	BLOQ	5.92E-01	2.53E+02	4.80E-02
CH_4 (μM)	1.83E+00	2.01E-02	2.30E-02	1.06E-01	1.48E+01	1.06E+02	1.53E-02
DIC (mM)	3.00E+03	3.50E+03	3.50E+03	2.90E+03	1.20E+02	1.30E+02	2.00E+01
Na (total) (μM)	3.49E+03	5.92E+02	6.58E+02	4.12E+03	4.95E+03	1.02E+04	5.85E+00
Ca (total) (μM)	1.33E+03	2.69E+02	1.03E+02	5.40E+01	4.07E+03	4.34E+03	1.60E-01
Mg (total) (μM)	1.44E+03	1.69E+03	1.91E+03	2.75E+03	2.00E+00	2.00E+01	5.90E-02
K (total) (μM)	3.92E+01	2.72E+01	2.95E+01	2.10E+02	2.51E+02	2.45E+02	8.26E-01
Al (total) (μM)	8.00E-01	8.00E-01	1.00E+00	BLOQ	1.80E+00	2.00E+00	7.60E-01
Fe (total) (μM)	4.00E-01	5.00E+00	2.00E+00	2.50E+00	1.57E-01	2.00E+00	6.00E-03
Si (total) (μM)	3.69E+02	2.67E+02	1.22E+02	3.00E+00	2.10E+01	6.00E+00	4.00E-01
Cl^- (μM)	5.04E+03	8.55E+02	8.01E+02	7.24E+03	1.16E+04	1.62E+04	2.82E+00
Br^- (μM)	2.00E+00	BLOQ	BLOQ	5.00E+00	1.20E+01	2.50E+01	1.25E+00

^{a} indicates data from 2017 was not available and replaced with 2016 data published by Rempfert et al. (2017); BLOQ indicates the parameter was below the limit of quantification (limit indicated in column LOQ).

configurations to include mixed acyl/ether glycerol (AEG), monoether glycerol (MEG), diether glycerol (DEG), ceramide (Cer), 1,2 alkanediol (AD), and fatty amide (FA) backbone structures in addition to the diacyl glycerol (DAG) and monoacyl glycerol (MAG) backbones already included in the package structure (Figure 1). Additionally, the number of allowed chains was increased from 2 to 4 to include cardiolipins and triglyceride lipids. We also expanded the headgroups considered by compiling previously identified headgroup structures of environmental IPLs from published literature; the chemical formulas and references for 91 included headgroups are reported in Supplementary Table S1. The final database consisted of over 2 million lipid species.

3.3. Inventory of intact polar lipids

We were able to identify a diversity of IPLs with varying headgroup and backbone structures in serpentinite-hosted fluids using our custom environmental IPL database coupled with data-dependent MS2 screening. A total of 96 IPLs were identified; the most abundant 20 IPL compounds across all sampled wells are presented in a relative abundance heatmap in Figure 2 (see Supplementary Table S4). Notably, these 20 IPLs constituted ≥98% of the observed IPL diversity across sampled fluids.

Total IPL concentrations (normalized by liter of filtered well water) showed no trend with planktonic cell abundances previously reported for these wells from paraformaldehyde-fixed samples collected at the time of lipid sampling (Fones et al., 2019). For example, the maximum concentration of polar lipids was observed in hyperalkaline well NSHQ14 where the lowest cell abundance (1.16×10^5 cells mL^{-1}) was reported (Supplementary Figure S2).

IPLs for both Bacteria (non-isoprenoidal) and Archaea (isoprenoidal) were dominated by glycolipids, which comprised 91 to 99% of the total intact lipidome (Figure 3). Apart from well WAB71, the most abundant glycolipid in subsurface fluids was monoglycosyl archaeol (1G-AR). This archaeal diether lipid made up 77% of measured IPLs in well WAB188 and 69% of IPLs in well NSHQ14. Bacterial monoglycosyl diethers (1G-DEGs) were prevalent in all fluids with the greatest relative abundance observed in WAB71 where 93% of IPLs could be attributed to just two 1G-DEG compounds (1G-DEG 32:1 and 1G-DEG 33:1; Figure 2). In all other wells, the relative abundance of 1G-DEG lipids varied from 15 to 52%.

Altogether, the combined relative abundance of bacterial and archaeal monoglycosyl diether lipids constituted 89 to 98% of the measured polar lipids (Figure 4), with the remaining glycolipids consisting of either glycosphingolipids (up to 4% in WAB71; primarily 1G-Cer, but 2G-Cer was present at <1% relative abundance), monoglycosyl glycoronic acid diacylglycerol (1G-GA-DAG) lipids (<1% relative abundance in NSHQ14), or diglycosyl isoprenoidal lipids (up to 14% relative abundance in NSHQ14).

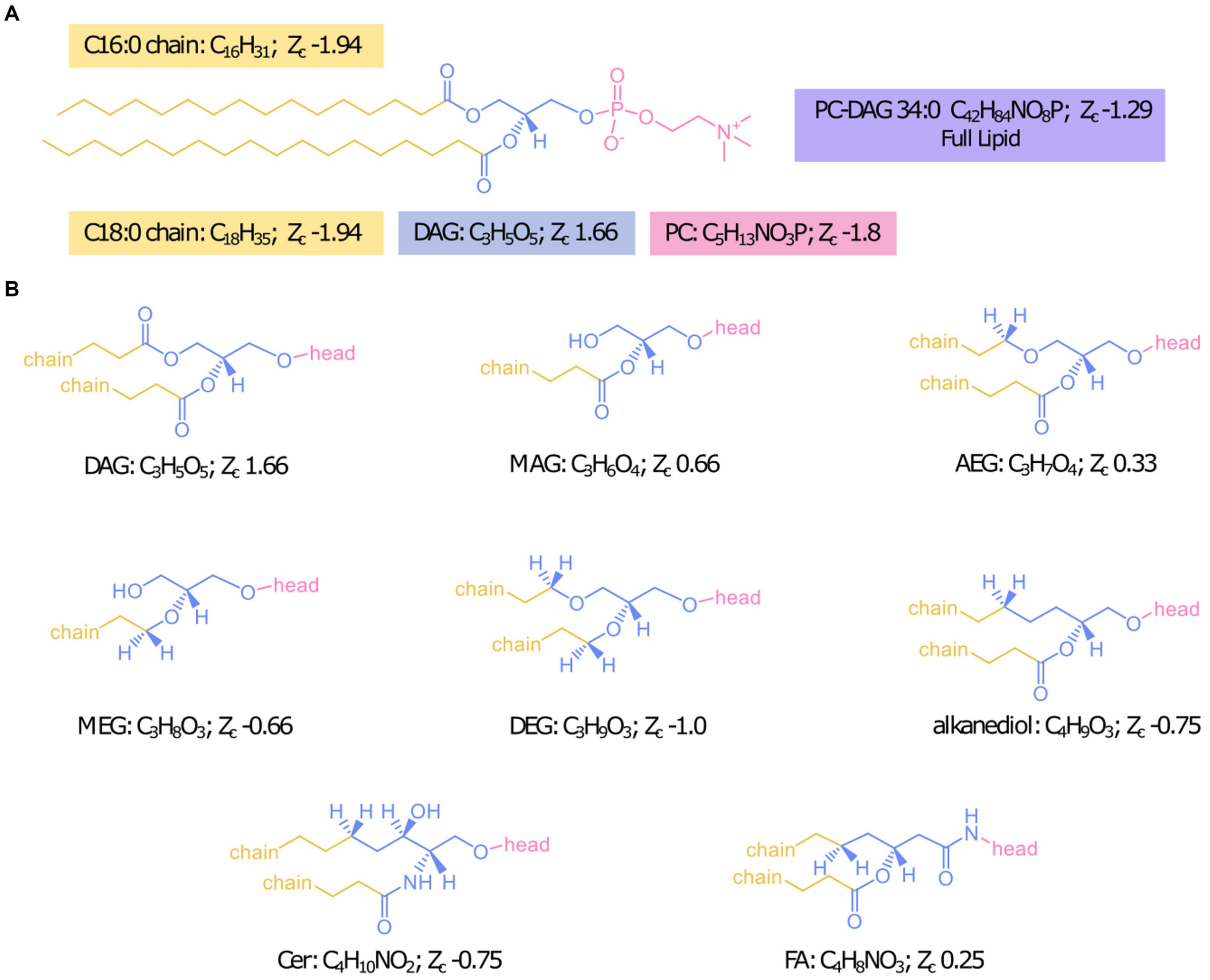

FIGURE 1
Designation of headgroup, backbone, and chains for Zc calculations with the example IPL PC-DAG 34:0 **(A)** and structures of all backbone linkages investigated **(B)**.

Membrane-spanning archaeal tetraethers were not detected in high abundance but were observed primarily in well NSHQ14 where 2G-GDGT-0 was present at 2% relative abundance.

Phospholipids were present at less than 1.1% relative abundance in all wells. Due to the predominance of archaeal and bacterial 1G-diether lipids, the lower barplot in Figure 4 displays the relative abundances of minor lipids (<12%) excluding these major lipid classes. Phospholipid classes included phosphocholine (PC) diacylglycerol (DAG), dietherglycerol (DEG), monoetherglycerol (MEG) and mixed acyl/ether glycerol (AEG) lipids, phosphoethanolamine sphingolipids (PE-Cer), and phosphatidylglycerol diacylglycerol (PG-DAG) lipids. Aminolipids were relatively more abundant than phospholipids, comprising up to 5.5% relative abundance of detected IPLs. Betaine lipids were particularly abundant in well WAB104 where diacylglyceryl-trimethylhomoserine (DGTS)-DAG 36:2 constituted 4% of the lipidome. Ornithine lipids (OL), particularly trimethylated ornithine (3Me-OL) lipids, were detected in all fluids with the greatest relative abundance in WAB105 and WAB188, where cumulatively this class made up 0.7 and 1.5% of the lipidome, respectively. In addition, two classes of lipids with N-acetylglucosaminyl (NAcG) headgroups and diether backbones were detected at <1% combined relative abundance across fluids.

3.4. Correlation of intact polar lipidome with potential source organisms

We coupled lipidomic analyses with 16S rRNA gene amplicon sequencing of DNA and RNA transcripts (RNA converted to cDNA) generated from biomass collected from the same fluids at the time of IPL sampling to infer potential source organisms for observed IPL compounds (Figure 5).

While archaeal lipids constituted >40% of the lipidome in all but one well, archaeal amplicon sequence variants (ASVs) comprised at most only 10.9% of the DNA and 34.4% of the cDNA (Figure 6). In wells WAB105 and WAB55, archaeal ASVs made up less than 2.5% of all ASVs; yet, 1G-AR accounted for 46 and 67% of the measured IPLs, respectively. However, fluids that exhibited the greatest relative abundance of lesser archaeal IPLs (e.g., 2G headgroups, GDGTs) did also have the greatest relative abundance of archaeal ASVs. Predominant archaeal ASVs varied considerably between wells;

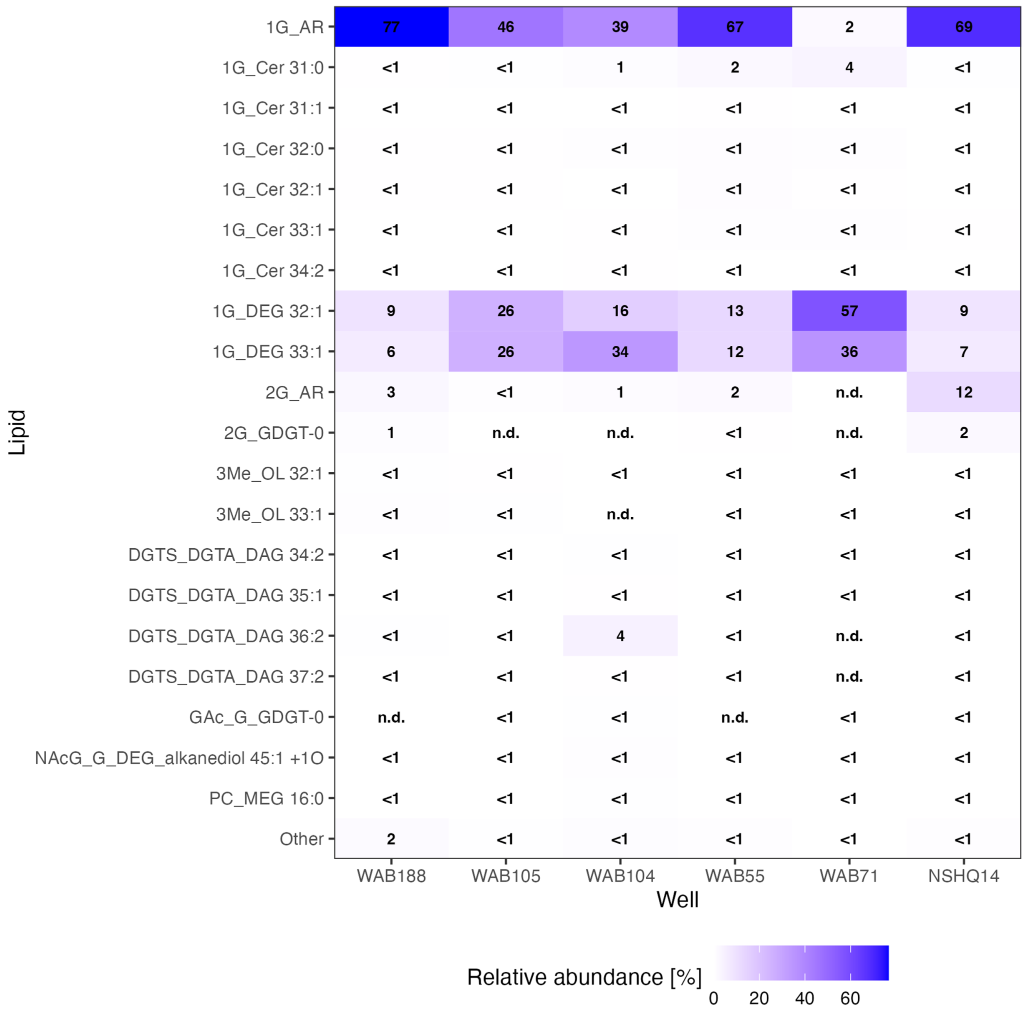

FIGURE 2
Relative abundance heatmap of the 20 most abundant intact polar lipid (IPL) compounds detected.

NSHQ14 and WAB188 were dominated by Methanobacteria, WAB55 and WAB104 by Nitrosopumiliaceae, and WAB105 by Woesarchaeales (Supplementary Table S5).

Pearson's correlation was used to evaluate relationships between non-isoprenoidal IPL and bacterial ASV relative abundances. A total of 48 bacterial IPL compounds were correlated significantly (Bonferroni-corrected value of $p < 0.005$) with 84 bacterial ASVs (Supplementary Figure S3). Generally, most compounds within a lipid class correlated with the same ASV, but multiple ASVs demonstrated equivalent correlation coefficients and value of ps per lipid class. 1G and 2G ceramides correlated with an entirely different set of ASVs; 1G ceramides were associated with Acidobacteria, Ignavibacteria, Desulfomonile, Candidate Phylum DTB120, Nitrospinota, and Verrucomicrobiota, while 2G ceramides were associated primarily with Acetothermia and Meiothermus. Both glycosphingolipid classes correlated with different ASVs assigned to Firmicutes, Thermodesulfovibriona, Chloroflexi, Alphaproteobacteria, and Gammaproteobacteria. Trimethylated ornithine lipids were correlated with the same set of ASVs as 1G-ceramides, and NAcG-containing classes were correlated with the same set of ASVs as 2G-ceramides. Betaine lipids correlated with Gammaproteobacteria (primarily Pseudomonas), Pedosphaeraceae, Planctomycetiota, Nitrospirota, Firmicutes, Acidobacteria, and Bacteriodota (primarily Kryptioniales).

3.5. Trends in lipid composition with aqueous geochemistry

To evaluate the relationship between the distribution of IPLs and subsurface fluid chemistry, we performed constrained analysis of principle coordinates (CAP) using the Gower dissimilarity matrix of IPL compound relative abundances for each site. For this analysis, we omitted 1G-AR from the calculation of IPL relative abundances, as this compound was strongly overrepresented in the intact polar lipidome compared to the relative abundance of any potential source organism as inferred by sequencing. Three explanatory variables (pH, [CH_4], [SO_4^{2-}]) explained 77.7% of the observed variance ($R^2 = 0.77$; 500 permutations: pseudo $F = 2.33$, value of $p = 0.046$) in the lipidome (Figure 7). Due to multicollinearity of geochemical parameters, replacing NO_3^- for SO_4^{2-} and H_2 for CH_4 yielded a similar ordination of samples and IPL compounds. The triplot for the CAP displayed a prevalence of trimethylated ornithine and betaine lipids in wells

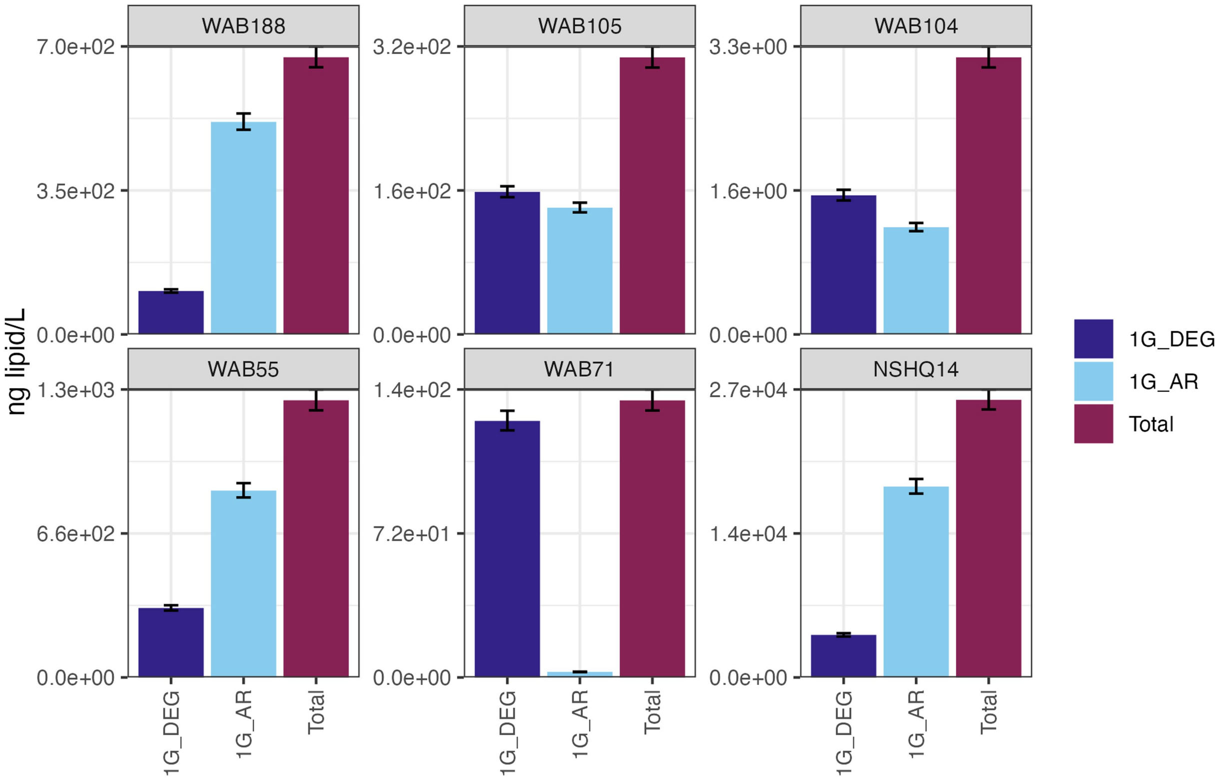

FIGURE 3
The abundances (ng of lipid/L) of bacterial non-isoprenoidal monoglycosyl diether (1G-DEG) lipids and the archaeal isoprenodial monoglycosyl diether lipid, archaeol (1G-AR), in comparison with total lipid abundances in each well.

associated with higher concentrations of sulfate. Additionally, a trend toward 2G instead of 1G headgroups of glycolipids was demonstrated in wells with higher methane concentrations and more hyperalkaline pH.

Differences in overall lipid structure across wells were also assessed through calculation of the average oxidation state of carbon (Z_c) in IPLs. Lower values of Z_c in a molecule indicate more reduced carbon (e.g., −4 in CH_4) and higher values represent more oxidized carbon (e.g., +4 in CO_2). Across sampled fluids, the abundance-weighted Z_c of the full lipid and of the lipid chains were remarkably consistent, with the full lipid Z_c varying from −1.52 to −1.56 and the chain Z_c from −1.88 to −1.90. The Z_c of headgroups and backbones were slightly more variable across samples, ranging from −0.12 to −0.32 and from −0.62 to −0.96, respectively (Supplementary Table S6). Notably, all calculated components of the IPL exhibited negative carbon oxidation states. The abundance-weighted Z_c of IPL backbones was the only component of the IPL to display any significant trend with geochemistry (Figure 8), which demonstrated a positive correlation with Eh ($R^2 = 0.81$, $p = 0.014$).

The proportion of ether-linked chains was greatest in hyperalkaline wells NSHQ14 and WAB71, where negative Eh values were measured (Supplementary Figure S4). Ester linkages were nearly absent in both these wells, but were the second most common linkage in all other sampled wells. Amide linkages were most abundant in well WAB55 (7% of linkages). There was little variation in both the abundance-weighted average number of aliphatic carbon (nC: 16.5–17.6) and unsaturations (nUns: 0.3–0.51) in lipid chains across sampled fluids. The maximum nC and minimum nUns for lipid chains was reported in NSHQ14, the well with the most negative Eh, however, there was no statistically significant trend of chain-linkage, nC, or nUns with Eh or any other measured geochemical parameter.

4. Discussion

4.1. Subsurface intact polar lipidome of a terrestrial serpentinite

Archaeal IPLs in the Samail Ophiolite were dominated by those with an archaeol core. Diether lipids are not typically found as the dominant class of archaeal lipids in ecosystems (Koga and Morii, 2005; Biddle et al., 2006; Sollai et al., 2019). However, a predominance of diether over tetraether IPLs has been described at a marine serpentinizing system- the Lost City hydrothermal vent field (Bradley et al., 2009b; Lincoln et al., 2013), in ophiolites (Rattray et al., 2022), as well as in deep oceanic crust drilled from the Atlantis Bank (Li et al., 2020) and some sites of methane seeps (Rossel et al., 2011). It has been postulated that archaeol abundance may serve as an indicator for methanogenic biomass, particularly where the Thaumarchaeotal GDGT lipid crenarchaeol (GDGT-5) is low in abundance (Lim et al., 2012). We found 2G-AR and 2G-GDGT-0 to be most abundant in the well NSHQ14 where methane concentrations were highest, ASVs assigned to *Methanobacterium* were the most prominent, and cDNA for this organism was comparatively enriched (Figures 2–4). In

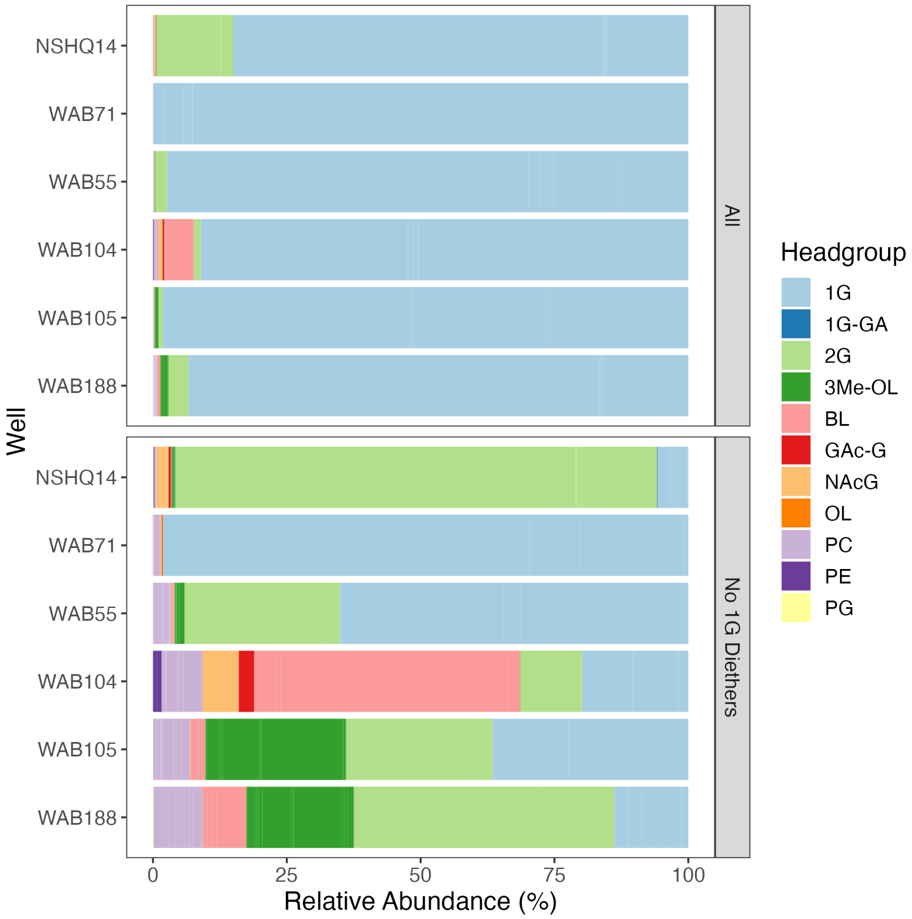

FIGURE 4
Relative abundances of IPLs by headgroup type with and without bacterial and archaeal monoglycosyl diether lipids included. Abbreviations: 1G, monoglycosyl; 1G-GA, monoglycosyl glycuronic acid; 2G, diglycosyl; 3Me-OL, trimethylated ornithine; BL, betaine lipid (DGTS and DGCC); GAc-G, acetylglycosyl monoglycosyl; NAcG, N-acetyl glycosaminyl (both NAcG-P and NAcG-G); OL, ornithine lipid, PC, phosphatidylcholine; PE, phosphatidylethanolamine; PG, phosphatidylglycerol.

culture, isolates of *Methanobacterium* have been reported to produce both archaeol and GDGT-0 with glycosyl and phosphate-containing headgroups (Nishihara and Koga, 1987). While we did detect Thaumarcheota of the family Nitrososphaeraceae (Supplementary Table S5), especially in alkaline peridotite-hosted fluids, we did not detect crenarchaeol, the major lipid constituent of this family (Elling et al., 2017). It is possible intact crenarchaeol lipids are present at low abundances in sampled fluids, but not in high enough concentrations to be detected by MS2 analysis. Accordingly, it is possible that some small fraction of isoprenoidal IPLs, including a proportion of 1G-AR, could be produced by Nitrososphaeraceae and other archaeal taxa, but these organisms are unlikely to be the major contributor of isoprenoidal diether lipids (Pitcher et al., 2010). We instead suggest the abundance of archaeol-based lipids in these fluids likely represent primarily a methanogenic source. The idea that at least some fraction of the archaeal IPL pool is actively produced by methanogens can be supported by previous studies of the biomass in these fluids by Fones et al. (2019) showing active biological $^{14}CH_4$ production from ^{14}C-labeled bicarbonate and by Kraus et al. (2021) identifying transcripts for key genes encoding methanogenesis enzymes.

Glycolipids with non-isoprenoidal diether cores were ubiquitous in biomass sampled from the Samail serpentinite-hosted fluids. Bacterial diether glycolipids were the major lipid class detected at the Lost City Hydrothermal Field (Bradley et al., 2009a,b). Non-isoprenoidal diether core lipids have additionally been described in fossilized serpentinite systems in the Iberian Margin (Klein et al., 2015), in serpentinite rock in ophiolites (Zwicker et al., 2018; Newman et al., 2020), and in drill cores of deep oceanic crust at Atlantis Bank (Li et al., 2020), suggesting this lipid class is common across ecosystems supported by water-rock interaction. Only a limited number of cultured bacteria have been found to synthesize DEG backbones, stemming mostly from thermophilic clades such as *Thermodesulfobacterium* (Langworthy et al., 1983), *Ammonifex* (Huber et al., 1996), *Aquifex* (Huber et al., 1992), *Rhodothermus* (Jorge et al., 2015), and *Thermatoga* (Damsté et al., 2007), along with some mesophilic sulfate-reducers (Rütters et al., 2001; Grossi et al., 2015). The only cultured isolate that has been reported to produce DEG lipids with a glycosyl headgroup is *Thermodesulfobacterium* (Langworthy et al., 1983). We observed the greatest relative abundance of 1G-DEG lipids in well WAB71 where the most predominant ASV was assigned to the family Thermodesulfovibriona

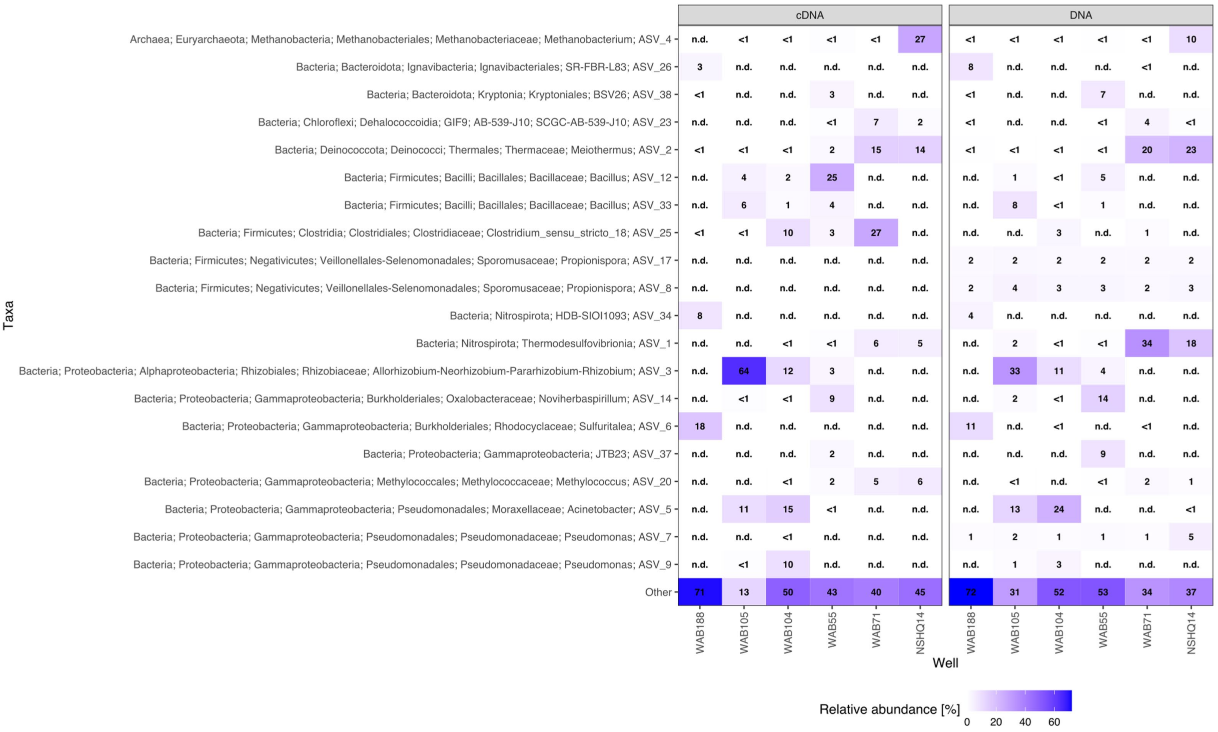

Taxa	cDNA						DNA					
	WAB188	WAB105	WAB104	WAB55	WAB71	NSHQ14	WAB188	WAB105	WAB104	WAB55	WAB71	NSHQ14
Archaea; Euryarchaeota; Methanobacteria; Methanobacteriales; Methanobacteriaceae; Methanobacterium; ASV_4	n.d.	<1	<1	<1	<1	27	<1	<1	<1	<1	<1	10
Bacteria; Bacteroidota; Ignavibacteria; Ignavibacteriales; SR-FBR-L83; ASV_26	3	n.d.	n.d.	n.d.	n.d.	n.d.	8	n.d.	n.d.	n.d.	<1	n.d.
Bacteria; Bacteroidota; Kryptonia; Kryptoniales; BSV26; ASV_38	<1	n.d.	n.d.	3	n.d.	n.d.	<1	n.d.	n.d.	7	n.d.	n.d.
Bacteria; Chloroflexi; Dehalococcoidia; GIF9; AB-539-J10; SCGC-AB-539-J10; ASV_23	n.d.	n.d.	n.d.	<1	7	2	<1	n.d.	n.d.	<1	4	<1
Bacteria; Deinococcota; Deinococci; Thermales; Thermaceae; Meiothermus; ASV_2	<1	<1	<1	2	15	14	<1	<1	<1	<1	20	23
Bacteria; Firmicutes; Bacilli; Bacillales; Bacillaceae; Bacillus; ASV_12	n.d.	4	2	25	n.d.	n.d.	n.d.	1	<1	5	n.d.	n.d.
Bacteria; Firmicutes; Bacilli; Bacillales; Bacillaceae; Bacillus; ASV_33	n.d.	6	1	4	n.d.	n.d.	n.d.	8	<1	1	n.d.	n.d.
Bacteria; Firmicutes; Clostridia; Clostridiales; Clostridiaceae; Clostridium_sensu_stricto_18; ASV_25	<1	<1	10	3	27	n.d.	n.d.	n.d.	3	n.d.	1	n.d.
Bacteria; Firmicutes; Negativicutes; Veillonellales-Selenomonadales; Sporomusaceae; Propionispora; ASV_17	n.d.	n.d.	n.d.	n.d.	n.d.	n.d.	2	2	2	2	2	2
Bacteria; Firmicutes; Negativicutes; Veillonellales-Selenomonadales; Sporomusaceae; Propionispora; ASV_8	n.d.	n.d.	n.d.	n.d.	n.d.	n.d.	2	4	3	3	2	3
Bacteria; Nitrospirota; HDB-SIOI1093; ASV_34	8	n.d.	n.d.	n.d.	n.d.	n.d.	4	n.d.	n.d.	n.d.	n.d.	n.d.
Bacteria; Nitrospirota; Thermodesulfovibrionia; ASV_1	n.d.	n.d.	<1	<1	6	5	n.d.	2	<1	<1	34	18
Bacteria; Proteobacteria; Alphaproteobacteria; Rhizobiales; Rhizobiaceae; Allorhizobium-Neorhizobium-Pararhizobium-Rhizobium; ASV_3	n.d.	64	12	3	n.d.	n.d.	n.d.	33	11	4	n.d.	n.d.
Bacteria; Proteobacteria; Gammaproteobacteria; Burkholderiales; Oxalobacteraceae; Noviherbaspirillum; ASV_14	n.d.	<1	<1	9	n.d.	n.d.	n.d.	2	<1	14	n.d.	n.d.
Bacteria; Proteobacteria; Gammaproteobacteria; Burkholderiales; Rhodocyclaceae; Sulfuritalea; ASV_6	18	n.d.	n.d.	n.d.	n.d.	n.d.	11	n.d.	<1	n.d.	<1	n.d.
Bacteria; Proteobacteria; Gammaproteobacteria; JTB23; ASV_37	n.d.	n.d.	n.d.	2	n.d.	n.d.	n.d.	n.d.	n.d.	9	n.d.	n.d.
Bacteria; Proteobacteria; Gammaproteobacteria; Methylococcales; Methylococcaceae; Methylococcus; ASV_20	n.d.	n.d.	<1	2	5	6	n.d.	<1	n.d.	<1	2	1
Bacteria; Proteobacteria; Gammaproteobacteria; Pseudomonadales; Moraxellaceae; Acinetobacter; ASV_5	n.d.	11	15	<1	n.d.	n.d.	n.d.	13	24	n.d.	n.d.	<1
Bacteria; Proteobacteria; Gammaproteobacteria; Pseudomonadales; Pseudomonadaceae; Pseudomonas; ASV_7	n.d.	n.d.	<1	n.d.	n.d.	n.d.	1	2	1	1	1	5
Bacteria; Proteobacteria; Gammaproteobacteria; Pseudomonadales; Pseudomonadaceae; Pseudomonas; ASV_9	n.d.	<1	10	n.d.	n.d.	n.d.	n.d.	1	3	n.d.	n.d.	n.d.
Other	71	13	50	43	40	45	72	31	52	53	34	37

FIGURE 5
Relative abundance heatmap of top 20 ASVs for cDNA and DNA.

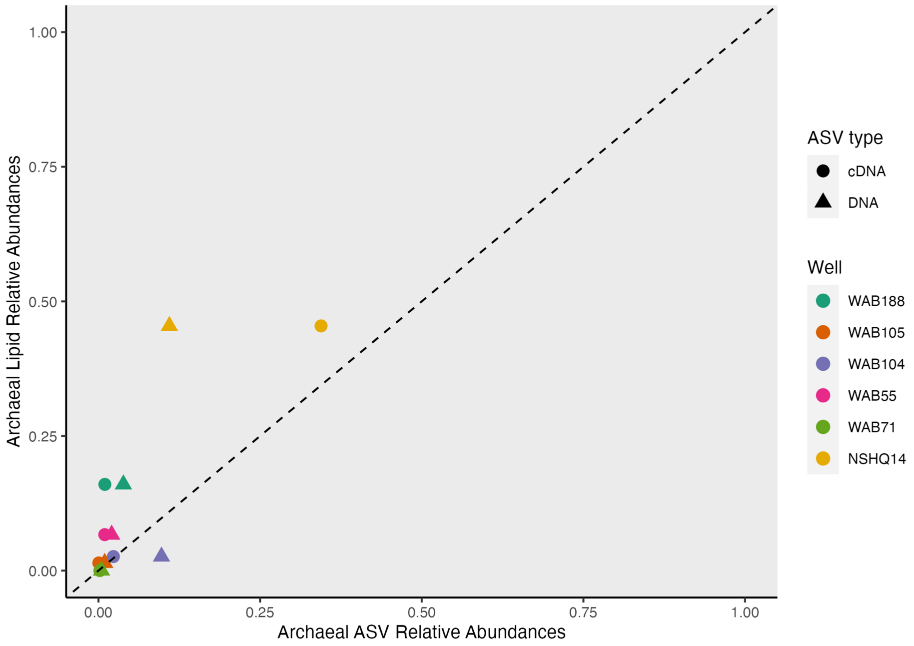

FIGURE 6
Overrepresentation of archaea in IPL compared to genomic and transcriptomic assays.

(Figure 5), supporting the hypothesis put forth by Bradley et al. (2009a) that sulfate-reducing organisms could be the source of these enigmatic lipids in serpentinized fluids (Bradley et al., 2009a). However, at Lost City, no known strains of bacteria capable of producing DEG lipids were detected via 16S rRNA gene sequencing, and so it was postulated that Clostridial sulfate-reducers instead could be a possible source (Bradley et al., 2009a). We did observe Clostridial ASVs enriched in the cDNA fraction of WAB71 as well as

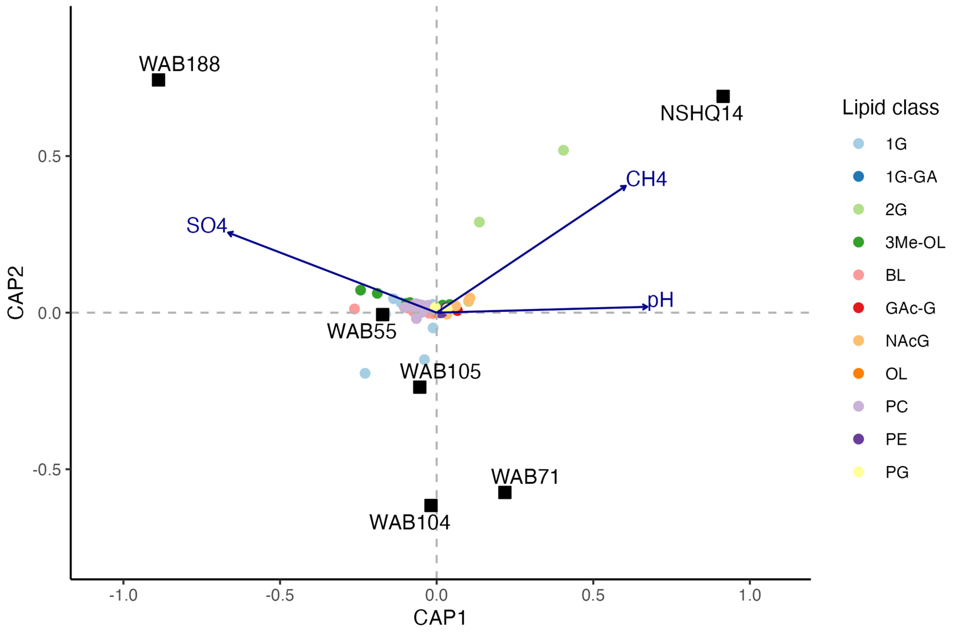

FIGURE 7
Constrained analysis of principle coordinates (CAP) of the Gower dissimilarity matrix of Hellinger-transformed IPL compound relative abundances. Permutations test of 500 iterations indicated significance of analysis (pseudo $F = 2.33$, value of $p = 0.046$).

minor relative abundances of ASVs assigned to Aquificales, Ammonifexales (e.g., *Desulforudis*), and Desulfobacteriota, so other potential source organisms cannot be ruled out.

Although diether glycolipids were measured in high abundance across all measured samples, it is important to note that there is no apparent instrumental bias toward the detection of this class of lipids. Instead, the ionization response of both mono- and di-glycosyl standards was an order of magnitude lower (1.84E+05 and 1.21E+06, respectively) than that of aminolipids (2.37E+08) and most phospholipids (1.81E+06 to 1.59E+08; Supplementary Table S3, Supplementary Figure S1) with no observed effect on ionization response for ether compared to ester linkages to the glycerol backbone (e.g., PC-AR and PC-DAG 32:0 standards: 8.85E+07 and 7.04E+07, respectively).

Minor bacterial IPLs in the lipidome included betaine and ornithine (including trimethylated ornithine) aminolipids, glycosphingolipids, aminoglycolipids with a N-acetyl glucosaminyl headgroup (NAcG), and to a lesser degree, phospholipids. We used Pearson's correlations between the relative abundances of non-isoprenoidal lipids and bacterial ASVs to discern possible sources of these largely cosmopolitan IPLs (Supplementary Figure S3). The significant correlation of highly specific lipids with NAcG headgroups to *Meiothermus* ASVs lends credence to the use of this approach because this class of lipids has only been found in members of the Thermus/Meiothermus clade (Ferreira et al., 1999; Yang et al., 2006). However, 14 other ASVs also significantly correlated with NAcG structures (Supplementary Figure S3). Because microbial community composition in Samail Ophiolite fluids is associated with aqueous geochemistry (Rempfert et al., 2017), it is to be expected that the relative abundance of many taxa co-vary, thus complicating source assignment.

Ceramide-linked sphingolipids were common across sampled fluids. Ceramide backbone linkages are only known to be synthesized by a few bacterial groups. Sphingolipids have been reported in organisms belonging to the Fibrobacteres-Chlorobi-Bacteriodetes superphylum, Alphaproteobacteria (e.g., *Sphingomonadales*), and some Deltaproteobacteria (Olsen and Jantzen, 2001; Keck et al., 2011; Stankeviciute et al., 2022), however, the genetic biosynthetic potential is found in a wider range of Gram-negative and several Gram-positive genera including *Thermodesulfovibrio* and *Ignavibacter* (Sohlenkamp and Geiger, 2016; Stankeviciute et al., 2022). 1G sphingolipids were correlated with Bacteriodota, Ignavibacteriales, and Thermodesulfovibriona ASVs, and both 1G and 2G glycosphingolipids were significantly correlated with ASVs belonging to Alpha- and Gammaproteobacteria (Supplementary Figure S3); we tentatively attribute ceramide IPLs to a combination of these taxa. While ceramide lipids are much more common in Eukarya, Kraus et al. (2021) reported only low eukaryotic 18S rRNA gene sequence counts in complimentary samples (0.11% of all sequences from all wells), and so we assume a bacterial source.

Aminolipids, such as betaine and ornithine lipids, were relatively abundant to the greatest degree in alkaline wells and were associated with higher concentrations of oxidants (e.g., sulfate) in constrained principle coordinate analysis (Figure 7). To the best of our knowledge, betaine lipids have only been reported in Alphaproteobacteria, Gammaproteobacteria, Actinobacteria, Verrucomicrobia, and Bacteriodetes (Benning et al., 1995; Geiger et al., 1999; Geske et al., 2013; Sebastián et al., 2016; Yao et al., 2016). Betaine lipids with DGTS/DGTA headgroups were significantly correlated with all these clades (Supplementary Figure S3), and thus we speculate this IPL class is produced by multiple bacterial sources in this setting. DGTS and DGTA have identical fragmentation patterns in MS2, but we presume these aminolipids have DGTS headgroups because DGTA has not yet been identified in bacteria (Geiger et al., 2010;

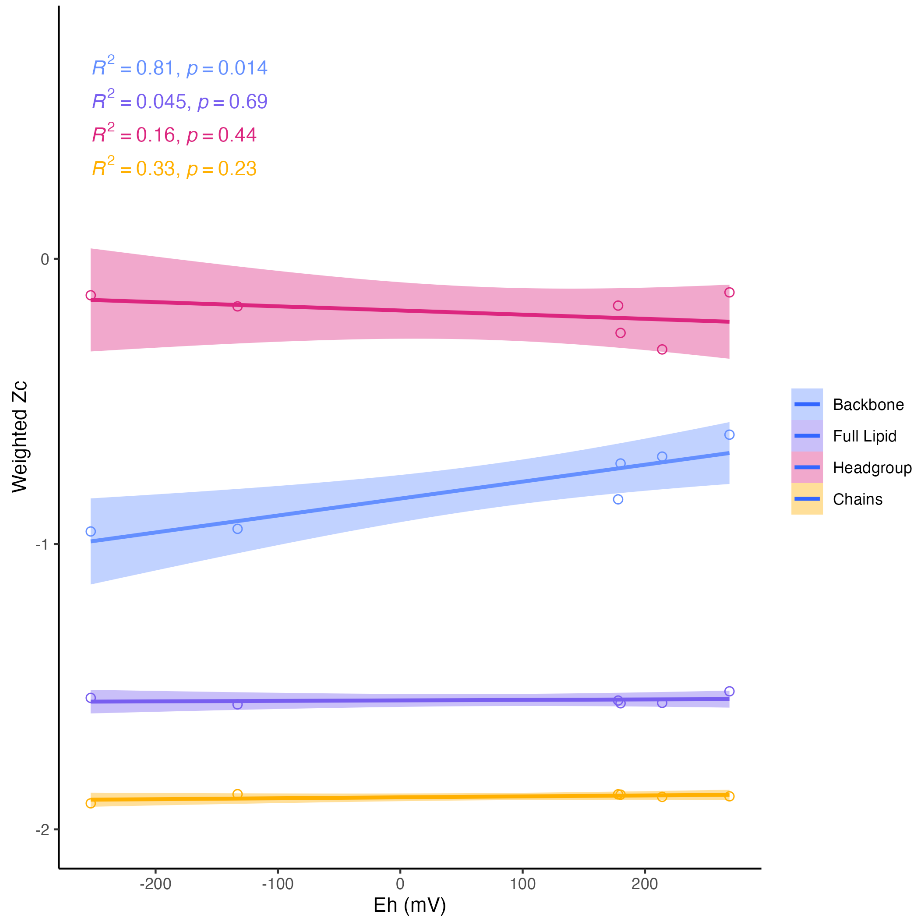

FIGURE 8
Abundance-weighted carbon oxidation state (Zc) of intact lipids, headgroups, backbones, and chains in relation to Eh. Backbone Zc is significantly ($R^2 = 0.81$, $p = 0.014$) correlated with Eh (mV) of fluids.

López-Lara and Geiger, 2017). Ornithine lipids are only present in Bacteria (Vences-Guzmán et al., 2012) and have been widely reported in Proteobacteria and other Gram-negative bacterial strains (Geiger et al., 2010; Sohlenkamp and Geiger, 2016). Like betaine lipids, ornithine lipids are likely produced by many taxa in this environment. Interestingly, while Planctomycetes groups were detected in low relative abundances in alkaline wells, there was no significant correlation of these groups with the abundance of trimethylated ornithine lipids (3Me-OL). Planctomycetes is the only known source of 3Me-OL signatures (Moore et al., 2013; Moore, 2021). However, 3Me-OL IPLs did correlate with Verrucromicrobia ASV abundance, a phylum that also belongs to the PVC superphylum (Planctomycetes-Verrucomicrobia-Chlamydiae). It is thus possible that the ability to produce this trimethylated structure is more widely spread across phyla than previously described.

4.2. Membrane adaptations in a polyextreme environment

The abundance of glycolipids and aminolipids compared to phospholipids in serpentinized fluids resembles the headgroup assemblages typically observed in the oligotrophic open ocean where phosphate is limiting (Van Mooy et al., 2009; Schubotz et al., 2018; Schubotz, 2019). All wells sampled did not have any detectable phosphate (detection limit 5 µM), which indicates subsurface fluid phosphate concentrations are below the 10 µM concentration at which heterotrophic (Sebastián et al., 2016) and sulfate-reducing bacteria (Bosak et al., 2016), as well as methanogenic archaea (Yoshinaga et al., 2015), have been observed to replace phospholipid membrane lipids with amino- and/or glycolipids in culture. Peridotite rocks have exceedingly low bulk phosphorus concentrations (median of 131 ppm from 577 samples in the EarthChem database; Porder and Ramachandran, 2013), with harzburgites in the Samail Ophiolite containing only 0.009–0.012 wt.% P_2O_5 (Hanghøj et al., 2010). Thus, limited phosphorus is available in the host rock to be liberated as phosphate during water-rock reaction. Additionally, the limited availability of phosphate in subsurface fluids within the ophiolite may be due to the formation of insoluble Ca-phosphates in hyperalkaline Ca-OH fluids, as well as the presence of the mineral brucite, which was found to comprise up to 8 wt% of the mineral assemblage in Samail Ophiolite dunite (Templeton et al., 2021) and is known to be an effective scavenger of phosphate from fluids (Holm et al., 2006; Templeton and Ellison, 2020). Accordingly, we suggest that the predominance of glycolipids and aminolipids in serpentinized fluids in Oman represents a phosphorus conservation strategy of organisms adapted to living within serpentinite systems with notably low phosphate availability.

Through culturing experiments, it has been documented that anionic phospholipids (e.g., PG) are often replaced with anionic glycolipids (e.g., GAc), and that neutral or zwitterionic phospholipids (e.g., PE, PC, PME, PDME) are replaced with neutral or zwitterionic amino or glycolipids (e.g., 1G, 2G, DGTS, OL) during phosphate limitation (Geske et al., 2013; Carini et al., 2015; Bosak et al., 2016; Sebastián et al., 2016). However, the ratio of anionic to neutral or zwitterionic lipids is not always conserved through membrane remodeling, which may impact the integrity of the lipid membrane (Bosak et al., 2016; Schubotz, 2019). Additionally, the shape of the membrane may be altered during remodeling (Bosak et al., 2016) if the configuration of cylindrical bilayer-forming IPLs and conical non-bilayer-forming IPLs is adjusted (Schubotz, 2019). For organisms that cannot synthesize DGTS, zwitterionic ornithine lipids have been implicated as important for maintaining membrane lipid charge (López-Lara et al., 2005). The addition of three methyl groups on the terminal nitrogen of trimethylated ornithine lipids mimics the structure of a phosphocholine headgroup, which likely imparts a greater polarity and similar cylindrical shape (Moore et al., 2013; Moore, 2021). Phosphocholine is a bilayer-stabilizing IPL common in heat-stressed microorganisms (Hazel and Williams, 1990; Hazel, 1995; Sollich et al., 2017) and was the most abundant phospholipid in sampled fluids. Accordingly, the predominance of zwitterionic 3Me-OL and DGTS aminolipids in the Samail Ophiolite lipidome likely reflect a preservation of membrane charge, structure, and integrity through membrane adaptation.

In addition to the apparent adaptation of IPL headgroup composition to phosphate limitation in serpentinite-hosted fluids, we observed an influence of fluid geochemistry on IPL backbone linkage structures. The average carbon oxidation state (Z_c) of IPL backbones was significantly and positively correlated with the measured reduction potential (Eh) of sampled fluids (Figure 8). Fones et al. (2019) noted a similar trend with the proteome's Z_c in complimentary samples, with the lowest Z_c observed in the most hyperalkaline, reduced well, NSHQ14. It has been interpreted that this relationship reflects an evolutionary convergence to minimize cellular biosynthetic costs, as reduced biomolecules are energetically more cost-effective to synthesize under reducing conditions (Dick and Shock, 2011; Dick, 2014; Fones et al., 2019; Boyer et al., 2020). Boyer et al. (2020) thus postulated that the Z_c of lipids represents an adaptation of organisms to the availability of reduction potential (i.e., concentrations of electron donors and acceptors) in their environment. However, we did not observe any significant correlation of full lipid Z_c with Eh, as was reported for hot spring IPL samples from Yellowstone (Boyer et al., 2020). The invariance of IPL Z_c in Samail Ophiolite aquifers can likely be attributed to the pervasiveness of phosphate limitation. Due to the weight of nitrogen and phosphorus in the calculation of lipid Z_c, the ubiquity of headgroup modifications across sampled fluids overprints the observed signature from backbone modifications.

The reduced IPL-backbone Z_c in NSHQ14 corresponds to a prevalence of ether linkages, the most reduced backbone configuration explored in this study (Figure 1). Ether-linked backbones have commonly been described in deep marine sediments (Evans et al., 2017), hydrothermal ecosystems (Jahnke et al., 2001; Pancost et al., 2006), and anerobic methane oxidizing and sulfate-reducing consortia at cold methane seeps (Hinrichs et al., 2000; Orphan et al., 2001; Pancost et al., 2001; Rossel et al., 2011) where their abundance was attributed to the robustness of these lipid structures. However, it is also possible ether linkages were prevalent in these environments in part due to the energetic favorability of producing this backbone structure under the prevailing reducing conditions. Ether-bound lipids have a lower proton permeability relative to ester-bound lipids (van de Vossenberg et al., 1998; Mathai et al., 2001) which may reduce energetic costs to cellular maintenance in energy-limiting environments (Valentine, 2007). Ether-bound lipids are also produced by soil bacteria during starvation-induced sporulation (Ring et al., 2006; Lorenzen et al., 2014), further implicating an influence of energy availability on membrane lipid backbone structure in serpentinizing settings where oxidants and inorganic carbon are deficient.

Ceramide backbone linkages also correspond to a reduced Z_c (−0.75) and were observed in the lipidome of all sampled fluids (Supplementary Figure S4). Ceramides have been reported as a major component of the lipidome in hyperthermic marine sediments in Spathi Bay (Sollich et al., 2017), as well as minor components in serpentine rock in the Chimera ophiolite (Rattray et al., 2022), the anoxic water column of the Black Sea (Schubotz et al., 2009), and in hot springs (Schubotz et al., 2013). However, ceramides are more commonly described for their hypothesized role in virulence and stress survival in host-associated taxa (e.g., Kunz and Kozjak-Pavlovic, 2019). Sollich et al. (2017) hypothesized that ceramides may confer increased membrane rigidity and stability through tighter membrane packing facilitated by the strong hydrogen-bonding potential of ceramide backbones. This hypothesis is supported by multiple studies that confirm intramolecular hydrogen bonding of amino and hydroxyl groups in the ceramide backbone with the headgroup of sphingomyelin lipids (Talbott et al., 2000; Mombelli et al., 2003; Venable et al., 2014). Interestingly, the availability of an amino group near the lipid headgroup also occurs in the fatty amide backbone structure of ornithine lipids, implying similar potential for increased hydrogen bonding. Overall, ceramide lipids likely provide increased membrane stability in IPLs and perhaps represent an alternative to ether linkages for organisms not genetically capable of synthesizing DEG backbones.

We observed little variation in the abundance-weighted average number of aliphatic carbons and unsaturations in IPL chains across wells; however, we did note the maximum nC and the minimum nUns in the chains of IPLs from the well NSHQ14 where pH was highest. Increasing length and saturation of alkyl chains has been shown to decrease membrane permeability (de Gier et al., 1968; Paula et al., 1996) which could modulate the maintenance of an ion gradient across the membrane at high pH. The methods employed for IPL characterization do not allow us to distinguish between branched non-isoprenoidal chains (e.g., iso- and anteiso- fatty acids) and straight-chain counterparts, and so nC is not necessarily equivalent to chain length. However, increased branching of aliphatic chains, which would similarly increase nC, has been reported in laboratory cultures of organisms belonging to the Bacillus/Clostridium subphylum when grown at high pH (Clejan et al., 1986; Li et al., 1994; Prowe and Antranikian, 2001). Thus, the observed trend of increasing nC and decreasing nUns could represent a strategy to cope with hyperalkaline pH. Importantly, unlike headgroup modifications, adjustments to IPL chains such as increased methylations or chain length could ultimately be preserved in fossil biomarker structures such as hydrocarbons as a record of past geochemical conditions.

4.3. IPLs as biomarkers for living biomass in terrestrial serpentinizing environments

A key assumption in the use of IPLs to characterize the abundance and physiology of microorganisms is that IPLs are a proxy for living biomass. This has been widely assumed because the bond linking the polar headgroup to the lipid backbone is labile and can easily be cleaved after cell death on the order of hours to days (White et al., 1979; Harvey et al., 1986). However, the lack of a meaningful correlation of estimated IPL concentrations with enumerated planktonic cells in Samail Ophiolite subsurface fluids (Supplementary Figure S2) demonstrates a stark difference in relative turnover times between at least some fraction of IPLs and microbial communities. This, in conjunction with the predominance of 1G-AR in wells that exhibited very low relative abundances of archaeal DNA and RNA (Figure 6) suggests an unknown, but large, proportion of IPLs in this setting does not represent viable biomass. An overrepresentation of archaea by IPL analyses in comparison to other biomass quantification techniques has been reported in multiple marine deep biosphere surveys (Biddle et al., 2006; Lipp et al., 2008; Lenggere et al., 2014). The prevalence of archaeal IPLs in deep, subsurface environments has been interpreted to be an artifact of the differential lability of ester-bound bacterial and ether-bound archaeal IPLs (Schouten et al., 2010). Laboratory studies of IPL degradation kinetics demonstrate that glycosidic archaeal IPLs degrade at a rate of one to two orders of magnitude slower than bacterial phosphatidic ester-bound IPLs (Logemann et al., 2011; Xie et al., 2013). In deep biosphere systems with very low cellular turnover rates, it has been extrapolated that glycosidic archaeal lipids could persist for 10 of 1,000 of years (Lin et al., 2013; Xie et al., 2013). Because of the persistence of at least some classes of IPLs in serpentinite-hosted fluids, the intact polar lipidome must be considered as a cumulative record of longer-scale patterns of microbial diversity and geochemistry, and not as a snapshot of a dynamic system.

4.4. Lipid preservation potential

The persistence of IPLs in fluids beyond the presence of their source organisms is promising for the detection of extinct life through lipid biomarker signatures. Intact diether lipids were found to be highly abundant in hyperalkaline fluids (Figure 3) despite low planktonic cell abundances, indicating a potential for these biomolecules to accumulate in fluids. Over time, these IPLs could amass to concentrations far surpassing living biomass, thus facilitating the detection of lipid signatures if these biomarkers were to be preserved in mineral precipitants. Fossil lipid signatures have been observed in carbonate and brucite veins at both terrestrial and marine sites of serpentinization (Klein et al., 2015; Zwicker et al., 2018; Newman et al., 2020), supporting the hypothesis that fluid-sourced microbial membrane lipids can be preserved in this type of geologic setting. Although, the apparent difference in residence times between diether lipids and other IPL classes suggests the preserved lipid biomarker record would not be a representative snapshot of the full diversity of the microbial community. Nevertheless, the detectability of IPLs (3.3 ng/L – 27 mg/L) in fluids with low (~1×10^5 cells/mL) cellular abundances merits further investigation into serpentinites as targets for life detection on other planetary bodies. Specifically, it supports the concept that life detection could be achieved via analysis of organic molecules in serpentinite fluids or in secondary mineral assemblages, to search for degradation products of cell membranes.

4.5. Reinterpretation of the fossil lipid biomarker record of the Samail ophiolite

The intact polar lipidome of serpentinized fluids hosted within the Samail Ophiolite can provide valuable context to aid in the reconstruction of past microbial activity from core lipid records of terrestrial serpentinites. Newman et al. (2020) surveyed core lipid biomarkers in travertine deposits and carbonate veins of serpentinized rock in the Samail Ophiolite. This record represents an integrated signature of microbial life over the time at which carbonate was precipitated, which could span ~50,000 years (Clark and Fontes, 1990; Kelemen and Matter, 2008; Kelemen et al., 2011; Mervine et al., 2014). The core structures observed here in IPLs from subsurface Samail Ophiolite fluids most closely resemble the assemblage of lipids detected in layered carbonate and travertine outcrops (Subset A in Newman et al., 2020), which were categorized by an abundance of archaeol and non-isoprenoidal ether lipids as well as a high ratio of GDGT-0 to crenarchaeol. These lipids were interpreted as signatures of surficial microbial communities because the source carbonates were presumed to have precipitated from surface outflow of Ca^{2+} and OH^- rich, serpentinized fluids (Newman et al., 2020). We posit that microorganisms inhabiting deep, highly reacted fluids could alternatively be the source of these biomarkers.

In wells such as NSHQ14, we sampled highly reacted fluids that exhibited a hyperalkaline pH (11.3) with reduced Eh (−253 mV), as well as characteristically high calcium (4,340 μM) and low magnesium (5 μM) and DIC (130 μM) concentrations consistent with the expected chemistry for source fluids of travertines in serpentinizing settings (Barnes and O'neil, 1969; Neal and Stanger, 1985; Paukert et al., 2012). Highly reduced fluids contained co-occurring intact diglycosyl archaeol and GDGT-0 lipids with non-isoprenoidal glycosyl diether bacterial lipids which were associated with high relative abundances of cDNA of methanogenic *Methanobacteria* and sulfate-reducing Thermodesulfovibriona. Because we found archaeal diether IPLs to be so recalcitrant in serpentinized fluids, we hypothesize archaeol, and perhaps other ether-linked lipids, comparatively accumulate in subsurface fluids with respect to more labile lipids, and thus are preferentially preserved upon rapid carbonate precipitation as reacted, subsurface fluids reemerge near the surface and are exposed to atmospheric carbon dioxide. We also note that the abundance of GDGT-0 could primarily be sourced by *Methanobacteria*, and not methanotrophic archaea, Crenarcheota, or Thaumarcheota as suggested by Newman et al. (2020), because we observed such high relative abundances of

2G-GDGT-0 in association with *Methanobacteria*. A subsurface, methanogenic source of archaeal biomarkers in serpentinites is consistent with the findings by Zwicker et al. (2018) for the serpentinite-hosted Chimera seeps of Turkey, as well as the distribution of methanogenic biomarkers in marine serpentinites where archaeol and acyclic GDGTs were most abundant within chimneys (Bradley et al., 2009a; Lincoln et al., 2013) and subsurface veins (Klein et al., 2015). The co-occurrence of bacterial non-isoprenoidal ether-linked lipids with archaeol in all intact and fossil lipid surveys of alkaline sites of serpentinization suggests these biomarkers could be a hallmark signature of serpentinized fluids (Bradley et al., 2009a,b; Lincoln et al., 2013; Méhay et al., 2013; Klein et al., 2015; Zwicker et al., 2018; Newman et al., 2020).

4.6. Implications for the detection of biomarkers on Mars

The detection of serpentine minerals by the Compact Reconnaissance Imaging Spectrometer for Mars (CRISM) in conjunction with olivine-rich basalts, carbonates, and other alteration mineral phases (e.g., talc, saponite) indicates serpentinization on Mars was once active, and potentially widespread (Ehlmann et al., 2008, 2009, 2010; Brown et al., 2010). Spectroscopic evidence from the Perseverance rover for aqueously-altered, olivine-rich rocks (Farley et al., 2022) imply there may even be the potential for sample collection of serpentinized Martian rock in the near future. We suggest these serpentine mineral assemblages are promising potential targets in the search for preserved organic signatures of ancient biomass on Mars. The abundance of recalcitrant IPLs in subsurface serpentinite-hosted fluids reported in this study in combination with the detection of fossil signatures in Samail Ophiolite travertines reported by Newman et al. (2020) support the theory that subsurface microbial communities inhabiting serpentinite-hosted aquifers could be preserved within mineral products of fluid-rock reaction. Travertine deposits form where deep-seated, highly reacted fluids discharge at the surface from bedrock fissures (Giampouras et al., 2020). Thus, travertine deposits facilitate the accessibility of sampling fossil subsurface, fluid-hosted biomass. On Mars, faults from impacts, the buildup of Tharsis, the dichotomy-forming event, or local tectonics (e.g., subsidence, uplift) could penetrate deep into the subsurface and potentially act as conduits for fluid seepage (Oehler and Etiope, 2017), thus providing near-surface access to subsurface material. A subsurface source of biomass may promote its preservation in carbonate veins below the surface, as a major challenge for the persistence of organic signatures on the Martian surface is degradation from exposure to ionizing radiation or prevalent chemical oxidants such as perchlorates (Hays et al., 2017). Accordingly, locations such as Nilli Fossae where fractured, serpentinized rocks have been detected from orbit should be prioritized for detection of preserved cell-derived organics in future missions.

5. Conclusion

This study represents the first intact polar lipid biomarker survey of subsurface fluids from a terrestrial site of active serpentinization, sampling high pH fluids characterized by challenging states of nutrient and energy limitation, thus greatly increasing the astrobiologically relevant physicochemical conditions explored in lipid biomarker investigations. To probe the anticipated diversity of intact lipid structures in this setting, IPLs were inventoried using an expansive, custom environmental lipid database, which expands the application of targeted and untargeted lipidomics in the study of microbial and biogeochemical processes. The intact polar lipidome across fluids was dominated by archaeal and bacterial glycosyl diether lipids that bore a surprising resemblance to the biomarker assemblages described for the marine serpentinizing system, Lost City Hydrothermal Field (Bradley et al., 2009a), despite differing microbial community compositions. In Oman, we interpret these lipids to most likely be signatures of methanogenic archaea belonging to the genus *Methanobacteria* and sulfate-reducing bacteria, possibly of the family Thermodesulfovibriona or Clostridiaceae. The co-occurrence of bacterial and archaeal diether glycolipids at Lost City and in the Samail Ophiolite suggests these biomarkers are potentially diagnostic signatures for serpentinizing systems.

The prominence of non-phospholipids such as betaine, trimethyl-ornithine, and glycosphingolipids suggests extensive membrane modifications of polar headgroups, likely as a conservation strategy of organisms adapted to living in phosphate-depleted conditions within serpentinite rock and fluids. Additionally, backbone linkages in highly reduced fluids exhibited low carbon oxidation states and were characterized by primarily ether and amide linkages, which may reflect an energy-conservation strategy of cells and an adaptation to reduce membrane permeability.

An unknown, but possibly dominant, proportion of IPLs in this setting were not representative of living biomass as commonly assumed for intact lipids. The accumulation of recalcitrant IPLs could facilitate the detectability of lipid biosignatures in mineral precipitates of serpentinized fluids, thus improving prospects for life detection efforts in serpentinites. We invoke this mechanism in a reinterpretation of the core lipid biomarker record for travertines in the Samail Ophiolite published by Newman et al. (2020), and hypothesize these biomarkers are representative of deep, highly reacted fluids rather than surficial microbial communities. This hypothesis merits further investigation because it implies that travertines should be a high priority target for organic biosignature detection on Mars or other planetary bodies. Overall, this work provides context for the interpretation of molecular fossil records in serpentinite-hosted settings, such as those potentially left on early Earth, Mars, or similar planetary systems, which will help guide future efforts to detect signatures of subsurface life.

Data availability statement

The datasets presented in this study can be found in online repositories. Raw mass spectral data are deposited in the EBI MetaboLights repository under accession number MTBLS7570: https://www.ebi.ac.uk/metabolights/MTBLS7570. Raw sequences are deposited in the NCBI Sequence Read Archive (SRA) under accession number PRJNA560313. All data and source code used to produce the figures and data tables in this manuscript are available at https://github.com/krempfert/Samail_fluid_IPLs.

Author contributions

AT, KR, and JuS conceived the study. KR, DN, EK, JoS, and AT collected the samples in the field. KR, DN, EK, ND, and JuS analyzed the samples. KR produced the expansive custom environmental lipid database, processed data, performed statistical analyses, and wrote the manuscript. All authors interpreted data and critically revised the manuscript text and figures. All authors contributed to the article and approved the submitted version.

Funding

This research was directly supported through the Rock-Powered Life NASA Astrobiology Institute (NNA15BB02A), the NASA Exobiology program (80NSSC21K0489), and a NASA Earth and Space Science Fellowship awarded to KR (80NSSC17K0488). JuS acknowledges partial support from NSF CAREER award 2047057.

Acknowledgments

We thank the Ministry of Regional Municipalities and Water Resources in the Sultanate of Oman for access to NSHQ and WAB groundwater wells and permits to export fluids, Peter Kelemen and Juerg Matter for supporting access to these field sites, and Eric Ellison, Eric Boyd, Laura Bueter, and Lauren Seyler for aid in sampling and insightful discussion in field. We also thank Sebastian Cantarero and Jon Raberg at CU Boulder for their assistance in IPL analyses.

Conflict of interest

The authors declare that the research was conducted in the absence of any commercial or financial relationships that could be construed as a potential conflict of interest.

Publisher's note

Supplementary material

The Supplementary material for this article can be found online at: https://www.frontiersin.org/articles/10.3389/fmicb.2023.1198786/full#supplementary-material

References

Adusumilli, R., and Mallick, P. (2017). "Data conversion with ProteoWizard msConvert" in *Proteomics: Methods and protocols, methods in molecular biology*. eds. L. Comai, J. E. Katz and P. Mallick (New York, NY: Springer), 339–368.

Bale, N. J., Rijpstra, W. I. C., Sahonero-Canavesi, D. X., Oshkin, I. Y., Belova, S. E., Dedysh, S. N., et al, (2019). Fatty acid and hopanoid adaption to cold in the methanotroph methylovulum psychrotolerans. *Front Microbiol* 10. doi: 10.3389/fmicb.2019.00589

Barnes, I., and O'neil, J. R. (1969). The relationship between fluids in some fresh alpine-type Ultramafics and possible modern serpentinization, Western United States. *Geol. Soc. Am. Bull.* 80, 1947–1960. doi: 10.1130/0016-7606(1969)80[1947:TRBFIS]2.0.CO;2

Becker, K. W., Elling, F. J., Yoshinaga, M. Y., Söllinger, A., Urich, T., and Hinrichs, K.-U., (2016). Unusual butane- and pentanetriol-based tetraether lipids in methanomassiliicoccus luminyensis, a representative of the seventh order of methanogens. *Appl Environ Microbiol* 82, 4505–4516. doi: 10.1128/AEM.00772-16

Benning, C., Huang, Z. H., and Gage, D. A. (1995). Accumulation of a novel glycolipid and a betaine lipid in cells of *Rhodobacter sphaeroides* grown under phosphate limitation. *Arch. Biochem. Biophys.* 317, 103–111. doi: 10.1006/abbi.1995.1141

Benton, H. P., Want, E. J., and Ebbels, T. M. D. (2010). Correction of mass calibration gaps in liquid chromatography-mass spectrometry metabolomics data. *Bioinforma. Oxf. Engl.* 26, 2488–2489. doi: 10.1093/bioinformatics/btq441

Biddle, J. F., Lipp, J. S., Lever, M. A., Lloyd, K. G., Sørensen, K. B., Anderson, R., et al. (2006). Heterotrophic Archaea dominate sedimentary subsurface ecosystems off Peru. *Proc. Natl. Acad. Sci.* 103, 3846–3851. doi: 10.1073/pnas.0600035103

Bligh, E. G., and Dyer, W. J. (1959). A rapid method of Total lipid extraction and purification. *Can. J. Biochem. Physiol.* 37, 911–917. doi: 10.1139/o59-099

Bosak, T., Schubotz, F., Santiago-Torio, A., de Kuehl, J. V., Carlson, H. K., Watson, N., et al. (2016). System-wide adaptations of *Desulfovibrio alaskensis* G20 to phosphate-limited conditions. *PLoS One* 11:e0168719. doi: 10.1371/journal.pone.0168719

Boyd, E. S., Amenabar, M. J., Poudel, S., and Templeton, A. S. (2020). Bioenergetic constraints on the origin of autotrophic metabolism. *Philos. Transact. A Math. Phys. Eng. Sci.* 378:20190151. doi: 10.1098/rsta.2019.0151

Boyer, G. M., Schubotz, F., Summons, R. E., Woods, J., and Shock, E. L. (2020). Carbon oxidation state in microbial polar lipids suggests adaptation to hot spring temperature and redox gradients. *Front. Microbiol.* 11, 1–20. doi: 10.3389/fmicb.2020.00229

Bradley, A. S., Fredricks, H., Hinrichs, K.-U., and Summons, R. E. (2009a). Structural diversity of diether lipids in carbonate chimneys at the lost City hydrothermal field. *Org. Geochem.* 40, 1169–1178. doi: 10.1016/j.orggeochem.2009.09.004

Bradley, A. S., Hayes, J. M., and Summons, R. E. (2009b). Extraordinary 13C enrichment of diether lipids at the lost City hydrothermal field indicates a carbon-limited ecosystem. *Geochim. Cosmochim. Acta* 73, 102–118. doi: 10.1016/j.gca.2008.10.005

Brazelton, W. J., Morrill, P. L., Szponar, N., and Schrenk, M. O. (2013). Bacterial communities associated with subsurface geochemical processes in continental Serpentinite Springs. *Appl. Environ. Microbiol.* 79, 3906–3916. doi: 10.1128/AEM.00330-13

Broadhurst, D., Goodacre, R., Reinke, S. N., Kuligowski, J., Wilson, I. D., Lewis, M. R., et al. (2018). Guidelines and considerations for the use of system suitability and quality control samples in mass spectrometry assays applied in untargeted clinical metabolomic studies. *Metabolomics* 14, 1–17. doi: 10.1007/s11306-018-1367-3

Brocks, J. J., and Summons, R. E. (2003). "8.03 - sedimentary hydrocarbons, biomarkers for early life" in *Treatise on geochemistry*. eds. H. D. Holland and K. K. Turekian (Oxford: Pergamon), 63–115.

Brown, A. J., Hook, S. J., Baldridge, A. M., Crowley, J. K., Bridges, N. T., Thomson, B. J., et al. (2010). Hydrothermal formation of clay-carbonate alteration assemblages in the Nili fossae region of Mars. *Earth Planet. Sci. Lett.* 297, 174–182. doi: 10.1016/j.epsl.2010.06.018

Callahan, B. J., McMurdie, P. J., Rosen, M. J., Han, A. W., Johnson, A. J. A., and Holmes, S. P. (2016). DADA2: high-resolution sample inference from Illumina amplicon data. *Nat. Methods* 13, 581–583. doi: 10.1038/nmeth.3869

Cardace, D., Meyer-Dombard, D. R., Woycheese, K. M., and Arcilla, C. A. (2015). Feasible metabolisms in high pH springs of the Philippines. *Front. Microbiol.* 6, 1–16. doi: 10.3389/fmicb.2015.00010

Carini, P., Van Mooy, B. A. S., Thrash, J. C., White, A., Zhao, Y., Campbell, E. O., et al. (2015). SAR11 lipid renovation in response to phosphate starvation. *Proc. Natl. Acad. Sci. U. S. A.* 112, 7767–7772. doi: 10.1073/pnas.1505034112

Chavagnac, V., Monnin, C., Ceuleneer, G., Boulart, C., and Hoareau, G. (2013). Characterization of hyperalkaline fluids produced by low-temperature serpentinization of mantle peridotites in the Oman and Ligurian ophiolites. *Geochem. Geophys. Geosystems* 14, 2496–2522. doi: 10.1002/ggge.20147

Chwastek, G., Surma, M. A., Rizk, S., Grosser, D., Lavrynenko, O., Rucińska, M., et al. (2020). Principles of membrane adaptation revealed through environmentally induced bacterial lipidome Remodeling. *Cell Rep.* 32:108165. doi: 10.1016/j.celrep.2020.108165

Clark, I. D., and Fontes, J.-C. (1990). Paleoclimatic reconstruction in northern Oman based on carbonates from hyperalkaline groundwaters. *Quat. Res.* 33, 320–336. doi: 10.1016/0033-5894(90)90059-T

Clejan, S., Krulwich, T. A., Mondrus, K. R., and Seto-Young, D. (1986). Membrane lipid composition of obligately and facultatively alkalophilic strains of Bacillus spp. *J. Bacteriol.* 168, 334–340.

Collins, J. R., Edwards, B. R., Fredricks, H. F., and Van Mooy, B. A. S. (2016). LOBSTAHS: an adduct-based Lipidomics strategy for discovery and identification of oxidative stress biomarkers. *Anal. Chem.* 88, 7154–7162. doi: 10.1021/acs.analchem.6b01260

Crespo-Medina, M., Twing, K. I., Sánchez-Murillo, R., Brazelton, W. J., McCollom, T. M., and Schrenk, M. O. (2017). Methane dynamics in a tropical Serpentinizing environment: the Santa Elena ophiolite, Costa Rica. *Front. Microbiol.* 8, 1–14. doi: 10.3389/fmicb.2017.00916

Damsté, J. S. S., Rijpstra, W. I. C., Hopmans, E. C., Schouten, S., Balk, M., and Stams, A. J. M. (2007). Structural characterization of diabolic acid-based tetraester, tetraether and mixed ether/ester, membrane-spanning lipids of bacteria from the order Thermotogales. *Arch. Microbiol.* 188, 629–641. doi: 10.1007/s00203-007-0284-z

de Gier, J., Mandersloot, J. G., and van Deenen, L. L. (1968). Lipid composition and permeability of liposomes. *Biochim. Biophys. Acta* 150, 666–675. doi: 10.1016/0005-2736(68)90056-4

Dick, J. M. (2014). Average oxidation state of carbon in proteins. *J. R. Soc. Interface* 11:20131095. doi: 10.1098/rsif.2013.1095

Dick, J. M., and Shock, E. L. (2011). Calculation of the relative chemical stabilities of proteins as a function of temperature and redox chemistry in a hot spring. *PLoS One* 6:e22782. doi: 10.1371/journal.pone.0022782

Diercks, H., Semeniuk, A., Gisch, N., Moll, H., Duda, K. A., and Hölzl, G. (2015). Accumulation of novel glycolipids and ornithine lipids in *Mesorhizobium loti* under phosphate deprivation. *J. Bacteriol.* 197, 497–509. doi: 10.1128/JB.02004-14

Dixon, P. (2003). VEGAN, a package of R functions for community ecology. *J. Veg. Sci.* 14, 927–930. doi: 10.1111/j.1654-1103.2003.tb02228.x

Ehlmann, B. L., Mustard, J. F., and Murchie, S. L. (2010). Geologic setting of serpentine deposits on Mars. *Geophys. Res. Lett.* 37, 1–5. doi: 10.1029/2010GL042596

Ehlmann, B. L., Mustard, J. F., Murchie, S. L., Poulet, F., Bishop, J. L., Brown, A. J., et al. (2008). Orbital identification of carbonate-bearing rocks on Mars. *Science* 322, 1828–1832. doi: 10.1126/science.1164759

Ehlmann, B. L., Mustard, J. F., Swayze, G. A., Clark, R. N., Bishop, J. L., Poulet, F., et al. (2009). Identification of hydrated silicate minerals on Mars using MRO-CRISM: geologic context near Nili fossae and implications for aqueous alteration. *J. Geophys. Res. Planets* 114, 1–33. doi: 10.1029/2009JE003339

Eigenbrode, J. L. (2008). Fossil lipids for life-detection: a case study from the early earth record. *Space Sci. Rev.* 135, 161–185. doi: 10.1007/s11214-007-9252-9

Elling, F. J., Könneke, M., Nicol, G. W., Stieglmeier, M., Bayer, B., Spieck, E., et al. (2017). Chemotaxonomic characterisation of the thaumarchaeal lipidome. *Environ. Microbiol.* 19, 2681–2700. doi: 10.1111/1462-2920.13759

Evans, T. W., Wörmer, L., Lever, M. A., Lipp, J. S., Lagostina, L., Lin, Y.-S., et al. (2017). Size and composition of subseafloor microbial community in the Benguela upwelling area examined from intact membrane lipid and DNA analysis. *Org. Geochem.* 111, 86–100. doi: 10.1016/j.orggeochem.2017.06.008

Farley, K. A., Stack, K. M., Shuster, D. L., Horgan, B. H. N., Hurowitz, J. A., Tarnas, J. D., et al. (2022). Aqueously altered igneous rocks sampled on the floor of Jezero crater, Mars. *Science* 377:eabo2196. doi: 10.1126/science.abo2196

Ferreira, A. M., Wait, R., Nobre, M. F., and da Costa, M. S. (1999). Characterization of glycolipids from Meiothermus spp. *Microbiol. Read. Engl.* 145, 1191–1199. doi: 10.1099/13500872-145-5-1191

Fones, E. M., Colman, D. R., Kraus, E. A., Nothaft, D. B., Poudel, S., Rempfert, K. R., et al. (2019). Physiological adaptations to serpentinization in the Samail ophiolite, Oman. *ISME J.* 13, 1750–1762. doi: 10.1038/s41396-019-0391-2

Foster, J. M., Moreno, P., Fabregat, A., Hermjakob, H., Steinbeck, C., Apweiler, R., et al. (2013). LipidHome: a database of theoretical lipids optimized for high throughput mass spectrometry Lipidomics. *PLoS One* 8:e61951. doi: 10.1371/journal.pone.0061951

Gatto, L., Gibb, S., and Rainer, J. (2021). MSnbase, efficient and elegant R-based processing and visualization of raw mass spectrometry data. *J. Proteome Res.* 20, 1063–1069. doi: 10.1021/acs.jproteome.0c00313

Gatto, L., and Lilley, K. S. (2011). MSnbase-an R/Bioconductor package for isobaric tagged mass spectrometry data visualization, processing and quantitation. *Bioinformatics* 28, 288–289. doi: 10.1093/bioinformatics/btr645

Geiger, O., González-Silva, N., López-Lara, I. M., and Sohlenkamp, C. (2010). Amino acid-containing membrane lipids in bacteria. *Prog. Lipid Res.* 49, 46–60. doi: 10.1016/j.plipres.2009.08.002

Geiger, O., Röhrs, V., Weissenmayer, B., Finan, T. M., and Thomas-Oates, J. E. (1999). The regulator gene phoB mediates phosphate stress-controlled synthesis of the membrane lipid diacylglyceryl-N,N,N-trimethylhomoserine in Rhizobium (Sinorhizobium) meliloti. *Mol. Microbiol.* 32, 63–73. doi: 10.1046/j.1365-2958.1999.01325.x

Geske, T., Vom Dorp, K., Dörmann, P., and Hölzl, G. (2013). Accumulation of glycolipids and other non-phosphorous lipids in *Agrobacterium tumefaciens* grown under phosphate deprivation. *Glycobiology* 23, 69–80. doi: 10.1093/glycob/cws124

Giampouras, M., Garrido, C. J., Bach, W., Los, C., Fussmann, D., Monien, P., et al. (2020). On the controls of mineral assemblages and textures in alkaline springs, Samail ophiolite, Oman. *Chem. Geol.* 533:119435. doi: 10.1016/j.chemgeo.2019.119435

Grossi, V., Mollex, D., Vinçon-Laugier, A., Hakil, F., Pacton, M., and Cravo-Laureau, C. (2015). Mono- and Dialkyl glycerol ether lipids in anaerobic Bacteria: biosynthetic insights from the mesophilic Sulfate reducer *Desulfatibacillum alkenivorans* PF2803T. *Appl. Environ. Microbiol.* 81, 3157–3168. doi: 10.1128/AEM.03794-14

Hanghøj, K., Kelemen, P. B., Hassler, D., and Godard, M. (2010). Composition and genesis of depleted mantle peridotites from the Wadi Tayin massif, Oman ophiolite; major and trace element geochemistry, and Os isotope and PGE systematics. *J. Petrol.* 51, 201–227. doi: 10.1093/petrology/egp077

Harvey, H. R., Fallon, R. D., and Patton, J. S. (1986). The effect of organic matter and oxygen on the degradation of bacterial membrane lipids in marine sediments. *Geochim. Cosmochim. Acta* 50, 795–804. doi: 10.1016/0016-7037(86)90355-8

Haug, K., Cochrane, K., Nainala, V. C., Williams, M., Chang, J., Jayaseelan, K. V., et al. (2020). MetaboLights: a resource evolving in response to the needs of its scientific community. *Nucleic Acids Res.* 48, D440–D444. doi: 10.1093/nar/gkz1019

Hays, L. E., Graham, H. V., Des Marais, D. J., Hausrath, E. M., Horgan, B., McCollom, T. M., et al. (2017). Biosignature preservation and detection in Mars Analog environments. *Astrobiology* 17, 363–400. doi: 10.1089/ast.2016.1627

Hazel, J. R. (1995). Thermal adaptation in biological membranes: is homeoviscous adaptation the explanation? *Annu. Rev. Physiol.* 57, 19–42. doi: 10.1146/annurev.ph.57.030195.000315

Hazel, J. R., and Williams, E. E. (1990). The role of alterations in membrane lipid composition in enabling physiological adaptation of organisms to their physical environment. *Prog. Lipid Res.* 29, 167–227. doi: 10.1016/0163-7827(90)90002-3

Hewelt-Belka, W., Nakonieczna, J., Belka, M., Bączek, T., Namieśnik, J., and Kot-Wasik, A. (2016). Untargeted Lipidomics reveals differences in the lipid pattern among clinical isolates of *Staphylococcus aureus* resistant and sensitive to antibiotics. *J. Proteome Res.* 15, 914–922. doi: 10.1021/acs.jproteome.5b00915

Hinrichs, K.-U., Summons, R. E., Orphan, V., Sylva, S. P., and Hayes, J. M. (2000). Molecular and isotopic analysis of anaerobic methane-oxidizing communities in marine sediments. *Org. Geochem.* 31, 1685–1701. doi: 10.1016/S0146-6380(00)00106-6

Holm, N. G., Dumont, M., Ivarsson, M., and Konn, C. (2006). Alkaline fluid circulation in ultramafic rocks and formation of nucleotide constituents: a hypothesis. *Geochem. Trans.* 7:7. doi: 10.1186/1467-4866-7-7

Huber, R., Rossnagel, P., Woese, C. R., Rachel, R., Langworthy, T. A., and Stetter, K. O. (1996). Formation of ammonium from nitrate during chemolithoautotrophic growth of the extremely thermophilic bacterium *ammonifex degensii* gen. Nov. sp. nov. *Syst. Appl. Microbiol.* 19, 40–49. doi: 10.1016/S0723-2020(96)80007-5

Huber, R., Wilharm, T., Huber, D., Trincone, A., Burggraf, S., König, H., et al. (1992). *Aquifex pyrophilus* gen. Nov. sp. nov., represents a novel group of marine Hyperthermophilic hydrogen-oxidizing Bacteria. *Syst. Appl. Microbiol.* 15, 340–351. doi: 10.1016/S0723-2020(11)80206-7

Jahnke, L. L., Eder, W., Huber, R., Hope, J. M., Hinrichs, K.-U., Hayes, J. M., et al. (2001). Signature lipids and stable carbon isotope analyses of Octopus spring Hyperthermophilic communities compared with those ofAquificales representatives. *Appl. Environ. Microbiol.* 67, 5179–5189. doi: 10.1128/AEM.67.11.5179-5189.2001

Jorge, C. D., Borges, N., and Santos, H. (2015). A novel pathway for the synthesis of inositol phospholipids uses cytidine diphosphate (CDP)-inositol as donor of the polar head group. *Environ. Microbiol.* 17, 2492–2504. doi: 10.1111/1462-2920.12734

Kampbell, D. H., Wilson, J. T., and McInnes, D. M. (1998). Determining dissolved hydrogen, methane, and vinyl chloride concentrations in aqueous solution on a nanomolar scale with the bubble strip method, p 176–190. In *proceedings of the 1998 conference on hazardous waste research*, snowbird, UT, 18 to 21 may 1998.

Karlsson, A. Å., Michélsen, P., and Odham, G., (1998). Molecular species of sphingomyelin: determination by high-performance liquid chromatography/mass spectrometry with electrospray and high-performance liquid chromatography/tandem mass spectrometry with atmospheric pressure chemical ionization. *Journal of Mass Spectrometry* 33, 1192–1198. doi: 10.1002/(SICI)1096-9888(199812)33:12<1192::AID-JMS735>3.0.CO;2-J

Kates, M. (1993). Biology of halophilic bacteria, part II. Membrane lipids of extreme halophiles: biosynthesis, function and evolutionary significance. *Experientia* 49, 1027–1036. doi: 10.1007/BF01929909

Kawahara, K., Tsukano, H., Watanabe, H., Lindner, B., and Matsuura, M., (2002). Modification of the structure and activity of lipid A in Yersinia pestis lipopolysaccharide by growth temperature. *Infect Immun* 70, 4092–4098. doi: 10.1128/IAI.70.8.4092-4098.2002

Keck, M., Gisch, N., Moll, H., Vorhölter, F.-J., Gerth, K., Kahmann, U., et al. (2011). Unusual outer membrane lipid composition of the gram-negative, lipopolysaccharide-lacking myxobacterium *Sorangium cellulosum* so ce56. *J. Biol. Chem.* 286, 12850–12859. doi: 10.1074/jbc.M110.194209

Kelemen, P. B., and Matter, J. (2008). In situ carbonation of peridotite for CO2 storage. *Proc. Natl. Acad. Sci.* 105, 17295–17300. doi: 10.1073/pnas.0805794105

Kelemen, P. B., Matter, J., Streit, E. E., Rudge, J. F., Curry, W. B., and Blusztajn, J. (2011). Rates and mechanisms of mineral carbonation in peridotite: natural processes and recipes for enhanced, in situ CO2 capture and storage. *Annu. Rev. Earth Planet. Sci.* 39, 545–576. doi: 10.1146/annurev-earth-092010-152509

Klein, F., Humphris, S. E., Guo, W., Schubotz, F., Schwarzenbach, E. M., and Orsi, W. D. (2015). Fluid mixing and the deep biosphere of a fossil lost City-type hydrothermal system at the Iberia margin. *Proc. Natl. Acad. Sci.* 112, 12036–12041. doi: 10.1073/pnas.1504674112

Koga, Y., and Morii, H. (2005). Recent advances in structural research on ether lipids from archaea including comparative and physiological aspects. *Biosci. Biotechnol. Biochem.* 69, 2019–2034. doi: 10.1271/bbb.69.2019

Kraus, E. A., Beeler, S. R., Mors, R. A., Floyd, J. G., Stamps, B. W., Nunn, H. S., et al. (2018). Microscale biosignatures and abiotic mineral Authigenesis in little Hot Creek, California. *Front. Microbiol.* 9, 1–13. doi: 10.3389/fmicb.2018.00997

Kraus, E. A., Nothaft, D., Stamps, B. W., Rempfert, K. R., Ellison, E. T., Matter, J. M., et al. (2021). Molecular evidence for an active microbial methane cycle in subsurface serpentinite-hosted groundwaters in the Samail ophiolite, Oman. *Appl. Environ. Microbiol.* 87:e02068–20. doi: 10.1128/AEM.02068-20

Kuhl, C., Tautenhahn, R., Böttcher, C., Larson, T. R., and Neumann, S. (2012). CAMERA: an integrated strategy for compound spectra extraction and annotation of LC/MS data sets. *Anal. Chem.* 84, 283–289. doi: 10.1021/ac202450g

Kunz, T. C., and Kozjak-Pavlovic, V. (2019). Diverse facets of sphingolipid involvement in bacterial infections. *Front. Cell Dev. Biol.* 7, 1–10. doi: 10.3389/fcell.2019.00203

Langworthy, T. A., Holzer, G., Zeikus, J. G., and Tornabene, T. G. (1983). Iso- and Anteiso-branched glycerol diethers of the thermophilic anaerobe Thermodesulfotobacterium commune. *Syst. Appl. Microbiol.* 4, 1–17. doi: 10.1016/S0723-2020(83)80029-0

Lengger, S. K., Hopmans, E. C., Sinninghe Damsté, J. S., and Schouten, S. (2014). Fossilization and degradation of archaeal intact polar tetraether lipids in deeply buried marine sediments (Peru margin). *Geobiology* 12, 212–220. doi: 10.1111/gbi.12081

Libiseller, G., Dvorzak, M., Kleb, U., Gander, E., Eisenberg, T., Madeo, F., et al. (2015). IPO: a tool for automated optimization of XCMS parameters. *BMC Bioinformatics* 16:118. doi: 10.1186/s12859-015-0562-8

Li, J., Mara, P., Schubotz, F., Sylvan, J. B., Burgaud, G., Klein, F., et al. (2020). Recycling and metabolic flexibility dictate life in the lower oceanic crust. *Nature* 579, 250–255. doi: 10.1038/s41586-020-2075-5

Lim, K. L. H., Pancost, R. D., Hornibrook, E. R. C., Maxfield, P. J., and Evershed, R. P. (2012). Archaeol: an Indicator of methanogenesis in water-saturated soils. *Archaea* 2012:896727. doi: 10.1155/2012/896727

Lincoln, S. A., Bradley, A. S., Newman, S. A., and Summons, R. E. (2013). Archaeal and bacterial glycerol dialkyl glycerol tetraether lipids in chimneys of the lost City hydrothermal field. *Org. Geochem.* 60, 45–53. doi: 10.1016/j.orggeochem.2013.04.010

Lin, Y.-S., Lipp, J. S., Elvert, M., Holler, T., and Hinrichs, K.-U. (2013). Assessing production of the ubiquitous archaeal diglycosyl tetraether lipids in marine subsurface sediment using intramolecular stable isotope probing. *Environ. Microbiol.* 15, 1634–1646. doi: 10.1111/j.1462-2920.2012.02888.x

Lipp, J. S., Morono, Y., Inagaki, F., and Hinrichs, K.-U. (2008). Significant contribution of Archaea to extant biomass in marine subsurface sediments. *Nature* 454, 991–994. doi: 10.1038/nature07174

Li, Y., Engle, M., Weiss, N., Mandelco, L., and Wiegel, J. (1994). *Clostridium thermoalcaliphilum* sp. nov., an anaerobic and thermotolerant facultative alkaliphile. *Int. J. Syst. Evol. Microbiol.* 44, 111–118. doi: 10.1099/00207713-44-1-111

Li, Y., Lou, Y., Mu, T., Xu, J., Zhou, C., and Yan, X. (2017). Simultaneous structural identification of diacylglyceryl-N-trimethylhomoserine (DGTS) and diacylglycerylhydroxymethyl-N,N,N-trimethyl-β-alanine (DGTA) in microalgae using dual Li+/H+ adduct ion mode by ultra-performance liquid chromatography/quadrupole time-of-flight mass spectrometry. *Rapid Commun. Mass Spectrom.* 31, 457–468. doi: 10.1002/rcm.7818

Lobasso, S., Pérez-Davó, A., Vitale, R., Sánchez, M. M.-, Corcelli, A., (2015). Deciphering archaeal glycolipids of an extremely halophilic archaeon of the genus Halobellus by MALDI-TOF/MS. *Chemistry and Physics of Lipids* 186, 1–8. doi: 10.1016/j.chemphyslip.2014.11.002

Logemann, J., Graue, J., Köster, J., Engelen, B., Rullkötter, J., and Cypionka, H. (2011). A laboratory experiment of intact polar lipid degradation in sandy sediments. *Biogeosciences* 8, 2547–2560. doi: 10.5194/bg-8-2547-2011

López-Lara, I. M., Gao, J.-L., Soto, M. J., Solares-Pérez, A., Weissenmayer, B., Sohlenkamp, C., et al. (2005). Phosphorus-free membrane lipids of *Sinorhizobium meliloti* are not required for the symbiosis with alfalfa but contribute to increased cell yields under phosphorus-limiting conditions of growth. *Mol. Plant-Microbe Interact. MPMI* 18, 973–982. doi: 10.1094/MPMI-18-0973

López-Lara, I. M., and Geiger, O. (2017). Bacterial lipid diversity. Biochim. Biophys. Acta BBA - mol. Cell biol. *Lipids, Bacterial Lipids* 1862, 1287–1299. doi: 10.1016/j.bbalip.2016.10.007

Lorenzen, W., Ahrendt, T., Bozhüyük, K. A. J., and Bode, H. B. (2014). A multifunctional enzyme is involved in bacterial ether lipid biosynthesis. *Nat. Chem. Biol.* 10, 425–427. doi: 10.1038/nchembio.1526

Luo, Y., Javed, M. A., Deneer, H., and Chen, X., (2018). Nutrient depletion-induced production of tri-acylated glycerophospholipids in Acinetobacter radioresistens. *Scientific Reports* 8, 1–11. doi: 10.1038/s41598-018-25869-9

Martin, M. (2011). Cutadapt removes adapter sequences from high-throughput sequencing reads. *EMBnet.journal* 17, 10–12. doi: 10.14806/ej.17.1.200

Mathai, J. C., Sprott, G. D., and Zeidel, M. L. (2001). Molecular mechanisms of water and solute transport across archaebacterial lipid membranes. *J. Biol. Chem.* 276, 27266–27271. doi: 10.1074/jbc.M103265200

Méhay, S., Früh-Green, G. L., Lang, S. Q., Bernasconi, S. M., Brazelton, W. J., Schrenk, M. O., et al. (2013). Record of archaeal activity at the serpentinite-hosted lost City hydrothermal field. *Geobiology* 11, 570–592. doi: 10.1111/gbi.12062

Mervine, E. M., Humphris, S. E., Sims, K. W. W., Kelemen, P. B., and Jenkins, W. J. (2014). Carbonation rates of peridotite in the Samail ophiolite, Sultanate of Oman, constrained through 14C dating and stable isotopes. *Geochim. Cosmochim. Acta* 126, 371–397. doi: 10.1016/j.gca.2013.11.007

Meyer-Dombard, D. R., Woycheese, K. M., Yargıçoğlu, E. N., Cardace, D., Shock, E. L., Güleçal-Pektas, Y., et al. (2015). High pH microbial ecosystems in a newly discovered, ephemeral, serpentinizing fluid seep at Yanartaş (chimera), Turkey. *Front. Microbiol.* 5, 1–13. doi: 10.3389/fmicb.2014.00723

Miller, H. M., Matter, J. M., Kelemen, P., Ellison, E. T., Conrad, M. E., Fierer, N., et al. (2016). Modern water/rock reactions in Oman hyperalkaline peridotite aquifers and implications for microbial habitability. *Geochim. Cosmochim. Acta* 179, 217–241. doi: 10.1016/j.gca.2016.01.033

Mombelli, E., Morris, R., Taylor, W., and Fraternali, F. (2003). Hydrogen-bonding propensities of sphingomyelin in solution and in a bilayer assembly: a molecular dynamics study. *Biophys. J.* 84, 1507–1517. doi: 10.1016/S0006-3495(03)74963-7

Moore, E. K. (2021). Trimethylornithine membrane lipids: discovered in Planctomycetes and identified in diverse environments. *Meta* 11:49. doi: 10.3390/metabo11010049

Moore, E. K., Hopmans, E. C., Rijpstra, W. I. C., Sánchez-Andrea, I., Villanueva, L., Wienk, H., et al, (2015). Lysine and novel hydroxylysine lipids in soil bacteria: amino acid membrane lipid response to temperature and pH in Pseudopedobacter saltans. *Front Microbiol* 6. doi: 10.3389/fmicb.2015.00637

Moore, E. K., Hopmans, E. C., Rijpstra, W. I. C., Villanueva, L., and Damsté, J. S. S., (2016). Elucidation and identification of amino acid containing membrane lipids using liquid chromatography/high-resolution mass spectrometry. *Rapid Communications in Mass Spectrometry* 30, 739–750. doi: 10.1002/rcm.7503

Moore, E. K., Hopmans, E. C., Rijpstra, W. I. C., Villanueva, L., Dedysh, S. N., Kulichevskaya, I. S., et al. (2013). Novel mono-, Di-, and Trimethylornithine membrane lipids in northern wetland Planctomycetes. *Appl. Environ. Microbiol.* 79, 6874–6884. doi: 10.1128/AEM.02169-13

Murphy, R. C., and Axelsen, P. H. (2011). Mass spectrometric analysis of Long-chain lipids. *Mass Spectrom. Rev.* 30, 579–599. doi: 10.1002/mas.20284

Neal, C., and Stanger, G. (1985). "Past and present serpentinisation of ultramafic rocks; an example from the Semail ophiolite nappe of northern Oman" in *The chemistry of weathering*. ed. J. I. Drever (Netherlands, Dordrecht: Springer), 249–275.

Newman, S. A., Lincoln, S. A., O'Reilly, S., Liu, X., Shock, E. L., Kelemen, P. B., et al. (2020). Lipid biomarker record of the serpentinite-hosted ecosystem of the Samail ophiolite, Oman and implications for the search for biosignatures on Mars. *Astrobiology* 20, 830–845. doi: 10.1089/ast.2019.2066

Nishihara, M., and Koga, Y. (1987). Extraction and composition of polar lipids from the archaebacterium, Methanobacterium thermoautotrophicum: effective extraction of tetraether lipids by an acidified solvent. *J. Biochem. (Tokyo)* 101, 997–1005. doi: 10.1093/oxfordjournals.jbchem.a121969

Nothaft, D. B. (2019). *Bubble strip aqueous gas sampling*. protocols.io

Nowak, A., Greń, I., and Mrozik, A. (2016). Changes in fatty acid composition of *Stenotrophomonas maltophilia* KB2 during co-metabolic degradation of monochlorophenols. *World J. Microbiol. Biotechnol.* 32:198. doi: 10.1007/s11274-016-2160-y

Oehler, D. Z., and Etiope, G. (2017). Methane seepage on Mars: where to look and why. *Astrobiology* 17, 1233–1264. doi: 10.1089/ast.2017.1657

Okur, H. I., Tarun, O. B., and Roke, S. (2019). Chemistry of lipid membranes from models to living systems: a perspective of hydration, surface potential, curvature, confinement and heterogeneity. *J. Am. Chem. Soc.* 141, 12168–12181. doi: 10.1021/jacs.9b02820

Olsen, I., and Jantzen, E. (2001). Sphingolipids in Bacteria and Fungi. *Anaerobe* 7, 103–112. doi: 10.1006/anae.2001.0376

Orphan, V. J., Hinrichs, K.-U., Ussler, W., Paull, C. K., Taylor, L. T., Sylva, S. P., et al. (2001). Comparative analysis of methane-oxidizing Archaea and Sulfate-reducing

Bacteria in anoxic marine sediments. *Appl. Environ. Microbiol.* 67, 1922–1934. doi: 10.1128/AEM.67.4.1922-1934.2001

Pancost, R. D., Bouloubassi, I., Aloisi, G., and Sinninghe Damsté, J. S.Scientific Party, the M.S. (2001). Three series of non-isoprenoidal dialkyl glycerol diethers in cold-seep carbonate crusts. *Org. Geochem.* 32, 695–707. doi: 10.1016/S0146-6380(01)00015-8

Pancost, R. D., Pressley, S., Coleman, J. M., Talbot, H. M., Kelly, S. P., Farrimond, P., et al. (2006). Composition and implications of diverse lipids in New Zealand geothermal sinters. *Geobiology* 4, 71–92. doi: 10.1111/j.1472-4669.2006.00069.x

Parada, A. E., Needham, D. M., and Fuhrman, J. A. (2016). Every base matters: assessing small subunit rRNA primers for marine microbiomes with mock communities, time series and global field samples. *Environ. Microbiol.* 18, 1403–1414. doi: 10.1111/1462-2920.13023

Parsons, J. B., and Rock, C. O. (2013). Bacterial lipids: metabolism and membrane homeostasis. *Prog. Lipid Res.* 52, 249–276. doi: 10.1016/j.plipres.2013.02.002

Paukert, A. N., Matter, J. M., Kelemen, P. B., Shock, E. L., and Havig, J. R. (2012). Reaction path modeling of enhanced in situ CO2 mineralization for carbon sequestration in the peridotite of the Samail ophiolite, Sultanate of Oman. *Chem. Geol.* 330–331, 86–100. doi: 10.1016/j.chemgeo.2012.08.013

Paula, S., Volkov, A. G., Van Hoek, A. N., Haines, T. H., and Deamer, D. W. (1996). Permeation of protons, potassium ions, and small polar molecules through phospholipid bilayers as a function of membrane thickness. *Biophys. J.* 70, 339–348.

Pitcher, A., Rychlik, N., Hopmans, E. C., Spieck, E., Rijpstra, W. I. C., Ossebaar, J., et al. (2010). Crenarchaeol dominates the membrane lipids of Candidatus Nitrososphaera gargensis, a thermophilic group I.1b archaeon. *ISME J.* 4, 542–552. doi: 10.1038/ismej.2009.138

Popendorf, K. J., Fredricks, H. F., and Van Mooy, B. A. S., (2013). Molecular Ion-Independent Quantification of Polar Glycerolipid Classes in Marine Plankton Using Triple Quadrupole MS. *Lipids* 48, 185–195. doi: 10.1007/s11745-012-3748-0

Porder, S., and Ramachandran, S. (2013). The phosphorus concentration of common rocks—a potential driver of ecosystem P status. *Plant Soil* 367, 41–55. doi: 10.1007/s11104-012-1490-2

Postec, A., Quéméneur, M., Bes, M., Mei, N., Benaïssa, F., Payri, C., et al. (2015). Microbial diversity in a submarine carbonate edifice from the serpentinizing hydrothermal system of the Prony Bay (New Caledonia) over a 6-year period. *Extreme Microbiol.* 857, 1–19. doi: 10.3389/fmicb.2015.00857

Probst, A. J., Elling, F. J., Castelle, C. J., Zhu, Q., Elvert, M., Birarda, G., et al. (2020). Lipid analysis of CO 2 -rich subsurface aquifers suggests an autotrophy-based deep biosphere with lysolipids enriched in CPR bacteria. *ISME J.* 1–14. doi: 10.1038/s41396-020-0624-4

Prowe, S. G., and Antranikian, G. (2001). *Anaerobranca gottschalkii* sp. nov., a novel thermoalkaliphilic bacterium that grows anaerobically at high pH and temperature. *Int. J. Syst. Evol. Microbiol.* 51, 457–465. doi: 10.1099/00207713-51-2-457

Quast, C., Pruesse, E., Yilmaz, P., Gerken, J., Schweer, T., Yarza, P., et al. (2013). The SILVA ribosomal RNA gene database project: improved data processing and web-based tools. *Nucleic Acids Res.* 41, D590–D596. doi: 10.1093/nar/gks1219

Quesnel, Y., Sotin, C., Langlais, B., Costin, S., Mandea, M., Gottschalk, M., et al. (2009). Serpentinization of the martian crust during Noachian. *Earth Planet. Sci. Lett.* 277, 184–193. doi: 10.1016/j.epsl.2008.10.012

Rattray, J. E., Zetterlind, A., Smittenberg, R. H., Potiszil, C., and Neubeck, A. (2022). Complexity of the serpentinization lipidome. *Org. Geochem.* 174:104514. doi: 10.1016/j.orggeochem.2022.104514

R Core Team. (2020). *R: A language and environment for statistical computing.* R Foundation for Statistical Computing: Vienna, Austria.

Rempfert, K. R., Miller, H. M., Bompard, N., Nothaft, D., Matter, J. M., Kelemen, P., et al. (2017). Geological and geochemical controls on subsurface microbial life in the Samail ophiolite. *Oman. Front. Microbiol.* 8, 1–21. doi: 10.3389/fmicb.2017.00056

Ring, M. W., Schwär, G., Thiel, V., Dickschat, J. S., Kroppenstedt, R. M., Schulz, S., et al. (2006). Novel iso-branched ether lipids as specific markers of developmental sporulation in the myxobacterium *Myxococcus xanthus*. *J. Biol. Chem.* 281, 36691–36700. doi: 10.1074/jbc.M607616200

Rossel, P. E., Elvert, M., Ramette, A., Boetius, A., and Hinrichs, K.-U. (2011). Factors controlling the distribution of anaerobic methanotrophic communities in marine environments: evidence from intact polar membrane lipids. *Geochim. Cosmochim. Acta* 75, 164–184. doi: 10.1016/j.gca.2010.09.031

Rowlett, V. W., Mallampalli, V. K. P. S., Karlstaedt, A., Dowhan, W., Taegtmeyer, H., Margolin, W., et al. (2017). Impact of membrane phospholipid alterations in *Escherichia coli* on cellular function and bacterial stress adaptation. *J. Bacteriol.* 199, e00849–e00816. doi: 10.1128/JB.00849-16

Russell, M. J., Hall, A. J., and Martin, W. (2010). Serpentinization as a source of energy at the origin of life. *Geobiology* 8, 355–371. doi: 10.1111/j.1472-4669.2010.00249.x

Rütters, H., Sass, H., Cypionka, H., and Rullkötter, J. (2001). Monoalkylether phospholipids in the sulfate-reducing bacteria Desulfosarcina variabilis and Desulforhabdus amnigenus. *Arch. Microbiol.* 176, 435–442. doi: 10.1007/s002030100343

Sabuda, M. C., Brazelton, W. J., Putman, L. I., McCollom, T. M., Hoehler, T. M., Kubo, M. D. Y., et al. (2020). A dynamic microbial sulfur cycle in a serpentinizing continental ophiolite. *Environ. Microbiol.* 22, 2329–2345. doi: 10.1111/1462-2920.15006

Schouten, S., Middelburg, J. J., Hopmans, E. C., and Sinninghe Damsté, J. S. (2010). Fossilization and degradation of intact polar lipids in deep subsurface sediments: a theoretical approach. *Geochim. Cosmochim. Acta* 74, 3806–3814. doi: 10.1016/j.gca.2010.03.029

Schrenk, M. O., Brazelton, W. J., and Lang, S. Q. (2013). Serpentinization, carbon, and deep life. *Rev. Mineral. Geochem.* 75, 575–606. doi: 10.2138/rmg.2013.75.18

Schubotz, F., Meyer-Dombard, D. R., Bradley, A. S., Fredricks, H. F., Hinrichs, K.-U., Shock, E. L., et al. (2013). Spatial and temporal variability of biomarkers and microbial diversity reveal metabolic and community flexibility in streamer biofilm communities in the lower Geyser Basin, Yellowstone National Park. *Geobiology* 11, 549–569. doi: 10.1111/gbi.12051

Schubotz, F. (2019). "Membrane homeostasis upon nutrient (C, N, P) limitation" in *Biogenesis of fatty acids, lipids and membranes, handbook of hydrocarbon and lipid microbiology*. ed. O. Geiger (Cham: Springer International Publishing), 823–847.

Schubotz, F., Santiago Toro, A., De Rahn-Lee, L., Grant, C., Kuehl, J., Summons, R. E., et al, (2015). Elucidating the role of non-phosphorus lipids in anaerobic environments.

Schubotz, F., Wakeham, S. G., Lipp, J. S., Fredricks, H. F., and Hinrichs, K.-U. (2009). Detection of microbial biomass by intact polar membrane lipid analysis in the water column and surface sediments of the Black Sea. *Environ. Microbiol.* 11, 2720–2734. doi: 10.1111/j.1462-2920.2009.01999.x

Schubotz, F., Xie, S., Lipp, J. S., Hinrichs, K.-U., and Wakeham, S. G. (2018). Intact polar lipids in the water column of the eastern tropical North Pacific: abundance and structural variety of non-phosphorus lipids. *Biogeosciences* 15, 6481–6501. doi: 10.5194/bg-15-6481-2018

Schulte, M., Blake, D., Hoehler, T., and McCollom, T. (2006). Serpentinization and its implications for life on the early earth and Mars. *Astrobiology* 6, 364–376. doi: 10.1089/ast.2006.6.364

Sebastián, M., Smith, A. F., González, J. M., Fredricks, H. F., Van Mooy, B., Koblížek, M., et al. (2016). Lipid remodelling is a widespread strategy in marine heterotrophic bacteria upon phosphorus deficiency. *ISME J.* 10, 968–978. doi: 10.1038/ismej.2015.172

Seyler, L. M., Brazelton, W. J., McLean, C., Putman, L. I., Hyer, A., Kubo, M. D. Y., et al. (2020). Carbon assimilation strategies in ultrabasic groundwater: Clues from the integrated study of a serpentinization-influenced aquifer. *mSystems* 5:607. doi: 10.1128/mSystems.00607-19

Siliakus, M. F., van der Oost, J., and Kengen, S. W. M. (2017). Adaptations of archaeal and bacterial membranes to variations in temperature, pH and pressure. *Extrem. Life Extreme Cond.* 21, 651–670. doi: 10.1007/s00792-017-0939-x

Slavetinsky, C., Kuhn, S., and Peschel, A., (2017). Bacterial aminoacyl phospholipids – Biosynthesis and role in basic cellular processes and pathogenicity. Biochimica et Biophysica Acta (BBA) - Molecular and Cell Biology of Lipids, *Bacterial Lipids* 1862, 1310–1318. doi: 10.1016/j.bbalip.2016.11.013

Sleep, N. H., Bird, D. K., and Pope, E. C. (2011). Serpentinite and the dawn of life. *Philos. Trans. R. Soc. B Biol. Sci.* 366, 2857–2869. doi: 10.1098/rstb.2011.0129

Smith, C. A., Want, E. J., O'Maille, G., Abagyan, R., and Siuzdak, G. (2006). XCMS: processing mass spectrometry data for metabolite profiling using nonlinear peak alignment, matching, and identification. *Anal. Chem.* 78, 779–787. doi: 10.1021/ac051437y

Smułek, W., Zdarta, A., Guzik, U., Dudzińska-Bajorek, B., and Kaczorek, E. (2015). Rahnella sp. strain EK12: cell surface properties and diesel oil biodegradation after long-term contact with natural surfactants and diesel oil. *Microbiol. Res.* 176, 38–47. doi: 10.1016/j.micres.2015.04.008

Sohlenkamp, C., and Geiger, O. (2016). Bacterial membrane lipids: diversity in structures and pathways. *FEMS Microbiol. Rev.* 40, 133–159. doi: 10.1093/femsre/fuv008

Sollai, M., Villanueva, L., Hopmans, E. C., Keil, R. G., and Sinninghe Damsté, J. S. (2019). Archaeal sources of intact membrane lipid biomarkers in the oxygen deficient zone of the eastern tropical South Pacific. *Front. Microbiol.* 10:765. doi: 10.3389/fmicb.2019.00765

Sollich, M., Yoshinaga, M. Y., Häusler, S., Price, R. E., Hinrichs, K.-U., and Bühring, S. I. (2017). Heat stress dictates microbial lipid composition along a thermal gradient in marine sediments. *Front. Microbiol.* 8, 1–19. doi: 10.3389/fmicb.2017.01550

Stankeviciute, G., Tang, P., Ashley, B., Chamberlain, J. D., Hansen, M. E. B., Coleman, A., et al. (2022). Convergent evolution of bacterial ceramide synthesis. *Nat. Chem. Biol.* 18, 305–312. doi: 10.1038/s41589-021-00948-7

Sturt, H. F., Summons, R. E., Smith, K., Elvert, M., and Hinrichs, K.-U., (2004). Intact polar membrane lipids in prokaryotes and sediments deciphered by high-performance liquid chromatography/electrospray ionization multistage mass spectrometry—new biomarkers for biogeochemistry and microbial ecology. *Rapid Communications in Mass Spectrometry* 18, 617–628. doi: 10.1002/rcm.1378

Suzuki, S., Ishii, S., Hoshino, T., Rietze, A., Tenney, A., Morrill, P. L., et al. (2017). Unusual metabolic diversity of hyperalkaliphilic microbial communities associated with subterranean serpentinization at the cedars. *ISME J.* 11, 2584–2598. doi: 10.1038/ismej.2017.111

Suzuki, S., Ishii, S., Wu, A., Cheung, A., Tenney, A., Wanger, G., et al. (2013). Microbial diversity in the cedars, an ultrabasic, ultrareducing, and low salinity serpentinizing ecosystem. *Proc. Natl. Acad. Sci.* 110, 15336–15341. doi: 10.1073/pnas.1302426110

Talbott, C. M., Vorobyov, I., Borchman, D., Taylor, K. G., DuPré, D. B., and Yappert, M. C. (2000). Conformational studies of sphingolipids by NMR spectroscopy. II. Sphingomyelin. *Biochim. Biophys. Acta BBA - Biomembr.* 1467, 326–337. doi: 10.1016/S0005-2736(00)00229-7

Tarnas, J. D., Mustard, J. F., Sherwood Lollar, B., Bramble, M. S., Cannon, K. M., Palumbo, A. M., et al. (2018). Radiolytic H2 production on Noachian Mars: implications for habitability and atmospheric warming. *Earth Planet. Sci. Lett.* 502, 133–145. doi: 10.1016/j.epsl.2018.09.001

Tautenhahn, R., Böttcher, C., and Neumann, S. (2008). Highly sensitive feature detection for high resolution LC/MS. *BMC Bioinformatics* 9:504. doi: 10.1186/1471-2105-9-504

Templeton, A. S., and Ellison, E. T. (2020). Formation and loss of metastable brucite: does Fe(II)-bearing brucite support microbial activity in serpentinizing ecosystems? *Philos. Trans. R. Soc. Math. Phys. Eng. Sci.* 378:20180423. doi: 10.1098/rsta.2018.0423

Templeton, A. S., Ellison, E. T., Glombitza, C., Morono, Y., Rempfert, K. R., Hoehler, T., et al. (2021). Accessing the subsurface biosphere within rocks undergoing active low-temperature serpentinization in the Samail ophiolite. Jour of Geophy rese: solid. *Earth* 126:e2021JG006315. doi: 10.1029/2021JG006315

Tsugawa, H., Ikeda, K., Takahashi, M., Satoh, A., Mori, Y., Uchino, H., et al. (2020). A lipidome atlas in MS-DIAL 4. *Nat. Biotechnol.* 38, 1159–1163. doi: 10.1038/s41587-020-0531-2

Twing, K. I., Brazelton, W. J., Kubo, M. D. Y., Hyer, A. J., Cardace, D., Hoehler, T. M., et al. (2017). Serpentinization-influenced groundwater Harbors extremely low diversity microbial communities adapted to high pH. *Front. Microbiol.* 8, 1–16. doi: 10.3389/fmicb.2017.00308

Valentine, D. L. (2007). Adaptations to energy stress dictate the ecology and evolution of the Archaea. *Nat. Rev. Microbiol.* 5, 316–323. doi: 10.1038/nrmicro1619

Vance, S., Harnmeijer, J., Kimura, J., Hussmann, H., Demartin, B., and Brown, J. M. (2007). Hydrothermal systems in small ocean planets. *Astrobiology* 7, 987–1005. doi: 10.1089/ast.2007.0075

van de Vossenberg, J. L. C. M., Driessen, A. J. M., and Konings, W. N. (1998). The essence of being extremophilic: the role of the unique archaeal membrane lipids. *Extremophiles* 2, 163–170. doi: 10.1007/s007920050056

Van Mooy, B. A. S., Fredricks, H. F., Pedler, B. E., Dyhrman, S. T., Karl, D. M., Koblízek, M., et al. (2009). Phytoplankton in the ocean use non-phosphorus lipids in response to phosphorus scarcity. *Nature* 458, 69–72. doi: 10.1038/nature07659

Venable, R. M., Sodt, A. J., Rogaski, B., Rui, H., Hatcher, E., MacKerell, A. D., et al. (2014). CHARMM all-atom additive force field for sphingomyelin: elucidation of hydrogen bonding and of positive curvature. *Biophys. J.* 107, 134–145. doi: 10.1016/j.bpj.2014.05.034

Vences-Guzmán, M. Á., Geiger, O., and Sohlenkamp, C. (2012). Ornithine lipids and their structural modifications: from a to E and beyond. *FEMS Microbiol. Lett.* 335, 1–10. doi: 10.1111/j.1574-6968.2012.02623.x

Walters, C. C., Moldowan, J. M., and Peters, K. E. (2004). "Biomarkers and isotopes in the environment and human history" in *The biomarker guide: biomarkers and isotopes in the environment and human history*, vol. *1* (Cambridge: Cambridge University Press), 1–2.

Wang, Q., Garrity, G. M., Tiedje, J. M., and Cole, J. R. (2007). Naive Bayesian classifier for rapid assignment of rRNA sequences into the new bacterial taxonomy. *Appl. Environ. Microbiol.* 73, 5261–5267. doi: 10.1128/AEM.00062-07

Wang, X. T., Sigman, D. M., Cohen, A. L., Sinclair, D. J., Sherrell, R. M., Weigand, M. A., et al, (2015). Isotopic composition of skeleton-bound organic nitrogen in reef-building symbiotic corals: A new method and proxy evaluation at Bermuda. *Geochimica et Cosmochimica Acta* 148, 179–190. doi: 10.1016/j.gca.2014.09.017

Weiss, M. C., Sousa, F. L., Mrnjavac, N., Neukirchen, S., Roettger, M., Nelson-Sathi, S., et al. (2016). The physiology and habitat of the last universal common ancestor. *Nat. Microbiol.* 1, 1–8. doi: 10.1038/nmicrobiol.2016.116

White, D. C., Davis, W. M., Nickels, J. S., King, J. D., and Bobbie, R. J. (1979). Determination of the sedimentary microbial biomass by extractible lipid phosphate. *Oecologia* 40, 51–62. doi: 10.1007/BF00388810

Wörmer, L., Lipp, J. S., and Hinrichs, K.-U. (2015). "Comprehensive analysis of microbial lipids in environmental samples through HPLC-MS protocols" in *Hydrocarbon and lipid microbiology protocols: Petroleum, hydrocarbon and lipid analysis*. eds. T. J. McGenity, K. N. Timmis and B. Nogales (Berlin, Heidelberg: Springer Protocols Handbooks. Springer), 289–317.

Wörmer, L., Lipp, J. S., Schröder, J. M., and Hinrichs, K.-U. (2013). Application of two new LC–ESI–MS methods for improved detection of intact polar lipids (IPLs) in environmental samples. *Org. Geochem.* 59, 10–21. doi: 10.1016/j.orggeochem.2013.03.004

Woycheese, K. M., Meyer-Dombard, D. R., Cardace, D., Argayosa, A. M., and Arcilla, C. A. (2015). Out of the dark: transitional subsurface-to-surface microbial diversity in a terrestrial serpentinizing seep (Manleluag, Pangasinan, the Philippines). *Extreme Microbiol.* 6:44. doi: 10.3389/fmicb.2015.00044

Xie, S., Lipp, J. S., Wegener, G., Ferdelman, T. G., and Hinrichs, K.-U. (2013). Turnover of microbial lipids in the deep biosphere and growth of benthic archaeal populations. *Proc. Natl. Acad. Sci.* 110, 6010–6014. doi: 10.1073/pnas.1218569110

Yang, Y.-L., Yang, F.-L., Huang, Z.-Y., Tsai, Y.-H., Zou, W., and Wu, S.-H., (2010). Structural variation of glycolipids from Meiothermus taiwanensis ATCC BAA-400 under different growth temperatures. *Org. Biomol. Chem.* 8, 4252–4254. doi: 10.1039/C0OB00169D

Yang, Y.-L., Yang, F.-L., Jao, S.-C., Chen, M.-Y., Tsay, S.-S., Zou, W., et al. (2006). Structural elucidation of phosphoglycolipids from strains of the bacterial thermophiles Thermus and Meiothermus. *J. Lipid Res.* 47, 1823–1832. doi: 10.1194/jlr.M600034-JLR200

Yao, M., Elling, F. J., Jones, C., Nomosatryo, S., Long, C. P., Crowe, S. A., et al. (2016). Heterotrophic bacteria from an extremely phosphate-poor lake have conditionally reduced phosphorus demand and utilize diverse sources of phosphorus. *Environ. Microbiol.* 18, 656–667. doi: 10.1111/1462-2920.13063

Yoshinaga, M. Y., Gagen, E. J., Wörmer, L., Broda, N. K., Meador, T. B., Wendt, J., et al. (2015). *Methanothermobacter thermautotrophicus* modulates its membrane lipids in response to hydrogen and nutrient availability. *Front. Microbiol.* 6, 1–9. doi: 10.3389/fmicb.2015.00005

Yoshinaga, M. Y., Kellermann, M. Y., Rossel, P. E., Schubotz, F., Lipp, J. S., and Hinrichs, K.-U., (2011). Systematic fragmentation patterns of archaeal intact polar lipids by high-performance liquid chromatography/electrospray ionization ion-trap mass spectrometry. *Rapid Communications in Mass Spectrometry* 25, 3563–3574. doi: 10.1002/rcm.5251

Yoshinaga, M. Y., Wörmer, L., Elvert, M., and Hinrichs, K.-U., (2012). Novel cardiolipins from uncultured methane-metabolizing archaea [WWW Document]. *Archaea*. doi: 10.1155/2012/832097

Zhang, X., Ferguson-Miller, S. M., and Reid, G. E., (2009). Characterization of ornithine and glutamine lipids extracted from cell membranes of rhodobacter sphaeroides. *J Am Soc Mass Spectrom* 20, 198–212. doi: 10.1016/j.jasms.2008.08.017

Zwicker, J., Birgel, D., Bach, W., Richoz, S., Smrzka, D., Grasemann, B., et al. (2018). Evidence for archaeal methanogenesis within veins at the onshore serpentinite-hosted Chimaera seeps, Turkey. *Chem. Geol.* 483, 567–580. doi: 10.1016/j.chemgeo.2018.03.027

Frontiers in Microbiology

Explores the habitable world and the potential of microbial life

The largest and most cited microbiology journal which advances our understanding of the role microbes play in addressing global challenges such as healthcare, food security, and climate change.

Discover the latest Research Topics

See more →

Frontiers
Avenue du Tribunal-Fédéral 34
1005 Lausanne, Switzerland
frontiersin.org

Contact us
+41 (0)21 510 17 00
frontiersin.org/about/contact